Transactions of the ASME

Journal of Applied Mechanics

Published Quarterly by The American Society of Mechanical Engineers

VOLUME 53 • NUMBER 4 • DECEMBER 1986

Technical Editor, **L. B. FREUND**
Division of Engineering
Brown University
Providence, R.I. 02912

APPLIED MECHANICS DIVISION

Chairman, **J. R. RICE**
Secretary, **THOMAS L. GEERS**
Associate Editors,
D. B. BOGY
R. M. CHRISTENSEN
R. J. CLIFTON
THOMAS J. R. HUGHES
W. D. IWAN
W. G. KNAUSS
F. A. LECKIE
J. T. C. LIU
FRANCIS C. MOON
J. W. NUNZIATO
R. H. PLAUT
J. G. SIMMONDS
K. R. SREENIVASAN
Z. WARHAFT
L. T. WHEELER
S. E. WIDNALL

BOARD ON COMMUNICATIONS
Chairman and Vice-President
K. N. REID, JR.

Members-at-Large
W. BEGELL
J. T. COKONIS
M. FRANKE
W. G. GOTTENBERG
M. KUTZ
F. LANDIS
J. R. LLOYD
T. C. MIN
R. E. NICKELL
R. E. REDER
F. W. SCHMIDT

President, **N. D. FITZROY**
Exec. Dir.
PAUL ALLMENDINGER
Treasurer, **ROBERT A. BENNETT**

PUBLISHING STAFF
Mng. Dir., Pub., **J. J. FREY**
Dep. Mng. Dir., Pub.
JOS. SANSONE
Managing Editor,
CORNELIA MONAHAN
Production Editor, **REMO SALTA**
Prod. Asst., **MARISOL ANDINO**

Transactions of the ASME, Journal of Applied Mechanics (ISSN 0021-8936) is published quarterly (Mar., June, Sept., Dec.) for $105 per year by The American Society of Mechanical Engineers, 345 East 47th Street, New York, NY 10017. Second class postage paid at New York, NY and additional mailing offices. POSTMASTER: Send address changes to The Journal of Applied Mechanics, c/o THE AMERICAN SOCIETY OF MECHANICAL ENGINEERS, 22 Law Drive, Box 2300, Fairfield, NJ 07007-2300. **CHANGES OF ADDRESS** must be received at Society headquarters seven weeks before they are to be effective. Please send old label and new address.

PRICES: To members, $24.00, annually; to nonmembers, $100.00. Add $6.00 for postage to countries outside the United States and Canada.

STATEMENT from By-Laws. The Society shall not be responsible for statements or opinions advanced in papers or . . . printed in its publications (B7.1, Par. 3).

COPYRIGHT © 1986 by the American Society of Mechanical Engineers. Reprints from this publication may be made on condition that full credit be given the TRANSACTIONS OF THE ASME, JOURNAL OF APPLIED MECHANICS, and the author, and date of publication be stated.

INDEXED by the Engineering Information

TECHNICAL PAPERS

(Contents continued on Inside Back Cover)

Downloaded 04 May 2010 to 171.66.16.49. Redistribution subject to ASME license or copyright; see http://www.asme.org/terms/Terms_Use.cfm

CONTENTS (CONTINUED)

BRIEF NOTES

DISCUSSION

BOOK REVIEWS

Thermal Expansion of Elastic-Plastic Composite Materials

G. J. Dvorak
Department of Civil Engineering,
Rensselaer Polytechnic Institute,
Troy, NY 12180
Fellow, ASME

Exact relationships are derived between instantaneous overall thermal stress or strain vectors and instantaneous overall mechanical stiffness or compliance, for two binary composite systems in which one of the phases may deform plastically. Also, the local instantaneous thermal strain and stress concentration factors are related in an exact way to the corresponding mechanical concentration factors. The results depend on instantaneous thermoelastic constants and volume fractions of the phases. They are found for fibrous composites with two distinct elastically isotropic or transversely isotropic phases, and for any binary composite with elastically isotropic phases. The results indicate that in the plastic range the thermal and mechanical loading effects are coupled even if the phase properties do not depend on changes in temperature. The derivation is based on a novel decomposition procedure which shows that spatially uniform elastic strain fields can be created in certain heterogeneous media by superposition of uniform phase eigenstrains with local strains, caused by piecewise uniform stress fields which are in equilibrium with prescribed surface tractions. The method is extended to discretized microstructures, and also to the analysis of moisture absorption and phase transformation effects on overall response and on local fields in the two composite materials.

1 Introduction

The response of elastic composite materials to spatially uniform changes in temperature is well understood. An essential contribution to the solution of this problem was made by Levin (1967), who found that macroscopic thermal expansion coefficients of a composite medium, consisting of two distinct isotropic phases of arbitrary shape, depend in a unique way on overall elastic moduli of the aggregate and on thermoelastic constants of the phases. Thus, if the elastic moduli are known, the thermal expansion coefficients can be calculated. This line of inquiry was extended by Shapery (1968), who derived bounds on thermal expansion coefficients of multi-phase composites with isotropic phases, while Rosen and Hashin (1970) applied Levin's approach to binary composites consisting of anisotropic phases, and they also found bounds on overall thermal expansion coefficients of multiphase materials. Budiansky (1970) gave self-consistent estimates of several thermal and thermoelastic properties of multiphase isotropic mixtures. Among the more recent contributions to the subject are the papers by Laws (1973) and Craft and Christensen (1981).

The response of elastic-plastic composite materials to uniform thermal changes has been explored only to a limited extent. This is a more difficult problem because at least one of the phases is inelastic, and the deformation of the phases and of the composite is affected both by the overall thermal change and by the current macroscopic mechanical loading. In the plastic state the thermal and mechanical loading effects are coupled, even if the mechanical properties of the phases do not depend on temperature. The problem is, of course, nonlinear and must be solved in an incremental way. Therefore, the connection between the two effects must be examined within a combined load increment. A representative volume element of the composite is first subjected to a certain uniform initial macroscopic stress or strain and to a uniform thermal change; then, both the stress or strain and the temperature experience a small simultaneous change to another uniform state. Overall instantaneous stiffness and compliance, and thermal stress and strain vectors are sought.

Earlier solutions of problems of this kind have been limited to simple loading situations in fibrous composites, such as pure thermal change (De Silva and Chadwick, 1969) or thermal change combined with axisymmetric mechanical loads (Dvorak and Rao, 1976). More recently (Dvorak, 1983) it was shown that the total overall strain increment caused in a prestressed fibrous composite by a small uniform thermal change can be related in an exact way to thermoelastic constants of the phases and to instantaneous overall compliance. No restrictions need to be imposed on the type of prestress or on the matrix constitutive law except for plastic incompressibility, but the fiber must be isotropic or transversely isotropic and remain elastic. This result has been applied in analysis of a composite cylinder element (Dvorak and Wung, 1984) subjected to axisymmetric mechanical loading, uniform thermal changes, and variations in matrix yield stress.

The present paper develops the connections between overall instantaneous mechanical and thermal properties in a more

---

Contributed by the Applied Mechanics Division for publication in the JOURNAL OF APPLIED MECHANICS.

Discussion on this paper should be addressed to the Editorial Department, ASME, United Engineering Center, 345 East 47th Street, New York, N.Y. 10017, and will be accepted until two months after final publication of the paper itself in the JOURNAL OF APPLIED MECHANICS. Manuscript received by ASME Applied Mechanics Division, October 21, 1985.

general way. First, it is shown that the overall thermal stress and strain vectors for an elastic fibrous composite with transversely isotropic phases can be obtained through superposition of certain uniform fields in the phases, and local fields caused by a uniform stress or strain. A similar result is derived for any composite consisting of two isotropic phases. These results are then utilized to find instantaneous thermoplastic properties and local fields of these composite systems for simultaneous mechanical and thermal load increments. Extensions of the results to discretized microstructures, and to additional load effects, such as phase transformations and moisture absorption, are discussed as well.

2 Elastic Fibrous Composite

A binary composite material consists of a matrix reinforced by aligned and bonded cylindrical fibers. Both phases are assumed to be homogeneous and transversely isotropic about the fiber direction x_3. In the transverse x_1x_2 plane, the cross sections and distribution of the phases can be arbitrary providing that the composite is statistically homogeneous, transversely isotropic, and free of voids.

A representative volume element V of the composite is selected and subjected to a certain loading or deformation history which is imposed through application of uniform overall stresses $\bar{\sigma}^o$ or strains $\bar{\epsilon}^o$ to the surface S of volume V. Also, a certain uniform thermal change has been applied such that the current temperature in V is constant and equal to θ_o. At this particular point of the loading sequence simultaneous increments of $d\bar{\sigma}$ and $d\theta$, or $d\bar{\epsilon}$ and $d\theta$, are applied to V.

The response of the composite to these load increments is described by constitutive equations:

$$d\bar{\epsilon} = M d\bar{\sigma} + \mathbf{m} d\theta, \quad d\bar{\sigma} = L d\bar{\epsilon} - \mathbf{l} d\theta, \tag{1}$$

where L,M are (6×6) overall stiffness and compliance matrices, and $\mathbf{m},\mathbf{l}$ are (6×1) overall thermal strain and stress vectors.[1]

While M and L are known, we wish to determine the vectors **m** and **l**. To this end it is necessary to specify the constitutive equations for field averages of the phases:

$$d\epsilon_r = M_r d\sigma_r + \mathbf{m}_r d\theta, \quad d\sigma_r = L_r d\epsilon_r - \mathbf{l}_r d\theta \quad (r = f,m) \tag{2}$$

which are analogous to equation (1); f,m indicate the "fiber" and "matrix" phases. In elastic composites, these phases are interchangeable and f,m are used merely for convenience of notation.

Since both the composite and each of the phases are transversely isotropic about x_3, it is possible to write a subset of equations (1) and (2) which relates the first two stress and strain invariants. With top bars and subscripts r, f,m omitted in equations (1) and (2), one obtains (Dvorak and Bahei-El-Din, 1979):

$$\begin{Bmatrix} d\epsilon_1 \\ d\epsilon_2 \end{Bmatrix} = \frac{1}{kE} \begin{bmatrix} n & -\ell \\ -\ell & k \end{bmatrix} \begin{Bmatrix} d\sigma_1 \\ d\sigma_2 \end{Bmatrix} + \begin{Bmatrix} \alpha \\ \beta \end{Bmatrix} d\theta \tag{3}$$

$$\begin{Bmatrix} d\sigma_1 \\ d\sigma_2 \end{Bmatrix} = \begin{bmatrix} k & \ell \\ \ell & n \end{bmatrix} \begin{Bmatrix} d\epsilon_1 \\ d\epsilon_2 \end{Bmatrix} - \begin{bmatrix} k\alpha + \ell\beta \\ \ell\alpha + n\beta \end{bmatrix} d\theta \tag{4}$$

where k,ℓ,n are Hill's (1964) elastic moduli, $E = n - \ell^2/k$, $\alpha = 2\alpha_T$, $\beta = \alpha_L$, and α_T and α_L are linear coefficients of thermal expansion in the transverse plane and longitudinal direction, respectively. The strain and stress invariants are defined as:

$$d\epsilon_1 = d\epsilon_{11} + d\epsilon_{22} \qquad d\epsilon_2 = d\epsilon_{33} \tag{5}$$

$$d\sigma_1 = \frac{1}{2}(d\sigma_{11} + d\sigma_{22}) \qquad d\sigma_2 = d\sigma_{33} \tag{6}$$

With appropriate values of elastic moduli and coefficients α,β, equations (3) to (6) can be applied either to the composite medium or to each of the two phases.

As long as M,L do not depend on θ, **m** on $\bar{\sigma}$, and **l** on $\bar{\epsilon}$, the thermal and mechanical contributions to $d\bar{\epsilon}$ and $d\bar{\sigma}$ in equation (1) can be found separately and superimposed. By assumption M and L are known, hence the first terms on the right-hand side of equation (1) are evaluated without difficulty for any given $d\bar{\sigma}$ or $d\bar{\epsilon}$. To find **m** and **l**, and the second terms in equation (1), we utilize the decomposition procedure of Dvorak (1983).

In the first step of the procedure the fiber and matrix phases are separated and surface tractions which preserve the current local stresses σ_r^o and strains ϵ_r^o are applied to each phase $r = f,m$. Alternatively, surface displacements corresponding to ϵ_r^o may be prescribed to preserve σ_r^o. In addition, a uniform thermal change $d\theta$ is applied to both phases. The local strains caused by $d\theta$ would make the phases incompatible if the composite was to be reassembled. Therefore, uniform stresses $d\hat{\sigma}_1^r$, $d\hat{\sigma}_2^r$ of as yet unknown magnitude are applied to the phases simultaneously with $d\theta$. (The top hats indicate auxiliary uniform fields used in the decomposition and reassembly of the composite.) This leads to the following uniform strain increments in the separated phases:

$$\begin{aligned} d\hat{\epsilon}_1^f &= (n_f d\hat{\sigma}_1^f - \ell_f d\hat{\sigma}_2^f)/k_f E_f + \alpha_f d\theta \\ d\hat{\epsilon}_2^f &= (-\ell_f d\hat{\sigma}_1^f + k_f d\hat{\sigma}_2^f)/k_f E_f + \beta_f d\theta \\ d\hat{\epsilon}_1^m &= (n_m d\hat{\sigma}_1^m - \ell_m d\hat{\sigma}_2^m)/k_m E_m + \alpha_m d\theta \\ d\hat{\epsilon}_2^m &= (-\ell_m d\hat{\sigma}_1^m + k_m d\hat{\sigma}_2^m)/k_m E_m + \beta_m d\theta \end{aligned} \tag{7}$$

In the second step of the procedure, the stresses $d\hat{\sigma}_1^r$ and $d\hat{\sigma}_2^r$ must be adjusted to assure compatibility of the phases and equilibrium of these stresses at phase interfaces and on the surface S of the representative volume V. The strain and stress increments in equation (7) obviously satisfy the equations $d\hat{\epsilon}_1^r = 2d\hat{\epsilon}_{11}^r = 2d\hat{\epsilon}_{22}^r$ and $d\sigma\hat{\epsilon}_1^r = d\hat{\sigma}_{11}^r = d\hat{\sigma}_{22}^r$ in each phase $r = f,m$. Shear components vanish in V, except in the immediate vicinity of fiber ends. Since the magnitude of average fiber diameter is assumed to be very small, the shear components may be neglected. Therefore, compatibility and equilibrium conditions for the increments can be written in terms of the invariants as follows:

$$d\hat{\epsilon}_1^m = d\hat{\epsilon}_1^f, \quad d\hat{\epsilon}_2^m = d\hat{\epsilon}_2^f \tag{8}$$

$$d\hat{\sigma}_1^f = d\hat{\sigma}_1^m = dS_T \tag{9}$$

$$c_f d\hat{\sigma}_2^f + c_m d\hat{\sigma}_2^m = dS_A. \tag{10}$$

The dS_T and dS_A are surface stresses which need to be added on S to preserve overall equilibrium of V while $d\hat{\sigma}_1^r$ and $d\hat{\sigma}_2^r$ are applied to the phases. The magnitudes of phase volume fractions $c_f + c_m = 1$ need also be known at this point; $c_f > 0$.

All strain and stress increments in equation (7) are uniform and transversely isotropic, hence equations (8) to (10) are exact for any transverse plane geometry. These relations suggest that spatially uniform strain fields can be created in certain heterogeneous media by superposition of uniform eigenstrains $\alpha_r d\theta$, $\beta_r d\theta$ in the phases, with local strains caused by piecewise uniform stress fields which are in equilibrium with surface stresses dS_A, dS_T.

Internal equilibrium and compatibility of the phases in V depend only on the eight unknown strains and stresses $d\hat{\epsilon}_1^r$, $d\hat{\epsilon}_2^r$, $d\hat{\sigma}_1^r$, $d\hat{\sigma}_2^r$, and not on dS_A, dS_T. These unknowns can be determined from equations (7), (8), and (9), when an additional constraint is imposed.

A particular choice which will be useful in the sequel is:

---

[1] We use the customary notation (Hill, 1963; Laws, 1973) where, except as noted, (6×6) matrices are denoted by lightface uppercase Latin letters, and (6×1) vectors by boldface lowercase Latin or Greek letters. Top bars denote overall volume averages.

$$d\hat{\sigma}_2^m = \rho d\hat{\sigma}_1^m, \tag{11}$$

where $\rho \neq 0$ is a constant.

Now, dS_T and dS_A follow from equation (7), after a substitution of equations (9) and (10), and from equation (8):

$$a_1 dS_T + a_2 dS_A + a_3 d\theta = 0 \tag{12}$$

$$b_1 dS_T + b_2 dS_A + b_3 d\theta = 0 \tag{13}$$

where:

$$a_1 = \frac{n_f}{k_f E_f} - \frac{n_m}{k_m E_m} + \rho\left[\frac{c_m \ell_f}{c_f k_f E_f} + \frac{\ell_m}{k_m E_m}\right]$$

$$a_2 = -\frac{1}{c_f}\,\frac{\ell_f}{k_f E_f}\,, \quad a_3 = \alpha_f - \alpha_m$$

$$b_1 = \frac{\ell_f}{k_f E_f} - \frac{\ell_m}{k_m E_m} + \rho\left[\frac{c_m}{c_f E_f} + \frac{1}{E_m}\right]$$

$$b_2 = -\frac{1}{c_f E_f}\,, \qquad b_3 = -\beta_f + \beta_m$$

and:

$$dS_T = s_T d\theta, \quad dS_A = s_A d\theta \tag{14}$$

$$s_T = (a_2 b_3 - a_3 b_2)/(a_1 b_2 - a_2 b_1) \tag{15}$$

$$s_A = (a_3 b_1 - a_1 b_3)/(a_1 b_2 - a_2 b_1) \tag{16}$$

At this point we change from the invariants (5), (6) to the (6×1) stress and strain vectors and write

$$\begin{aligned} d\hat{\epsilon}_{11}^f = d\hat{\epsilon}_{22}^f = \frac{1}{2}\, d\hat{\epsilon}_1^f = g_1 d\theta \\ d\hat{\epsilon}_{33}^f = d\hat{\epsilon}_2^f = g_2 d\theta \end{aligned} \tag{17}$$

$$\begin{aligned} d\hat{\epsilon}_{11}^m = d\hat{\epsilon}_{22}^m = \frac{1}{2}\, d\hat{\epsilon}_1^m = h_1 d\theta \\ d\hat{\epsilon}_{33}^m = d\hat{\epsilon}_2^m = h_2 d\theta \end{aligned} \tag{18}$$

From equation (7), with equations (8) to (10), (15), and (16):

$$\begin{aligned} g_1 &= \left[\frac{1}{2}\,(n_f - \gamma \ell_f)/(k_f E_f)\right] s_T + \frac{1}{2}\,\alpha_f \\ g_2 &= [(-\ell_f + \gamma k_f)/(k_f E_f)] s_T + \beta_f \\ h_1 &= \left[\frac{1}{2}\,(n_m - \rho \ell_m)/(k_m E_m)\right] s_T + \frac{1}{2}\,\alpha_m \\ h_2 &= [(-\ell_m + \rho k_m)/(k_m E_m)] s_T + \beta_m \end{aligned} \tag{19}$$

where

$$\gamma = (s_A - \rho c_m s_T)/(c_f s_T), \tag{20}$$

and, according to equation (8):

$$g_1 = h_1, \quad g_2 = h_2. \tag{21}$$

Analogous results for stresses are:

$$\begin{aligned} d\hat{\sigma}_{11}^f = d\hat{\sigma}_{22}^f = d\hat{\sigma}_1^f = s_T d\theta \\ d\hat{\sigma}_{33}^f = d\hat{\sigma}_2^f = \gamma s_T d\theta \end{aligned} \tag{22}$$

$$\begin{aligned} d\hat{\sigma}_{11}^m = d\hat{\sigma}_{22}^m = d\hat{\sigma}_1^m = s_T d\theta \\ d\hat{\sigma}_{33}^m = d\hat{\sigma}_2^m = \rho s_T d\theta \end{aligned} \tag{23}$$

In the final step of the decomposition procedure, the composite is reassembled and the surface stresses dS_T, dS_A removed. Of course, the local strains and stresses (17) to (23) already assure that the phases are compatible and in internal equilibrium; in fact thet are equal to local fields caused in the composite by simultaneous application of $d\theta$, dS_A, and dS_T. They must now be added to local fields caused in the composite by surface stresses $-dS_T$, $-dSA\cdot$

The final results assume a concise form with the definitions

$$\begin{aligned} \mathbf{h} &= [h_1\ h_1\ h_2\ 0\ 0\ 0]^T \\ \mathbf{s}_a &= [s_T\ s_T\ s_A\ 0\ 0\ 0]^T \\ \boldsymbol{\gamma} &= [1\ 1\ \gamma\ 0\ 0\ 0]^T \\ \boldsymbol{\rho} &= [1\ 1\ \rho\ 0\ 0\ 0]^T \end{aligned} \tag{24}$$

where $[\ ]^T$ denotes a transpose and the coefficients appear in equations (11), (15), (16), and (19) to (21).

Therefore, for $d\bar{\sigma} = \mathbf{0}$, $d\theta \neq 0$ in (1_1):

$$d\bar{\epsilon} = \mathbf{m} d\theta \tag{25}$$

$$\mathbf{m} = \mathbf{h} - M\mathbf{s}_a \tag{26}$$

where $\mathbf{m}$ is the overall thermal strain vector and M is the known overall compliance.

Also, suppose that the local stresses in the phases are written in terms of concentration factors:

$$d\sigma_r = B_r d\bar{\sigma} + \mathbf{b}_r d\theta, \quad (r = f, m) \tag{27}$$

and that B_m, B_f are known.

With regard to equations (22) and (23) one obtains:

$$\begin{aligned} \mathbf{b}_f &= s_T \boldsymbol{\gamma} - B_f \mathbf{s}_a \\ \mathbf{b}_m &= s_T \boldsymbol{\rho} - B_m \mathbf{s}_a \end{aligned} \tag{28}$$

Similar results can be found for a fully constrained composite subjected to a uniform thermal change. Recall that the strains (17) and (18) are actually equal to overall strains under $d\theta$, dS_A, dS_T. This follows immediately from equations (8) and (21). These overall strains must be removed, and the local fields adjusted accordingly.

Therefore, for $d\bar{\epsilon} = \mathbf{0}$, $d\theta \neq 0$ in (1_2):

$$\begin{aligned} d\bar{\sigma} &= -\mathbf{l} d\theta \\ \mathbf{l} &= -\mathbf{s}_a + L\mathbf{h} \end{aligned} \tag{29}$$

where $\mathbf{l}$ is the overall thermal stress vector, and L is the known overall stiffness.

Also, if the local strains are written in terms of concentration factors:

$$d\epsilon_r = A_r d\bar{\epsilon} - \mathbf{a}_r d\theta, \quad (r = f, m) \tag{30}$$

and if A_m, A_f are known, one obtains with the help of equations (17) to (21):

$$\mathbf{a}_f = (A_f - I)\mathbf{h}, \quad \mathbf{a}_m = (A_m - I)\mathbf{h} \tag{31}$$

To facilitate applications we note that

$$\mathbf{m} = [\alpha_T\ \alpha_T\ \alpha_L\ 0\ 0\ 0]^T \tag{32}$$

where α_T, α_L are linear coefficients of thermal expansion in the transverse plane, and in the longitudinal direction.

For any binary fibrous composite with known phase properties and phase volume fractions, the effect of thermal change is reduced to equivalent mechanical loads and to certain uniform fields in the phases. Thus $\mathbf{m}$ and $\mathbf{l}$ are found in terms of M and L, and $\mathbf{a}_r$, $\mathbf{b}_r$ in terms of A_r, B_r. All these relations are exact. While the constant ρ is a free parameter, none of the results actually depend on ρ. For each ρ one obtains by superposition a solution to the same boundary value problem. According to the uniqueness theorem in the theory of elasticity, all such solutions must coincide. This can be verified by numerical calculations.

3 Two Isotropic Elastic Phases

Suppose that a composite aggregate consists of two perfectly bonded elastic phases, which are distinct but isotropic. The microstructural geometry can be arbitrary, providing that the composite is statistically homogeneous and free of voids. The composite itself need not be isotropic, it can be reinforced by aligned, braided, or otherwise distributed continuous fibers, short fibers, particles of any shape, and by combinations of such reinforcements.

Assume that the overall constitutive relations are again given by equation (1) and that the overall compliance M and stiffness L are known. Also, let local fields be described by equations (27) and (30), and assume that A_r, B_r are known. As in the previous section we utilize the subscripts f,m to identify the two phases, even though we no longer require that either phase be of cylindrical shape. Local phase properties need be known only in terms of bulk moduli K_f, K_m, and linear thermal expansion coefficients α_f, α_m.

We again pose the problem described in the previous section: The composite has been loaded by a certain uniform overall stress $\bar{\sigma}^o$, or strain $\bar{\epsilon}^o$, and uniform temperature θ_o. Simultaneous increments $d\bar{\sigma}$ and $d\theta$, or $d\bar{\epsilon}$ and $d\theta$ are applied. The response of the aggregate is sought in terms of the overall thermal strain and stress vectors $\mathbf{m}$ and $\mathbf{l}$, and phase concentration factors $\mathbf{a}_r$, $\mathbf{b}_r$, $(r = f,m)$.

As in Section 2, the phases are first separated, and loaded by $d\theta$ and by certain unknown tractions which correspond to isotropic stresses $d\hat{\boldsymbol{\sigma}}_r$. The nonvanishing stress and strain increments are

$$\begin{aligned} &d\hat{\sigma}^f_{11} = d\hat{\sigma}^f_{22} = d\hat{\sigma}^f_{33} = dS_f \\ &d\hat{\sigma}^m_{11} = d\hat{\sigma}^m_{22} = d\hat{\sigma}^m_{33} = dS_m \\ &d\hat{\epsilon}^f_{11} = d\hat{\epsilon}^f_{22} = d\hat{\epsilon}^f_{33} = dS_f/(3K_f) + \alpha_f d\theta \\ &d\hat{\epsilon}^m_{11} = d\hat{\epsilon}^m_{22} = d\hat{\epsilon}^m_{33} = dS_m/(3K_m) + \alpha_m d\theta \end{aligned} \qquad (33)$$

To assure equilibrium and compatibility:

$$dS_f = dS_m = dS, \quad d\epsilon^f_{ij} = d\epsilon^m_{ij}, \qquad (34)$$

and

$$dS = s\, d\theta, \quad s = -3(\alpha_f - \alpha_m)/(1/K_f - 1/K_m) \qquad (35)$$

The composite is now loaded by three equal overall normal stresses dS, and by $d\theta$. Local strain and stress fields follow from equations (33) and (34).

Finally, the composite is reassembled and surface stresses dS are removed.

Let

$$\begin{aligned} &q = s/(3K_f) + \alpha_f = s/(3K_m) + \alpha_m \\ &\mathbf{q} = q[1\,1\,1\,0\,0\,0]^T \\ &\mathbf{s} = s[1\,1\,1\,0\,0\,0]^T \end{aligned} \qquad (36)$$

In analogy with equations (25) to (30), one obtains

For $d\bar{\sigma} = \mathbf{0}$, $d\theta \neq 0$, in equation (1)

$$\begin{aligned} &d\bar{\epsilon} = \mathbf{m}\, d\theta \\ &\mathbf{m} = \mathbf{q} - M\mathbf{s} \end{aligned} \qquad (37)$$

$$\begin{aligned} &d\sigma_r = \mathbf{b}_r d\theta \quad (r = f,m) \\ &\mathbf{b}_f = (I - B_f)\mathbf{s}, \quad \mathbf{b}_m = (I - B_m)\mathbf{s} \end{aligned} \qquad (38)$$

For $d\bar{\epsilon} = \mathbf{0}$, $d\theta \neq 0$ in equation (1):

$$\begin{aligned} &d\bar{\sigma} = -\mathbf{l} d\theta \\ &\mathbf{l} = -\mathbf{s} + L\mathbf{q} \end{aligned} \qquad (39)$$

$$\begin{aligned} &d\epsilon_r = \mathbf{a}_r d\theta \quad (r = f,m) \\ &\mathbf{a}_f = (A_f - I)\mathbf{q}, \quad \mathbf{a}_m = (A_m - I)\mathbf{q} \end{aligned} \qquad (40)$$

If the composite is macroscopically anisotropic, then M and L can depend on up to 21 elastic constants, and

$$\mathbf{m} = [\alpha_1\ \alpha_2\ \alpha_3\ \alpha_4\ \alpha_5\ \alpha_6]^T \qquad (41)$$

where α_1 to α_6 are overall linear thermal expansion coefficients, defined by (1_1) at $d\bar{\sigma} = \mathbf{0}$. For a fibrous composite which is transversely isotropic one recovers equation (32). For an isotropic composite all α in equation (32) become equal to

$$\alpha = \alpha_m + \frac{(\alpha_f - \alpha_m)}{\left(\dfrac{1}{K_f} - \dfrac{1}{K_m}\right)} \left(\frac{1}{K} - \frac{1}{K_m}\right) \qquad (42)$$

where K is the overall bulk modulus.

This last equation was derived in a different way by Levin (1967).

4 Elastic-Plastic Composites

(*i*) Fibrous Composites. Consider again the fibrous composite system of Section 2. Suppose that the matrix phase is elastic within a certain stress region, but becomes elastic-plastic when a given yield condition has been satisfied. The fiber remains elastic until failure. This suggests a metal matrix, which is usually elastically isotropic. Thus the matrix elastic moduli in equations (3) and (4) become related as follows:

$$\begin{aligned} &\ell_m = k_m - m_m, \qquad n_m = k_m + m_m, \qquad E_m = n_m - \ell_m^2/k_m \\ &\frac{n_m}{k_m E_m} = \frac{2(1-\nu_m)}{E_m}, \quad \frac{\ell_m}{k_m E_m} = \frac{2\nu_m}{E_m}, \quad \alpha_m = 2\beta_m \end{aligned} \qquad (43)$$

where E_m, ν_m are the isotropic constants, and β_m is the linear thermal expansion coefficient of the matrix.

In the plastic range the matrix response is assumed to be piecewise linear and given by equation (2), but M_m and L_m, $\mathbf{m}_m$ and $\mathbf{l}_m$ are now instantaneous compliance and stiffness matrices, and thermal vectors, at a particular point of a loading path. We assume that M_m and L_m are symmetric, satisfy the requirement of plastic incompressibility of the matrix, and do not depend on θ; $\mathbf{m}_m$ and $\mathbf{l}_m$ are piecewise constant, within each $d\theta$, but their values may change with θ.

Furthermore, we assume that the response of the composite to any purely mechanical loading by uniform $d\bar{\sigma}$ or by $d\bar{\epsilon}$ is also piecewise linear and described by equation (1). Suppose that instantaneous overall properties M and L in equation (1), as well as instantaneous phase concentration factors A_r, B_r in equation (27) can be evaluated for any given mechanical loading step. The instantaneous thermal properties $\mathbf{m}$, $\mathbf{l}$, and concentration factors $\mathbf{a}_r$ and $\mathbf{b}_r$ are to be determined.

Therefore, we again pose the problem stated in Section 2: A representative volume V of the composite has been subjected to a certain loading or deformation history such that the current overall stresses and strains in V are uniform and have magnitudes $\bar{\sigma}^o$ and $\bar{\epsilon}^o$. Also, the current temperature in V is constant and equal to θ_o. At this particular point of the loading sequence we apply simultaneous increments of $d\bar{\sigma}$ and $d\theta$, or $d\bar{\epsilon}$ and $d\theta$ in V, and wish to evaluate instantaneous values of M, L, $\mathbf{m}$, $\mathbf{l}$, and of the concentration factors A_r, B_r, $\mathbf{a}_r$, $\mathbf{b}_r$ during the loading step.

This problem is solved by the decomposition procedure of Section 2. Initially, the composite is subjected to the prescribed thermal change $d\theta$ and to simultaneously applied surface stresses dS_T and dS_A given by equations (14) to (16). These thermal and mechanical loads create local strain increments $d\boldsymbol{\epsilon}_m$ in equation (18) and stress increments $d\boldsymbol{\sigma}_m$ in equation (23). In general, these strain increments may be inelastic. *However, since the matrix is plastically incompressible, it is possible to assure that these increments correspond to purely elastic deformation in both phases under $d\theta$, dS_A and dS_T.* This is obviously the case when one chooses $\rho = 1$ in equation (11), so that the stress and strain increments in the matrix are isotropic.

The stresses dS_A and dS_T must now be removed. This may lead to plastic straining in the matrix, which corresponds to or is caused by $d\theta$. Also, if an overall stress increment $d\bar{\sigma}$ is applied simultaneously with $d\theta$, then dS_A, dS_T, and $d\bar{\sigma}$ must be added and applied together.

The final results for a plastically deforming composite can now be written on the basis of equations (24) to (31). With $\rho = 1$ in equations (11) to (23), we retain the definitions (24) of vectors $\mathbf{h}$, $\mathbf{s}_a$ and γ and of their components but replace that of ρ with

$$\mathbf{1} = [1\,1\,1\,0\,0\,0]^T. \tag{44}$$

For loading by $d\bar{\sigma}$ and $d\theta$, the overall strain increment $d\bar{\epsilon}$ is:

$$d\bar{\epsilon} = \mathbf{h}\,d\theta + M(d\bar{\sigma} - \mathbf{s}_a d\theta). \tag{45}$$

A comparison with (1_1) again yields the form (26)

$$\mathbf{m} = \mathbf{h} - M\mathbf{s}_a \tag{46}$$

We note that for $\rho = 1$ and an isotropic matrix one obtains from equations (19) and (43) the following expression for $\mathbf{h}$ in equation (24):

$$\mathbf{h} = h\mathbf{1} \tag{47}$$

where

$$h = h_1 = h_2 = s_T/(3K_m) + \beta_m,$$

and s_T is given by equation (15).

Therefore, the first term in equation (45) is an overall isotropic strain increment, and, according to equation (18), it is equal to the matrix strain increment. The loading vector $d\bar{\sigma} - \mathbf{s}_a\,d\theta$ represents total mechanical load that must be applied to the composite to reflect the effect of simultaneous application of $d\bar{\sigma}$ and $d\theta$. M is the instantaneous overall compliance corresponding to this loading vector.

The stresses caused in the phases by simultaneous application of $d\bar{\sigma}$ and $d\theta$ are:

$$\begin{aligned} d\sigma_f &= s_T\boldsymbol{\gamma} d\theta + B_f(d\bar{\sigma} - \mathbf{s}_a d\theta) \\ d\sigma_m &= s_T\mathbf{1} d\theta + B_m(d\bar{\sigma} - \mathbf{s}_a d\theta) \end{aligned} \tag{48}$$

where B_f, B_m are the instantaneous concentration factors for the overall mechanical load increment $d\bar{\sigma} - \mathbf{s}_a d\theta$. If these increments are described by equation (27), then the instantaneous thermal stress concentration factors become:

$$\begin{aligned} \mathbf{b}_f &= s_T\boldsymbol{\gamma} - B_f\mathbf{s}_a \\ \mathbf{b}_m &= s_T\mathbf{1} - B_m\mathbf{s}_a \end{aligned} \tag{49}$$

Equations (45) to (49) convert in an exact way the thermomechanical problem into a mechanical loading problem along the incremental path $d\bar{\sigma} - \mathbf{s}_a\,d\theta$.

Next, consider loading by $d\bar{\epsilon}$ and $d\theta$. The composite is first subjected to loading by $d\theta$, dS_A, and dS_T, which causes isotropic strains $\mathbf{h}\,d\theta$ in both the composite and matrix. Since the overall strain increment is now prescribed, the $\mathbf{h}\,d\theta$ and any additional overall strains must be equal to $d\bar{\epsilon}$. Hence, the overall stress increment is:

$$d\bar{\sigma} = \mathbf{s}_a\,d\theta + L(d\bar{\epsilon} - \mathbf{h}\,d\theta) \tag{50}$$

A comparison with (1_2) again yields (29):

$$\mathbf{l} = -\mathbf{s}_a + L\mathbf{h}. \tag{51}$$

While $\mathbf{s}_a$ is not isotropic, together with $d\theta$ it causes an isotropic stress increment $s_T\,\mathbf{1}\,d\theta$ in the matrix. This is found from equation (23) at $\rho = 1$. Accordingly, plastic loading of the composite is caused only by the second term in equation (50). The overall mechanical strain is equal to $d\bar{\epsilon} - \mathbf{h}\,d\theta$. L is the instantaneous overall stiffness corresponding to this strain increment.

The strain increments in the phases are:

$$\begin{aligned} d\epsilon_f &= \mathbf{h}\,d\theta + A_f(d\bar{\epsilon} - \mathbf{h}d\theta) \\ d\epsilon_m &= \mathbf{h}\,d\theta + A_m(d\bar{\epsilon} - \mathbf{h}d\theta) \end{aligned} \tag{52}$$

where A_f, A_m are instantaneous strain concentration factors for overall strain $d\bar{\epsilon} - \mathbf{h}d\theta$. If equation (30) is used, then the instantaneous thermal strain concentration factors are:

$$\begin{aligned} \mathbf{a}_f &= (A_f - I)\mathbf{h} \\ \mathbf{a}_m &= (A_m - I)\mathbf{h} \end{aligned} \tag{53}$$

Inasmuch as the instantaneous M and L may have as many as 21 independent coefficients, the vectors $\mathbf{m}$ in equation (46) and $\mathbf{l}$ in equation (51) may have 6 independent coefficients. For example, $\mathbf{m}$ assumes the form (41), with α_i (i = 1 to 6) representing instantaneous thermal expansion coefficients of the composite.

As in the previous case, equations (50) to (52) convert in an exact way the thermomechanical problem into a mechanical deformation problem along the path $d\bar{\epsilon} - \mathbf{h}d\theta$. It is seen that in both cases the thermal and mechanical effects are coupled, even though phase mechanical properties do not depend directly on temperature.

(ii) **Two-Phase Composites.** Finally, we consider the two-phase composite with isotropic phases of arbitrary geometry, Section 3. The reinforcement phase (f) is assumed to remain elastic, while the matrix phase (m) may become elastic-plastic when a given yield condition has been satisfied. In the plastic region, the matrix constitutive relation is described by equation (2), with M_m and L_m replaced by instantaneous compliance and stiffness. Again, M_m and L_m are assumed to be piecewise linear, symmetric, and satisfy the requirement of plastic incompressibility of the matrix. Also, we assume that overall instantaneous properties M and L of the composite, as well as the instantaneous concentration factors A_r, B_r can be evaluated for any purely mechanical overall stress or strain increment in the elastic and plastic range.

To find instantaneous thermal properties $\mathbf{m}$, $\mathbf{l}$, and the concentration factors $\mathbf{a}_r$, $\mathbf{b}_r$, we again consider a representative volume V of the composite which has been loaded to current uniform overall stress $\bar{\sigma}^o$, strain $\bar{\epsilon}^o$, and temperature θ_o. The volume V is now subjected to additional increments of $d\bar{\sigma}$ and $d\theta$, or $d\bar{\epsilon}$ and $d\theta$. As in Section 3, we apply overall increments of temperature $d\theta$ and of isotropic stress dS, with dS given by equation (35). Resulting phase stresses and strains follow from equation (33), they are isotropic and by assumption cannot cause plastic deformation in the matrix. The surface tractions or strains must now be adjusted to satisfy the prescribed $d\bar{\sigma}$ or $d\bar{\epsilon}$ at the boundary S of V.

For the case $d\theta$ and $d\bar{\sigma}$ applied simultaneously one obtains the overall composite strain increment

$$d\bar{\epsilon} = \mathbf{q}d\theta + M(d\bar{\sigma} - \mathbf{s}d\theta) \tag{54}$$

where $\mathbf{q}$ and $\mathbf{s}$ are given by equations (35) and (36), and M is the overall instantaneous compliance for the mechanical stress increment $d\bar{\sigma} - \mathbf{s}\,d\theta$.

A comparison with (1_1) again yields the form (37)

$$\mathbf{m} = \mathbf{q} - M\mathbf{s} \tag{55}$$

The stresses caused in the phases are:

$$\begin{aligned} d\sigma_f &= \mathbf{s}\,d\theta + B_f(d\bar{\sigma} - \mathbf{s}\,d\theta) \\ d\sigma_m &= \mathbf{s}\,d\theta + B_m(d\bar{\sigma} - \mathbf{s}\,d\theta) \end{aligned} \tag{56}$$

where B_f, B_m are instantaneous stress concentration factors for the overall mechanical load increment $d\bar{\sigma} - \mathbf{s}\,d\theta$. From equations (27) and (56), the instantaneous thermal stress concentration factors are:

$$\mathbf{b}_f = (I - B_f)\mathbf{s}, \quad \mathbf{b}_m = (I - B_m)\mathbf{s} \tag{57}$$

For the case of $d\theta$ and $d\bar{\epsilon}$ applied together, one obtains the overall stress increment

$$d\bar{\sigma} = \mathbf{s}\,d\theta + L(d\bar{\epsilon} - \mathbf{q}d\theta) \tag{58}$$

and

$$\mathbf{l} = -\mathbf{s} + L\mathbf{q} \tag{59}$$

where L is the instantaneous composite stiffness for the overall strain increment $d\bar{\epsilon} - \mathbf{q}\,d\theta$, and $\mathbf{q}$ is given by equation (36). The phase strain increments in this case are

$$\begin{aligned} d\epsilon_f &= \mathbf{q}\,d\theta + A_f(d\bar{\epsilon} - \mathbf{q}\,d\theta) \\ d\epsilon_m &= \mathbf{q}\,d\theta + A_m(d\bar{\epsilon} - \mathbf{q}\,d\theta) \end{aligned} \tag{60}$$

and the instantaneous concentration factors:

$$\mathbf{a}_f = (A_f - I)\mathbf{q}, \quad \mathbf{a}_m = (A_m - I)\mathbf{q} \tag{61}$$

where A_f, A_m are instantaneous strain concentration factors for an overall mechanical strain increment equal to $d\bar{\epsilon} - \mathbf{q}\, d\theta$.

Equations (54), or (58), again convert in an exact way the thermomechanical loading problem into a mechanical one along a loading path $d\bar{\sigma} - \mathbf{s}\, d\theta$, or a strain path $d\bar{\epsilon} - \mathbf{q}\, d\theta$, respectively. As in the case of a fibrous composite, the thermal and mechanical loading effects are coupled in the instantaneous M, L, and A_r, B_r.

5 Discretization of the Phases

Results of the previous sections depend on the availability of overall instantaneous mechanical stiffnesses, compliances, and phase concentration factors in each loading step. These quantities need to be evaluated for a certain model geometry of the composite material. An important consideration in the choice of a material model is the fact that the thermal loading paths $d\bar{\sigma} - \mathbf{s}_a\, d\theta$ in equation (45) and $d\bar{\sigma} - \mathbf{s}\, d\theta$ in equation (54), as well as the thermal strain paths $d\bar{\epsilon} - \mathbf{h}\, d\theta$ in equation (50) and $d\bar{\epsilon} - \mathbf{q}\, d\theta$ in equation (58), may have a significant isotropic component. That is easily seen from the definitions (24), (36), and (47) of $\mathbf{s}_a$, $\mathbf{s}$, $\mathbf{h}$ and $\mathbf{q}$. It follows that the material model chosen for analysis of the mechanical response must give reasonably accurate predictions when the composite is loaded by isotropic overall stresses or strains. This restriction may exclude certain models which are primarily useful in predicting the behavior of a fibrous lamina under in-plane loads, such as the VFD model (Dvorak and Bahei-El-Din, 1982).

Another important consideration in the choice of a material model is the fact that when the matrix phase becomes plastic, the local properties (2) are stress-dependent, and therefore, L_m and M_m are no longer spatially uniform. Even if (2) are regarded as relations for averages in the phases, the phase properties need to be determined for the actual local fields or their approximations. This excludes application of certain averaging techniques, such as the self-consistent method, which assume that phase fields are uniform.

These considerations suggest that the chosen composite model should be based on a specific representative geometry of the microstructure, which allows for discretization of each phase into a number of subelements with locally uniform fields. An example of such an approach was outlined by Dvorak and Teply (1985). In general, if the representative volume of the composite and the phase geometry in this volume are specified, then each phase can be subdivided into a certain number of finite elements, and the overall properties L, M, local properties in the plastically deforming subelements, as well as the concentration factors for each subelement can be calculated for any load or strain increment.

Suppose that the subelement stresses, strains, as well as the stiffnesses and compliances of plastically deformed subelements have been found for a certain increment $d\bar{\sigma}$ or $d\bar{\epsilon}$ applied to the representative volume at $d\theta = 0$. Let subscripts i, and j, denote subelements in the matrix and fiber, respectively. If the partial contributions of each row of $d\bar{\sigma}$ or $d\bar{\epsilon}$ are identified, one can write the uniform subelement fields in the form

$$\begin{aligned} d\sigma_{im} &= B_{im} d\bar{\sigma} \qquad & d\sigma_{jf} &= B_{jf} d\bar{\sigma} \\ d\epsilon_{im} &= A_{im} d\bar{\sigma} \qquad & d\epsilon_{jf} &= A_{jf} d\bar{\epsilon} \end{aligned} \tag{62}$$

where the A, B are instantaneous subelement concentration factors.

One can also write the following relations between the overall averages and the uniform local fields in the subelements of the representative volume:

$$\begin{aligned} d\bar{\sigma} &= \Sigma c_i d\sigma_{im} + \Sigma c_j d\sigma_{jf} \\ d\bar{\epsilon} &= \Sigma c_i d\epsilon_{im} + \Sigma c_j d\epsilon_{jf} \end{aligned} \tag{63}$$

where c_i, c_j are subelement volume fractions such that

$$\Sigma c_i = c_m, \quad \Sigma c_j = c_f, \quad c_f + c_m = 1 \tag{64}$$

Using equations (62) and (63) one can obtain the average phase concentration factors

$$\begin{aligned} A_m &= \frac{1}{c_m} \Sigma c_i A_{im} \qquad & B_m &= \frac{1}{c_m} \Sigma c_i B_{im} \\ A_f &= \frac{1}{c_f} \Sigma c_i A_{jf} \qquad & B_f &= \frac{1}{c_f} \Sigma c_j B_{jf} \end{aligned} \tag{65}$$

From the local instantaneous L_{im}, M_{im} in the plastically deforming subelements, known L_m, M_m, L_f, M_f in the elastic subelements, and equations (62) to (65), one can find the overall instantaneous properties as:

$$\begin{aligned} L &= \Sigma c_i L_{im} A_{im} + \Sigma c_j L_f A_{jf} \\ M &= \Sigma c_i M_{im} B_{im} + \Sigma c_j M_f B_{jf} \end{aligned} \tag{66}$$

The local thermal strain vectors $\mathbf{m}_m$ and $\mathbf{m}_f$ remain constant in each subelement, at least for a given $d\theta$, and equal to those of the elastic phase. These thermal stress vectors are:

$$\mathbf{l}_{im} = L_{im} \mathbf{m}_m, \quad \mathbf{l}_f = L_f m_f \tag{67}$$

The decomposition procedure can now be applied to the discretized representative volume. The results follow from those presented in Section 4.

In the fibrous composite one obtains: For $d\bar{\sigma} \neq \mathbf{0}$, $d\theta \neq 0$, the overall strain increment $d\bar{\epsilon}$, and overall $\mathbf{m}$, follow from equation (45) and (46), with M taken from equation (66). The local subelement stresses and thermal stress concentration factors are, in analogy with equations (48) and (49):

$$\begin{aligned} d\bar{\sigma}_{jf} &= s_T \gamma d\theta + B_{jf}(d\bar{\sigma} - \mathbf{s}_a d\theta) \\ d\bar{\sigma}_{im} &= s_T \mathbf{1} d\theta + B_{im}(d\bar{\sigma} - \mathbf{s}_a d\theta) \\ \mathbf{b}_{jf} &= s_T \gamma - B_{jf} \mathbf{s}_a \\ \mathbf{b}_{im} &= s_T \gamma - B_{im} \mathbf{s}_a \end{aligned} \tag{68}$$

For $d\bar{\epsilon} \neq 0$ $d\theta \neq 0$, the overall stress increment $d\bar{\sigma}$ and overall $\mathbf{l}$, follow from equations (50), (51), and (66), and the local fields and thermal strain concentration factors are as in equations (52), (53):

$$\begin{aligned} d\bar{\epsilon}_{jf} &= \mathbf{h} d\theta + A_{jf}(d\bar{\epsilon} - \mathbf{h} d\theta) \\ d\bar{\epsilon}_{im} &= \mathbf{h} d\theta + A_{im}(d\bar{\epsilon} - \mathbf{h} d\theta) \\ \mathbf{a}_{jf} &= (A_{jf} - I)\mathbf{h} \\ \mathbf{a}_{im} &= (A_{im} - I)\mathbf{h} \end{aligned} \tag{69}$$

These results can be utilized to find average instantaneous thermal strain concentration factors in the phases as:

$$\begin{aligned} \mathbf{a}_f &= \frac{1}{c_f} \Sigma c_j \mathbf{a}_{jf} \qquad & \mathbf{b}_f &= \frac{1}{c_f} \Sigma c_j \mathbf{b}_{jf} \\ \mathbf{a}_m &= \frac{1}{c_m} \Sigma c_i \mathbf{a}_{im} \qquad & \mathbf{b}_m &= \frac{1}{c_m} \Sigma c_i \mathbf{b}_{im} \end{aligned} \tag{70}$$

6 Related Applications

In addition to mechanical and thermal loading, the composite may also undergo a phase transformation such that one or both phases, if free, experience a volume change over an increment of temperature $d\theta$:

$$dV_r/V = d\epsilon_{kk}^T = 3\omega_r d\theta \quad (r = f,m) \tag{71}$$

Furthermore, composites with polymer matrices may absorb moisture. This causes swelling of the unconstrained matrix material. If the moisture concentration is uniform, then

$$d\epsilon_{kk}^{H} = 3\gamma_m dc \qquad (72)$$

where γ_m is the linear swelling coefficient and c is moisture concentration. If the matrix remains elastic in dilatation, and inviscid, then the above theory may be applied with the following adjustments.

Suppose that $d\theta$ and dc are applied simultaneously and that a free phase r undergoes total volume change

$$d\epsilon_{kk}^{r} = (d\epsilon_{kk}^{\theta} + d\epsilon_{kk}^{T} + d\epsilon_{kk}^{H})_r \qquad (73)$$

If this superposition holds in a piecewise linear manner, then one can write in phase r for each loading step

$$d\epsilon_{kk}^{r} = 3(\alpha_r + \xi_n^r \omega_r + \zeta_n^r \gamma_r) d\theta \qquad (74)$$

where, in a particular loading step n:

$$\xi_n^r = (d\epsilon_{kk}^{\theta} / d\epsilon_{kk}^{T})_r, \quad \zeta_n^r = (d\epsilon_{kk}^{\theta} / d\epsilon_{kk}^{H})_r$$

are known distribution coefficients. Hence,

$$d\epsilon_{kk}^{r} = 3(1 + \xi_n^r + \zeta_n^r)\alpha_r d\theta. \qquad (75)$$

This suggests that for each loading step n one can evaluate a certain multiplier of $3d\theta$ that can be substituted for the instantaneous linear thermal expansion coefficient of phase r in equation (2). Indeed, even in the case of thermal loading alone it may be appropriate to change α_r with temperature, and that is obviously possible in the present theory.

7 Discussion

Although the results are valid only for the two binary systems, they apply to most composite materials of practical interest. For the composite systems in question, the elastic values of **m** and **l** found from equations (26) and (29) are identical with those that can be calculated from Levin (1967) formulae, or equation (2.20) in Rosen and Hashin (1970) and equation (33) in Laws (1973) which are all similar and valid only for elastic composites. However, the methods used in deriving these equations, and their internal structure, are entirely different from those in the present paper. The decomposition used herein makes it possible to find overall thermomechanical response of the composite in the plastic range in terms of instantaneous overall mechanical properties and thermoelastic constants of the phases. Also, average instantaneous phase stresses and strains are found in terms of mechanical concentration factors. All these relations are exact. They make it possible to convert any available facility, such as a computer program for analysis of isothermal elastic-plastic behavior of the two composite systems to one which can analyze the effect of both mechanical loads and uniform changes in temperature, as well as other transformation strains in the phases.

It has not escaped our attention that equations similar to (7) to (10) can be written for three-phase fibrous composites. The resulting system has at most one solution, and if it exists it leads to evaluation of overall thermal vectors and local thermal concentration factors for the elastic three-phase materials which are analogous to those derived in Section 2. However, no additional constraints are allowed in this case, hence equation (11) cannot be introduced, and, therefore, it is not possible to analyze elastic-plastic deformation of the three-phase aggregate by the method of Section 4(*i*).

Acknowledgment

This work was supported by a grant from the Office of Naval Research, Dr. Yapa Rajapakse served as contract monitor. Dr. Zvi Hashin and Dr. Iradj Tadjbakhsh offered useful comments. Mr. A. Kaveh Ahangar performed numerical calculations.

References

Budiansky, B., 1970, "Thermal and Thermoelastic Properties of Isotropic Composites," *Journal of Composite Materials*, Vol. 4, pp. 286–295.

Craft, W. J., and Christensen, R. M., 1981, "Coefficient of Thermal Expansion for Composites with Randomly Oriented Fibers," *Journal of Composite Materials*, Vol. 15, pp. 1–20.

De Silva, A. R. T., and Chadwick, G. A., 1969, "Thermal Stresses in Fiber Reinforced Composites," *Journal of the Mechanics and Physics of Solids*, Vol. 17, pp. 387–403.

Dvorak, G. J., and Rao, M. S. M., 1976, "Thermal Stresses in Heat-Treated Fibrous Composites," ASME JOURNAL OF APPLIED MECHANICS, Vol. 98, pp. 619–624.

Dvorak, G. J., and Bahei-El-Din, Y. A., 1979, "Elastic-Plastic Behavior of Fibrous Composites," *Journal of Mechanics and Physics of Solids*, Vol. 27, No. 1, pp. 51–72.

Dvorak, G. J., and Bahei-El-Din, Y. A., 1982, "Plasticity Analysis of Fibrous Composites," ASME JOURNAL OF APPLIED MECHANICS, Vol. 49, pp. 327–335.

Dvorak, G. J., 1983, "Metal Matrix Composites: Plasticity and Fatigue," *Mechanics of Composite Materials: Recent Advances*, Hashin, Z., and Herakovich, C. T., eds., Pergamon Press, pp. 73–91.

Dvorak, G. J., and Teply, J. L., 1985, "Periodic Hexagonal Array Models for Plasticity Analysis of Composite Materials," *Plasticity Today: Modelling, Methods and Applications, W. Olszak Memorial Volume*, Sawczuk, A., and Bianchi, V., eds., Elsvier Scientific Publishing Co., Amsterdam, pp. 623–642.

Dvorak, G. J., and Wung, C. J., 1984, "Thermoplasticity of Unidirectional Metal Matrix Composites," *Mechanics of Material Behavior*, Dvorak, G. J., and Shield, R. T., eds., Elsvier Scientific Publishing Co., Amsterdam, pp. 87–116.

Hill, R., 1963, "Elastic Properties of Reinforced Solids: Some Theoretical Principles," *Journal of the Mechanics and Physics of Solids*, Vol. 11, pp. 357–372.

Hill, R., 1964, "Theory of Mechanical Properties of Fiber-Strengthened Materials: I. Elastic Behaviour," *Journal of the Mechanics and Physics of Solids*, Vol. 12, pp. 199–212.

Laws, N., 1973, "On the Thermostatics of Composite Materials," *Journal of the Mechanics and Physics of Solids*, Vol. 21, pp. 9–17.

Levin, V. M., 1967, "Thermal Expansion Coefficients of Heterogeneous Materials," *Mekhanika Tverdogo Tela*, Vol. 2, pp. 88–94.

Rosen, B. W., and Hasin, Z., 1970, "Effective Thermal Expansion Coefficients and Specific Heats of Composite Materials," *International Journal of Engineering Science*, Vol. 8, pp. 157–173.

Schapery, R. A., 1968, "Thermal Expansion Coefficients of Composite Materials Based on Energy Principles," *Journal of Composite Materials*, Vol. 2, No. 3, pp. 380–404.

An Efficient Method for the Calculation of Interlaminar Stresses in Composite Materials

C. Kassapoglou[1]

P. A. Lagace
Associate Professor.

Technology Laboratory for Advanced Composites,
Department of Aeronautics and Astronautics,
Massachusetts Institute of Technology,
Cambridge, MA 02139

A simple and efficient method is presented to determine the interlaminar stresses in a symmetric composite laminate under uniaxial loading. Expressions for the interlaminar stresses are assumed in terms of exponentials based on shapes that the interlaminar stresses must take in order to assure overall (integral) force and moment equilibrium. The boundary conditions and the traction continuity between plies are satisfied exactly. The exponential terms in the stress expressions are determined by minimizing the laminate complementary energy. Typical results are presented and compared with previous results found in the literature. The current method is shown to efficiently deal with the problem including the ability to perform the analysis of thick laminates (100 plies or more) with relative ease and cost-effectiveness.

1 Introduction

It is well-established (Pipes and Pagano, 1970) that at free edges in composite laminates, interlaminar stresses arise due to a mismatch in elastic properties between plies. Thus, in this region near the free edge known as the boundary layer, Classical Laminated Plate Theory is not valid and a full three-dimensional state of stress is present. These interlaminar stresses can lead to delamination and failure of the laminate at in-plane loads which are significantly lower than the loads at which the laminate would fail if only in-plane fracture were the failure mechanism (e.g., Lagace, 1983).

Numerous investigators have used a variety of methods to attempt to calculate these interlaminar stresses at straight free edges. These methods include finite difference (e.g., Pipes and Pagano, 1970), finite elements (e.g., Rybicki, 1970, and Wang and Crossman, 1977), and stress potentials (e.g., Wang and Choi, 1982a). There are two main problems in the current methods used to calculate interlaminar stresses. The various methods often yield different results for the same problem (Whitcomb et al., 1982). In addition, the methods require large amounts of computer storage and computer time and are therefore not cost-effective. In addition, some of these analyses do not exactly satisfy the boundary condition that the free edge is stress free.

The computation limitations are inherent in the methods which are utilized. Finite difference methods involve the solution of very large systems of equations and require tedious extrapolations. Pipes and Pagano (1970) report using 120 CPU seconds on an IBM 360-365 to solve the 1200 by by 1200 problem for a simple four-ply laminate. Finite element methods require the use of meshes with a large number of elements even for the case of four-ply laminates. Other methods proposed are also limited to few plies either because intermediate numbers generated are so large that most computers cannot store them (Pagano, 1978) or involve the use of unknown parameters, the value of which cannot be determined exactly (Hsu and Herakovich, 1977). The eigenfunction method developed by Wang and Choi (1982a, 1982b) involves the solution of a complicated and tedious eigenvalue problem and requires the use of a collocation technique at every ply interface in order to satisfy traction continuity. This limits the application of this technique to relatively thin laminates.

These limitations make it hard for the methods to deal with laminates that have more than ten to twelve plies. Thicker laminates generally cannot be handled by the methods developed or require an inordinate amount of computer time and storage, and thus cost. In the preliminary design phase, it is necessary for the designer to have access to an efficient means to analyze laminates in order to select a few for final consideration. Current restrictions on analysis limit the laminates which can be considered.

There is only one method, to the authors' knowledge, that is capable of analyzing thick laminates. This is a global-local model developed by Pagano and Soni (1983). However, this method involves substituting part of the laminate with an equipollent system. The solution is very sensitive to the substructuring scheme and the results may differ significantly from one scheme to another. Furthermore, a different "lumping" scheme is required for different plies in the same laminate which makes the procedure inefficient in that it must be repeated for different plies within the same laminate and there are no specific guidelines as to how this "lumping" should be done.

The solution method presented herein, based on overall force and moment equilibrium and the principle of minimum complementary energy, calculates the three-dimensional stress state in laminated plates. The analysis is meant to fulfill the

---

[1] Currently Research Assistant, Beech Aircraft Company, Wichita, KS.

Contributed by the Applied Mechanics Division for publication in the JOURNAL OF APPLIED MECHANICS.

Discussion on this paper should be addressed to the Editorial Department, ASME, United Engineering Center, 345 East 47th Street, New York, N.Y. 10017, and will be accepted until two months after final publication of the paper itself in the JOURNAL OF APPLIED MECHANICS. Manuscript received by ASME Applied Mechanics Division, April 23, 1985; final revision February 18, 1986.

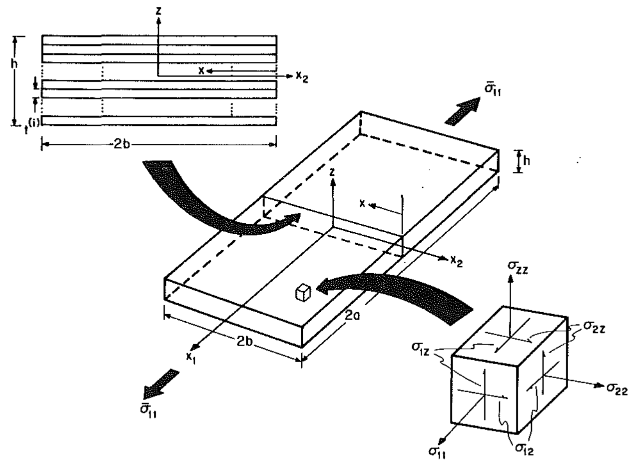

Fig. 1 Geometry for problem of a laminated plate under uniaxial loading

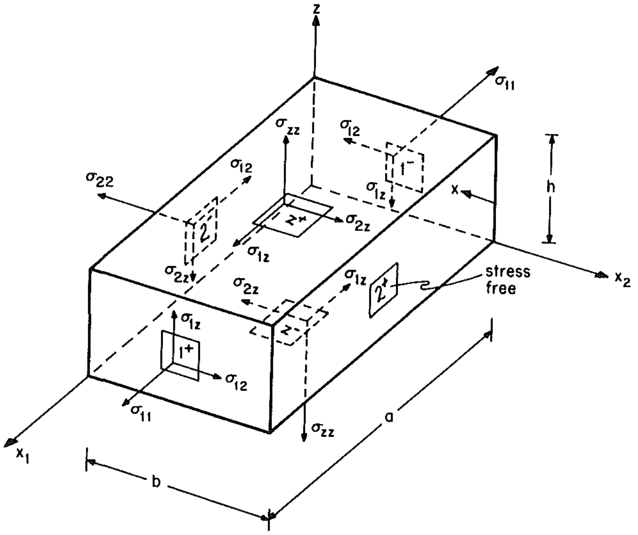

Fig. 2 Free body diagram of a section of a laminate at the free edge

need for a simple, efficient, and cost-effective technique to calculate interlaminar stresses which the designer can use, especially in preliminary design stages, to avoid delamination-prone laminates.

2 Formulation

A composite laminate under uniaxial load is illustrated in Fig. 1. The out-of-plane direction is denoted by z, as opposed to x_3. In order to determine the three-dimensional state of stress in the laminate, three assumptions are made. One, each ply is treated as macroscopically homogenous and is represented by its three-dimensional elastic constants. This effective modulus approach has the effect of "smearing out" the individual behavior of the fiber and matrix and is valid over distances sufficiently larger than the size of an individual fiber (0.0076 mm for typical graphite). Two, far from the free edge, the classical laminated plate theory solution is recovered and the interlaminar stresses are thus zero. Three, away from the effects of load introduction, stresses do not depend on the longitudinal direction x_1.

In addition to these assumptions, the stress field must satisfy several boundary conditions. One, the top and bottom surfaces of the laminate at z equal to $\pm h/2$, where h is the total laminate thickness, are stress free. Two, the x_2 faces of the laminate at x_2 equal to $\pm b$, with $2b$ as the total laminate width, are stress free. Three, the boundary condition in the x_1 direction is that there is some applied uniform traction $\bar{\sigma}_{11}$. Four, traction continuity must be satisfied from ply to ply.

3 Solution

The solution is based upon the qualitative description of the interlaminar stress field obtained by enforcing overall equilibrium (Pagano and Pipes, 1971) and the application of the principle of minimum complementary energy. By judiciously placing a rectangular parallelepiped element so that its x_2 faces correspond with the stress-free edge and center plane of a laminate, as shown in Fig. 2, six general equations are derived from overall force and moment equilibrium considerations (Lagace and Kassapoglou, 1985):

$$\int_{Z^+} \sigma_{1z} dx - \int_{Z^-} \sigma_{1z} dx - \int_{2^-} \sigma_{12} dz = 0 \tag{1}$$

$$-\int_{2^-} \sigma_{22} dz + \int_{Z^+} \sigma_{2z} dx - \int_{Z^-} \sigma_{2z} dx = 0 \tag{2}$$

$$\int_{Z^+} \sigma_{zz} dx - \int_{Z^-} \sigma_{zz} dx = 0 \tag{3}$$

$$\int_{2^-} \sigma_{22} z dz - \int_{Z^+} \sigma_{zz} x dx + \int_{Z^-} \sigma_{zz} x dx - h \int_{Z^+} \sigma_{2z} dx = 0 \tag{4}$$

$$-\int_{1^+} \sigma_{1z} dx dz - \int_{2^-} \sigma_{12} z dz + h \int_{Z^+} \sigma_{1z} dx = 0 \tag{5}$$

$$\int_{1^+} \sigma_{12} dx dz - \int_{Z^+} \sigma_{1z} (b-x) dx + \int_{Z^-} \sigma_{1z} (b-x) dx = 0 \tag{6}$$

where the subscript on the integral sign represents the face over which the integral is taken as referenced to Fig. 2. For convenience, a coordinate transformation has been introduced:

$$x = b - x_2 \tag{7}$$

such that the origin of x is at the free edge. The choice of x_1 faces for this parallelepiped is arbitrary due to the assumption that there is no variation of stress in the x_1 direction. The z faces can also be chosen at any location. The location choice will depend on the z location which is to be considered. It will later be convenient to choose ply interfaces as z face locations.

Given these equilibrium equations, the solution procedure is a three step process: one, stress shapes are chosen that satisfy equilibrium on an integral (equations (1) through (6)) as well as differential basis; two, the specified boundary conditions and traction continuity at ply interfaces are satisfied; and three, the remaining unknown parameters are determined by minimizing the complementary energy of the entire laminate.

3.1 Choice of Stress Shapes. It is assumed that for each stress (except $\sigma_{11}^{(k)}$) the x_2 dependence and z dependence can be functionally separated. Using the axis transformation of equation (7), the stresses in the kth ply of an n-ply laminate can be expressed as (with no sum on i and j):

$$\sigma_{ij}^{(k)} = f_{ij}^{(k)}(x) g_{ij}^{(k)}(z) \tag{8}$$

given that the stresses do not depend on x_1. The $f_{ij}^{(k)}(x)$ and $g_{ij}^{(k)}(z)$ are functions to be determined for each ply. It will later be shown that the longitudinal stress $\sigma_{11}^{(k)}$ can be expressed as a combination of the other stresses. For simplicity, the laminate will be assumed to be symmetric and balanced. However, the analysis can easily be generalized to other types of laminates.

The use of these expressions in the three equations of differential equilibrium yields equations for the unknown functions which can be placed in four functional groups:

$$\frac{df_{12}^{(k)}}{dx} = f_{13}^{(k)} \tag{9}$$

$$\frac{df_{22}^{(k)}}{dx} = f_{23}^{(k)}, \quad \frac{df_{23}^{(k)}}{dx} = f_{33}^{(k)} \tag{10}$$

$$g_{12}^{(k)} = \frac{dg_{13}^{(k)}}{dz} \tag{11}$$

$$g_{22}^{(k)} = \frac{dg_{23}^{(k)}}{dz}, \; g_{23}^{(k)} = \frac{dg_{33}^{(k)}}{dz} \tag{12}$$

Thus, the minimum number of functions that must be assumed is four, with the remaining functions determined using equations (9) through (12).

Consider the $g_{ij}^{(k)}(z)$ functions first. The assumption that far from the free edge the classical laminated plate theory solution is recovered shows that $\tilde{\sigma}_{22}^{(k)}$ and $\tilde{\sigma}_{12}^{(k)}$ are constants outside the boundary layer in a given ply. (Note that the $\tilde{}$ denotes the in-plane stress value determined from classical laminated plate theory). This implies that the $g_{ij}^{(k)}(z)$ functions corresponding to these two stresses are constants. Using this fact and equations (11) and (12) yields the basic expressions for the five $g_{ij}^{(k)}(z)$ functions:

$$g_{12}^{(k)}(z) = B_1^{(k)} \tag{13}$$

$$g_{22}^{(k)}(z) = B_3^{(k)} \tag{14}$$

$$g_{13}^{(k)}(z) = B_1^{(k)} z + B_2^{(k)} \tag{15}$$

$$g_{23}^{(k)}(z) = B_3^{(k)} z + B_4^{(k)} \tag{16}$$

$$g_{33}^{(k)}(z) = B_3^{(k)} \frac{z^2}{2} + B_4^{(k)} z + B_5^{(k)} \tag{17}$$

where the $B_i^{(k)}$ are constants to be determined for a specific ply.

The determination of the $f_{ij}^{(k)}(x)$ requires the well-known fact (Pagano and Pipes, 1971) that σ_{zz} must cross the x axis at least once and must decay to zero away from the free edge in order to satisfy overall equilibrium. To satisfy these conditions, $f_{33}^{(k)}(x)$ is chosen to be a linear combination of two exponential functions in x. Exponential functions are needed since σ_{zz} must drop rapidly to zero away from the free edge. The algebra is more straightforward if, instead of a shape for $f_{33}^{(k)}(x)$, a shape for $f_{22}^{(k)}(x)$ is assumed:

$$f_{22}^{(k)}(x) = A_1^{(k)} e^{-\phi x} + A_2^{(k)} e^{-\lambda\phi x} + A_3^{(k)} \tag{18}$$

where the $A_i^{(k)}$ and λ and ϕ are unknown constants to be determined. The constant $A_3^{(k)}$ is introduced so that far from the free edge the constant value of $\tilde{\sigma}_{22}^{(k)}$ predicted by classical laminated plate theory can be recovered. The dimensions of ϕ are 1/length and λ is dimensionless. The exponents λ and $\lambda\phi$ are assumed in that particular form since the final form of the equations for λ and ϕ becomes less cumbersome.

As previously noted, the requirements of integral equilibrium imply that σ_{zz} must cross the x axis at least once. However, this does not preclude multiple crossings. For each additional crossing, another exponential term would be necessary, although additional exponential terms would not guarantee additional crossings. The solution for the unknowns will be obtained by minimizing the complementary energy of the laminate. A mode which has more crossings of the x axis intuitively represents a higher energy mode. This is analogous to higher modes in plate vibration and buckling. Thus, the assumed mode with two exponentials and only one crossing represents the lowest energy state while still satisfying the requirements of overall equilibrium. It is thus proposed that if a solution exists using this mode, it represents the minimum energy and is thus the proper solution.

Similar requirements lead to an assumed shape for $f_{12}^{(k)}(x)$:

$$f_{12}^{(k)}(x) = A_4^{(k)} + A_5^{(k)} e^{-\phi x} \tag{19}$$

The same exponent is used for $f_{12}^{(k)}(x)$ as is used for $f_{22}^{(k)}(x)$. This is mandated from the following argument. If the assumption that stresses do not depend on x_1 is relaxed and a more general problem is considered, the stresses $\sigma_{12}^{(k)}$ and $\sigma_{22}^{(k)}$ become coupled via the equations of differential equilibrium. Maintaining the assumption that the functional dependencies are separable implies that $\sigma_{12}^{(k)}$ and $\sigma_{22}^{(k)}$ must have the same form for their x dependency. The case considered here is a degenerate case of the more general problem. However, this argument should still apply and thus the same exponent can be used for $f_{12}^{(k)}(x)$ as for $f_{22}^{(k)}(x)$.

The utilization of equations (9) and (10) enable the determination of the remaining $f_{ij}^{(k)}(x)$ functions:

$$f_{33}^{(k)}(x) = A_1^{(k)} \phi^2 e^{-\phi x} + \lambda^2 \phi^2 A_2^{(k)} e^{-\lambda\phi x} \tag{20}$$

$$f_{23}^{(k)}(x) = -A_1^{(k)} \phi e^{-\phi x} - \lambda\phi A_2^{(k)} e^{-\lambda\phi x} \tag{21}$$

$$f_{13}^{(k)}(x) = -\phi A_5^{(k)} e^{-\phi x} \tag{22}$$

The choice of stress shapes is now complete.

3.2 Boundary Conditions and Traction Continuity. The $A_i^{(k)}$ for each ply can be expressed in terms of the stresses determined from classical laminated plate theory by applying the traction free condition at x equal to 0:

$$A_1^{(k)} = -\frac{\lambda \tilde{\sigma}_{22}^{(k)}}{(\lambda - 1)} \tag{23a}$$

$$A_2^{(k)} = \frac{\tilde{\sigma}_{22}^{(k)}}{(\lambda - 1)} \tag{23b}$$

$$A_3^{(k)} = \tilde{\sigma}_{22}^{(k)} \tag{23c}$$

$$A_4^{(k)} = \tilde{\sigma}_{12}^{(k)} \tag{23d}$$

$$A_5^{(k)} = -\tilde{\sigma}_{12}^{(k)} \tag{23e}$$

The $B_i^{(k)}$ are determined by applying traction continuity at ply interfaces starting from the bottom surface of the laminate and proceeding towards the midplane (as defined in Fig. 1). At the interface between ply $k+1$ and ply k, the three interlaminar tractions (stresses) σ_{2z}, σ_{1z}, and σ_{zz}, must be continuous. The constants $B_i^{(k)}$ are determined in succession by this process by utilizing the traction free condition at the top and bottom surfaces of the laminate. The $B_i^{(k)}$ for a particular ply will therefore be dependent on the value of $B_i^{(k)}$ in all the plies below that particular ply:

$$B_1^{(k)} = 1 \tag{24a}$$

$$B_2^{(k)} = \sum_{j=k+1}^{n} \tilde{\sigma}_{12}^{(j)} t^{(j)} \tag{24b}$$

$$B_3^{(k)} = 1 \tag{24c}$$

$$B_4^{(k)} = \sum_{j=k+1}^{n} \tilde{\sigma}_{22}^{(j)} t^{(j)} \tag{24d}$$

$$B_5^{(k)} = \sum_{j=k+1}^{n} t^{(j)} \tilde{\sigma}_{22}^{(j)} \left\{ \frac{1}{2} t^{(j)} + \sum_{m=k+1}^{j-1} t^{(m)} \right\} \tag{24e}$$

where both $B_1^{(k)}$ and $B_3^{(k)}$ can be set to one without loss of generality. The $t^{(k)}$ are the thicknesses of the individual layers.

The final general expressions for the stresses in the kth ply can now be summarized using the results for $B_i^{(k)}$, $A_i^{(k)}$, $g_{ij}^{(k)}(z)$, and $f^{(k)}(x)$:

$$\sigma_{22}^{(k)} = \tilde{\sigma}_{22}^{(k)} \left[1 - \frac{\lambda}{\lambda - 1} \left(e^{-\phi x} - \frac{1}{\lambda} e^{-\lambda\phi x} \right) \right] \tag{25}$$

$$\sigma_{zz}^{(k)} = \phi^2 \frac{\lambda}{\lambda - 1} \left(\lambda e^{-\lambda\phi x} - e^{-\phi x} \right) \left(\tilde{\sigma}_{22}^{(k)} \frac{z^2}{2} + B_4^{(k)} z + B_5^{(k)} \right) \tag{26}$$

$$\sigma_{2z}^{(k)} = \phi \frac{\lambda}{\lambda - 1} \left(e^{-\phi x} - e^{-\lambda\phi x} \right) \left(\tilde{\sigma}_{22}^{(k)} z + B_4^{(k)} \right) \tag{27}$$

$$\sigma_{1z}^{(k)} = \phi e^{-\phi x}\left(\tilde{\sigma}_{12}^{(k)} z + B_2^{(k)}\right) \tag{28}$$

$$\sigma_{12}^{(k)} = \tilde{\sigma}_{12}^{(k)}\left(1 - e^{-\phi x}\right) \tag{29}$$

The constants $B_i^{(k)}$ contain the stacking sequence information in their expressions.

Different values for λ and ϕ could have been assumed for each ply. However, the condition of traction continuity at each ply interface would result in λ and ϕ being constant throughout the laminate as is assumed here. To illustrate this concept, consider the σ_{zz} stress at any ply interface defined by some value of z. Since σ_{zz} must cross the x axis in order to satisfy integral equilibrium, σ_{zz} will equal zero at some point x. This point must be the same within two plies in order to satisfy the requirements of traction continuity. This can only be satisfied if λ and ϕ are the same throughout the laminate. Similar arguments can be made for the σ_{1z} and σ_{2z} stresses as well.

Since it was assumed that stresses do not depend on x_1, $\sigma_{11}^{(k)}$ dropped out of the equilibrium equations. To determine the expression for $\sigma_{11}^{(k)}$ in each ply, the stress-strain and strain-displacement equations are utilized. This procedure, presented in Appendix A, results in the equation:

$$\sigma_{11}^{(k)} = \frac{1}{S_{11}^{(k)}}\left[\left\{S_{11}^{(k)}\tilde{\sigma}_{11}^{(k)} + S_{12}^{(k)}\tilde{\sigma}_{22}^{(k)} + S_{16}^{(k)}\tilde{\sigma}_{12}^{(k)}\right\} - \left\{S_{12}^{(k)}\sigma_{22}^{(k)} - S_{13}^{(k)}\sigma_{zz}^{(k)} - S_{16}^{(k)}\sigma_{12}^{(k)}\right\}\right] \tag{30}$$

where the $S_{ij}^{(k)}$ are the ply compliances.

The expressions for the stresses in each ply are now complete and all the constants can be found except for λ and ϕ. All the requirements of equilibrium have now been satisfied.

3.3 Minimization of the Laminate Complementary Energy.

The remaining two undetermined constants λ and ϕ are found by minimizing the complementary energy of the entire laminate. The expression for the laminate complementary energy, Π_c, is the sum of the contributions of each of the individual plies:

$$\Pi_c = \sum_{k=1}^{n} \Pi_c^{(k)} = \sum_{k=1}^{n} \frac{1}{2}\iiint_{V^{(k)}} \boldsymbol{\sigma}^T \mathbf{S}^{(k)} \boldsymbol{\sigma}\, dV - \iint_{A_\sigma} \mathbf{T}^T \bar{\mathbf{u}}\, dA \tag{31}$$

where $\boldsymbol{\sigma}$ is the stress vector, $\mathbf{S}$ is the compliance tensor, $V^{(k)}$ is the volume of the kth ply, A_σ is the area over which displacements $\bar{\mathbf{u}}$ are prescribed, and $\mathbf{T}$ is the traction vector corresponding to those displacements.

Due to the geometrical symmetry about the x_2 plane at x_2 equal to zero (or x equal to the width b), only half of the laminate need be considered. In addition, the current analysis is restricted to the case of midplane symmetric laminates. The problem is the same independent of which outer z face is considered to be the "top" or "bottom" of the laminate. Thus, only one-half of the stacking sequence need be considered in minimizing the energy. Finally, since stresses do not depend on x_1, the expression for Π_c can be evaluated per unit of length without changing the final expressions for λ and ϕ.

The stress expressions of equations (25) through (30) are used in the equation for the complementary energy. It is assumed that the laminate is wide enough so that $e^{-\lambda\phi b}$ and $e^{-\phi b}$ are approximately zero. This is valid if the thickness to width ratio of the laminate is less than 0.1.

The value of Π_c is made stationary by taking partial derivatives of the expression for Π_c with respect to the two unknowns λ and ϕ to yield the two equations:

$$\frac{\partial \Pi_c}{\partial \lambda} = \lambda^4\phi^4 f_2 + 2\lambda^3\phi^4 f_2 + \lambda^2\left\{2(f_6 + f_9 + f_1) + \phi^2(2f_{11} + f_3 - 2f_{10} - 2f_8)\right\} + \lambda(4f_6 + 8f_9 + 6f_1) + 2f_6 + 4f_9 + 3f_1 = 0 \tag{32}$$

and

$$\frac{\partial \Pi_c}{\partial \phi} = 3\phi^4\lambda^3 f_2 + \phi^2\left\{\lambda^2(f_4 + 2f_{11} + f_3 - 2f_{10} - 2f_8) + \lambda f_4\right\} + \lambda^2\left\{f_5 + 6f_9 + 3f_1 + 2(f_7 + f_6)\right\} + \lambda\left\{f_5 + 8f_9 + 5f_1 + 2(f_7 + 2f_6)\right\} + 4f_9 + 3f_1 + 2f_6 = 0 \tag{33}$$

which are to be solved simultaneously for λ and ϕ. The f_i are coefficients given in Appendix B.

Both equations (32) and (33) are biquadratic in ϕ. This makes their solution simpler and is a direct consequence of the way the exponential terms were assumed in the expressions for $f_{22}^{(k)}$ and $f_{12}^{(k)}$. In general, there are sixteen pairs of λ and ϕ values which satisfy equations (32) and (33). From these, only the pairs with real and positive λ and ϕ are admissible and, if there are more than one such pair, the one that minimizes Π_c is the correct solution pair. Since equation (33) is cubic in λ, there is at least one real λ value that is a solution to both equations for a given value of ϕ.

It is important to point out that the procedure used here is general and that other stress expressions could be used and results obtained provided that these stress expressions satisfy the requirements of integral and different equilibrium. It was felt that the two-exponential form of the expressions best represented the physical reality of the situation. It is also important to note that in assuming stress shapes, interface displacement continuity is not satisfied. It is felt that this is not a serious drawback since the interlaminar stresses are the important factors in delamination.

4 Computer Implementation

The two resulting equations for λ and ϕ must be solved numerically. This involves a five-step process:

(1) A starting value is picked for ϕ. An order of magnitude analysis shows that the product ϕh is of order 1, where h is the total laminate thickness. This fact was used in arriving at the expression for the starting value of ϕ of $4.4/h$.

(2) This initial value of ϕ is substituted into equation (32) and solutions for λ (both real and complex) are obtained using the Newton-Raphson method.

(3) The λ value which, along with the ϕ value utilized, minimizes Π_c, is substituted into equation (33). This equation is quadratic in ϕ^2, and thus relatively easy to solve for ϕ.

(4) Of these solutions for ϕ, the one which, along with the λ value utilized, minimizes the complementary energy is used as the corrected value for ϕ in repeating this process beginning with step two.

(5) The procedure is repeated until a predetermined degree of accuracy for ϕ and λ is achieved.

In this investigation, the scheme was considered to have converged if the ϕ values for two successive iterations differed by less than one part in a million.

The above scheme was implemented in FORTRAN on a PDP-11/34 computer. The computer program uses the laminate information (ply orientations, ply thicknesses, elastic constants for each material type) and the classical laminated plate theory solution as input. The output consists of the com-

Table 1 Computation times for various laminates

Number of Plies	Number of Iterations	CPU Time On VAX 11/782, seconds	Actual Run Time On PDP-11/34, seconds
4	0*	0.20	2
6	8	1.01	15
12	15	2.66	30
50	50	3.29	80
100	69	5.37	120

*Solution is obtained in closed form.

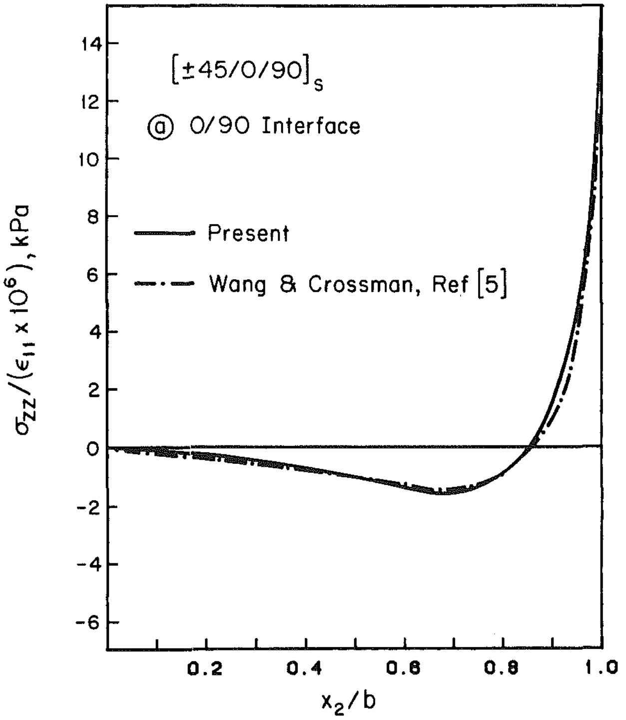

Fig. 3 Interlaminar normal stress σ_{zz} at 0/90 interface of a [±45/0/90]$_S$ laminate

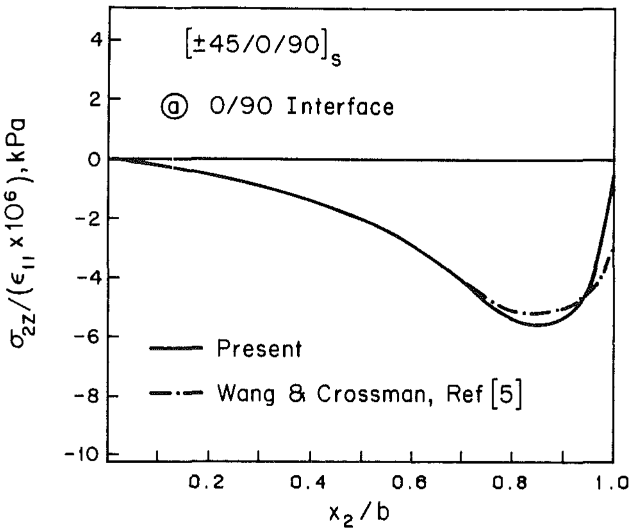

Fig. 4 Interlaminar shear stress σ_{2z} at 0/90 interface of a [±45/0/90]$_S$ laminate

pliances for each ply, the value of λ and ϕ, and the constants in the stress expressions of equations (25) through (30) for various z locations (chosen as the ply interfaces in this case).

5 Results

Many different cases with laminates of different thicknesses and different materials (within the same laminate) were solved using this procedure. The computer program is very efficient and convergence is generally achieved after relatively few iterations (see Table 1). There are some cases where no iterations are needed and the running time for the program is very small.

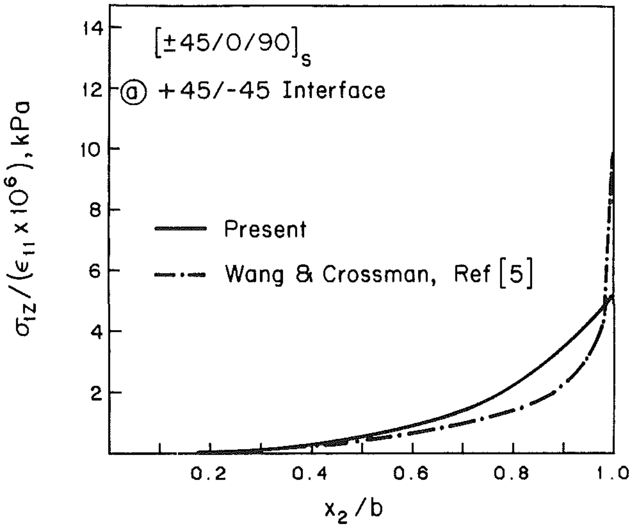

Fig. 5 Interlaminar shear stress σ_{1z} at +45/−45 interface of [±45/0/90]$_S$ laminate

In order to gain some insight into the accuracy of the approach and program, similar cases to those reported in the literature were analyzed. Specifically, the case of a [±45/0/90]$_s$ graphite/epoxy laminate under uniaxial loading was analyzed. The following basic ply properties were used:

$$E_{11}=138\ \text{GPa} \quad G_{12}=5.9\ \text{GPa} \quad \nu_{12}=0.21$$

$$E_{22}=14.5\ \text{GPa} \quad G_{13}=5.9\ \text{GPa} \quad \nu_{13}=0.21$$

$$E_{33}=14.5\ \text{GPa} \quad G_{23}=5.9\ \text{GPa} \quad \nu_{23}=0.21$$

This laminate, with these ply properties, was analyzed by Wang and Crossman (1977) using a finite element scheme with constant strain triangular elements and 792 degrees of freedom.

The current technique yields a solution in under 15 seconds of run time on the PDP-11/34 computer. The resulting values for ϕ and λ are 42.01 1/m and 2.381, respectively. Generally, the two methods yield relatively the same results. Three examples of the results for the interlaminar stresses are presented in Figs. 3, 4, and 5 to illustrate the similarities and differences in the solutions. The results presented in Figs. 3, 4, and 5 are for the interlaminar stresses σ_{zz} and σ_{2z} at the 0 deg/90 deg interface and for σ_{1z} at the +45deg/−45 deg interface, respectively.

For the interlaminar normal stress, the two techniques yield virtually the same result as evidenced in Fig. 3. However, the results are not as similar for the interlaminar shear stresses as evidenced in Figs. 4 and 5. For these cases, the two methods produce similar results away from the free edge, but diverge slightly as the free edge is approached. In the case of σ_{2z} at the 0 deg/90 deg interface, the current solution technique exactly satisfies the traction free boundary condition, while the finite element technique of Wang and Crossman predicts a finite value at the free edge. Several other previous solution procedures also do not exactly satisfy the traction free boundary conditions.

This may be related to the existence of a weak stress singularity at the free edge. This is suggested in the solution of Wang and Crossman for σ_{1z} shown in Fig. 5 while the current technique does not capture this behavior. S. S. Wang and Choi (1982b) have shown that the stress field is indeed singular at the free edge based on the assumption that a composite ply can be represented by effective elastic moduli (i.e., "smeared" properties). However, Soni and Pagano (1982) have noted that these free edge stress singularities simply represent an artifact of the effective modulus approach. It has been further noted by Wang and Crossman (1977) that these singularities would probably dissipate themselves into the laminate resulting in stress redistribution and/or relaxation. Furthermore, the strength of the stress singularities reported by Wang and Choi is so small that it becomes dominant over a region that is so close to the free edge (a few fiber diameters away) that the assumption of material homogeneity breaks down. This does not invalidate their solution, but it also means that methods which do not predict/incorporate a stress singularity, such as the present technique, are equally valid. In that small region very close to the free edge, any analysis that treats the material as homogeneous is not truly valid and a modified theory that accounts for the bimaterial nature of the laminate must be used. However, over the remainder of the boundary layer, all these analyses are valid.

Thus, especially in a solution technique oriented toward preliminary design, the exact value of the stresses at the free edge is not important. This is further emphasized by recent results on delamination reported by Kim and Soni (1984) where they suggest that delamination is controlled by the stresses averaged over some distance from the free edge. Therefore, the current technique provides sufficiently accurate results for the purpose intended, and these results do exactly satisfy the stress-free boundary conditions.

6 Efficiency of Solution Technique

The efficiency of the present method was better assessed by transferring the program to a VAX-11/782 computer so that CPU time measurements could be made. Cases ranging from four to one hundred plies were successfully run. It should be noted that for all cases, the stacking sequences were chosen in such a way that no simplifications could be made by lumping part of the laminate or treating a sequence of plies as a single ply. For the fifty and one hundred ply cases, more than fifteen different ply orientations were used. The CPU times needed to obtain solutions for the various laminates are shown in Table 1. The approximate run times (actual and not CPU time) on the PDP-11/34 computer are also given.

Previous investigators have reported CPU times for their analysis techniques. Pipes and Pagano (1970) report using 120 CPU seconds on an IBM 360-365 for the analysis of a simple four-ply laminate using a finite difference scheme. Wang and Crossman (1977) report using 12 CPU seconds on a UNIVAC-1108, again for the same four-ply laminate using a finite element method.

Three different computers were used in these three cases, VAX-11/782, IBM 360-365, and a UNIVAC-1108. Thus, a direct comparison of CPU time cannot be easily made. However, these three computers are of relatively the same class and thus order-of-magnitude comparisons can be made. The CPU times reported in Table 1 show that the current solution technique is more efficient than the other techniques. Even for one hundred ply laminates, the CPU time used by the present method is still less than that reported for four-ply laminates in the two other cases. Furthermore, doubling the number of plies increases the computation time in the current case by less than double indicating that laminates with even larger numbers of plies can be efficiently analyzed.

The actual run times on the PDP-11/34, a much less powerful computer, are also small. Furthermore, the program requires relatively little memory space for operation. This implies that the program can be successfully and efficiently implemented on personal computers. Thus, the technique allows a cost-effective method for the calculation of interlaminar stresses in composite laminates.

7 Summary

A simple and efficient method was presented to determine the interlaminar stress field at straight free edges in symmetric composite laminates under uniaxial load. The method is based on assumed stress shapes suggested by the considerations of integral equilibrium and the final solution is obtained by the minimization of the complementary energy of the entire laminate. The solutions obtained compare well with a previous solution in the literature which utilizes a tedious finite element analysis.

The present method is at least an order of magnitude more efficient (in terms of CPU time) than previous analyses reported in the literature. Solutions were obtained for laminates of up to one hundred plies, and even thicker laminates could be solved with relative ease. This efficient analysis technique gives the designer the ability to cost-effectively perform parametric studies early in the design process and to look at the effects of various parameters such as ply thickness, material type, and stacking sequence on the interlaminar stress state and, ultimately, on delamination. This results in greater flexibility in design without a substantial increase in effort or cost. The adaptability of the computer program to personal computers also makes it a valuable research and teaching tool.

The present analysis is limited to the case of a straight-edged laminate under uniaxial load. However, the approach is general and could be adapted to more complex situations such as the interlaminar stress field around a hole in a laminate.

Acknowledgments

This work was supported by the Boeing Military Airplane Company. Mr. Robert Waner was the technical monitor. The authors wish to thank Mr. Waner and his staff for the useful suggestions and discussions during the course of this work.

References

Hsu, P. W., and Herakovich, C. T., 1982, "Edge Effect in Angle-Ply Composite Laminates," *Journal of Composite Materials*, Vol. 11, pp. 541-548.

Kim, R. Y., and Soni, S. R., 1984, "Experimental and Analytical Studies On the Onset of Delamination in Laminated Composites," *Journal of Composite Materials*, Vol. 18, pp. 70-80.

Lagace, P. A., 1983, "Delamination Fracture Under Tensile Loading," *Proceedings of the Sixth Conference on Fibrous Composites*, AMMRC MS 83-2, Army Materials and Mechanics Research Center, Watertown, MA, pp. IX 53-70.

Lagace, P. A., and Kassapoglou, C., 1985, "An Efficient Method for the Calculation of Interlaminar Stresses in Composite Materials: Part 1 – The Force Balance Method," Technology Laboratory for Advanced Composites Report 85-5, Massachusetts Institute of Technology, Cambridge, MA.

Pagano, N. J., "Free Edge Fields in Composite Laminates," 1978, *International Journal of Solids and Structures*, Vol. 14, pp. 401-406.

Pagano, N. J., and Pipes, R. B., 1971, "The Influence of Stacking Sequence on Laminate Strength," *Journal of Composite Materials*, Vol. 5, pp. 50-58.

Pagano, N. J., and Soni, S. R., 1983, "Global-Local Laminate Variational Model," *International Journal of Solids and Structures*, Vol. 19, pp. 207-228.

Pipes, R. B., and Pagano, N. J., 1970, "Interlaminar Stresses in Composite Materials Under Uniform Axial Extension," *Journal of Composite Materials*, Vol. 4, pp. 538-548.

Rybicki, E. F., 1971, "Approximate Three-Dimensional Solutions for Symmetric Laminates Under In-Plane Loading," *Journal of Composite Materials*, Vol. 5, pp. 354-361.

Soni, S. R., and Pagano, N. J., 1982, "Elastic Response of Composite Laminates," in *Mechanics of Composite Materials, Recent Advances*, Pergamon Press, New York.

Wang, A. S. D., and Crossman, F. W., 1977, "Some New Results on Edge Effect in Symmetric Composite Laminates," *Journal of Composite Materials*, Vol. 11, pp. 92-106.

Wang, S. S., and Choi, I., 1982, "Boundary-Layer Effects in Composite Laminates: Part 2—Free Edge Stress Solutions and Basic Characteristics," ASME JOURNAL OF APPLIED MECHANICS, Vol. 49, pp. 549-560.

Wang, S. S., and Choi, I., 1982, "Boundary-Layer Effects in Composite Laminates: Part 1—Free Edge Stress Singularities," ASME JOURNAL OF APPLIED MECHANICS, Vol. 49, pp. 541-548.

Whitcomb, J. D., Raju, I. S., and Goree, J. G., 1982, "Reliability of the Finite Element Method for Calculating Free Edge Stresses in Composite Laminates," *Journal of Computers and Structures*, Vol. 15, pp. 23-37.

APPENDIX A

Since it was assumed, in the main text, that the stresses do not depend on x_1, the longitudinal stress $\sigma_{11}^{(k)}$ drops out of the equilibrium equations. To determine $\sigma_{11}^{(k)}$ in each ply, the stress-strain and strain-displacement equations are utilized. The general stress-strain relations can be inverted and placed in the strain-displacement equations to yield:

$$\epsilon_{ij} = S_{ijkl}\sigma_{kl} = \frac{1}{2}\left(\frac{\partial u_i}{\partial x_j} + \frac{\partial u_j}{\partial x_i}\right) \quad i,j,k,l = 1,2,3 \tag{A1}$$

where the S_{ijkl} are the material compliances. These equations can be integrated (engineering notation is now used for the compliances) to give the general expressions:

$$u = (S_{11}\sigma_{11} + S_{12}\sigma_{22} + S_{13}\sigma_{zz} + S_{16}\sigma_{12})x_1 + F(x_2,z) \tag{A2}$$

$$v = S_{12}\int\sigma_{12}dx_2 + S_{22}\int\sigma_{22}dx_2 + S_{23}\int\sigma_{zz}dx_2 + S_{26}\int\sigma_{12}dx_2 + G(x_1,z) \tag{A3}$$

and

$$w = S_{13}\int\sigma_{11}dz + S_{23}\int\sigma_{22}dz + S_{33}\int\sigma_{zz}dz + S_{36}\int\sigma_{12}dz + H(x_1,x_2) \tag{A4}$$

where the F, G, and H are unknown functions. These expressions are substituted in the equations which relate the shear strains to the displacements in order to obtain the two equations:

$$x_1\frac{\partial}{\partial x_2}\left(S_{11}\sigma_{11} + S_{12}\sigma_{22} + S_{13}\sigma_{zz}\right) + \frac{\partial F}{\partial x_2} + \frac{\partial G}{\partial x_1} = S_{16}\sigma_{11} + S_{26}\sigma_{22} + S_{36}\sigma_{zz} + S_{66}\sigma_{12} \tag{A5}$$

and

$$x_1\frac{\partial}{\partial z}\left(S_{11}\sigma_{11} + S_{12}\sigma_{22} + S_{13}\sigma_{zz} + S_{16}\sigma_{12}\right) + \frac{\partial F}{\partial z} + \frac{\partial H}{\partial x_1} = S_{45}\sigma_{23} + S_{55}\sigma_{1z} \tag{A6}$$

which are valid for any ply.

Functional dependencies are now matched and the assumption that stresses do not depend on x_1 is utilized to yield:

$$S_{11}^{(k)}\sigma_{11}^{(k)} + S_{12}^{(k)}\sigma_{22}^{(k)} + S_{13}^{(k)}\sigma_{zz}^{(k)} + S_{16}\sigma_{12}^{(k)} = K^{(k)} \tag{A7}$$

for any ply, where $K^{(k)}$ is some unknown constant. This equation can be solved for $\sigma_{11}^{(k)}$ and matched with the classical laminated plate solution for $\tilde{\sigma}_{11}^{(k)}$ in order to determine $K^{(k)}$. This results in the following expression for $\sigma_{11}^{(k)}$ in each ply:

$$\sigma_{11}^{(k)} = \frac{1}{S_{11}^{(k)}}\left[\left\{S_{11}^{(k)}\tilde{\sigma}_{11}^{(k)} + S_{12}^{(k)}\tilde{\sigma}_{22}^{(k)} + S_{16}^{(k)}\tilde{\sigma}_{12}^{(k)}\right\} - \left\{S_{12}^{(k)}\sigma_{22}^{(k)} - S_{13}^{(k)}\sigma_{zz}^{(k)} - S_{16}^{(k)}\sigma_{12}^{(k)}\right\}\right] \tag{A8}$$

The σ_{ij} are the stresses in the kth ply as defined in equations (25) through (29) in the main text.

APPENDIX B

The values for the f_i of equations (32) and (33) are:

$$f_1 = \frac{1}{2}\sum_{k=1}^{n}[\tilde{\sigma}_{22}^{(k)}]^2 t^{(k)}\left\{S_{22}^{(k)} - \frac{[S_{12}^{(k)}]^2}{S_{11}^{(k)}}\right\}$$

$$f_2 = \frac{1}{120}\sum_{k=1}^{n} t^{(k)}\Big\{3[\tilde{\sigma}_{22}^{(k)}]^2[t^{(k)}]^4 + 15\tilde{\sigma}_{22}^{(k)}B_4^{(k)}[t^{(k)}]^3 + 20\tilde{\sigma}_{22}^{(k)}B_5^{(k)}[t^{(k)}]^2 + 20[B_4^{(k)}]^2[t^{(k)}]^2 + 60B_4^{(k)}B_5^{(k)}t^{(k)} + 60[B_5^{(k)}]^2\Big\}\left\{S_{33}^{(k)} - \frac{[S_{13}^{(k)}]^2}{S_{11}^{(k)}}\right\}$$

$$f_3 = \frac{1}{6}\sum_{k=1}^{n} t^{(k)}\Big\{[\tilde{\sigma}_{22}^{(k)}]^2[t^{(k)}]^2 + 3\tilde{\sigma}_{22}^{(k)}B_4^{(k)}t^{(k)} + 3[B_4^{(k)}]^2\Big\}S_{44}^{(k)}$$

$$f_4 = \frac{1}{6}\sum_{k=1}^{n} t^{(k)}\Big\{[\tilde{\sigma}_{12}^{(k)}]^2[t^{(k)}]^2 + 3\tilde{\sigma}_{12}^{(k)}B_2^{(k)}t^{(k)} + 3[B_2^{(k)}]^2\Big\}S_{55}^{(k)}$$

$$f_5 = \frac{3}{2}\sum_{k=1}^{n}[\tilde{\sigma}_{12}^{(k)}]^2 t^{(k)}\left\{S_{66}^{(k)} - \frac{[S_{16}^{(k)}]^2}{S_{11}^{(k)}}\right\}$$

$$f_6 = \sum_{k=1}^{n}\tilde{\sigma}_{22}^{(k)}t^{(k)}\frac{S_{12}^{(k)}}{S_{11}^{(k)}}\left\{S_{11}^{(k)}\tilde{\sigma}_{11}^{(k)} + S_{12}^{(k)}\tilde{\sigma}_{22}^{(k)} + S_{16}^{(k)}\tilde{\sigma}_{12}^{(k)}\right\}$$

$$f_7 = \sum_{k=1}^{n}\tilde{\sigma}_{12}^{(k)}t^{(k)}\frac{S_{16}^{(k)}}{S_{11}^{(k)}}\left\{S_{11}^{(k)}\tilde{\sigma}_{11}^{(k)} + S_{12}^{(k)}\tilde{\sigma}_{22}^{(k)} + S_{16}^{(k)}\tilde{\sigma}_{12}^{(k)}\right\}$$

$$f_8 = \frac{1}{12}\sum_{k=1}^{n}\tilde{\sigma}_{22}^{(k)}t^{(k)}\Big\{\tilde{\sigma}_{22}^{(k)}[t^{(k)}]^2 + 3B_4^{(k)}t^{(k)} + 6B_5^{(k)}\Big\}\left\{S_{23}^{(k)} - \frac{[S_{12}^{(k)}S_{13}^{(k)}]}{S_{11}^{(k)}}\right\}$$

$$f_9 = \frac{1}{2}\sum_{k=1}^{n}\tilde{\sigma}_{12}^{(k)}\tilde{\sigma}_{22}^{(k)}t^{(k)}\left\{S_{26}^{(k)} - \frac{[S_{12}^{(k)}S_{16}^{(k)}]}{S_{11}^{(k)}}\right\}$$

$$f_{10} = \frac{1}{12}\sum_{k=1}^{n}\tilde{\sigma}_{12}^{(k)}t^{(k)}\Big\{\tilde{\sigma}_{22}^{(k)}[t^{(k)}]^2 + 3B_4^{(k)}t^{(k)} + 6B_5^{(k)}\Big\}\left\{S_{36}^{(k)} - \frac{[S_{13}^{(k)}S_{16}^{(k)}]}{S_{11}^{(k)}}\right\}$$

$$f_{11} = \frac{1}{12}\sum_{k=1}^{n} t^{(k)}\Big\{2\tilde{\sigma}_{12}^{(k)}\tilde{\sigma}_{22}^{(k)}[t^{(k)}]^2 + 3\tilde{\sigma}_{22}^{(k)}B_2^{(k)}t^{(k)} + 3\tilde{\sigma}_{12}^{(k)}B_4^{(k)}t^{(k)} + 6B_4^{(k)}B_2^{(k)}\Big\}S_{45}^{(k)}$$

W. B. Avery

C. T. Herakovich
Mem. ASME

Department of Engineering Science
and Mechanics,
Virginia Polytechnic Institute
and State University,
Blacksburg, VA 24061

Effect of Fiber Anisotropy on Thermal Stresses in Fibrous Composites

An elasticity solution is utilized to analyze an orthotropic fiber in an isotropic matrix under uniform thermal load. The analysis reveals that stress distributions in the fiber are singular in the radial coordinate when the radial fiber stiffness (C_{rr}) *is greater than the hoop stiffness* ($C_{\theta\theta}$). *Conversely, if* $C_{rr} < C_{\theta\theta}$ *the maximum stress in the composite is finite and occurs at the fiber-matrix interface. In both cases the stress distributions are radically different than those predicted assuming the fiber to be transversely isotropic* ($C_{rr} = C_{\theta\theta}$). *It is also shown that fiber volume fraction greatly influences the stress distribution for transversely isotropic fibers, but has little effect on the distribution if the fibers are transversely orthotropic.*

I Introduction

High axial stiffness in graphite fibers is obtained by processing the fiber precursor such that the stiff basal planes of the graphite crystals (Fig. 1) are oriented nearly parallel to the longitudinal axis of the fiber (Johnson, 1982; Reynolds and Sharp, 1974; Diefendorf and Tokarsky, 1975; Brydges, et al., 1969; Kirk-Othmer, 1978). In the transverse direction, however, the orientation of the basal planes can result in many different microstructures. Examples of four types of microstructures observed in graphite fibers are shown in Fig. 2. In Fig. 2(*a*) the basal planes are arranged circumferentially around the fiber. This structure is commonly called an "onionskin" structure, and it would be expected that $E_\theta > E_r$. In Fig. 2(*b*) the basal planes are arranged radially, for which $E_r > E_\theta$. Figures 2(*c*) and 2(*d*) show combinations of radial and circumferential microstructures. Figure 2(*c*) shows a radially oriented core with an onionskin sheath. Figure 2(*d*) shows a random core with a radially oriented sheath. The structures shown in Figs. 2(*a*) and 2(*c*) are normally associated with polyacronitrile-based (PAN) fibers and the structures shown in Figs. 2(*b*) and 2(*d*) are commonly associated with pitch-base fibers (Lemaistre and Diefendorf, 1973; Bennett and Johnson, 1978 and 1979; Guigon and Oberlin, 1983; Ng et al., 1983).

The elasticity formulation used in this paper follows the previous works of St. Venant (1865), Voigt (1866), Mitinskii (1936), Lekhnitskii (1950, 1957), and Cohen et al. (1984a,b,c). Lekhnitskii (1950) provides the form of the solution for a variety of loading conditions on solid and hollow cylinders possessing "cylindrical anisotropy." Cohen and coworkers provided explicit forms of the equations for laminated composite tubes subjected to thermal loading.

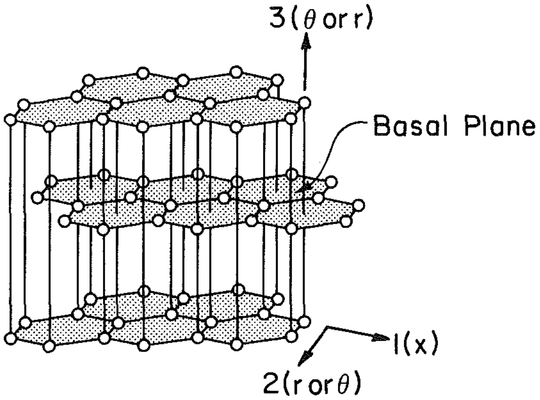

Fig. 1 The graphite crystal structure

In this paper, the anisotropic elasticity solution is used to explore the interrelationshp between fiber orthotropy, as exhibited by the transverse microstructures, and the stress distributions in a fiber-matrix composite under uniform thermal load. As will be shown, the type of orthotropy radically affects the thermal stress distribution in the fiber. In particular, radial orthotropy ($C_{rr} > C_{\theta\theta}$) in the center of the fiber (Figs. 2(*b*)-2(*c*)) results in singular stresses at the center of the fiber for all three normal components of stress. This has obvious negative consequences for the development of damage in the form of fiber splitting and fiber breakage.

The results of this analysis provide helpful insight into the structural integrity of the fiber as a function of microstructure. Such insight may prove helpful in choosing a fiber for a particular application, such as in carbon-carbon composites, which are subjected to large thermal loads. In addition, the results may aid in guiding fiber development for improved properties.

Contributed by the Applied Mechanics Division for publication in the JOURNAL OF APPLIED MECHANICS.

Discussion on this paper should be addressed to the Editorial Department, ASME, United Engineering Center, 345 East 47th Street, New York, N.Y. 10017, and will be accepted until two months after final publication of the paper itself in the JOURNAL OF APPLIED MECHANICS. Manuscript received by ASME Applied Mechanics Division, August 5, 1985; final revision April 12, 1986.

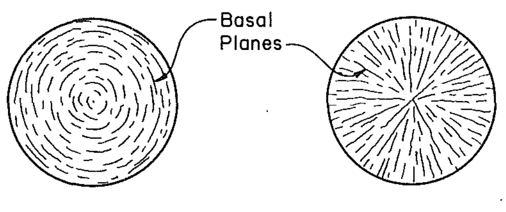

(a) Circumferentially Orthotropic

(b) Radially Orthotropic

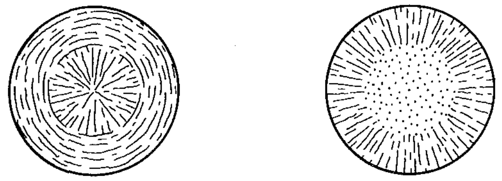

(c) Radially Orthotropic Core; Circumferentially Orthotropic Sheath

(d) Transversely Isotropic Core; Radially Orthotropic Sheath

Fig. 2 Transverse microstructures of graphite fibers

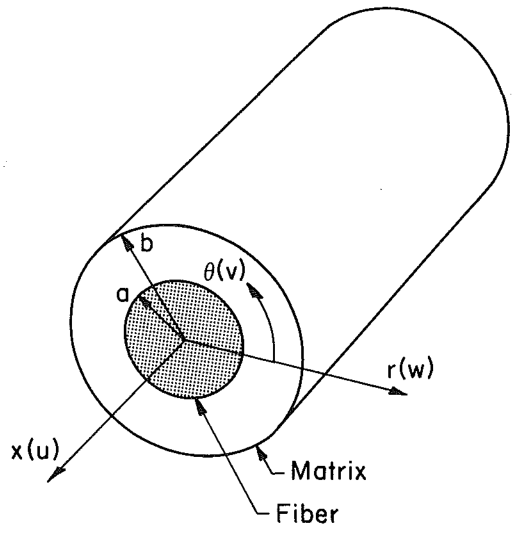

Fig. 3 Composite geometry and coordinate system

II Mathematical Formulation

Consider a long fiber of radius **a** in an isotropic matrix of thickness **b** − **a** under uniform thermal load (Fig. 3).

Due to axial symmetry the hoop displacements are zero, stresses and strains are independent of θ, and there is no shear-extension coupling. Therefore, the thermoelastic stress-strain relations are

$$\begin{Bmatrix}\sigma_x\\ \sigma_\theta\\ \sigma_r\end{Bmatrix}=\begin{bmatrix}C_{xx} & C_{x\theta} & C_{xr}\\ C_{\theta x} & C_{\theta\theta} & C_{\theta r}\\ C_{rx} & C_{r\theta} & C_{rr}\end{bmatrix}\begin{Bmatrix}\epsilon_x-\alpha_x\Delta T\\ \epsilon_\theta-\alpha_\theta\Delta T\\ \epsilon_r-\alpha_r\Delta T\end{Bmatrix} \qquad (1)$$

$$\tau_{r\theta}=G_{r\theta}\gamma_{r\theta};\ \tau_{xr}=G_{xr}\gamma_{xr};\ \tau_{\theta x}=G_{\theta x}\gamma_{\theta x}$$

where C_{ij} are stiffness coefficients and $[C]$ represents the appropriate matrix for the three normal components of stress, α_i are coefficients of thermal expansion, and ΔT is the uniform temperature change. The nonvanishing equilibrium equations for this axisymmetric problem are

$$\frac{\partial\sigma_r}{\partial r}+\frac{1}{r}(\sigma_r-\sigma_\theta)=0 \qquad (2a)$$

$$\frac{\partial\tau_{xr}}{\partial r}+\frac{1}{r}\tau_{xr}=0 \qquad (2b)$$

The strain-displacement relations can be written

$$\epsilon_r=\frac{\partial w}{\partial r} \qquad (3a)$$

$$\epsilon_\theta=\frac{w}{r} \qquad (3b)$$

$$\epsilon_x=\frac{\partial u}{\partial x} \qquad (3c)$$

$$\gamma_{r\theta}=0 \qquad (3d)$$

$$\gamma_{xr}=\frac{\partial u}{\partial r} \qquad (3e)$$

$$\gamma_{\theta x}=0 \qquad (3f)$$

where u, v, and w are axial, hoop, and radial displacements, respectively.

Substituting equations (3a)-(3f) into equation (1) and substituting the resulting equations into the equilibrium equation (2a) yields the governing differential equation

$$C_{rr}\left[\frac{\partial^2 w}{\partial r^2}+\frac{1}{r}\frac{\partial w}{\partial r}\right]-C_{\theta\theta}\frac{w}{r^2}=\frac{1}{r}(C_{\theta x}-C_{rx})\epsilon_x+\frac{1}{r}(C_{rj}-C_{\theta j})\alpha_j\Delta T \qquad (4)$$

for generalized plane strain with uniform axial strain ϵ_x. Here and throughout the paper repeated subscripts i, j are summed over x, r, and θ. Equation (4) may be solved for the case of applied thermal load or the case of applied axial strain.

The general solutions to equation (4), following Cohen and Hyer's (1984b) treatment of an orthotropic tube under uniform thermal load are:

a) transversely orthotropic fiber ($C_{\theta\theta}\neq C_{rr}$),

$$w(r)=A_1r^{\lambda_1}+A_2r^{\lambda_2}+H_1\epsilon_xr+H_2\Delta Tr \qquad (5a)$$

where

$$H_1=\frac{C_{\theta x}-C_{rx}}{C_{rr}-C_{\theta\theta}} \qquad (5b)$$

$$H_2=\frac{(C_{ri}-C_{\theta i})\alpha_i}{(C_{rr}-C_{\theta\theta})} \qquad (5c)$$

b) transversely isotropic fiber ($C_{\theta\theta}=C_{rr}$),

$$w(r)=A_1r^{\lambda_1}+A_2r^{\lambda_2}+G_1\epsilon_xr\ ln\ r+G_2\Delta T\ r\ ln\ r \qquad (6a)$$

where

$$G_1=\frac{C_{\theta x}-C_{rx}}{2C_{\theta\theta}} \qquad (6b)$$

$$G_2=\frac{(C_{ri}-C_{\theta i})\alpha_i}{2C_{\theta\theta}} \qquad (6c)$$

In both of the above displacement fields (5a and 6a), $\lambda_{1,2}$ are defined

$$\lambda_{1,2}=\pm\sqrt{\frac{C_{\theta\theta}}{C_{rr}}} \qquad (7)$$

The solution of the second equilibrium equation (2b) is

$$\tau_{xr}=\frac{K}{r} \qquad (8)$$

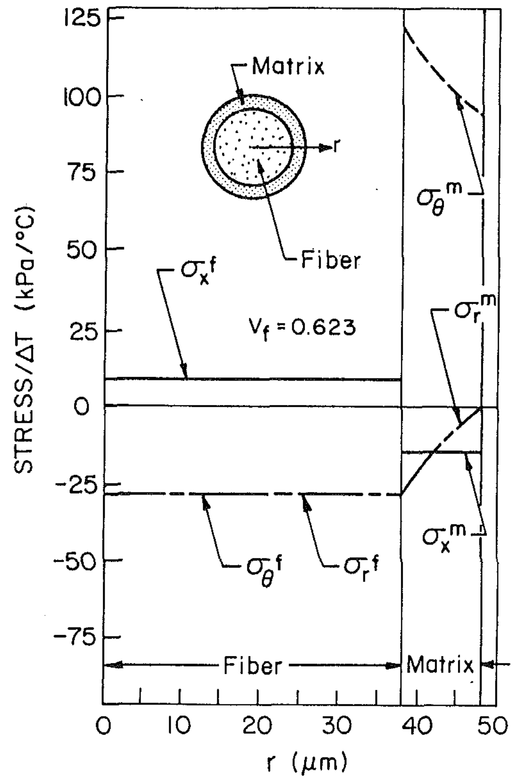

Fig. 4 Thermal stress distribution in a composite with a transversely isotropic fiber

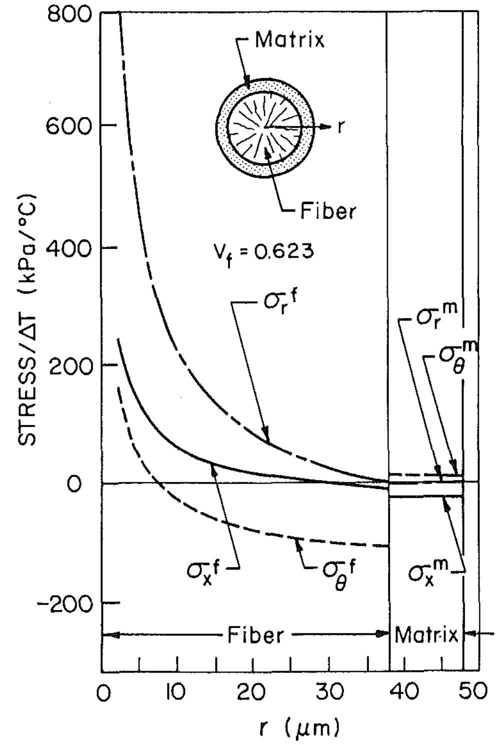

Fig. 5 Thermal stress distribution in a composite with a radially orthotropic fiber

where K is a constant of integration determined from the boundary condition on τ_{xr} at $r = \mathbf{b}$.

For a composite with an orthotropic fiber and an isotropic matrix the equations for the radial displacements are

$$w^f(r) = A_1^f r^{\lambda_1^f} + A_2^f r^{\lambda_2^f} + H_1^f \epsilon_x r + H_2^f \Delta T r \tag{9a}$$

Table 1 Fiber and matrix properties

	Radially Orthotropic Fiber	Circumferentially Orthotropic Fiber	Transversely Isotropic Fiber	Matrix
E_x(GPa)	220	220	220	34.5
E_θ(GPa)	27.5	220	27.5	34.5
E_r(GPa)	220	27.5	27.5	34.5
$\nu_{x\theta}$	0.20	0.20	0.20	0.12
ν_{xr}	0.25	0.25	0.20	0.12
$\nu_{\theta r}$	0.025	0.25	0.25	0.12
$\alpha_x(10^{-6}/^\circ C)$	0.28	0.28	0.28	1.11
$\alpha_\theta(10^{-6}/^\circ C)$	5.56	0.28	5.56	1.11
$\alpha_r(10^{6}/^\circ C)$	0.28	5.56	5.56	1.11

$$w^m(r) = A_1^m r + A_2^m \frac{1}{r} \tag{9b}$$

where the superscripts f and m refer to the fiber and matrix, respectively, $\lambda_{1,2}^m = \pm 1$, and $G_1^m = G_2^m = 0$ for a material wich is transversely isotropic in both elastic and thermal constants.

The equations for the normal components of stress, for the fiber and matrix, can be obtained by substituting equations (5)–(6) into equations (3a)–(3b) and then substituting the results into the constitutive relations (equation (1)). The resulting equations are:

a) transversely isotropic fiber ($C_{rr}^f = C_{\theta\theta}^f$, $\lambda_{1,2} = \pm 1$),

$$\sigma_i^f = A_1^f(C_{i\theta}^f + C_{ir}^f) + A_2^f(C_{i\theta}^f - C_{ir}^f)\frac{1}{r^2} + C_{ix}^f\epsilon_x - C_{ij}^f\alpha_j^f\Delta T \tag{10a}$$

b) transversely orthotropic fiber ($C_{rr}^f \neq C_{\theta\theta}^f$),

$$\sigma_i^f = A_1^f(C_{i\theta}^f + C_{ir}^f\lambda_1^f)r^{\lambda_1 - 1} + A_2^f(C_{i\theta}^f + C_{ir}^f\lambda_2^f)r^{\lambda_2 - 1} + L_i^f\epsilon_x + N_i^f\Delta T \tag{10b}$$

where

$$L_i^f = C_{ix}^f + H_1^f(C_{i\theta}^f + C_{ir}^f)$$

$$N_i^f = H_2^f(C_{i\theta}^f + C_{ir}^f) - C_{ij}^f\alpha_j^f$$

c) isotropic matrix,

$$\sigma_i^m = A_1^m(C_{i\theta}^m + C_{ir}^m) + A_2^m(C_{i\theta}^m - C_{ir}^m)\frac{1}{r^2} + C_{ix}^m\epsilon_x - C_{ij}^m\alpha_j^m\Delta T \tag{10c}$$

The five constants A_1^f, A_2^f, A_1^m, A_2^m, and ϵ_x, are determined from the following five conditions:

1) The radial displacement w must be zero at $r = 0$. This condition, plus the fact that $\lambda_2^f < 0$ (equation (7)), requires A_2^f be zero to avoid a singularity in w at $r = 0$ for both transversely orthotropic and transversely isotropic fibers (equations (5) and (6)).

2) Continuity of w at the fiber-matrix interface $w^f(a) = w^m(a)$ requires that:

a) for a transversely orthotropic fiber ($C_{rr}^f \neq C_{\theta\theta}^f$),

$$A_1^f a^{\lambda_1^f} + a(H_1^f\epsilon_x + H_2^f\Delta T) = A_1^m a + A_2^m \frac{1}{a} \tag{11a}$$

b) for a transversely isotropic fiber ($C_{rr}^f = C_{\theta\theta}^f$)

$$A_1^f a = A_1^m a + A_2^m \frac{1}{a} \tag{11b}$$

3) Continuity of the radial stress σ_r at the fiber matrix interface, $\sigma_r^f(a) = \sigma_r^m(a)$ requires that:

a) for a transversely orthotropic fiber

$$A_1^f(C_{j\theta}^f + C_{jr}^f\lambda_1^f)a^{\lambda_1^f-1} + L_j^f\epsilon_x + N_j^f\Delta T \tag{12a}$$

$$= A_1^m(C_{r\theta}^m + C_{rr}^m) + A_2^m(C_{r\theta}^m - C_{rr}^m)\frac{1}{a^2} - C_{rj}^m\alpha_j^m\Delta T + C_{rx}^m\epsilon_x$$

or

b) for a transversely isotropic fiber

$$A_1^f(C_{r\theta}^f + C_{rr}^f) + C_{rx}^f\epsilon_x - C_{rj}^f\alpha_j^f\Delta T + \tag{12b}$$

$$= A_1^m(C_{r\theta}^m + C_{rr}^m) + A_2^m(C_{r\theta}^m - C_{rr}^m)\frac{1}{a^2} + C_{rx}^m\epsilon_x - C_{rj}^m\alpha_j^m\Delta T$$

4) Since there are no tractions applied at the outer boundary of the matrix $\sigma_r(b)$ and $\tau_{xr}(b)$ equal zero. The condition on σ_r requires that

$$A_1^m(C_{r\theta}^m + C_{rr}^m) + A_2^m\frac{1}{b^2}(C_{r\theta}^m - C_{rr}^m) + C_{rx}^m\epsilon_x - C_{rj}^m\alpha_j^m\Delta T = 0 \tag{13}$$

The traction free condition on τ_{xr} requires that K in equation (8) equal zero. Thus, there are no shear stresses in the fiber or matrix.

5) The final condition for the case of pure thermal loading is that the net axial force P on the fiber-matrix composite be zero. This is expressed mathematically as

$$P = 2\pi\int_0^b \sigma_x r\,dr = 0 \tag{14}$$

and for a transversely orthotropic fiber results in the condition

$$A_1^f(C_{x\theta}^f + C_{xr}^f\lambda_1^f)\frac{a^{\lambda_1^f+1}}{\lambda_1^f+1} + A_1^m(C_{xr}^m)(b^2 - a^2)$$

$$+\frac{1}{2}[C_{xx}^m(b^2 - a^2)$$

$$+ L_x^f a^2]\epsilon_x + \frac{1}{2}[N_x^f a^2 - C_{xj}^m\alpha_j^m(b^2 - a^2)]\Delta T = 0 \tag{15a}$$

For a transversely isotropic fiber ($C_{rr}^f = C_{\theta\theta}^f$), the form of equation (14) is:

$$A_1^f\frac{1}{2}(C_{x\theta}^f + C_{xr}^f)a^2 + A_1^m\frac{1}{2}C_{xr}^m(b^2 - a^2)$$

$$+\frac{1}{2}[C_{xx}^m(b^2 - a^2) + C_{xx}^f a^2]\epsilon_x - \frac{1}{2}[C_{xj}^f\alpha_j^f a^2$$

$$+ C_{xj}^m\alpha_j^m(b^2 - a^2)]\Delta T = 0 \tag{15b}$$

The constants A_1^f, A_1^m, A_2^m, and ϵ_x are obtained by solving equations (11)–(13) and (15) simultaneously. It is noted that the axial loading case can be considered for a given axial strain ϵ_x or a given axial force P. In addition, the radial loading case may also be considered by appropriate modification of equation (13).

III Results and Discussion

Thermal stress distributions were determined for three types of fiber properties: (1) transversely isotropic ($C_{rr} = C_{\theta\theta}$); (2) circumferentially orthotropic ($C_{rr} < C_{\theta\theta}$); (3) radially orthotropic ($C_{rr} > C_{\theta\theta}$). The matrix was considered to be isotropic. The fiber and matrix properties used for the calculations are given in Table 1. A uniform temperature increase of 1°C was used for loading. Results for a fiber volume fraction $V_f = 0.623$ are presented in Figs. 4–6 and results for variable V_f are presented in Figs. 7–9.

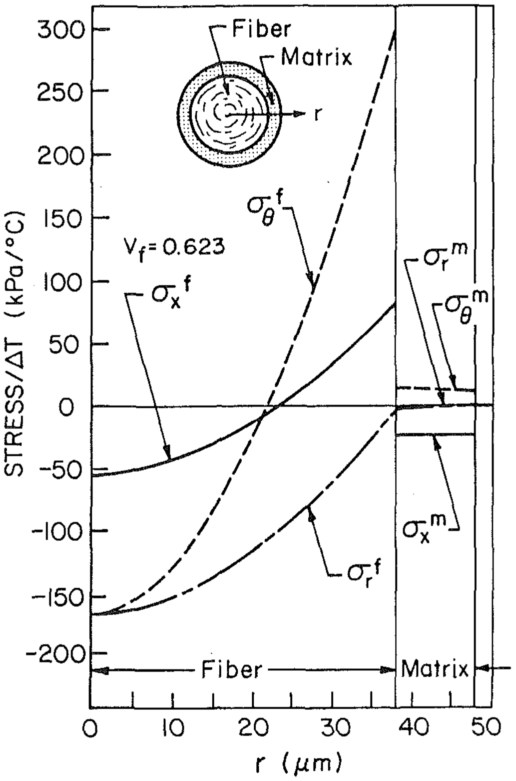

Fig. 6 Thermal stress distribution in a composite with a circumferentially orthotropic fiber

Transversely Isotropic Fiber ($C_{rr} = C_{\theta\theta}$). The stress distributions for the case of a transversely isotropic fiber (Fig. 4) exhibit a uniform positive axial stress and uniform compressive hoop and radial stresses in the fiber. These distributions can be explained by examining the equation of the stress distribution in a transversely isotropic fiber (equation (10*a*)). Recalling that $A_2^f = 0$ in order to eliminate singular w displacements at $r = 0$ allows equation (10*a*) to be restated as

$$\sigma_i^f = A_1^f(C_{i\theta}^f + C_{ir}^f) + C_{ix}^f\epsilon_x - C_{ij}^i\alpha_j^f\Delta T \tag{16}$$

It is evident from equation (16) that the fiber stresses are independent of radial coordinate. The stress distributions in the matrix are described by equation (10*c*). A relatively large, positive hoop stress is present in the matrix. The hoop stress attains a maximum at the fiber-matrix interface (Fig. 4). The decay in the magnitude of the radial and hoop matrix stresses with radial coordinate can be explained by examining the A_2^m term in equation (10*c*). The stresses decay as a function of $1/r^2$. The axial stress is constant in the matrix because $C_{i\theta}^m = C_{ir}^m$ when $i = x$. Thus the A_2^m term in equation (10*c*) is zero and there is no axial stress dependence on the radial coordinate. For these stress distributions, fiber failure (if present) is expected to be an axial tensile fracture.

Radially Orthotropic Fiber ($C_{rr} > C_{\theta\theta}$). Figure 5 shows the thermal stress distributions for the case of a fiber with radial orthotropy. All three components of stress are positive and singular at the center of the fiber. These distributions can be explained by examining equation (10*b*). For radial orthotropy $C_{rr} > C_{\theta\theta}$ and λ_1^f is less than unity. Defining $\delta = (1 - \lambda_1^f)$, and recalling once again that $A_2^f = 0$, equation (10*b*) can be written

$$\sigma_i^f = A_1^f(C_{i\theta}^f + C_{ir}^f\lambda_1^f)\frac{1}{r^\delta} + L_i^f\epsilon_x + N_i^f\Delta T \tag{17}$$

For the example problem considered here $\lambda_1^f = 0.343$ and $\delta = 0.657$. Therefore, a stress singularity of order δ exists at $r = 0$ for $\lambda_1^f < 1.0$. It should be noted that δ is a function only of the

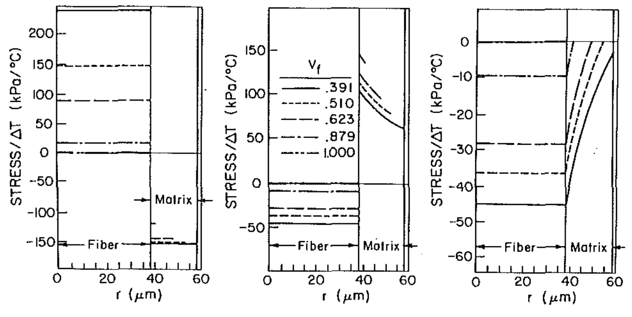

(a) Axial Stress (b) Hoop Stress (c) Radial Stress

Fig. 7 Effect of volume fraction on thermal stress distributions in a composite with a transversely isotropic fiber

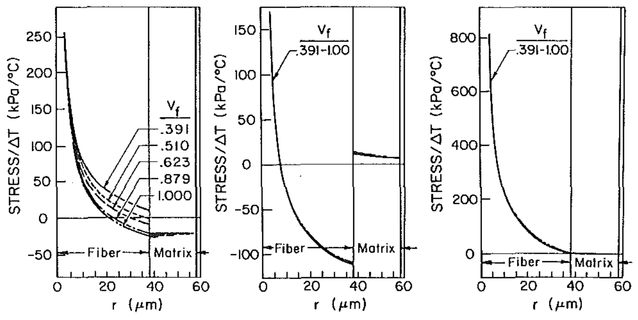

(a) Axial Stress (b) Hoop Stress (c) Radial Stress

Fig. 8 Effect of volume fraction on thermal stress distributions in a composite with a radially orthotropic fiber

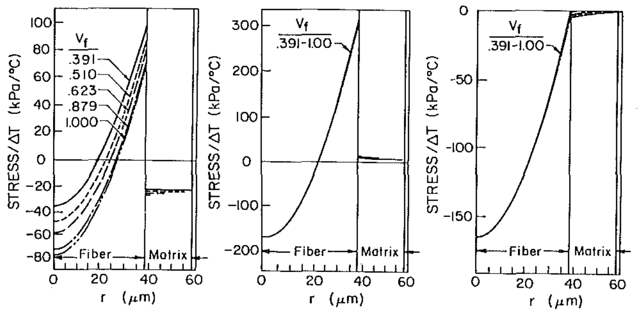

(a) Axial Stress (b) Hoop Stress (c) Radial Stress

Fig. 9 Effect of volume fraction on thermal stress distributions in a composite with a circumferentially orthotropic fiber

fiber properties C_{rr}^f and $C_{\theta\theta}^f$. The term A_1^f ($C_{i\theta}^f$ + C_{ir}^f λ_1^f), which defines the strength of the singularity, is a function of fiber and matrix properties, fiber volume fraction, and boundary conditions.

A similar singularity was shown by Lekhnitskii (1957) to exist in an anisotropic disk under radial compression. Lekhnitskii also notes that for the limiting case $r = 0$ there is no difference in material properties between the r and θ directions; therefore, the fiber must be transversely isotropic at $r = 0$. Such a condition precludes the existence of a mathematical singularity at the center of the fiber. (This point is also mentioned in a latter paper by Olson and Bert, 1966.) However, the singular nature of the stress distributions as r approaches zero remains valid for the actual case.

The potential failure mode of the fiber can be addressed by examining the relationship between the orientation of the graphite crystals in the fiber and the mechanical properties of a graphite crystal. For a radially orthotropic fiber, the basal planes of the graphite crystals (Fig. 1), which exhibit maximum strength (Kirk-Othmer, 1978) are oriented parallel to the radial and axial directions. Thus, the direction of minimum strength is in the hoop direction. Therefore, fiber splitting due to σ_θ is a potential failure mode for a radially orthotropic fiber which exhibits singular hoop stresses.

Circumferentially Orthotropic Fiber ($C_{\theta\theta}$ > C_{rr}). Stress distributions for circumferentially orthotropic fibers are shown in Fig. 6. The stresses in the fiber are governed by the reduced form of equation (10*b*), which is now written in the form

$$\sigma_i^f = A_1^f (C_{i\theta}^f + C_{ir}^f \lambda_1^f) r^{\lambda_1^f - 1} + L_i^f \epsilon_x + N_i^f \Delta T \tag{18}$$

and it is noted that $\lambda_1^f - 1 > 0$. Comparison of the stress distributions in Figs. 5 and 6 (or comparison of equations (17) and (18)) shows that the distributions in fibers with circumferential orthotropy (Fig. 6) are completely different from those in radially orthotropic fibers (Fig. 5). The distribution of axial and hoop stresses in circumferentially orthotropic fibers varies uniformly from compression along the centerline (r = 0) to tension at the fiber-matrix interface. The radial stress is compressive throughout the fiber. For this case $\lambda_1^f = 2.876$; therefore, equation (18) reveals that the stresses have a power function distribution. The matrix exhibits compressive radial and axial stresses, but positive hoop stresses. All matrix stresses are relatively small in magnitude.

In the circumferentially orthotropic fiber, the basal planes are oriented parallel to the axial and circumferential directions. Thus, the directions of maximum fiber strength are expected to be in the axial and hoop directions with minimum fiber strength in the radial direction. Therefore, the maximum tensile stresses are in the directions of maximum strength. The direction of minimum strength is under compression throughout the fiber. For this type of fiber orthotropy, failure, should it occur, would be expected to be via fiber splitting at the fiber-matrix interface. It is interesting to note that under a uniform temperature decrease the signs of the stresses will change, resulting in a positive radial stress. In this case the maximum tensile stress will be in the direction of minimum strength. Therefore, the fiber may be more likely to fail during a cooling cycle than a heating cycle.

It is noted that the solution presented here for a fiber in an isotropic matrix is quite different than that of Chen and Diefendorf (1985) for a single fiber.

Influence of Fiber Volume Fraction. The influence of fiber volume fraction on the distribution of thermal stresses is demonstrated in Figs. 7–9. Figure 7 shows the results for a transversely isotropic fiber, Fig. 8 for a fiber with radial orthotropy, and Fig. 9 a fiber with circumferential orthotropy. The fiber volume fraction was varied by changing the thickness of the matrix layer surrounding the fiber and holding the fiber radius constant. Results are presented for fiber volume fractions in the range 0.391–1.0.

These figures show that the axial component of stress is a function of fiber volume fraction for all three types of fiber microstructure. This is a direct consequence of the equilibrium requirement of zero axial force for pure thermal loading. Equilibrium must always be satisfied regardless of material properties. A somewhat surprising result is the fact that the distributions of radial and hoop stresses are essentially independent of fiber volume fraction for both types of transversely orthotropic fibers considered (Figs. 8*b*–*c*, 9*b*–*c*), but the distributions of these two stress components varies considerably with fiber volume fraction for the case of a transversely isotropic fiber. These results can be explained by considering the equations for the stress distributions in each type of fiber (equations (16)–(18)).

In the transversely orthotropic fibers, A_1^f is relatively independent of volume fraction, differing by less than 4 percent in the volume fraction range 0.391–1.0. In contrast, ϵ_x differs by more than 30 percent in the same volume fraction range.

Detailed examination of the equations shows that the hoop and radial stresses are a strong function of the term containing A_1^f and a weak function of the term containing ϵ_x since $(C_{i\theta}^f + \lambda_1^f C_{ir}^f)$ is large and L_i is small for $i = r$ or θ. Thus, it can be concluded that in transversely orthotropic fibers the hoop and radial stresses are relatively independent of fiber volume fraction. The axial stresses in the transversely orthotropic fibers, however, show a greater dependence on fiber volume fraction. In this case $(C_{x\theta}^f + \lambda_1^f C_{xr}^f)$ is smaller and L_x is more than two orders of magnitude greater than the corresponding terms mentioned above. Consequently, the axial stresses are a stronger function of fiber volume fraction through the term associated with axial strain. In transversely isotropic fibers, however, both A_1^f and ϵ_x are strong functions of fiber volume fraction. A_1^f and ϵ_x vary by approximately 23 and 40 percent, respectively, in the fiber volume fraction range 0.391-1.0. Thus, all stresses will be greatly influenced by fiber volume fraction.

An equally surprising result is that the stresses in transversely orthotropic fibers are nonzero for a fiber volume fraction of 1.0, which corresponds to a fiber with no matrix surrounding it. The physical explanation is that as the fiber expands radially it also expands in the hoop direction; however, if there is a mismatch in the thermal expansion coefficients in the radial and hoop directions the expansion in the hoop direction can't compensate for the radial expansion. Thus, an internal constraint exists which gives rise to internal stresses. It should be noted that the presence of nonzero stresses in a single fiber is a function of the mismatch in radial and hoop thermal expansion coefficients only and not a function of material stiffness coefficients.

IV Conclusions

The distribution of thermal stresses in a fiber reinforced composite material is affected significantly by the microstructure of the fiber. If the fiber exhibits radial orthotropy, the distributions of all three components of normal stress exhibit a singularity of type $r^{-\delta}$ where the order of the singularity is a function of the radial and circumferential stiffness coefficients of the fiber. For circumferentially orthotropic and transversely isotropic fibers there is no singularity in the stresses.

Fiber volume fraction has essentially no influence on the radial and hoop stresses in orthotropic fibers. The axial stresses in orthotropic fibers and all three components of normal stress in transversely isotropic fibers are a function of fiber volume fraction.

Single fibers exhibit nonzero stresses when there is a mismatch in the radial and circumferential thermal expansion coefficients.

Acknowledgment

This work was supported by the NASA-Virginia Tech Composites Program under NASA Grant NAG-1-343. The authors express their appreciation to Professor M. W. Hyer for many helpful discussions regarding the elasticity solution.

References

Bennett, S. C., and Johnson, D. J., 1978, "Structural Heterogeneity in Carbon Fibers," *Proceedings of the Fifth London International Carbon and Graphite Conference*, Society of Chemical Industry, London, p. 377.

Bennett, S. C., and Johnson, D. J., 1979, "Electron-Microscope Studies of Structural Heterogeneity in PAN-based Carbon Fibers," *Carbon*, Vol. 17, No. 25.

Brydges, W. T., Badam, D. V., Joiner, J. C., and Jones, G. A., 1969, "The Structure and Elastic Properties of Carbon Fibers," *Applied Polymer Symposia*, Vol. 9, pp. 225-261.

Chen, K. J., and Diefendorf, R. J., 1985, "A Theoretical Calculation of Residual Stresses in Carbon Fibers," *Proceedings of the 17th Biennial Conference on Carbons.*

Cohen, D., and Hyer, M. W., 1984a, "Residual Thermal Stresses in Cross-Ply Graphite-Epoxy Tubes," *Advances in Aerospace Sciences and Engineering*, Yuceoglu, U., and Hesser, R., eds., ASME Publication AD-08, pp. 87-93.

Cohen, D., and Hyer, M. W., 1984b, "Residual Stresses in Cross-Ply Composite Tubes," CCMS-84-04, Virginia Polytechnic Institute and State University, Blacksburg, Va.

Cohen, D., Hyer, M. W., and Tompkins, S. S., 1984c, "The Effects of Thermal Cycling on Matrix Cracking and Stiffness Changes in Composite Tubes," CCMS-84-12, Virginia Polytechnic Institute and State University, Blacksburg, Va.

Diefendorf, R. J., and Tokarsky, E., 1975, "High Performance Carbon Fibers," *Polymer Engineering and Science*, Vol. 15, pp. 150-159.

Guigon, M., and Oberlin, A., 1983, "Structure and Microstructure of Some Pitch-Base Fibers," *Extended Abstracts and Program of the 16th Biennial Conference on Carbon*, p. 513.

Johnson, D. L., 1982, "Structure and Physical Properties of Carbon Fibers," *Chemistry and Industry*, 18 Sept., pp. 692-698.

Kirk-Othmer, 1978, *Encyclopedia of Chemical Technology*, 3rd Ed., Vol. 4, New York, John Wiley and Sons, p. 622.

Lekhnitskii, S. G., 1957, "Anisotropic Plates," Moscow, translation by Foreign Technology Division, Air Force Systems Command FTD-HT-23-608-67.

Lekhnitskii, S. G., 1950, *Theory of Elasticity of an Anisotropic Body*, pp. 68-70. reprinted by Mir Publishers, Moscow, 1981.

Lemaistre, C. W., and Diefendorf, R. J., 1973, "The Origin of Structure in Carbonized PAN Fibers," *SAMPE Quarterly*, Vol. 4, pp. 1-6.

Mitinskii, A. N., 1936, "The Calculation of Stresses in a Drilled Wood Tube," *Vestnik Inzhenerov i Tekhnikov*, No. 5.

Ng, C. B., Henderson, G. W., Buechler, M., and White, J. L., 1983, "Fracture Behavior of Mesophase Carbon Fibers," *Extended Abstracts and Program of the 16th Biennial Conference on Carbon*, p. 515.

Olson, W. A., and Bert, C. W., 1966, "Analysis of Residual Stresses in Bars and Tubes of Cylindrically Orthotropic Materials," *Experimental Mechanics*, Vol. 6, No. 9, pp. 451-457.

Reynolds, W. N., and Sharp, J. V., 1974, "Crystal Shear Limit to Carbon Fiber Strength," *Carbon*, Vol. 12, pp. 103-110.

St. Venant, B., 1865, Mémoire sur les divers genres d'homogénéite des corps solides," *Journal de Math. pures et appl.*, Louiville, p. 10.

Voigt, W., 1886, "Ueber die Elastizitätsverhältnisse zylinrisch aufgebauter Körper," Nachrichten v. d. Königl. Gesellschaft der Wissenschaften und der Georg-Augustin zu Göttingen, No. 16.

Stresses and Deformations in Composite Tubes Due to a Circumferential Temperature Gradient

M. W. Hyer
Professor,
Department of Mechanical Engineering,
University of Maryland,
College Park, MD 20742
Mem. ASME

D. E. Cooper
Structures Technology,
Boeing Aerospace Company,
Seattle, WA 98124

This paper presents a linear elasticity solution for determining the response of composite tubes subjected to a circumferential temperature gradient of the form $\Delta T_0 + \Delta T_1 \cos(\theta)$. *The temperature does not vary with distance along the tube nor through the wall. Temperature-independent material properties are assumed and a displacement approach is used. The results are limited to tubes with the fibers in each layer oriented axially or circumferentially, so-called cross-ply tubes. It is shown that for both single layer and multiple layer tubes, one constant characterizes overall bending of the tube and one constant characterizes overall axial deformation. Numerical results show that fiber orientation strongly influences the stresses in a single layer tube. When the fibers are aligned axially, all components of stress in the tube are small. When the fibers are aligned circumferentially, the hoop stress becomes large. This is due to the large difference between the radial and circumferential coefficients of thermal expansion when the fibers are oriented circumferentially. Also, for a single layer tube constructed of a material with no thermal expansion in the axial direction, the overall change of length of the tube due to the temperature gradient will be zero only if the material is transversely isotropic. However, even if the material is transversely isotropic, the tube will still experience overall bending.*

Introduction

Considerable work has been done to understand the response of single and multiple layers of fiber-reinforced material in tubular form to bending, torsion, and tensile loads (Whitney and Halpin, 1968; Pagano and Whitney, 1970; Rizzo and Vacario, 1970; Pagano, 1971; Whitney, 1971; Whitney et al., 1972; Rizzo and Vacario, 1972, Pagano, 1973). This work was done in conjunction with the possible use of tubular specimens, rather than traditional flat coupons, to study the mechanical behavior of fiber-reinforced materials. To a lesser extent some work has been done to understand the thermally-induced stresses in single (Kalam and Tauchert, 1978) and multilayer tubes (Whitney, 1971; Birger, 1971; Tauchert and Hsu, 1977; Tauchert, 1980; Hyer et al., 1986). This paper summarizes a portion of the analytical work developed to help understand the response of fiber-reinforced tubes exposed to a temperature change that varies sinusoidally with the circumferential coordinate but does not vary with distance along the tube or through the tube wall. The analysis is limited to tubes with the fibers in each layer aligned either axially or circumferentially, so-called cross-ply tubes. Numerical examples are presented for a single layer and a specially-constructed three-layer tube.

In this work each layer is idealized as a homogeneous orthotropic material with respect to the global geometry of the tube. The material properties are assumed temperature-independent. An elasticity approach, as opposed to a shell-like approach, is used. An elasticity approach is used because tube radius to wall thickness ratios less than 10 are of interest. While radial stresses are expected to be small, radial thermal expansion effects can cause axial and circumferential stresses in the tube wall. A higher-order shell theory (Whitney, 1971) could be used to account for the through-the-thickness effects but an elasticity approach is felt to be more direct. Since interest centers on the behavior of the tube away from the ends, a planar elasticity approach is used.

The limitation of a temperature-independent theory is fully appreciated. However, there is little documentation on the variation with temperature of the nine elastic constants and the three expansion coefficients of fiber-reinforced materials. Developing an analysis which required data that was unavailable was not felt to be a useful first exercise in understanding tube response. A forthcoming publication, however, examines the issue of temperature-dependent properties. In addition to providing valuable insight into the thermal response of cross-ply tubes, the solution presented here served as a basis for that temperature-dependent work.

Contributed by the Applied Mechanics Division for publication in the JOURNAL OF APPLIED MECHANICS.

Discussion on this paper should be addressed to the Editorial Department, ASME, United Engineering Center, 345 East 47th Street, New York, N.Y. 10017, and will be accepted until two months after final publication of the paper itself in the JOURNAL OF APPLIED MECHANICS. Manuscript received by ASME Applied Mechanics Division, December 26, 1985; final revision April 12, 1986.

Problem Definition and Derivation of the Governing Equations

A cylindrical coordinate system is used, x being the axial coordinate and θ and r being the circumferential and radial coordinates, respectively. The inner and outer radii are denoted as r_i and r_o, respectively, and r_k is the radial location of the interface between the kth and $(k+1)-st$ layers. Pagano's (1972) most general work, though addressing neither thermal effects nor layered tubes, was consulted frequently and so the nomenclature and approach used here somewhat parallel that work. In this work the temperature variation around the tube is given by

$$\Delta T_o = \Delta T + \Delta T_1 \cos(\theta), \tag{1}$$

ΔT_o and ΔT_1 being constants representing the temperature change measured relative to some reference temperature. The specific reference temperature will be discussed further when numerical examples are presented.

For the cross-ply tubes being considered, the constitutive behavior for each layer can be written in the form

$$\begin{Bmatrix} \sigma_x \\ \sigma_\theta \\ \sigma_r \\ \tau_{\theta r} \\ \tau_{xr} \\ \tau_{x\theta} \end{Bmatrix} = \begin{bmatrix} C_{11} & C_{12} & C_{13} & 0 & 0 & 0 \\ C_{12} & C_{22} & C_{23} & 0 & 0 & 0 \\ C_{13} & C_{23} & C_{33} & 0 & 0 & 0 \\ 0 & 0 & 0 & C_{44} & 0 & 0 \\ 0 & 0 & 0 & 0 & C_{55} & 0 \\ 0 & 0 & 0 & 0 & 0 & C_{66} \end{bmatrix} \begin{Bmatrix} \epsilon_x - \alpha_x \Delta T \\ \epsilon_\theta - \alpha_\theta \Delta T \\ \epsilon_r - \alpha_r \Delta T \\ \gamma_{\theta r} \\ \gamma_{xr} \\ \gamma_{x\theta} \end{Bmatrix}, \tag{2}$$

where the C_{ij} are the elastic constants and the α's the thermal expansion coefficients of the layer. Since the study focuses on tube response away from the ends, and in light of the independence of temperature on the axial coordinate, it is assumed that the stresses are independent of x. With this assumption, the equilibrium equations become

$$\begin{aligned} &\frac{\partial \sigma_r}{\partial r} + \frac{1}{r}(\sigma_r - \sigma_\theta) + \frac{1}{r}\frac{\partial \tau_{\theta r}}{\partial \theta} = 0 \\ &\frac{\partial \tau_{xr}}{\partial r} + \frac{1}{r}\frac{\partial \tau_{x\theta}}{\partial \theta} + \frac{1}{r}\tau_{xr} = 0 \\ &\frac{\partial \tau_{\theta r}}{\partial r} + \frac{1}{r}\frac{\partial \sigma_\theta}{\partial \theta} + \frac{2}{r}\tau_{\theta r} = 0 \end{aligned} \tag{3}$$

The strain-displacement relations for the problem are

$$\begin{aligned} &\epsilon_r = \frac{\partial u}{\partial r} && \epsilon_\theta = \frac{1}{r}\left(\frac{\partial v}{\partial \theta} + u\right) \\ &\epsilon_x = \frac{\partial w}{\partial x} && \gamma_{\theta r} = \frac{1}{r}\left(\frac{\partial u}{\partial \theta} - v + r\frac{\partial v}{\partial r}\right) \\ &\gamma_{xr} = \frac{\partial w}{\partial r} + \frac{\partial u}{\partial x} && \gamma_{x\theta} = \frac{\partial v}{\partial x} + \frac{1}{r}\frac{\partial w}{\partial \theta}, \end{aligned} \tag{4}$$

where u, v, and w are the r, θ, and x components of displacements, respectively. Finally, the rotations are given by

$$\omega_{x\theta} = \frac{1}{2}\left(\frac{1}{r}\frac{\partial w}{\partial x} - \frac{\partial v}{\partial x}\right); \quad \omega_{xr} = \frac{1}{2}\left(\frac{\partial u}{\partial x} - \frac{\partial w}{\partial r}\right);$$

$$\omega_{\theta r} = \frac{1}{2}\left(\frac{1}{r}\frac{\partial (rv)}{\partial r} - \frac{1}{r}\frac{\partial u}{\partial \theta}\right). \tag{5}$$

For this class of problems Leknitskii (1963) has shown that the displacements in each layer have the following form:

$$\begin{aligned} u(x,\theta,r) &= U(\theta,r) + \frac{1}{2}x^2(b_1\cos\theta - b_2\sin\theta) \\ &\quad - x(\omega_1\sin\theta - \omega_2\cos\theta) + u_o\cos\theta + v_o\sin\theta \\ v(x,\theta,r) &= V(\theta,r) - \frac{1}{2}x^2(b_1\sin\theta + b_2\cos\theta) \\ &\quad + xb_3r - x(\omega_1\cos\theta + \omega_2\sin\theta) - u_o\sin\theta + v_o\cos\theta + \omega_3 r \\ w(x,\theta,r) &= W(\theta,r) - rx(b_1\cos\theta - b_2\sin\theta) + b_4x + \omega_1 r\sin\theta \\ &\quad - \omega_2\cos\theta + w_o. \end{aligned} \tag{6}$$

Lekhnitskii shows this for the case of no thermal expansion effects. However, it can be shown that the form holds when thermal expansion effects are present. The physical interpretation of some of the constants in equation (6) is interesting and will be emphasized when numerical examples are presented. Of course the rigid body displacement terms are u_o, v_o, w_o, ω_1, ω_2, and ω_3. The constant b_1 represents displacements due to overall bending of the layer and the constant b_4 represents axial expansion. For a layered tube there is a set of constants $u_o, \ldots, b_1, b_4$, and a set of functions U, V, and W for each layer.

Using a displacement approach, the equilibrium equations lead to the following three governing equations for U, V, and W for each layer:

$$\begin{aligned} &C_{33}\left(\frac{\partial^2 U}{\partial r^2} + \frac{1}{r}\frac{\partial U}{\partial r}\right) + \frac{C_{44}}{r^2}\frac{\partial^2 U}{\partial \theta^2} - \frac{C_{22}}{r^2}U \\ &\qquad + \left(\frac{C_{44}+C_{23}}{r}\right)\frac{\partial^2 V}{\partial r \partial \theta} - \left(\frac{C_{22}+C_{44}}{r^2}\right)\frac{\partial V}{\partial \theta} = P_1 \\ &\qquad C_{55}\frac{\partial^2 W}{\partial r^2} + \frac{1}{r}\frac{\partial W}{\partial r} + \frac{C_{66}}{r^2}\frac{\partial^2 W}{\partial \theta^2} = 0 \\ &\frac{(C_{44}+C_{23})}{r}\frac{\partial^2 U}{\partial r \partial \theta} + \frac{(C_{44}+C_{22})}{r^2}\frac{\partial U}{\partial \theta} \\ &\qquad + C_{44}\left(\frac{\partial^2 V}{\partial r^2} + \frac{1}{r}\frac{\partial V}{\partial r} - \frac{V}{r^2}\right) + \frac{C_{22}}{r^2}\frac{\partial^2 V}{\partial \theta^2} = P_3, \end{aligned} \tag{7}$$

where

$$\begin{aligned} P_1(\theta,r) &= \frac{1}{r}[(C_{12}-C_{13})b_4 + \tilde{M}] + \left[(2C_{13}-C_{12})b_1 + \frac{\tilde{N}}{r}\right]\cos\theta \\ P_3(\theta,r) &= -\left[C_{12}b_1 + \frac{\tilde{N}}{r}\right] \end{aligned} \tag{8}$$

and

$$\begin{aligned} \tilde{N} &= [(C_{13}-C_{12})\alpha_x + (C_{23}-C_{22})\alpha_\theta + (C_{33}-C_{23})\alpha_r]\Delta T_1 \\ \tilde{M} &= [(C_{13}-C_{12})\alpha_x + (C_{23}-C_{22})\alpha_\theta + (C_{33}-C_{23})\alpha_r]\Delta T_o \\ \hat{N} &= (C_{12}\alpha_x + C_{22}\alpha_\theta + C_{23}\alpha_r)\Delta T_1. \end{aligned} \tag{9}$$

It should be noted that the equation governing the axial displacement component, W, is uncoupled from the other two equations. For layers with fibers other than circumferentially or axially oriented, there would be coupling of all three displacement components.

Solution of Governing Equations

Since each layer in the tube is orthotropic in the x-θ-r system, and since the temperature distribution is an even function of θ, it is to be expected that in each layer u and w will be even functions of θ and w will be an odd function of θ. Therefore, in equation (6)

$$b_2 = \omega_1 = v_o = b_3 = \omega_3 = 0. \tag{10}$$

More importantly, solutions for U, V, and W in the form

$$\begin{aligned} U(\theta,r) &= \sum_{n=0}^{\infty} U_n(r)\cos n\theta + U_p(\theta,r) \\ V(\theta,r) &= \sum_{n=0}^{\infty} V_n(r)\sin n\theta + V_p(\theta,r) \qquad (11) \\ W(\theta,r) &= \sum_{n=0}^{\infty} W_n(r)\cos n\theta. \end{aligned}$$

will be sought. The functions U_p and V_p are the particular solutions for U and V due to P_1 and P_3. The summation in each expression represents the homogeneous solution to the governing equations. Recall that there is a solution of the above form for each layer.

Homogeneous Solution. The homogeneous solution to the governing equations has several special features corresponding to the $n=0$ and $n=1$ cases. These special features deal mainly with the presence of repeated eigenvalues and the fact that some of the solutions represent rigid body motions already accounted for in the general form equation (6).

If the rigid body terms are eliminated (because they are accounted for in equation (6)), the $n=0$ solution leads to

$$\begin{aligned} U_0(r) &= A_{01}r^{\lambda_1} + A_{02}r^{-\lambda_1} \\ W_0(r) &= D_{02}\ln r. \end{aligned} \tag{12}$$

A_{01}, A_{02}, D_{02} being constants and

$$\lambda_1 = \sqrt{\frac{C_{22}}{C_{33}}}\,. \tag{13}$$

The solution for $n=1$ leads to the eigenvalues

$$\lambda_2 = 0,0,\pm\left(\frac{C_{23}C_{33} - C_{23}^2 - 2C_{23}C_{44} + C_{33}C_{44} + C_{22}C_{44}}{C_{33}C_{44}}\right)^{1/2} \tag{14}$$

for the u and v displacements. If the rigid body motions are eliminated from the $n=1$ solution, U and V take the form

$$\begin{aligned} U_1(r) &= A_{13}r^{\lambda_2} + A_{14}r^{-\lambda_2} \\ V_1(r) &= \phi_{13}A_{13}r^{\lambda_2} + \phi_{14}A_{14}r^{-\lambda_2} \end{aligned} \tag{15}$$

where

$$\begin{aligned} \phi_{13} &= \frac{C_{22} + C_{44} - C_{33}\lambda_2^2}{(C_{23} + C_{44})\lambda_2 - (C_{22} + C_{44})} \\ \phi_{14} &= \frac{C_{33}\lambda_2^2 - C_{22} - C_{44}}{(C_{23} + C_{44})\lambda_2 + (C_{22} + C_{44})}\,, \end{aligned} \tag{16}$$

λ_2 being the nonzero eigenvalue from equation (14).

The solution for $n \geq 2$ for U and V and for $n \geq 1$ for W follow regular patterns. For W the solutions for $n \geq 1$ are

$$W_n(r) = D_{n1}r^{\gamma_n} + D_{n2}r^{-\gamma_n}, \tag{17}$$

$$\gamma_n = n\sqrt{\frac{C_{66}}{C_{55}}}\,. \tag{18}$$

The U and V solutions for $n \geq 2$ are of the form

$$U_n(r) = \sum_{s=1}^{4} A_{ns}r^{\lambda_{ns}}; \quad V_n(r) = \sum_{s=1}^{4} B_{ns}r^{\lambda_{ns}}. \tag{19}$$

The λ_{ns} are eigenvalues and A_{ns} and B_{ns} are related through the eigenvectors, i.e., $B_{ns} = \phi_{ns}A_{ns}$. As will be seen, the solutions for $n \geq 2$ are not involved in predicting the response of the tube.

It can be shown that the particular solutions are

$$\begin{aligned} U_p &= (r^2A_5 + rA_4)\cos\theta + r(a_1b_4 + D_4) \\ V_p &= (r^2H_5 + rH_4)\sin\theta, \end{aligned} \tag{20}$$

where

$$a_1 = \frac{C_{12} - C_{13}}{C_{33} - C_{22}}\,; \quad D_4\,\frac{\tilde{M}}{C_{33} - C_{22}} \tag{21}$$

and

$$\begin{aligned} A_4 &= (C_{22}\tilde{N} + (C_{22} - C_{23})\hat{N})/\Delta_1, \\ H_4 &= ((C_{33} - C_{22} - C_{44})\hat{N} - (C_{23} + 2C_{44} + C_{22})\tilde{N})/\Delta_1, \\ &\qquad A_5 = a_5b_1,\ H_5 = h_5b_1, \end{aligned} \tag{22}$$

where

$$\begin{aligned} a_5 &= ((C_{22} - 3C_{44})(2C_{13} - C_{12}) - C_{12}(C_{44} \\ &\qquad + 2C_{23} - C_{22}))/\Delta_2 \\ h_5 &= ((4C_{33} - C_{44} - C_{22})C_{12} - (2C_{13} - C_{12})(3C_{44} \\ &\qquad + 2C_{23} + C_{22}))/\Delta_2 \end{aligned} \tag{23}$$

and

$$\begin{aligned} \Delta_1 &= (C_{33} - C_{22} - C_{44})C_{22} - (C_{23} - C_{22})(2C_{44} + C_{22} + C_{23}) \\ \Delta_2 &= (4C_{33} - C_{44} - C_{22})(C_{22} - 3C_{44}) \\ &\qquad - (3C_{44} + 2C_{23} + C_{22})(C_{44} + 2C_{23} - C_{22}). \end{aligned} \tag{24}$$

The complete solution for the three components of displacement is:

$$\begin{aligned} u &= A_{01}r^{\lambda_1} + A_{02}r^{-\lambda_1} + (A_{13}r^{\lambda_2} + A_{14}r^{-\lambda_2})\cos\theta \\ &\quad + \sum_{n=2}^{\infty}\left(\sum_{s=1}^{4} A_{ns}r^{\lambda_{ns}}\right)\cos n\theta + (r^2A_5 + rA_4)\cos\theta \\ &\quad + r(a_1b_4 + D_4) + \frac{1}{2}x^2b_1\cos\theta + x\omega_2\cos\theta + u_o\cos\theta \end{aligned} \tag{25a}$$

$$\begin{aligned} v &= (\phi_{13}A_{13}r^{\lambda_2} + \phi_{14}A_{14}r^{-\lambda_2})\sin\theta \\ &\quad + \sum_{n=2}^{\infty}\left(\sum_{s=1}^{4} B_{ns}r^{\lambda_{ns}}\right)\sin n\theta + (r^2H_5 + rH_4)\sin\theta \\ &\quad - \frac{1}{2}x^2b_1\sin\theta - x\omega_2\sin\theta - u_o\sin\theta \end{aligned} \tag{25b}$$

$$\begin{aligned} w &= D_{02}\ln r + \sum_{n=1}^{\infty}(D_{1n}r^{\gamma_n} + D_{2n}r^{-\gamma_n})\cos n\theta \\ &\quad - b_1rx\cos\theta + b_4x - \omega_2r\cos\theta + w_o. \end{aligned} \tag{25c}$$

From the expressions for the displacements, expressions for the stresses in terms of the unknown constants can be determined. With these displacement and stress expressions, boundary and interface continuity conditions can be applied to a particular problem. In addition, because of the planar nature of the analysis, there are certain integral conditions that must be satisfied. The totality of the conditions lead to a set of linear algebraic equations for the unknown constants in each layer.

Application to a Single Layer

Because of orthotropy, a single layer tube provides an interesting numerical example of the theory with which the effect of fiber orientation can be studied. In addition, a single layer tube can be used to study the consequences of having the coefficient of thermal expansion of the tube material in the axial direction being zero. For some applications of composite tubes, the condition of no axial dimensional changes due to a temperature change is desirable. Usually, this condition is in the context of a uniform temperature change of the tube. Since graphite fibers contract when heated, they can be combined in the proper proportion with a matrix material that expands when heated so that in the fiber direction the composite has a coefficient of thermal expansion of zero. It is interesting to study the response of such a material in tubular form to a circumferential temperature gradient condition.

For a single layer tube the inner and outer surfaces are traction free, i.e.,

$$\sigma_r(\theta,r_i)=\sigma_r(\theta,r_o)=\tau_{\theta r}(\theta,r_i)=\tau_{\theta r}(\theta,r_o)$$
$$=\tau_{xr}(\theta,r_i)=\tau_{xr}(\theta,r_o)=0. \qquad (26a\text{-}f)$$

In addition, the following integrals must be satisfied:

$$\int_0^{2\pi}\int_{r_i}^{r_o}\sigma_x r dr d\theta=0 \qquad (27a)$$

$$\int_0^{2\pi}\int_{r_i}^{r_o}\sigma_x r^2\cos\theta dr d\theta=0. \qquad (27b)$$

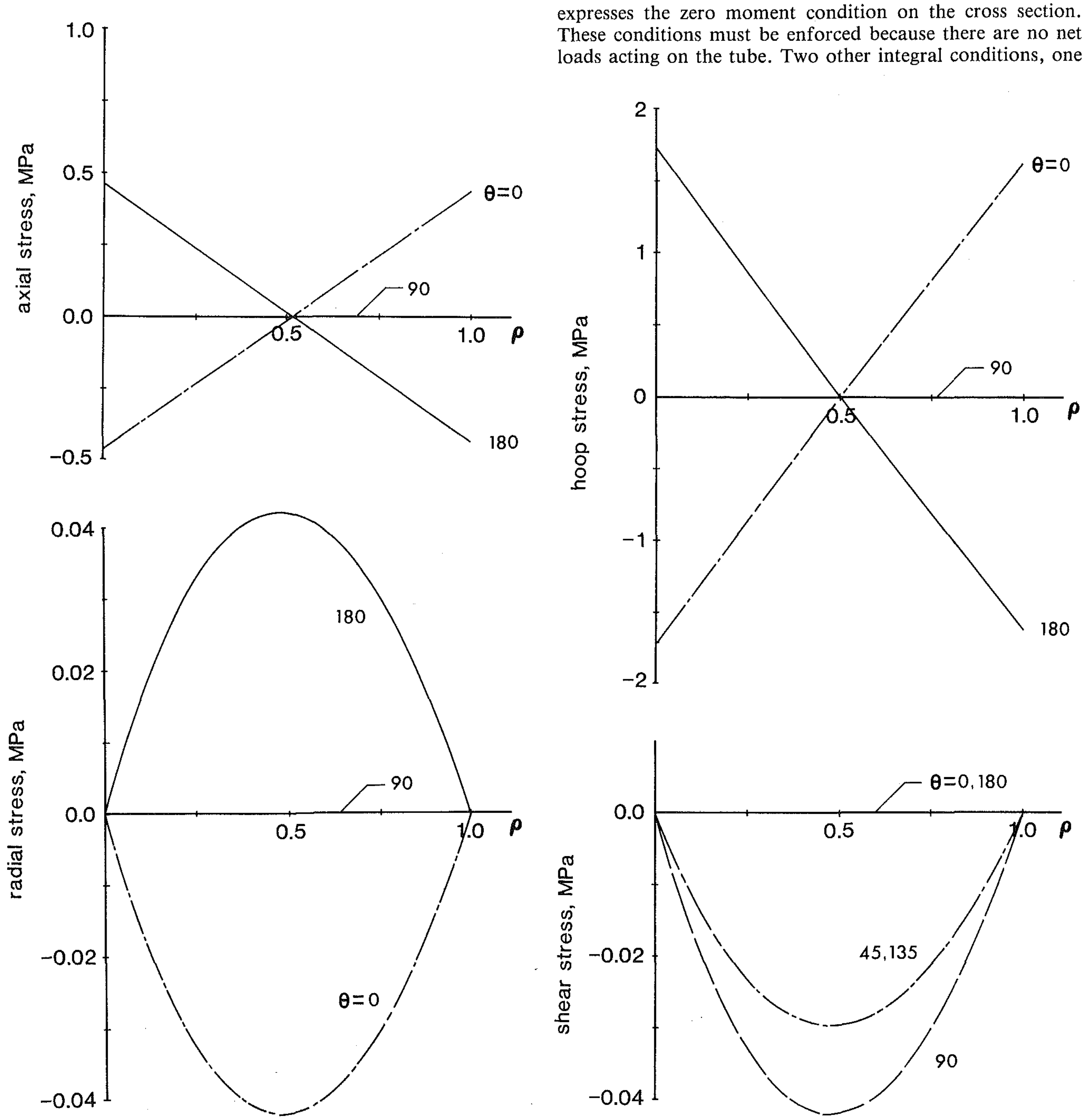

Fig. 1 Stresses in a 0 deg tube

The first integral represents the fact that the net axial force on the cross section of the tube must be zero. The second integral expresses the zero moment condition on the cross section. These conditions must be enforced because there are no net loads acting on the tube. Two other integral conditions, one representing another cross-sectional moment and the other representing torsion acting on the cross section, can be written. However, for this problem those conditions are automatically satisfied. To complete the statement of the problem, rigid body translations and the rotations are specified at some point. Here the motions at the point $(x, \theta, r) = (0, 0, r_o)$, a point at the outer radius of the tube, are chosen to be zero. Because of the assumed functional form of the displacements, equation (10), some of the six rigid body conditions are automatically satisfied.

When applying the traction boundary conditions, equation (26), it can be shown that for a single layer

$$A_{ns}=0, s=1,4 \text{ and } n\geq 2; D_{n1}=D_{n2}=0, n\geq 1 \qquad (28a)$$

and

$$D_{02}=0. \qquad (28b)$$

Thus harmonics $n\geq 2$ do not appear in any of the displacement components and $W(\theta, r)$ of equation (6) is identically zero. Also, the shear stresses τ_{xr} and $\tau_{x\theta}$ are identically zero throughout the tube.

Suppressing axial rigid body translation and rotation component ω_{xr} at $(x, \theta, r) = (o, o, r_o)$ requires

$$w_o=\omega_2=0. \qquad (29)$$

The remaining unknown constants u_o, A_{01}, A_{02}, b_4, A_{13}, A_{14}, and b_1 are determined by using equations (26*a*) and (26*b*) and equations (27) for the harmonics that do remain in u and v. These lead to seven simultaneous algebraic equations for the unknowns. (Actually, the seven equations separate into one group of three and another group of four equations. The group of three represent the response to the tube to a uniform temperature change ΔT_o. The group of four represents the response to the temperature change $\Delta T_1\cos(\theta)$). Equations (26*c*) and (26*d*) must also be enforced, but when doing so they provide the same information as equations (26*a*) and (26*b*) and so are not used.

Figure 1 shows the four nonzero components of stress for a graphite-epoxy tube with all the fibers oriented axially. The tube has a mean radius to wall thickness ratio of 10 and is subjected to the temperature condition

$$\Delta T= -177+100\cos\theta. \qquad (30)$$

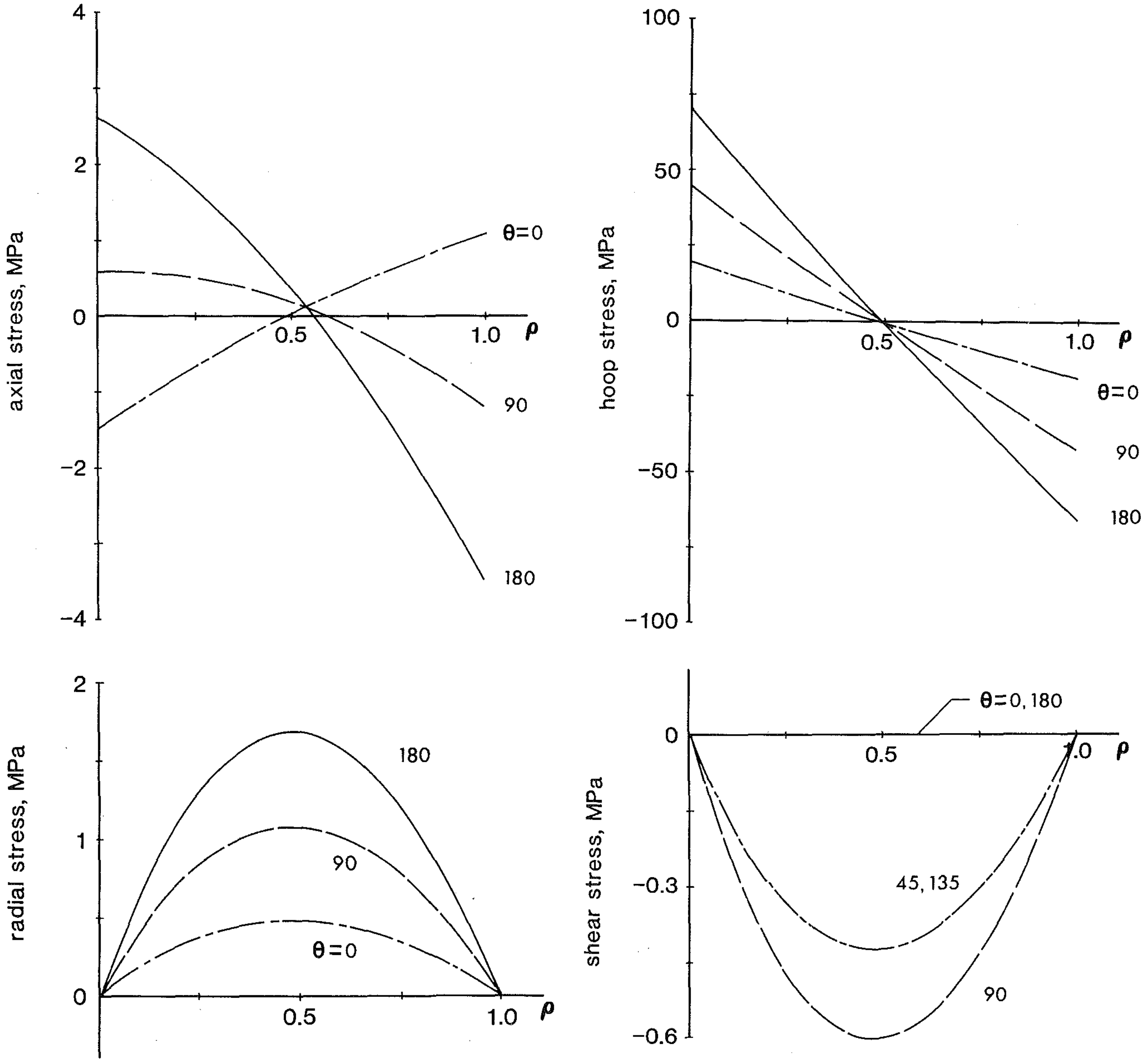

Fig. 2 Stresses in a 90 deg tube

Specifically, the mean radius is 10 mm and the wall thickness is 1 mm. This tube will be referred to as a 0 deg tube. The tube is made of a material which is assumed to cure, and be free of stress, at 177°C. This will be the reference temperature in all examples. With equation 30, at $\theta = 0$ deg the tube temperature is 100°C, while at $\theta = 180$ deg the tube temperature is -100°C. Table 1 lists the material properties used in the examples. The subscript notation in the table follows the usual notations for fiber-reinforced materials, i.e., 1 being the fiber direction, etc. Because the temperatures are measured relative to the stress-free state, the stresses can be intrepreted as residual stresses.

In the figures the stresses are plotted as a function of nondimensional distance through the wall at $\theta=0$ deg, $\theta=90$ deg, and $\theta=180$ deg. The nondimensional distance ρ is defined to be

$$\rho=\frac{r-r_i}{r_o-r_i}\,. \tag{31}$$

As can be seen, the stresses are quite small when the fibers are aligned axially. The axial and hoop stresses vary nearly linearly with distance through the wall. In addition, the maximum value of the axial stress at $\theta=0$ deg is very close to the maximum value at $\theta=180$ deg. The same is true of the hoop stress. The other two stress components vary in a nonlinear fashion. It should be noted that although they are negligible, the axial, hoop and radial stresses are not zero at $\theta=90$ deg. If the tube was transversely isotropic, then these three components of normal stress would be exactly zero at $\theta=90$ deg. In all cases the shear stress is exactly zero at $\theta=0$ deg and 180 deg.

Table 1 Material properties

$E_1=147$ GPa $G_{12}=4.27$ GPa
$E_2=9.10$ GPa $G_{13}=4.69$ GPa
$E_3=9.93$ GPa $G_{23}=5.93$ GPa
$\nu_{12}=\nu_{13}=0.3$ $\nu_{23}=0.49$
$\alpha_1=-0.077\times10^{-6}/°\mathrm{C}$
$\alpha_2=\alpha_3=33.7\times10^{-6}/°\mathrm{C}$

The stresses in the 0 deg tube are in sharp contrast to the stresses in the 90 deg tube shown in Fig. 2, a tube made of the same material and subjected to the same temperature gradient except that the fibers are in the circumferential direction. The axial stresses for this case, though still low, are nonlinear functions of distance through the wall. The maximum values at $\theta=0$ deg and $\theta=180$ deg are not equal. However, the most significant contrast with the 0 deg case is with the hoop stresses. These stresses are much larger than in the 0 deg tube and are due to the difference between the radial and circumferential thermal expansions coefficients when the fibers are oriented circumferentially. These stresses are not actually of concern because they are in the fiber direction and are much below the material failure level. However, a comparison of Figs. 1 and 2 illustrates the strong influence of fiber orientation.

Returning to the 0 deg tube, Fig. 3(*a*) shows the radial and tangential displacements at various circumferential locations as a function of length along the tube. The displacements shown are the displacements at the outer radius at the particular θ. The tube is assumed to be perfectly straight and circular at the stress-free temperature. The parabolic shape of the displacements, with the axial coordinate, is due to the con-

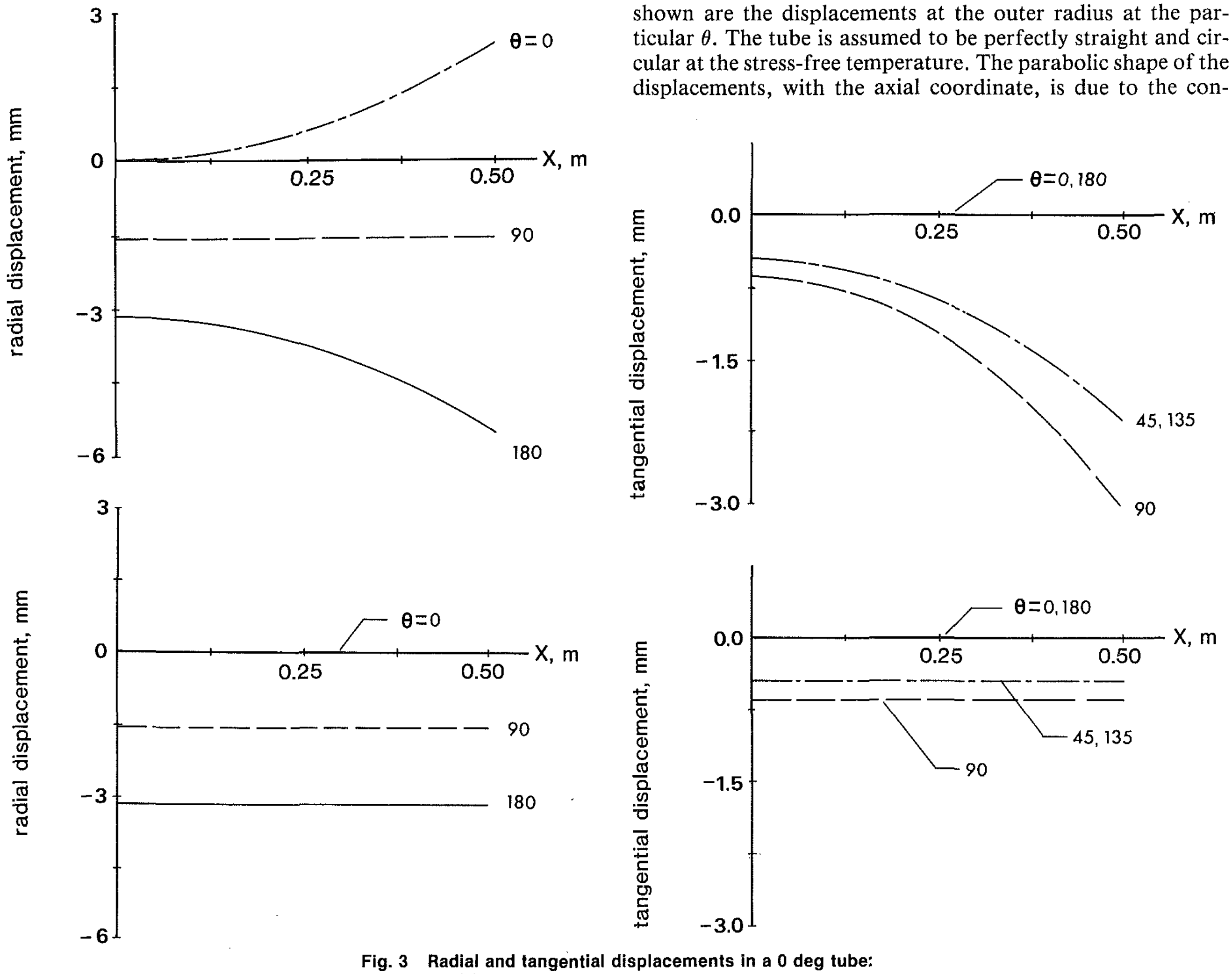

Fig. 3 Radial and tangential displacements in a 0 deg tube: (*a*) $\alpha_x \neq 0$; (*b*) $\alpha_x = 0$

stant b_1 and the figure indicates $b_1 \geq 0$. This is due to α_x being negative. In particular, $b_1 = 0.761 \times 10^{-6}\text{mm}^{-1}$. Comparing the displacements at $\theta = 0$ deg, 90 deg, and 180 deg, the figure indicates the tube cross section shortens along the 0–180 deg diameter about the same as it does along the 90–270 deg diameter, the cross section remaining almost circular. Since the tangential displacements are zero at $\theta = 0$ deg and 180 deg, the displacements at $\theta = 45$ deg, 90 deg and 135 deg are shown in Fig. 3. For this tube the quantity b_4 is positive, namely $b_4 = 13.7 \times 10^{-6}$. This means the tube has expanded axially, in addition to bending. The expansion, relative to the stress-free state, is again due to α_x being negative.

It is interesting to consider the case of a material with no thermal expansion in one direction. Figure 3(*b*) shows the displacements for the 0 deg tube subjected to the thermal conditions under discussion, but with the coefficient of thermal expansion α_x arbitrarily set to zero. Being a 0 deg tube, this means the tube is made of a material with no thermal expansion in the direction aligned with the axial direction. The figure seems to indicate that, relative to the $\alpha_x \neq 0$ case, there is no variation in the displacements along the length and so the tube remains straight. However, the figure must be viewed with caution. For this $\alpha_x = 0$ case, the values of b_1 and b_4 are actually $1.48 \times 10^{-21}\ \text{mm}^{-1}$ and -0.854×10^{-20}, respectively. These nonzero values mean that the tube actually bends and changes length, even though the deformations are orders of magnitude less than for the $\alpha_x \neq 0$ case. The tube must be transversely isotropic in the θr plane with $\alpha_x = 0$ if the tube is to not change length. However, the tube will still bend. The bending effects will be quite small and like the tube of Fig. 3(*a*), the cross section of the tube will decrease in diameter but remain almost circular. In the numerical examples presented here, the material is very close to being transversely isotropic and so the variations of the deformations with x in Fig. 3(*b*) are imperceptible.

As a matter of comparison, for the 90 deg tube $b_1 = -332 \times 10^{-6}\ \text{mm}^{-1}$ and $b_4 = -5980 \times 10^{-6}$.

Application to a Multilayer Tube

For a multilayer tube, the displacements of equation (25) are used but with the superscript k added to the nomenclature to denote that the displacements are associated with the kth layer, e.g., $A_{01}^{(k)}$, . . . $\lambda_1^{(k)}$, ... $A_4^{(k)}$, . . . , $b_1^{(k)}$, . . . $D_{01}^{(k)}$ . . . $w_o^{(k)}$. The application of the theory to multiple layers is straightforward. Here application will be limited to three-layer tubes but the extension to more layers is obvious.

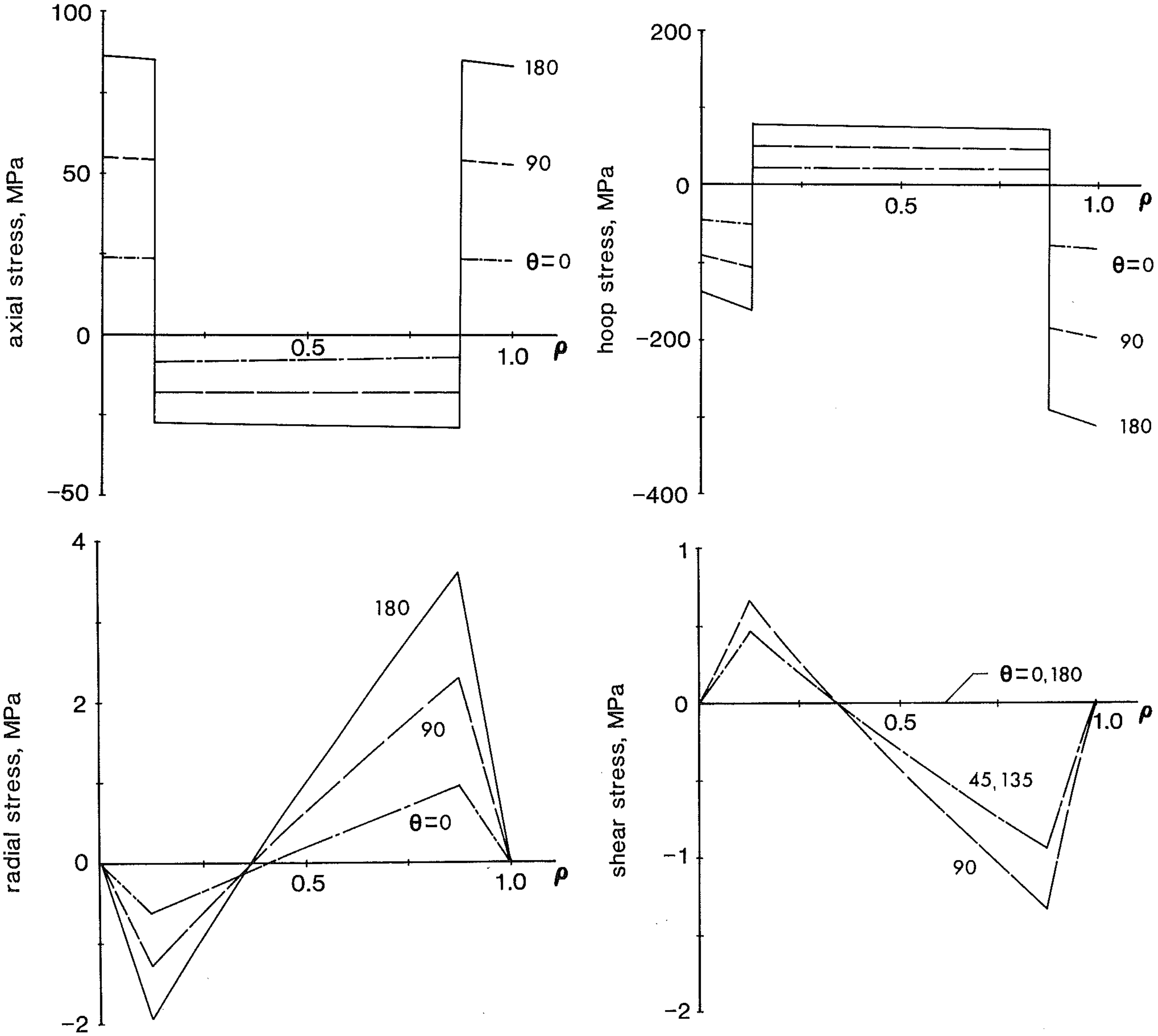

Fig. 4 Stresses in a (90/0_6/90) tube

For a three-layer tube the following conditions must be satisfied at the inner and outer boundaries.

$$\sigma_r^{(1)}(\theta,r_i)=\sigma_r^{(3)}(\theta,r_o)=\tau_{\theta r}^{(1)}(\theta,r_i)$$
$$=\tau_{\theta r}^{(3)}(\theta,r_o)=\tau_{xr}^{(1)}(\theta,r_i)=\tau_{xr}^{(3)}(\theta,r_o)=0. \tag{32a–f}$$

In addition, three of the six components of stress and the displacements must be continuous across the layer interfaces, namely,

$$\left.\begin{aligned}\sigma_r^{(k)}(\theta,r)&=\sigma_r^{(k+1)}(\theta,r)\\ \tau_{\theta r}^{(k)}(\theta,r)&=\tau_{\theta r}^{(k+1)}(\theta,r)\\ \tau_{xr}^{(k)}(\theta,r)&=\tau_{xr}^{(k+1)}(\theta,r)\\ u^{(k)}(x,\theta,r)&=u^{(k+1)}(x,\theta,r)\\ v^{(k)}(x,\theta,r)&=v^{(k+1)}(x,\theta,r)\\ w^{(k)}(x,\theta,r)&=w^{(k+1)}(x,\theta,r)\end{aligned}\right\} @r=r_k,\ k=1,2 \tag{33a–f}$$

Equations (27*a*) and (27*b*) must also be applied to the multilayer tube, the integration involving the cross section of all the layers. Finally, as with the single layer case, rigid body translations and rotations are set to zero at $(x,\theta,r)\ =\ (0,0,r_o)$.

Application of the above conditions leads to several important conclusions. They are:

$$\left.\begin{aligned}&1)\ A_{ns}^{(k)}=0,\ n\geq 2,\ s=1,4\\ &2)\ D_{02}^{(k)}=0,\ D_{n1}^{(k)}=D_{n2}^{(k)}=0,\ n\geq 1,\\ &3)\ \omega_2^{(k)}=w_o^{(k)},\end{aligned}\right\} k=1,3 \tag{34}$$

$$4)\ b_1^{(1)}=b_1^{(2)}=b_1^{(3)}=b_1,\ b_4^{(1)}=b_4^{(2)}=b_4^{(3)}=b_4.$$

The first three conclusions parallel the findings for the single layer case. The fourth conclusion indicates that even for the multilayer tube the planar cross section of the stress-free underformed tube remains planar after deformation. This is true despite the fact the material properties change from layer to layer. Because of this, the constants b_1 and b_4 describe the deformations of the tube as-a-whole, as they did for the single layer case. The remaining 17 constants, $A_{01}^{(k)}$, $A_{02}^{(k)}$, $u_o^{(k)}$, $A_{13}^{(k)}$, $A_{14}^{(k)}$, $k=1,3$ and b_1 and b_4 are determined by enforcing equations (32*a*) and (32*b*), equations (33*a*), (33*d*), and (33*e*), equations (27*a*) and (27*b*) and the condition

$$u^{(3)}(0,0,r_o)=0 \tag{35}$$

for the harmonics that do remain in u and v. As with a single layer tube, application of equations (32*c*) and (32*d*), and equation (33*b*) for the harmonics that remain lead to redundant information and are not used.

Figure 4 illustrates the stresses in an 8-layer ($90/0_6/90$) tube subjected to the temperature gradient of equation (30). The six 0 deg layers, called the core, are treated as a single layer and hence the tube is analyzed as a three-layer tube. The inner and outer circumferential layers are referred to as skins. As with the single layer examples, the stresses are illustrated as a function of nondimensional wall thickness at several circumferential locations. Like the single layer case, $\tau_{\theta r}$ is the nonzero shear stress.

As can be seen, three of the four components of stress have their largest magnitude at $\theta=180$ deg, where the tube is the coldest. The two major components of stress are the axial and the hoop stresses. The stress components are discontinuous functions of ρ, a characteristic of layered materials. In the skins the axial stresses are tensile and they act perpendicular to the fiber direction. As $\theta=180$ deg these stresses are large enough to crack the material. Also, in the core the hoop stresses at $\theta=180$ deg are tensile and act perpendicular to the fibers. They are also large enough to cause cracking in the material. The radial and shear stresses are much smaller than the other components of stress. These stresses peak at the interfaces between layers, the outer interface experiencing both the highest radial and the highest shear stress. The quantities b_1 and b_4, which characterize the overall deformations of the tubes, have the values -11.6×10^{-6} mm^{-1} and -208×10^{-6}. This means the tube bends and contracts axially like the 90 deg tube. This is due to the fact that the skins, with positive axial thermal expansion coefficients, overpower the six 0 deg core layers with negative axial expansion coefficients and determine the sign of the thermally induced deformations.

Concluding Comments

An analysis has been presented for studying the stresses and deformations of composite tubes subjected to a circumferential temperature gradient. Numerical examples have shown that in a single layer tube fiber orientation strongly influences response. In the multilayer tubes studied, the stresses were quite high. Even for a multiple-layer tube, just two constants, b_1 and b_4, characterize the overall bending and axial deformations of the tube.

Acknowledgments

The authors are grateful for the support of Cooperative Agreement NAG-1-343 between the NASA Langley Research Center and Virginia Polytechnic Institute and State University. Both authors were formerly associated with the latter institution. S. S. Tompkins of the Center monitored the work.

References

Birger, B. I., 1971, "Thermal Stresses in an Anisotropic Cylinder," *Izvestiya VUZ, Aviatsionnaya Technika*, Vol. 14, No. 1, pp. 24-28.

Hyer, M. W., Cooper, D. E., and Cohen, D., 1986, "Stresses and Deformations in Cross-Play Tubes Subjected to a Uniform Temperature Change," *J. Thermal Stresses*, Vol. 9, pp. 97-117.

Kalman, A. A., and Tauchert, T. R., 1978, "Stresses in an Orthotropic Cylinder Due to a Plane Temperature Distribution $T(r,\theta)$," *Journal of Thermal Stress*, Vol. 1, pp. 13-24.

Lekhnitskii, S. G., 1963, *"Theory of Elasticity of a Anisotropic Elastic Body,"* Translated by P. Fern, Holden-Day, Inc., San Francisco.

Pagano, N. J., 1971, "Stress Gradients in Laminated Composite Cylinders," *J. Composite Materials*, Vol. 5, pp. 260-265.

Pagano, N. J., 1972, "The Stress Field in a Cylindrically Anisotropic Body Under Two-Dimensional Surface Tractions," ASME JOURNAL APPLIED MECHANICS, Vol. 39, pp. 791-796.

Pagano, N. J., 1973, "Pure Bending of Helical Wound Composite Cylinders," *Analysis and Test Method for High Modulus Fibers and Composites*, ASTM STP 521, American Society for Testing and Materials, pp. 255-263.

Pagano, N. J., and Whitney, J. M., 1970, "Geometric Design of Composite Cylindrical Characterization Specimens," *J. Composite Materials*. Vol. 4, pp. 360-378.

Rizzo, R. R., and Vacario, A. A., 1970, "A Finite-Element Analysis of Laminated Anisotropic Tubes," *J. Composite Materials*, Vol. 4, pp. 344-349.

Rizzo, R. R., and Vacario, A. A., 1972, "A Finite-Element Analysis for Stress Distribution in Gripped Tubular Specimens," *Composite Materials: Testing and Design*, ASTM STP 497, American Society for Testing and Materials, pp. 68-88.

Tauchert, T. R., 1980, "Thermal Stresses in Coal Conversion Pressure Vessels Built of Layered Construction," in *Thermal Stresses in a Severe Environment*, Hasselman, D. P. H., and Heller, R., eds., Plenum Press, N.Y., pp. 183-205.

Tauchert, T. R., and Hsu, N. N., 1977, "Shrinkage Stresses in Wood Logs Considered as Layered Cylindrical Orthotropic Material," *Wood Science Technology*, Vol. 11, pp. 51-58.

Whitney, J. M., 1971, "On the Use of Shell Theory for Determining Stresses in Composite Cylinders," *J. Composite Materials*, Vol. 5, pp. 340-353.

Whitney, J. M., and Halpin, J. C., 1968, "Analysis of Laminated Anisotropic Tubes under Combined Loading," *J. Composite Materials*, Vol. 2, No. 3, pp. 360-364.

Whitney, J. M., Pagano, N. J., and Pipes, R. B., 1972, "Design and Fabrication of Tubular Specimens for Composite Characterization," *Composite Materials: Testing and Design*, ASTM STP 497, American Society for Testing and Materials, pp. 52-67.

H. Murakami

G. A. Hegemier

Department of Applied
Mechanics and Engineering Sciences,
University of California at San Diego,
La Jolla, Calif. 92023

A Mixture Model for Unidirectionally Fiber-Reinforced Composites

A binary mixture theory with microstructure is constructed for unidirectionally fiber-reinforced elastic composites. Model construction is based on an asymptotic scheme with multiple scales and the application of Reissner's new mixed variational principle (1984). In order to assess the accuracy of the model, comparison of the mixture model predictions with available experimental data on dispersion of harmonic waves is made for boron/epoxy and tungsten/aluminum composites. Formulas for the effective moduli are also presented, and the results are compared with test data and other available predictions.

1 Introduction

With the advent of high strength and stiffness fibers such as boron and carbon, and the development of techniques for binding such materials to plastic or metal, fibrous composites have become important elements of modern structures. Such composites, due to their microstructural heterogeneity, may exhibit response phenomena for some environments that are not observed for homogeneous materials. An example of these phenomena for dynamic environments is wave dispersion, an understanding of which is important both from the standpoints of direct response prediction and indirect analyses associated with such topics as nondestructive testing. For fibrous composites, wave dispersion has been amply demonstrated via ultrasonic techniques by such investigators as Tauchert and Guzelsu (1972), and Sutherland and Lingle (1972).

Simulation of response phenomena associated with the material microstructure, such as wave dispersion, requires a higher-order continuum description. Several such models have been proposed, some phenomenological, some nonphenomenological.

A higher-order continuum model which simulates wave dispersion was first proposed by Achenbach and Herrmann (1968) for unidirectionally fiber-reinforced composites. This theory called the "effective stiffness theory", has been further studied and applied to fibrous composites by Bartholomew and Torvick (1972), Hlaváček (1975), Achenbach (1976), and Aboudi (1981). The aforementioned works concerned linear materials. By modifying the original methodology, Aboudi (1982, 1983) extended the linear model to account for inelastic responses of the composite constituents.

In addition to the effective stiffness modeling concept, a mixture approach has been followed by a number of investigators. A phenomenological version of this model type was adopted by Martin, Bedford and Stern (1971). Deterministic, nonphenomenological mixture theories were introduced by Hegemier, Gurtman and Nayfeh (1973), Hegemier and Gurtman (1974), Nayfeh (1977), Murakami, Maewal and Hegemier (1979), and Nayfeh, Crane and Hoppe (1984). Although capable of simulating nonlinear component responses and interfacial slip, this work was limited to waveguide-type problems. This limitation was removed in the mixture theory developed for laminated composites by Hegemier, Murakami and Maewal (1979), and Murakami, Maewal, and Hegemier (1982). In their papers, it was demonstrated that the mixture-type model was capable of simulating harmonic wave dispersion in laminated composites more accurately than the effective stiffness theories. Further, the mixture-type model requires fewer governing equations. The accuracy and efficiency of the mixture theory is due to the use of appropriate displacement and stress microstructural fields, and a judicious smoothing technique. These are obtained by an asymptotic procedure with multiple scales. This procedure yields a series of microboundary value problems (MBVP's) defined over a unit cell, which in turn represents the (periodic) microstructure of a composite. The lowest order version of the MBVP method is equivalent to the "$O(1)$ homogenization theory" summarized by Bensoussan, Lions, and Papanicolaou (1978), and Sanchez-Palencia (1980). The latter, while it generates appropriate static moduli, is nondispersive. Simulation of wave dispersion requires at least a theory which is classified as an $O(\epsilon)$ homogenization theory in which ϵ denotes the representative ratio of micro-to-macrodimensions of a composite.

To date an $O(\epsilon)$ mixture theory has not been constructed for fibrous composites subject to *arbitrary* wave motion. Construction and validation of such a 3D model for unidirectional binary composites with periodic microstructure are the objectives of this paper. To facilitate this task, the asymptotic procedure with multiple scales noted previously is combined with a variational technique (Murakami, 1985). Following development of the basic equations, the dispersion of time-harmonic waves is studied and the results are compared with experimen-

---

Contributed by the Applied Mechanics Division for publication in the JOURNAL OF APPLIED MECHANICS.

Discussion on this paper should be addressed to the Editorial Department, ASME, United Engineering Center, 345 East 47th Street, New York, NY 10017, and will be accepted until two months after final publication of the paper itself in the JOURNAL OF APPLIED MECHANICS. Manuscript received by ASME Applied Mechanics Division, September 5, 1985; final revision April 7, 1986.

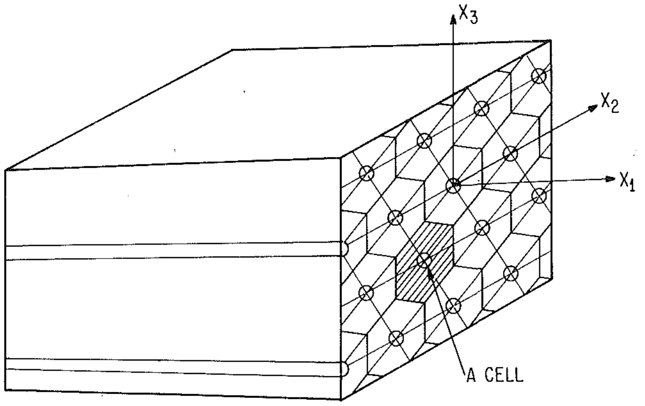

Fig. 1 A unidirectionally fiber-reinforced composite

tal data for boron/epoxy (Tauchert and Guzelsu, 1972) and tungsten/aluminum (Sutherland and Lingle, 1972) composites. The good correlation obtained with experimental data indicates that the proposed mixture model furnishes a basic tool by which dynamic responses of elastic composites can be investigated. While the model construction procedure is applicable to inelastic component response and interface slip, extension and investigation of the nonlinear problem is deferred to later publications.

2 Formulation

Consider a domain $\bar{V}$ which contains a uniaxial periodic array of fibers embedded in the matrix, as shown in Fig. 1. Let a rectangular system $\bar{x}_1$, $\bar{x}_2$, $\bar{x}_3$ be selected with $\bar{x}_1$ in the axial direction of the fibers. In the $\bar{x}_2$, $\bar{x}_3$ plane, a typical cell that represents the geometrical microstructure of the composite is shown in Fig. 2 for a hexogonal array.

For notational convenience forms $(\ )^{(\alpha)}$; $\alpha=1,2$ denote quantities associated with material α with $\alpha=1$ representing fiber and $\alpha=2$ matrix. Cartesian indicial notation will be employed in which Latin indices range from 1 to 3 and repeated indices imply the summation convention unless otherwise stated. In addition, the notations $(\bar{\ })_{,i}\equiv\partial(\bar{\ })/\partial\bar{x}_i$ and $(\bar{\ })_{,t}\equiv\partial(\bar{\ })/\partial\bar{t}$ will be employed in which $\bar{t}$ represents time. Quantities of the form $(\bar{\ })$ and $(\ )$ denote dimensional and nondimensional variables, respectively.

The governing relations for the displacement vector $\bar{u}_i^{(\alpha)}$ and the stress tensor $\bar{\sigma}_{ij}^{(\alpha)}$ in the two constituents are:

(*a*) Equations of motion

$$\bar{\sigma}^{(\alpha)}_{ji,j}=\bar{\rho}^{(\alpha)}\bar{u}^{(\alpha)}_{i,tt},\ \ \bar{\sigma}^{(\alpha)}_{ji}=\bar{\sigma}^{(\alpha)}_{ij} \tag{1}$$

where $\bar{\rho}^{(\alpha)}$ is the mass density;

(*b*) Constitutive relations

$$\bar{\sigma}^{(\alpha)}_{ij}=\bar{\lambda}^{(\alpha)}\delta_{ij}e^{(\alpha)}_{kk}+2\bar{\mu}^{(\alpha)}e^{(\alpha)}_{ij} \tag{2}$$

where $\bar{\lambda}^{(\alpha)}$, $\bar{\mu}^{(\alpha)}$ are Lamé's constants, $e^{(\alpha)}_{ij}$ is the infinitesimal Cauchy strain, and δ_{ij} is the Kronecker delta;

(*c*) Strain-displacement relations

$$e^{(\alpha)}_{ij}=\frac{1}{2}\ (\bar{u}^{(\alpha)}_{i,j}+\bar{u}^{(\alpha)}_{j,i}); \tag{3}$$

(*d*) Interface continuity relations

$$\bar{u}^{(1)}_i=\bar{u}^{(2)}_i,\bar{\sigma}^{(1)}_{ji}\nu^{(1)}_j=\bar{\sigma}^{(2)}_{ji}\nu^{(1)}_j\ \text{ on }\ \bar{\mathcal{I}} \tag{4}$$

where $\nu^{(1)}_1\equiv 0$ on the fiber-matrix interface $\bar{\mathcal{I}}$;

(*e*) Initial conditions at $\bar{t}=0$ and appropriate boundary data along the boundary $\partial\bar{V}$.

Conditions (*a*)–(*e*) define a well posed initial boundary value problem. However, due to the large number of fiber-matrix interfaces the direct solution to this problem is extremely difficult. The objective of the subsequent analysis is to alleviate such difficulties by deriving a set of partial differential equations with constant coefficients whose solution can be utilized to approximate the solution of the problem. To this end, it will be convenient to nondimensionalize the basic equations by using the following quantities:

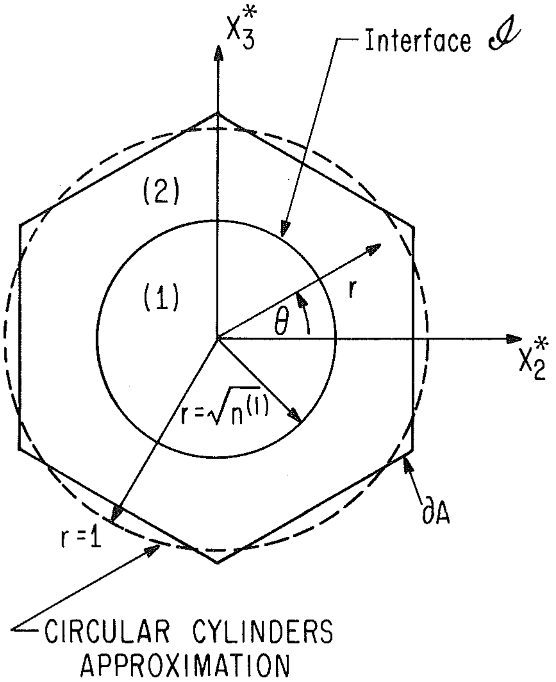

Fig. 2 A typical cell

$\bar{\Lambda}$ =	typical macrosignal wavelength
$\bar{\Delta}$ =	typical fiber spacing or cell dimension
$\bar{C}_{(m)},\bar{\rho}_{(m)}$ =	reference wave velocity and macrodensity
$\bar{E}_{(m)}\equiv\bar{\rho}_{(m)}\bar{C}^2_{(m)}$ =	reference modulus
$\bar{t}_{(m)}\equiv\bar{\Lambda}/\bar{C}_{(m)}$ =	typical macrosignal travel time
$\epsilon\equiv\bar{\Delta}/\bar{\Lambda}$ =	ratio of micro-to-macrodimensions.

With the aid of the above notation, nondimensional variables are now introduced according to

$$(x_1,x_2,x_3)=(\bar{x}_1,\bar{x}_2,\bar{x}_3)/\bar{\Lambda},\ \ t=\bar{t}/\bar{t}_{(m)},$$
$$(\lambda,\mu)^{(\alpha)}=(\bar{\lambda},\bar{\mu})^{(\alpha)}/\bar{E}_{(m)},\ \ \rho^{(\alpha)}=\bar{\rho}^{(\alpha)}/\bar{\rho}_{(m)}. \tag{5}$$

With the variables defined according to (5), the material properties are seen to be periodic in the x_2, x_3 plane in which the periodicity of the fiber lattice structure may be defined by the cell. It is expected that stress and deformation fields will vary significantly with respect to two basic length scales: (1) a "global" or "macro" length typical of the body size or loading condition, and (2) a "micro" length typical of "cell" planar dimensions. Further, it is expected that these scales will differ by at least one order of magnitude in most cases. This suggests the use of multivariable asymptotic techniques (Bensoussan, Lion, and Papanicolaou, 1978; Hegemier, Murakami, and Maewal, 1979; Sanchez-Palencia, 1980). This approach commences by introducing new independent microvariables according to

$$x_i^*\equiv x_i/\epsilon. \tag{6}$$

Therefore, all field variables are considered to be functions of the microvariables x_2^* and x_3^*, as well as the macrovariables x_i, $i=1-3$:

$$f(x_1,x_2,x_3,t)=f^*(x_1,x_2,x_3,x_2^*,x_3^*,t;\epsilon) \tag{7a}$$

Spacial derivatives of a function f then takes the form

$$\frac{\partial}{\partial x_i}f(x_k,t)=\frac{\partial}{\partial x_i}f^*(x_k,x_j^*,t;\epsilon)+\frac{1}{\epsilon}\ \frac{\partial}{\partial x_i^*}f^*(x_k,x_j^*,t;\epsilon) \tag{7b}$$

where $\partial(\ )/\partial x_1^* \equiv 0$. By introducing the notation $(\ )_{,j^*} \equiv \partial(\ )/\partial x_j^*$ equation (7b) can be rewritten as:

$$f_{,i} = f^*_{,i} + \frac{1}{\epsilon} f^*_{,i^*}. \tag{7c}$$

In the sequel f^* will be written as f for notational simplicity.

The operations (7), when applied to all field variables, lead to the following "synthesized" governing field relations:

(a) Equations of motion

$$\sigma^{(\alpha)}_{ji,j} + \frac{1}{\epsilon}\sigma^{(\alpha)}_{ji,j^*} = \rho^{(\alpha)} u^{(\alpha)}_{i,tt}, \ \ \sigma^{(\alpha)}_{ji} = \sigma^{(\alpha)}_{ij}; \tag{8}$$

(b) Constitutive relations

$$\sigma^{(\alpha)}_{ij} = \lambda^{(\alpha)}\delta_{ij} e^{(\alpha)}_{kk} + 2\mu^{(\alpha)} e^{(\alpha)}_{ij}\ ; \tag{9}$$

(c) Strain-displacement relations

$$e^{(\alpha)}_{ij} = \frac{1}{2}\left\{u^{(\alpha)}_{i,j} + u^{(\alpha)}_{j,i} + \frac{1}{\epsilon}\left(u^{(\alpha)}_{i,j^*} + u^{(\alpha)}_{j,i^*}\right)\right\}; \tag{10}$$

(d) Interface continuity conditions

$$u_i^{(1)} = u_i^{(2)}, \ \ \sigma^{(1)}_{ji}\nu^{(1)}_j = \sigma^{(2)}_{ji}\nu^{(1)}_j \ \text{ on } \mathcal{I}. \tag{11}$$

At this point, the variation of field variables which satisfy the periodicity with respect to x_i^* is assumed. According to this condition field variables take equal values on opposite sides of the cell boundary. The premise allows one to analyze a single cell in an effort to determine the distribution of any field variable with respect to the microcoordinates x_i^*. The x^*-periodicity condition is motivated by the Floquet and Block theorems (Brillouin, 1946) for harmonic wave in periodic structures. Certainly, it eliminates boundary layer effects. However, it is expected to provide a good model for the global wave phenomena in fibrous composites with periodic microstructure.

For the construction of a mixture model it is convenient to cast the field equations in a variational form by using the Reissner new mixed variational principle (Reissner, 1984). In the Reissner variational principle the variations of displacement, strain with equation (10) as definition and transverse stresses, i.e., all stress-components except $\sigma^{(\alpha)}_{11}$, are considered. Thus, it is convenient to rewrite the constitutive relation (9) in terms of the axial strain $e^{(\alpha)}_{11}$ and the transverse stresses:

$$\sigma^{(\alpha)}_{11} \equiv (\lambda + 2\mu)^{(\alpha)} e^{(\alpha)}_{11} + \lambda^{(\alpha)}\{e^{(\alpha)}_{22}(\ldots) + e^{(\alpha)}_{33}(\ldots)\},$$

$$\begin{bmatrix} e^{(\alpha)}_{22}(\ldots) \\ e^{(\alpha)}_{33}(\ldots) \end{bmatrix} \equiv \begin{bmatrix} (\lambda+2\mu)^{(\alpha)} & \lambda^{(\alpha)} \\ \lambda^{(\alpha)} & (\lambda+2\mu)^{(\alpha)} \end{bmatrix}^{-1}$$

$$\left(\begin{bmatrix} \sigma_{22} \\ \sigma_{33} \end{bmatrix}^{(\alpha)} - \lambda^{(\alpha)} e^{(\alpha)}_{11} \begin{bmatrix} 1 \\ 1 \end{bmatrix}\right),$$

$$[2e^{(\alpha)}_{23}(\ldots), 2e^{(\alpha)}_{31}(\ldots), 2e^{(\alpha)}_{12}(\ldots)]$$

$$\equiv \frac{1}{\mu^{(\alpha)}}[\sigma^{(\alpha)}_{23}, \sigma^{(\alpha)}_{31}, \sigma^{(\alpha)}_{12}] \tag{12}$$

Using the equations of motion (8), Gauss' theorem, and the x^*-periodicity condition, it can be demonstrated that the Reissner mixed variational principle, applied to the synthesized fields by the multivariable representation, takes the form:

$$\iiint_V \left[\sum_{\alpha=1}^{2} \iint_{A^{(\alpha)}} \left\{\delta e^{(\alpha)}_{11}\sigma^{(\alpha)}_{11} + \delta e^{(\alpha)}_{22}\hat\sigma^{(\alpha)}_{22} + \delta e^{(\alpha)}_{33}\hat\sigma^{(\alpha)}_{33}\right.\right.$$

$$+ 2\delta e^{(\alpha)}_{23}\hat\sigma^{(\alpha)}_{23} + 2\delta e^{(\alpha)}_{31}\hat\sigma^{(\alpha)}_{31} + 2\delta e^{(\alpha)}_{12}\hat\sigma^{(\alpha)}_{12}$$

$$+ \delta\hat\sigma^{(\alpha)}_{22}\left(u^{(\alpha)}_{2,2} + \frac{1}{\epsilon}u^{(\alpha)}_{2,2^*} - e^{(\alpha)}_{22}(\ldots)\right)$$

$$+ \delta\hat\sigma^{(\alpha)}_{33}\left(u^{(\alpha)}_{3,3} + \frac{1}{\epsilon}u^{(\alpha)}_{3,3^*} - e^{(\alpha)}_{33}(\ldots)\right)$$

$$+ \delta\hat\sigma^{(\alpha)}_{23}\left(u^{(\alpha)}_{2,3} + u^{(\alpha)}_{3,2} + \frac{1}{\epsilon}u^{(\alpha)}_{2,3^*} + \frac{1}{\epsilon}u^{(\alpha)}_{3,2^*} - 2e^{(\alpha)}_{23}(\ldots)\right)$$

$$+ \delta\hat\sigma^{(\alpha)}_{31}\left(u^{(\alpha)}_{1,3} + u^{(\alpha)}_{3,1} + \frac{1}{\epsilon}u^{(\alpha)}_{1,3^*} - 2e^{(\alpha)}_{31}(\ldots)\right)$$

$$\left.+ \delta\hat\sigma^{(\alpha)}_{12}\left(u^{(\alpha)}_{1,2} + u^{(\alpha)}_{2,1} + \frac{1}{\epsilon}u^{(\alpha)}_{1,2^*} - 2e^{(\alpha)}_{12}(\ldots)\right)\right\} dx_2^*\, dx_3^*$$

$$+ \int_{\mathcal{I}} \frac{1}{\epsilon}\{(\delta u_i^{(2)} - \delta u_i^{(1)})\,{}^{\nu}T_i^* + \delta\,{}^{\nu}T_i^*(u_i^{(2)}$$

$$\left.- u_i^{(1)})\}\, ds^*\right] dx_1\, dx_2\, dx_3$$

$$= \iiint_V \left\{\sum_{\alpha=1}^{2} \iint_{A^{(\alpha)}} \delta u_i^{(\alpha)}\right.$$

$$\left.(-\rho^{(\alpha)} u^{(\alpha)}_{i,tt})\, dx_2^*\, dx_3^*\right\} dx_1\, dx_2\, dx_3$$

$$+ \iint_{\partial V_T}\left(\sum_{\alpha=1}^{2}\iint_{A^{(\alpha)}} \delta u_i^{(\alpha)}\,{}^{\nu}T_i^{(\alpha)}\, dx_2^*\, dx_3^*\right) dA, \tag{13}$$

where $A^{(\alpha)}$ denotes the x_2^*, x_3^* domain of the cell occupied by material α (Fig. 2), $\hat\sigma^{(\alpha)}_{ij}$ is used for the approximate transverse stress, ${}^{\nu}T_i^{(\alpha)}$ denotes the traction vector on the surface ∂V_T where the traction is specified, ds^* is an infinitesimal line element on $\mathcal{I}$, and dA is an infinitesimal surface element on the boundary of $V{:}\partial V$. In (13) basic variables are the displacements $u_i^{(\alpha)}$, the transverse stresses $\hat\sigma^{(\alpha)}_{ij}$ and the interface traction vector ${}^{\nu}T_i^*$. The Euler-Lagrange equations of (13) include (8a), (11a), (12b, c), and

$${}^{\nu}T_i^* \equiv \hat\sigma^{(\alpha)}_{ji}\nu_j^{(1)} \ \text{ on } \mathcal{I}. \tag{14}$$

The above variational equation (13) furnishes a tool with which a mixture model can be obtained with appropriate trial displacement and transverse stress fields. The basic requirement for the variables is the x^*-periodicity condition on the cell boundary ∂A. The microstructural variation of the trial functions can be obtained by the asymptotic procedure (Murakami, Maewal, and Hegemier, 1981).

3 Asymptotic Analysis

The premise that the composite macrodimension is much larger than the microdimension, $\epsilon \ll 1$, and the form of scaled equations (8) and (10), suggest the expansion of the dependent variables in the asymptotic series:

$$\{u_i, \sigma_{ij}\}^{(\alpha)}(x_k, x_l^*, t; \epsilon) = \sum_{n=0}^{\infty} \epsilon^n \{u_{i(n)}, \sigma_{ij(n)}\}^{(\alpha)}(x_k, x_l^*, t). \tag{15}$$

If equation (15) is substituted into equations (8)-(11) and the coefficients of different powers of ϵ are equated to zero, a sequence of problems defined on the cell is obtained. The first of the equations in this sequence furnishes

$$u^{(\alpha)}_{i(o),j^*} = 0, \ \ \sigma^{(\alpha)}_{ji(o),j^*} = 0. \tag{16}$$

Equation (16a) implies that $u^{(\alpha)}_{i(o)}$ is independent of x_j^* and yields with the zero-th order expansion of (11a):

$$u^{(\alpha)}_{i(o)} = U_{i(o)}(x_k, t). \tag{17}$$

The remaining systems of equations obtained from equations (8)-(10) are, for $n \geq 0$:

$$\sigma^{(\alpha)}_{ji\,(n+1),\,j^*} = \rho^{(\alpha)} u^{(\alpha)}_{i(n),tt} - \sigma^{(\alpha)}_{ji(n),\,j},\ \sigma^{(\alpha)}_{ji(n)} = \sigma^{(\alpha)}_{ij(n)}, \tag{18}$$

$$\sigma^{(\alpha)}_{ij\,(n)} = \lambda^{(\alpha)} \delta_{ij} e^{(\alpha)}_{kk\,(n)} + 2\mu^{(\alpha)} e^{(\alpha)}_{ij\,(n)}, \tag{19}$$

$$e^{(\alpha)}_{ij(n)} = \frac{1}{2}\,(u^{(\alpha)}_{i(n),\,j} + u^{(\alpha)}_{j(n),i} + u^{(\alpha)}_{i(n+1),\,j^*} + u^{(\alpha)}_{j(n+1),i^*}). \tag{20}$$

To be added to the foregoing are the interface conditions and the x^*-periodicity conditions for $n \geq 0$:

$$u^{(1)}_{i(n)} = u^{(2)}_{i(n)},\ \sigma^{(1)}_{ji(n)} \nu^{(1)}_j = \sigma^{(2)}_{ji(n)} \nu^{(1)}_j \ \text{ on } \ \mathcal{I}, \tag{21}$$

$$u^{(2)}_{i(n)} \text{ and } \sigma^{(2)}_{ji(n)} \nu^{(2)}_j \text{ are } x^*\text{-periodic on } \partial A. \tag{22}$$

The first set of microboundary value problems (MBVP's) for $\sigma^{(\alpha)}_{ji(o)}$ and $u^{(\alpha)}_{i(1)}$, called the $O(1)$ MBVP's, is defined by equations (16*b*), (18*b*), (19), (20), (21*b*), (22*b*) with $n=0$, and (21*a*), (22*a*) with $n=1$. The $O(1)$ MBVP's are excited by $U_{i(o),\,j}$. Similarly, a sequence of MBVP's is defined for each n from equations (18)–(22). With appropriate integrability and normalization conditions, higher order terms may be computed by solving the MBVP's. In particular, the $O(1)$ MBVP's are the ones solved for the $O(1)$ homogenization theory proposed by Bensoussan, Lions, and Papanicolaou (1978) and Sanchez-Palencia (1980), and, also, form the basis of the mixture theory which may be classified as an $O(\epsilon)$ homogenization theory. The asymptotic approach yields the microstructures of displacement and stress fields after solving a multitude of MBVP's which are complicated.

In order to use the approximate solutions of the MBVP's in the course of developing a mixture model, and to ease the burden of solving the MBVP's exactly, a variational procedure was adopted by Murakami (1985) for laminated composites with the help of the Reissner new mixed variational principle (Reissner, 1984). A similar approach is adopted here for fibrous composites. To obtain the lowest order mixture theory by using equation (13), it is necessary to obtain trial displacement and transverse stress to $O(\epsilon)$. In the sequel, the trial functions are obtained for a hexagonal cell with a concentric cylinder approximation as shown in Fig. 2. In Fig. 2, (r, θ) are micro-polar coordinates:

$$r = \sqrt{x^{*2}_2 + x^{*2}_3}, \quad \tan\theta = x^*_3 / x^*_2, \tag{23}$$

by which $r=1$ constitutes the cell boundary and $r = \sqrt{n^{(1)}}$, denotes the interface $\mathcal{I}$. The quantities $n^{(\alpha)}$ indicate the volume fraction of material α and satisfy

$$n^{(1)} + n^{(2)} = 1. \tag{24}$$

In terms of the polar coordinates the x^*-periodicity conditions for a hexagonal cell with the concentric cylinders approximation reduce to the form:

$$f(x, r, \theta, t) = f(x_k, r, \pi + \theta, t) \text{ at } r = 1. \tag{25}$$

4 Trial Displacements and Transverse Stresses

The $O(1)$ stress and $O(\epsilon)$ displacement fields are obtained by solving the $O(1)$ MBVP's which are defined by equations (16*b*), (18*b*), (19)–(22) and (25). These MBVP's are excited by $U_{i(o),\,j}$. The exact solution of $u^{(\alpha)}_{i(1)}$ is furnished in the Appendix. For the mixture formulation it is convenient to introduce an $O(\epsilon)$ displacement variable which represents $U_{i(o),\,j} + U_{j(o),\,i}$ according to:

$$\overset{j}{S}_i(x_k, t) \equiv \frac{1}{\epsilon A} \int_{\mathcal{I}} u^{(\alpha)}_i \nu^{(1)}_j ds^* = \frac{1}{A} \int_{\mathcal{I}} u^{(\alpha)}_{i(1)} \nu^{(1)}_j ds^* \tag{26}$$

where $A(=\pi)$ is the area of the cell. Due to the fact that $u^{(\alpha)}_{i(1)}$ is excited by $U_{i(o),\,j} + U_{j(o),\,i}$ one obtains

$$\overset{3}{S}_2 = \overset{2}{S}_3. \tag{27}$$

Equation (27) can also be obtained if one substitutes the exact $u^{(\alpha)}_{i(1)}$ in Appendix A into equation (26) and eliminates $U_{i(o),\,j}$. To render the analysis tractable, it is preferable to utilize an approximate form of the exact solution for $u^{(\alpha)}_{i(1)}$. The exact solution indicates that the following form of the $O(\epsilon)$ displacement yields a good approximation:

$$u^{(\alpha)}_{i(1)}(x_k, x_{j^*}, t) = \overset{2}{S}_i(x_k, t) g^{(\alpha)}(r)\cos\theta + \overset{3}{S}_i(x_k, t) g^{(\alpha)}(r)\sin\theta \tag{28a}$$

where

$$g^{(1)}(r) = \frac{r}{n^{(1)}}\ ,\ g^{(2)}(r) = \frac{1}{n^{(2)}}\left(-r + \frac{1}{r}\right). \tag{28b}$$

Anticipating the $O(\epsilon^2)$ difference of the average of $u^{(\alpha)}_i$ on $A^{(\alpha)}$, equations (17) and (28) yield the following trial displacement field:

$$u^{(\alpha)}_i(x_k, x_{j^*}, t) = U^{(\alpha)}_i(x_k, t) + \epsilon u^{(\alpha)}_{i(1)}(x_k, x_{j^*}, t) \tag{29}$$

where $u^{(\alpha)}_{i(1)}$ is defined by equations (28). Equations (29) and (28) indicate that the mixture displacement variables are $U^{(1)}_i$, $U^{(2)}_i$, ${}^2S_i$ and ${}^3S_i$ with the constraint (27).

By using equations (29) in (19) with $n=0$ and considering the $O(\epsilon^2)$ differences of the average transverse stresses, the $O(1)$ trial stress field may be expressed as:

$$\begin{bmatrix} \hat{\sigma}_{22(o)} \\ \hat{\sigma}_{33(o)} \\ \hat{\sigma}_{23(o)} \end{bmatrix}^{(\alpha)} = \begin{bmatrix} \tau_{22}(x_k, t) \\ \tau_{33}(x_k, t) \\ \tau_{23}(x_k, t) \end{bmatrix}^{(\alpha)} + \frac{\delta_{\alpha 2}}{r^2} \left\{ t^{(2)}_{22}(x_k, t) \begin{bmatrix} \cos 2\theta \\ \cos 2\theta \\ 0 \end{bmatrix} + t^{(2)}_{33}(x_k, t) \begin{bmatrix} \cos 2\theta \\ -\cos 2\theta \\ \sin 2\theta \end{bmatrix} + t^{(2)}_{23}(x_k, t) \begin{bmatrix} \sin 2\theta \\ \sin 2\theta \\ 0 \end{bmatrix} \right\}, \tag{30a}$$

$$\begin{bmatrix} \hat{\sigma}_{31(o)} \\ \hat{\sigma}_{12(o)} \end{bmatrix}^{(\alpha)} = \begin{bmatrix} \tau_{31}(x_k, t) \\ \tau_{12}(x_k, t) \end{bmatrix}^{(\alpha)} + \frac{\delta_{\alpha 2}}{r^2} \left\{ t^{(2)}_{12}(x_k, t) \begin{bmatrix} \sin 2\theta \\ \cos 2\theta \end{bmatrix} + t^{(2)}_{31}(x_k, t) \begin{bmatrix} \cos 2\theta \\ -\sin 2\theta \end{bmatrix} \right\}. \tag{30b}$$

In order to define the $O(\epsilon)$ trial stress field it is convenient to define the $O(\epsilon)$ stress variable according to

$$P_i(x_k, t) \equiv \frac{1}{\epsilon A} \int_{\mathcal{I}} \sigma^{(\alpha)}_{ji} \nu^{(1)}_j ds^* = \frac{1}{A} \int_{\mathcal{I}} \sigma^{(\alpha)}_{ji(1)} \nu^{(1)}_j ds^*. \tag{31}$$

If one integrates (8*a*) over $A^{(\alpha)}$ and utilizes the x^*-periodicity condition, one obtains the mixture momentum equations:

$$n^{(\alpha)} \sigma^{(\alpha a)}_{ji,\,j} + (-1)^{\alpha+1} P_i = n^{(\alpha)} \rho^{(\alpha)} u^{(\alpha a)}_{i,tt} \tag{32}$$

where the average operation is defined by

$$f^{(\alpha a)}(x_k, t) \equiv \frac{1}{n^{(\alpha)} A} \iint_{A^{(\alpha)}} f^{(\alpha)}(x_k, x^*_j, t) dx^*_2 dx^*_3 \tag{33}$$

From equation (32) it can be seen that P_i represents an interaction body force between the two constituents across the interface. Also, the form of equation (32) with P_i defined by (31) satisfies the integrability condition adopted by the $O(1)$ MBVP's for $\sigma^{(\alpha)}_{ij(1)}$ which are defined by equations (18)–(20)

with appropriate n's and equation (31). As an $O(\epsilon)$ trial stress field which satisfies (31b) one may use the following approximate fields:

$$\begin{bmatrix} \hat{\sigma}_{22(1)} \\ \hat{\sigma}_{33(1)} \\ \hat{\sigma}_{23(1)} \end{bmatrix}^{(\alpha)} = \frac{1}{4}\left\{ P_2(x_k, t)g^{(\alpha)}(r) \begin{bmatrix} 3\cos\theta \\ \cos\theta \\ \sin\theta \end{bmatrix} + P_3(x_k, t)g^{(\alpha)}(r) \begin{bmatrix} \sin\theta \\ 3\sin\theta \\ \cos\theta \end{bmatrix} \right\}, \qquad (34a)$$

$$\begin{bmatrix} \hat{\sigma}_{31(1)} \\ \hat{\sigma}_{12(1)} \end{bmatrix}^{(\alpha)} = \frac{1}{2} P_1(x_k, t)g^{(\alpha)}(r) \begin{bmatrix} \sin\theta \\ \cos\theta \end{bmatrix}. \qquad (34b)$$

As a result, the trial transverse stresses are expressed as:

$$\hat{\sigma}_{ij}^{(\alpha)} \equiv \hat{\sigma}_{ij(o)}(x_k, x_l^*, t) + \epsilon\hat{\sigma}_{ij(1)}^{(\alpha)}(x_k, x^*{}_l, t) \qquad (35)$$

where $\hat{\sigma}_{ij(o)}^{(\alpha)}$ and $\hat{\sigma}_{ij(1)}^{(\alpha)}$ are defined by equations (30) and (34), respectively.

5 Mixture Equations

By substituting the displacement and transverse stress trial functions defined by equations (29) and (35), respectively, into the Reissner variational equation (13), one obtains the following relations as the Euler-Lagrange equations:

(a) Equations of motion

$$n^{(\alpha)}\sigma_{ji,j}^{(\alpha a)} + (-1)^{\alpha+1}P_i = n^{(\alpha)}\rho^{(\alpha)}U_{i,tt}^{(\alpha)}, \; i = 1-3, \qquad (36)$$

$$\overset{2}{M}_{ji,j} + \frac{1}{\epsilon^2}\left(\sigma_{2i}^{(2a)} - \sigma_{2i}^{(1a)} + R_{2i}^{(2)}\right) = I\overset{2}{S}_{i,tt}, \; i = 1,2, \qquad (37a, b)$$

$$\overset{3}{M}_{ji,j} + \frac{1}{\epsilon^2}\left(\sigma_{3i}^{(2a)} - \sigma_{3i}^{(1a)} + R_{3i}^{(2)}\right) = I\overset{3}{S}_{i,tt}, \; i = 1,3, \qquad (37c,d)$$

$$\frac{1}{2}\left(\overset{3}{M}_{j2,j} + \overset{2}{M}_{j3,j}\right) + \frac{1}{\epsilon^2}\left(\sigma_{23}^{(2a)} - \sigma_{23}^{(1a)} + R_{23}^{(2)}\right) = I\overset{3}{S}_{2,tt}. \qquad (37e)$$

where

$$\sigma_{ij}^{(\alpha a)} \equiv \frac{1}{n^{(\alpha)}A}\iint_{A^{(\alpha)}} \sigma_{ij}^{(\alpha)}\, dx_2^*\, dx_3^*,$$

$$\epsilon(\overset{2}{M}_{ij}, \overset{3}{M}_{ij}) \equiv \frac{1}{A}\sum_{\alpha=1}^{2}\iint_{A^{(\alpha)}} \sigma_{ij}^{(\alpha)} g^{(\alpha)}(\cos\theta, \sin\theta)\, dx_2^*\, dx_3^*, \qquad (38)$$

and

$$I \equiv \sum_{\alpha=1}^{2} h^{(\alpha)}\rho^{(\alpha)}, \; h^{(1)} = \frac{1}{4},$$

$$h^{(2)} = \frac{-1}{4n^{(2)}}\left(2 + n^{(2)} + \frac{2}{n^{(2)}}\ln n^{(1)}\right); \qquad (39)$$

(b) Constitutive relations

$$\begin{bmatrix} \sigma_{22} \\ \sigma_{33} \end{bmatrix}^{(\alpha a)} = \begin{bmatrix} \tau_{22} \\ \tau_{33} \end{bmatrix}^{(\alpha)} = \begin{bmatrix} \lambda + 2\mu & \lambda \\ \lambda & \lambda + 2\mu \end{bmatrix}^{(\alpha)}$$

$$\begin{bmatrix} U_{2,2}^{(\alpha)} + (-1)^{\alpha+1}\overset{2}{S}_2/n^{(\alpha)} \\ U_{3,3}^{(\alpha)} + (-1)^{\alpha+1}\overset{3}{S}_3/n^{(\alpha)} \end{bmatrix} + \lambda^{(\alpha)}U_{1,1}^{(\alpha)} \begin{bmatrix} 1 \\ 1 \end{bmatrix},$$

$$\begin{bmatrix} \sigma_{23} \\ \sigma_{31} \\ \sigma_{12} \end{bmatrix}^{(\alpha a)} = \begin{bmatrix} \tau_{23} \\ \tau_{31} \\ \tau_{12} \end{bmatrix}^{(\alpha)} = \mu^{(\alpha)}\left\{ \begin{bmatrix} U_{2,3} + U_{3,2} \\ U_{3,1} + U_{1,3} \\ U_{1,2} + U_{2,1} \end{bmatrix}^{(\alpha)} + \frac{(-1)^{\alpha+1}}{n^{(\alpha)}} \begin{bmatrix} 2\overset{3}{S}_2 \\ \overset{3}{S}_1 \\ \overset{2}{S}_1 \end{bmatrix} \right\}; \qquad (40)$$

$$\begin{aligned} P_1 &= \beta_1[(U_1^{(2)} - U_1^{(1)})/\epsilon^2 + (h/2)\{\overset{2}{S}_{1,2} + \overset{2}{S}_{2,1} + \overset{3}{S}_{3,1} + \overset{3}{S}_{1,3}\}] \\ P_2 &= \beta_2[(U_2^{(2)} - U_2^{(1)})/\epsilon^2 + \gamma\overset{2}{S}_{1,1} + h(3\overset{2}{S}_{2,2} + 2\overset{2}{S}_{2,3} + \overset{3}{S}_{3,2})/4] \\ P_3 &= \beta_3[(U_3^{(2)} - U_3^{(1)})/\epsilon^2 + \gamma\overset{3}{S}_{1,1} + h(\overset{2}{S}_{2,3} + 2\overset{3}{S}_{2,2} + 3\overset{3}{S}_{3,3})/4] \end{aligned} \qquad (41)$$

where

$$\beta_1 = 1/\left\{\sum_{\alpha=1}^{2} h^{(\alpha)}/(2\mu^{(\alpha)})\right\},$$

$$\beta_2 = \beta_3 = 1/\left\{\sum_{\alpha=1}^{2} h^{(\alpha)}(\lambda + 3\mu)^{(\alpha)}/8(\lambda + \mu)^{(\alpha)}\right\},$$

$$\gamma = \sum_{\alpha=1}^{2} h^{(\alpha)}\lambda^{(\alpha)}/2(\lambda + \mu)^{(\alpha)}, \; h = \sum_{\alpha=1}^{2} h^{(\alpha)}; \qquad (42)$$

$$\overset{2}{M}_{22} = \frac{3}{4}hP_2, \overset{2}{M}_{33} = \frac{h}{4}P_2, \overset{2}{M}_{12} = \frac{h}{2}P_1, \overset{3}{M}_{22} = \frac{h}{4}P_3,$$

$$\overset{3}{M}_{33} = \frac{3}{4}hP_3, \overset{3}{M}_{31} = \frac{h}{2}P_1,$$

$$\overset{2}{M}_{23} = \overset{2}{M}_{31} = \overset{3}{M}_{23} = \overset{3}{M}_{12} = 0 \qquad (43)$$

where it is understood that

$$\overset{2}{M}_{ij} = \overset{2}{M}_{ji}, \overset{3}{M}_{ij} = \overset{3}{M}_{ji}; \qquad (44)$$

$$R_{21}^{(2)} \equiv t_{12}^{(2)}/n^{(1)}, R_{22}^{(2)} \equiv (t_{22}^{(2)}/2 + t_{33}^{(2)})/n^{(1)}, R_{31}^{(2)} \equiv -t_{31}^{(2)}/n^{(1)},$$

$$R_{23}^{(2)} \equiv t_{23}^{(2)}/2n^{(1)}, R_{33}^{(2)} \equiv (-t_{22}^{(2)}/2 + t_{33}^{(2)})/n^{(1)} \qquad (45)$$

and

$$t_{12}^{(2)} = -\mu^{(2)}\overset{2}{S}_1/n^{(2)}, t_{31}^{(2)} = \mu^{(2)}\overset{3}{S}_1/n^{(2)},$$

$$t_{22}^{(2)} = -(\lambda + \mu)^{(2)}(\overset{2}{S}_2 - \overset{3}{S}_3)/n^{(2)}, t_{33}^{(2)} = -\mu^{(2)}(\overset{2}{S}_2 + \overset{3}{S}_3)/n^{(2)},$$

$$t_{23}^{(2)} = -(\lambda + \mu)^{(2)}(2\overset{3}{S}_2)/n^{(2)}. \qquad (46)$$

The remaining constitutive relations associated with $\sigma_{11}^{(\alpha)}$ are obtained from (12a); the results are

$$\sigma_{11}^{(\alpha a)} = (\lambda + 2\mu)^{(\alpha)}U_{1,1}^{(\alpha)} + \lambda^{(\alpha)}\{U_{2,2}^{(\alpha)} + U_{3,3}^{(\alpha)} + (-1)^{\alpha+1}(\overset{2}{S}_2 + \overset{3}{S}_3)/n^{(\alpha)}\}, \qquad (47)$$

$$\begin{bmatrix} \overset{2}{M}_{11} \\ \overset{3}{M}_{11} \end{bmatrix} = \sum_{\alpha=1}^{2} h^{(\alpha)}\left[(\lambda + 2\mu)^{(\alpha)} - \frac{\lambda^{(\alpha)2}}{(\lambda + \mu)^{(\alpha)}}\right] \begin{bmatrix} \overset{2}{S}_{1,1} \\ \overset{3}{S}_{1,1} \end{bmatrix}$$

$$+\gamma\begin{bmatrix} P_2 \\ P_3 \end{bmatrix}. \tag{48}$$

The associated boundary conditions are on ∂V

$$n^{(\alpha)}\sigma_{ji}^{(\alpha a)}\nu_j = {}^{\nu}T_i^{(\alpha p)} \quad \text{or} \quad \delta U_i^{(\alpha)} = 0 \quad , i=1,2,3, \tag{49}$$

$$\overset{2}{M}_{ji}\nu_j = {}^{2\nu}T_i \quad \text{or} \quad \delta\overset{2}{S}_i = 0 \quad , i=1,2, \tag{50a}$$

$$\overset{3}{M}_{ji}\nu_j = {}^{3\nu}T_i \quad \text{or} \quad \delta\overset{3}{S}_i = 0 \quad , i=1,3, \tag{50b}$$

$$(\overset{3}{M}_{j2} + \overset{2}{M}_{j3})\nu_j = {}^{3\nu}T_2 + {}^{2\nu}T_3 \quad \text{or} \quad \delta\overset{3}{S}_2 = 0. \tag{50c}$$

where

$${}^{\nu}T_i^{(\alpha p)} \equiv \frac{1}{A}\iint_{A^{(\alpha)}} {}^{\nu}T_i^{(\alpha)} dx_2^* \, dx_3^*,$$

$$\epsilon({}^{2\nu}T_i, {}^{3\nu}T_i) = \frac{1}{A}\sum_{\alpha=1}^{2}\iint_{A^{(\alpha)}} {}^{\nu}T_i^{(\alpha)} g^{(\alpha)}(\cos\theta, \sin\theta) dx_2^* \, dx_3^* \tag{51}$$

Equations (36)–(50) and the initial conditions

$$U_i^{(\alpha)}, U_{i,t}^{(\alpha)}, \overset{j}{S}_i, \overset{j}{S}_{i,t} \text{ at } t=0 \text{ on } V \tag{52}$$

define a well posed initial boundary value problem with respect to time t and the macrocoordinates x_k.

6 Harmonic Wave Dispersion Spectra

In an attempt to test the accuracy of the mixture model, the phase velocity and group velocity spectra of the mixture theory have been compared with available experimental data for time harmonic waves. For the comparison harmonic waves which are propagating at an arbitrary angle of incidence in a full space of the following form are considered:

$$\begin{aligned}&[U_1^{(1)}, U_1^{(2)}, U_2^{(1)}, U_2^{(2)}, U_3^{(1)}, U_3^{(2)}, \\ &\quad \overset{2}{S}_1/ik, \overset{2}{S}_2/ik, 2\overset{3}{S}_2/ik, \overset{3}{S}_1/ik, \overset{3}{S}_3/ik]^T \\ &= \exp\{ik(x_1\cos\phi + x_2\sin\phi\cos\theta + x_3\sin\phi\sin\theta) - i\omega t\}\mathbf{U}^*\end{aligned} \tag{53}$$

where

$$\begin{aligned}\mathbf{U}^* = [&\overset{*}{U}{}_1^{(1)}, \overset{*}{U}{}_1^{(2)}, \overset{*}{U}{}_2^{(1)}, \overset{*}{U}{}_2^{(2)}, \overset{*}{U}{}_3^{(1)}, \\ &\overset{*}{U}{}_3^{(2)}, \overset{2}{s}_1, \overset{2}{s}_2, 2\overset{3}{s}_2, \overset{3}{s}_1, \overset{3}{s}_3]^T\end{aligned} \tag{54}$$

and $[\ ]^T$ denotes the transpose of $[\ ]$. In equation (53) $\overset{*}{U}{}_i^{(\alpha)}$ and ${}^{j}s_i$ are constant amplitudes, k denotes the wave number, ω represents angular frequency, ϕ is the azimuth measured from the x_1 axis, and θ is the longitude; the direction of the wave propagation may be best represented by the wave vector $\mathbf{k}$:

$$\mathbf{k} = k[\cos\phi, \sin\phi\cos\theta, \sin\phi\sin\theta]^T, \tag{55}$$

Substitution of (53) into equations (36) and (37), which are expressed by the displacement variables with equations (40)–(48), yields an eigenvalue problem for $\epsilon\omega$ of the form:

$$[K]\overset{*}{\mathbf{U}} = (\epsilon\omega)^2[M]\overset{*}{\mathbf{U}} \tag{56}$$

where $[K]$ and $[M]$ are 11 × 11 real symmetric matrices, the elements of which are functions of the mixture constants and the wave vector. Furthermore, $[M]$ is a diagonal matrix. Upon calculation of the eigenvalue $\epsilon\omega$ for a given ϵk, one obtains the phase velocity C_p as

$$C_p = (\epsilon\omega)/(\epsilon k). \tag{57}$$

For each computed eigen pairs $(\epsilon\omega, \overset{*}{\mathbf{U}})_j$, $j = 1,2, \ldots 11$ the group velocity

$$C_g = \frac{d\omega}{dk} \tag{58}$$

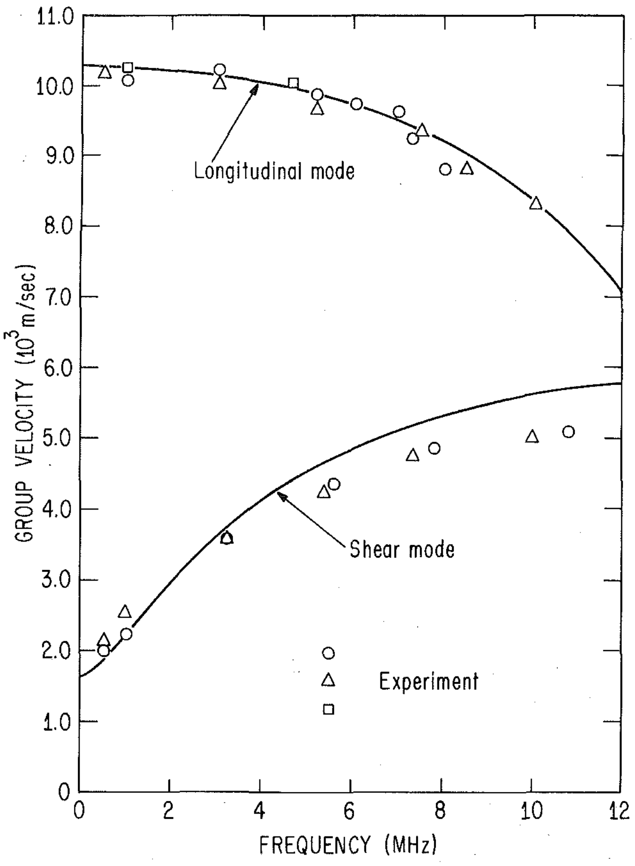

Fig. 3 Group velocity spectra of waveguide modes for a boron/epoxy composite (Tauchert and Guzelsu, 1972)

Table 1 Material properties of the boron/epoxy composite tested by Tauchert and Guzelsu (1972)

	Volume Fraction $n^{(\alpha)}$	Young's Modulus $\bar{E}^{(\alpha)}$	Poisson's Ratio $\nu^{(\alpha)}$	Mass Density $\bar{\rho}^{(\alpha)}$
$^{(1)}$Boron	0.54	379.2 GPa (55 × 10^6 psi)	0.18	2682 kg/m^3 (251 × 10^{-6} *lb* sec^2/*in*^{4})
$^{(2)}$Epoxy	0.46	5.033 GPa (0.73 × 10^6 psi)	0.40	1261 kg/m^3 (118 × 10^{-6} *lb* sec^2/*in*^{4})

Table 2 Material properties of the tungsten/aluminum composite tested by Sutherland and Lingle (1972)

	Volume Fraction $n^{(\alpha)}$	Young's Modulus $\bar{E}^{(\alpha)}$	Poisson's Ratio $\nu^{(\alpha)}$	Mass Density $\bar{\rho}^{(\alpha)}$
$^{(1)}$Tungsten	0.022	398 GPa	0.28	19194 kg/m^3
$^{(2)}$Aluminum	0.978	71.0 GPa	0.34	2700 kg/m^3

can be obtained by taking the derivative of equation (56) with respect to ϵk:

$$[K']_j\overset{*}{\mathbf{U}}_j = \{2(\epsilon\omega)C_g[M] + (\epsilon\omega)^2[M']\}_j\overset{*}{\mathbf{U}}_j. \tag{59}$$

For the jth eigenpair equation (59) yields

$$(C_g)_j = \frac{\overset{*}{\mathbf{U}}{}^T\{[K'] - (\epsilon\omega)^2[M']\}\overset{*}{\mathbf{U}}}{2(\epsilon\omega)_j(\overset{*}{\mathbf{U}}{}^T[M]\overset{*}{\mathbf{U}})_j}. \tag{60}$$

In the subsequent simulation a typical cell dimension $\tilde{\Delta}$ was

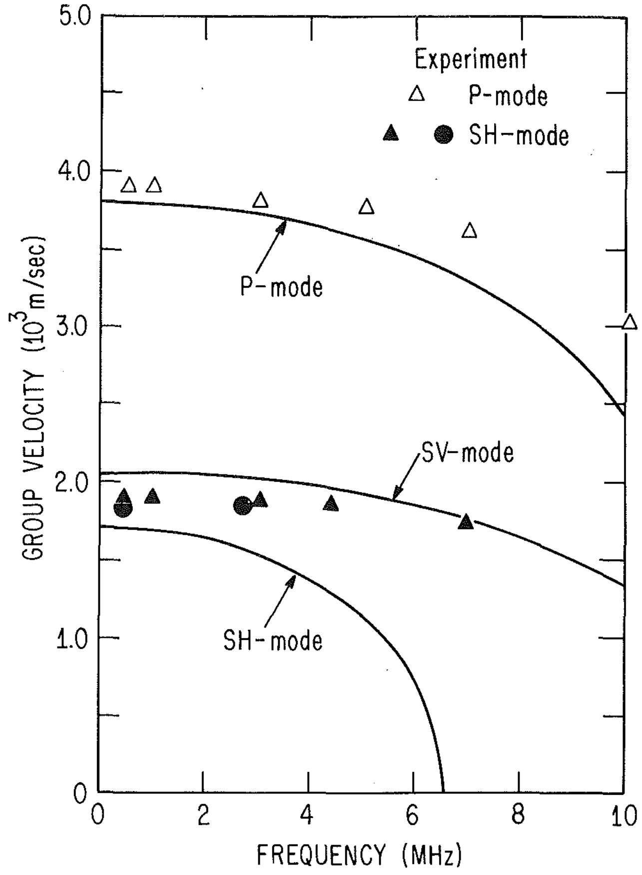

Fig. 4 Group velocity spectra of wavereflect modes for a boron/epoxy composite (Tauchert and Guzelsu, 1972)

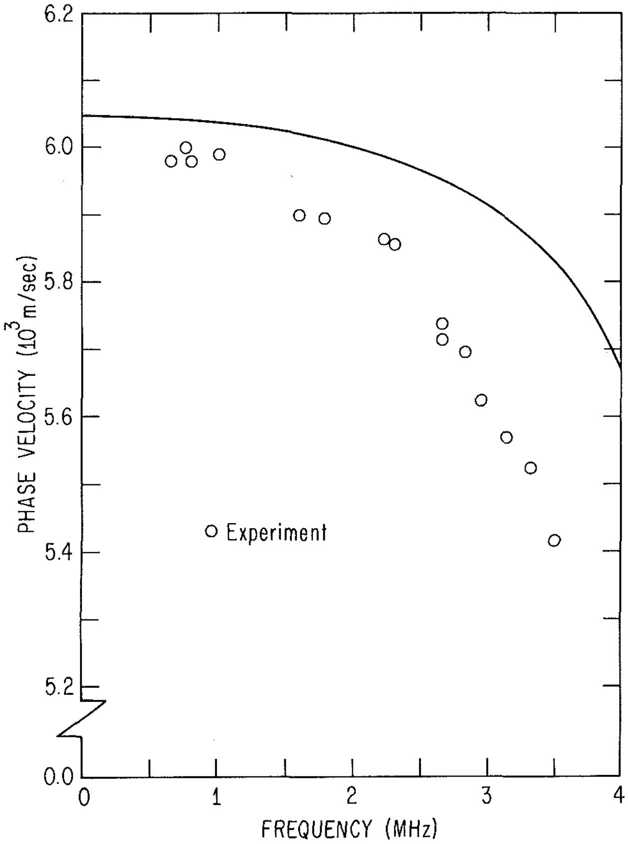

Fig. 5 A phase velocity spectrum of a longitudinal wavereflect mode for tungsten/aluminum composite (Sutherland and Lingle, 1972)

Table 3 Comparison of effective moduli of a boron/aluminum unidirectionally fiber-reinforced composite

	Data[a]	Mixture Model	Square Cell[a] Model	Hexagonal Cell[a] Model
$E_{11}^{(m)}$	2.450	2.551	2.480	2.551
$E_{22}^{(m)}$	1.825	1.868	1.856	1.872
$E_{23}^{(m)}$	0.779	0.661	-----	0.661
$E_{12}^{(m)}$	0.604	0.578	----	0.578
$E_{44}^{(m)}$	0.526	0.604	-----	0.606
$E_{55}^{(m)}$	0.566	0.559	0.451	0.561

[a] After Datta and Ledbetter (1983)

chosen to be a cell radius by introducing the concentric cylinders approximation of the equal area. The reference elastic modulus and density used for the scaling are

$$\bar{E}_{(m)} = \sum_{\alpha=1}^{2} n^{(\alpha)} \bar{E}^{(\alpha)}, \ \bar{\rho}_{(m)} = \sum_{\alpha=1}^{2} n^{(\alpha)} \bar{\rho}^{(\alpha)} \tag{61}$$

where $\bar{E}^{(\alpha)}$ is Young's modulus. The dimensional frequency $\nu(Hz)$ can be computed from $\epsilon\omega$ by

$$\nu = (\epsilon\omega)\sqrt{\bar{E}_{(m)}/\bar{\rho}_{(m)}}/(2\pi\bar{\Delta}). \tag{62}$$

Numerical results are presented for a boron-epoxy composite, for which experimental results were presented by Tauchert and Guzelsu (1972) for a waveguide case $\phi = 0$ deg and a wavereflect case $\phi = 90$ deg. The material properties are summarized in Table 1 in which the values for Poisson's ratio are estimated. In the simulation $\bar{\Delta}$ was computed from the fiber diameter $(= 2\sqrt{n^{(1)}}\bar{\Delta})$ which was 1.016×10^{-4} m. The group velocity spectra for a waveguide case $\phi = \theta = 0$ deg are shown in Fig. 3 for two acoustic modes: a "gross" longitudinal model and a "gross" shear mode. In the figure the same symbols as the reference of Tauchert and Guzelsu are used for the experimental data points. It is noted that reasonable agreement is achieved for the waveguide case in which pronounced dispersion is observed. The group velocity spectra for a wavereflect case $\phi = 90$ deg, $\theta = 0$ deg in which the wave vector is normal to the fiber axis are shown in Fig. 4 with the experimental data. The figure includes three acoustic modes: a "gross" longitudinal wave (*P*-mode), a "gross" vertically polarized shear wave (SV-mode), and a "gross" horizontally polarized shear wave (SH-mode). The sets of experimental data correspond to the "gross" P-mode and the "gross" SH-mode. It is noted that there are significant deviations from the "gross" SH-mode, but the overall agreement is not unsatisfactory if one admits the scarcity of the experimental data and the difficulties associated with the measurement of shear wave velocities. It was reported by Tauchert and Guzelsu (1972) that a shear wave exhibited extremely high damping of the pulse. A similar observation and the scatter of shear wave data were reported by Sachse (1974) who conducted modulus measurements of boron/epoxy composites by using pulse-echo techniques. He concluded that "the measurement of the present investigation indicate that shear waves propagating along and across fibers in the composite materials tested do not always propagate at the same speed."

Sutherland and Lingle (1972) reported phase velocity measurements for tungsten/aluminum composites whose material properties are shown in Table 2. The equivalent cell radius $\bar{\Delta}$ was computed from the given fiber spacings which yield the area of a typical cell $\bar{A}(= \pi\bar{\Delta}^2)$ 0.579×10^{-6} m^2. Figure 5 shows the phase velocity versus frequency relation for the "gross" longitudinal mode. Reasonable agreement is observed between the experimental data and the theoretical prediction.

7 Effective Moduli

The $O(1)$ homogenization theory which yields the effective moduli of composites can be obtained by taking the limit of $\epsilon \rightarrow 0$ and equating the constituents' displacements

$$U_i^{(1)} = U_i^{(2)} = U_i \tag{63}$$

By introducing the above constraints, equations (36) yield

$$\sigma_{ji,j}^{(m)} = \rho^{(m)} U_{i,tt} \tag{64}$$

where

$$\sigma_{ij}^{(m)} = \sum_{\alpha=1}^{2} n^{(\alpha)} \sigma_{ij}^{(\alpha a)}, \ \rho^{(m)} = \sum_{\alpha=1}^{2} n^{(\alpha)} \rho^{(\alpha)}. \tag{65}$$

Equations (37) yield

$$\sigma_{2i}^{(2a)} - \sigma_{2i}^{(1a)} + R_{2i}^{(2)} = 0, \ i = 1,2,3 \tag{66a}$$

$$\sigma_{3i}^{(2a)} - \sigma_{3i}^{(1a)} + R_{3i}^{(2)} = 0, \ i = 1,3. \tag{66b}$$

By eliminating ${}^jS_i$ by equations (66), equations (65a), (40), and (47) with (63) furnish

$$\boldsymbol{\sigma}^{(m)} = [E^{(m)}]\mathbf{e}^{(m)} \tag{67}$$

where

$$\boldsymbol{\sigma}^{(m)} = [\sigma_{11}^{(m)}, \sigma_{22}^{(m)}, \sigma_{33}^{(m)}, \sigma_{23}^{(m)}, \sigma_{31}^{(m)}, \sigma_{12}^{(m)}]^T,$$

$$\mathbf{e}^{(m)} = [U_{1,1}, U_{2,2}, U_{3,3}, U_{2,3} + U_{3,2}, U_{3,1} + U_{1,3}, U_{1,2} + U_{2,1}]^T, \tag{68}$$

and $[E^{(m)}]$ is the effective modulus matrix with transverse isotropy due to the concentric cylinders approximation and is defined in Appendix B.

The formulas for the effective moduli (B2) are assessed by comparing the results with the experimental data reported by Datta and Ledbetter (1983) for boron/aluminum composites. The results are shown in Table 3 in which the moduli computed from the effective stiffness theories for the square cell by Achenbach (1976) and for the hexagonal cell by Hlaváček (1975) are included by using the formulas reported by Datta and Ledbetter (1983). The comparison has revealed that all high-order theories yield almost similar results. It can be easily shown that the formulas for the effective moduli yield values which fall between the upper and the lower bounds obtained by Hashin and Rosen (1964) for fiber-reinforced composites.

8 Concluding Remarks

An asymptotic mixture theory with multiple scales was applied to unidirectionally fiber-reinforced elastic composites with periodic microstructure. In the model construction, Reissner's new mixed variational principle was applied to the synthesized fields with multivariable field representations. In order to assess the accuracy of the model the mixture dispersion spectra were compared with the experimental data obtained for the boron/epoxy composite by Tauchert and Guzelsu (1972) and for the tungsten/aluminum composite by Sutherland and Lingle (1972).

A satisfactory correlation with the experimental data indicates that the proposed mixture model furnishes a basic tool by which dynamic responses of the composite structures can be investigated.

Acknowledgment

The research was supported by the Office of Naval Research under Contract N00014-84-K-0468 to the University of California at San Diego. The authors are grateful to Dr. A. S. Kushner for his support.

References

Aboudi, J., 1981, "Generalized Effective Stiffness Theory for the Modeling of Fiber-Reinforced Composites," *International Journal of Solids and Structures*, Vol. 17, pp. 1005–1018.

Aboudi, J., 1982, "A Continuum Theory for Fiber-Reinforced Elastic-Viscoplastic Composites," *International Journal of Engineering Science*, Vol. 20, pp. 605–621.

Aboudi, J., 1985, "The Effective Thermomechanical Behavior of Inelastic Fiber-Reinforced Materials," *International Journal of Engineering Science*, Vol. 23, pp. 773–787.

Achenbach, J. D., and Herrmann, G., 1968, "Dispersion of Free Harmonic Waves in Fiber-Reinforced Composites," *AIAA Journal*, Vol. 6, pp. 1832–1836.

Achenbach, J. D., 1976, "Generalized Continuum Theory for Directionally Reinforced Solids," *Archives of Mechanics*, Vol. 28, pp. 257–278.

Bartholomew, R. A., and Torvick, P. J., 1972, "Elastic Wave Propagation in Filamentary Composite Materials," *International Journal of Solids and Structures*, Vol. 8, pp. 1389–1405.

Bensoussan, A., Lions, J. L., and Papanicolaou, G., 1978, *Asymptotic Analysis for Periodic Structures*, North-Holland Publishing Co., Amsterdam.

Brillouin, L., 1946, *Wave Propagation in Periodic Structures*, Dover Publication Inc., New York.

Datta, S. K., and Ledbetter, H. M., 1983, "Elastic Constants of Fiber-Reinforced Boron-Aluminum: Observation and Theory," *International Journal of Solids and Structures*, Vol. 19, pp. 885–894.

Hashin, Z., and Rosen, B. W., 1968, "The Elastic Moduli of Fiber-Reinforced Materials," ASME JOURNAL OF APPLIED MECHANICS, Vol. 31, pp. 223–232.

Hegemier, G. A., and Gurtman, G. A., 1974, "Finite-Amplitude Elastic-Plastic Wave Propagation in Fiber-Reinforced Composites," *Journal of Applied Physics*, Vol. 45, pp. 4245–4261.

Hegemier, G. A., Gurtman, G. A., and Nayfeh, A. H., 1973, "A Continuum Mixture Theory of Wave Propagation in Laminated and Fiber Reinforced Composites," *International Journal of Solids and Structures*, Vol. 9, pp. 395–414.

Hegemier, G. A., Murakami, H., and Maewal, A., 1979, "On Construction of Mixture Theories for Composite Materials by the Method of Multi-Variable Asymptotic Expansion," *Proceedings of the Third International Symposium on Continuum Models of Discrete Systems*, Freudenstadt, Germany, pp. 423–441.

Hlaváček, M., 1975, "A Continuum Theory for Fiber-Reinforced Composites," *International Journal of Solids and Structures*, Vol. 11, pp. 199–217.

Martin, S. E., Bedford, A., and Stern, M., 1971, "Steady State Wave Propagation in Fiber Reinforced Elastic Materials," *Proceedings of the 12th Midwestern Mechanics Conference, Developments in Mechanics*, Vol. 6, pp. 515–528.

Murakami, H., 1985, "A Mixture Theory for Wave Propagation in Angle-Ply Laminates, Part 1: Theory," ASME JOURNAL OF APPLIED MECHANICS, Vol. 52, pp. 331–337.

Murakami, H., Maewal, A., and Hegemier, G. A., 1979, "Mixture Theory for Longitudinal Wave Propagation in Unidirectional Composites with Cylindrical Fibers of Arbitrary Cross-Section – I. Formulation," *International Journal of Solids and Structures*, Vol. 15, pp. 325–334.

Murakami, H., Maewal, A., and Hegemier, G. A., 1981, " A Mixture Theory with a Director for Linear Elastodynamics of Periodically Laminated Media," *International Journal of Solids and Structures*, Vol. 17, pp. 155–173.

Nayfeh, A. H., 1977, "Thermomechanically Induced Interfacial Stresses in Fibrous Composites," *Fiber Science and Technology*, Vol. 10, pp. 195–209.

Nayfeh, A. H., Crane, R. L., and Hoppe, W. L., 1984, "Reflection of Acoustic Waves from Water/Composite Interfaces," *Journal of Applied Physics*, Vol. 55, pp. 685–689.

Reissner, E., 1984, "On a Certain Mixed Variational Theorem and a Proposed Application," *International Journal for Numerical Methods in Engineering*, Vol. 20, pp. 1366–1368.

Sachse, W., 1974, "Measurement of the Elastic Moduli of Continuous-Filament and Eutectic Composite Materials," *Journal of Composite Materials*, Vol. 8, pp. 378–390.

Sanchez-Palencia, E., 1980, *Non-Homogeneous Media and Vibration Theory*, Lecture Notes in Physics 127, Springer-Verlag, Berlin.

Sutherland, H. J., and Lingle, R., 1972, "Geometric Dispersion of Acoustic Waves by a Fibrous Composite," *Journal of Composite Materials*, Vol. 6, pp. 490–502.

Tauchert, T. R., and Guzelsu, A. N., 1972, "An Experimental Study of Dispersion of Stress Waves in a Fiber-Reinforced Composite," ASME JOURNAL OF APPLIED MECHANICS, Vol. 39, pp. 98–102.

APPENDIX A

Exact $u_{i(1)}^{(\alpha)}$ of the $O(1)$ MBVP's

$$\begin{aligned} u_{1(1)}^{(\alpha)} &= Gg^{(\alpha)}(r)\{(U_{1(0),2} + U_{2(0),1})\cos\theta + (U_{3(0),1} + U_{1(0),3})\sin\theta\}, \\ u_{2(1)}^{(\alpha)} &= b_o(U_{2(0),2} + U_{3(0),3} + \hat{\lambda} U_{1(0),1}) g^{(\alpha)}(r)\cos\theta \\ &+ a_2^{(\alpha)}[\{g^{(\alpha)}(r)\cos\theta + \hat{\kappa}^{(\alpha)} g_{II}^{(\alpha)}(r)\cos 3\theta\}(U_{2(0),2} - U_{3(0),3}) \\ &\quad + \{g^{(\alpha)}(r)\sin\theta + \hat{\kappa}^{(\alpha)} g_{II}^{(\alpha)}(r)\sin 3\theta\}(U_{2(0),3} + U_{3(0),2})] \end{aligned}$$

$$
\begin{aligned}
&+ b_2^{(\alpha)}[\{3(1-\hat{\kappa}^{(\alpha)})g_I^{(\alpha)}(r)\cos\theta + (1\\
&+ \hat{\kappa}^{(\alpha)})g_{III}^{(\alpha)}(r)\cos 3\theta\}(U_{2(0),2} - U_{3(0),3})\\
&+ \{3(1-\kappa^{(\alpha)})g_I^{(\alpha)}(r)\sin\theta + (1\\
&+ \hat{\kappa}^{(\alpha)})g_{III}^{(\alpha)}(r)\sin 3\theta\}(U_{2(0),3} + U_{3(0),2})],\\
u_{3(1)}^{(\alpha)} &= b_o(U_{2(0),2} + U_{3(0),3} + \hat{\lambda} U_{1(0),1})g^{(\alpha)}(r)\sin\theta\\
&+ a_2^{(\alpha)}[\{g^{(\alpha)}(r)\sin\theta - \hat{\kappa}^{(\alpha)} g_{II}^{(\alpha)}\sin 3\theta\}(-U_{2(0),2} + U_{3(0),3})\\
&+ \{g^{(\alpha)}(r)\cos\theta - \hat{\kappa}^{(\alpha)} g_{II}^{(\alpha)}(r)\cos 3\theta\}(U_{2(0),3} + U_{3(0),2})]\\
&+ b_2^{(\alpha)}[\{3(1-\kappa^{(\alpha)})g_I^{(\alpha)}(r)\sin\theta - (1\\
&+ \kappa^{(\alpha)})g_{III}^{(\alpha)}(r)\sin 3\theta\}(-U_{2(0),2} + U_{3(0),3})\\
&+ \{3(1-\kappa^{(\alpha)})g_I^{(\alpha)}(r)\cos\theta - (1\\
&+ \kappa^{(\alpha)})g_{III}^{(\alpha)}(r)\cos 3\theta\}(U_{2(0),3} + U_{3(0),2})] \qquad (A1)
\end{aligned}
$$

where

$$
\begin{aligned}
b_o &\equiv \{(\lambda+\mu)^{(2)} - (\lambda+\mu)^{(1)}\}/(2d_1),\\
&d_1 \equiv \sum_{\alpha=1}^{2} (\lambda+\mu)^{(\alpha)}/n^{(\alpha)} + \mu^{(2)}/(n^{(1)}n^{(2)}),\\
G &\equiv -(\mu^{(1)} - \mu^{(2)})/d_3, d_3 \equiv \sum_{\alpha=1}^{2} \mu^{(\alpha)}/n^{(\alpha)} + \mu^{(2)}/(n^{(1)}n^{(2)}),\\
\hat{\lambda} &\equiv (\lambda^{(1)} - \lambda^{(2)})/\{(\lambda+\mu)^{(1)} - (\lambda+\mu)^{(2)}\}\\
\kappa^{(\alpha)} &\equiv (\lambda+2\mu)^{(\alpha)}/\mu^{(\alpha)}, \hat{\kappa}^{(\alpha)} \equiv (1-\kappa^{(\alpha)})/(1+\kappa^{(\alpha)}) \qquad (A2)\\
g_I^{(1)}(r) &= g_{III}^{(1)}(r) = r^3,\ g_{II}^{(1)}(r) = 0\\
g_I^{(2)}(r) &= -r^3 + r^{-1},\ g_{II}^{(2)}(r) = (-r^{-1} + r^{-3})/n^{(2)},\\
g_{III}^{(2)}(r) &= r^3 - (1+\kappa^{(2)})^{-2}\{4(1-\kappa^{(2)} + {\kappa^{(2)}}^2)r^{-3}\\
&\qquad - 3(1-\kappa^{(2)})^2 r^{-1}\}. \qquad (A3)
\end{aligned}
$$

In equations $(A1)$ $a_2^{(\alpha)}$ and $b_2^{(\alpha)}$ are obtained by solving the linear equations for $\mathbf{x} = [a_2^{(1)}, b_2^{(1)}, a_2^{(2)}, b_2^{(2)}]^T$:

$$
\underset{4\times 4}{[A]}\ \underset{4\times 1}{\mathbf{x}} = \underset{4\times 1}{\mathbf{B}} \qquad (A4)
$$

where

$$
\begin{aligned}
A_{11} &= 1, A_{21} = 0, A_{31} = \mu^{(1)}/n^{(1)}, A_{41} = 0\\
A_{12} &= 3(1-\kappa^{(1)}){n^{(1)}}^2,\ A_{22} = (1+\kappa^{(1)}){n^{(1)}}^2\\
A_{32} &= -A_{42} = 3n^{(1)}\mu^{(1)}(1-\kappa^{(1)}),\quad A_{13} = -1,\\
A_{23} &= -\hat{\kappa}^{(2)}/n^{(1)},\\
A_{33} &= \mu^{(2)}/n^{(2)}\{1 - \hat{\kappa}^{(2)}/n^{(1)}\},\ A_{43} = 3\hat{\kappa}^{(2)}\mu^{(2)}/{n^{(1)}}^2\\
A_{14} &= -3n^{(2)}(1+n^{(1)})(1-\kappa^{(2)})\\
A_{24} &= (1+\kappa^{(2)}){n^{(1)}}^2 - (4-3n^{(1)})(1-\kappa^{(2)} + {\kappa^{(2)}}^2)\\
&\qquad /\{n^{(1)}(1+\kappa^{(2)})\}\\
A_{34} &= 3\mu^{(2)}(1-\kappa^{(2)})(n^{(1)} - \hat{\kappa}^{(2)}/n^{(1)})\\
A_{44} &= -3\mu^{(2)}(1-\kappa^{(2)})(n^{(1)} + 3\hat{\kappa}^{(2)}/n^{(1)})\\
&\qquad + 12\mu^{(2)}(1-\kappa^{(2)} + {\kappa^{(2)}}^2)/\{{n^{(1)}}^2(1+\kappa^{(2)})\}, \qquad (A5)
\end{aligned}
$$

and

$$
B_1 = B_2 = B_4 = 0,\ B_3 = -(\mu^{(1)} - \mu^{(2)})/2. \qquad (A6)
$$

It is interesting to note that for most of practical composites $b_2^{(\alpha)}$, $\alpha = 1,2$ are small compared with $a_2^{(\alpha)}$.

APPENDIX B

The Definition of $[E^{(m)}]$ in (67)

$$
\begin{bmatrix} \sigma_{11}\\ \sigma_{22}\\ \sigma_{33}\\ \sigma_{23}\\ \sigma_{31}\\ \sigma_{12} \end{bmatrix}^{(m)}
=
\begin{bmatrix}
E_{11} & E_{12} & E_{12} & 0 & 0 & 0\\
E_{12} & E_{22} & E_{23} & 0 & 0 & 0\\
E_{12} & E_{23} & E_{22} & 0 & 0 & 0\\
0 & 0 & 0 & E_{44} & 0 & 0\\
0 & 0 & 0 & 0 & E_{55} & 0\\
0 & 0 & 0 & 0 & 0 & E_{55}
\end{bmatrix}^{(m)}
\begin{bmatrix} U_{1,1}\\ U_{2,2}\\ U_{3,3}\\ U_{2,3} + U_{3,2}\\ U_{3,1} + U_{1,3}\\ U_{1,2} + U_{2,1} \end{bmatrix}
\qquad (B1)
$$

where

$$
\begin{aligned}
E_{11}^{(m)} &= \sum_{\alpha=1}^{2} n^{(\alpha)}(\lambda+2\mu)^{(\alpha)} - (\lambda^{(1)} - \lambda^{(2)})^2/d_1,\\
E_{12}^{(m)} &= \sum_{\alpha=1}^{2} n^{(\alpha)}\lambda^{(\alpha)} - (\lambda^{(1)} - \lambda^{(2)})\{(\lambda+\mu)^{(1)} - (\lambda+\mu)^{(2)}\}/d_1,\\
E_{22}^{(m)} &= \sum_{\alpha=1}^{2} n^{(\alpha)}(\lambda+2\mu)^{(\alpha)} - \{(\lambda+\mu)^{(1)}\\
&\qquad - (\lambda+\mu)^{(2)}\}^2/d_1 - (\mu^{(1)} - \mu^{(2)})^2/d_2,\\
E_{23}^{(m)} &= \sum_{\alpha=1}^{2} n^{(\alpha)}\lambda^{(\alpha)} - \{(\lambda+\mu)^{(1)}\\
&\qquad - (\lambda+\mu)^{(2)}\}^2/d_1 + (\mu^{(1)} - \mu^{(2)})^2/d_2,\\
E_{44}^{(m)} &= (E_{22}^{(m)} - E_{23}^{(m)})/2,\\
E_{55}^{(m)} &= \sum_{\alpha=1}^{2} n^{(\alpha)}\mu^{(\alpha)} - (\mu^{(1)} - \mu^{(2)})^2/d_3, \qquad (B2)
\end{aligned}
$$

and where

$$
d_2 = \sum_{\alpha=1}^{2} \mu^{(\alpha)}/n^{(\alpha)} + (\lambda+\mu)^{(2)}/(2n^{(1)}n^{(2)}). \qquad (B3)
$$

Shear Stress Intensity Factors for a Planar Crack With Slightly Curved Front

Huajian Gao
James R. Rice
Division of Applied Sciences,
Harvard University,
Cambridge, Mass. 02138

Recent work (Rice, 1985a) has presented the calculations of the first order variation in an elastic displacement field associated with arbitrary incremental planar advance of the location of the front of a half-plane crack in a loaded elastic full space. That work also indicated the relation of such calculations to a three-dimensional weight function theory for crack analysis and derived an expression for the distribution of the tensile mode stress intensity factor along a slightly curved crack front, to first order accuracy in the deviation of the crack front location from a reference straight line. Here we extend the results on stress intensity factors to the shear modes, solving to similar first order accuracy for the in-plane (Mode 2) and antiplane (Mode 3) shear stress intensity factors along a slightly curved crack front. Implications of results for the configurational stability of a straight crack front are discussed. It is also shown that the concept of line tension, while qualitatively useful in characterizing the crack extension force (energy release rate) distribution exerted on a tough heterogeneity along a fracture path as the crack front begins to curve around it, does not agree with the exact first order effect that is derived here.

Introduction

For a half-plane crack lying in an infinite space, the stress intensity factors due to point force pairs acting on the crack surface have been derived by many authors (Uflyand, 1965; Sih and Liebowitz, 1968; Kassir and Sih, 1973; Bueckner, 1977; Meade and Keer, 1984a; etc) in the case when the crack front lies along a straight line. Hence, by integration, the solution due to arbitrary loading on the crack surface can be found.

Rice (1985a) showed how the knowledge of such solutions enables one to calculate the changes in crack surface displacement distribution, exact to the first order in the deviation of the crack front position from a reference straight line, when the crack front position is altered slightly to lie along a general curved arc in the same plane as that of the crack. He gave full details for the case of tensile (Mode 1) loading and derived an expression for the stress intensity factor K_1 along such a nonstraight crack front (again, exact to the first order). The latter work was motivated by the interesting approach to the wavy crack front problem based on asymptotic expansions by Meade and Keer (1984b), although it turned out that their results required correction.

Here we carry through details of the slightly curved crack front analysis for general shear loading, deriving the analogous expressions for the inplane (Mode 2) and antiplane (Mode 3) stress intensity factors, K_2 and K_3, along a nonstraight crack front.

Crack Surface Displacement

We now present the basic equation for crack surface displacements associated with incremental crack growth, following Rice (1985a).

An infinite, homogeneous, isotropic elastic solid contains a half-plane crack with a straight crack front and is subjected to an "original" load system, consisting of some fixed forces and/or imposed boundary displacements, that induces mixed modes with distributions $K_\alpha^0(z')$ of stress intensity factors along the crack front. Here $\alpha = 1, 2, 3$ and z' denotes the location along the crack front. A Cartesian x, y, z coordinate system is attached such that the crack plane lies on $y = 0$ and the z axis lies along the crack front (Fig. 1).

Now imagine that the original loading is supplemented by a set of concentrated force pairs $\pm P_j$, $j = x, y, z$, acting at $x, 0^+, z$ and $x, 0^-, z$ resulting in opening, inplane shear and antiplane shear relative displacements of the crack surface. Let $\Delta u_j(x, z)$ be the relative displacements of crack surfaces at the load location. (These are unbounded for point forces; see Rice (1985a) for a refinement of the argument by distributing the forces over finite discs whose radius is later allowed to approach zero.) Suppose that under the combined load system described, the crack front is advanced normal to itself by some infinitesimal variable distance $\delta a(z')$, where z' is the location

---

Contributed by the Applied Mechanics Division for presentation at the Winter Annual Meeting, Anaheim, CA, December 7-12, 1986, of The American Society of Mechanical Engineers.

Discussion on this paper should be addressed to the Editorial Department, ASME, United Engineering Center, 345 East 47th Street, New York, N.Y. 10017, and will be accepted until two months after final publication of the paper itself in the JOURNAL OF APPLIED MECHANICS. Manuscript received by ASME Applied Mechanics Division, September 20, 1985; *final revision, April 14, 1986.* Paper No. 86-WA/APM-43.

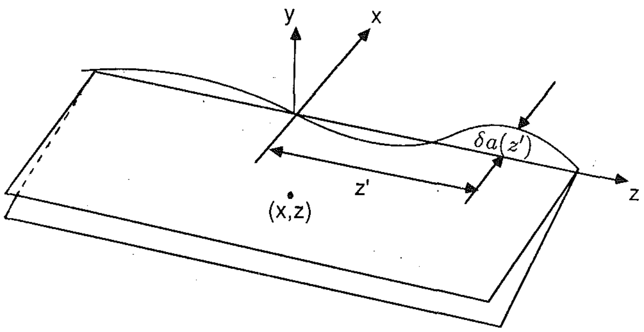

Fig. 1 Half-plane crack on $y = 0$ in an infinite elastic body. Reference straight crack front along z axis; z' denotes location along front and $\delta a(z')$ denotes advance of crack location in the plane $y = 0$

along the front. The change in strain energy U plus the potential energy V_0 of the fixed forces of the "original load system", associated with incremental crack growth and/or variation of the point force amplitudes P_j, is

$$\delta(U+V_0)=P_j\delta[\Delta u_j(x,z)]-\int_{-\infty}^{+\infty}G(z')\delta a(z')dz' \qquad (1)$$

($j = x, y, z$; summation implied on repeated j.)

Here G is the energy release rate per unit crack area of elastic fracture mechanics, and by Irwin's relation

$$G=(1-\nu^2)(K_1^2+K_2^2)/E+(1+\nu)K_3^2/E \qquad (2)$$

(E = Young's modulus, ν = Poisson's ratio.)

Since U and V_0 can depend only on the P_j (or Δu_j) and the location of the crack front, the right-hand side of equation (1) is a perfect differential. Rice (1985a) then showed, using a Legendre transformation and the reciprocal property of coefficients in perfect differentials, that the variation of surface displacemnets due to incremental crack front advance under fixed applied forces is

$$\begin{aligned}\delta[\Delta u_j(x,z)]&=\int_{-\infty}^{+\infty}\frac{\partial G(P_j;z')}{\partial P_j}\,\delta a(z')dz'\\&=\int_{-\infty}^{+\infty}\Bigg(2\,\frac{1-\nu^2}{E}\Bigg[K_1(P_j;z')\,\frac{\partial K_1(P_j;z')}{\partial P_j}\\&\qquad+K_2(P_j;z')\,\frac{\partial K_2(P_j;z')}{\partial P_j}\Bigg]\\&+2\,\frac{1+\nu}{E}\,K_3(P_j;z')\,\frac{\partial K_3(P_j;z')}{\partial P_j}\Bigg)\delta a(z')dz' \qquad (3)\end{aligned}$$

Here the derivations of G and the K_α with respect to the P_j are taken with a fixed position of the crack front. Letting the P_j = 0, one has

$$K_\alpha(0;z')=K_\alpha^0(z')$$

$$\partial K_\alpha(0;z')/\partial P_j=k_{\alpha j}(z';x,z)$$

($\alpha = 1, 2, 3, j = x, y, z$) where $K_\alpha^0(z')$ is the mode α stress intensity factor induced along the reference straight crack front by the original loading while $k_{\alpha j}$ is the mode α stress intensity factor induced by a unit force pair at (x, 0^+, z) and (x, 0^-, z) in the ±j directions. Thus equation (3) becomes

$$\begin{aligned}\delta[\Delta u_j(x,z)]&=\int_{-\infty}^{+\infty}\Bigg(\frac{2(1-\nu^2)}{E}\,[k_{1j}(z';x,z)K_1^0(z')\\&\qquad+k_{2j}(z';x,z)K_2^0(z')]\\&+\frac{2(1+\nu)}{E}\,k_{3j}(z';x,z)K_3^0(z')\Bigg)\delta a(z')dz' \qquad (4)\end{aligned}$$

Equation (4) is the first order variation of $\Delta u_j(x,z)$ when the crack advances by $\delta a(z')$ in presence of the original load system only. In fact, equation (4) can be regarded as a special version of a general three-dimensional relation in Rice's (1972) formulation (see Rice 1985 a, b also), based on displacement field variations associated with incremental crack growth, of the theory of Bueckner's (1970, 1972, 1977) "weight functions" for crack analysis.

As we stated before, $k_{\alpha j}$ can be found for the present half-plane crack configuration from many sources in the literature, and they are also listed in the form

$$k_{1x}=k_{1z}=k_{2y}=k_{3y}=0$$

$$k_{1y}=k=\frac{(-2x/\pi^3)^{1/2}}{[x^2+(z'-z)^2]}$$

$$k_{2x}=\left[1+\frac{2\nu}{2-\nu}\,\frac{x^2-(z'-z)^2}{x^2+(z'-z)^2}\right]k$$

$$k_{3z}=\left[1-\frac{2\nu}{2-\nu}\,\frac{x^2-(z'-z)^2}{x^2+(z'-z)^2}\right]k$$

$$k_{2z}=k_{3x}=-\frac{4\nu}{2-\nu}\,\frac{x(z'-z)}{x^2+(z'-z)^2}\,k \qquad (5)$$

by Rice (1985a).

Shear Mode Stress Intensity Factors

Substituting equations (5) into equation (4), for the shear displacements we obtain

$$\begin{aligned}\delta[\Delta u_x(x,z)]&=\frac{8(1-\nu^2)}{E}\left(-\frac{x}{2\pi}\right)^{1/2}\Bigg[\frac{1}{2\pi}\int_{-\infty}^{+\infty}\frac{K_2^0(z')}{x^2+(z'-z)^2}\\&\qquad\left(1+\frac{2\nu}{2-\nu}\,\frac{x^2-(z'-z)^2}{x^2+(z'-z)^2}\right)\delta a(z')dz'\\&\qquad-\frac{2\nu}{\pi(2-\nu)(1-\nu)}\int_{-\infty}^{+\infty}\frac{K_3^0(z')x(z'-z)}{[x^2+(z'-z)^2]^2}\,\delta a(z')dz'\Bigg]\\\delta[\Delta u_z(x,z)]&=\frac{8(1+\nu)}{E}\left(-\frac{x}{2\pi}\right)^{1/2}\Bigg[\frac{1}{2\pi}\int_{-\infty}^{+\infty}\frac{K_3^0(z')}{x^2+(z'-z)^2}\\&\qquad\left(1-\frac{2\nu}{2-\nu}\,\frac{x^2-(z'-z)^2}{x^2+(z'-z)^2}\right)\delta a(z')dz'\\&\qquad-\frac{2\nu(1-\nu)}{\pi(2-\nu)}\int_{-\infty}^{+\infty}\frac{K_2^0(z')x(z'-z)}{[x^2+(z'-z)^2]^2}\,\delta a(z')dz'\Bigg] \qquad (6)\end{aligned}$$

correct to first order in $\delta a(z')$.

Very near the crack front the stress intensity factors are related to the relative displacements by the asymptotic formulae

$$\Delta u_n(x,z)=\frac{8(1-\nu^2)}{E}\left(\frac{r}{2\pi}\right)^{1/2}K_2+0[(r)^{3/2}]$$

$$\Delta u_t(x,z)=\frac{8(1+\nu)}{E}\left(\frac{r}{2\pi}\right)^{1/2}K_3+0[(r)^{3/2}] \qquad (7)$$

where n and t are the normal and tangential directions along the curved crack front (Fig. 2), with n lying in the x, z plane, and r is the distance as measured from the crack front in the negative normal direction (Fig. 2). Denoting the angle between the normal and the x direction (very small) by ϕ, we find from geometric relations that

$$-r\cos\phi=x-\delta a(z),\ \tan\phi=\mathrm{d}[\delta a(z)]/dz \qquad (8)$$

Now consider a particular z at which $\delta a(z) = 0$ but $d[\delta a(z)]/dz$ exists. Then the first of equations (6) becomes, when $x \to 0^-$,

$$\delta[\Delta u_x(x,z)]\sim\frac{8(1-\nu^2)}{E}\left(-\frac{x}{2\pi}\right)^{1/2}[\ldots]$$

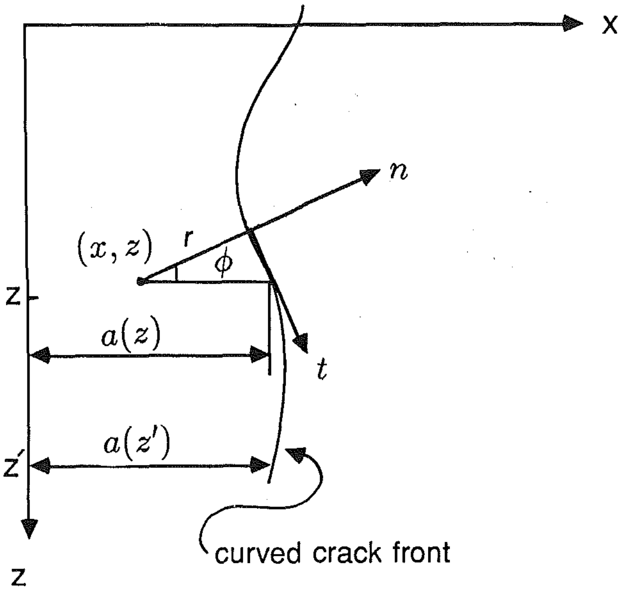

Fig. 2 Normal (*n*) and tangential (*t*) directions for deviated half-plane crack

where now the bracketed terms of equation (6) have reduced to

$$[\ldots]=\frac{1}{2\pi}\,\frac{2-3\nu}{2-\nu}\,PV\int_{-\infty}^{+\infty}\frac{K_2^0(z')\delta a(z')}{(z'-z)^2}\,dz'$$

$$+\frac{\nu}{(2-\nu)(1-\nu)}\,K_3^0(z)\,\frac{d[\delta a(z)]}{dz} \tag{9}$$

and where the PV in the first term of equation (9) denotes the principal value in the Cauchy sense.

Equation (9) can be proven as follows. Breaking the $\int_{-\infty}^{+\infty}$ in the first of equation (6) into $\int_{-\infty}^{z-\eta}+\int_{z-\eta}^{z+\eta}+\int_{z+\eta}^{+\infty}$, the $[\int_{-\infty}^{z-\eta}+\int_{z+\eta}^{+\infty}]$ part, when letting $x\to 0^-$ and then $\eta\to 0$, gives the PV term in (9) above, whereas the remaining $\int_{z-\eta}^{z+\eta}$ part of the bracketed term in equation (6) becomes

$$\frac{1}{2\pi}\int_{z-\eta}^{z+\eta}\frac{K_2^0(z')}{x^2+(z'-z)^2}\left[1+\frac{2\nu}{2-\nu}\,\frac{x^2-(z'-z)^2}{x^2+(z'-z)^2}\right]\delta a(z')dz'$$

$$-\frac{2\nu}{\pi(2-\nu)(1-\nu)}\int_{z-\eta}^{z+\eta}\frac{K_3^0(z')x(z'-z)}{[x^2+(z'-z)^2]^2}\,\delta a(z')dz'$$

Let us now observe that

$$K_\alpha^0(z')\delta a(z')=K_\alpha^0(z)\,\frac{d[\delta a(z)]}{dz}\,(z'-z)+O[(z'-z)^2]$$

and that the error term $O\,[(z'-z)^2]$ will have a bound of form $|O\,[(z'-z)^2]|\le B(z'-z)^2$ on $z-\eta\le z'\le z+\eta$ for some finite $B>0$. Then since the term linear in $(z'-z)$ gives zero contribution to the first integral above, i.e., to the integral involving K_2^0, we have

$$\left|\frac{1}{2\pi}\int_{z-\eta}^{z+\eta}\frac{K_2^0(z')}{x^2+(z'-z)^2}\left[1+\frac{2\nu}{2-\nu}\,\frac{x^2-(z'-z)^2}{x^2+(z'-z)^2}\right]\delta a(z')dz'\right|$$

$$\le\frac{B}{2\pi}\int_{z-\eta}^{z+\eta}\frac{(z'-z)^2}{x^2+(z'-z)^2}\left[1+\frac{2\nu}{2-\nu}\right]dz'<\frac{2+\nu}{2-\nu}\,\frac{B}{\pi}\,\eta$$

for any x. Hence, letting $x\to 0^-$ and then $\eta\to 0$, the upper bound on the first integral, and therefore the integral itself, vanishes. In the same limit the second integral, involving K_3^0, becomes with the substitution $z'-z=-tx$

$$\frac{2\nu}{\pi(2-\nu)(1-\nu)}\int_{-\infty}^{+\infty}\frac{t^2}{(1+t^2)^2}\,dtK_3^0(z)\,\frac{d[\delta a(z)]}{dz}$$

$$=\frac{\nu}{(2-\nu)(1-\nu)}\,K_3^0(z)\,\frac{d[\delta a(z)]}{dz}$$

We thus have the two contributions noted in equation (9), the PV term from $[\int_{-\infty}^{z-\eta}+\int_{z+\eta}^{+\infty}]$ $(\eta\to 0^+)$, which represents the influence of the rest of the nonstraight crack front on the special point z at which $\delta a(z)=0$, and the term involving $K_3^0(z)$ from $\int_{z-\eta}^{z+\eta}$ which represents the coupling effect due to local slope. The sum of these two is given as equation (9). In the above argument we have implicitly assumed, in writing the error terms as $O\,[(z'-z)^2]$, that $K_\alpha^0(z')\delta a(z')$ has a good second derivative at z. However, the steps leading to equation (9) above, and equation (10) below, may be justified under weaker assumption that the first derivative of $K_\alpha^0(z')\delta a(z')$ exists and is merely Holder continuous at z, such that the bounded term above may be written as $B|z'-z|^{1+\epsilon}$ where $0<\epsilon\le 1$.

Similary, when $x\to 0^-$ the second of equation (6) reduces to

$$\delta[\Delta u_z(x,z)]\sim\frac{1+\nu}{E}\left(-\frac{x}{2\pi}\right)^{1/2}[\ldots]$$

where now

$$[\ldots]=\frac{1}{2\pi}\,\frac{2+\nu}{2-\nu}\,PV\int_{-\infty}^{+\infty}\frac{K_3^0(z')\delta a(z')}{(z'-z)^2}\,dz'$$

$$+\frac{\nu(1-\nu)}{2-\nu}\,K_2^0(z)\,\frac{d[\delta a(z)]}{dz} \tag{10}$$

in which we can also observe the coupling due to local slope.

To find $\delta[\Delta u_x(x,z)]$ and $\delta[\Delta u_z(x,z)]$ near some location z along the crack front where $\delta a(z)\neq 0$, we use the concept developed by Rice (1985a) of relocating the reference straight crack front by moving it along the x direction an amount equal to $\delta a(z)$. Then, redefining the origin of the x axis so that $x=0$ along the relocated reference straight crack tip, we have $\delta a(z)=0$ at the location z considered and can use the results just given above. Note that the reference straight crack location is aribtrary, so that we can locate it at will. In other words we always choose the reference straight crack as the one that when $x\to 0^-$ we approach simultaneously both the reference straight crack and the actual front. This is equivalent to interpreting $\delta a(z')$ in the above formulae as $a(z')-a(z)$, where $x=a(z)$ is the slightly curved arc describing the crack front location relative to any convenient choice of origin for the x axis, and interpreting $d[\delta a(z)]/dz$ as $da(z)/dz$. In using this notation one also needs expressions for the stress intensity factors induced at location z along the crack front when the front is straight but located at a general x coordinate, say, $x=a$. We let the functions $K_\alpha^0[z;a]$, $\alpha=1,2,3$, denote these distributions. Then, at a given point x, z on the crack faces, equations (9) and (10) become

$$\delta[\Delta u_x(x,z)]\sim\frac{8(1-\nu^2)}{E}\left[\frac{a(z)-x}{2\pi}\right]^{1/2}\times$$

$$\left\{\frac{1}{2\pi}\,\frac{2-3\nu}{2-\nu}\,PV\int_{-\infty}^{+\infty}\frac{K_2^0[z';a(z)][a(z')-a(z)]}{(z'-z)^2}\,dz'\right.$$

$$\left.+\frac{\nu}{(2-\nu)(1-\nu)}\,K_3^0[z;a(z)]\,\frac{da(z)}{dz}\right\}$$

and

$$\delta[\Delta u_z(x,z)]\sim\frac{8(1+\nu)}{E}\left[\frac{a(z)-x}{2\pi}\right]^{1/2}\times$$

$$\left\{\frac{1}{2\pi}\,\frac{2+\nu}{2-\nu}\,PV\int_{-\infty}^{+\infty}\frac{K_3^0[z';a(z)][a(z')-a(z)]}{(z'-z)^2}\,dz'\right.$$

$$\left.+\frac{\nu(1-\nu)}{(2-\nu)}\,K_2^0[z;a(z)]\,\frac{da(z)}{dz}\right\} \tag{11}$$

to first order in $a(z')-a(z)$ and in $da(z)/dz$. These last equations are now understood to represent the change in surface displacement at a point x, z very near crack front in going from the hypothetical reference state, in which the crack front is everywhere straight and of depth equal to that at z, to the actual state in which the crack front is curved.

Referring to Fig. 2, we can get the relative displacement components in the normal and tangential directions along the crack front in terms of $\Delta u_z(x, z)$ and $\Delta u_x(x, z)$,

$$\begin{aligned}\Delta u_n(x,z) &= \Delta u_x(x,z)\cos\phi - \Delta u_z(x,z)\sin\phi\\ \Delta u_t(x,z) &= \Delta u_x(x,z)\sin\phi + \Delta u_z(x,z)\cos\phi \qquad (12)\end{aligned}$$

As ϕ is small for a small perturbation we have to the first order

$$\begin{aligned}\Delta u_n(x,z) &= \Delta u_x - \Delta u_z da(z)/dz\\ \Delta u_t(x,z) &= \Delta u_z + \Delta u_x da(z)/dz \qquad (13)\end{aligned}$$

In equations (13) we now write Δu_x as $(\Delta u_x)^0 + \delta(\Delta u_x)$ and Δu_z as $(\Delta u_z)^0 + \delta(\Delta u_z)$, where $(\Delta u_x)^0$ and $(\Delta u_z)^0$ are the near-tip crack face displacements in the reference straight crack front configuration and, again, $\delta(\Delta u_x)$ and $\delta(\Delta u_z)$ are the variations of equation (11) due to the crack front being curved, i.e., due to the crack front advancing by $\delta a(z') = a(z') - a(z)$:

$$\begin{aligned}\Delta u_n(x,z) &= (\Delta u_x)^0 + \delta[\Delta u_x] - (\Delta u_z)^0 da(z)/dz\\ \Delta u_t(x,z) &= (\Delta u_z)^0 + \delta[\Delta u_z] + (\Delta u_x)^0 da(z)/dz \qquad (14)\end{aligned}$$

Everything here is exact to first order in $\delta a(z)$. Comparing these expressions, as evaluated with the help of equations (11), to equations (7) (and recognizing that $r = a(z) - x$ to first order) we get the stress intensity factors K_2 and K_3 to first order when the crack front deviates from a reference straight line. The results, supplemented for completeness with the result for the Mode 1 stress intensity factor derived by Rice (1985a), are as follows:

$$K_1(z) = K_1^0[z;a(z)] + \frac{1}{2\pi} PV\int_{-\infty}^{+\infty} \frac{K_1^0[z';a(z)][a(z')-a(z)]}{(z'-z)^2}\,dz'$$

$$K_2(z) = K_2^0[z;a(z)] - \frac{2}{2-\nu} K_3^0[z;a(z)]\,\frac{da(z)}{dz} + \frac{1}{2\pi}\,\frac{2-3\nu}{2-\nu}\, PV\int_{-\infty}^{+\infty} \frac{K_2^0[z';a(z)][a(z')-a(z)]}{(z'-z)^2}\,dz'$$

$$K_3(z) = K_3^0[z;a(z)] + \frac{2(1-\nu)}{2-\nu} K_2^0[z;a(z)]\,\frac{da(z)}{dz} + \frac{1}{2\pi}\,\frac{2+\nu}{2-\nu}\, PV\int_{-\infty}^{+\infty} \frac{K_3^0[z';a(z)][a(z')-a(z)]}{(z'-z)^2}\,dz' \qquad (15)$$

Equations (15) are not consistent with the stress intensity factors presented for this case by Meade and Keer (1984b) as

$$\begin{aligned}K_1(z) &= K_1^0[z;a(z)]\\ K_2(z) &= K_2^0[z;a(z)] - K_3^0[z;a(z)]da(z)/dz\\ K_3(z) &= K_3^0[z;a(z)] + K_2^0[z;a(z)]da(z)/dz \qquad (16)\end{aligned}$$

Rice (1985a, just after his equation (65)), explained the source of oversight in the Meade and Keer results for Mode 1, in that Meade and Keer assumed in their asymptotic analysis a double scaling of the z dependence of the solution but not of the x and y dependence; in fact, just the opposite was found to be true in the solution developed (without *a priori* assumptions on scaling) by Rice. Similar remarks apply to the Meade and Keer results for Modes 2 and 3.

The results of equations (15) for $K_\alpha(z)$ can be inserted into equation (2) to compute the energy release rate $G(z)$ along the slightly curved crack front. When this is done and we retain only those terms consistent with first order accuracy in $a(z') - a(z)$ and $da(z)/dz$, we find that the cross terms involvig $da(z)dz$ in equations (15) cancel one another. A specific illustration of this is given in the next section.

It may sometimes prove convenient to rewrite the various principal value integrals of equation (15) by the rearrangement, following from integration by parts,

$$PV\int_{-\infty}^{+\infty} \frac{K_\alpha^0[z';a(z)][a(z')-a(z)]}{(z'-z)^2}\,dz'$$

$$= PV\int_{-\infty}^{+\infty} \frac{K_\alpha^0[z';a(z)]da(z')/dz' + [a(z')-a(z)]\partial K_\alpha^0[z';a(z)]/\partial z'}{(z'-z)}\,dz'$$

The last term of the second numerator vanishes when, as in the next section, we consider loadings which would induce uniform K_α along a straight crack front.

Cosine-Wave Crack Front; Configurational Stability

Now we apply the results in equations (15) to the case of a wavy crack front with the profile

$$a(z) = a_0 + A\cos(2\pi z/\lambda) \qquad (17)$$

where $A/\lambda << 1$, a_0 is arbitrary and $\lambda > 0$. It is assumed for convenience that the stress intensity factors induced along the reference straight crack are uniform along the crack front i.e., $K_\alpha^0[z;a] = K_\alpha^0[a]$. Going through some algebraic calculations and further assuming that $(AdK^0/da)/K^0 << 1$, we get the results to the first order in A

$$K_1(z) = K_1[a_0] + \left[\frac{dK_1^0[a_0]}{da_0} - \pi K_1^0[a_0]/\lambda\right] A\cos\left(\frac{2\pi z}{\lambda}\right)$$

$$K_2(z) = K_2[a_0] + \left[\frac{dK_2^0[a_0]}{da_0} - \frac{2-3\nu}{2-\nu}\,\pi K_2^0[a_0]/\lambda\right] A\cos\left(\frac{2\pi z}{\lambda}\right) + \frac{4\pi}{2-\nu}(A/\lambda)K_3^0[a_0]\sin\left(\frac{2\pi z}{\lambda}\right)$$

$$K_3(z) = K_3[a_0] + \left[\frac{dK_3^0[a_0]}{da_0} - \frac{2+\nu}{2-\nu}\,\pi K_3^0[a_0]/\lambda\right] A\cos\left(\frac{2\pi z}{\lambda}\right) - \frac{4\pi(1-\nu)}{2-\nu} K_2^0[a_0](A/\lambda)\sin\left(\frac{2\pi z}{\lambda}\right) \qquad (18)$$

From equations (18) we observe that when both shear modes are present the extremal values of a given shear stress intensity factor do not occur at the extremal locations of the crack front where $\cos(2\pi z/\lambda) = \pm 1$.

We may also compute the energy release rate G, defined by equation (2), along the perturbed crack front from the results just given for the K_α. Consistent with the first order accuracy in A, the result is

$$G(z) = G^0[a_0] + \{dG^0[a_0]/da_0 - 2\pi F[a_0]/\lambda\}A\cos(2\pi z/\lambda) \qquad (19)$$

Here

$$G^0[a_0] = \frac{1-\nu^2}{E}\left\{(K_1^0[a_0])^2 + (K_2^0[a_0])^2 + \frac{1}{1-\nu}(K_3^0[a_0])^2\right\} \qquad (20)$$

and

$$F[a_0] = \frac{1-\nu^2}{E}\left\{(K_1^0[a_0])^2 + \frac{2-3\nu}{2-\nu}\,(K_2^0[a_0])^2 + \frac{2+\nu}{(2-\nu)(1-\nu)}\,(K_3^0[a_0])^2\right\} \qquad (21)$$

Note that the extrema of $G(z)$ do coincide with the extrema of $a(z)$ since the sine terms of equation (18) have cancelled one another.

We have not been able to find an energetic interpretation for F in equation (21) but we can confirm that the result derived for $G(z)$ in equation (19) is not compatible with a string-like model with a "line tension" effect, as used frequently to analyze curved dislocation lines. In particular, G is sometimes called the "crack extension force" since it is the generalized force, in the sense of equation (1), conjugate to crack growth. One might optimistically hope that the effect of curvature on the crack extension force would be analogous to the effect of curvature on a string under tension. Such would form a useful conceptual picture of, e.g., the crack extension force distribution exerted as a crack front meets and begins to surround a localized, hard-to-fracture heterogeneity lying in the path of the advancing crack. However, while the string model is qualitatively correct in predicting the proper sign of the effect of curvature shown in equation (19), it fails quantitatively since elementary calculations show that a line tension model would require a $1/\lambda^2$ effect for a cosine wave rather than the proper $1/\lambda$ effect that we have derived.

Rice (1985a) considered the configurational stability of quasi-static tensile mode crack growth (e.g., by fatigue or corrosion) by observing that if the crack growth rate is an increasing function of K_1, then the amplitude of a cosine component of $a(z)$ will grow if the maxima of $K_1(z)$ and $a(z)$ are in phase but decay if they are out of phase. Thus, from the first of equations (18), disturbances of wavelength λ in the crack front profile will decay in amplitude during crack growth if

$$dK_1^0[a_0]/da_0 < \pi K_1^0[a_0]/\lambda \qquad (22)$$

This is met for all λ when $dK_1^0/da_0 < 0$ and will be met for sufficiently small λ when $dK_1^0/da_0 > 0$. It generally turns out that the critical λ values, λ_{cr}, at which the inequality fails (e.g., $\lambda_{cr} = 2\pi L$ for an edge crack of depth L in a large body under remote tensile loading) are sufficiently large that the model of a half plane crack in an infinite body is inappropriate to analyze perturbations of those wavelengths; the actual finite body dimensions must be considered instead for a suitable analysis. Thus we conclude that planar crack growth should be configurationally stable to perturbations involving wavelengths that are small compared to overall body or crack dimensions. This seems to be generally in accord with experience in that cracks, when approximately planar, in subcritical growth are generally observed to have fronts that lie along smoothly curving arcs at the macroscale and to be devoid of structure except for that directly relatable to microstructure heterogeneity or large scale plastic flow. See, e.g., Colangelo and Heiser (1974, chapter 4).

The stability issue is less readily addressed under general mixed-mode loadings as we have analyzed them here since a mixed-mode crack will seldom grow along a plane. One case which may meet that condition of planarity involves the tectonic shear crack whose slip surface is channeled by a preexisting fault plane. If in that case or others it is approriate to describe crack advance under mixed-mode loading by a unique (independent of mode combination) increasing relation between G and the crack growth rate, then it is evident by comparing equations (19) to the first of equation (18) that a similar stability condition to that for Mode 1 growth will result. In particular, crack position $a(z)$ and $G(z)$ will be out of phase, thus smoothing out initial irregularities during growth, for wavelengths λ satisfying

$$dG^0[a_0]/da_0 < 2\pi F[a_0]/\lambda \qquad (23)$$

This reduces to equation (22) for pure Mode 1 conditions.

Meade and Keer (1984b) emphasized that crack front segmentation is observed in laboratory study of brittle materials under combined Mode 1 and Mode 3 loading. They suggest that this may be attributed to the coupling effect between the shear modes. For example, as is evident from the exact first order results in equations (15), or in equations (18) for the cosine wave, and as is also seen in the less complete Meade and Keer results reported here as equations (16), Mode 3 loading induces a Mode 2 stress intensity wherever $da(z)/dz \neq 0$. This induced K_2 reverses sign with the change in sign of $da(z)/dz$ in going from one side to the other of a localized protrusion. This change in sign of K_2 is expected to promote deviations from planarity of opposite sense (up versus down relative to the y direction) on the two sides of the protrusions during tensile crack growth, so that localized protrusions of the crack front grow into nonplanar segments. It is not yet clear how to test this proposed mechanism against observations.

Acknowledgments

The work reported was supported by the ONR Mechanics Division contract N00014-85-K-0405, USGS Earthquake Hazards Reduction Program grant 14-08-0001-G1167, and NSF Earth Sciences Division grant EAR-84-11201.

References

Bueckner, H. F., 1970, "A Novel Principle for the Computation of Stress Intensity Factors," *Zeitschrift fuer angewandte Mathematik und Mechanik*, Vol. 50, pp. 529–546.

Bueckner, H. F., 1972, "Field Singularities and Related Integral Representations," *Mechanics of Fracture 1: Methods of Analysis and Solution of Crack Problems*, Sih, G. C., ed., Noordhoff, Leyden, pp. 329–314.

Bueckner, H. F., 1977, 'The Weight Functions of Mode I of the Penny-Shaped and of the Elliptic Crack," *Fracture Mechanics and Technology*, Sih, G. C., and Chow, eds., Vol. II, pp. 1069–1107, Sijthoff and Noordhoff publishers.

Colangelo, V. J., and Heiser, F. A., 1974, *Analysis of Metallurgical Failures*, Wiley, New York.

Kassir, M. K., and Sih, G. C., 1973, "Application of Papkovich-Neuber Potentials to a Crack Problem," *International Journal of Solids and Structures*, Vol. 9, pp. 643–645.

Meade, K. P., and Keer, L. M., 1984a, "On the Problem of a Pair of Point Forces Applied to the Faces of a Semi-Infinite Plane Crack," *Journal of Elasticity*, Vol. 14, pp. 3–14.

Meade, K. P., and Keer, L. M., 1984b, "Stress Intensity Factors for Semi-infinite Plane Crack with a Wavy Front," *Journal of Elasticity*, Vol. 14, pp. 79–92.

Rice, J. R., 1972, "Some Remarks on Elastic Crack Tip Stress Fields," *International Journal of Solids and Structures*, Vol. 8, pp. 751–758.

Rice, J. R., 1985a, "First Order Variations in Elastic Fields Due to Variation in Location of a Planar Crack Front," ASME *Journal of Applied Mechanics*, Vol. 52, pp. 571–579.

Rice, J. R., 1985b, "Three Dimensional Elastic Crack Tip Interactions with Transformation Strains and Dislocations," *International Journal of Solids and Structures*, Vol. 21, pp. 781–791.

Sih, G. C., and Liebowitz, H., 1968, "Mathematical Theories of Brittle Fracture," *Treatise on Fracture*, Liebowitz, H., ed., Vol. II, Academic Press, New York, pp. 67–190.

Uflyand, Y. S., 1965, "Survey of Articles on the Application of Integral Transforms in the Theory of Elasticity," *North Carolina State University, Department of Applied Mathematics Research Group*, File No. PSR-24/6, Raleigh, N.C.

The Effect of Surface Depressions on Conformal and Nonconformal Contact Pressure Distributions

H. H. Chen

K. M. Marshek

Department of Mechanical Engineering,
University of Texas at Austin,
Austin, Texas 78712

This paper presents a numerical method for analyzing the stress concentration around one or several shallow longitudinal surface depressions. The modified iterative method and modified influence function are used in conjunction with an automatic mesh generation technique to avoid solving the ill-condition of the large scale linear system and therefore a wide range of contact problems having multiply-connected regions can be solved. The effect of the blending radius and the pit size on the stress concentration for a pitted copper cylinder contacting an elastic half space are examined. The conformal pressure distributions for a smooth steel journal contacting a self-lubricated bearing with various radial clearances and material properties are also determined. The numerical results show that the smaller the blend radii, the higher the stress concentration for a given pit size. A large deviation from the Hertzian solution is observed for a surface with large pits because of the loss of pressure supporting area. The results of the analysis provides a design tool for predicting the magnitude and location of the peak stress for the rolling and sliding contact elements.

1 Introduction

The Hertz contact theory was developed based on the conditions that (1) the contacting surfaces are frictionless, (2) the bodies are homogeneous and isotropic, (3) the undeformed surface profiles near the point of contact are continuous and may each be represented by a second degree polynomial, (4) the bodies are isothermal and free of any internal stresses caused by plastic strain, and (5) the dimensions of the deformed contact area are small compared to the radii of the undeformed contact surfaces. Contact problems are classified as nonconformal, if condition (3) is violated. If the applied load produces a contact area with dimensions nearly equal to the radii of curvature of the undeformed surfaces and thus the contact patch cannot be approximated by a plane (i.e., condition (5) is also violated), the problem is classified as a conformal contact problem. Some examples of the conformal contact problem are self-lubricated journal bearings, connecting joints in robotic manipulators, pistons sliding in cylinders, and worn surface bodies in sliding contact.

Small surface depressions can cause high stress concentrations and therefore rapid surface fatigue failure. Because of the limitations of Hertzian contact theory, contact problems involving surface depressions have received little attention in the literature. Experimental work (Bayer, 1968; Beagley, 1976; Littman and Widner, 1966; Marshek, 1979) has shown that repeated stressing beyond the endurance strength in rolling or sliding contact can result in the formation of fatigue cracks on or near the surface, which will propagate until pieces of the surface material break out, leaving pits or spalls. Repeated loading might also cause furrow-shape depressions on the surface.

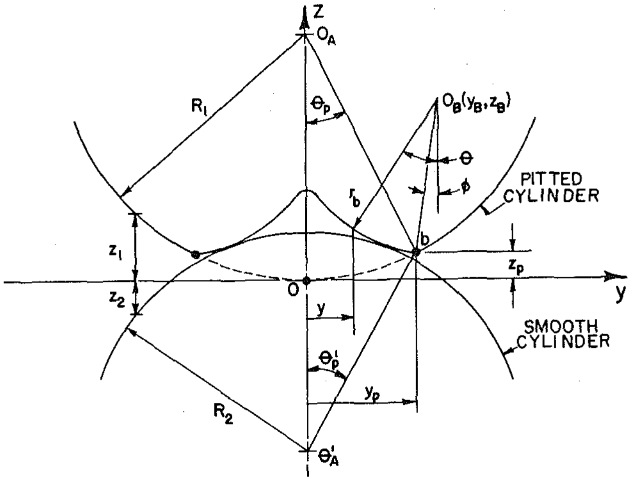

Fig. 1 Coordinate systems for a smooth cylinder contacting a cylinder with a longitudinal surface depression

Chiu (1969) analytically solved the problem of an infinitely long rigid cylinder having an axial groove in contact with an elastic half space. Paul et al. (1975) solved the problem of a pitted sphere in contact with a nonpitted elastic sphere with a restriction on symmetry and the requirement of a functional regularization parameter to make his solution quasi-stable. He

---

Contributed by the Applied Mechanics Division for publication in the JOURNAL OF APPLIED MECHANICS.

Discussion on this paper should be addressed to the Editorial Department, ASME, United Engineering Center, 345 East 47th Street, New York, N.Y. 10017, and will be accepted until two months after final publication of the paper itself in the JOURNAL OF APPLIED MECHANICS. Manuscript received by ASME Applied Mechanics Division, August 20, 1985; final revision February 5, 1986.

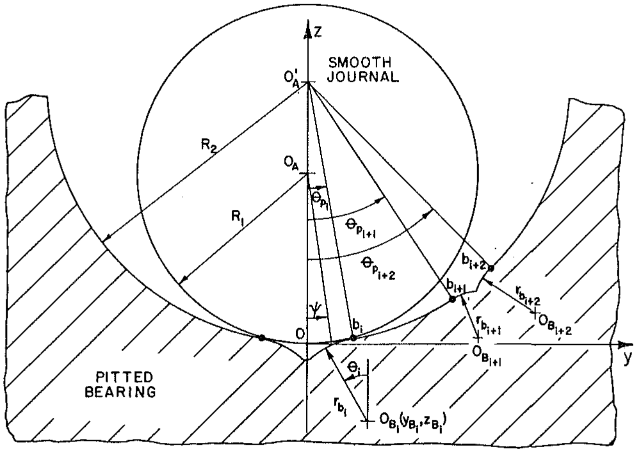

Fig. 2 Coordinate systems for a smooth journal contacting a bearing with several longitudinal surface defects

treated the relative approach δ_r as an unknown which needed to be determined along with the contact pressure. Their method was limited in its range of application because of a numerical instability encountered in their linear system of equations. Since their matrix was not diagonally dominant, and had a partial pivoting, the system was ill-conditioned. The ill-conditioned phenomenon results from round-off error in either the calculation of the inverse of a matrix or in the solution of the sets of simultaneous linear equations (Young, 1971).

In the work to be discussed herein, the modified iterative method and modified influence function will be used in conjunction with an automatic mesh generation technique to avoid solving the ill-condition of the large scale linear system. By guessing a relative approach instead of treating it as an unknown, the matrix becomes strictly diagonally dominant. This improves solution efficiency and accuracy and, more importantly, provides stability and convergence.

In the analysis to be presented, consider the contact of two cylinders, one which is smooth and one which contains one or several shallow longitudinal surface depressions. In what follows, a brief review of a theory for analyzing multiply connected contact problems will be described. Numerical results and conclusions will be given.

2 Formulation of the Profile Function for Multiply Connected Region

Case 1: Smooth Cylinder Contacting a Cylinder With a Longitudinal Surface Depression. Consider a cylinder of radius R_1, having a shallow surface depression, perfectly aligned with a smooth cylinder of radius R_2. Let (x, y, z) be a coordinate system with origin at point 0 with the z axis along the common normal between two contact bodies, and the x axis along the axial direction as shown in Fig. 1. The origin of the pitted contour O_B is arbitrarily located at a distance y_B from the z axis, with the pit radii r_b connected to the cylindrical surface at the blending point b. The z coordinate of a point on body 1 located at a distance y from the z axis *within* the blended region is given by

$$z_1 = Z_p + r_b\cos\phi - r_b\cos\theta \tag{1}$$

where

$$Z_p = R_1(1-\cos\theta_p)$$

and

$$\theta_p = \sin^{-1}(y_p/R_1)$$

$$\phi = \sin^{-1}[(y_B - y_p)/r_b]$$

$$\theta = \sin^{-1}[(y_B - y)/r_b)]$$

and the z coordinate of the candidate contact point on the smooth cylinder, located at a distance $y\,(\leqq y_p)$ from the z axis is given by

$$z_2 = [R_2{}^2 - y^2]^{1/2} - (R_2\cos\theta_p{}' - Z_p) \tag{2}$$

where

$$\theta_p{}' = \sin^{-1}(y_p/R_2)$$

For points *outside* the depression $(y > y_p)$, the variables z_1 and z_2 are, respectively, written as

$$z_1 = R_1 - [R_1{}^2 - y^2]^{1/2} \tag{3}$$

$$z_2 = Z_p + [R_2{}^2 - y^2]^{1/2} - R_2\cos\theta_p' \tag{4}$$

Therefore, the *profile function h* (initial separation) for contact of a cylinder having an axial surface defect on a smooth cylinder can be determined by combining equation (1) with equation (2) and equation (3) with equation (4) leading to

$<i>$ Inside pitted contour; $|y| \leqq y_p$

$$\begin{aligned} h(r_b, y_B, y_p, y) &= z_1 - z_2 \\ &= [R_2{}^2 - y_p{}^2]^{1/2} - [R_2{}^2 - y^2]^{1/2} \\ &\quad + [r_b{}^2 - (y_B - y_p)^2]^{1/2} - [r_b{}^2 - (y_B - y)^2]^{1/2} \end{aligned} \tag{5}$$

$<ii>$ Outside pitted contour; $|y| > y_p$

$$\begin{aligned} h(y_p, y) &= z_1 - z_2 \\ &= [R_1{}^2 - y_p{}^2]^{1/2} + [R_2{}^2 - y_p{}^2]^{1/2} - [R_1{}^2 - y^2]^{1/2} - [R_2{}^2 - y^2]^{1/2} \end{aligned} \tag{6}$$

Case 2: Smooth Journal Contacting a Bearing Containing Several Longitudinal Surface Defects. Consider a long smooth shaft of radius R_1 perfectly aligned with a finite bearing, of length L, and radius R_2, having several shallow longitudinal surface defects. Let (x, y, z) be a coordinate system with origin at point 0, with z axis along the common normal between the journal and the bearing, with y axis tangent to the smooth shaft at point 0, and with x axis parallel to the shaft axis as indicated in Fig. 2. The center of each of the pit blending arcs lies along the line joining the center of the bearing $O_A{}'$ and the blended point b_i. Let the pitted radii r_{bi} connect smoothly to the bearing main surface at each blending point. The z coordinate of a point on the journal (or bearing) located at a distance y from the z axis *within* the blended region are, respectively, determined as

$$z_1 = R_1 - [R_1{}^2 - y^2]^{1/2} \tag{7}$$

$$z_2 = R_2 - (R_2 + r_{bi})\cos\theta_{pi} + r_{bi}\cos\theta_i \tag{8}$$

where

$$\theta_i = \sin^{-1}[(y_{Bi} - y)/r_{bi}]$$

and

$$y_{Bi} = (R_2 + r_{bi})\sin\theta_{pi}$$

and θ_{pi}, r_{bi}, y are as defined in Fig. 2.

Therefore, the profile function in the mean radial direction for contact of a rigid unpitted journal on an elastic bearing with several longitudinal surface defects can be determined by combining equation (7) with equation (8).

(*i*) Within the *pitted* bearing surface

$$\begin{aligned} h(r_{bi}, \theta_{pi}, \Psi) &= (z_1 - z_2)\cos\Psi \\ &= [(R_1 - R_2) + (R_2 + r_{bi})\cos\theta_{pi} - [R_1{}^2 - y^2]^{1/2} - r_{bi}\cos\theta_i]\cos\Psi \end{aligned} \tag{9}$$

where $\Psi = \sin^{-1}(y/R_1)$; (angular contact angle).

(*ii*) Outside the *pitted* bearing surface for highly conforming contact problems, the profile function in the radial direction can be approximated by

$$h(\Psi) = (R_2 - R_1)(1 - \cos\Psi). \tag{10}$$

3 Formulation of General Contact Criteria

Assume that the point M_1 on body 1 and point M_2 on body

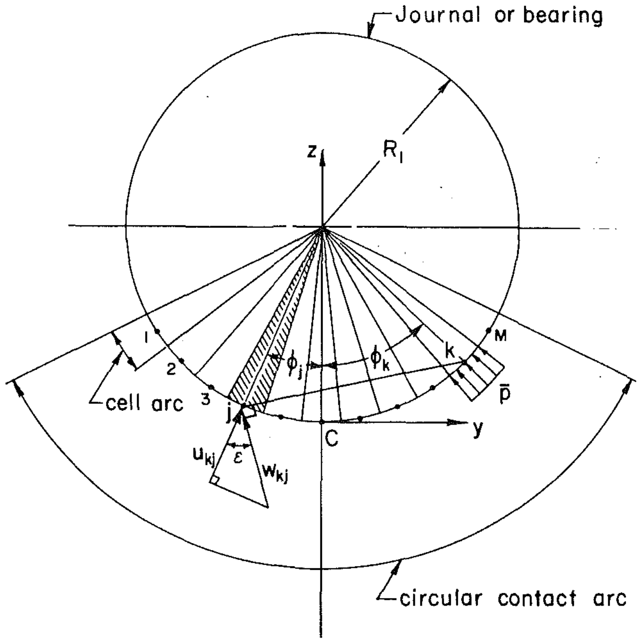

Fig. 3 Modified influence function for conformal contact

2 have an initial separation distance h, and that the points will come into contact after deformation. Then the final separation S_f (along the common normal direction) of those two candidate contact points becomes

$$S_f = u^{(1)} + u^{(2)} + h - \delta_r \tag{11}$$

where δ_r is the relative approach along the common normal direction and h is the profile function. In general, the normal displacement $u^{(1)}$, $u^{(2)}$ can be written in terms of an unknown contact pressure $\bar{p}(\bar{x},\bar{y})$ and the Fredholm integral equation for nonconformal contact problems. The normal displacements can be expressed as

$$u^{(i)}(x,y)$$
$$= K^{(i)} \int_\Omega \bar{p}(\bar{x},\bar{y})(d\bar{x}d\bar{y}) / [(x-\bar{x})^2 + (y-\bar{y})^2]^{1/2}$$

where

$$K^{(i)} = 1 - \nu_i{}^2/\Pi E_i \qquad i = 1,2 \tag{12}$$

and E_i, ν_i are the modulus of elasticity and Poisson's ratio of body i and Ω is the contact area.

Substituting equation (12) into equation (11) yields

$$S_f = K_m \int_\Omega \bar{p}(\bar{x},\bar{y})(d\bar{x}d\bar{y}) / [(x-\bar{x})^2 + (y-\bar{y})^2]^{1/2} + h - \delta_r \tag{13}$$

where $K_m = K^{(1)} + K^{(2)}$

The boundary conditions require that

$$\text{(1)} \quad S_f = 0 \quad \bar{p}(\bar{x},\bar{y}) \geqq 0$$
$$\text{(2)} \quad S_f > 0 \quad \bar{p}(\bar{x},\bar{y}) = 0 \tag{14}$$

and the equilibrium condition requires

$$\int_{\Omega_A} \bar{p}(\bar{x},\bar{y}) d\Omega_A = F \tag{15}$$

where F in the applied load along the z direction, and Ω_A is the projected pressure area.

4 Modified Influence Function for Conformal Contact

One of the major difficulties in the solution of the conformal contact problem is the determination of an appropriate influence function for the surface in contact, since the Boussinesq's point force and displacement half-space influence function is no longer suitable for this curved contact surface area. It is necessary to generate a modified influence function for the conformal contact problem.

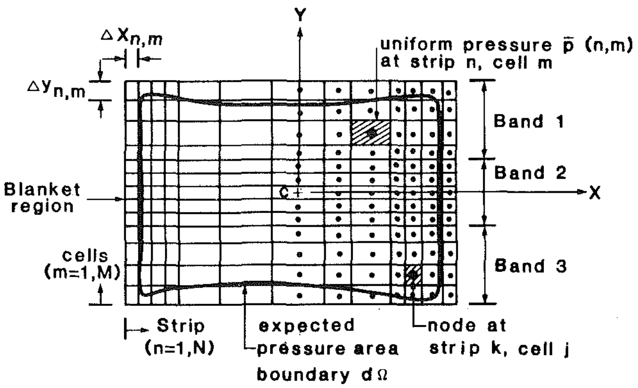

Fig. 4 Grid generation for multiply-connected region

For the case of a highly conformal surface when the relative distance r_{kj} of nodal points k and j is larger than the maximum dimensions of the arc cell on the shaft, the influence function will be approximated by assuming that points k and j on the curved surface are the points on the half-space as shown in Fig. 3. The radial displacement $u^{(i)}{}_{kj}$ of body i at point j subject to a uniform pressure over cell k becomes

$$u_{kj}^{(i)} = w_{kj}^{(i)} \cos\epsilon \tag{16}$$

where

$$w_{kj}^{(i)} = K^{(i)} / r_{kj}^{(i)} \quad i = 1,2$$

and $\epsilon = (\phi_k + \phi_j)/2$ is the angle formed between the direction perpendicular to r_{kj} and the radial direction of point j. Thus, the modified influence function for the conformal contact is given by

$$g_{kj}^{(i)} = D_{kj}^{(i)} \cos\epsilon \quad i = 1,2 \tag{17}$$

where $D_{kj}^{(i)}$ is the influence function for the nonconformal contact.

5 Mesh Generation and Discretization of Integral Equation for Multiply-Connected Regions

A blanket region is chosen to be larger than the upper boundary of the multiply-connected contact regions for a given rigid body approach δ_r as indicated in Fig. 4. The estimated axial and lateral contact length within the blanket region may be divided into any number of segments along the x and y directions, respectively. Each segment is then partitioned into a number of strips and a number of cells. The total number of strips along the axial direction is N, and the number of cells for each strip is M. Fine grids will be chosen near the high stress concentration regions. The discretization method of the integral equation will be implemented in conjunction with the modified Boussinesq point force displacement influence function. By assuming a uniform pressure distribution over each cell, equation (13) can be written as follows:

$$\sum_{n=1}^{N} \sum_{m=1}^{M} g_{kj,nm}^{(i)} \bar{P}_{nm} = \delta_r - h_{kj} \qquad \begin{matrix} k = 1,N \\ j = 1,M \end{matrix} \tag{18}$$

where $g_{kj,nm}^{(i)}$ is the modified influence function which represents the normal deflection of body i at strip k, cell j due to a uniform pressure $\bar{P}_{nm}$ over strip n, cell m. The variable h_{kj} is the profile function at strip k, cell j. Equation (18) represents a system of linear equations which can be solved to determine contact pressure for a given normal relative approach δ_r. The automatic mesh generation technique is im-

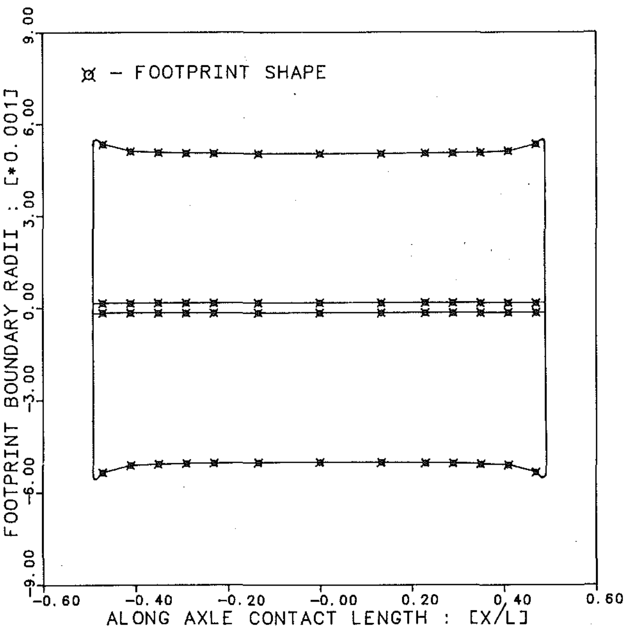

Fig. 5 Footprint shape with one surface depression

plemented to redefine the pressure area boundary by a numerical method of interpolation and extrapolation (Hildebrand, 1953). The process is repeated until both the boundary conditions and the equilibrium condition are satisfied.

6 Modified Iterative Method

To avoid having to solve a large linear system of equations, the modified interative method (Hartnett, 1980) can be introduced by employing the local and remote influence concept combined with the modified influence function to determine a solution for a small set of linear algebraic equations. Equation (18) can be rearranged in the following form:

$$\sum_{m=1}^{M} g_{kj,km}^{(i)} \bar{P}_{km}$$

$$= \delta_r - h_{kj} - \sum_{n=1}^{N} \sum_{m=1}^{M} g_{kj,nm} \bar{P}_{nm} (1 - \delta_{kn}) \quad \begin{matrix} k = 1,M \\ j = 1,N \end{matrix} \tag{19}$$

where $g_{kj,km}^{(i)}\ \bar{P}_{km}$ represents the normal displacement of body i at strip k, cell j due to a uniform pressure at strip k, cell m and δ_{kn} is the Kronecker delta.

To solve for the strip pressure $\bar{P}_{km}$ in equation (19), an initial estimate is made for the pressure distribution outside the strip k. Subsequently, this estimated pressure is updated until all the strip pressures within the blanket area are found. The boundary conditions in equation (14) and equilibrium condition (15) are applied to determine the *iterated applied load* F_{iter}. The process is repeated until the change in the iterated applied load falls within a chosen limit of accuracy. The latest iterated applied load is called the *estimated applied load*, F_e. The automatic mesh generation technique is implemented to redefine the new pressure area boundary region from which the new mesh grids are generated. The iterating process is repeated to solve for all the strip pressures within the pressure area boundary, and finally the new estimated applied load is determined. The whole process continues until the change of the estimated applied load falls within a second tolerance of accuracy.

7 Presentation and Discussion of Numerical Results

A wide range of contact problems having multiply connected regions can be solved by using the analysis presented in this paper. The program CONPITS was written to solve for either nonconformal or conformal type of contact problems involving one or several surface depressions. As a specific example, contact of a cylinder containing a shallow longitudinal surface depression at the center of the contact zone in contact with an elastic half space is considered. The effect of the blending radius r_b and the pit size y_p on the stress concentration will be discussed. In addition, the effect of clearance and material properties on journal bearing contact pressure will be presented.

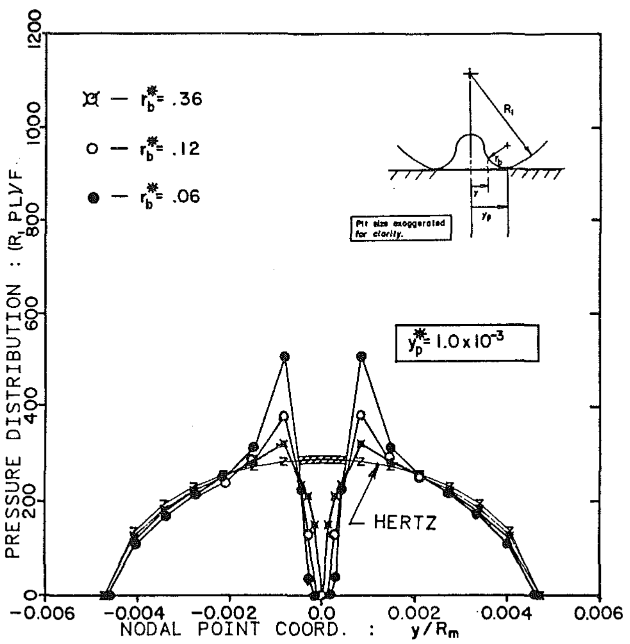

Fig. 6 Pressure distribution for various blend radius r_b*, y_p* = 1.0 × 10^{-3}

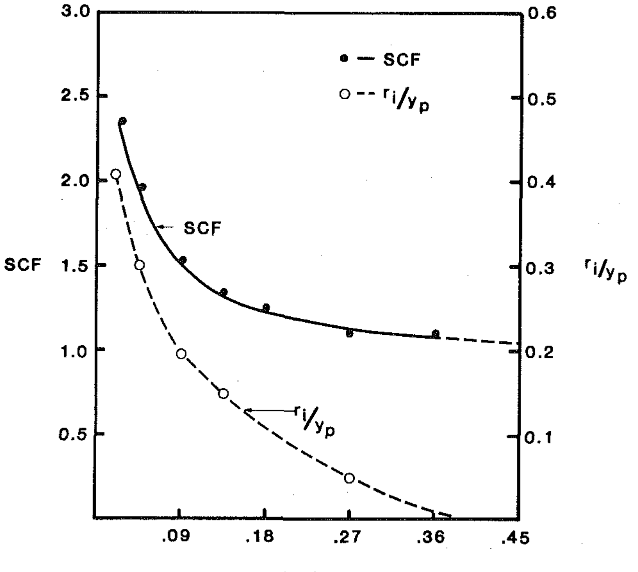

Fig. 7 The dimensionless quantity $C_o(=K_mP_or_b/y_p)$ versus SCF and $r_i(=r_i/y_p)$

Example 1: Copper Cylinder of Finite Length L (With an Axial Surface Depression) Contacting an Elastic Half Space.

$R_1{}^* = R_1/R_m$ = radius of copper cylinder = 1.0
$L^* = L/R_m$ = straight length of cylinder = 0.5 where
$R_m = R_1R_2/(R_1 + R_2)$

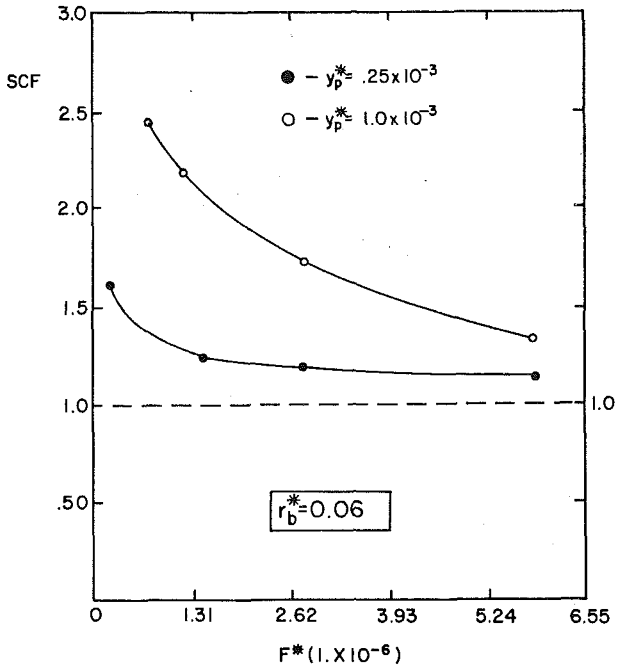

Fig. 8 The stress concentration factor (SCF) versus load F^* for various pit sizes y_p^*, $r_b^* = 0.06$

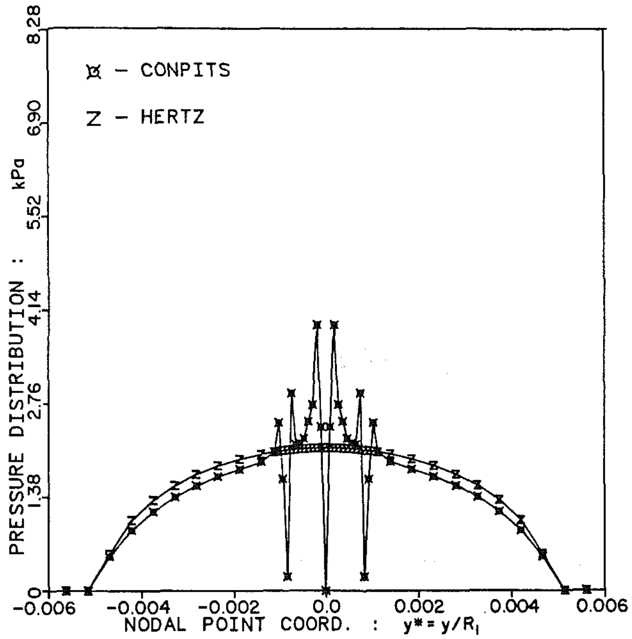

Fig. 9 Nonconformal pressure distribution for several *small* pits

$E_1 = 119$ GPa, $\nu_1 = 0.326$
$E_2 = 207$ GPa, $\nu_2 = 0.30$

$r_b^* = r_b/R_m =$ blend radius $= 0.06,\ 0.12,\ 0.36$

$y_p^* = y_p/R_m =$ pit size $= 0.25 \times 10^{-3},\ 1.0 \times 10^{-3},\ 2.0 \times 10^{-3}$

For $F = 444.8\ N$, numerical results were obtained using a 15 × 21 cell, (i.e., 15 strips along the axial contact length with each strip containing 21 cells). Fine grids were chosen near the high stress concentration region. The footprint contact area involving one surface depression was plotted in Fig. 5 for $y_p^* = 0.001$ and $r_b^* = 0.12$. For a given pit size y_p^*, the pressure distributions $P^* = (R_1PL/F)$ were plotted for various blend radius r_b^* as shown in Fig. 6. The smaller the blend radius r_b^*, the higher the pressure gradient near the pitted region. In each case, the pressure distribution far away from the pit agrees closely with that from the Hertzian solution for a smooth cylinder.

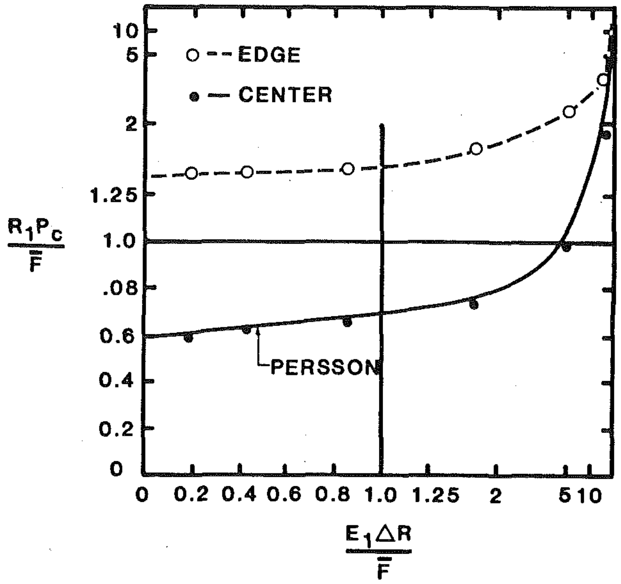

Fig. 10 Relationship between $R_1P_c/\bar{F}$ and $E_1\Delta R/\bar{F}$

Figure 7 shows the dimensionless quantity $C_o = K_mP_or_b/y_p$ as a function of stress concentration factor (SCF) and inner contact radius $\bar{r}_i = r_i/y_p$ at the center of the axial contact length. The SCF is defined as the ratio of the maximum pressure at the center of the finite cylinder to the Hertzian maximum pressure P_o for the smooth cylinder for the same loading conditions. As expected, the smaller the ratio of blend radius r_b to pit size y_p the higher the SCF. When the blend radius r_b tends to zero, an infinite pressure concentration occurs at the sharp edge of the contact. An increase of C_o will make the blend contour conform to the main surface and produce a smaller inner contact radius $\bar{r}_i$ and therefore a close agreement with the Hertzian solution (i.e., SCF approaches 1.0). For a given blend radius, the increase of the pit size produces an increase in stress concentration due to the loss of load supporting area. Due to the nonlinear properties of the contact problem, the SCF is found to decrease with an increase in the applied load $F^*(=K_mF/R_m^2)$ as illustrated in Fig. 8.

Example 2: Copper Cylinder of Finite Length L (Containing Several Axial Surface Depressions) Contacting an Elastic Half Space. Dimensions and properties are the same as in Example 1 except for the blend radius r_{bi}^* and the pit size y_{pi}^*

$$y_{pi}^* = 0.25 \times 10^{-3}, 0.75 \times 10^{-3}, 1.0 \times 10^{-3}$$
$$r_{bi}^* = 0.015$$

The numerical solutions for problems involving several small pits were obtained using a 15×45 cell. Figure 9 shows the pressure distribution at the center of the axial contact length for small pits located near the axis of symmetry. A peak pressure gradient near the innermost pit and the pressure distribution far from the outer pit agrees reasonably well with the Hertzian prediction.

Example 3: Perfectly Aligned Journal Bearing in Contact. R_1 = radius of the shaft = 19.25mm; R_2 = radius of the bearing = −19.30mm; L = straight length of the bearing = 16.83mm.

The effect of clearance and material properties on journal bearing conformal pressure are examined and the results are compared with the analytical solution of Persson (Persson, 1964), thus lending support to the use of the approximate influence function of Section 4 for this problem.

The dimensionless quantity $E_1 \Delta R/\bar{F}$ is represented in Fig. 10 as a function of $R_1 P_c/\bar{F}$, where P_c is the maximum contact pressure at either the center or the edge of the axial contact length, ΔR is the radial clearance and $\bar{F}$ is the load per unit bearing length. There is close agreement with the Persson's analytical solution at the center of the axial contact length. However, owing to a high stress concentration at the bearing edge, the edge pressure distribution will differ significantly from the Persson's plane stress analysis.

8 Conclusion

A general numerical method has been presented to solve contact problems involving multiply connected regions. The program CONPITS was written to solve for either conformal or nonconformal contact problems containing several surface depressions. Numerical results were presented for several example problems. The first example was a copper cylinder having a shallow axial surface defect aligned with and contacting a steel surface. The numerical results show that the smaller the blend radii r_b^*, the higher the stress concentration for a given pit size. For a given blend radius, the SCF increases with an increase of pit size. A large deviation from the Hertzian solution is observed for a surface with large pits because of the loss of pressure supporting area. The SCF can also be reduced by increasing the applied load. The second example gives the high stress concentration for a cylinder containing several small pits. The third example solves for the three dimensional conformal contact pressure distribution for various moduli and radial clearances.

The analysis presented in this paper contributes to bearing technology by providing an analysis of the effect of surface defects on bearing stress and therefore provides a means for estimating bearing operating life.

Acknowledgment

This material is based upon work supported by the National Science Foundation under grant MSM-8416143.

References

Bayer, R. G., 1968, "The Significance of Surface Fatigue in Sliding Wear," *Wear*, Vol. 12, pp. 173-183.

Beagley, T. M., 1976, "Severe Wear of Rolling/Sliding Contacts," *Wear*, Vol. 36, pp. 317-335.

Chiu, Y. P., 1969, "On the Contact Problem of Cylinders Containing a Shallow Longitudinal Surface Depression," ASME *Journal of Applied Mech.*, Vol. 91, Ser. E, No. 4, pp. 852-858.

Hartnett, M. J., 1980, "A General Numerical Solution for Elastic Body Contact Problem," *Solid Contact and Lubrication, The Winter Annual Meeting of the ASME*, Chicago, IL, pp. 51-66.

Hildebrand, F. B., 1953, *Introduction to Numerical Analysis*, McGraw-Hill, New York.

Littman, W. E., Widner, R. L., 1966, "Propagation of Contact Fatigue From Surface and Subsurface Origin," ASME *J. of Basic Engr.*, Vol. 88, Ser. D, pp. 624-636.

Marshek, K. M., 1979, "Failures in Plastic Ball Bearings," *Wear*, Vol. 52, pp. 141-146.

Paul, B., Singh, K. P., and Woodard, W., 1975, "Contact Stresses for Multiply-Connected Regions – The Case of Pitted Spheres," *Proceedings of the Symposium on the Mechanics of Deformable Bodies*, Delft University Press, pp. 264-281.

Persson, A., 1964, "On the Stress Distribution of Cylindrical Elastic Bodies in Contact," PhD Dissertation, Chalmers Tekniska, Hogskola, Goteborg, Sweden.

Young, D. M., 1971, *Iterative Solution of Large Linear Systems*, Academic Press, New York, pp. 120-129.

In-Plane Indentation and Separation of a Flat, or Rounded Rigid Stamp from an Elastic, Finite Layer

R. Solecki
Department of Mechanical Engineering,
University of Connecticut,
Storrs, CT 06268
Mem. ASME

This paper describes symmetric, frictionless indentation of a two-dimensional, rectangular, elastic solid, with two parallel edges constrained against displacements, by a flat, rigid, or rounded stamp pressed against one of the remaining edges. Comparison with the classical problem of indentation of the elastic half-plane by a flat rigid stamp reveals new interesting features of the present analysis: 1) For each relative stamp length a critical aspect ratio of the indented rectangle exists such that for a narrower rectangle the separation of the midsection of the stamp occurs. 2) The stress intensity factors at the ends of the stamp are found to depend strongly on the relative depth of the "beam"; they also depend, but to a lesser degree, on the relative length of the stamp. 3) Unlike in the classical problem here the penetration of the stamp is uniquely determined. Numerical results are provided. The numerical results obtained for the case of the rounded stamp are compared with the results available from earlier studies.

1 Introduction

The problem of frictionless indentation of a half-plane by a plane, rigid stamp was solved first by Sadowsky (1928) (see also Gladwell, 1980, for further references and for a historical overview). The solution of this classical problem depicted in Fig. 1 revealed that the interface stress has square-root singularities at the ends of the stamp. It was also determined that the interface stress is negative everywhere under the stamp hence there was no question of separation of it from the half-plane. Furthermore, an important feature of the classical solution consisted of its inability to determine the penetration of the stamp. The present paper attempts to remove the restrictions imposed on the solution of the stamp problem by the assumption of the infinity of the indented solid. This is achieved by replacing the infinite solid by a finite two-dimensional isotropic elastic solid in the form of a rectangle whose vertical edges are prevented from deforming as shown in Fig. 2. To simplify the analysis the symmetry with respect to x axis is assumed. The state of stress and displacement is found by first applying finite double Fourier transformation to the two-dimensional Navier equations of elasticity. Subsequent application of the inversion formulas and of the boundary conditions expanded into Fourier series with unknown coefficients (and with built-in singularities at the ends of the stamp and at the corners of the layer) leads to an infinite system of algebraic equations.

These are then solved numerically for various $\psi = c/b$ and $\phi = a/b$ ratios and for fixed material characteristics in an attempt to decide whether and under what circumstances the stamp separates (a phenomenon foreseen by Nied and Erdogan 1979), how the boundaries affect the stress intensity

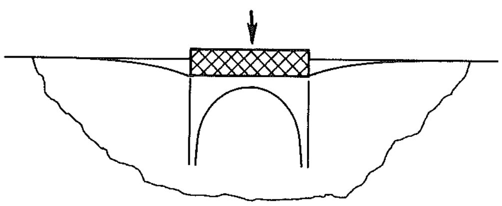

Fig. 1 Indentation of an elastic half-plane

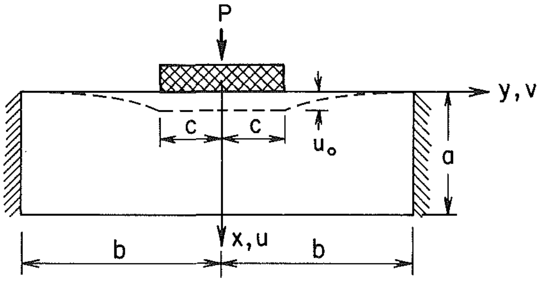

Fig. 2 Indentation of a finite layer by a flat stamp

Contributed by the Applied Mechanics Division for publication in the Journal of Applied Mechanics.

Discussion on this paper should be addressed to the Editorial Department, ASME, United Engineering Center, 345 East 47th Street, New York, N.Y. 10017, and will be accepted until two months after final publication of the paper itself in the Journal of Applied Mechanics. Manuscript received by ASME Applied Mechanics Division, July 16, 1985; final revision March 26, 1986.

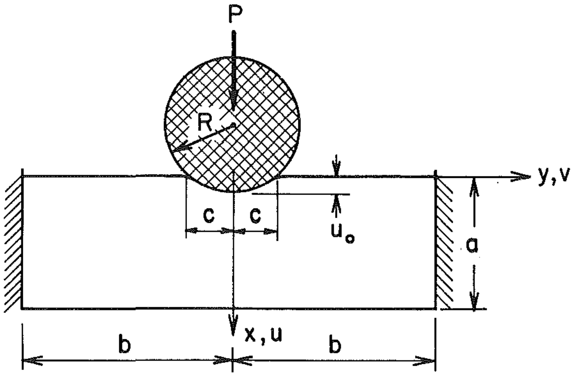

Fig. 3 Indentation of a finite layer by a rounded stamp

factors and what is the magnitude of the penetration of the stamp for selected dimensions. A simple change in one of the boundary conditions makes the present study also applicable to the case of a rounded stamp indenting a finite layer with two built-in edges (Fig. 3). Here the results were compared with the data obtained by Keer and Miller (1983) and confirmed by Sankar and Sun (1983) who used a different method. It should be noted that the present method is valid for any aspect ratio of the indented layer while the previous results, based on combination of simple beam theory and the theory of elasticity, are valid only for relatively thin beams.

2 Basic Equations – A Flat Stamp

For the two-dimensional state of strain assumed here the equations of equilibrium in the absence of body forces take the form:

$$\frac{\partial \sigma_{xx}}{\partial x}+\frac{\partial \sigma_{xy}}{\partial y}=0 \tag{1}$$

$$\frac{\partial \sigma_{xy}}{\partial x}+\frac{\partial \sigma_{yy}}{\partial y}=0 \tag{2}$$

The geometric and physical symmetry of the problem suggests that only the portion $y > 0$ of the beam (Fig. 2) must be analyzed. The corresponding boundary conditions are:

$$v=0,\ \sigma_{xy}=0 \text{ at } y=0 \tag{3}$$

$$\sigma_{xx}=0,\ \sigma_{xy}=0 \text{ at } x=a \tag{4}$$

$$u=0,\ v=0 \text{ at } y=b \tag{5}$$

$$\sigma_{xy}=0,\ u=u_0=\text{const at } x=0,\ 0\le y\le c \tag{6}$$

$$\sigma_{xy}=0,\ \sigma_{xx}=0 \text{ at } x=0,\ c\le y\le b \tag{7}$$

where u and v are components of the displacement vector along Ox and Oy axes, respectively. Substituting stress-strain relations for an isotropic, Hookean solid

$$\sigma_{xx}=\mu\left[(\gamma+2)\frac{\partial u}{\partial x}+\gamma\frac{\partial v}{\partial y}\right], \tag{8}$$

$$\sigma_{yy}=\mu\left[\gamma\frac{\partial u}{\partial x}+(\gamma+2)\frac{\partial v}{\partial y}\right], \tag{9}$$

$$\sigma_{xy}=\mu\left(\frac{\partial u}{\partial y}+\frac{\partial v}{\partial x}\right) \tag{10}$$

where

$$\gamma=\lambda/\mu \tag{11}$$

λ and μ being Lame's constants, into equations (3) ÷ (7) results finally in

$$v=0 \text{ at } y=0 \tag{12}$$

$$\frac{\partial u}{\partial y}+\frac{\partial v}{\partial x}=0 \text{ at } y=0 \tag{13}$$

$$\gamma\frac{\partial v}{\partial y}+(\gamma+2)\frac{\partial u}{\partial x}=0 \text{ at } x=a \tag{14}$$

$$\frac{\partial u}{\partial y}+\frac{\partial v}{\partial x}=0 \text{ at } x=a \tag{15}$$

$$u=0 \text{ at } y=b \tag{16}$$

$$v=0 \text{ at } y=b \tag{17}$$

$$\frac{\partial u}{\partial y}+\frac{\partial v}{\partial x}=0 \text{ at } x=0 \tag{18}$$

$$u=u_o \text{ at } x=0,\ y<c \tag{19}$$

$$\gamma\frac{\partial v}{\partial y}+(\gamma+2)\frac{\partial u}{\partial x}=0 \text{ at } x=0,\ y>c \tag{20}$$

Next equations (1) and (2) are subject to finite Fourier transformations by multiplying them by $\cos(m\pi x/a)\cos(n\pi y/b)$ and $\sin(m\pi x/a)\sin(n\pi y/b)$, respectively, and then integrating over the rectangle $x\epsilon[0,\ a]$, $y\epsilon[0,\ b]$. This is followed by integration by parts of some integrals appearing in the transformed equations and by application of the boundary conditions (12) ÷ (20). The final form the transformed field equations include four integrals with the following unknown integrands: $v(0,y)$, $v(a,y)$, $\sigma_{xy}(x,b)$, $\sigma_{xx}(0,y)$. The first two integrands are regular functions and are expanded into Fourier series:

$$v(0,y)=\frac{2}{b}\sum_{n=1}^{\infty} G_n \sin\beta_n y, \tag{21}$$

$$v(a,y)=\frac{2}{b}\sum_{n=1}^{\infty} H_n \sin\beta_n y, \tag{22}$$

The third integrand has a singularity of strength p at $x=0$ and $x=a$ (see Benthem and Minderhoud, 1972) where p is the solution of the transcendental equation

$$\cos^2\frac{p\pi}{2}=\frac{4(1-\nu)^2}{3-4\nu}-\frac{(1-p)^2}{3-4\nu} \tag{23.1}$$

It is therefore represented in the following form

$$\sigma_{xy}(x,b)=\frac{\mu}{a}\left[\frac{S_1}{\left(1-\frac{x}{a}\right)^p}+\frac{S_2}{\left(\frac{x}{a}\right)^p}\right]$$

$$+\frac{\mu}{a}\left(K_o+2\sum_{n=1}^{\infty}K_n\cos\alpha_n x\right) \tag{23.2}$$

where S_1 and S_2 are unknown stress intensity factors and where

$$\alpha_n=n\pi/a, \quad \beta_n=n\pi/b \tag{24}$$

The numerical results were obtained for $\nu = 0.3$. In this case from equation (23.1) we have

$$p=0.28883$$

The last of the unknown functions, $\sigma_{xx}(0,\ y)$, which equals zero for $y>c$, is square-root singular at $y=c$. Therefore it is represented as:

$$\sigma_{xx}(0,y)=\mu\left\{\frac{C}{\sqrt{1-(y/c)^2}}\right.$$

$$\left.+\frac{1}{c}\left[F_0+2\sum_{n=1}^{\infty}F_n\cos(n\pi y/c)\right]\right\} \tag{25}$$

where in addition to the Fourier coefficients F_n also the stress intensity factor C is unknown. Solving the transformed field equations with respect to the transforms of the displacements

$$u_{mn} \equiv \int_o^a \int_o^b u(x,y) \cos\alpha_m x \cos\beta_n y \, dx \, dy, \quad m,n=0,1, \ldots \infty \tag{26}$$

$$v_{mn} \equiv \int_o^a \int_o^b v(x,y) \sin\alpha_m x \sin\beta_n y \, dx \, dy, \quad m,n=1, \ldots \infty \tag{27}$$

one obtains the relation between those transforms and the unknown Fourier coefficients appearing in equations (21)–(25):

$$\begin{aligned} u_{mo} = {} & [P/2\mu + K_m + S_1\epsilon_m \\ & + (-1)^m S_2 \epsilon_m]/[(\gamma+2)\alpha_m^2], \qquad m=1, \ldots \infty \end{aligned} \tag{28}$$

$$\begin{aligned} u_{on} = {} & \{(Cc\pi/2)Y_n + (P/2\mu)[\sin(n\pi\psi)/(n\pi\psi) - (-1)^n] \\ & - 2\sum_{k=1}^{\infty} F_k a_{nk} - \beta_n(G_n - H_n)\Big\}/\beta_n^2, \qquad n=1, \ldots \infty \end{aligned} \tag{29}$$

$$\begin{aligned} u_{mn} = {} & \Big\{[\alpha_m^2 + (2+\gamma)\beta_n^2]X_{1mn} \\ & + (1+\gamma)\alpha_m\beta_n X_{2mn}\Big\}/[(2+\gamma)(\alpha_m^2+\beta_n^2)^2] \end{aligned} \tag{30}$$

$$\begin{aligned} v_{mn} = {} & \{(1+\gamma)\alpha_m\beta_n X_{1mn} \\ & + [(2+\gamma)\alpha_m^2 + \beta_n^2]X_{2mn}\}/[(2+\gamma)(\alpha_m^2+\beta_n^2)^2] \end{aligned} \tag{31}$$

where

$$\begin{aligned} X_{1mn} = {} & (Cc\pi/2)Y_n + P\sin(n\pi\psi)/(2\mu n\pi\psi) - 2\sum_{n=1}^{\infty} F_k a_{nk} \\ & + (-1)^n[K_m + S_1\epsilon_m + (-1)^m S_2\epsilon_m] \\ & - \beta_n[G_n - (-1)^m H_n], \qquad m,n=1, \ldots \infty \end{aligned}$$

$$X_{2mn} = \alpha_m[G_n - (-1)^m H_n], \qquad m,n=1, \ldots \infty \tag{32}$$

$$Y_n = \sin(n\pi\psi)/(n\pi\psi) = J_o(n\pi\psi), \qquad n=1, \ldots \infty \tag{33}$$

and

$$\phi = a/b, \quad \psi = c/b$$

$$a_{nk} = (-1)^k n\psi\sin(n\pi\psi)/[\pi(n^2\psi^2 - k^2)] \tag{34}$$

Here $J_0(x)$ is the Bessel function of the first kind of order zero, while ϵ_m represents an integral evaluated numerically:

$$\epsilon_m = \frac{1}{1-p} + (-1)^m \frac{m\pi}{1-p} \int_0^1 t^{1-p} \sin m\pi t \, dt$$

Remaining two Fourier coefficients are determined from the global equilibrium equations

$$K_o = -P/2\mu - S_1 - S_2, \quad F_o = -(Cc\pi/2 + P/2\mu) \tag{35}$$

Next the inversion formulae are used

$$\begin{aligned} u(x,y) = {} & u_{oo} + 2\sum_{m=1}^{\infty} u_{mo}\cos\alpha_m x + 2\sum_{n=1}^{\infty} u_{on}\cos\beta_n y \\ & + 4\sum_{m=1}^{\infty}\sum_{n=1}^{\infty} u_{mn}\cos\alpha_m x \cos\beta_n y]/ab \end{aligned} \tag{36}$$

$$v(x,y) = \left[4\sum_{m=1}^{\infty}\sum_{n=1}^{\infty} v_{mn}\sin\alpha_m x \sin\beta_n y\right]/ab \tag{37}$$

Finally the boundary conditions, equations (15), (16), (18), and (19), are also subject to finite Fourier transformations (the remaining boundary conditions are identically satisfied). After numerous manipulations in which the symbolic manipulation package muMATH-muSIMP (1981) was very useful, the following infinite system of linear algebraic equations was obtained.

$$\begin{aligned} & Cc\pi w_{1i} + 2(\pi/a)\sum_{k=1}^{\infty}[G_k - (-1)^i H_k]r_{1ik} - 4\sum_{k=1}^{\infty} F_k r_{2ik} \\ & \quad + 2K_i w_{5i} + 2[S_1 + (-1)^i S_2]\epsilon_i w_{5i} + (P/\mu)w_{4i} = 0, \\ & Cc\pi w_{2i} - (\pi/a)\sum_{k=1}^{\infty}[G_k w_{7k} - H_k w_{6k}]a_{ki} + \sum_{k=1}^{\infty} F_k \, r_{3ik} \\ & \quad + 2\sum_{k=1}^{\infty} K_k \, r_{2ki} + 2\sum_{k=1}^{\infty}[S_1 + (-1)^k S_2]\epsilon_k r_{2ki} \\ & \quad + (P/\mu)w_{3i} = 0, \\ & Cc\pi w_{8i} - 8(\pi/a)(1+\gamma)i^2\phi^2(G_i w_{10i} - H_i w_{9i}) + 2\sum_{k=1}^{\infty} K_k \, r_{1ki} \\ & \quad + \sum_{k=1}^{\infty}[S_1 + (-1)^k S_2]\epsilon_k \, r_{1ki} \\ & \quad + 2\sum_{k=1}^{\infty} F_k \, a_{ik} w_{7i} + (P/\mu)w_{11i} = 0, \\ & Cc\pi w_{12i} - 8(\pi/a)(1+\gamma)i^2\phi^2(G_i w_{9i} - H_i w_{10i}) \\ & \quad + 2\sum_{k=1}^{\infty}(-1)^k K_k \, r_{1ki} \\ & \quad + 2\sum_{k=1}^{\infty}[(-1)^k S_1 + S_2]\epsilon_k \, r_{1ki} \\ & \quad + 2\sum_{k=1}^{\infty} F_k \, a_{ik} w_{6i} + (P/\mu)w_{13i} = 0 \\ & \qquad i=1, \ldots \infty \end{aligned} \tag{38}$$

where

$$w_{1i} = \sum_{n=1}^{\infty}(-1)^n[(2+\gamma)n^2\phi^2 + i^2]Y_n/D_{in},$$

$$w_{2i} = \sum_{n=1}^{\infty} a_{ni} \, Y_n \, B_n,$$

$$w_{3i} = \sum_{n=1}^{\infty} a_{ni}[B_n \sin(n\pi\psi)/(n\pi\psi) - (-1)^n(2+\gamma)/(2n^2\phi^2)],$$

$$\begin{aligned} w_{4i} = {} & [(1+\gamma)i\pi\psi \sinh(i\pi/\phi)\cosh(i\pi\psi/\phi) \\ & - (1+\gamma)i\pi\cosh(i\pi/\phi)\sinh(i\pi\psi/\phi) \\ & + 2\phi\sinh(i\pi/\phi)\sinh(i\pi\psi/\phi)]/[4i^2\phi\psi\sinh^2(i\pi/\phi)], \end{aligned}$$

$$\begin{aligned} w_{5i} = {} & [-(1+\gamma)i\pi^2 \\ & + (3+\gamma)\phi\pi\sinh(2i\pi/\phi)/2]/[4i\phi^2\sinh^2(i\pi/\phi)], \end{aligned}$$

$$w_{6i} = \pi[\sinh(i\pi\phi) + (1+\gamma)i\pi\phi\cosh(i\pi\phi)]/\sinh^2(i\pi\phi),$$

$$w_{7i} = \pi[(1+\gamma)i\pi\phi + \sinh(2i\pi\phi)/2]/\sinh^2(i\pi\phi),$$

$$w_{8i} = -Y_i w_{7i}/2,$$

$$
\begin{aligned}
w_{9i} &= -\pi[i\pi\phi\cosh(i\pi\phi)-\sinh(i\pi\phi)]/[4i\phi\sinh^2(i\pi\phi)],\\
w_{10i} &= [-i\pi\phi+\sinh(2i\pi\phi)/2]/[4i\phi\sinh^2(i\pi\phi)],\\
w_{11i} &= [-w_{7i}\phi\sin(i\pi\psi)+(-1)^i(2+\gamma)\pi\psi]/(2i\pi\phi\psi),\\
w_{12} &= -Yw_{6i}/2,\\
w_{13i} &= [-w_{6i}\phi\sin(i\pi\psi)+(-1)^i(2+\gamma)\pi\psi]/(2i\pi\phi\psi),\\
r_{1ik} &= (-1)^k k\phi[\gamma i^2-(2+\gamma)k^2\phi^2]/D_{ik},\\
r_{2ik} &= (1-1)^k\psi\{-(1+\gamma)i\pi(i^2\psi^2\\
&\quad +k^2\phi^2)\cosh(i\pi/\phi)\sinh(i\pi\psi/\phi)\\
&\quad +2\phi[(2+\gamma)k^2\phi^2\\
&\quad +i^2\psi^2]\sinh(i\pi/\phi)\sinh(i\pi\psi/\phi)+(1+\gamma)i\pi\psi\\
&\quad\ (i^2\psi^2+k^2\phi^2)\sinh(i\pi/\phi)\cosh(i\pi\psi/\phi)\\
r_{3ik} &= -4\sum_{n=1}^{\infty} a_{ni}a_{nk}B_n,\\
B_n &= \pi[(1+\gamma)n\pi\phi+(3+\gamma)\sinh(2n\pi\phi)/2]/[4n\phi\sinh^2(n\pi\phi)],\\
D_{ik} &= (i^2+k^2\phi^2)^2 \qquad (39)
\end{aligned}
$$

Solution of the infinite system of algebraic equations (38) and application of the formulae (35) yield the values of Fourier coefficients of the unknown boundary stresses. In particular, for the normal stress under the stamp we obtain:

$$
\begin{aligned}
\sigma_{xx}(0,y) &= (\mu/c)\{C\pi[1-(y/c)^2]^{1/2}-Cc\pi/2-P/2\mu\\
&\quad +2\sum_{k=1}^{\infty}F_k\cos(k\pi y/c)\} \qquad (40)
\end{aligned}
$$

Note that since the solutions of equations (38) are proportional to P, therefore $\sigma_{xx}(0,y)$ above is also proportional to P.

To calculate the displacements we must first find u_{oo}. This is obtained from the condition that $u=0$ at $y=b$ yielding:

$$u_{oo}+2\sum_{n=1}^{\infty}(-1)^n u_{on}=0 \qquad (41)$$

where u_{on} is substituted from equation (29).

Now Fourier coefficients in equations (36) and (37) are known to any desired degree of accuracy and hence the displacements can be evaluated. The penetration u_o is of particular interest since in the classical problem it has been an undeterminable quantity. Presently it is determined from the following equation:

$$
\begin{aligned}
u_o &= 2\sum_{k=1}^{\infty}\frac{u_{ko}}{ab}[\sin(k\pi\psi)/(k\pi\psi)-(-1)^k]\\
&\quad +4\sum_{k-1}^{\infty}\sum_{l=1}^{\infty}\frac{u_{kl}}{ab}\sin(l\pi\psi)/(l\pi\psi) \qquad (42)
\end{aligned}
$$

This equation resulted by performing transformation on the boundary condition (19). It is also worth noting, as pointed out by one of the reviewers of this paper, that the slope $\partial u/\partial y$ is infinite at the punch corner ($x=0$, $y=\pm b$). That this is so results from inspection of formula (36). It follows from it that:

$$
\begin{aligned}
\left.\frac{\partial u}{\partial y}\right|_{x=0,y=c} &= -\frac{2}{ab}\sum_{n=1}^{\infty}\beta_n u_{on}\sin n\pi\psi\\
&\quad -\frac{4}{ab}\sum_{m=1}^{\infty}\sum_{n=1}^{\infty}\beta_n u_{mn}\sin n\pi\psi \qquad (43)
\end{aligned}
$$

Once the expressions (32) and (34) are substituted here it is seen that one of the terms is represented by a divergent series of the order

$$\sum_{n=1}^{\infty}\sin^2 n\pi\psi/\beta_n.$$

Hence in fact expression (43) tends to infinity.

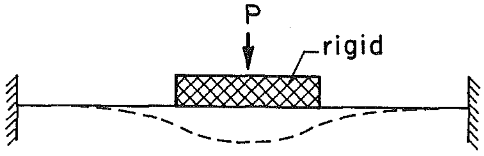

Fig. 4 Rigid load on a beam with built-in ends

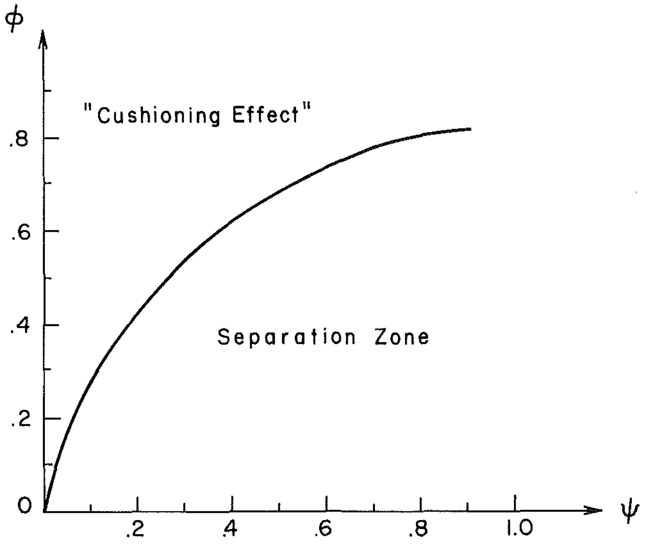

Fig. 5 The threshhold curve ϕ_{cr}

3 Basic Equations – A Rounded Stamp

In this section symmetric indentation by a rounded stamp is investigated (Fig. 3). All equations and results from Section 2 are still valid except that the following changes must be made.

(1) Boundary condition (6), or (19), reads now:

$$\sigma_{xy}=0,\ u=u_o-\frac{1}{2}\frac{y^2}{R}\quad \text{at } x=0,\ 0\le y\le c \qquad (44)$$

(2) In addition, since the normal stress under the stamp vanishes now at the ends of the contact zone, the stress intensity factor C appearing in equation (25) and in the following equations, must be set equal to zero

$$C=0 \qquad (45)$$

(3) Finally an inverse method is used here: the width of the contact $2c$ is assumed to be known and the force needed to generate an indentation of such a width is calculated. The condition that the normal stress vanishes at the ends of contact zone is also used to eliminate some of the Fourier coefficients.

4 Numerical Results

Inspection of the problem of deflection of a beam with both ends fixed, subject to a rigid load (Fig. 4), from the point of view of elementary theory led to the conclusion, anticipated first by Nied and Erdogan (1979), that also here, when $\phi = a/b$ is sufficiently small, separation under a portion of the rigid load will occur. To test this, one had to solve first the system of equations (38) using the method of reduction as described by Kantorowitsch and Krylow (1956) and then calculate the stresses under that stamp from equation (40).

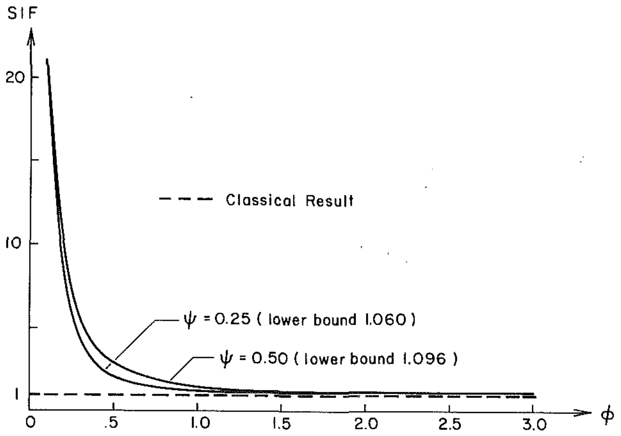

Fig. 6 The dependence of stress intensity factor on ϕ and ψ

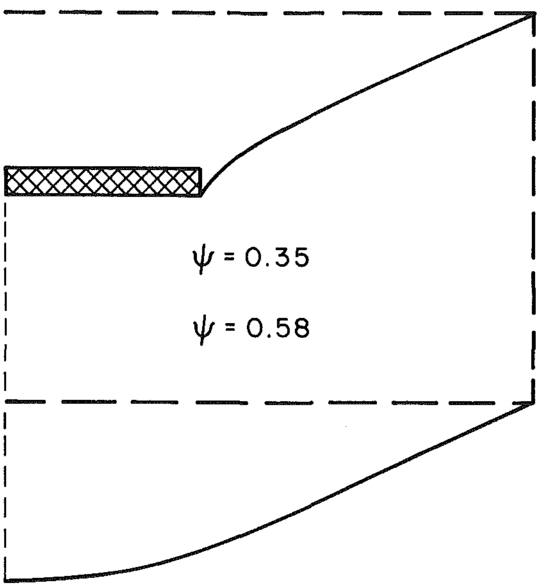

Fig. 7 Example of the deformed shape of the indented rectangle

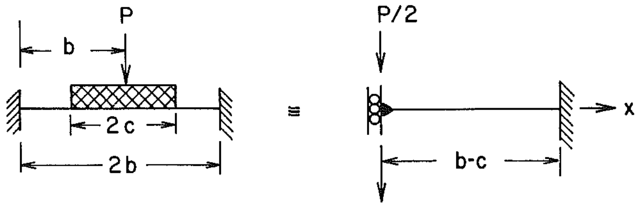

Fig. 8 2D stamp problem with two sided constraints modeled as a simple beam

The numerical results obtained from the approximate solution of this system (reduced to 200 equations) fully confirmed that expectation revealing also other interesting properties of this modified flat punch problem:

(1) For each fixed $\psi = c/b$ such critical value ϕ_{cr} of $\phi = a/b$ exists that indicates the onset of separation of the stamp from the substrate at the midpoint. When $\phi < \phi_{cr}$ then the separation of the central portion of the stamp occurs. When $\phi > \phi_{cr}$, there is no separation ("cushioning" effect). It is to be noted that ϕ_{cr} does not depend on the magnitude P of the applied load and that for an isotropic material assumed here it depends only on the Poisson's ratio ν. The values of ϕ_{cr} calculated for $\nu = 0.3$ are plotted against ψ in Fig. 5.

Table 1 Depth of penetration by the flat stamp for $\psi = 0.25$, $\nu = 0.30$

ϕ	.10	.20	.30	.40	.50	.60	.70	.80	.90	1.00
u_o	97.4	16.3	6.23	3.26	2.06	1.47	1.14	.945	.818	.731

1.25	1.50	1.75	2.00	3.00	5.00	10.00	20.00
.607	.546	.512	.493	.465	.458	.443	.441

(2) The nondimensional stress intensity factor SIF (it is the ratio of the actual stress intensity factor to the one obtained for the infinite case) at the ends of the flat stamp depends on both ψ and ϕ. Its dependence on ϕ is particularly striking: it grows considerably with decreasing ϕ, reaching for instance about 23 for $\phi = 0.1$ and $\psi = 0.5$ (data obtained for the case when separation is prevented by two-sided constraints under the stamp). For fixed ϕ, SIF increases very slowly with ψ. The dependence of SIF on ϕ is shown in Fig. 6 for $\psi = 0.25$ and $\psi = 0.5$.

The presence of two-sided constraints in the contact zone is assumed here. It is evident that for each fixed ψ, SIF has a lower bound > 1. The smaller ψ is the closer this lower bound is to 1, as can be expected. In Fig. 6 it is shown that this lower bound equals 1.096 for $\psi = 0.5$ and equals 1.060 for $\psi = 0.25$.

(3) For each combination of ψ and ϕ the displacements at any point, including those directly under the stamp, can be uniquely determined. Hence the penetration is no longer unknown as it is in the classical problem. The typical shape of the deformed solid is shown in Fig. 7 for $\phi = 0.58$ and $\psi = 0.35$ (the onset of the separation) and for $P/\mu = 1$. It must be noted that the calculated vertical displacement under the edge of the stamp differs by about 5 percent from the displacements of other points under the stamp. This can be attributed to Gibbs phenomenon. For the purpose of illustration the values of the penetration u_o, by the flat stamp, calculated for $\psi = 0.25$, $\nu = 0.30$, and $P/\mu = 1$ are listed in Table 1. These results suggest that for fixed ψ and growing ϕ, u_o approaches a limiting value.

(4) If the flat stamp is assumed to be permanently bonded to the indented substrate, then the calculated value of the displacement under the stamp, u_o, matches the one obtained from the simple beam theory. The latter is determined in the following way: since the deflection is constant under the stamp, all its derivatives are zero and the problem is equivalent to one represented in Fig. 8.

Solving the differential equation for bending of a beam

$$EIy^{IV} = 0 \tag{46}$$

and applying the boundary conditions

$$\begin{aligned} &y' = 0, \quad EIy''' = P/2 \quad \text{at } x = 0 \\ &y = 0, \quad y' = 0 \quad \text{at } x = (1-\psi)b \end{aligned} \tag{47}$$

one obtains maximum deflection at $x = 0$:

$$y_{\max} = P(1-\psi)^3 b^3/24EI \tag{48}$$

Using here, as before $P = \mu = E/2(1+\nu)$ and $I = 1 \cdot a^3/12$ one obtains finally

$$y_{\max} = (1-\psi)^3/4(1+\nu)\phi^3 \tag{49}$$

For $\psi = 0.05$ and $\phi = 0.10$ this yields $y_{\max} = 165$ as compared to $u_o = 176$. For deeper beam the discrepancy between u_o and $y_{\max}$ grows larger due to shear effects among others. For the round stamp (Fig. 3) the calculations made by Keer and Miller (1983) were duplicated. It should be emphasized that their

Table 2 Comparison of the results for a rounded stamp with Keer and Miller (KM) (1983)

						Load/displ.		Max. stress		
c/h	ψ	L/h	ϕ	Pres.	KM	Pres.	KM	Pres.	KM	Comments
0.25	.0167				.04434		26.31			er*
0.50	.0333		.0667	.0586	.0578	34.92	34.84	.625	.622	
1.00	.0667	15.0		.06620	.06634	39.29	39.20	.564	.560	
2.00	.1333			.07629	.07654	44.34	44.26	.985	.979	
4.00	.2667			.1043	.1051	54.31	54.28	1.98	1.97	ps*
0.25	.025			.0574	.0578	10.30	10.23	.637	.635	
0.50	.050			.0846	.0851	15.15	15.02	.628	.622	
1.00	.100	10.0	.1	.1012	.1018	17.99	17.83	.560	.560	
2.00	.200			.1259	.1271	21.38	21.22	.977	.981	
4.00	.400			.2112	.2153	28.12	27.92	1.97	1.97	
0.25	.05			.0820	.0834	2.002	1.912	.640	.635	
0.50	.10			.1517	.1548	3.662	3.506	.627	.622	
1.00	.20	5.0	.2	.2140	.2197	5.004	4.807	.567	.560	
2.00	.40			.3445	.3606	6.778	6.527	.976	.981	
4.00	.80			1.513	1.887	10.55	10.03	1.98	1.97	ps*
0.05	.05			.0055		.0068		.640		
0.25	.25	1.0	1.0	.1238		.1074		.640		
0.50	.50			.3972		.2739		.627		

*er = erratic results
*ps = partial separation

method, as a combination of the solution for an infinite layer and a finite simple beam is applicable to relatively slender beams. The present method is: (1) free of this limitation; (2) satisfies exactly the boundary conditions at fixed ends (at Keer and Miller the ends are allowed to move freely in vertical direction what is of no consequence for slender beams, but this and disregard of corner singularities may affect the results for deeper beams).

The results of the calculation and the comparison with the results of Keer and Miller (1983) are given in Table 2. It seems that except for the value of $\bar{P}^{(R)}$ for $c/h = 4.0$ and $L/h = 5.0$ the correlation of the results is very good. The case of a very deep beam ($L/h = 1.0$) was not calculated by Keer and Miller.

Acknowledgments

This research was sponsored in part by the US Department of Energy under Contract DEA CO-281-ER 10910. This support, and that of Dr. Robert Gottschall of the US Department of Energy, is gratefully acknowledged. Fruitful discussion with Professor G. Adams from Northeastern University, Boston, Mass., is also greatly appreciated.

References

Gladwell, G. M. L., 1980, *Contact Problems in Classical Theory of Elasticity*, Sijthoff & Noordhoff.

Kantorowitsch, L. W., Krylow, W. I., 1956, Naherungsmethoden der Hoherenanalysis, V. E. B.

Nied, H. F., Erdogan, R., 1979, "A Cracked Beam or Plate Transversely Loaded by a Stamp," *Int. J. Solids Structures*, Vol. 15, p. 951-965.

Sadowsky, M. A., 1928, "Zweidimensionale Probleme der Elastizitatstheorie," *ZAMM*, Vol. 8, p. 107-121.

Benthem, J. P., Minderhoud, P., 1972, "The Problem of the Solid Cylinder Compressed Between Rough Rigid Stamps," *Int. J. Solids Structures*, Vol. 8, p. 1027-1042.

Keer, L. M., Miller, G. R., 1983, "Smooth Indentation of a Finite Layer," *ASCE J. of Engineering Mechanics*, Vol. 109, p. 706-717.

Sanhar, B. V., Sun, C. T., 1983, "Identation of a Beam by a Rigid Cylinder," *Int. J. Solids Structure*, Vol. 19, p. 293-303.

muMATH-muSIMP Symbolic Manipulation Package, 1981, Microsoft.

Howard L. Schreyer
Mem. ASME

Z. Chen

Department of Mechanical Engineering and
The New Mexico Engineering Research
Institute,
University of New Mexico,
Albuquerque, NM 87131

One-Dimensional Softening With Localization

The relationship between material softening and structural softening is investigated through the use of a model problem in one dimension. If the size of the softening zone is large the structural softening response is stable under displacement-prescribed loading. For a small size, the softening response is unstable and the loading regime is sensitive to imperfections in stiffness. A nonlocal constitutive equation in which the limit stress is a function of strain and strain gradient is introduced to provide an approach for simulating softening with localization. Implications for the numerical modeling of softening phenomena are given.

Introduction

Numerous computational codes contain numerical algorithms for strain-hardening plasticity. To develop a capability for predicting large deformations, strain softening must be incorporated. Strain softening is associated with localization, and if no precautions are taken, the region of localization will depend on the size of the mesh used for spatial discretization. This mesh-dependence is clearly unacceptable, and therefore an approach that can provide basic equations governing the phenomena of softening and localization is needed. Several studies concerning the conditions necessary for the onset of localization are available (Rudnicki and Rice, 1975; Vermeer, 1982; Prevost, 1984), but it is still not clear which procedure is optimal for predicting postlimit states.

From a continuum point of view, Bazant (1976) has pointed out that the region of localization must condense to what might be considered a surface. However, such an idealization is rarely observed in experiments. On the other hand, there is no doubt that a region of localization exists and may consist of a band whose lateral dimension appears to depend on the physical characteristic of the materials. Because of the complexity of the problems involving a material instability, a numerical technique such as the finite-element method has been used to obtain most solutions. Inherent in such a technique is the problem that a region of localization that is smaller than the element size cannot be accurately represented. In fact, the predicted response will generally depend on the element size in which case the modeling of actual physical phenomena is lost.

Recently, considerable effort has been made to obtain a suitable approach to handling strain softening and localization. A promising approach (Bazant, 1984b; Pietruszczack and Mroz, 1981) involves the assumption that the size of the localization is fixed with the size related to the material being studied. Softening characteristics are adjusted to take element size into account or to ensure that an appropriate amount of energy dissipation is provided. However, Willam (1984) suggests that in order to take into account what appear to be different modes of softening, a composite damage formulation is necessary. A motivation for the use of a nonlocal constitutive equation is that the aspects discussed by Willam can perhaps be synthesized into one theory, although Bazant and Chang (1984) point out that certain precautions must be taken. Recently, Bazant, Belytschko, and Chang (1984) and Bazant (1984b) have introduced the concept of an imbricated continuum which is a method for capturing nonlocal constitutive features. Physically realistic results have been obtained for

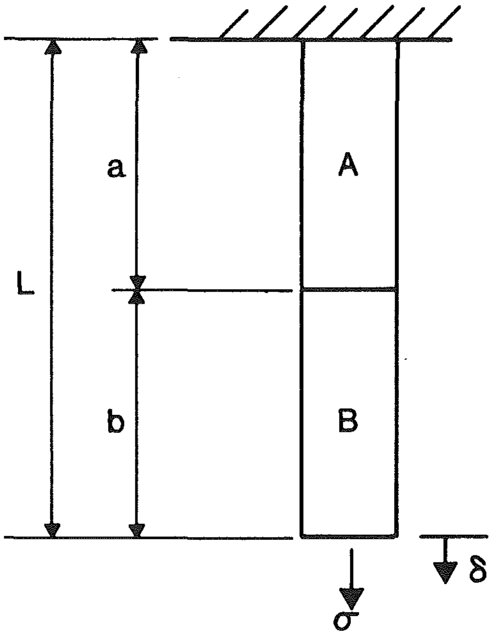

Fig. 1 One-dimensional model problem

Contributed by the Applied Mechanics Division for publication in the JOURNAL OF APPLIED MECHANICS.

Discussion on this paper should be addressed to the Editorial Department, ASME, United Engineering Center, 345 East 47th Street, New York, N.Y., 10017, and will be accepted until two months after final publication of the paper itself in the JOURNAL OF APPLIED MECHANICS. Manuscript received by ASME Applied Mechanics Division, June 13, 1985; final revision February 20, 1986.

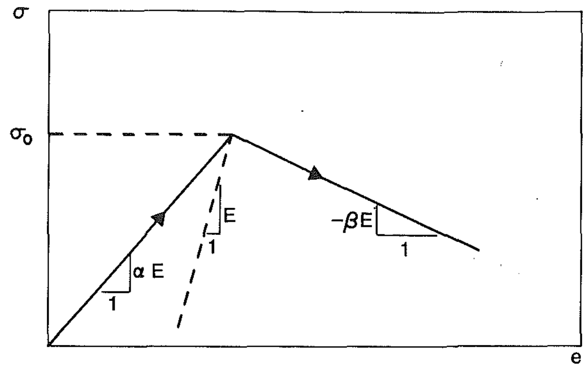

Fig. 2 Constitutive relation for segments *A* and *B*

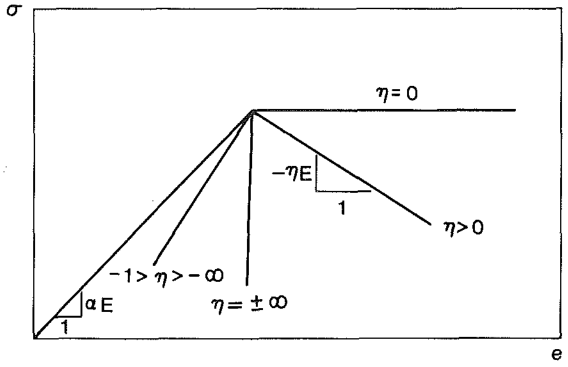

Fig. 3 Composite constitutive relation

wave propagation in a bar. The arguments of Sandler (1984) and Read and Hegemier (1985) that strain softening is not a true material property has been circumvented to a certain extent by the use of nonlocal continuum laws which do involve softening.

Triantafyllidas and Aifantis (1984) and Aifantis (1984) point out the need for an approach to localization that will automatically generate in a predictive and natural way solutions with localized deformations. For hyperelastic materials they have shown that such a procedure is possible by introducing higher-order deformation gradients in the constitutive equations. The result is a static problem that is well-posed in the softening region, and consequently, well-posedness probably exists for the dynamic problem, especially in light of the solution provided by Bazant and Belytschko (1985).

At least two aspects of strain softening and localization have not been addressed. First, the effect of initial imperfections is unknown; and second, the potential usefulness of a nonlocal constitutive relation has not been conclusively demonstrated. In this paper, the implications of softening, localization, stiffness imperfections, and the assumption that stress is a function of both strain and the gradient of strain are explored by means of a one-dimensional model problem. It is believed that the insight provided can be useful for the construction of more general theories to address the issues that have been raised in connection with softening.

Model Problem

Willam, Pramono, and Sture (1985) argue that a series arrangement of intact elastic and strain-softening zones is more representative of post-critical experiments on concrete than a parallel arrangement. Therefore, to simulate the softening phenomenon (Crisfield, 1982; Schreyer and Chen, 1984) consider a body of length $L = a + b$ and a unit cross-sectional area as shown in Fig. 1. This body can be considered a bar or, in a more general sense, a structural member or even a finite element of a continuum. The element is considered to be composed of two segments described by similar constitutive equations, the only difference being that the limit stress for segment B is slightly less than that for segment A. If the stress on the element is such that the strain in region B exceeds the value at the limit state, then softening will be exhibited. It is assumed that softening occurs uniformly over a localized region B whose dimension is given by the parameter b. It is also assumed that the length of the element is greater than that of the softening regime, i.e., $L > b$.

For simplicity, the constitutive relation for both regions is considered to be bilinear. The slopes of the loading and softening segments are αE and $-\beta E$, respectively. If unloading occurs, a line with slope E is followed so that if $\alpha < 1$, the effect of strain hardening can be simulated in an approximate sense. The limit stress for region A, denoted by σ_a, is assumed to be infinitesimally larger than the limit stress for region B, denoted by σ_0. These details are sketched in Fig. 2.

There is a cogent argument that strain softening does not exist. It is the essence of damage theory (Krajcinovic, 1983) that a decrease in apparent stress occurs not by strain softening but by a reduction in effective area due to the coalescence of voids and microcracks. The viewpoint adopted here is that for an engineering approach, the choice of a procedure for providing a drop in nominal stress with strain can be based on convenience because a rigorous development of the two methods should provide the same results on a macroscopic basis. For the current development, the assumption of strain softening provides a suitable basis for deriving general results that would not change if an alternative approach were used.

For given values of strain in regions A and B, which are denoted by e_a and e_b, respectively, the corresponding elongations are

$$\delta_a = a e_a \quad \delta_b = b e_b \tag{1}$$

Then the elongation and the composite strain for the complete element are given by

$$\delta = \delta_a + \delta_b \quad e = \delta / L \tag{2}$$

The composite constitutive equation is characterized by the relation between stress, σ, and strain, e, or equivalently, a P-δ curve.

For monotonically increasing stress from zero up to the limit stress, the composite constitutive equation is identical to the constitutive equation for either segment. However, the postlimit response is different. To obtain this part of the curve, suppose that e_b is given an increment, Δe_b. From equilibrium in segment B,

$$\Delta\sigma = -\beta E \Delta e_b \tag{3}$$

and the change in strain in segment A is

$$\Delta e_a = \frac{\Delta\sigma}{E} = -\beta \Delta e_b \tag{4}$$

It follows from equation (2) that the increment in total strain is

$$\Delta e = \frac{(b - \beta a)}{L} \Delta e_b \tag{5}$$

The result of substituting equation (3) in equation (5) is

$$\Delta\sigma = -\eta E \Delta e \tag{6}$$

where

$$\eta = \frac{\beta L}{b(1+\beta) - \beta L} \tag{7}$$

The composite, or smeared, constitutive relation is shown schematically in Fig. 3. The case of an infinite value of η corresponds to a vertical drop in stress, and the stress-strain curve displays a decrease in strain with a decrease in stress for

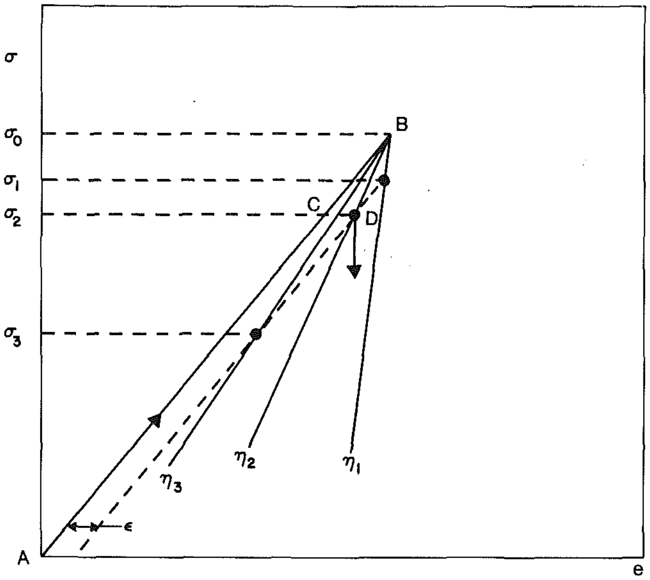

Fig. 4 The effect of an initial imperfection on a stable equilibrium state

negative values of η. The parameter α, which characterizes strain hardening, does not appear in the expression for η. As L increases, η approaches asymptotically the limiting value of -1.

Implications

Experimental data are often obtained with stress-prescribed devices, in which case failure occurs when the limit load is reached. For some devices, however, displacements are prescribed, in which case postlimit data can be obtained unless the case corresponding to negative values of η exists. If the model problem represents an element in a continuum, for example, then because of the basic indeterminacy of such a system, the situation is probably closer to a displacement or strain-controlled problem than to one of load or stress control.

If the loading condition can be represented adequately by increasing the strain monotonically, and if η is negative, then it is apparent from Fig. 3 that it is impossible to follow the actual stress-strain curve. If an increment in load forces e to be larger than $e_0 = \sigma_0/\alpha E$, the result will be a snapdown to zero stress with a corresponding release of energy. Because loss of stability is often associated with failure, a condition of negative η is assumed to be undesirable. However, no matter how small a value (positive) of β is appropriate, equation (7) shows that η can be made negative for a sufficiently large value of L with b fixed. In the context of a structural member, the dependence of instability on the size of the structure is a manifestation of a size effect that has not been investigated extensively. For example, fracture can be used to justify the argument that strain softening is not observed in metals. However, an alternate interpretation for fracture can be given. The phenomenon of crack growth occurs in such a small zone compared to the length of the specimen that the terms involving L in equation (7) dominate, and η is negative. In other words, fracture is usually an unstable process because of the size of the specimen, not because strain softening does not exist. In fact, since crack widening has been controlled for concrete (Shah and Gopalaratnam, 1984), it would be interesting to know whether one could obtain a similar result for metals by using sufficiently small specimens.

An energy interpretation is apparent. Once softening occurs, the energy dissipated in region B must be provided from region A and from any work added by an external agency. The situation defined by $\eta = \pm\infty$ is the critical case in which region A can provide enough energy to match that dissipated in region B with no additional work, a case corresponding to $\Delta e = 0$.

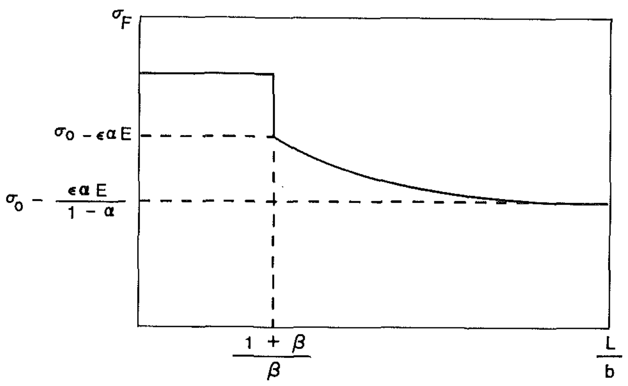

Fig. 5 Failure stress as a function of element length

In many finite-element codes that use explicit time integration, the total strain increment is fixed at each time step. Some algorithms incorporate the conventional softening identified with $\eta > 0$, but almost none incorporate the possibility associated with $\eta < 0$. From equation (7), the need for the latter case can be averted by selecting the element size h, such that

$$0 < h < L^* \equiv \frac{b(1+\beta)}{\beta} \tag{8}$$

It is assumed, of course, that b is known.

Willam, Pramono, and Sture (1985) have theoretically developed the weak restriction $\eta \leq 1$ which must hold for uniqueness. If such a condition is invoked, then the maximum allowable element size is $L^*/2$ rather than L^* given by equation (8). The primary problem is that elements larger than L^* are desirable. In addition to the problem of uniqueness, the use of large elements would require a constitutive equation that incorporates a negative value of η. To the authors' knowledge, such an algorithm has not been developed. This feature may not be difficult to incorporate because plasticity algorithms automatically incorporate an elastic unload feature. In the postpeak regime, which is not unloading because energy is being dissipated, a pseudoelastic behavior could be incorporated as a three-dimensional representation of the case corresponding to negative η. Simultaneously, the limit surface must contract to exclude any path that involves an increase in stress. With such a constitutive model, the static analysis of structures would require a special numerical algorithm to predict the possible snap-down and snap-back response features. Although the arc-length method holds considerable promise, a general and robust procedure has not been demonstrated for applications to strain softening and localization.

Initial Imperfections

So far, the development for the model problem indicates a size effect based on the softening feature of an element, but there is no implication that the apparent failure or fracture stress varies with the size of the structural member. To show that there may be a size effect for the failure stress as well, consider the case in which $L \gg b$, so that η is close to (slightly less than) -1. The situation is illustrated in Fig. 4 with $\eta_1 < \eta_2 < \eta_3 \leq -1$. The fact that the pre- and postlimit equilibrium states can be close suggests that the response of the structural member will be sensitive to initial imperfections or loading disturbances. Rather than being geometrical in

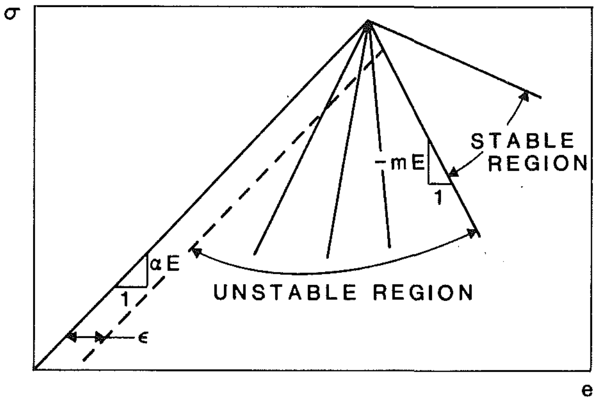

Fig. 6 **Reduction in failure stress for initial imperfections on a spring-loaded element**

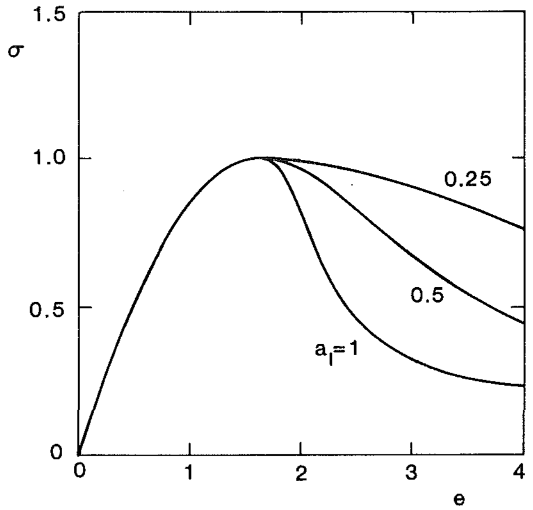

Fig. 7 **The effect of the parameter a_1 on strain-softening**

nature, the imperfections of concern here are those associated with variations in stiffness, αE, as the structure is loaded. Suppose such variations are bounded on one side by the dotted line in Fig. 4, where the imperfection is characterized by the strain parameter, ϵ. Then, for strain-prescribed loading, it is possible for a snap-down response to occur at stress values of σ_1, σ_2, and σ_3 for softening conditions characterized by η_1, η_2, and η_3, respectively. To be specific, if $\eta = \eta_2$ and the load increases from point A to point C, then the possibility of reaching an alternative equilibirum state exists at $\sigma = \sigma_2$, and snap-down from D is feasible.

The presence of initial imperfections provides the rationale for a potential size effect on the limit stress (or limit load) that can be exhibited by a structural member. As the size of the element increases, the softening parameter approaches -1, and the probability of snap-down at a stress less than the ultimate stress becomes greater.

Geometrical arguments based on Fig. 4 can be used to show that the failure stress, in the presence of imperfections, is

$$\sigma_F = \sigma_0 \quad \eta \geq 0$$

$$\sigma_F = \sigma_0 - \frac{\epsilon\alpha E}{1+\alpha/\eta} \quad \eta \leq -1 \tag{9}$$

For brittle materials, modeled by a value of α close to unity, the failure stress is sensitive to imperfections as exhibited through ϵ; whereas for ductile materials, modeled by small values of α, the decrease in the failure stress from σ_0 is not as abrupt. The idealized post-peak response, as reflected through η in equation (7), does not depend on α, whereas a consideration of initial imperfections shows that strain hardening, as exhibited by values of α less than one, is an important characteristic.

A plot of failure stress as a function of L/b is shown in Fig. 5. For strain-controlled loading, no reduction in failure stress occurs if the structural element is small enough. When L/b reaches the critical value of $(1 + \beta)/\beta$, the failure stress decreases sharply. The magnitude of the jump depends on the degree of inelasticity in the loading part of the stress-strain curve. With a further increase in structural size, or a decrease in the size of the region of localization, the failure stress asymptotically approaches a limiting value, which also depends on the parameter α. In fact, if α is close to one, the limiting value can be zero for large values of L/b.

These results must be ameliorated to a certain extent because neither total strain nor a stress-controlled loading condition describes a typical problem. Instead, a stable post-peak response may be the line with a slope of $-m$, where $0 \leq m < \infty$, so that an additional regime of instability exists for values of η between m and ∞ as shown in Fig. 6. Except for a change in some of the details, the basic concepts outlined previously are still valid, and the matter will not be pursued further except to say that alternate considerations also imply a decrease in strength with an increase in the size of a structural member. For example, Bazant and Panula (1978) made such a claim based on the assumptions that material properties are randomly distributed and that a model structure can be represented by a set of elements in parallel rather than in series. Another size effect due to blunting at a fracture front has been described by Bazant (1984a).

A Nonlocal Constitutive Model

The existence of a localized region with strains much larger than those in the adjacent region implies that the strain gradient must be large. For cases in which softening and localization occur, it is not clear whether the region of localization remains fixed in size or changes monotonically with deformation. One approach is to postulate that a characteristic dimension of localization depends on the material (Bazant, 1984a) while another involves dependence on the post-peak stress (Shah and Gopalaratnam, 1984). A disadvantage of these assumptions is that a separate procedure for handling softening must be established for numerical computations. On the other hand, an alternate approach involving an assumption on the constitutive equation might provide equivalent results, but with the advantage that the softening mechanism would be a consequence of the loading path. As a result, existing numerical algorithms could be used with a minimal degree of modification.

To explore the potential usefulness of a nonlocal constitutive equation, a modified form of the relation shown in Fig. 2 is used. The nomenclature of conventional plasticity is used to suggest a possible three-dimensional generalization. Suppose the yield function is given by

$$F = \bar{\sigma} - H \tag{10}$$

where $\bar{\sigma}$ is the second invariant of the stress deviator normalized such that $\bar{\sigma} = |\sigma|$ for uniaxial stress. The strain hardening function is prescribed to be continuous with a continuous first derivative as follows:

$$H = H_o + (H_L - H_o)\sin\left[\frac{\pi}{2}\left(\frac{e^i}{e^i_L}\right)^n\right] \quad o \leq e^i \leq e^i_L$$

$$H = H_a + (H_L - H_a)(1 + a_1 e^*)e^{-a_1 e^*} \quad e^i > e^i_L \tag{11}$$

with

$$e^* = \frac{e^i - e^i_L}{e^i_L} \tag{12}$$

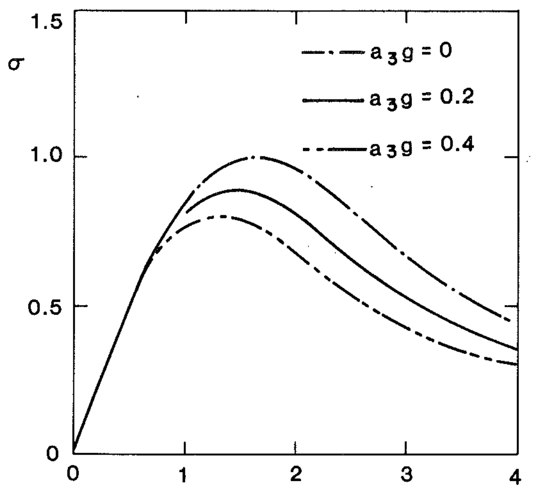

Fig. 8 The assumed effect of strain-gradient on stress-strain behavior

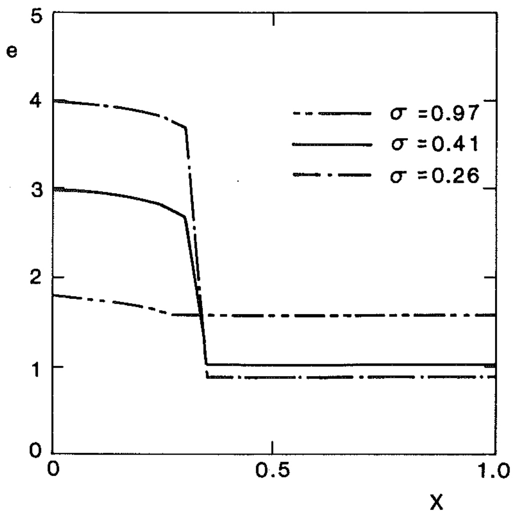

Fig. 9 Distribution of strain for various levels of stress in the post-peak regime

The inelastic strain invariant, e^i, is also considered to be scaled so that for uniaxial stress, e^i is equal to the absolute value of the principal inelastic strain. The value of e^i at the limit state is e^i_L. Initial and peak values of yield stress are denoted by H_o and H_L, respectively. The parameter n controls the shape of the strain hardening part of the stress-strain curve. In the strain softening regime, the function H decreases to the asymptote H_a. For a Young's modulus of $E = 1$, and with $H_o = 0.5$, $H_L = 1$, $H_a = 0.2$, $e^i_L = 0.1$, and $n = 0.5$, the effect of the parameter a_1 is shown in Fig. 7.

Suppose further that an inelastic strain gradient causes a decrease in both the limit stress and the inelastic strain at the limit state. Although it will be shown that realistic localization features are predicted for uniaxial tension, the assumption appears to be contrary to experimental evidence obtained from simple bending tests where both strain gradients and an enhancement of the tensile limit stress are exhibited. However, the strain field in beams displays different strain gradients in two directions which is a topic beyond the scope of this investigation.

A smooth characterization of the assumed effect of the strain gradient is given by

$$\begin{aligned} H_L &= H_{L0}G \\ e^i_L &= e^i_{L0}G \qquad (13) \\ G &= a_2 + (1-a_2)e^{-a_3 g} \end{aligned}$$

where g denotes the absolute value of the gradient of the inelastic strain invariant normalized to equal the absolute value of the inelastic strain gradient under uniaxial stress. For $H_{L0} = 1$, $e^i_{L0} = 0.1$, $a_1 = 0.5$ and $a_2 = 0.4$, the postulated effect of strain gradient on the stress-strain curve is shown in Fig. 8. The material parameter a_3 has the dimension of length and its effect can only be exhibited for cases involving nonuniform strain.

To show the effect of g, consider a bar under uniaxial stress loaded such that the strain in the softening region is increased monotonically. For model parameters listed previously except for $a_1 = 0.8$, and $a_3 = 0.05$, the evolution of strain distribution for a bar discretized with 20 uniform elements is shown in Fig. 9. Initially the strain is uniform. Once the peak stress is reached at a point chosen arbitrarily to be $x = 0$, a portion of the bar in the softening zone will continue to elongate, while elastic retraction will cause the remainder of the bar to shrink. The region of continued extension is the localized softening region which develops to a maximum size and thereafter remains fixed. The listed values for stress are less than one because the structure is in the post-peak regime. The lower the value of stress, the more extensive is the strain softening.

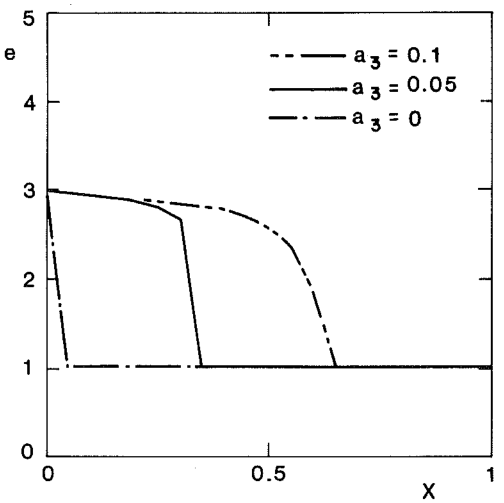

Fig. 10 The effect of the parameter a_3 on the region of localization for $\sigma = 0.41$

Strain distributions for a fixed value of stress in the post-peak regime are shown in Fig. 10 for various values of a_3. When $a_3 = 0$, which corresponds to a conventional constitutive equation with no consideration of strain gradients, the softening localizes into a single element as expected. An increase in the value of a_3 corresponds to a widening of the softening region; thus, if softening is very localized, which occurs with cracking for example, then a small value of a_3 should be used.

The effect of element size is shown in Fig. 11, in which convergence is displayed.

For a length of one unit, the stress-deflection relation for the bar is shown in Fig. 12 for various values of a_3. When $a_3 = 0$, unstable behavior is predicted for displacement-prescribed loading whereas larger values of a_3 yield results that are stable. All of the softening curves will be steeper if a longer bar is analyzed.

Shah and Gopalaratnam (1984) performed tensile tests on concrete under carefully controlled loading conditions and with refined measuring techniques. The response of the con-

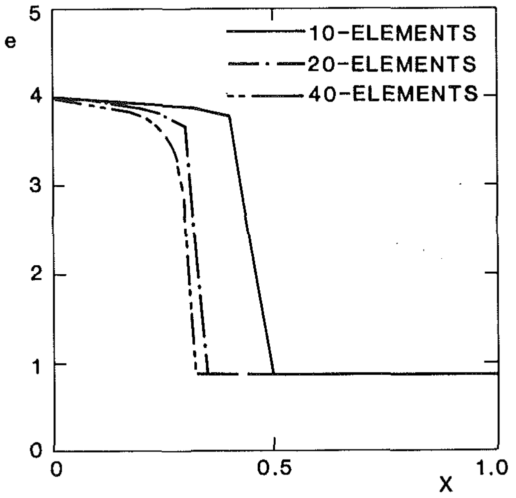

Fig. 11 Effect of element size in which convergence is shown for $\sigma = 0.26$ ($a_1 = 0.8$, $a_3 = 0.05$)

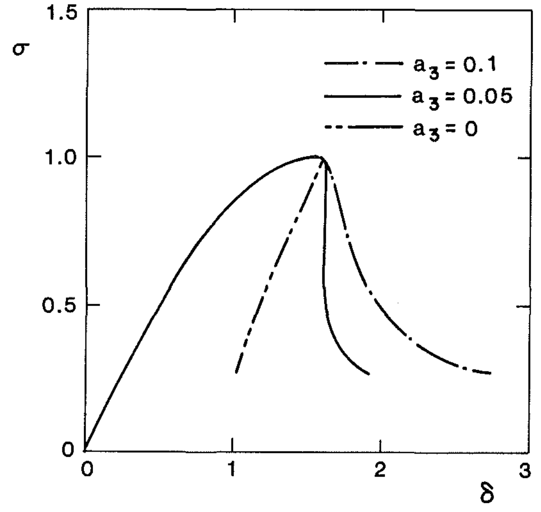

Fig. 12 Effect of the parameter a_3 on the stress-deflection relation for a bar of unit length

crete specimen was modeled with 20 elements and the following material parameters:

$E = 5 \times 10^6$ psi
$H_{L0} = 530$ psi
$a_1 = 0.03$
$a_3 = 60$ in.
$e^i_{L0} = 3.8 \times 10^{-6}$
$H_o = 370$ psi
$H_a = 53$ psi
$a_2 = 0.4$
$n = 0.5$

The theoretical stress-elongation relation for a gage length of 3.25 in. is compared with the experimental result in Fig. 13 which shows that the softening response has been captured with a nonlocal plasticity model. However the size of the predicted softening zone is 0.16 in. which is considerably larger than the measured crack width. This difference between theoretical and experimental values may be due to the existence of a softening region outside the crack zone, or to a deficiency in the model. An interesting feature is the small value of a_1 which indicates that very little strain softening is required to obtain a reasonable result. This absence of a significant amount of strain softening is close in spirit to the argument of Read and Hegemier (1984) that experimental evidence does not support the concept of strain softening.

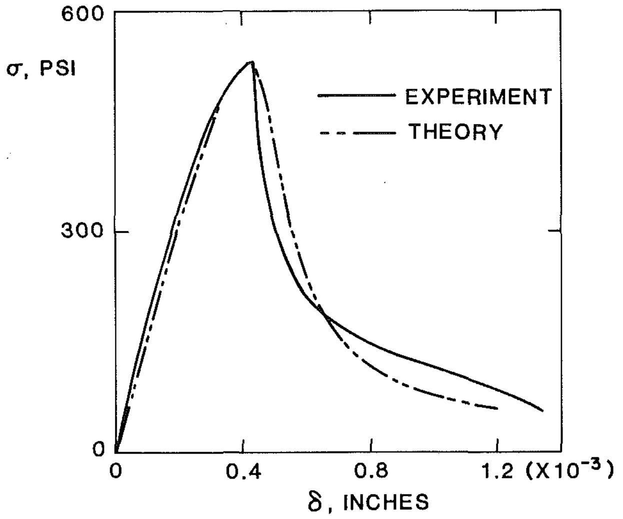

Fig. 13 Tensile stress-deflection relation for a concrete specimen; experimental data from Shah and Gopalaratnam (1984)

Conclusion

With the use of an elementary model problem, the significance of both strain softening and the ratio of the size of the softening region to the size of the structure has been demonstrated. For a given strain softening relation and for structural elements that are small enough, the slope of the softening part of the load-deflection curve will depend on the size of the structural element. This conclusion is in agreement with three-dimensional softening data obtained by Van Mier (1984) who performed experiments on cubical specimens. The experimental results show that the descending branch of the stress-strain curve should be considered a structural characteristic rather than a material property. Similar implications follow from the examples given by Read and Hegemier (1984).

If the structural element is large enough, the assumption of strain softening implies that unstable equilibrium states exist even if the problem is one of displacement-controlled loading. The presence of unstable equilibrium states adjacent to stable equilibrium states suggests that such a structure is sensitive to variations in stiffness. Consequently, the failure load may be less than the load associated with the nominal peak stress. The possible reduction in dimensionless failure load with an increase in the size of a structural element is a size effect that has been noted previously from alternate viewpoints.

One approach for predicting the various manifestations of softening in a continuous medium without being overwhelmed with detail is to assume that the constitutive equation incorporates strain softening and is nonlocal. If the mesh size used for structural discretization is small enough, then structural softening and the region of localization are predicted in an evolutionary manner. Comparisons between theoretical and experimental data associated with the cracking of concrete indicate that the method is useful and that a generalization to three dimensions is feasible.

From a practical viewpoint for numerical calculations, a mesh size larger than the region of localization is desirable in which case the constitutive equation must be modified to incorporate a reversal in strain in the post-peak regime. The theoretical and computational issues associated with strain reversals must be resolved before softening and localization can be routinely handled.

Acknowledgment

This research was supported by the US Air Force Office of Scientific Research.

References

Aifantis, E. C., 1984, "On the Microstructural Origin of Certain Inelastic Models," *Journal of Engineering Materials and Technology*, Vol. 106, pp. 326-330.

Bazant, Z. P., 1976, "Instability, Ductility, and Size Effect in Strain-Softening Concrete," *ASCE Journal of the Engineering Mechanics Division*, EM2, pp. 331-334.

Bazant, Z. P., and Panula, Z., 1978, "Statistical Stability Effects in Concrete Failure," *ASCE Journal of the Engineering Mechanics Division*, EM5, pp. 1195-1212.

Bazant, Z. P., 1984a, "Size Effect in Blunt Fracture: Concrete, Rock, Metal," *ASCE Journal of Engineering Mechanics*, Vol. 110(4), pp. 518-535.

Bazant, Z. P., 1984b, "Imbricate Continuum and its Variational Derivation," *Journal of Engineering Mechanics*, Vol. 110(12), pp. 1693-1712.

Bazant, Z. P., Belytshko, T. B., and Chang, T. P., 1984, "Continuum Theory for Strain Softening," *Journal of Engineering Mechanics*, Vol. 110(12), pp. 1666-1692.

Bazant, Z. P., and Belytschko, T. B., 1985, "Wave Propagation in a Strain-Softening Bar: Exact Solution," *Journal of Engineering Mechanics*, Vol. III(3), pp. 381-389.

Bazant, Z. P., and Chang, T. P., 1984, "Instability of Nonlocal Continuum and Strain Averaging," *ASCE Journal of Engineering Mechanics*, Vol. 110(10), pp. 1441-1450.

Crisfield, M. A., 1982, "Local Instabilities in the Nonlinear Analysis of Reinforced Concrete Beams and Slabs," *Proceedings of the Institution for Civil Engineers*, Vol.73(12), pp. 135-145.

Krajcinovic, D., 1983, "Constitutive Equations for Damaging Materials," ASME JOURNAL OF APPLIED MECHANICS, Vol. 50, pp. 355-360.

Pietruszczak, St., and Mroz, A., 1981, "Finite Element Analysis of Deformation of Strain-Softening Materials," *International Journal of Numerical Methods in Engineering*, Vol. 17, pp. 327-334.

Prevost, J. H., 1984, "Localization of Deformation in Elastic-Plastic Solids," *International Journal for Numerical and Analytical Methods in Geomechanics*, Vol. 8, pp. 187-196.

Read, H. E., and Hegemier, G. A., 1984, "Strain Softening of Rock, Soil and Concrete—A Review Article," *Mechanics of Materials*, Vol. 3, pp. 271-294.

Rudnicki, J. W., and Rice, J. R., 1975, "Conditions for the Localization of Deformation in Pressure-Sensitive Dilatant Materials," *Journal of the Mechanics and Physics of Solids*, Vol. 23, pp. 371-394.

Sandler, I. S., 1984, "Strain Softening for Static and Dynamic Problems," *Proceedings of the Symposium on Constitutive Equations: Micro, Macro, and Computational Aspects*, Willam, K., ed., ASME Winter Annual Meeting, New Orleans, 10-14, Dec. 1984, pp. 217-231.

Schreyer, H. L., and Chen, Z., 1984, "The Effect of Localization on the Softening Behavior of Structural Members," *Proceedings of the Symposium on Constitutive Equations: Micro, Macro, and Computational Aspects*, Willam, K., ed., ASME Winter Annual Meeting, New Orleans, 10-14, Dec. 1984, pp. 193-203.

Shah, S. P., and Gopalaratnam, V. S., 1985, "Softening Response of Plain Concrete in Direct Tension," *Journal of the American Concrete Institute*, Vol. 82, pp. 310-323.

Triantafyllidis, N., and Aifantis, E. C., 1984, "A Gradient Approach to Localization of Deformation: I. Hyperelastic Materials," MM Report No. 6, Dept. of Mechanical Engineering—Engineering Mechanics, Michigan Technological University, Houghton, Michigan.

Van Mier, J. G. M., 1984, "Strain-Softening of Concrete Under Multiaxial Loading Conditions," Ph.D. Dissertation, University of Eindhoven, The Netherlands.

Vermeer, P. A., 1982, "A Simple Shear-Band Analysis Using Compliances," *International Union of Theoretical and Applied Mechanics, Proceedings of the Symposium on Deformation and Failure of Granular Material*, Delft, The Netherlands, 31 Aug.-3 Sept., Vermeer, P. A., and Luger, H. J., eds., published by A. A. Balkema, Rotterdam.

Willam, K. J., 1984, "Experimental and Computational Aspects of Concrete Fracture," Invited Paper, International Conference on Computer-Aided Analysis and Design of Concrete Structures, Split, Yugoslavia, Sept. 17-21.

Willam, K. J., Pramono, E., and Sture, S., 1985, "Stability and Uniqueness of Strain-Softening Computations," Structural Research Series 8503, Department of Civil, Environmental and Architectural Engineering, University of Colorado, Boulder.

Inclined Flat Punch of Arbitrary Shape on an Elastic Half-Space

V. I. Fabrikant
Department of Mechanical Engineering,
Concordia University,
Montreal, Canada H3G 1M8

A new method is proposed for the analysis of elastic contact problems for a flat inclined punch of arbitrary planform under the action of a normal noncentrally applied force. The method is based on an integral representation for the reciprocal distance between two points obtained by the author earlier. Some simple yet accurate relationships are established between the tilting moments and the angles of inclination of an arbitrary flat punch. Specific formulae are derived for a punch whose planform has a shape of a polygon, a triangle, a rectangle, a rhombus, a circular sector and a circular segment. All the formulae are checked against the solutions known in the literature, and their accuracy is confirmed.

Introduction

The theory of elastic contact problems for classical domains (a circle and an ellipse) is well developed (Galin, 1961). There are quite a few publications treating the case of a flat nonelliptical punch under the action of a centrally applied force (Rvachev and Protsenko, 1977). There are almost no reports on the case of a noncentrally applied force and a nonclassical domain of contact. We are aware of only one report (Rvachev and Protsenko, 1977) considering an inclined circular punch, with a zone of separation between the punch and the elastic half-space. Slightly better is the situation in Electrical Engineering where the mathematically equivalent problem of the magnetic polarizabilty coefficients was solved numerically for several specific shapes (de Smedt, 1979; De Meulenaere and Van Bladel, 1977; Okon and Harrington, 1981). Though their results sometimes differ by more than the accuracy they claim, we have no other source for verification of the accuracy of the formulae to be derived here.

This paper constitutes the second part of a three-part project. In the first part (Fabrikant, 1986) we derived a universal formula for the relationship between the punch settlement and a centrally applied force which compares favorably with the numerical results available for a regular polygon, a rectangle, a triangle, a rhombus, a circular sector, and a segment. Here, the same method is used for the solution of the problem of an inclined punch of arbitrary planform. Some general relationshps are derived between the tilting moments and the angles of inclination of the punch. Specific formulae are derived for various punch planforms, and their accuracy proves to be quite satisfactory when compared with the numerical results available. The third part of the project will deal with an arbitrary curved punch.

Theory

It is well known (Galin, 1961) that the problem of an arbitrary punch on an elastic half-space can be reduced to the solution of the following integral equation

$$w(N)=H\iint_S \frac{\sigma(M)}{R(M,N)}\,dS \tag{1}$$

where S is a two-dimensional domain of contact, $R(M,N)$ stands for the distance between the points M and N, w denotes the normal displacements under the punch (known function), σ stands for the normal stress exerted by the punch (unknown function), and H is a constant which in the case of an isotropic elastic half-space takes on the value $H=(1-\nu^2)/\pi E$, ν and E being, respectively, the Poisson coefficient and the elasticity modulus. In the case of a transversely isotropic body, the explicit expression for H can be found in Fabrikant (1971b).

The presentation in this paper will be made in terms of the elastic contact problems but one should keep in mind that all the results will be applicable in other branches of engineering science. Here we outline the analytical treatment of the elastic contact problems which allows to derive simple yet accurate formulae for various punch shapes. The approach is based on the integral representation for the reciprocal distance established in Fabrikant (1971a)

$$\frac{1}{\left[\rho^2+\rho_0{}^2-2\rho\rho_0\cos(\phi-\phi_0)\right]^{1/2}}=\frac{2}{\pi}\int_0^{\min(\rho_0,\rho)}\frac{\lambda\left(\dfrac{x^2}{\rho\rho_0},\,\phi-\phi_0\right)dx}{\left[(\rho^2-x^2)(\rho_0{}^2-x^2)\right]^{1/2}} \tag{2}$$

where

$$\lambda(k,\psi)=\frac{1-k^2}{1+k^2-2k\cos\psi} \tag{3}$$

Substitution of equation (2) into equation (1) gives, after changing the order of integration,

---

Contributed by the Applied Mechanics Division for publication in the JOURNAL OF APPLIED MECHANICS.

Discussion on this paper should be addressed to the Editorial Department, ASME, United Engineering Center, 345 East 47th Street, New York, N.Y. 10017, and will be accepted until two months after final publication of the paper itself in the JOURNAL OF APPLIED MECHANICS. Manuscript received by ASME Applied Mechanics Division, December 30, 1985; final revision April 11, 1986.

$$w(\rho,\phi)=\frac{2}{\pi}H\int_0^{\rho}\frac{dx}{(\rho^2-x^2)^{1/2}}\int_0^{2\pi}d\phi_0\int_x^{a(\phi_0)}\frac{\lambda\left(\frac{x^2}{\rho\rho_0},\phi-\phi_0\right)}{({\rho_0}^2-x^2)^{1/2}}\sigma(\rho_0,\phi_0)\rho_0 d\rho_0 \tag{4}$$

Consider a flat-ended punch with a planform S whose boundary is given in the polar coordinates as

$$\rho=a(\phi)$$

where the function $a(\phi)$ is bounded and single-valued. The punch is pressed against an elastic half-space by a normal force P applied at the point with cartesian coordinates x_0 and y_0. This loading is statically equivalent to a centrally applied force P and two tilting moments $M_x = Py_0$ and $M_y = -Px_0$. The case of a centrally applied force was considered in Part 1 (Fabrikant, 1986). It remains here to consider the punch under the action of the tilting moments, and to superpose the results. Let the normal displacements under the punch be

$$w=\alpha_x y-\alpha_y x \tag{5}$$

where α_x and α_y are the tilting angles about the axes Ox and Oy, respectively. It is necessary to relate these angles with the tilting moments.

Let the normal stress distribution under the punch be

$$\sigma=\frac{a(\phi)\rho(p_1\cos\phi+p_2\sin\phi)}{\left[a^2(\phi)-\rho^2\right]^{1/2}} \tag{6}$$

where p_1 and p_2 are yet unknown constants. Make use of the condition that the integral of σ over S should be equal zero. Since p_1 and p_2 are independent, this leads to two equations

$$\int_0^{2\pi}(a(\phi))^3\cos\phi\, d\phi=0,\quad \int_0^{2\pi}(a(\phi))^3\sin\phi\, d\phi=0 \tag{7}$$

One can note that the left-hand side of each equation (7) is proportional to the x or y coordinates of the center of gravity. This means that the origin of the system of coordinates should be located at the center of gravity of the domain of contact. The axis orientation will be discussed later.

The relationships between the tilting moments and the parameters p_1 and p_2 can be established from the statics conditions

$$M_x=Py_0=\iint_S \sigma y\, dS,\quad M_y=-Px_0=-\iint_S \sigma x\, dS$$

which leads to

$$M_x=\frac{8}{3}(p_1I_{xy}+p_2I_x),\quad M_y=-\frac{8}{3}(p_1I_y+p_2I_{xy}) \tag{8}$$

where I_x, I_y, and I_{xy} are the well known quantities of the moments of inertia and the product of inertia, respectively. Now it is necessary to relate p_1 and p_2 to the angles α_x and α_y. This can be done by substitution of equation (6) into equation (4) which yields after integration with respect to ρ_0

$$w(\rho,\phi)=H\sum_{n=-\infty}^{\infty}\int_0^{\rho}\left(\frac{x}{\rho}\right)^{|n|}\frac{x^2dx}{(\rho^2-x^2)^{1/2}}\int_0^{2\pi}e^{in(\phi-\phi_0)}F\left(\frac{3-|n|}{2},\frac{1}{2};1;1-\frac{x^2}{a^2(\phi_0)}\right)(p_1\cos\phi_0+p_2\sin\phi_0)d\phi_0 \tag{9}$$

Here F stands for the Gauss hypergeometric function. Further evaluation of the normal displacements can be done separately for each harmonic. Note that the zeroth and all the even harmonics of w will be zero if $a(\phi)$ contains only the even harmonics. The first harmonic will take the form

$$w_1(\rho,\phi)=\frac{\pi}{2}H\rho\int_0^{2\pi}\cos(\phi-\phi_0)(p_1\cos\phi_0+p_2\sin\phi_0)a(\phi_0)d\phi_0$$

which can be simplified as

$$w_1(\rho,\phi)=\frac{\pi}{2}H\rho[(p_1J_y+p_2J_{xy})\cos\phi+(p_1J_{xy}+p_2J_x)\sin\phi] \tag{10}$$

where the following quantities were introduced

$$J_x=\int_0^{2\pi}a(\phi)\sin^2\phi d\phi,\quad J_y=\int_0^{2\pi}a(\phi)\cos^2\phi d\phi,$$

$$J_{xy}=\int_0^{2\pi}a(\phi)\sin\phi\cos\phi d\phi \tag{11}$$

These quantities do not seem to have been used before in engineering practice so they do not have an accepted name. Since their tensor properties are similar to those of the moments of inertia, we shall call J_x and J_y *the linear moments of a two-dimensional domain about the axes Ox and Oy*, respectively; J_{xy} will be called *the linear product of a two-dimensional domain about the axes Ox and Oy.*

It is important to note that the third harmonic is equal to zero for an arbitrary contour. Here is the expression for the fifth harmonic

$$w_5(\rho,\phi)=\frac{128}{315}H\rho^4\int_0^{2\pi}\frac{\cos5(\phi-\phi_0)}{a^2(\phi_0)}(p_1\cos\phi_0+p_2\sin\phi_0)d\phi_0$$

which can be modified as

$$w_5(\rho,\phi)=\frac{64}{315}H\rho^4\{[(A_{c6}+A_{c4})p_1+(A_{s6}-A_{s4})p_2]\cos5\phi+[(A_{s6}+A_{s4})p_1+(A_{c4}-A_{c6})p_2]\sin5\phi\} \tag{12}$$

Here, the following geometrical characteristics of the domain of contact were introduced

$$A_{c4}=\int_0^{2\pi}\frac{\cos4\phi\, d\phi}{(a(\phi))^2},\quad A_{c6}=\int_0^{2\pi}\frac{\cos6\phi\, d\phi}{(a(\phi))^2},$$

$$A_{s4}=\int_0^{2\pi}\frac{\sin4\phi\, d\phi}{(a(\phi))^2},\quad A_{s6}=\int_0^{2\pi}\frac{\sin6\phi\, d\phi}{(a(\phi))^2}$$

Investigation of further harmonics shows that their amplitude decreases.

Now consider in more detail the case of a square with the side $2l$. The equation of the boundary in this case is $a(\phi) = l/\cos\phi$ for $-\pi/4<\phi<\pi/4$, and the pattern is repeated outside this range. We can evaluate the first two nonzero harmonics:

$$w_1=\pi Hl\rho\, ln(1+\sqrt{2})(p_1\cos\phi+p_2\sin\phi),$$

$$w_5=\frac{128H\rho^4}{945l^2}(p_1\cos5\phi+p_2\sin5\phi) \tag{13}$$

Since the amplitude of w_5 is significantly less than that of w_1, it seems natural to assume $w \approx w_1$, and the remaining harmonics may be called the solution error. Direct computations show that the error is less than 3 percent inside the circle $\rho\leq l$. The error is reasonably small outside the circle, reaching about 20 percent at the apex and decreasing very rapidly with the distance from the apex. Taking into consideration that the error sign fluctuation will result in even smaller error in the integral characteristics sought, a direct comparison of equations (5) and (10) leads to

$$\alpha_x = \frac{\pi}{2} H(p_1 J_{xy} + p_2 J_x), \quad \alpha_y = -\frac{\pi}{2} H(p_1 J_y + p_2 J_{xy}) \tag{14}$$

The inversion of (14) gives

$$p_1 = -\frac{2}{\pi H} \frac{J_{xy}\alpha_x + J_x \alpha_y}{J_x J_y - J_{xy}^2}, \quad p_2 = \frac{2}{\pi H} \frac{J_y \alpha_x + J_{xy}\alpha_y}{J_x J_y - J_{xy}^2} \tag{15}$$

Substitution of (15) into (8) finally gives the required relationship

$$M_x = \frac{16}{3\pi H}(m_{11}\alpha_x + m_{12}\alpha_y), \quad M_y = \frac{16}{3\pi H}(m_{21}\alpha_x + m_{22}\alpha_y) \tag{16}$$

where

$$m_{11} = \frac{J_y I_x - J_{xy} I_{xy}}{J_x J_y - J_{xy}^2}, \quad m_{12} = \frac{J_{xy} I_x - J_x I_{xy}}{J_x J_y - J_{xy}^2}$$

$$m_{21} = \frac{J_{xy} I_y - J_y I_{xy}}{J_x J_y - J_{xy}^2}, \quad m_{22} = \frac{J_x I_y - J_{xy} I_{xy}}{J_x J_y - J_{xy}^2}$$

It is clear that all these results can be rewritten in a matrix or a tensor form. One can verify that formulae (16) are invariant with respect to an arbitrary rotation of the axes. The same property holds for $m_{11} + m_{22}$ and $m_{12} - m_{21}$. Strictly speaking, according to the reciprocal theorem, m_{12} should be equal m_{21}, so that formulae (16) generally do not satisfy this theorem. But we may state that this theorem is satisfied "approximately." We mean by this the following property which has been verified by several direct computations, namely, $|m_{12} - m_{21}|/m_{11} \ll 1$ and $|m_{12} - m_{21}|/m_{22} \ll 1$. This theorem will be satisfied exactly for any domain which has at least one axis of symmetry because in this case $m_{12} = m_{21} = 0$ provided that the coordinate axes coincide with the central principal axes of the domain of contact. Since we have no numerical data for nonsymmetrical domains which could be used to verify the accuracy of (16), we shall consider further only the case when the domain of contact has an axis of symmetry. In this case formulae (8), (14), and (16) simplify significantly

$$M_x = \frac{8}{3} I_x p_2, \qquad M_y = -\frac{8}{3} I_y p_1 \tag{17}$$

$$\alpha_x = \frac{\pi}{2} H J_x p_2, \qquad \alpha_y = -\frac{\pi}{2} H J_y p_1 \tag{18}$$

$$M_x = \frac{16}{3\pi H} \frac{I_x}{J_x} \alpha_x, \qquad M_y = \frac{16}{3\pi H} \frac{I_y}{J_y} \alpha_y \tag{19}$$

Returning back to our problem of noncentrally applied force and using the results of Part 1 (Fabrikant, 1986), we can write the following expression for the stress distribution under the punch in terms of the applied force P and the coordinates of its point of application x_0 and y_0

$$\sigma = \frac{P\,a(\phi)}{2A\left[a^2(\phi) - \rho^2\right]^{1/2}} \left[1 + \frac{3}{4} A\left(\frac{x x_0}{I_y} + \frac{y y_0}{I_x}\right)\right] \tag{20}$$

where A is the area of the domain S. An expression equivalent to equation (20) can be written in terms of the normal displacement δ and the tilting angles α_x and α_y

$$\sigma = \frac{2a(\phi)}{\pi H\left[a^2(\phi) - \rho^2\right]^{1/2}} \left[\frac{\delta}{J_0} + \frac{\alpha_x y}{J_x} - \frac{\alpha_y y}{J_y}\right] \tag{21}$$

where

$$J_0 = \int_0^{2\pi} a(\phi)\, d\phi$$

The quantity J_0 may be called *the polar linear moment* due to the analogy with the moments of inertia and the property $J_0 = J_x + J_y$. One can note also that J_0 is proportional to the average polar radius. Expressions (20) and (21) are *exact* for an ellipse. We expect them to be reasonably accurate in the neighborhood of the coordinate origin for an arbitrary punch planform with at least one axis of symmetry, while the error might become quite significant close to the boundary of the domain S.

Let us rewrite formula (19) in the form

$$M_x = \frac{A^{3/2}}{2\pi H} h_x \alpha_x, \quad M_y = \frac{A^{3/2}}{2\pi H} h_y \alpha_y \tag{22}$$

where

$$h_x = \frac{32 I_x}{3A^{3/2} J_x}, \quad h_y = \frac{32 I_y}{3A^{3/2} J_y} \tag{23}$$

We introduced the coefficients h_x and h_y for two reasons: since they are dimensionless they characterize the shape of S and do not depend on its size; both h_x and h_y are equal to the corresponding coefficients of magnetic polarizability which will simplify the comparison of our results with the numerical data available. There is an advantage of formulae (22) over the equivalent (19): the factors depending on the shape of S are separated from those depending on its size. One can draw from equations (22) an immediate conclusion that in the case when a domain S is magnified so that its linear dimensions double, its area quadruples, and the tilting moment should be multiplied by 8 in order to produce the same tilting angle. This conclusion is not so clear in equations (19). The remaining part of the paper will be devoted to the evaluation of the coefficients h_x and h_y for various punch planforms.

Applications

Several punch planforms are considered here. Each configuration is related to its central principal axes and assumed to have at least one axis of symmetry coinciding with the axis Ox. A high degree of accuracy of formulae (23) is confirmed by comparison with available numerical solutions.

Polygon. Consider a polygon with n sides. The function $a(\phi)$ describing its boundary is bounded and single-valued. The origin of the coordinate system is located at the center of gravity, as before. Let us number the polygon sides in a counterclockwise direction from 1 to n, a_k being the length of the kth side. The apex, at which the sides a_k and a_{k+1} are intersecting, is numbered $k+1$. It is clear that the value of index equal $n+1$ is understood as 1. Denote b_k the distance from the center of gravity to the kth apex; ψ_k stands for the angle between the axis Ox and the perpendicular to the side a_k. Let A_k be the area of the triangle formed by a_k, b_k, and b_{k+1}, the total area A of the polygon being equal to the sum of A_k. The following expressions can be obtained for the moments of inertial

$$I_x = \sum_{k=1}^{n} \frac{2A_k^3}{a_k^2}\left[\sin^2\psi_k + \frac{b_{k+1}^2 - b_k^2}{4A_k} \sin 2\psi_k + \frac{a_k^4 + 3\left(b_{k+1}^2 - b_k^2\right)^2}{48A_k^2} \cos^2\psi_k\right] \tag{24}$$

$$I_y = \sum_{k=1}^{n} \frac{2A_k^3}{a_k^2}\left[\cos^2\psi_k - \frac{b_{k+1}^2 - b_k^2}{4A_k} \sin 2\psi_k\right.$$

$$+\frac{a_k{}^4+3\left(b_{k+1}{}^2-b_k{}^2\right)^2}{48A_k{}^2}\sin^2\psi_k\Big] \tag{25}$$

The linear moments can be computed in the form

$$J_x=\sum_{k=1}^{n}\frac{A_k}{a_k{}^2}\Big[-\left(\frac{1}{b_k}+\frac{1}{b_{k+1}}\right)[a_k^2-(b_k-b_{k+1})^2]\cos2\psi_k$$

$$+4A_k\left(\frac{1}{b_k}-\frac{1}{b_{k+1}}\right)\sin2\psi_k+2a_k ln\,\frac{b_k+b_{k+1}+a_k}{b_k+b_{k+1}-a_k}\cos^2\psi_k\Big] \tag{26}$$

$$J_y=\sum_{k=1}^{n}\frac{A_k}{a_k{}^2}\Big[\left(\frac{1}{b_k}+\frac{1}{b_{k+1}}\right)[a_k^2-(b_k-b_{k+1})^2]\cos2\psi_k$$

$$-4A_k\left(\frac{1}{b_k}-\frac{1}{b_{k+1}}\right)\sin2\psi_k+2a_k ln\,\frac{b_k+b_{k+1}+a_k}{b_k+b_{k+1}-a_k}\sin^2\psi_k\Big] \tag{27}$$

Substitution of equations (24)–(27) into (23) gives the coefficients h_x and h_y for an arbitrary polygon. In the case of a regular polygon $a_k = a$, $b_k = b = a/[2\sin(\pi/n)]$, $\psi_k = 2\pi(k-1)/n$, $A_k = [a^2\cot(\pi/n)]/4 = [b^2\sin(2\pi/n)]/2$, $A = nA_k$, and formulae (24)–(27) simplify to

$$I_x=I_y=\frac{na^4}{64}\cot\frac{\pi}{n}\left[\cot^2\frac{\pi}{n}+\frac{1}{3}\right]$$

$$=\frac{nb^4}{24}\sin\frac{2\pi}{n}\left[2+\cos\frac{2\pi}{n}\right] \tag{28}$$

$$J_x=J_y=\frac{1}{4}\,na\cot\frac{\pi}{n}\,ln\,\frac{1+\sin(\pi/n)}{1-\sin(\pi/n)}$$

$$=\frac{1}{2}\,nb\cos\frac{\pi}{n}\,ln\,\frac{1+\sin(\pi/n)}{1-\sin(\pi/n)} \tag{29}$$

Substituting equations (18) and (29) into (23) leads to

$$h_x=h_y=\frac{16\left(2+\cos\frac{2\pi}{n}\right)}{9\left(n^3\sin\frac{\pi}{n}\cos^3\frac{\pi}{n}\right)^{1/2}ln\,\frac{1+\sin(\pi/n)}{1-\sin(\pi/n)}} \tag{30}$$

Consider several particular values of n. For an equilateral triangle ($n=3$) formula (30) gives $h_x=h_y=3^{1/4}16/[27ln(2+\sqrt{3})]=0.5922$. We did not find any numerical data to compare with this result. In the case of a square $n=4$, and $h_x=h_y=4/[9ln(1+\sqrt{2})]=0.5043$ which is inside the interval from 0.4973 to 0.5162 given by Okon and Harrington (1981) and within 3 percent from the result of de Smedt (1979) 0.5193. Since formula (30) in the limiting case $n\to\infty$ gives the exact result for a circle $h_x=h_y=8/(3\pi^{3/2})=0.4789$, we should expect that the error of equation (30) will decrease with n. The value of the coefficients for a regular hexagon is $h_x=h_y=40\sqrt{2}/(3^{1/4}81ln3)=0.4830$ which differs by 1.4 percent from the result 0.49 due to Okon and Harrington (1981), and it is quite clear that the maximum possible error indeed decreases with n. It is noteworthy that the value of the coefficients does not change significantly in the whole range $3\le n<\infty$.

Isosceles Triangle. In the case of a triangle with the sides $a_1=a_2=l$ and the angle between them equal to α formulae (23)–(27) give

$$I_x=\frac{1}{12}\,l^4\sin\alpha\,\sin^2(\alpha/2),\quad I_y=\frac{1}{36}\,l^4\sin\alpha\,\cos^2(\alpha/2),$$

$$J_x=\frac{2}{3}\,l\cos\frac{\alpha}{2}\Big[\sin\alpha+\sin(\alpha+\gamma)-2\sin\gamma$$

$$+2\sin^3\frac{\alpha}{2}\,ln\left(\cot\frac{2\gamma-\alpha}{4}\cot\frac{\alpha}{4}\right)+ln\tan\left(\frac{\pi}{4}+\frac{\gamma}{2}\right)\Big],$$

$$J_y=\frac{2}{3}\,l\cos\frac{\alpha}{2}\Big[-\sin\alpha-\sin(\alpha+\gamma)+2\sin\gamma$$

$$+\sin\alpha\cos\frac{\alpha}{2}\,ln\left(\cot\frac{2\gamma-\alpha}{4}\cot\frac{\alpha}{4}\right)\Big],$$

with the result for the coefficients

$$h_x=8\left(\tan(\alpha/2)\right)^{3/2}\Big\{3\Big[\sin\alpha+\sin(\alpha+\gamma)-2\sin\gamma$$

$$+2\sin^3\frac{\alpha}{2}\,ln\left(\cot\frac{2\gamma-\alpha}{4}\cot\frac{\alpha}{4}\right)$$

$$+ln\tan\left(\frac{\pi}{4}+\frac{\gamma}{2}\right)\Big]\Big\}^{-1},$$

$$h_y=8\sqrt{\cot(\alpha/2)}\Big\{9\Big[-\sin\alpha-\sin(\alpha+\gamma)+2\sin\gamma$$

$$+\sin\alpha\cos\frac{\alpha}{2}\,ln\left(\cot\frac{2\gamma-\alpha}{4}\cot\frac{\alpha}{4}\right)\Big]\Big\}^{-1}, \tag{31}$$

where $\gamma = \tan^{-1}(3\tan(\alpha/2))$.

The isosceles right triangle was considered by Okon and Harrington (1981) who gave the interval between 0.9829 and 1.021 for only one coefficient which in our notation is h_x. Our result for h_x is 0.9255 which differs less than 10 percent from theirs. The second formula (31) gives $h_y = 0.3995$, and there is nothing in the literature to compare with this result.

Rectangle. Consider a punch with a rectangular base, a_1 and a_2 being its semiaxes. Introduce the aspect ratio $\epsilon = a_2/a_1$. Formulae (24)–(27) in this case reduce to

$$I_x=\frac{4}{3}\,a_1a_2{}^3,\qquad I_y=\frac{4}{3}\,a_1{}^3a_2,$$

$$J_x=4a_1\sinh^{-1}\epsilon,\qquad J_y=4a_2\sinh^{-1}(1/\epsilon)$$

and formulae (23) yield

$$h_x=\frac{4\epsilon^{3/2}}{9\sinh^{-1}\epsilon},\quad h_y=\frac{4\epsilon^{-3/2}}{9\sinh^{-1}(1/\epsilon)} \tag{32}$$

We have found in the literature some numerical results which seem to be more or less accurate. The coefficients of magnetic polarizability were computed by de Smedt (1979) for a rectangle with different aspect ratio ϵ. Here, we present his results along with those given by equations (32):

$\epsilon =$	0.1000	0.2000	0.3333	0.5000	0.7500	0.8000	1.0000
de Smedt $h_x =$	0.1287	0.1881	0.2531	0.3249	0.4240	0.4436	0.5193
Formula (32) $h_x =$	0.1408	0.2001	0.2612	0.3265	0.4165	0.4341	0.5043
de Smedt $h_y =$	4.1070	2.0260	1.2600	0.8892	0.6426	0.6130	0.5193
Formula (32) $h_y =$	4.6876	2.1488	1.2701	0.8708	0.6228	0.5929	0.5043
Discrepancy in h_x(%)	−9.4	−6.4	−3.2	−0.5	1.8	2.2	2.9
Discrepancy in h_y(%)	−14.1	−6.1	−0.8	2.1	3.1	3.3	2.9

Our formula (32) seems to perform satisfactorily in a sufficiently wide range of aspect ratio. The approximate expression for the stress distribution under the punch according to (20) takes the form

$$\sigma = \frac{Pa(\phi)}{8a_1a_2\left[a^2(\phi)-\rho^2\right]^{1/2}}\left[1+\frac{9}{4}\left(\frac{xx_0}{a_1{}^2}+\frac{yy_0}{a_2{}^2}\right)\right] \qquad (33)$$

Expression (33) can be used for analyzing the process of movement of the applied force P, say, along the axis Ox. This analysis can be done by requiring that the contact traction vanish at the edge. One can conclude from equation (20) that the boundary at which this occurs will always be a straight line. It is clear from equation (33) that the punch will be in contact with the half-space as long as $x_0 \leq 4a_1/9$, after which the punch will start separating from the half-space. Assuming that the new domain of contact is also a rectangle (of course, with a different aspect ratio), one can again apply the formulae of this paragraph to analyze the process further. If one can denote by c the width of the zone of separation, the following relationship holds:

$$c = \frac{2}{5}(9x_0 - 4a_1), \quad \text{for } x_0 \geq \frac{4}{9}a_1$$

The last formula states, for example, that when the force P is applied at $x_0 = 13a_1/18$ only a half of the punch will be in contact with the half-space. Unfortunately, there is no data to verify these relationships. Further analysis reveals that the core inside which the force can be applied without causing any separation is a rhombus with semiaxes $4a_1/9$ and $4a_2/9$, respectively. As one knows, in the case of a circular punch the core is a circle of radius equal to one third of the radius of the punch. The results due to equation (33) can be compared with the numerical data received in personal communication from de Smedt. In order to make the comparison possible, one should put in equation (33) $P=0$, $M_x=0$, replace M_y with equations (22), with the result

$$\sigma H = \frac{9\sqrt{\epsilon}a(\phi)h_y x}{4a_1\left[a^2(\phi)-\rho^2\right]^{1/2}} \qquad (34)$$

Computations due to equation (34) were made for $\epsilon = 0.5$ along the axis Ox, the value h_y was taken 0.8708 (see the table above). Here are the results compared to those communicated by de Smedt:

x/a_1	0.0833	0.1667	0.2500	0.3333	0.4167	0.5000	0.5833	0.6667	0.7500	0.8333	0.9167
de Smedt $\sigma H=$	0.1143	0.2303	0.3501	0.4759	0.6093	0.7523	0.9367	1.1460	1.4304	1.8303	2.8182
Formula (34) $\sigma H=$	0.1159	0.2342	0.3577	0.4898	0.6350	0.7999	0.9950	1.2392	1.5709	2.0886	3.1777
Discrepancy (%)	−1.3	−1.7	−2.2	−2.9	−4.2	−6.3	−6.2	−8.1	−9.8	−14.1	−12.8

One should expect the error of equation (34) to be monotonous (or to have one extremum). This expectation is not met around $x/a_1 = 0.5$ and $x/a_1 = 0.9$ which most probably indicates some computational errors in the data by de Smedt. This is why we are using the word *discrepancy* rather than the word *error* in the tables throughout the paper. The situation becomes even more evident if we compare the same values along the axis Oy. One can use a formula similar to (34) replacing all x by y and interchanging a_1 and a_2, the value of h_x was taken to be 0.3265.

$y/a_2=$	0.1667	0.3333	0.5000	0.6667	0.8333
de Smedt $\sigma H=$	0.1756	0.3663	0.6011	0.9014	1.6413
our result $\sigma H=$	0.1756	0.3673	0.5998	0.9292	1.5662
Discrepancy (%)	0.0	−0.3	0.2	−3.1	4.6

Changing sign in the discrepancy indicates some "noise" in the numerical solution by de Smedt.

Rhombus. Let α be the angle at one of the rhombus apexes, and l be its side Formulae (24)–(27) in this case yield

$$I_x = \frac{1}{6}\, l^4 \sin\alpha \sin^2\frac{\alpha}{2}, \quad I_y = \frac{1}{6}\, l^4 \sin\alpha \cos^2\frac{\alpha}{2},$$

$$A = l^2 \sin\alpha,$$

$$J_x = 2l\sin\alpha\left[\cos\frac{\alpha}{2} - \sin\frac{\alpha}{2} + \sin^2\frac{\alpha}{2}\, ln\, \frac{\cos(\alpha/2)+\sin(\alpha/2)+1}{\cos(\alpha/2)+\sin(\alpha/2)-1}\right],$$

$$J_y = 2l\sin\alpha\left[-\cos\frac{\alpha}{2} + \sin\frac{\alpha}{2} + \cos^2\frac{\alpha}{2}\, ln\, \frac{\cos(\alpha/2)+\sin(\alpha/2)+1}{\cos(\alpha/2)+\sin(\alpha/2)-1}\right]$$

The coefficients will be defined as

$$h_x = \frac{8\sin^2\frac{\alpha}{2}}{9(\sin\alpha)^{3/2}\left[\cos\frac{\alpha}{2} - \sin\frac{\alpha}{2} + \sin^2\frac{\alpha}{2}\, ln\, \frac{\cos(\alpha/2)+\sin(\alpha/2)+1}{\cos(\alpha/2)+\sin(\alpha/2)-1}\right]}$$

$$h_y = \frac{8\cos^2\frac{\alpha}{2}}{9(\sin\alpha)^{3/2}\left[-\cos\frac{\alpha}{2} + \sin\frac{\alpha}{2} + \cos^2\frac{\alpha}{2}\, ln\, \frac{\cos(\alpha/2)+\sin(\alpha/2)+1}{\cos(\alpha/2)+\sin(\alpha/2)-1}\right]} \qquad (35)$$

The same formulae in terms of the rhombus semiaxes a and b and the aspect ratio $\epsilon = b/a$ has the form

$$h_x = \frac{2\sqrt{2}\epsilon(1+\epsilon^2)}{9\left[1-\epsilon+\frac{\epsilon^2}{(1+\epsilon^2)^{1/2}}\, ln\, \frac{1+\epsilon+(1+\epsilon^2)^{1/2}}{1+\epsilon-(1+\epsilon^2)^{1/2}}\right]},$$

$$h_y = \frac{2\sqrt{2}(1+\epsilon^2)}{9\epsilon^{3/2}\left[\epsilon-1+\frac{1}{(1+\epsilon^2)^{1/2}}\, ln\, \frac{1+\epsilon+(1+\epsilon^2)^{1/2}}{1+\epsilon-(1+\epsilon^2)^{1/2}}\right]}, \qquad (36)$$

We did not find in mechanics literature any result related to a punch with a rhombus planform. In electrical sciences, the mathematically equivalent problem of the coefficients of

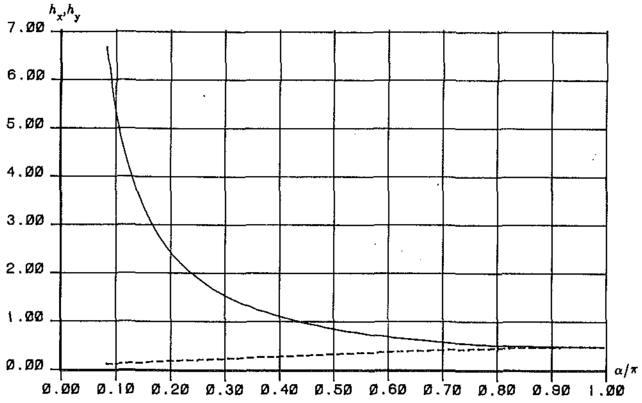

Fig. 1 Coefficients h_x and h_y for a circular segment

magnetic polarizability of a diamond was solved numerically by de Smedt (1979). Here, we present his results compared to those given by formula (36):

$\epsilon =$	0.1000	0.2000	0.3333	0.5000	0.7500	0.8000	1.0000
de Smedt $h_x =$	0.1181	0.1729	0.2341	0.3052	0.4101	0.4323	0.5193
Formula (36) $h_x =$	0.1078	0.1627	0.2258	0.2986	0.4026	0.4230	0.5043
de Smedt $h_y =$	6.1820	2.7060	1.5240	0.9946	0.6703	0.6323	0.5193
Formula (36) $h_y =$	4.5987	2.1982	1.3254	0.9095	0.6388	0.6052	0.5043
Discrepancy of h_x(%)	8.7	5.9	3.6	2.2	1.8	2.1	2.9
Discrepancy of h_y(%)	25.6	18.8	13.0	8.6	4.7	4.3	2.9

The deterioration of the accuracy of (36) for small values of ϵ is the result of erroneous assumption of a square root singularity in equation (6) which is grossly incorrect for domains with sharp angles.

The stress distribution under the punch can be expressed according to equation (20)

$$\sigma = \frac{Pa(\phi)}{2A\left[a^2(\phi)-\rho^2\right]^{1/2}}\left[1+\frac{9}{2}\left(\frac{xx_0}{a^2}+\frac{yy_0}{b^2}\right)\right]$$

Further analysis of the last expression reveals that the core inside which the force can be applied without causing any separation is a rectangle with semiaxes $2a/9$ and $2b/9$, respectively. In the case of $\epsilon = 1$ the rhombus transforms into a square, and all the results are in agreement with those of the previous paragraph.

Circular Segment. Let the radius r and the angle 2α be the segment parameters. The location of its center of gravity is defined by $x_c = kr$, where

$$k = \frac{2\sin^3\alpha}{3\left(\alpha - \frac{1}{2}\sin 2\alpha\right)} \tag{37}$$

The equation of the segment boundary with respect to its center of gravity takes the form

$$a(\phi) = \begin{cases} r\left[-k\cos\phi + \left(1-k^2\sin^2\phi\right)^{1/2}\right] & \text{for } 0 \le \phi \le \pi-\gamma \text{ or } \pi+\gamma \le \phi < 2\pi \\ r\,\dfrac{k-\cos\alpha}{\cos(\pi-\phi)} & \text{for } \pi-\gamma \le \phi \le \pi+\gamma \end{cases} \tag{38}$$

Computation of the moments (24)–(27) yields

$$A = r^2\left(\alpha - \frac{1}{2}\sin 2\alpha\right), \quad I_x = \frac{1}{4}Ar^2(1-k\cos\alpha),$$

$$I_y = \frac{1}{4}Ar^2(1+3k\cos\alpha-4k^2),$$

$$J_x = \frac{3}{2}r\Big\{-k\sin^3\gamma + (1-k^2\sin^2\gamma)^{1/2}\sin\gamma\cos\gamma + \frac{1-k^2}{k^2}F(\pi-\gamma,k) + \frac{2k^2-1}{k^2}E(\pi-\gamma,k) + 3(k-\cos\alpha)\Big[-\sin\gamma + \ln\tan\Big(\frac{\pi}{4}+\frac{\gamma}{2}\Big)\Big]\Big\}$$

$$J_y = \frac{2}{3}r\Big\{\sin\gamma\Big[k\sin^2\gamma - 3\cos\alpha - (1-k^2\sin^2\gamma)^{1/2}\cos\gamma\Big] - \frac{1-k^2}{k^2}F(\pi-\gamma,k) + \frac{1+k^2}{k^2}E(\pi-\gamma,k)\Big\}$$

where $\gamma = \tan^{-1}(\sin\alpha/(k-\cos\alpha))$. Substituting in (23) leads to

$$h_x = \frac{4(1-k\cos\alpha)}{\left[\alpha-\frac{1}{2}\sin 2\alpha\right]^{1/2}}\Big\{-k\sin^3\gamma + (1-k^2\sin^2\gamma)^{1/2}\sin\gamma\cos\gamma + \frac{1-k^2}{k^2}F(\pi-\gamma,k) + \frac{2k^2-1}{k^2}E(\pi-\gamma,k) + 3(k-\cos\alpha)\Big[-\sin\gamma + ln\,\tan\Big(\frac{\pi}{4}+\frac{\gamma}{2}\Big)\Big]\Big\}^{-1}, h_y = \frac{4(1+3k\cos\alpha-4k^2)}{\left[\alpha-\frac{1}{2}\sin 2\alpha\right]^{1/2}}$$

$$\Big\{\sin\gamma\Big[k\sin^2\gamma - 3\cos\alpha - (1-k^2\sin^2\gamma)^{1/2}\cos\gamma\Big] - \frac{1-k^2}{k^2}F(\pi-\gamma,k) + \frac{1+k^2}{k^2}E(\pi-\gamma,k)\Big\}^{-1}$$

A plot of h_x (solid line) and h_y (broken line) against the ratio α/π is given in Fig. 1. We are unaware of any data to verify the accuracy of (39).

One can now investigate the case of a circular punch under the action of a normal force P applied at $x_0 > r/3$. From the classical theory we know that there should be a separation between the punch and the half-space. Assuming that the domain of contact after separation is a circular segment, one can get the following relationship between the coordinate x_0 and the size of the segment characterized by the angle α

$$x_0 = r\,\frac{(1-k)(1+4k)}{3(k-\cos\alpha)} \tag{40}$$

The last expression is exact in two limiting cases: the complete circle $\alpha=\pi$ gives $x_0 = r/3$, and $\alpha \to 0$ results in $x_0 = \tau$. The problem of an inclined circular punch was considered numerically in the book by Rvachev and Protsenko (1977). Here, we compare the results

α(deg) =	158.4	108.1	102.0
Rvachev et al. $x_0 =$	0.3583	0.5833	0.6250
Formula (40) $x_0 =$	0.3543	0.5418	0.5750
Discrepancy (%)	1.1	7.1	8.0

The agreement should be considered as surprisingly good, especially taken into consideration that Rvachev et al. considered the domain of contact not in the form of a segment but having a more complicated shape.

Circular Sector. Repetition of the procedure, described in the previous paragraph, leads to the following results for a circular sector with the angle 2α:

$$A = r^2\alpha, \quad I_x = \frac{1}{4}\,r^4\left(\alpha - \frac{1}{2}\,\sin 2\alpha\right),$$

$$I_y = r^4\,\frac{9\alpha^2 + 9\alpha\sin\alpha\cos\alpha - 16\sin^2\alpha}{36\alpha}$$

$$J_x = \frac{2}{3}\,r\Big\{-k\sin^3\gamma - (1-k^2\sin^2\gamma)^{1/2}\sin\gamma\cos\gamma + \frac{1-k^2}{k^2}\,F(\gamma,k)$$

$$+\frac{2k^2-1}{k^2}\,E(\gamma,k) + 3k\sin\alpha\Big[\cos\alpha + \cos(\alpha+\gamma)$$

$$+\sin^2\alpha\; ln\left(\cot\frac{\alpha}{2}\,\cot\frac{\gamma-\alpha}{2}\right)\Big]\Big\}$$

$$J_y = \frac{2}{3}\,r\Big\{k\sin\gamma(\sin^2\gamma - 3) + (1-k^2\sin^2\gamma)^{1/2}\sin\gamma\cos\gamma$$

$$-\frac{1-k^2}{k^2}\,F(\gamma,k)$$

$$+\frac{1+k^2}{k^2}\,E(\gamma,k) + 3k\sin\alpha\Big[-\cos\alpha - \cos(\alpha+\gamma)$$

$$+\cos^2\alpha\; ln\left(\cot\frac{\alpha}{2}\,\cot\frac{\gamma-\alpha}{2}\right)\Big]\Big\}$$

Here, $k = 2\sin\alpha/(3\alpha)$, and $\gamma = \tan^{-1}(\sin\alpha/(\cos\alpha - k))$. The coefficients sought are expressed as follows

$$h_x = 2\alpha^{-3/2}(2\alpha - \sin 2\alpha)\Big\{-k\sin^3\gamma - (1-k^2\sin^2\gamma)^{1/2}\sin\gamma\cos\gamma$$

$$+\frac{1-k^2}{k^2}\,F(\gamma,k)$$

$$+\frac{2k^2-1}{k^2}\,E(\gamma,k) + 3k\sin\alpha\Big[\cos\alpha + \cos(\alpha+\gamma)$$

$$+\sin^2\alpha\; ln\left(\cot\frac{\alpha}{2}\,\cot\frac{\gamma-\alpha}{2}\right)\Big]\Big\}^{-1}$$

$$h_y = \frac{4(9\alpha^2 + 9\alpha\sin\alpha\cos\alpha - 16\sin^2\alpha)}{9\alpha^{5/2}}\Big\{k\sin\gamma(\sin^2\gamma - 3)$$

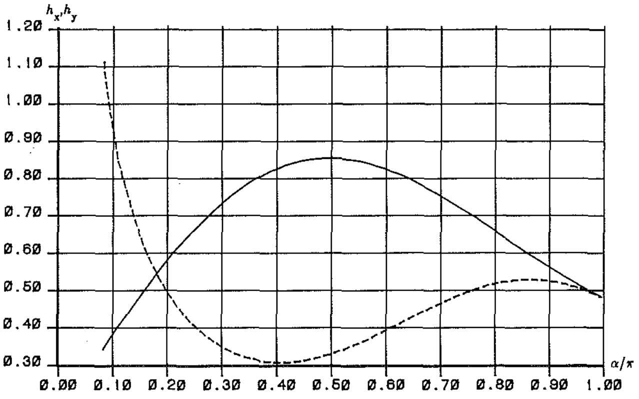

Fig. 2 Coefficients h_x and h_y for a circular sector

$$+(1-k^2\sin^2\gamma)^{1/2}\sin\gamma\cos\gamma - \frac{1-k^2}{k^2}\,F(\gamma,k)$$

$$+\frac{1+k^2}{k^2}\,E(\gamma,k) + 3k\sin\alpha\Big[-\cos\alpha - \cos(\alpha+\gamma)$$

$$+\cos^2\alpha\; ln\left(\cot\frac{\alpha}{2}\,\cot\frac{\gamma-\alpha}{2}\right)\Big]\Big\}^{-1} \tag{41}$$

Formulae (41) are exact for a complete circle ($\alpha=\pi$), and give the same results as (39) for a half-circle ($\alpha=\pi/2$). The plot of h_x (solid line) and h_y (broken line) against the ratio α/π is given in Fig. 2. We did not find in the literature anything to compare with these results.

Cross. Consider a punch configuration obtained by an orthogonal intersection of two equal rectangles with sides $2a$ and $2b$. Introduce the aspect ratio as $\epsilon = b/a$. The area and the moments will take the form

$$A = 4a^2\epsilon(2-\epsilon), \quad I_x = I_y = \frac{4}{3}\,a^4\epsilon(1+\epsilon^2-\epsilon^3)$$

$$J_x = J_y = 4a\left[ln\,(\epsilon + (1+\epsilon^2)^{1/2}) + \epsilon\; ln\,\frac{1+(1+\epsilon^2)^{1/2}}{(1+\sqrt{2})\epsilon}\right]$$

The coefficients will be defined as

$$h_x = h_y = \frac{4\epsilon(1+\epsilon^2-\epsilon^3)}{9\epsilon(2-\epsilon)^{3/2}}\Big[ln\,(\epsilon + (1+\epsilon^2)^{1/2})$$

$$+\epsilon\,\ln\frac{1+(1+\epsilon^2)^{1/2}}{(1+\sqrt{2})\epsilon}\Big]^{-1} \tag{42}$$

The comparison between the results due to (42) and those given by de Smedt (1979) are presented below:

$\epsilon =$	0.1000	0.2000	0.3333	0.4000	0.5000	0.6000	0.7500	0.8000	1.0000
de Smedt $h_x = h_y =$	1.5910	0.8720	0.6255	0.5725	0.5267	0.5069	0.4985	0.4997	0.5193
Formula (42)$h_x = h_y =$	1.7382	0.8758	0.6006	0.5465	0.5049	0.4890	0.4893	0.4926	0.5043
Discrepancy (%)	−9.3	−0.4	4.0	4.5	4.1	3.5	1.9	1.4	2.9

Taking into consideration the shape complexity, we should consider the results agreement as surprisingly good, not only quantitatively but qualitatively as well: both data display a relatively flat minimum around $\epsilon = 0.75$.

Discussion

It is noteworthy that the change of the order of integration which led to equation (4) is valid inside the circle $\rho \le \min\{a(\phi)\}$ only. Nevertheless, one can obtain from equation (4) an *exact* solution for an ellipse and sufficiently accurate formulae for various punch planforms as it was demonstrated in the previous Section.

The accuracy of formulae (23) can be improved by taking into consideration the fifth harmonic (12) in combination with the variational approach (Noble, 1960). The following functional assumes its maximum value at the exact solution of (1)

$$I(\sigma)=\frac{2}{H}\iint_S \sigma(M)\,w(M)\,dS_M - \iint_S \sigma(M)\left[\iint_S \frac{\sigma(N)}{R(M,N)}\,dS_N\right]dS_M \tag{43}$$

Taking

$$H\iint_S \frac{\sigma(N)}{R(M,N)}\,dS_N \approx w_1+w_5 \tag{44}$$

and substituting equations (6), (10), (12), and (44) into (43), one gets after integration with respect to ρ

$$\begin{aligned}I=\int_0^{2\pi} (a(\phi))^4\Big\{(p_1\cos\phi+p_2\sin\phi)\Big[\frac{4}{3H}(\alpha_x\sin\phi \\ -a_y\cos\phi)-\frac{\pi}{3}(p_1J_y+p_2J_{xy})\cos\phi \\ -\frac{\pi}{3}(p_1J_{xy}+p_2J_x)\sin\phi-\frac{4}{63}(a(\phi))^3([p_1(A_{c6}+A_{c4}) \\ +p_2(A_{s6}-A_{s4})]\cos5\phi+[p_1(A_{s6}+A_{s4}) \\ +p_2(A_{c4}-A_{c6})]\sin5\phi)\Big]\Big\}d\phi\end{aligned} \tag{45}$$

Considering now the functional I as a function of p_1 and p_2, the extremum conditions

$$\frac{\partial I}{\partial p_1}=0,\quad \frac{\partial I}{\partial p_2}=0$$

give two linear algebraic equations with respect to the unknowns p_1 and p_2. The complete solution is pretty cumbersome. Here, we present the final result for the coefficients h_x and h_y which are valid only for domains having at least one axis of symmetry, and the central principal axes taken as the coordinate axes

$$h_x=\frac{32I_x}{3A^{3/2}J_x(1+\eta_x)},\quad h_y=\frac{32I_y}{3A^{3/2}J_y(1+\eta_y)} \tag{46}$$

where the correction terms

$$\eta_x=\frac{(B_{c4}-B_{c6})(A_{c4}-A_{c6})}{42\pi I_xJ_x},\quad \eta_y=\frac{(B_{c4}+B_{c6})(A_{c4}+A_{c6})}{42\pi I_yJ_y}, \tag{47}$$

and

$$B_{c6}=\int_0^{2\pi} (a(\phi))^7\cos6\phi\,d\phi,\quad B_{c4}=\int_0^{2\pi} (a(\phi))^7\cos4\phi\,d\phi$$

Since expression (44) is approximate, there is no guarantee that equations (46) will be more accurate than (23). We performed the necessary computations for a rectangle. Here are the results compared to those by de Smedt (1979):

$\epsilon=$	0.1000	0.2000	0.3333	0.5000	0.7500	0.8000	1.0000
de Smedt $h_x=$	0.1287	0.1881	0.2531	0.3249	0.4240	0.4436	0.5193
Formula (46) $h_x=$	0.1405	0.1988	0.2577	0.3207	0.4165	0.4376	0.5331
de Smedt $h_y=$	4.1070	2.0260	1.2600	0.8892	0.6426	0.6130	0.5193
Formula (46) $h_y=$	4.5856	2.0985	1.2479	0.8714	0.6463	0.6190	0.5331
Discrepancy in h_x(%)	−9.2	−5.7	−1.8	1.3	1.8	1.3	−2.7
Discrepancy in h_y(%)	−11.7	−3.6	1.0	2.0	−0.6	−1.0	−2.7

Comparison with similar data computed on the basis of formula (32) shows that the correction terms η_x and η_y in this particular case resulted in decreasing the value of discrepancy, positive as well as negative. We caution again that there is no guarantee that this will be valid for an arbitrary domain. For example, here are the data computed for a rhombus:

$\epsilon=$	0.1000	0.2000	0.3333	0.5000	0.7500	0.8000	1.0000
de Smedt $h_x=$	0.1181	0.1729	0.2341	0.3052	0.4101	0.4323	0.5193
Formula (46) $h_x=$	0.2268	0.1860	0.2351	0.3031	0.4058	0.4264	0.5091
de Smedt $h_y=$	6.1820	2.7060	1.5240	0.9946	0.6703	0.6323	0.5193
Formula (46) $h_y=$	8.5600	2.5916	1.4196	0.9408	0.6490	0.6138	0.5091
Discrepancy of h_x(%)	−92.0	−7.6	−0.4	0.7	1.0	1.4	2.0
Discrepancy of h_y(%)	−38.5	4.2	6.8	5.4	3.2	2.9	2.0

Comparison with the data computed due to equation (36) indicates that the discrepancy decreased for $\epsilon \geq 0.2$ while for $\epsilon=0.1$ it has jumped in the opposite direction to −92 percent. The main reason for this is a jump in the value of the coefficients η_x and η_y when ϵ is very small. The following rule of thumb may be suggested for the user wishing to improve the accuracy: when the value of the correction coefficients η_x and η_y does not exceed a small percentage of unity, this generally means an improvement in accuracy, otherwise one should not use formulae (46).

It is worthwhile to give the solution due to (45) for the case when the domain of contact has no axis of symmetry, and only the first harmonic of the displacements w_1 is taken into consideration. The result is

$$\begin{aligned}p_1&=\frac{\alpha_x(c_{22}I_{xy}-c_{12}I_x)+\alpha_y(c_{12}I_{xy}-c_{22}I_y)}{c_{11}c_{22}-c_{12}^2}\\ p_2&=\frac{\alpha_x(c_{11}I_x-c_{12}I_{xy})+\alpha_y(c_{12}I_y-c_{11}I_{xy})}{c_{11}c_{22}-c_{12}^2}\end{aligned} \tag{48}$$

where

$$c_{11}=\frac{\pi H}{2}(J_yI_y+J_{xy}I_{xy}),\quad c_{22}=\frac{\pi H}{2}(J_xI_x+J_{xy}I_{xy}),$$

$$c_{12}=\frac{\pi H}{4}(J_{xy}(I_x+I_y)+I_{xy}(J_x+J_y))$$

Formulae (48) look different from the equivalent set (15) derived earlier. In the absence of any numerical data related to a general domain, it is impossible to say whether formulae (48) are more accurate than (15), but they are definitely more complicated. It is noteworthy that in the case of a domain with an axis of symmetry both (48) and (15) simplify to the same equations (18).

Conclusion

Formulae (22)-(23) give a simple and effective solution to the problem of a flat inclined punch of arbitrary planform on an elastic half-space. Their high accuracy is confirmed by numerous examples. One can notice a certain similarity between the formulae derived and those related to the Saint-Venant theory of bending. This similarity will become more evident if, for example, we rewrite equation (20) in the form

$$\sigma = \frac{a(\phi)}{2\left[a^2(\phi) - \rho^2\right]^{1/2}} \left[\frac{P}{A} + \frac{3}{4} \left(-\frac{M_y x}{I_y} + \frac{M_x y}{I_x} \right) \right]$$

We think that this similarity is not a pure coincidence since the method used in this paper can also be called semi-inverse. The method can be developed further into a complete Saint-Venant type theory of elastic contact problems which will combine the simplicity and the accuracy sufficient for a practical engineer. The case of a curved punch will be considered in the third part of this project. Results of this paper are useful for the solution of mathematically similar problems in the other branches of engineering science (Electrostatics, Fluid Mechanics, Acoustics, Heat Transfer, etc.)

References

De Smedt, R., 1979, "Low-Frequency Penetration through Apertures: Results for the Integral Equations," *Laboratorium voor Electromagnetisme en Acustica*, Internal report 79-9, University of Ghent.

Fabrikant, V. I., 1971a, "Closed Form Solution of a Two-dimensional Integral Equation," *Izvestiya Vysshikh Uchebnykh Zavedenii, Matematika*, in Russian, No. 2, pp. 102–104.

Fabrikant, V. I., 1971b, "Effect of Shearing Force and Tilting Moment on a Cylindrical Punch Attached to a Transversely Isotropic Half-space," *Journal of Applied Mathematics and Mechanics* (*PMM*), Vol. 35, pp. 147–151.

Fabrikant, V. I., 1986, "Flat Punch of Arbitrary Shape on an Elastic Half-space," *International Journal of Engineering Science*, in print.

Galin, L. A., 1961, *Contact Problems in the Theory of Elasticity*, in Russian, Gostekhteorizdat, 1953, translated by H. Moss, Dept. of Math., North Carolina State College, Raleigh.

De Meulenaere, F., and Van Bladel, J., 1977, "Polarizability of Some Small Apertures," *IEEE Trans. on Antennas and Propagation*, Vol. AP-25, pp. 198–205.

Noble, B., 1960, "The Numerical Solution of the Singular Integral Equation for the Charge Distribution on a Flat Rectangular Lamina," *Sympos. Numerical Treatment of Ordinary Differential Equations, Integral and Integrodifferential Equations*, (Proc. Rome Sympos. 20–24 September 1960), Birkhauser, Berlin-Stuttgart.

Okon, E. E., and Harrington, R. F., 1981, "The Polarizabilities of Electrically Small Aperatures of Arbitrary Shape," *IEEE Trans. on Electromagnetic Compatibility*, Vol. EMC-23, pp. 359–366.

Rvachev, V. L., and Protsenko, V. S., 1977, "Contact Problems of the Theory of Elasticity for Non-classical Domains," *Naukova Dumka*, in Russian, Kiev.

M. F. Beatty
Department of Engineering Mechanics,
University of Kentucky,
Lexington, KY 40506

D. O. Stalnaker
Central Research Laboratories,
The Firestone Tire and Rubber Co.,
Akron, OH 44317

The Poisson Function of Finite Elasticity

The Poisson function is introduced to study in a simple tension test the lateral contractive response of compressible and incompressible, isotropic elastic materials in finite strain. The relation of the Poisson function to the classical Poisson's ratio and its behavior for certain constrained materials are discussed. Some experimental results for several elastomers, including two natural rubber compounds of the same kind studied in earlier basic experiments by Rivlin and Saunders, are compared with the derived relations. A special class of compressible materials is also considered. It is proved that the only class of compressible hyperelastic materials whose response functions depend on only the third principal invariant of the deformation tensor is the class first introduced in experiments by Blatz and Ko. Poisson functions for the Blatz-Ko polyurethane elastomers are derived; and our experimental data are reviewed in relation to a volume constraint equation used in their experiments.

1 Introduction

Isotropic, linear elasticity theory is characterized by two important physical constants: Young's modulus and Poisson's ratio. It is well-known that their definitions are based upon the simple tension test[1]; and, for a specific homogeneous, isotropic and linearly elastic material, both may be found from this experiment (Love, 1927). We recall that Poisson's ratio is determined from kinematical measurements alone, and when the material is known to be incompressible it has the value of 1/2.

In isotropic, nonlinear elasticity theory, the traditional material constants play a less important role, but their use in characterization of the mechanical properties of highly elastic materials certainly is of no lesser importance. However, in this case, the material response generally is not described by constants; rather, it is represented by three scalar-valued functions $\beta_\Gamma = \beta_\Gamma(I_1, I_2, I_3)$ of the three principal invariants I_k of the Cauchy-Green deformation tensor $\mathbf{B}$ so that the principal Cauchy stress components t_k are determined by

$$t_k = \beta_0 + \beta_1 \lambda_k^2 + \beta_{-1} \lambda_k^{-2}, \quad k = 1, 2, 3, \tag{1.1}$$

(Truesdell and Noll, 1965). Herein λ_k^2, the squared principal stretches, are the principal values of $\mathbf{B}$; and $\Gamma = -1, 0, 1$. For an incompressible material, every deformation must satisfy the constant volume constraint relation

$$I_3^{1/2} = \lambda_1 \lambda_2 \lambda_3 = 1; \tag{1.2}$$

and the constitutive relation (1.1) is replaced by

$$t_k = -p + \beta_1 \lambda_k^2 + \beta_{-1} \lambda_k^{-2}, \ k = 1, 2, 3, \tag{1.3}$$

in which p is an unknown hydrostatic stress, and the two response functions $\beta_\Gamma = \beta_\Gamma(I_1, I_2)$ depend on the invariants indicated. The determination of the response functions for particular materials is a principal problem in experimental mechanics. Of course, it is reasonable to expect that the response functions, or combinations of them, ought to be related in some limited sense to the classical moduli of the linearized theory; and it is natural to ask how the usual physical parameters may be characterized in the general theory. The connection of the response functions with the Lamé constants is made in Truesdell and Noll (1965). This note concerns the definition of the Poisson function and its relation to the classical modulus known as Poisson's ratio.

The Poisson function is defined in Section 2; and its connection with the simple tension experiment and its behavior under certain constraints are described there. Some experimental results are then presented for demonstration in Section 3. Experimental data for a urethane elastomer, a certain blend of natural and synthetic rubbers, and two natural rubber compounds of the same kind used in early experiments by Rivlin and Saunders (1951) are compared with the universal Poisson function obtained for incompressible materials. Although every incompressible material has the universal constant, natural state limit value 1/2, the converse is shown generally to be false. A specific application to compressible materials is illustrated.

It is proved in Section 4 that the only class of compressible hyperelastic materials whose response functions depend on only the third principal invariant of the deformation tensor is the class first studied in experiments by Blatz and Ko (1962). Their constitutive equation for foamed, polyurethane rubber is shown to be related to the micro-structural theory of

---

[1] This does not preclude the use of other testing methods for the determination of these basic moduli. However, the Poisson ratio is defined in terms of strains in a simple extension produced by simple tensile loading. Although the same thing may be done in a simple compression experiment, a compression test usually is avoided because of eccentric loading and stability problems. Of course, compression data sometimes may be obtained by other means (See Rivlin and Saunders, 1951, p. 270).

Contributed by the Applied Mechanics Division for publication in the JOURNAL OF APPLIED MECHANICS.

Discussion on this paper should be addressed to the Editorial Department, ASME, United Engineering Center, 345 East 47th Street, New York, N.Y. 10017, and will be accepted until two months after final publication of the paper itself in the JOURNAL OF APPLIED MECHANICS. Manuscript received by ASME Applied Mechanics Division, December 26, 1985.

foamed rubbers due to Gent and Thomas (1959) and to the well-known controversial, classical molecular theory of elasticity (Todhunter and Pearson, 1960). Poisson functions are derived for the Blatz-Ko polyurethane materials and our demonstration data are reviewed in relation to an *ad hoc* Blatz-Ko constitutive equation of volume control in simple tension. It is shown that the natural state Poisson's ratio for every Blatz-Ko material is simply the ratio of the true lateral contractive strain to the true extensional strain for finite deformations and hence may be readily evaluated from measurements of corresponding stretches over the entire range of elastic extensibility of the material in a simple tension experiment. Discussion of some additional related literature is reserved for the end.

2 The Poisson Function

It is easy to show from the constitutive equation for isotropic, linearly elastic solids that a simple tension produces a simple extension provided that the shear modulus $\mu_o \neq 0$ nor ∞, and Poisson's ratio $\nu_o \neq -1$ nor ∞. In fact, on physical grounds, one usually requires $\infty > \mu_o > 0$ and $1/2 \geq \nu_o > 0$; and, in any case, $\nu_o > -1$ is necessary for material stability (Love, 1927). The corresponding result for isotropic, nonlinearly elastic solids is not as transparent. Therefore, to begin, it is necessary to recall Batra's theorem (Batra, 1976) that for every isotropic, compressible or incompressible elastic material, a simple tensile loading

$$t_3 = T, \quad t_1 = t_2 = 0 \tag{2.1}$$

produces a corresponding extensional deformation

$$\lambda_3 = \lambda, \ \lambda_1 = \lambda_2, \tag{2.2}$$

provided that the empirical inequalities

$$\beta_1 > 0, \quad \beta_{-1} \leq 0 \tag{2.3}$$

hold (Truesdell and Noll, 1965). Actually, the same result is obtained under the weaker condition that the Baker-Ericksen inequalities hold.

With Batra's result in hand, let us assume that a compressible material characterized by equations (1.1) and (2.3) is subjected to a simple tension (2.1). Then the familiar Young's modulus is defined as the slope of the axial stress/axial stretch function $T = t_3(\lambda)$ evaluated at $\lambda = 1$. However, its determination involves the further assumption that either of the identical transverse stress equations $(2.1)_{2,3}$ may be solved uniquely for the lateral stretch as a function of the axial stretch. In other words, $(2.1)_2$ may be interpreted in a simple tension test as a restriction on the response functions that defines a relation between the longitudinal extension $\lambda \geq 1$ and the lateral contractions $\lambda_1 = \lambda_2 \leq 1$. Hence, their ratio,

$$\alpha(\lambda) \equiv \frac{\lambda_1(\lambda)}{\lambda}, \tag{2.4}$$

defines one kind of *lateral contraction function* that derives from $(2.1)_2$ and (1.1). Subtraction of the second equation from the first in (1.1) and use of (2.3) shows that in simple tension $0 < \alpha(\lambda) \leq 1$. There exists the possibility that for some response functions the same equations may exhibit several solutions for $\lambda_1(\lambda)$. We consider only those elastic materials for which $\lambda_1(\lambda)$ may be determined uniquely. When this is so, we say that the extension is *simple*. Thus, if the empirical inequalities are met, it is in this sense that a simple tension produces a simple extension in every compressible, homogeneous, and isotropic elastic solid. In linear elasticity theory (Love, 1927), for example, the null relations $(2.1)_{2,3}$ yield a unique expression for the ratio of the principal transverse contractive and longitudinal engineering strains in terms of the Lamé constants; and this classical squeeze-stretch ratio is commonly known as Poisson's ratio (Love, 1927; Todhunter and Pearson, 1960).

Recalling that the three principal engineering strains ϵ_k are related to the principal stretches by $\epsilon_k = \lambda_k - 1$, we may define the *Poisson function* $\nu(\lambda)$ as the ratio of the lateral contractive strain to the extensional strain measured in a simple tension experiment; that is,

$$\nu(\lambda) \equiv -\frac{\epsilon_1}{\epsilon_3} = \frac{1-\lambda_1}{\lambda_3 - 1} = \frac{1 - \lambda\alpha(\lambda)}{\lambda - 1}, \tag{2.5}$$

wherein equations (2.2) and (2.4) have been used in the last relation. Then, for general homogeneous and isotropic elastic solids, *Poisson's ratio* ν_o is defined as the value of this function in the undistorted, natural state where $\lambda = 1$:

$$\nu_o \equiv \lim_{\lambda \to 1} \nu(\lambda) = -\frac{d\lambda_1(\lambda)}{d\lambda}\bigg|_{\lambda=1}, \tag{2.6}$$

wherein the last of equation (2.6) follows from $(2.5)_2$ provided $\lambda_1(1) = 1$.

It follows similarly by Batra's theorem that for the incompressible material (1.3) a simple tension produces an extension (2.2); and the constraint (1.2) determines uniquely the function

$$\lambda_1(\lambda) = \lambda^{-1/2}. \tag{2.7}$$

Thus, a simple tension produces a simple extension in every incompressible, homogeneous and isotropic elastic solid, provided the empirical inequalities (2.3) hold. We have seen that the condition $(2.1)_2$ is essential to the determination of the Poisson function (2.5) for an isotropic and compressible elastic material. On the other hand, in view of equation (2.7) and the arbitrariness of the stress p in equation (1.3), the condition $(2.1)_2$ in the case of an incompressible material is irrelative to the determination of the Poisson function, which may be found from the kinematics alone. By use of equation (2.7) in $(2.5)_2$, we obtain for every incompressible, homogeneous and isotropic material the *universal* Poisson function[2]

$$\nu(\lambda) = \frac{1}{\lambda + \lambda^{1/2}}. \tag{2.8}$$

Hence, we may conclude by (2.6) that for every incompressible, isotropic material Poisson's ratio has the unique value $\nu_o = 1/2$. The converse, however, is false, as we shall see in a moment. It may be mentioned that the lateral contraction function (2.4) for the incompressible case becomes $\alpha(\lambda) = \lambda^{-3/2}$; hence, $\alpha(1) = 1$ in the natural state.

The value of Poisson's ratio ν_o is defined by equation (2.6); hence, clearly, $\nu_o = 1/2$ does not imply that the isotropic elastic material need be incompressible. We shall illustrate this by a counterexample of a compressible, isotropic material whose Poisson function has the constant value $\nu_o = 1/2$. For this purpose it is useful to recall the results of experiments by Bell (1983) for certain homogeneous and isotropic metals in finite (plastic) strain. These data support the following constraint in a variety of deformations:

$$tr\mathbf{B}^{1/2} = \lambda_1 + \lambda_2 + \lambda_3 = 3. \tag{2.9}$$

A similar constraint $tr\mathbf{B} = 3$ has been investigated recently by Ericksen (1985) in a study of a constitutive theory for elastic crystals. Details of these applications need not concern us here. Rather, let us consider a homogeneous, isotropic elastic material for which the constraint (2.9) may hold; and let it be subjected to a simple tension to effect, under suitable restrictions on the response functions, an extensional deformation

---

[2] The function (2.8) and its limit value have been described in different ways by others (Claxton, 1958; Lindley, 1957; Pósfalvi, 1982). However, of these, only Pósfalvi derived them in the context of the simple tension test for general incompressible, homogeneous, and isotropic hyperelastic materials; but Pósfalvi does nothing with the results. We thank Dr. Joseph D. Walter, Assistant Director of the Firestone Central Research Laboratories, for bringing to our attention the papers by Claxton and Pósfalvi.

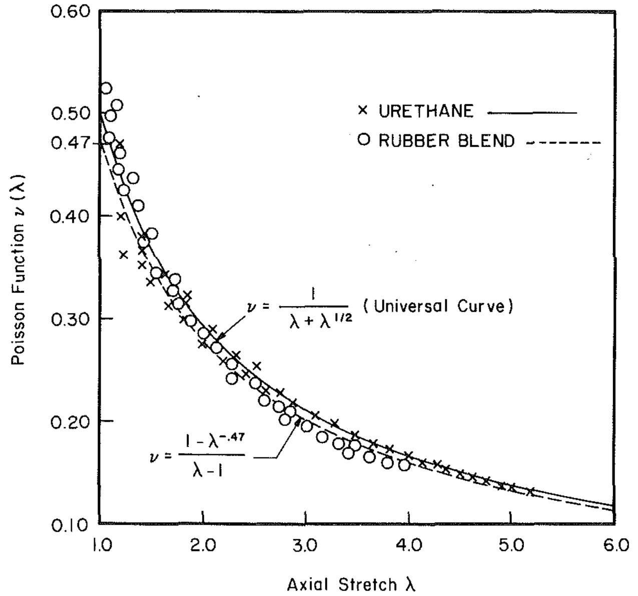

Fig. 1 Comparison of extension data for two elastomers with the Poisson function (2.8) for an incompressible material in a simple tension test

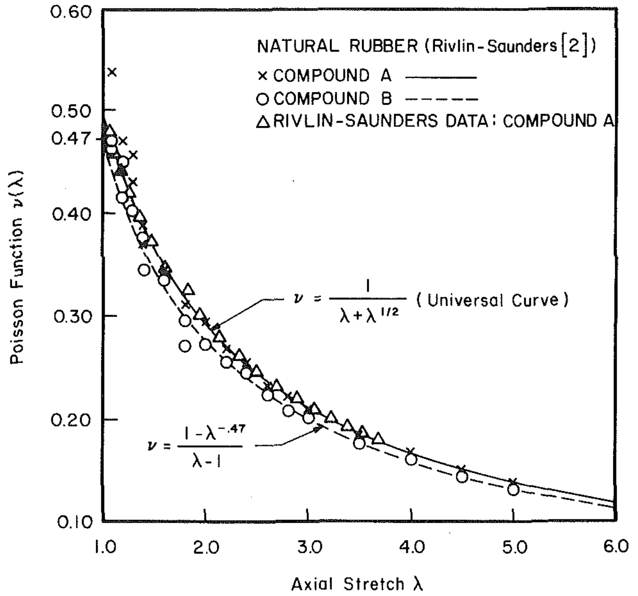

Fig. 2 Comparison of extension data for two rubber compounds with the Poisson function (2.8) for an incompressible material in a simple tension test. Data by Rivlin and Saunders (1951) for compound *A* also is shown.

(2.2). Then use of equation (2.2) in (2.9) yields the unique simple extension relation $2\lambda_1(\lambda) = 3 - \lambda > 0$, which also implies $1 \leq \lambda < 3$. It thus follows by $(2.5)_2$ and (2.6) that the Poisson function for this special class of constrained, compressible, homogeneous and isotropic elastic materials is a constant:

$$\nu(\lambda) = \frac{1}{2} = \nu_o \tag{2.10}$$

for all $\lambda \epsilon [1, 3)$. If, additionally, the material were assumed incompressible so that equation (1.2) must also hold for every admissible deformation, it may be seen that only the trivial deformation $\lambda_1 = \lambda_2 = \lambda_3 = 1$ would be possible. For sufficiently small deformations, however, the constraint (2.9) approximates the incompressibility constraint; hence, for small strains, the material behaves initially like an incompressible, isotropic elastic solid.

It is interesting to observe that in every extension (2.2), whatever may be the tractions required for its control in an incompressible material, the Poisson function (2.8) is independent of the elastic response and is valid whether the material be isotropic or not. However, this fact must be viewed with caution. Control of the deformation (2.2) plainly depends on the nature of the constitutive equation for the stress; and if the homogeneous deformation (2.2) is assigned, this stress distribution may be readily determined. But if the stress is given, conditions needed to assure that the deformation (2.2) is possible, as demonstrated above, must follow from careful examination of the constitutive equation for the prescribed loading situation. In particular, in a simple tension (or compression) test, the kinematic condition $(2.2)_2$ plainly cannot be expected to hold for arbitrary directions in an incompressible, anisotropic material. In such a material, even equal biaxial loading may not produce (2.2). For an isotropic material, we are assured by Batra's theorem that simple tensile loading will effect the deformation (2.2). Therefore, the formula (2.8), though universal for the deformation (2.2), must be viewed indirectly with regard for the nature of the material and of the loading needed to control the deformation. Parallel remarks apply to the Bell constraint (2.9) and the associated value (2.10) for the Poisson function valid in every equi-biaxial deformation (2.2).

On the other hand, contraction functions certainly may be defined in terms of other experiments; and, for distinction, these may be named *apparent* Poisson functions ν_a. For an incompressible material, the apparent Poisson function will be the same as equation (2.8) in any experiment for which equation (2.2) holds; but the loading needed to control the deformation will be determined by the particular constitutive equation for the material. In equal triaxial extension of a cube of any incompressible material, the only solution is the trivial solution $\lambda_1 = \lambda_2 = \lambda_3 = 1$; hence, for this case equation (2.8) yields the apparent value $\nu_a(\lambda) = \nu_o = 1/2$. We are reminded, however, that nonuniqueness of a pure homogeneous deformation is possible in all around tension of an incompressible material. Rivlin (1974) has shown, for example, that for a uniform tension $T > 0$ on all faces of a cube of neo-Hookean material for which $\beta_1 = \mu_o$ is constant and $\beta_{-1} = 0$, seven possible states exist. The trivial state $\lambda_1 = \lambda_2 = \lambda_3 = 1$ is always a solution for which $\nu_a = 1/2$. This state is stable provided that $T/\mu_o < 2$. The state $\lambda_1 = \lambda_2$, $0 < \lambda_3 = \lambda < T/\mu_o$, and two others obtained by cyclic permutation of the λ_k's, are stable equilibrium solutions; and the apparent Poisson function is also the same as (2.8). The remaining three solutions are unstable. Although each solution has the same apparent Poisson function (2.8), it cannot be measured in these unstable states. Other examples may be easily constructed.

3 Some Experimental Results

Experimental data obtained from at least two specimens of each of three considerably different elastomers are presented here. One is a polyether, polyurethane elastomer. Another is a carbon-black reinforced, sulfur-cured blend of natural and synthetic rubbers. A third variety is a natural gum rubber. The procedure for obtaining the axial and transverse stretch data is straightforward. Specimens having straight sides of length 42 mm and width of 6 mm were die stamped from thin sheets of uniform thickness of 1 to 3 mm. Each sample was quasistatically elongated in a tensile loading frame. The test was stopped periodically to allow measurement of the specimen width to the nearest 0.01 mm with a Gaertner traversing microscope equipped with a digital readout. At that time, the elongation was measured to the nearest 0.1 mm with a linear variable differential transformer fastened to the loading actuator. These techniques permitted reasonably accurate determination of the transverse and axial stretches suitable for demonstration purposes here. For the sake of

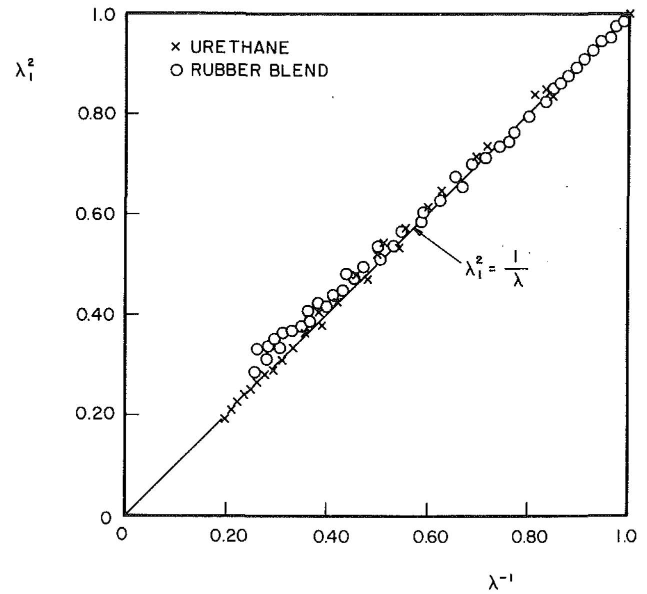

Fig. 3 Comparison of stretch data for two elastomers with the incompressibility condition $\lambda_1^2 = \lambda^{-1}$ in a simple tension test (see equation (2.7))

clarity in diagrams presented below, not all the data values collected will be shown.

It is seen that the Poisson function (2.8) for an incompressible material is a monotonically decreasing function for which $0 < \nu(\lambda) \leq 1/2$ in simple tension. The graph of equation (2.8) is shown in Figs. 1 and 2 together with tensile test stretch data for the three kinds of elastomers described above. It is seen that the urethane follows the universal function very nicely, particularly for axial stretches $\lambda > 1.5$, roughly. Although the data for the carbon-black reinforced blend of natural and synthetic rubbers, as shown in Fig. 1, follows the trend of the universal graph, its deviation at the larger deformations is evident. Two compounds of natural gum rubber of the same[3] kind used in the basic experiments by Rivlin and Saunders (1951) were fabricated from their recipes (see p. 285) provided for compounds described as A and B. Figure 2 shows that our compound A is exceptional in its comparison with the kinematical relation (2.8), while our compound B, though well-behaved, falls below and virtually parallel to the master curve. The scatter in the data for small deformations was typical for all the samples; and we feel no need to provide an explanation for it. The dotted curves shown in Figs. 1 and 2 have an analytical basis which will be explained in the next section; it suffices to mention here that these curves approximate the best fit for the data. The extension data obtained by Rivlin and Saunders for their compound A also is shown in Fig. 2. It is found that these data, for the same reason noted later, fit the universal relation (2.8). Our data for the same material is essentially coincident with theirs, except at small deformations, as noted before.

The same data may be viewed differently in Figs. 3 and 4, which emphasize the incompressibility relation (2.7) in simple tension. The data are to be compared with the line whose slope is one. The response appears to be about the same as described for Figs. 1 and 2, except that the small amount of scatter evident for the smaller stretches appears diminished in Figs. 3 and 4. It is quite clear from both graphs that the data for the urethane and the natural gum compound A fall reasonably close to the kinematical function described; therefore, these materials are virtually incompressible. The special rubber blend and the natural rubber compound B exhibit almost incompressible response that we shall examine again further on. The data for the Rivlin-Saunders compound A is also shown in Fig. 4. However, it must be mentioned that Rivlin and Saunders (1951) did not confirm by any tests described in their paper that the incompressibility constraint actually was obeyed by either compound they studied. Since the incompressibility condition was used to compute from measured values of λ alone the values for I_2 provided in their Table 6, it is not surprising that our calculation of values of λ_1 corresponding to their tabulated values for λ and I_2 results in their data falling smack on the line in Fig. 4. The same applies to Fig. 2. The representation of our stretch data in the universal plot in Fig. 2, however, is a genuine experimental result that demonstrates the incompressibility of the natural rubber compound A. The response of compound B is another matter that will be discussed later.

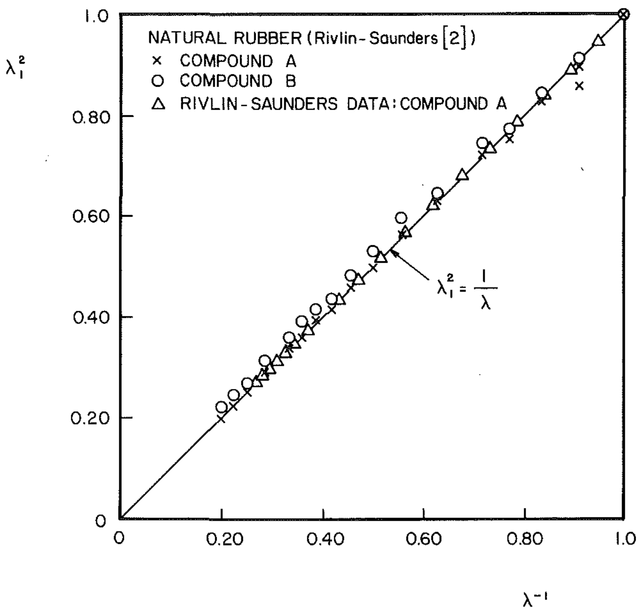

Fig. 4 Comparison of stretch data for two rubber compounds with the incompressibility condition $\lambda_1^2 = \lambda^{-1}$ in a simple tension test (see equation (2.7)). Data by Rivlin and Saunders (1951) for compound A is also shown.

4 Example for Compressible Rubbers

Let us consider a class of compressible, isotropic hyperelastic materials with strain energy function $W = W(J_1, J_2, J_3)$ per unit undeformed volume, and whose response functions in equation (1.1) depend on J_3 alone: $\beta_\Gamma = \beta_\Gamma(J_3)$. Herein we have introduced the invariants

$$J_1 \equiv I_1 = tr\mathbf{B},\; J_2 \equiv I_2/I_3 = tr\mathbf{B}^{-1},\; J_3 \equiv I_3^{1/2} = \det\mathbf{F}. \tag{4.1}$$

Then the following relations will be obtained for this hyperelastic material (Truesdell and Noll, 1965):

$$\beta_0(J_3) = \frac{\partial W}{\partial J_3},\; \beta_1(J_3) = \frac{2}{J_3}\frac{\partial W}{\partial J_1},$$

$$\beta_{-1}(J_3) = -\frac{2}{J_3}\frac{\partial W}{\partial J_2}. \tag{4.2}$$

Bearing in mind the assumed functional dependence, it may be seen that these relations will hold if and only if $2\partial W/\partial J_1 = \alpha$ and $2\partial W/\partial J_2 = \beta$ are constants. Thus, introducing these in equation (4.2) and writing $\partial W/\partial J_3 \equiv W_3(J_3)$, we obtain the response functions

$$\beta_0 = W_3(J_3),\; \beta_1 = \frac{\alpha}{J_3},\; \beta_{-1} = -\frac{\beta}{J_3}. \tag{4.3}$$

---

[3] There was a minor difference; the antioxidant nonox used by Rivlin and Saunders (1951) was replaced by another hindered phenol type antioxidant, tradename American Cyanamid A02246.

It is known that $\beta_1(1)-\beta_{-1}(1)=\alpha+\beta=\mu_o$, the usual constant shear modulus in the undistorted, natural state of the material (Truesdell and Noll, 1965). Thus, upon introducing $\alpha=\mu_o f$ and $\beta\equiv\mu_o(1-f)$, where f is another constant, and substituting equation (4.3) into (1.1), we reach the general form of the constitutive equation for our compressible, hyperelastic material:

$$\mathbf{T}=W_3(J_3)\mathbf{1}+\frac{\mu_o f}{J_3}\mathbf{B}-\frac{\mu_o(1-f)}{J_3}\mathbf{B}^{-1}. \tag{4.4}$$

This equation was first introduced in an altogether different way by Blatz and Ko (1962). It may be seen from equation (4.3) that the empirical inequalities (2.3) are satisfied for the Blatz-Ko material if and only if $\mu_o>0$ and $0<f\le 1$. These conditions were not noted by Blatz and Ko (1962); however, they are essential in the biaxial deformation problems described there. In order that the stress (4.4) may vanish in the undeformed state where $\mathbf{B}=\mathbf{1}$, it is necessary and sufficient that $W_3(1)+\mu_o(2f-1)=0$. Hence, by $(4.3)_1$, $-\mu_o\le\beta_0(1)<\mu_o$.

Experiments by Blatz and Ko (1962) on a certain compressible, foamed, polyurethane rubber revealed the specific response functions

$$\beta_0=\mu_o,\quad 0<\beta_1<<1,\quad \beta_{-1}=-\mu_o/J_3, \tag{4.5}$$

where β_1 was considered negligible so that $f=0$, very nearly, and $W_3=\mu_o=32$ psi. Thus, in general terms, equation (4.4) reduces to the following constitutive equation for the Blatz-Ko foamed, polyurethane rubber:

$$\mathbf{T}=\mu_o[\mathbf{1}-J_3^{-1}\mathbf{B}^{-1}]. \tag{4.6}$$

For the simple tension (2.1), (2.2) holds and $J_3=\lambda_1^2\lambda$. It follows that equation (4.6) yields

$$T=\mu_o(1-\lambda_1^{-2}\lambda^{-3}),\quad \lambda_1(\lambda)=\lambda^{-1/4}. \tag{4.7}$$

The extension, therefore, is simple. Application of equation (2.5) delivers the Poisson function

$$\nu(\lambda)=\frac{1-\lambda^{-1/4}}{\lambda-1}. \tag{4.8}$$

We thus find by equation (2.6) that the foamed, polyurethane rubber (4.6) has a Poisson ratio $\nu_o=1/4$, which is, in fact, the experimental value found by Blatz and Ko. However, they made no connection of their data with equation (4.8); rather, they used a clever *ad hoc* rule described below to determine ν_o.

The linearized form of equation (4.6) will be considered next. First we note that $E_o=5\mu_o/2$ is the usual Young's modulus for this model, and for a sufficiently small engineering strain ϵ, it can be easily shown that

$$\mathbf{B}=\mathbf{1}+2\epsilon,\quad J=1+\theta, \tag{4.9}$$

in which $\theta=tr\epsilon$ describes the small change in volume per unit initial volume. Then, to the first order in ϵ, equation (4.6) becomes

$$\mathbf{T}=\frac{2E_o}{5}[\theta\mathbf{1}+2\epsilon]. \tag{4.10}$$

We thus recover the linearized, uni-constant equation for general isotropic, foamed elastic materials derived by Gent and Thomas (1959) from a simple microstructural model consisting of a network of thin extensible rubber cords connected by rigid joints. It may be noted that equation (4.10) is the same equation obtained from linear, isotropic elasticity theory with $\nu_o=1/4$, i.e., with equal Lamé constants $\lambda_o=\mu_o$; it is the constitutive equation of the controversial 19th century rari-constant elasticity model that evolved from molecular theories of elasticity due by Poisson and Cauchy (Todhunter and Pearson, 1960; Bell, 1973). On the contrary side, we are reminded of Wertheim's many experiments on metals for which he claimed a universal average value $\nu_o=1/3$. The rari-constant theorists and experimentists were careful always to exclude from the uniconstant theory unusual materials that they believed ought not to be treated as elastic; caoutchouc was an example often cited (Todhunter and Pearson, 1960). It is strangely coincidental that Gent and Thomas (1959) found in their experiments on foamed natural rubber the average value $\nu_o=1/3$, as compared with their predicted universal value of 1/4.

There is a third empirical condition, $\beta_0\le 0$, that also should be considered (Truesdell and Noll, 1965). Hence, $\beta_0(1)\le 0$ with $\mu_o>0$ holds if and only if $f\ge(1/2)$, in which case $-\mu_o<\beta_0(1)\le 0$ for $(1/2)\le f\le 1$. We see from $(4.5)_1$ that the Blatz-Ko foamed, polyurethane rubber model fails to satisfy it (Beatty, 1984). It is possible, of course, that this results from the fact that a foamed rubber is not a homogeneous, materially uniform and isotropic continuum. Nonetheless, the test data share good agreement with this model. It should be emphasized also that the data for the Blatz-Ko compressible, solid polyurethane rubber material described below support all of the empirical inequalities.

It is also interesting, though apparently not well-known, that in the construction of their more general constitutive equation (4.4), which essentially is designed to reduce to the Mooney-Rivlin model when $\nu_0=1/2$, Blatz and Ko (1962) invoked the following additional *ad hoc* constitutive assumption of volume control in a simple tension:

$$J_3=\lambda^{1-2\nu_o} \tag{4.11}$$

It follows by Batra's theorem that $\lambda_1=\lambda_2$ in the simple tension; hence, equation (4.11) yields the unique relation

$$\lambda_1(\lambda)=\lambda^{-\nu_o}. \tag{4.12}$$

Therefore, the extension is indeed simple. This must hold in a simple tension of every Blatz-Ko material (4.4) for which (2.3) holds. Thus, the Poisson function for every such material is given by

$$\nu(\lambda)=\frac{1-\lambda^{-\nu_o}}{\lambda-1}. \tag{4.13}$$

It is readily seen that for small strains equation (4.12) may be linearized to $\epsilon_1=-\nu_o\epsilon_3$; hence, the constant exponent ν_o in equations (4.11) to (4.13) is the classical Poisson ratio for the material. Of course, the same thing derives from equation (2.6). Thus, the occurrence of Poisson's ratio $\nu_o=1/4$ in equation $(4.7)_2$ and (4.8) is not coincidental. Notice also that for this case the value $\nu_o=1/2$ reduces equation (4.11) to the incompressibility condition (1.2) in simple tension.

A material whose response in a simple tension test fails to obey the rule (4.12) cannot be a candidate for the Blatz-Ko model. Therefore, when attempting to model the constitutive behavior of an elastomer, the experimenter may find it helpful to first confirm the volume control relation (4.12) by plotting a graph of $\log(1/\lambda_1)$ against $\log\lambda$, which is a straight line of slope ν_o. For illustration, the tensile test data for the elastomers considered earlier are plotted accordingly in Figs. 5 and 6. A least squares fit of the data with straight lines through the origin shows in Fig. 5 that the urethane has a Poisson ratio $\nu_o=0.493$, while the rubber blend satisfies $\nu_o=0.468$. Similar tests on a second urethane and a second rubber blend, which differed from the others only slightly in their formulation and processing, yielded the same basic response with the respective values $\nu_o=0.463$ and $\nu_o=0.459$.

The data for the Rivlin-Saunders natural rubber compound *A* are shown in Fig. 6. However, as noted earlier, because they measured only λ and, in effect, used the incompressibility condition to compute λ_1, one should expect, as seen in Fig. 6, that their converted data should follow perfectly the ideal line for which $\nu_o=0.5$. It is seen, however, that our corresponding data for the natural rubber compound *A* also enjoys excellent

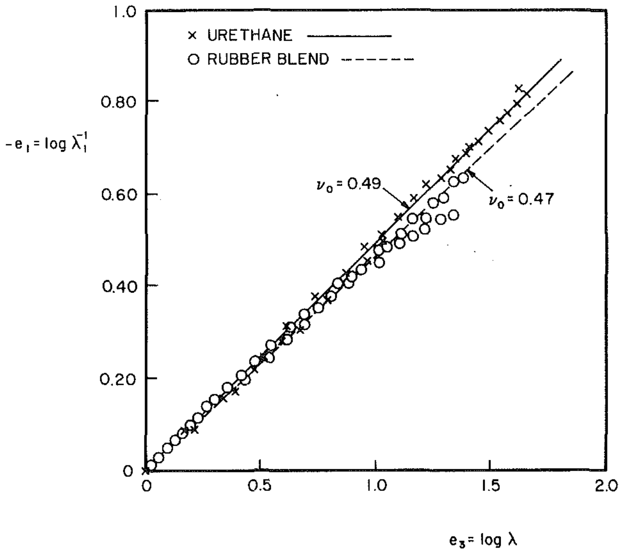

Fig. 5 Best fit comparison of tensile test data for two elastomers with the Blatz-Ko volume control relation (4.12), and evaluation of Poisson's ratio for the materials

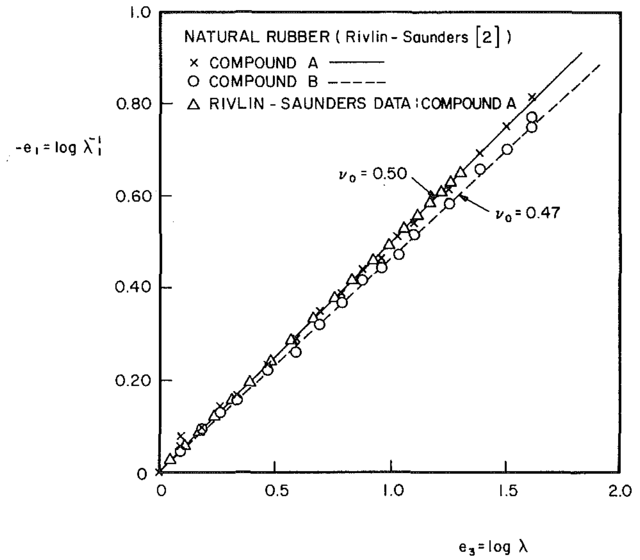

Fig. 6 Best fit comparison of tensile test data for two rubber compounds with the Blatz-Ko volume control relation (4.12), and evaluation of Poisson's ratio for the materials. Data by Rivlin and Saunders (1951) for compound *A* also is shown.

correlation with the volume control relation for incompressible materials. The compound *A* yielded, among all the elastomers we studied, the best fit correlation with $\nu_o = 0.499$. The natural rubber compound *B*, on the other hand, produced in our tests and best fit $\nu_o = 0.466$. The values of ν_o found in this manner were then used in equation (4.13), and the corresponding best fit graphs of their Poisson functions $\nu(\lambda)$ were plotted in Figs. 1 and 2. Of course, the curves for the urethane and the rubber compound *A* lay so close to the master curve that we let this curve represent their behavior, as shown therein. Although the elastomers for which $\nu_o \neq 0.5$, approximately, may thus be viewed as candidates for a Blatz-Ko constitutive model, considerable further evaluation would be necessary to establish this.

Based upon their volume control relation (4.11), Blatz and Ko graphed the straight line of $\log J_3$ against $\log \lambda$ and from its slope $1 - 2\nu_o$ determined for their foamed, polyurethane rubber the value $\nu_o = 0.25$; but they apparently were unable to apply the same method to their solid, polyurethane rubber. By an altogether different and unrelated argument, they arrived at the value $\nu_o = 0.463$. We encountered no serious difficulties in our graphical evaluations of ratios of similar value for other varieties of rubber based upon equation (4.12). Evaluation by Blatz and Ko (1962) of the tension data for their solid, polyurethane showed that $f = 1$ and $\mu_o = 34$ psi. Thus, in general terms, the reduced form of the Blatz-Ko constitutive relation (4.4) for their solid polyurethane rubber may be written as

$$\mathbf{T} = W_3(J_3)\mathbf{1} + \frac{\mu_o}{J_3}\mathbf{B}, \tag{4.14}$$

subject to the further empirical inequality $\beta_o = W_3(J_3) \leq 0$.

Finally, it may be observed that the true strain e_k in any direction k is defined by $e_k = \log \lambda_k$. Consequently, the volume control relation (4.12) may be rewritten as

$$\nu_o = -\frac{e_1}{e_3}, \tag{4.15}$$

which reveals that in finite strain Poisson's ratio for every Blatz-Ko model is the ratio of the true lateral contractive strain to the true extensional strain. Therefore, Figs. 5 and 6 actually are plots of the true transverse strain e_1 versus the true axial strain e_3 in a simple tension test. This simple fact has apparently gone unnoticed by others.

5 Conclusion

The tensile test possibly is the most important among all simple experiments used to characterize the phenomenological behavior of solid materials; and its application to rubbery materials provides an excellent opportunity for instruction in some interesting aspects of nonlinear elasticity. With this objective in mind, some data for the so-called Poisson's ratio (sic) as a function of engineering strain for an unspecified rubber material was illustrated by Coakman, Eastwood and Evans (1966); however, they provided no explanation or discussion of the phenomenon. This almost casual indication of a substantial variation in the lateral contraction ratio for rubber in finite strain prompted, we feel, an inaccurate critique by Lindley (1967) a year later.

Lindley observed correctly that Poisson's ratio is a material *constant*, hence independent of the strain from the natural state. But his subsequent remark that its definition is valid only for small strains, so that its use is inappropriate at large strains, is imprecise. He naturally *assumes* that regardless of the nonlinear constitutive description of the material, the transverse strains in a simple tension test must be equal; and based upon this assertion and the incompressibility of rubber, which he justifies in terms of the bulk modulus rather than the volume constraint for infinitesimal strains, he provides an equation in terms of (possibly) finite engineering strains that characterizes reasonably the data shown by Coakham et al. (1966). We agree with Lindley that the experiment in Coakham et al. and in our own Figs. 1 and 2 above, is an inappropriate method for evaluation of Poisson's ratio for natural rubber, though it may be an excellent demonstration in support of its incompressibility. However, since Poisson's ratio $\nu_o = 1/2$ for every incompressible, isotropic elastic material, these data obviously are not intended for this evaluation in the first place.

The fact that one can indeed define a Poisson function, or some other lateral contraction function, that accurately demonstrates the variation in the lateral contractive response of elastomers over a wide range of deformation in a simple tension test, as shown in Figs. 1 and 2, apparently is unappreciated by Lindley (1967) and ignored by Coakham, Eastwood and Evans (1966). Of course, not every elastomer need be incompressible; and based upon the Blatz-Ko volume control relation (4.11), it is seen in Figs. 5 and 6 that in special circumstances the kinematical data for finite deformations may be plotted in a manner that does allow for easy evaluation of their Poisson's ratio in the natural state. In fact, our equation (4.15), demonstrated by rough experiments, refutes Lindley's remark that use of Poisson's ratio is appropriate only for small strains. Moreover, Anand (1979) has found that equation (4.15) arises naturally in a linear theory of isotropic elasticity that uses the true strain $\mathbf{e} \equiv \log \mathbf{B}^{1/2}$ as a deformation measure for moderately large strains. He showed that Hencky's constitutive equation for the Kirchhoff stress shares good agreement with a variety of experimental data for moderately large deformations defined by stretches of roughly 1.3 to 1.4. Although it may be tempting to adopt equation (4.15) as the definition of Poisson's ratio for large deformations, we caution that this rule applies only to the class of materials for which equation (4.12) holds in a simple tension test. The Blatz-Ko material (4.6), in view of equation $(4.7)_2$, the linear Hencky model (Anand, 1979), by definition, and all others for which equation (4.12) may be valid, belong to this class. The definition (2.5), on the other hand, extends to all isotropic elastic materials that respect the empirical inequalities.

Finally, we are reminded that in numerical work involving elastomeric materials which often are *assumed* ideally incompressible, a value of ν_0 *close* to 0.5 commonly is used to avoid computational difficulties. But it may be useful to first evaluate the actual lateral contractive response for the special elastomeric material of interest. Indeed, it may happen that a plot of the kind used in Figs. 5 and 6 may provide useful data for a more appropriate and realistic estimate of Poisson's ratio for elastomers studied in numerical work.

Acknowledgment

Professor M. F. Beatty gratefully acknowledges support of this work through grants from the National Science Foundation and the University of Minnesota, Institute for Mathematics and its Applications, where the work was largely completed while he was on leave as a Senior Fellow during 1984–1985. The authors also wish to thank the Firestone Tire and Rubber Company for permission to use in this report experimental data generated at the Central Research Laboratories at Akron.

References

Anand, L., 1979, "On H. Hencky's Approximate Strain-Energy Function for Moderate Deformations," ASME JOURNAL OF APPLIED MECHANICS, Vol. 46, pp. 78–81.

Batra, R. C., 1976, "Deformation Produced by a Simple Tensile Load in an Isotropic Elastic Body," *Journal of Elasticity*, Vol. 6, pp. 109–111.

Beatty, M. F., 1984, "A Lecture on Some Topics in Nonlinear Elasticity and Elastic Stability," IMA Preprint Series #99, Institute for Mathematics and its Applications, University of Minnesota, MN.

Bell, J. F., 1973, "Mechanics of Solids, I. The Experimental Foundations of Solid Mechanics," *Flügge's Handbuch der Physik*, Vol. VIa/1, Springer-Verlag, Berlin, Heidelberg, New York.

Bell, J. F., 1983, "Continuum Plasticity at Finite Strain for Stress Paths of Arbitrary Composition and Direction," *Archive for Rational Mechanics and Analysis*, Vol. 84, pp. 139–170.

Blatz, P. J., and Ko, W. L., 1962, "Application of Finite Elasticity Theory to the Deformation of Rubbery Materials," *Transactions of the Society of Rheology*, Vol. 6, pp. 223–251.

Claxton, W. E., 1958, "Stress-Strain Equation for Rubber in Tension," *Journal of Applied Physics*, Vol. 29, pp. 1398–1406.

Coakham, J. W., Eastwood, W. M. K., and Evans, W., 1966, "Introductory Experiments in Materials Science for Engineers," *Bulletin of Mechanical Engineering Education*, Vol. 5, pp. 145–155.

Ericksen, J. L., 1985, "Constitutive Theory for Some Constrained Elastic Crystals," IMA Preprint Series #123, Institute for Mathematics and its Applications, University of Minnesota, MN.

Gent, A. N., and Thomas, A. G., 1959, "The Deformation of Foamed Elastic Materials," *Journal of Applied Polymer Science*, Vol. 1, pp. 107–113.

Lindley, P. B., 1958, "Poisson's Ratio and the Incompressibility of Rubber," *Bulletin of Mechanical Engineering Education*, Vol. 6, pp. 186–187.

Love, A. E. H., 1927, *A Treatise on the Mathematical Theory of Elasticity*, Fourth Ed., Dover Pub., New York, pp. 102–105.

Pósfalvi, Ö., 1982, "Zur Bestimmung der Poissonschen Zahl von gummielastischen Stoffen," *Kautschuk und Gummi Kunststoffe*, Vol. 35, pp. 940–941.

Rivlin, R. S., 1974, "Stability of Pure Homogeneous Deformations of an Elastic Cube Under Dead Loading," *Quarterly of Applied Mathematics*, Vol. 32, pp. 265–272.

Rivlin, R. S., and Saunders, D. W., 1951, "Large Elastic Deformations of Isotropic Materials; VII. Experiments on the Deformation of Rubber," *Philosophical Transactions of the Royal Society of London*, Vol. A 243, pp. 251–288.

Todhunter, I., and Pearson, K., 1960, *A History of the Theory of Elasticity and of the Strength of Materials*, Dover Pub. Inc., New York.

Truesdell, C., and Noll, W., 1965, "The Nonlinear Field Theories of Mechanics," *Flügge's Handbuch der Physik*, Vol. III/3, Springer-Verlag: Berlin, Heidelberg, New York, pp. 139–141, pp. 153–158, and pp. 317–319.

N. Hasebe
Professor.

T. Sugimoto
Assistant.

T. Nakamura
Associate Professor.

Department of Civil Engineering,
Nagoya Institute of Technology,
Gokisocho, Showaku, Nagoya, Japan 466

Longitudinal Shear Problem for an Elastic Body with Two Fixed Edges

A semi-infinite elastic body with an arbitrary shape and an infinite one with a hole under uniform longitudinal shear load are investigated. These bodies have a boundary with two fixed parts. The respective complex stress functions are obtained in closed form by using a conformal mapping function. Doubly connected elastic bodies with symmetry can also be treated. Examples of the stress distribution and expressions for the stress intensity factor are shown.

Introduction

The longitudinal shear problem is characterized by a single displacement component normal to the *x-y* plane, and independent of the coordinate perpendicular to this plane. The nonvanishing stress components are the shear stresses in the *x-y* plane. In this paper we consider a semi-infinite elastic body with an arbitrary shape and an infinite elastic body with a hole under uniform longitudinal shear load. These bodies have a boundary on which displacements are fixed at two parts. It is assumed here that the material of these bodies is homogeneous and isotropic. The exact solution of this mixed boundary value problem can be obtained in closed form. In the analysis, the complex stress function and a conformal mapping function which maps these shapes into the inside or outside of a unit circle are used.

The stress function for boundary condition of one fixed part can be obtained in closed form, but for that of two fixed parts the stress function contains an integral term which is difficult to integrate. However, the first derivative of this term can be obtained in closed form which does not contain an integral term. Finally, the complex stress function is obtained in its first derivative form.

Examples of stress distribution are shown for a doubly connected shape with symmetry. As examples of a crack problem, expressions for stress intensity factor are also shown.

Method of Analysis

A) Analysis of Semi-Infinite Elastic Body. A stress function is derived for a semi-infinite elastic body with an arbitrary shape. The body has two parts of the boundary on which displacements are given. Figure 1 shows the semi-infinite region in the z plane and the unit circle in the ζ plane. The parts of the boundary on which displacements are given are designated by M_1 and M_2, and the sum by $M = M_1 + M_2$. Similarly $L = L_1 + L_2$ designates the parts on which external forces are given. Γ designates $M + L$. Z_A and Z_B are endpoints of M_1 and Z_C and Z_D are those of M_2.

A conformal mapping function which maps the semi-infinite region into the unit circle is used (see Fig. 1). The rational mapping function is expressed as follows (Hasebe, 1979; Hasebe and Inohara, 1980)

$$z=\omega(\zeta)=\frac{E_h}{1-\zeta}+\sum_{k=1}^{n}\frac{E_k}{\zeta_k-\zeta}+E_{-1}, \tag{1}$$

in which E_h is imaginary if the semi-infinite region coincides with the lower half of the z plane, and ζ_k is a point outside of the unit circle. $\zeta = 1$ corresponds to infinity. The boundary of the unit circle is denoted by Γ. α, β, γ, and δ correspond to Z_A, Z_B, Z_C, and Z_D.

Next, we show several basic expressions for the longitudinal shear problem. Stresses τ_{xt} and τ_{yt}, the displacement w, and a complex function $\Phi(z)$ which is regular in the region obey the following relations (Benthem and Koiter, 1973)

$$\tau_{xt}=G\frac{\partial w}{\partial x}, \quad \tau_{yt}=G\frac{\partial w}{\partial y}$$

$$\tau_{xt}-i\tau_{yt}=G\Phi'(z), \quad w=[\Phi(z)+\overline{\Phi(z)}]/2, \tag{2}$$

where G is the shear modulous, the prime indicates differentiation and the bar indicates a conjugate term. The displacement w is a solution of Laplace equation to satisfy the

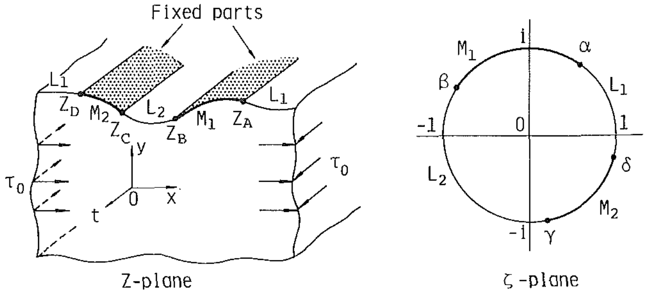

Fig. 1 A semi-infinite elastic body with an arbitrary shape and the unit circle

---

Contributed by the Applied Mechanics Division for publication in the JOURNAL OF APPLIED MECHANICS.

Discussion on this paper should be addressed to the Editorial Department, ASME, United Engineeing Center, 345 East 47th Street, New York, N.Y. 10017, and will be accepted until two months after final publication of the paper itself in the JOURNAL OF APPLIED MECHANICS. Manuscript received by ASME Applied Mechanics Division, December 26, 1985; fianl revision April 1, 1986.

equilibrium equation. The following expression is obtained from the equilibrium of external forces:

$$G[\Phi(\xi)-\overline{\Phi(\xi)}]=2i\{\textstyle\int\tau_{rt}ds+C_0\}, \tag{3}$$

in which ξ is a point on the boundary; τ_{rt} is the longitudinal shear stress on the boundary; s is the length along the boundary, and the sense of s is positive when the region lies to the left.

Introducing the mapping function $\omega(\zeta)$, and putting $\Phi(z) = \Phi(\omega(\zeta)) \equiv \phi(\zeta)$, the following expressions are obtained:

$$\tau_{xt}-i\tau_{yt}=G\,\frac{\phi'(\zeta)}{\omega'(\zeta)}\,,\quad w=[\phi(\zeta)+\overline{\phi(\zeta)}]/2$$

$$G[\phi(\sigma)-\overline{\phi(\sigma)}]=2i\{\textstyle\int\tau_{rt}ds+C_0\}, \tag{4}$$

in which σ is a point on the unit circle. If stresses τ_{rt} and $\tau_{\theta t}$ are components for the curvilinear coordinates expressed by the mapping function, the relations among τ_{rt}, $\tau_{\theta t}$, τ_{xt}, and τ_{yt} are,

$$\tau_{rt}-i\tau_{\theta t}=e^{i\rho}(\tau_{xt}-i\tau_{yt}),\quad e^{i\rho}=\frac{\zeta\omega'(\zeta)}{|\zeta\omega'(\zeta)|}\,. \tag{5}$$

The boundary condition is expressed from equation (4) as follows:

$$\phi(\sigma)+\delta(\sigma)\phi(\sigma)-\overline{\phi(\sigma)}=f(\sigma), \tag{6}$$

where

$$\delta(\sigma)=\begin{cases}0 & \text{on L}\\ -2 & \text{on } M\end{cases}\,,\quad f(\sigma)=\begin{cases}2i\{\int\tau_{rt}ds+C_0\}/G & \text{on } L\\ -2w & \text{on } M.\end{cases}$$

When equation (6) is multiplied by $d\sigma/[2\pi i(\sigma-\zeta)]$ and integrated along Γ, the following expression is obtained:

$$\phi(\zeta)-\frac{1}{\pi i}\int_M\frac{\phi(\sigma)}{\sigma-\zeta}\,d\sigma=M(\zeta)+\overline{\phi(0)},$$

$$M(\zeta)=\frac{1}{2\pi i}\int_\Gamma\frac{f(\sigma)}{\sigma-\zeta}\,d\sigma. \tag{7}$$

The solution of equation (7) is obtained as follows (Mikhlin, 1964):

$$\phi(\zeta)=M(\zeta)-\frac{\chi(\zeta)}{\pi i}\int_M\frac{M(\sigma)}{\chi(\sigma)(\sigma-\zeta)}\,d\sigma+P(\zeta)\chi(\zeta), \tag{8}$$

where

$$x(\zeta)=(\zeta-\alpha)^{1/2}(\zeta-\beta)^{1/2}(\zeta-\gamma)^{1/2}(\zeta-\delta)^{1/2},$$

$$\left(\lim_{\zeta\to\infty}\frac{\chi(\zeta)}{\zeta^2}=1\right).$$

$\chi(\zeta)$ is a Plemelj function chosen so that displacements are continuous at α, β, γ, and δ. $P(\zeta)\chi(\zeta)$ is a homogeneous solution of equation (7). Equation (8) is a general solution when arbitrary displacements and external forces are given.

When two parts of the boundary are fixed under uniform longitudinal shear load as shown in Fig. 1, the stress function $\phi(\zeta)$ is obtained as follows:

$$\phi(\zeta)=\phi_0(\zeta)+\phi_1(\zeta). \tag{9}$$

$\phi_0(\zeta)$ is the stress function which determines the uniform stress state at infinity, and from equation (4)

$$\phi_0(\zeta)=\frac{\tau_0}{G}\,\omega(\zeta). \tag{10}$$

Boundary conditions are,

$$f(\sigma)=0 \qquad \text{on } L_1,\quad f(\sigma)=0 \quad \text{on } M_1$$

$$f(\sigma)=2i\,\frac{C_h}{G} \qquad \text{on } L_2,\quad f(\sigma)=0 \quad \text{on } M_2 \tag{11}$$

C_h is a resultant force on M_1. In equation (11), we can also take $f(\sigma)=2iC_h/G$ on L_1 and $f(\sigma)=0$ on L_2, and then C_h represents a resultant force on M_2. If we substitute equations (9), (10), and (11) into equation (6), $\phi_1(\zeta)$ can be obtained from equation (8). Then $\phi(\zeta)$ is obtained from equation (9) as follows:

$$\phi(\zeta)=\frac{\tau_0}{G}\,\frac{E_h}{1-\zeta}\,\frac{\chi(\zeta)}{\chi(1)}+\frac{C_h}{G\pi}\,F(\zeta)+\text{Const},$$

$$F(\zeta)=\log\frac{\gamma-\zeta}{\beta-\zeta}-\frac{\chi(\zeta)}{\pi i}\int_M\frac{\log\dfrac{\gamma-\sigma}{\beta-\sigma}}{\chi(\sigma)(\sigma-\zeta)}\,d\sigma. \tag{12}$$

$\phi(\zeta)$ has to satisfy $\tau_{xt}\to\tau_0$ as $\zeta\to 1$, and the resultant force on M has to be equal to zero. Therefore, $P(\zeta)$ in equation (8) equals zero, and the constant term in equation (12) is determined from the condition on displacement. The integral in $F(\zeta)$ of equation (12) looks difficult, but the first derivative $\phi'(\zeta)$ of the stress function $\phi(\zeta)$ can be obtained by the following procedure. Looking at equation (12), $\phi(\zeta)$ does not contain E_k and ζ_k except E_h in equation (1). Hence $\phi(\zeta)$ for a semi-infinite elastic body with perfectly flat plane and for that with an arbitrary shape are the same; however, E_h, i.e., the coefficient of $1/(1-\zeta)$, for each shape has to be used in $\phi(\zeta)$. First we find $\Phi'(z)$ for a semi-infinite elastic body with a perfectly flat plane. Then $\phi'(\zeta)$ for a semi-infinite elastic body with an arbitrary shape can be obtained from $\Phi'(z)$, and $F'(\zeta)$ can also be obtained.

The semi-infinite elastic body is in the region of the lower half of the z plane, so the boundary is on the x axis. The uniform longitudinal shear $\tau_{xt}=\tau_0$ acts at infinity. Boundary conditions are expressed by using equation (2) and analytic continuation for stress-free boundary,

$$\Phi'^{+}(\xi)+\Phi'^{-}(\xi)=2\,\frac{\partial w}{\partial x}\quad\text{on } M$$

$$\Phi'^{+}(\xi)-\Phi'^{-}(\xi)=-2i\,\frac{\tau_{yt}}{G}\quad\text{on } L \tag{13}$$

where ξ is a point on the x axis. The solution to the Riemann-Hilbert problem of equation (13) is

$$\Phi'(z)=\frac{Y(z)}{2\pi i}\int_\Gamma\frac{f(\xi)}{Y(\xi)(\xi-z)}\,d\xi+Q(z)Y(z), \tag{14}$$

$$Y(z)=(z-z_A)^{-1/2}(z-z_B)^{-1/2}(z-z_C)^{-1/2}(z-z_D)^{-1/2},$$

in which $f(\xi)$ equals $2(\partial w/\partial x)$ on M, and $-2i\tau_{yt}/G$ on L. $Y(z)$ is a Plemelj function which is chosen so that the stresses are discontinuous at z_A, z_B, z_C and z_D, and the branch is chosen so that $z^2Y(z)\to 1$ as $z\to\infty$. $Q(z)Y(z)$ is a homogeneous solution of equation (13).

The desired stress function is expressed by $\Phi'(z)=\Phi_0{}'(z)+\Phi_1{}'(z)$ where $\Phi_0{}'(z)$ gives a uniform stress state at infinity, and $\Phi_0{}'(z)=\tau_0/G$ by equation (2).

Substituting the boundary condition $f(\xi)=0$ into equation (13), the boundary condition for $\Phi_1{}'(z)$ is given and $\Phi_1{}'(z)$ is given by equation (14). $Q(z)$ is a polynomial expression of second order, since the stress is τ_0 at infinity. Consequently $\Phi'(z)$ has the following form:

$$\Phi'(z)=\left\{\frac{\tau_0}{G}\,z^2+b_1z+b_0\right\}Y(z), \tag{15}$$

in which b_1 and b_0 are coefficients chosen to satisfy the condition of resultant force at infinity and relative displacement of parts M_1 and M_2. $\phi'(\zeta)$ can be obtained from equation (15) as follows: the mapping function which maps the region in the lower half of the z plane into a unit circle is expressed by

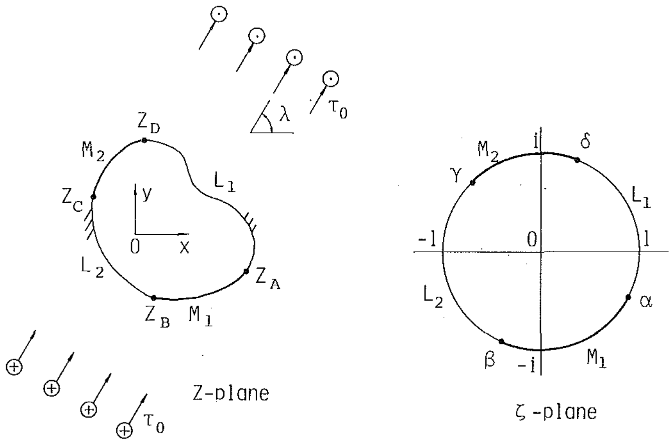

Fig. 2 An infinite elastic body with a hole and the unit circle

$$z=\omega(\zeta)=\frac{E_h}{1-\zeta}-\frac{E_h}{2}. \qquad (16)$$

Substituting equation (16) into equation (15), $\phi'(\zeta)$ can be obtained from $\Phi'(z) = \phi'(\zeta)/\omega'(\zeta)$:

$$\phi'(\zeta)=\frac{\tau_0}{G}E_h\left\{\frac{D_2}{(1-\zeta)^2}+\frac{D_1}{1-\zeta}+D_0\right\}\frac{y(\zeta)}{y(1)}, \qquad (17)$$

where

$$y(\zeta)=(\zeta-\alpha)^{-1/2}(\zeta-\beta)^{-1/2}(\zeta-\gamma)^{-1/2}(\zeta-\delta)^{-1/2}.$$

For convenience $(\tau_0/G)E_h$ is put before the bracket, as shown in equation (17). D_0, D_1, and D_2 are obtained by the following procedure: $D_2 = 1$ is obtained from $\phi'(1)/\omega'(1) = \tau_0/G$, since the stress is τ_0 at infinity. D_1 can be obtained from $[(1-\zeta)^2\phi'(\zeta)]'_{\zeta=1} = 0$ since the resultant force is equal to zero at infinity:

$$D_1=-\frac{1}{2}\left(\frac{1}{1-\alpha}+\frac{1}{1-\beta}+\frac{1}{1-\gamma}+\frac{1}{1-\delta}\right). \qquad (18)$$

D_0 can be obtained from the condition that the relative displacement of two fixed parts M_1 and M_2 is equal to zero and the part L_1 is a free boundary. From this condition and equation (4), the following expression is obtained:

$$\phi(\gamma)-\phi(\beta)=\int_\beta^\gamma \phi'(\sigma)d\sigma=0. \qquad (19)$$

We can take another part between α and δ instead of β and γ. Equation (19) is integrated along the arc on the unit circle. This integration is transformed into a real integral by using the transformation $\xi = E_0/(1-\sigma)-(E_0/2)$ in which E_0 is an arbitrary imaginary number. Hence D_0 is expressed as follows:

$$D_0=-\frac{I(2)+E_0(1+D_1)I(1)}{E_0^2 I(0)}-\frac{1}{4}-\frac{D_1}{2}, \qquad (20)$$

where $I(2)$, $I(1)$, and $I(0)$, are real integrals:

$$I(2)=\int_{\xi_B}^{\xi_C}\xi^2 Y^*(\xi)d\xi, \quad I(1)=\int_{\xi_B}^{\xi_C}\xi Y^*(\xi)d\xi,$$

$$I(0)=\int_{\xi_B}^{\xi_C}Y^*(\xi)d\xi,$$

in which

$$Y^*(\xi)=(\xi-\xi_A)^{-1/2}(\xi-\xi_B)^{-1/2}(\xi-\xi_C)^{-1/2}(\xi-\xi_D)^{-1/2}$$

$$\xi_A=E_0\left(\frac{1}{1-\alpha}-\frac{1}{2}\right), \quad \xi_B=E_0\left(\frac{1}{1-\beta}-\frac{1}{2}\right)$$

$$\xi_C=E_0\left(\frac{1}{1-\gamma}-\frac{1}{2}\right), \quad \xi_D=E_0\left(\frac{1}{1-\delta}-\frac{1}{2}\right).$$

To avoid complication, the derivations of $I(2)$, $I(1)$, and $I(0)$ are omitted, but these contain elliptic integrals in general. In a practical calculation, it is necessary to pay attention that the modulus of elliptic integral k^2 does not exceed 1. When the region and the fixed parts are symmetric to the y axis, i.e., $\xi_D = -\xi_A$, $\xi_C = -\xi_B$, then D_0 is simplified as follows:

$$D_0=-\left(\frac{1}{1-\alpha}-\frac{1}{2}\right)^2\left[1-\frac{E(k)}{K(k)}\right]+\frac{1}{4}, \qquad (21)$$

in which

$$k^2=\left[\frac{(1+\beta)(1-\alpha)}{(1-\beta)(1+\alpha)}\right]^2.$$

$K(k)$ and $E(k)$ are complete elliptic integrals of the first and second kind. Of course we may derive the expression by using γ and δ instead of α and β.

Thus $\phi'(\zeta)$ is obtained as follows:

$$\phi'(\zeta)=\frac{\tau_0}{G}E_h\left\{\frac{1}{(1-\zeta)^2}-\frac{1}{2}\left(\frac{1}{1-\alpha}+\frac{1}{1-\beta}+\frac{1}{1-\gamma}\right.\right.$$
$$\left.\left.+\frac{1}{1-\delta}\right)\frac{1}{1-\zeta}+D_0\right\}\frac{y(\zeta)}{y(1)}, \qquad (22)$$

where D_0 is given by equation (20), or by equation (21) for the symmetric case. Equation (22) is the solution for the semi-infinite elastic body with an arbitrary shape. As mentioned previously, E_h must be given by the coefficient of the term $1/(1-\zeta)$ in the mapping function for each shape.

When the first derivative $\omega'(\zeta)$ of the mapping function is given for the desired shape, stresses can be obtained by the first expression of equation (4). In this case the mapping function need not be a rational one. When the shape is polygonal, $\omega'(\zeta)$ is easily obtained from the Schwarz-Christoffel transformation.

Next $F'(\zeta)$ is obtained as follows: because equation (22) is equal to the first derivative of equation (12), $F'(\zeta)$ can be obtained,

$$F'(\zeta)=B\left[\zeta^2-\frac{1}{2}(\alpha+\beta+\gamma+\delta)\zeta+\frac{1}{2}(\alpha+\beta+\gamma+\delta)-1\right.$$
$$\left.+D_0(1-\alpha)(1-\beta)(1-\gamma)(1-\delta)\right]y(\zeta), \qquad (23)$$

in which $B = \pi\tau_0 E_h y(1)/C_h$, but B is not related to the shape and loading condition because $F(\zeta)$ is not related to the shape and loading condition (see equation (12)).

b) Analysis of Infinite Elastic Body. A stress function is derived for an infinite elastic body with a hole of arbitrary shape as shown in Fig. 2. The body has two fixed parts on the boundary. A rational mapping function which maps the physical region into the outside of the unit circle is expressed as follows (Hasebe and Ueda, 1980; Hasebe et al., 1984):

$$z=\omega(\zeta)=E_c\zeta+\sum_{k=1}^{n}\frac{E_k}{\zeta_k-\zeta}+E_{-1}, \qquad (24)$$

in which ζ_k is a point inside the unit circle. The uniform longitudinal shear load in the direction λ is considered. We assume the desired stress function $\phi(\zeta) = \phi_0(\zeta) + \phi_1(\zeta)$ in the same way as for the semi-infinite body. Then $\phi_0(\zeta) = \tau_0 e^{-i\lambda}\omega(\zeta)/G$, and the boundary conditions are $f(\sigma) = 2iC_c/G$ on L_2 and $f(\sigma) = 0$ on the other parts. C_c represents the resultant force on M_1. Using these expressions and equation (24), $\phi_1(\zeta)$ is obtained from equations (6) and (8). Hence $\phi(\zeta)$ is

$$\phi(\zeta)=\frac{\tau_0}{G}e^{i\lambda}\frac{\bar{E}_c}{\zeta}\frac{\chi(\zeta)}{\chi(0)}+\frac{C_c}{G\pi}F(\zeta)+\text{Const}, \qquad (25)$$

in which $F(\zeta)$ is the second term of equation (12). Equation (25) also does not involve E_k and ζ_k. $\phi'(\zeta)$ is given by

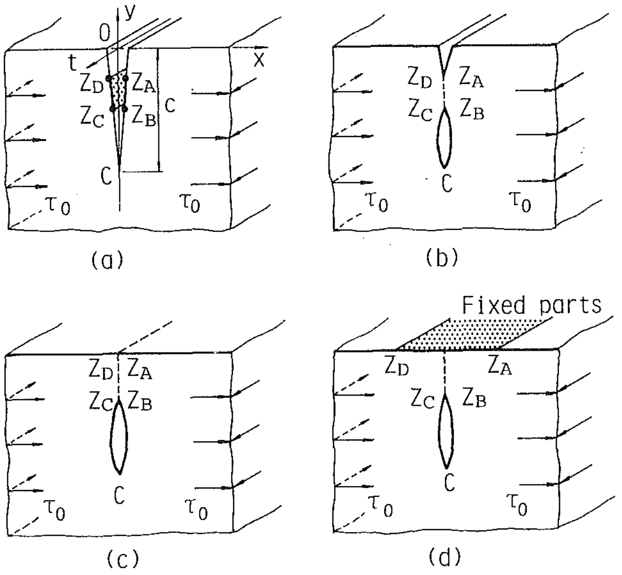

Fig. 3 Examples of analysis for a semi-infinite elastic body

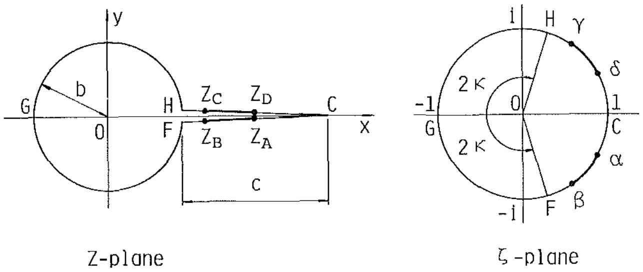

Fig. 4 An infinite elastic body with a crack on a rim of a circular hole and the unit circle

substituting equation (23) into the first derivative of equation (25). In this case, undetermined constant $BC_c/G\pi$ is determined by the stress condition at infinity, $\phi'(\infty)/\omega'(\infty) = e^{-i\lambda}\tau_0/G$. Finally $\phi'(\zeta)$ leads to

$$\phi'(\zeta) = -\frac{\tau_0}{G}e^{i\lambda}\bar{E}_c\left\{\frac{1}{\zeta^2}-\frac{1}{2}\left(\frac{1}{\alpha}+\frac{1}{\beta}+\frac{1}{\gamma}+\frac{1}{\delta}\right)\frac{1}{\zeta}\right\}\frac{y(\zeta)}{y(0)}$$
$$+\frac{\tau_0}{G}e^{-i\lambda}E_c\left\{\zeta^2-\frac{1}{2}(\alpha+\beta+\gamma+\delta)\zeta\right\}y(\zeta)$$
$$+\frac{\tau_0}{G}\{e^{-i\lambda}E_c-e^{i\lambda}\bar{E}_c y(0)\}\left\{\frac{1}{2}(\alpha+\beta+\gamma+\delta)-1+D_0(1-\alpha)(1-\beta)(1-\gamma)(1-\delta)\right\}y(\zeta). \tag{26}$$

The constant D_0 which contains elliptic integrals is given by equation (20), or equation (21) for the symmetric case. Equation (26) is the solution for the infinite elastic body with a hole of arbitrary shape. The stress components can be obtained by using the first expression of equation (4). The first derivative of the mapping function $\omega'(\zeta)$ and E_c of the shape to be analyzed have to be used. An irrational mapping function could also be used.

Examples of Analysis

Examples are shown for the analysis of a semi-infinite elastic body and an infinite one. First example is the semi-infinite elastic body with a crack of depth c as shown in Fig 3. Figure 3(*a*) shows that two parts on the crack sides are fixed.

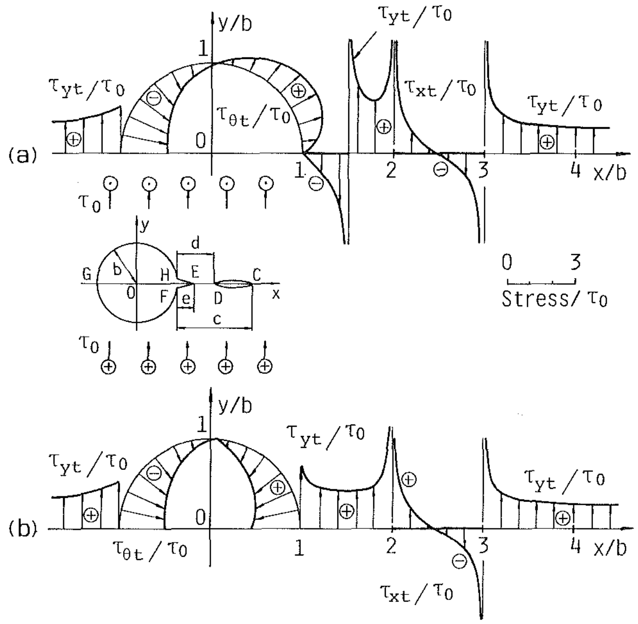

Fig. 5 Examples of a stress distribution of the infinite elastic body with a circular hole and a detouched crack: (*a*) *c/b* = 2, *d/b* = 1, *e/b* = 0.5; (*b*) *c/b* = 2, *d/b* = 1, *e/b* = 0

The stress function $\phi'(\zeta)$ is given by equation (22) and the mapping function is $\omega(\zeta) = -\sqrt{2}ic\sqrt{1+\zeta^2}/(1-\zeta)$ with $E_h = -2ic$. This shape is symmetric to the y axis and the loading is antisymmetric. When the fixed parts are symmetric, i.e., $z_D = z_A$ and $z_C = z_B$, this problem is one of a doubly-connected region as shown in Fig. 3(*b*). According to the position of the fixed parts the problem also becomes one for Figs. 3(*c*) or 3(*d*). In these cases $\delta = \bar{\alpha}$ and $\gamma = \bar{\beta}$ and D_0 of equation (21) are used in equation (22) because of symmetry.

In Fig. 3(*b*) the stress intensity factor $K_{\rm III}$ at the crack tip $z_A\,(=z_D)$ is given by using the singularity of the fixed edge

$$K_{\rm III} = \sqrt{2\pi}\,ie^{-\frac{\pi}{4}i}G\,\frac{[(\zeta-\alpha)^{1/2}\phi'(\zeta)]_{\zeta=\alpha}}{\sqrt{\omega'(\alpha)}}\,. \tag{27}$$

Similarly the stress intensity factor at the point $z_C\,(=z_B)$ is

$$K_{\rm III} = \sqrt{2\pi}\,ie^{\frac{\pi}{4}i}G\,\frac{[(\zeta-\gamma)^{1/2}\phi'(\zeta)]_{\zeta=\gamma}}{\sqrt{\omega'(\gamma)}} \tag{28}$$

and at the point C

$$K_{\rm III} = \sqrt{\pi}\,ie^{\frac{-\pi}{4}i}G\,\frac{\phi'(-1)}{\sqrt{\omega''(-1)}}\,. \tag{29}$$

where $\zeta = -1$ corresponds to the point C on the z plane. Further the problem of Figs. 3(*b*) or 3(*c*) are the same one as symmetric two or three cracks arranged on a straight line in the infinite elastic body. Sih's solution (Sih, 1964) for the infinite elastic body concides with one of this paper.

Next an example is shown for an infinite elastic body with a circular hole having a crack in the radial direction. The mapping function which maps this shape into the outside of the unit circle is given as follows (Bowie, 1956):

$$z=\omega(\zeta)=\frac{1}{2\sin^2\kappa}\left\{\zeta+\frac{1}{\zeta}+1+\cos 2\kappa+\left(1+\frac{1}{\zeta}\right)(\zeta^2+2\zeta\cos 2\kappa+1)^{1/2}\right\}, \tag{30}$$

$$c/b=\frac{2\cos\kappa}{1-\cos\kappa}\,,\quad E_c=\frac{1}{\sin^2\kappa}\,,$$

where c is the crack length and b is the radius of the circular hole. The loading direction is along the y axis, i.e., $\lambda = \pi/2$ in equation (26) (see Fig. 5). When parts of the sides of the crack are fixed at symmetric positions as shown in Fig. 4, i.e., $z_D = z_A$ and $z_C = z_B$, the problem is that of a doubly connected region as shown in Fig. 5. When the fixed part extends to the circular boundary, the problem becomes one of an infinite body which has a detouched crack for the circular rigid inclusion with debonding. And if $\beta = \gamma$, the problem becomes one without debonding, with one fixed part. Also $\delta = \bar{\alpha}$ and $\gamma = \bar{\beta}$ due to the symmetry and D_0 in equation (26) is given by equation (21). Figure 5(*a*) shows the stress distribution for a crack on a rim of a circular hole and a detouched crack. Figure 5(*b*) shows a circular hole and a detouched crack. Stress analysis for an arbitrary loading direction λ can be obtained by superposing the previous solution $\lambda = \pi/2$ on the solution of a semi-infinite body with a semi-circular notch under uniform shear ($\lambda = 0$).

Stress intensity factors are given by the following expressions for each crack tip in Fig. 5:

$$K_{\mathrm{III}} = \sqrt{\pi}\, iG \frac{\phi'(1)}{\sqrt{\omega''(1)}} \quad \text{at } C, \tag{31}$$

where $\zeta = 1$ corresponds to the point C. Using the singularity of the fixed edge

$$K_{\mathrm{III}} = -\sqrt{2\pi}\, G \frac{[(\zeta-\alpha)^{1/2}\phi'(\zeta)]_{\zeta=\alpha}}{\sqrt{\omega'(\alpha)}} \quad \text{at } D, \tag{32}$$

and

$$K_{\mathrm{III}} = \sqrt{2\pi}\, iG \frac{[(\zeta-\gamma)^{1/2}\phi'(\zeta)]_{\zeta=\gamma}}{\sqrt{\omega'(\gamma)}} \quad \text{at } E. \tag{33}$$

When the crack length $e = 0$ (see Fig. 5), i.e., only a detouched crack, the stress intensity factors at C and D have been shown in a figure by Yamada (1972). These values coinside with the values of equations (31) and (32).

Conclusion

The stress functions $\phi'(\zeta)$ are given by equations (22) or (26) under the uniform longitudinal shear load for semi-infinite or infinite elastic bodies with two fixed parts on the boundary. These functions are for arbitrary shapes. E_h and E_c in respective solutions are those of the shape to be analyzed. An irrational mapping function could also be used. Hence if the first derivative of the mapping function $\omega'(\zeta)$ is given for desired shape, stresses can be calculated by equation (4) with equations (22) or (26). Putting $\beta = \gamma$, equations (22) and (26) become the solutions of the problem for one fixed part. The first derivative $F'(\zeta)$ of the second term in equation (12) is given in the form of equation (23) containing undetermined constants.

Examples for the doubly connected region with symmetry were shown and the stress distributions were also shown. Furthermore by using symmetry, solutions of a semi-infinite or an infinite elastic body with a rigid inclusion, cracks, and debonding can also be obtained.

Problems of heat conduction (temperature- heat flow) and potential flow (potential-velocity) are mathematically equivalent to the longitudinal shear problem (displacement-stress) and so these mixed boundary value problems can be analyzed in the same way as in this paper.

References

Benthem, J. P., and Koiter, W. T., 1973, "Methods of Analysis and Solutions of Crack Problems," *Mechanics of Fracture 1*, Sih, G. C., ed., Noordhoff International Publishing, Chapter 3.

Bowie, O. L., 1956, "Analysis of an Infinite Plate Containing Radial Cracks Originating at the Boundary of an Internal Circular Hole," *Journal of Mathematics and Physics*, Vol. 35, pp. 60–71.

Hasebe, N., 1979, "Uniform Tension of a Semi-Infinite Plate with a Crack at an End of a Stiffened Edge," *Ingenieur-Archiv*, Heft 48, pp. 129–141.

Hasebe, N., and Inohara, S., 1980, "Stress Analysis of a Semi-Infinite Plate with an Oblique Edge Crack," *Ingenieur-Archiv*, Heft 49, pp. 51–62.

Hasebe, N., and Ueda, M., 1980, "Crack Originating from a Corner of a Square Hole," *Engineering Fracture Mechanics*, Vol. 13, No. 4, pp. 913–923.

Hasebe, N., Keer, L. M., and Nemat-Nasser, S., 1984, "Stress Analysis of a Kinked Crack Initiating from a Rigid Line Inclusion. Part I: Formulation," *Mechanics of Materials*, Vol. 3, pp. 131–145.

Mikhlin, S. G., 1964, *Integral Equations*, 2nd Ed., Pergamon Press, Oxford, pp. 126–131.

Sih, G. C., 1964, "Boundary Problems for Longitudinal Shear Cracks," *Proceedings of the Second Southeastern Conference on Theoretical and Applied Mechanics*, Pergamon Press, pp. 117–130.

Yamada, T., 1972, "The Effect of a Circular Inclusion on the Stress around a Line Crack in an Infinite Body under Longitudinal Shear," *Transactions of the Japan Society of Mechanical Engineers*, Vol. 38, No. 307, pp. 459–464.

Finite Elastic Deformation Governed by Linear Equations

Joseph B. Keller
Departments of Mathematics and Mechanical Engineering,
Stanford University,
Stanford, Calif. 94305

It is observed that the equations of motion governing finite elastic deformation are linear if and only if the Piola-Kirchhoff stress tensor is linear in the deformation gradient. Then the three components of displacement satisfy uncoupled linear equations. These equations are used to solve some problems of finite deformation.

1 Introduction

Finite elastic deformations, both static and dynamic, are governed by equations which are usually nonlinear. However, there is a particular material for which they are linear. For it the equations governing the three Cartesian components of displacement are uncoupled. The stress in this material is linear in the deformation gradient, so the natural or stress-free length of any element of it is zero. Therefore, it can represent only a real material which has been stretched to several times its stress-free size. Nevertheless for this material one can obtain exact solutions of problems in finite elasticity. They can be used, for example, to test numerical methods and other approximations.

The present considerations extend to two and three dimensions our previous analysis of the finite amplitude motion of strings (Keller, 1959).

In Section 2 we present the equations of motion, constitutive equation and boundary conditions for the particular material. Then in sections 3 and 4 we solve some simple problems for it.

2 Equations of Motion

Let $\mathbf{x}(\mathbf{p},t)$ be the position at time t of the material point $\mathbf{p}$ and let $\rho(\mathbf{p})$ be the density at $\mathbf{p}$ when the body is in its reference configuration $\mathbf{x}=\mathbf{p}$. Then the equation of motion satisfied by $\mathbf{x}$ is

$$\rho(\mathbf{p})\frac{\partial^2\mathbf{x}}{\partial t^2} = \nabla\cdot S + \mathbf{f}(\mathbf{p},t). \tag{2.1}$$

Here $\mathbf{f}$ is the external force per unit volume in the reference configuration and S is the Piola-Kirchhoff stress tensor. In an elastic material S is a function of the deformation gradient $\nabla\mathbf{x}$, of the form (Gurtin, 1981, p. 181, equation (15)).

$$S = (\nabla\mathbf{x})\bar{S}[(\nabla\mathbf{x})^T(\nabla\mathbf{x}),\mathbf{p}]. \tag{2.2}$$

The tensor $\bar{S}$ is symmetric so that $\bar{S}_{ij}=\bar{S}_{ji}$.

Now (2.1) will be linear in $\mathbf{x}$ if and only if S is linear in $\nabla\mathbf{x}$, so $\bar{S}=\bar{S}(\mathbf{p})$ must be independent of $(\nabla\mathbf{x})^T(\nabla\mathbf{x})$:

$$S = (\nabla\mathbf{x})\bar{S}(\mathbf{p}). \tag{2.3}$$

In the reference configuration $\nabla\mathbf{x}=\mathbf{I}$, so (2.3) shows that the residual stress is $\bar{S}(\mathbf{p})$. In component form (2.3) is

$$S_{ij} = (\partial x_i/\partial p_k)\bar{S}_{kj}(\mathbf{p}). \tag{2.3$'$}$$

Then (2.1) becomes

$$\rho(\mathbf{p})\frac{\partial^2\mathbf{x}}{\partial t^2} = \nabla\cdot[(\nabla\mathbf{x})\bar{S}(\mathbf{p})] + \mathbf{f}(\mathbf{p},t), \tag{2.4}$$

or in component form

$$\rho(\mathbf{p})\frac{\partial^2 x_i}{\partial t^2} = \frac{\partial}{\partial p_j}\left[\frac{\partial x_i}{\partial p_k}\bar{S}_{kj}\right] + f_i(\mathbf{p},t). \tag{2.4$'$}$$

We observe that (2.4) is linear and the ith equation involves only x_i, so the three equations of motion are linear and uncoupled. If we had required that the equations be uncoupled, rather than that they be linear, we would have been led to the same results (2.3)–(2.4′) in view of the form of S in (2.2).

For a homogeneous material $\bar{S}$ and ρ are constants so (2.4) and (2.4′) have constant coefficients. If the material is also isotropic $\bar{S}=2\mu I$, or in components $\bar{S}_{kj}=2\mu\delta_{kj}$, where μ is a constant. Then (2.4) becomes

$$\rho\frac{\partial^2\mathbf{x}}{\partial t^2} - 2\mu\Delta\mathbf{x} = \mathbf{f}(\mathbf{p},t). \tag{2.5}$$

This is just the wave equation with propagation speed $c=(2\mu/\rho)^{1/2}$ and forcing term $\mathbf{f}$, which is satisfied by each component of $\mathbf{x}$.

There is a strain-energy density $\sigma(\nabla\mathbf{x},\mathbf{p})$ corresponding to (2.3), so the material is hyperelastic:

$$\sigma(\nabla\mathbf{x},\mathbf{p}) = \frac{1}{2}\bar{S}_{ij}(\mathbf{p})\frac{\partial x_k}{\partial p_i}\frac{\partial x_k}{\partial p_j}. \tag{2.6}$$

For a homogeneous isotropic material this becomes a sum of squares:

$$\sigma(\nabla\mathbf{x}) = \mu\left(\frac{\partial x_k}{\partial p_i}\right)^2. \tag{2.7}$$

The traction $t_i(\mathbf{p},t)$ at a point on the surface of a body with unit normal n_j in the reference configuration, is from (2.3′),

$$t_i(\mathbf{p},t) = \left(\frac{\partial x_i}{\partial p_k}\right)\bar{S}_{kj}(\mathbf{p})n_j. \tag{2.8}$$

When the material is isotropic, (2.8) reduces to

$$t_i(\mathbf{p},,t) = 2\mu\left(\frac{\partial x_i}{\partial p_k}\right)n_k. \tag{2.9}$$

The right side of (2.9) is just 2μ times the normal derivative of

---

Contributed by the Applied Mechanics Division for publication in the JOURNAL OF APPLIED MECHANICS.

Discussion on this paper should be addressed to the Editorial Department, ASME, United Engineering Center, 345 East 47th Street, New York, N.Y. 10017, and will be accepted until two months after final publication of the paper itself in the JOURNAL OF APPLIED MECHANICS. Manuscript received by ASME Applied Mechanics Division, February 25, 1986.

x_i. We see that in (2.8) and (2.9) only one component x_i occurs in each equation. Thus if the t_i are prescribed, (2.8) or (2.9) become boundary conditions on the x_i and these conditions are uncoupled, just like the equations of motion are.

If the position of all or part of the body surface is a given function $x_i^{(0)}$ $(\mathbf{p},t)$ then on that surface x_i must satisfy the boundary condition

$$x_i(\mathbf{p},t) = x_i^{(0)}(\mathbf{p},t). \tag{2.10}$$

Again the conditions (2.10) for the different x_i are uncoupled.

3 Static Solutions for Cylindrical and Spherical Holes

Consider a circular hole cut out of a circular sheet of homogeneous isotropic material, so that an annulus remains. Let the inner and outer radii of the annulus be a and $b > a$, respectively, in the reference state. Suppose that the outer boundary is held fixed, while the inner boundary is stress-free. We shall find the equilibrium configuration of this annulus. The result applies equally well to a three dimensional cylinder with a concentric cylindrical hole. We shal write $R = |\mathbf{p}|$ and $r = |\mathbf{x}|$.

When $f_i = 0$ and $\partial^2 x_i/\partial t^2 = 0$ the equation of motion (2.5) becomes Laplace's equation

$$\Delta x_i = 0,\ a \leq R \leq b,\ i = 1,2. \tag{3.1}$$

The inner boundary condition (2.9) becomes, with $t_i = 0$,

$$\frac{\partial x_i}{\partial R} = 0 \text{ at } R = a,\ i = 1,2. \tag{3.2}$$

The outer boundary condition (2.10) becomes

$$x_1 = b \cos\theta,\ x_2 = b \sin\theta \text{ at } R = b. \tag{3.3}$$

The solution of (3.1)-(3.3) for x_1 and x_2 is readily found to be $(x_1, x_2) = r(R)(\cos\theta, \sin\theta)$ where $r(R)$ is given by

$$r(R) = (1 + a^2/b^2)^{-1}(R + a^2/R) \tag{3.4}$$

By setting $R = a$ in (3.4), we find that the equilibrium radiuis of the hole is $r(a) = 2a(1 + a^2/b^2)^{-1}$. Thus $r(a) > a$ and it increases from a when $b/a = 1$ to $2a$ as b/a tends to infinity.

Let us next consider a sphere of material with a concentric spherical hole in it. The formulation is the same as that above with $i = 1,2,3$ and with (3.3) replaced by

$$\mathbf{x} = b\omega,\ R = b. \tag{3.5}$$

Here $\omega = \mathbf{p}/R$ is a unit vector. The solution of (3.1), (3.2), and (3.5) is $\mathbf{x} = r(R)\omega$ with

$$r(R) = (1 + a^3/2b^3)^{-1}(R + a^3/2R^2). \tag{3.6}$$

The equilibrium radius of the hole is $r(a) = 3a/2$ $(1 + a^3/2b^3)^{-1}$. Again it exceeds a and increases from a when $b/a = 1$ to $3a/2$ as b/a tends to infinity.

For a balloon the boundary condition is $t_i = -pn_i$ at $R = a$ and $t_i = 0$ at $R = b$, where p is the pressure in the balloon. The solutions for cylindrical and spherical balloons are as above with $r(R)$ given by

$$r(R) = \frac{pR}{2\mu}\,\frac{(1 + b^2/R^2)}{(b^2/a^2 - 1)} \sim \frac{paR}{2\mu(b-a)}, \tag{3.7}$$

$$r(R) = \frac{pR}{2\mu}\,\frac{(1 + b^3/2R^3)}{(b^3/a^3 - 1)} \sim \frac{paR}{4\mu(b-a)}. \tag{3.8}$$

The second forms apply when the wall of the balloon is thin compared to its radius, i.e., $b - a << a$. They show that then the spherical balloon has half the radius of the cylindrical balloon for the same internal pressure.

4 Expansion of a Spherical Hole

We shall now consider the dynamic problem of the expansion of a spherical hole in an unbounded homogeneous isotropic medium. At $t = 0$ the medium is at rest and a hole of radius a is created, or the surface of a preexisting hole is released. We wish to find the subsequent motion of the medium, and especially the radius of the hole as a function of time. As t increases, the radius should tend to the static value $3a/2$ given in Section 3. With $f_i = 0$, (2.5) becomes the homogeneous wave equation

$$\Delta x_i - \frac{1}{c^2}\,\frac{\partial^2 x_i}{\partial t^2} = 0. \tag{4.1}$$

Initially we have

$$x_i(\mathbf{p},0) = x_i,\ \frac{\partial x_i(\mathbf{p},0)}{\partial t} = 0,\ R \geq a. \tag{4.2}$$

At the surface of the hole $t_i = 0$ and (2.9) becomes

$$\frac{\partial x_i}{\partial R} = 0,\ R = a. \tag{4.3}$$

To solve this problem we choose the polar axis along p_i and set $p_i = R\cos\theta$ and $x_i = f(R,t)\cos\theta$. Then from (4.1) it follows that r is of the form

$$r(R,t) = R + \frac{\partial}{\partial R}\left[\frac{f(R-ct)}{R}\right]. \tag{4.4}$$

Here f is arbitrary and we have omitted the incoming solution, since the initial conditions (4.2) require it to vanish. We see that (4.2) will be satisfied if

$$f(R-ct) = 0 \text{ for } R - ct \geq a. \tag{4.5}$$

Upon using (4.4) in (4.3) we get

$$\frac{1}{a}f''(a-ct) - \frac{2}{a^2}f'(a-ct) + \frac{2}{a^3}f(a-ct) = -1. \tag{4.6}$$

The solution of (4.6) must satisfy (4.5) and also make $r(R,t)$ continuous, which requires that $f'(a) = 0$. The unique solution satisfying these conditions is

$$f(z) = \frac{a^3}{2}\left[\frac{e^{(z-a)/a}}{\cos\pi/4}\cos\left(\frac{z-a}{a} + \frac{\pi}{4}\right) - 1\right], z \leq a, \tag{4.7}$$

and $f(z) = 0$ for $z \geq a$.

Now (4.4) yields

$$r(R,t) = R + \frac{a^3}{2R^2} + \frac{a^3}{2^{1/2}}\,\frac{\partial}{\partial R}\left[\frac{e^{(R-ct-a)/a}}{R}\right.$$
$$\left.\cos\left(\frac{R-ct-a}{a} + \frac{\pi}{4}\right)\right],\quad R - ct - a \leq 0 \tag{4.8}$$
$$r(R,t) = R,\quad R - ct - a \geq 0.$$

Then $x(\mathbf{p},t) = r(R,t)\omega$. We see from (4.8) that as t increases, $r(R,t)$ tends to $R + a^3/2R^2$. This is the solution of the static problem, given by (3.6) with $b/a = \infty$. The radial coordinate r of each particle, including the surface of the hole, tends to its limit via a damped oscillation.

Acknowledgment

Research was supported by the Office of Naval Research, the Air Force Office of Scientific Research, the Army Research Office, and the National Science Foundation.

References

Gurtin, M. E., 1981, *An Introduction to Continuum Mechanics*, Academic Press, New York.

Keller, J. B., 1959, "Large Amplitude Motion of a String," *American Journal of Physics*, Vol. 27, pp. 584-586.

P. M. Naghdi
Honorary Mem. ASME

D. J. Nikkel, Jr.
Assoc. Mem. ASME

Department of Mechanical Engineering,
University of California,
Berkeley, CA 94720

Two-Dimensional Strain Cycling in Plasticity

Detailed calculations are presented for strain cycling in a homogeneous deformation that can be sustained by a biaxial state of stress in thin-walled specimens of OFHC copper. These calculations are made with a set of relatively simple constitutive equations within the framework of the strain-space formulation of plasticity. The predicted theoretical calculations, carried out in the context of small deformation, are in good agreement with corresponding available experimental results for saturation hardening and erasure of memory in two-dimensional strain cycling. Also, with the use of the calculated results, a scalar quantity that characterizes strain-hardening is plotted as a function of plastic strains. Such plots are likely to be useful for computational purposes.

1 Introduction

In an interesting series of experiments pertaining to two-dimensional strain cycling in plasticity that can be sustained by a biaxial state of stress resulting from combined tension-compression and torsion in thin-walled specimens of OFHC copper,[1] Lamba and Sidebottom (1978a,b) observed the following three phenomena:

(a) The occurrence of saturation hardening after loading from an undeformed state and cycling along a strain path which is essentially an ellipse in the normal strain-shear strain plane;
(b) the erasure of memory after the material has reached a state of saturation; and
(c) the nature of the post-saturation stress response for cycling in a relatively "complex" nonproportional strain path.

With reference to the above two-dimensional strain cycling experiments, our main objective is to examine the predictive capability of a (rate-independent) theory of plasticity formulated in a strain space setting with the use of special constitutive equations employed previously by Naghdi and Nikkel (1984). Also, by employing the strain-hardening characterization which arises in the strain-space formulation of plasticity (Casey and Naghdi, 1981, 1983, 1984a) and which is represented by a scalar function Φ, we calculate (over the domain of interest) the values of Φ for the material used in the experiments of Lamba and Sidebottom (1978a,b) and plot this as a function of plastic strains. As in the experiments of Lamba and Sidebottom (1978a,b), our calculations are carried out in the context of small deformation.

In a previous paper (Naghdi and Nikkel, 1984) comparisons were made between the predictions of uniaxial stress and strain cycling in plasticity and corresponding available experiments. The previous calculations (Naghdi and Nikkel, 1984) were carried out in a strain space setting by means of special constitutive equations obtained on the basis of a theory first formulated relative to stress space by Green and Naghdi (1965, 1966) and subsequently reformulated relative to strain space by Naghdi and Trapp (1975a), along with some additional developments pertaining to loading criteria and hardening characterization by Casey and Naghdi (1984a,b).

Description of the Strain Cycling Problem. As in the experiments of Lamba and Sidebottom (1978a,b), we consider the combined tension-compression and torsion of a thin-walled circular cylinder whose axis is in the x_1 direction. As usual, we neglect the variation of stress and strain in the radial coordinate direction so that the stress and strain components referred to cylindrical polar coordinates are then independent of position. We denote the axial stress and axial strain, respectively, by s_{11} and e_{11}; and similarly denote the shear stress and shear strain, respectively, by s_{12} and e_{12}.

The analysis in Section 3 and the procedure for calculations in Section 4 require a reduction of the general loading criteria since not all components of strain (and strain rate) are known *a priori* in the context of the particular experiment considered. This reduction is discussed in Appendix A and the results are employed in all calculations of Section 4. Our calculations do not include those appropriate for two-dimensional stress cycling, even though it is relatively easier to calculate such cycles for materials exhibiting hardening behavior.[2]

In the remainder of this section, we discuss in some detail the main features of the calculated results. A summary of the calculations can be arranged in three groups corresponding to

---

[1] The abbreviation OFHC stands for "oxygen-free high conductivity."

Contributed by the Applied Mechanics Division for publication in the JOURNAL OF APPLIED MECHANICS.

Discussion on this paper should be addressed to the Editorial Department, ASME, United Engineering Center, 345 East 47th Street, New York, N.Y. 10017, and will be accepted until two months after final publication of the paper itself in the JOURNAL OF APPLIED MECHANICS. Manuscript received by ASME Applied Mechanics Division, November 4, 1985.

[2] This is because for materials exhibiting hardening behavior the loading criteria in stress space may be used (Casey and Naghdi, 1984b), and for two-dimensional stress cycling all of the components of stress are prescribed in contrast to two-dimensional strain cycling where some of the components of strain are not known *a priori*.

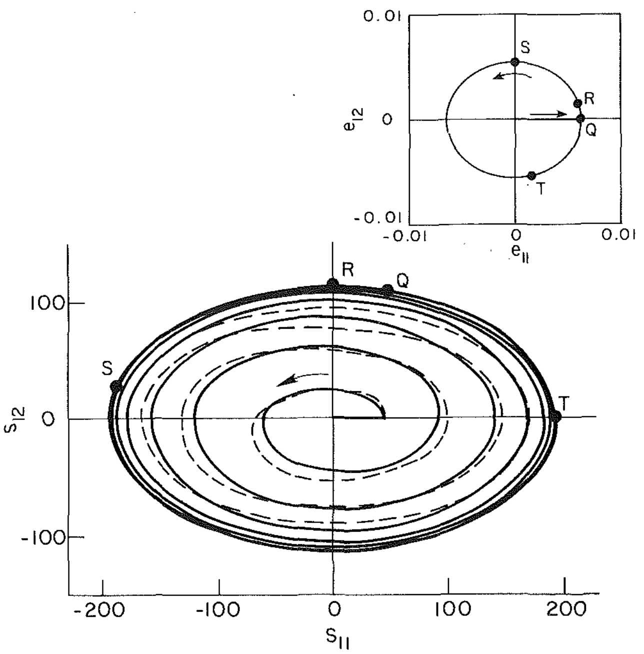

Fig. 1(*a*) Comparison of the stress trajectory in $s_{12}-s_{12}$ plane (measured in MPa) between the theoretical prediction (———) and the experimental data (---) from Lamba and Sidebottom (1978a) for OFHC copper; the numerical calculation of the theoretical trajectory was effected with the use of equations (3.4), (3.15), (3.16), and the constants (4.1). The prescribed strain path in the $e_{11}-e_{12}$ plane is shown in the inset. After initial elongation from the undeformed state to point Q, the nearly elliptical path QRSTQ is repeatedly traversed. Whie the path in the $e_{11}=e_{12}$ plane is cyclic, the remaining nonzero components of strain do not necessarily return to the same values at the end of each cycle. Comparison with the experimental data is shown for the first few cycles only since the portion of the trajectory for additional cycles would crowd the figure.

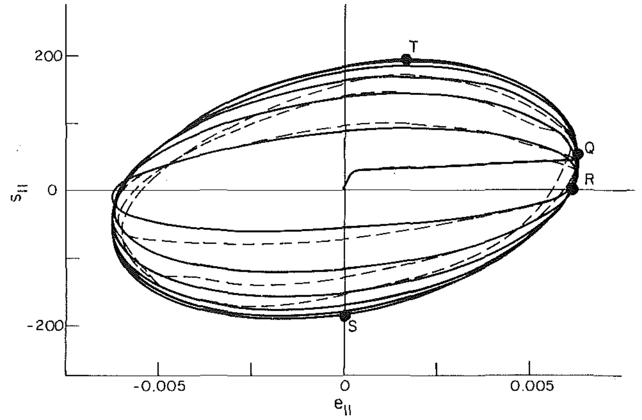

Fig. 1(*b*) Comparison of the theoretical (———) axial stress response, measured in MPa, with the corresponding experimental data (---) of Lamba and Sidebottom (1978a) for OFHC copper according to the prescribed strain path in the inset of Fig. 1(*a*). Comparison with the experimental data is shown for the first few cycles only, since the portion of the curve for additional cycles would crowd the figure.

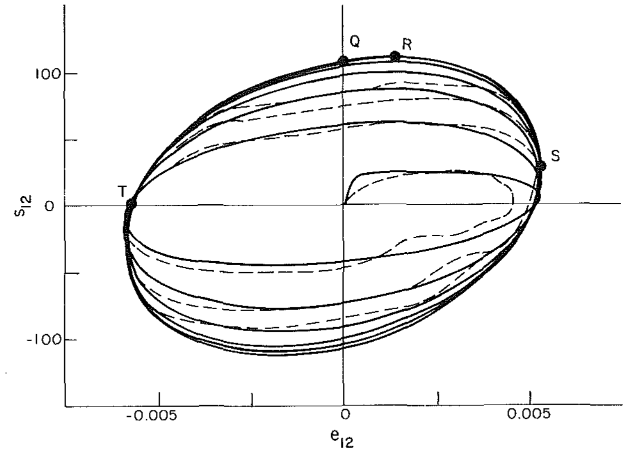

Fig. 1(*c*) Comparison of the theoretical (———) shear stress response, measured in MPa, with the corresponding experimental data (---) of Lamba and Sidebottom (1978a) for OFHC copper according to the prescribed strain path in the inset of Fig. 1(*a*). Comparison with the experimental data is shown for the first few cycles only, since the portion of the curve for additional cycles would crowd the figure.

the nonproportional strain cycling experiments of Lamba and Sidebottom (1978a,b) as listed in the opening paragraph of this section. The first experiment pertains to saturation hardening after loading from an undeformed state, and the second two concern the behavior after the material has reached a state of saturation. In each case, the strain path in the $e_{11}-e_{12}$ plane is the *input* to the problem, and the stress response (s_{11} and s_{12}) is calculated from the relevant constitutive equations. A graphical presentation of the calculated stress trajectory in the $s_{11}-s_{12}$ plane alone does not give all the relevant information, unless a knowledge of the correspondence between all points of the stress trajectory and all points of the input strain path in the $e_{11}-e_{12}$ plane is also known. It is, therefore, necessary to also plot the calculated results in either the $s_{11}-e_{11}$ or the $s_{12}-e_{12}$ plane. For clarity's sake, we have presented the calculated results in both the $s_{11}-e_{11}$ and $s_{12}-e_{12}$ planes.

Saturation Hardening. For two-dimensional saturation hardening, we prescribe e_{11} and e_{12} parametrically as functions of time such that in the $e_{11}-e_{12}$ plane the strain path is as depicted in the inset of Fig. 1(*a*). This corresponds to uniaxial tensile loading from the undeformed state until the axial strain reaches the value 0.00635 (point Q in Fig. 1(*a*)) followed by combined tension-compression and torsion controlled in such a way that e_{11} and e_{12} cycle in a counterclockwise direction around the nearly elliptical path in the inset of Fig. 1(*a*).[3] The strain components e_{11} and e_{12} were parametrically specified to be sinusoidal differing by a 90 deg phase shift. The calculated results for stresses are shown in Figs. 1(*a*-*c*) along with the experimental curves for the first few cycles only, since the portion of the trajectory for additional cycles would crowd the figure. Figure 1(*a*) represents the stress trajectory and Figs. 1(*b*,*c*) are alternative representations of the calculations in the $s_{11}-e_{11}$ and $s_{12}-e_{12}$ planes. Points corresponding to Q,R,S,T on the prescribed strain path in the inset of Fig. 1(*a*) have been labeled in Figs. 1(*a*-*c*) only for the portion of the path which represents a cycle at saturation and not for prior cycles. These results are in good qualitative agreement with the experimental results of Lamba and Sidebottom (1978a). In agreement with the experimental results, the theory predicts that saturation occurs after about four cycles. The main differences between the theoretical predictions and the experimental results are that the predicted maximum shear stress at saturation (point R in Figs. 1(*a*,*c*)) is slightly greater than the corresponding experimental value while the predicted maximum axial stress at saturation (point T in Figs. 1(*a*,*b*)) is slightly less than the corresponding experimental value. The reasons for these differences are discussed in Section 5. One further point may be

---

[3] The actual experimental strain path in Fig. 3(*a*) of Lamba and Sidebottom (1978a) is not perfectly elliptical. In the present calculations the portion of the path in the upper half of the $e_{11}-e_{12}$ plane is specified to be the upper half of an ellipse with vertices on the e_{11} axis at -0.00623 and 0.00635 and a semiaxis of 0.00531 in the e_{12} direction. The portion of the path in the lower half of the $e_{11}-e_{12}$ plane is specified to be the lower half of an ellipse with the same vertices on the e_{11} axis, but with a semiaxis of 0.00588 in the e_{12} direction.

mentioned with respect to Figs. 1(*b*,*c*). When some of the constitutive response functions are linear in the variables (such as generalized Hooke's law for the linear elastic range), in a plot associated with uniaxial loading the response exhibits a sharp corner. This is exemplified by the beginning portion of Fig. 1(*b*) which corresponds to the strain path from the origin to point *Q* in the inset of Fig. 1(*a*). On the other hand, corresponding to the portion of the strain path *QRS* in the first cycle (along which plastic deformation also occurs), because of the presence of two components of stress the response is no longer uniaxial and the beginning portion of the plot of the response in the $s_{12} - e_{12}$ plane in Fig. 1(*c*) exhibits a smooth transition between a rising portion and a portion which is fairly level.

Erasure of Memory. Consider next the erasure of memory property observed by Lamba and Sidebottom (1978a) in the case of OFHC copper. The phenomenon occurs when the material has reached a state of saturation after strain cycling along an elliptical path in the $e_{11} - e_{12}$ plane. If subsequent linear strain paths lie within the elliptical strain path (which was originally used to reach the state of saturation), then corresponding to a given linear path in the $e_{11} - e_{12}$ plane there is a particular limiting stress cycle response in the $s_{11} - s_{12}$ plane. This process is repeated as the material is cycled again along the strain path. Lamba and Sidebottom (1978a) observed that a larger cycle (not necessarily along a linear path) in the $e_{11} - e_{12}$ plane essentially erases the effect of any previously traversed smaller cycles and returns the material to a state in which the limiting stress cycle response corresponds to that of the larger cycle. With the use of the linear strain paths *BDB* and *BFB* (as the larger and smaller cycles) indicated in the inset of Fig. 2(*a*), a calculation leading to a state of saturation was arrived at by first cycling in shear along *B′D′B′* for four cycles followed by cyling along *B′CD′EB′* for an additional four cycles. Then, the effect of erasure of memory was calculated by further cycling which alternates along *BDB* and *BFB*. The results of calculations are shown in Figs. 2(*a*–*c*) along with the experimental curves from Lamba and Sidebottom (1978a, Figs. 5(*b*,*c*)), where for clarity only the portion of the response corresponding to cycling which alternates along *BDB* and *BFB* are indicated.[4] The erasure of memory phenomenon is best seen in Fig. 2(*c*), where along the segment of path *BD* the effect of the path *BFB* has become undetectable by the time the trajectory has reached point *D*. Thus, the larger cycle *BDB* erases the material's memory of the previously traversed smaller cycle *BFB*. In addition, the overall response is in qualitative agreement with the experimental results of Lamba and Sidebottom (1978a), while the predicted shear stress is again higher than the corresponding experimental results (Fig. 2(*c*)) and the predicted compressive axial stress has a larger absolute value than the corresponding experimental results (Fig. 2(*b*)). Also, the

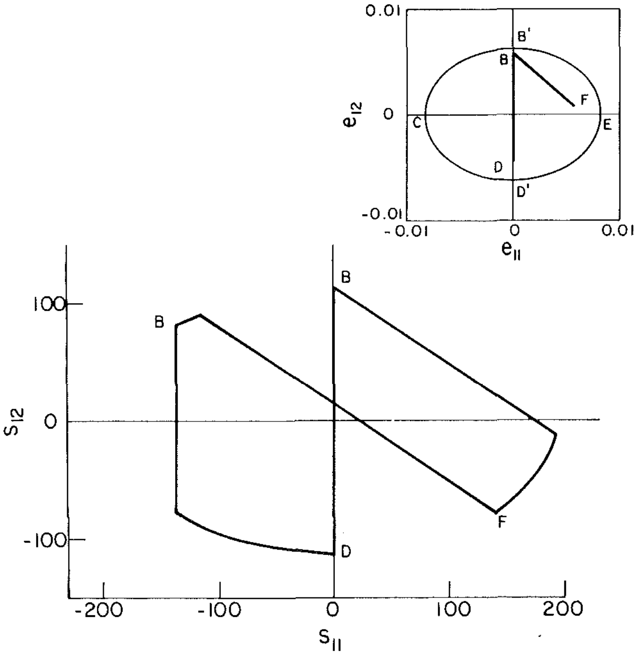

Fig. 2(*a*) The theoretical stress trajectory in $s_{11} - s_{12}$ plane (measured in MPa) calculated from equations (3.4), (3.15), and (3.16) for OFHC copper using the constants (4.1). The prescribed strain path in the $e_{11} - e_{12}$ plane is shown in the inset. Calculation for a state of saturation was obtained by first cycling in shear along *B′D′B′* in the e_{11}-e_{12} plane for four cycles followed by cycling along the elliptical path *B′CD′EB′* for four cycles. After this saturation was attained, the smaller path *BDBFB* was repeatedly traversed. Only the portion of the stress trajectory which corresponds to the (post saturation) strain path *BDBFB* is shown.

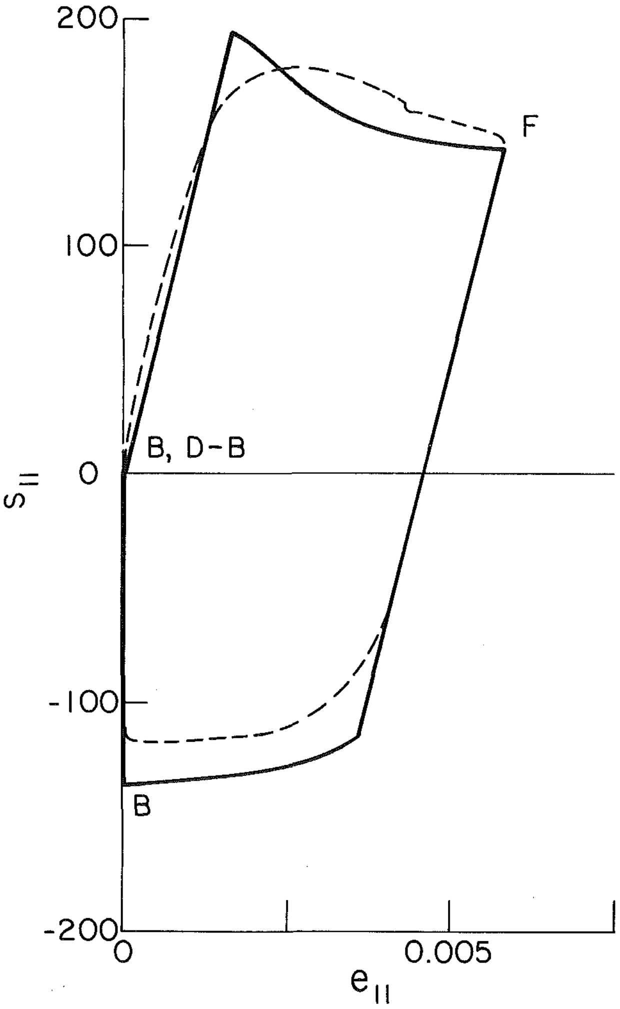

Fig. 2(*b*) Comparison of the theoretical (———) axial stress response, measured in MPa, with the corresponding experimental data (- - -) of Lamba and Sidebottom (1978a) for OFHC copper according to the prescribed strain path in the inset of Fig. 2(*a*). Only the portion of the stress response which corresponds to the (post saturation) strain path *BDBFB* is shown.

---

[4] In Lamba and Sidebottom (1978a), at the point we've labeled *D*, the value of the shear strain shown in Fig. 5(*a*) (the strain path in the axial strain-shear strain plane) is somewhat different from its value shown in Fig. 5(*b*) (the experimental results shown in the shear stress-shear strain plane). In prescribing the strain path for our calculations, in order to compare with the experimental results we specified the value of the shear strain at point *D* to be that indicated in Fig. 5(*b*) of Lamba and Sidbottom (1978a).

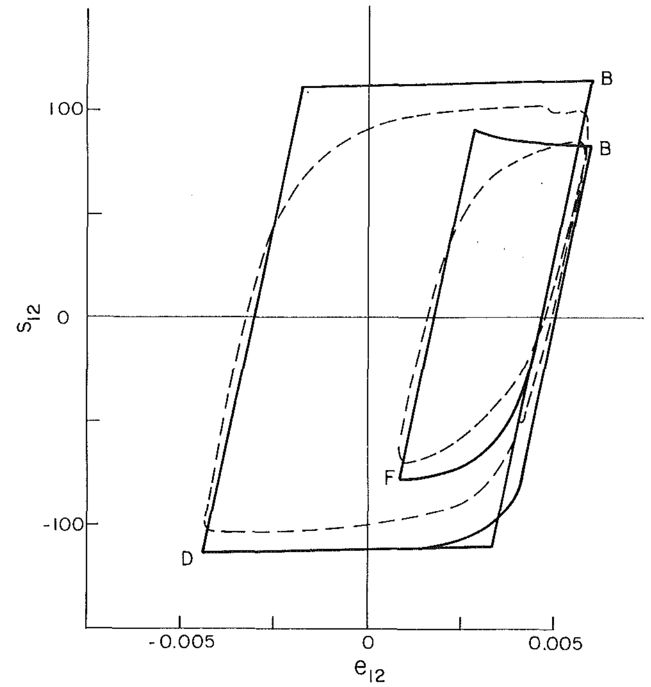

Fig. 2(c) Comparison of the theoretical (———) shear stress response, measured in MPa, with the corresponding experimental data (---) of Lamba and Sidebottom (1978a) for OFHC copper according to the prescribed strain path in the inset of Fig. 2(*a*). Only the portion of the stress response which corresponds to the (post saturation) strain path *BDBFB* is shown.

slope of the calculated $s_{12}-e_{12}$ curve in Fig. 2(*c*) during loading along *FB* is different than on the corresponding experimental curve. Again, these differences are discussed in some detail in Section 5.

Complex Nonproportional Strain-Path. Now, with reference to the third experiment of Lamba and Sidebottom (1978b), consider the predicted response for a "complex" nonporportional strain path (using the terminology of Lamba and Sidebottom) applied after the material has reached a state of saturation. The state of saturation is attained in the same way as discussed earlier in the preceding paragraph, namely by cycling first in shear followed by cycling along an elliptical path in the $e_{11}-e_{12}$ plane. After this, a path was prescribed which returned e_{11} and e_{12} to the origin of the $e_{11}-e_{12}$ plane (point 0 in Fig. 3(*a*)) while at the same time the plastic strains were returned to the value zero.[5] Next let e_{11} and e_{12} be prescribed parametrically as functions of time such that in the $e_{11}-e_{12}$ plane the strain path is represented by the linear segments 0–1, 1–2, 2–3, . . . ,7–8 in the inset of Fig. 3(*a*). The calculated results for stresses are shown in Fig. 3(*a–c*) which qualitatively agree well with the experimental results of Lamba and Sidebottom (1978b), Figs. 2(*a–d*)). Moreover, the theory again predicts the erasure of memory effect since as the path 0–1, . . . ,7–8 in the inset of Fig. 3(*a*) is traversed a second time, the stress path becomes indistinguishable from the first time the path was traversed. Thus, the larger path 6–7–8 erases the effect of the previously traversed smaller portion of the path 1–6.

Strain Hardening Behavior—The Function Φ. In view of the fundamental role played by a scalar function Φ that characterizes strain-hardening behavior of the material (Casey and Naghdi, 1984a), we represent Φ as a surface which exhibits the nature of strain-hardening at any elastic-plastic state with fixed values of the total strain components[6] e_{11} and e_{12}. The surface in Fig. 4 is a plot of Φ (defined in equation (2.10)) as a function of the plastic strains e^p_{11} and e^p_{12} for fixed values of the total strains e_{11} and e_{12} prescribed in the course of calculations; in the plot of Fig. 4 the prescribed total strains are specified to be $e_{11}=e_{12}=0$. For different values of e_{11} and e_{12}, the surface represented by Φ merely translates parallel to the plane of $e^p_{11}-e^p_{12}$. A choice of the total strains, say $(\bar{e}_{11},\bar{e}_{12})$, specifies a particular surface and elastic-plastic states reached by different strain paths ending at $(\bar{e}_{11},\bar{e}_{12})$ will in general correspond to different points on the surface Φ. The outer boundary of this surface (which has the smallest value of Φ) corresponds to the state of saturation, while the inner boundary corresponds to the largest value that Φ can take in the domain of interest. A further discussion of how the surface was calculated is found at the end of Section 4. As is evident from the plot in Fig. 4, Φ is always positive; and hence, in view of the conditions for strain-hardening characterization (see for example the conditions (8) in Naghdi and Nikkel, 1984), the material always exhibits hardening behavior.[7] It also shows how Φ decreases with additional plastic deformation, taking its largest value at initial yield and its smallest value at saturation. The value of Φ is constant at both initial yield and saturation.

2 General Background and Special Constitutive Equations

With reference to a strain-space formulation of plasticity and for the special constitutive equations used previously (Naghdi and Nikkel 1984), we include here a brief summary of the relevant equations of the purely mechanical theory contained in the papers of Green and Naghdi (1965, 1966), Naghdi and Trapp (1975a), and Casey and Naghdi (1981, 1983).[8]

In the context of infinitesimal deformation, we recall that the main ingredients of the rate-type theory of plasticity, in addition to the total strain e_{KL}, are plastic strain e^p_{KL} and a measure of work-hardening κ. Also, no distinction needs to be made between various measures of stress which we denote by s_{KL}. As usual, it is convenient to express the various constitutive response functions in terms of the components of deviatoric stress τ_{KL} and deviatoric strain γ_{KL}, namely

$$\begin{aligned} \tau_{KL} &= s_{KL}-\bar{s}\,\delta_{KL}, \quad \tau_{KK}=0, \\ \gamma_{KL} &= e_{KL}-\bar{e}\,\delta_{KL}, \quad \gamma_{KK}=0, \end{aligned} \tag{2.1}$$

with a similar definition for the deviatoric plastic strain γ^p_{KL}, where $\bar{s}$, $\bar{e}$, and $\bar{e}^p$ denote the mean normal stress, mean normal strain, and mean normal plastic strain, respectively. For materials which are isotropic in reference configuration and in the presence of plastic incompressibility ($\bar{e}^p=0$), we specify the stress response by generalized Hooke's law and the loading

---

[5] This calculation was performed by prescribing a path unloading from the elliptical path at a point such as B' in the insert of Fig. 2(*a*) on which $e_{11}=0$ and allowing reverse loading to take place until such a point where $e^p_{12}=0$. At this point e^p_{11} has also become essentially zero which is again indicative of erasure of memory. Reversing the direction along this path until point 0 in Fig. 3(*a*) is reached results in only elastic behavior.

[6] A topographical representation of this kind was used recently in a different context by Casey and Lin (1983).

[7] It should be emphasized that even though one component of the stress may be decreasing during loading while the corresponding strain component is increasing (e.g., as in Fig. 2(*b*)) the material is not exhibiting softening behavior in two-dimensional cycling.

[8] A more expanded summary is contained in Sections 2 and 3 of Naghdi and Nikkel (1984).

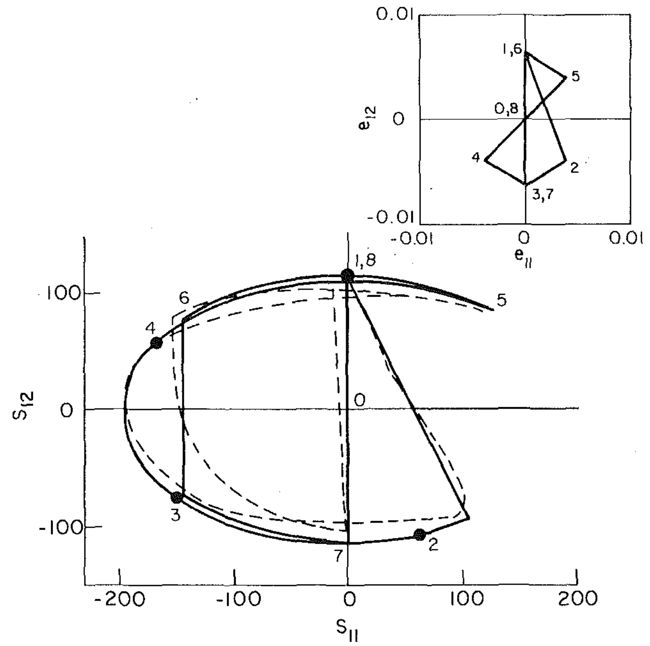

Fig. 3(a) *Comparison of the stress trajectory in $s_{11}-s_{12}$ plane* **(measured in MPa) between the theoretical prediction (———) an the experimental data (---) from Lamba and Sidebottom (1978b) for OFHC copper; the numerical calculation of the theoretical trajectory was effected with the use of equations (3.4), (3.15), (3.16), and the constants (4.1). The prescribed strain path in the $e_{11}-e_{12}$ plane is shown in the inset. Calculation for a state of saturation was obtained in a similar manner to that in Fig. 2(*a*). After the saturation was attained, the complex path 0-1, 1-2, . . . ,7-8 was repeatedly traversed. Only the portion of the stress trajectory which corresponds to the (post saturation) strain path 0-8 is shown.**

functions g and f in strain space and stress space, respectively, by[9]

$$g = 4\mu^2\left[\gamma_{KL} - \left(1+\frac{\hat{\alpha}(\kappa)}{4\mu}\right)\gamma^p_{KL}\right]\left[\gamma_{KL} - \left(1+\frac{\hat{\alpha}(\kappa)}{4\mu}\right)\gamma^p_{KL}\right] - \kappa$$

$$= \left(\tau_{KL} - \frac{1}{2}\,\hat{\alpha}(\kappa)\gamma^p_{KL}\right)\left(\tau_{KL} - \frac{1}{2}\,\hat{\alpha}(\kappa)\gamma^p_{KL}\right) - \kappa = f \qquad (2.2)$$

with

$$\hat{\alpha} = \hat{\alpha}(\kappa) = \frac{(\alpha_o - \alpha_s)\kappa + \alpha_s\kappa_o - \alpha_o\kappa_s}{\kappa_o - \kappa_s}. \qquad (2.3)$$

In equations (2.2) and (2.3) the coefficients α_o, α_s, κ_o, κ_s are constants and μ is the elastic shear modulus. The constants α_o and α_s are so chosen that $\hat{\alpha}(\kappa)$ takes the value α_o when $\kappa = \kappa_o$ and takes the value α_s when $\kappa = \kappa_s$.

We adopt the loading criteria of strain space as primary. Then, after invoking the work assumption of Naghdi and Trapp (1975b), the constitutive equations for the rate of plastic strain $\dot{e}^p_{KL}$ and the rate of work-hardening parameter $\dot{\kappa}$ may be expressed as (see the development among equations (36)-(42) in Casey and Naghdi 1981):

$$\dot{e}^p_{KL} = \dot{\gamma}^p_{KL} = \begin{cases} 0, \text{ when } g<0, \text{ or when } g=0 \text{ and } \hat{g}\le 0, \\[2ex] \dfrac{\hat{g}}{\Gamma+\Lambda}(2\tau_{KL} - \hat{\alpha}\gamma^p_{KL}), \text{ when } g=0 \text{ and } \hat{g}>0 \end{cases} \qquad (2.4a,b)$$

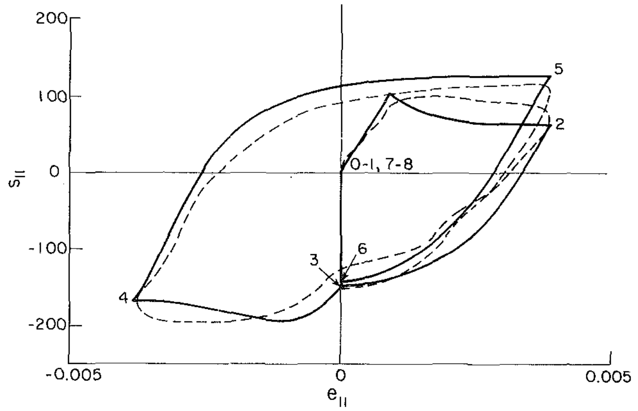

Fig. 3(*b*) Comparison of the theoretical (———) axial stress response, measured in MPa, with the corresponding experimental data (---) of Lamba and Sidebottom (1978b) for OFHC copper according to the prescribed strain path in the inset of Fig. 3(*a*). Only the portion of the stress response which corresponds to the (post saturation) strain path 0-8 is shown.

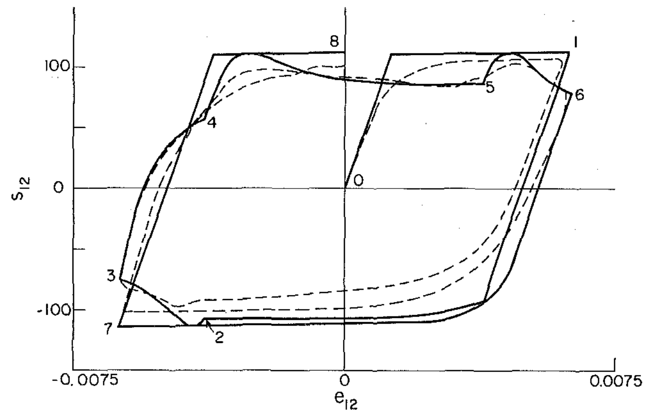

Fig. 3(c) Comparison of the theoretical (———) shear stress response, measured in MPa, with the corresponding experimental data (---) of Lamba and Sidebottom (1978b) for OFHC copper according to the prescribed strain path in the inset of Fig. 3(*a*). Only the portion of the stress response which corresponds to the (post saturation) strain path 0-8 is shown.

and

$$\dot{\kappa} = (\hat{\beta}(\kappa)\tau_{KL} + \hat{\eta}(\kappa)\gamma^p_{KL})\dot{e}^p_{KL}. \qquad (2.5)$$

In equations (2.4) and (2.5), the quantities $\hat{\beta}$,$\hat{\eta}$ are defined by

$$\hat{\beta} = \hat{\beta}(\kappa) = \left(\frac{\kappa-\kappa_s}{\kappa_o-\kappa_s}\right)\beta,\ \hat{\eta} = \hat{\eta}(\kappa) = \left(\frac{\kappa-\kappa_s}{\kappa_o-\kappa_s}\right)\eta, \qquad (2.6)$$

β,η are constants,

$$\hat{g} = \frac{\partial g}{\partial e_{KL}}\,\dot{e}_{KL} = 4\mu\left(\tau_{KL} - \frac{1}{2}\,\hat{\alpha}\gamma^p_{KL}\right)\dot{\gamma}_{KL}, \qquad (2.7)$$

and on the yield surface $g = 0$,

$$\Lambda = 8\mu\kappa > 0, \qquad (2.8)$$

$$\Gamma = 2\hat{\alpha}\kappa + 2\left[1 + \left(\frac{\alpha_o-\alpha_s}{\kappa_o-\kappa_s}\right)\left(\tau_{KL} - \frac{\hat{\alpha}}{2}\,\gamma^p_{KL}\right)\gamma^p_{KL}\right](\hat{\beta}\tau_{MN} + \hat{\eta}\gamma^p_{MN})\left(\tau_{MN} - \frac{\hat{\alpha}}{2}\,\gamma^p_{MN}\right). \qquad (2.9)$$

The yield function f in (2.2) is of the von Mises type: it is quadratic in the deviatoric stresses and allows for translation and change in size of the yield surface. The amount of transla-

---

[9] The loading functions in (2.2) with $\hat{\alpha}$ being regarded as constant (rather than a function of κ) were used in the paper of Caulk and Naghdi (1978) and, with $\hat{\alpha}$ as a function of κ, are the same as those used by Naghdi and Nikkel (1984).

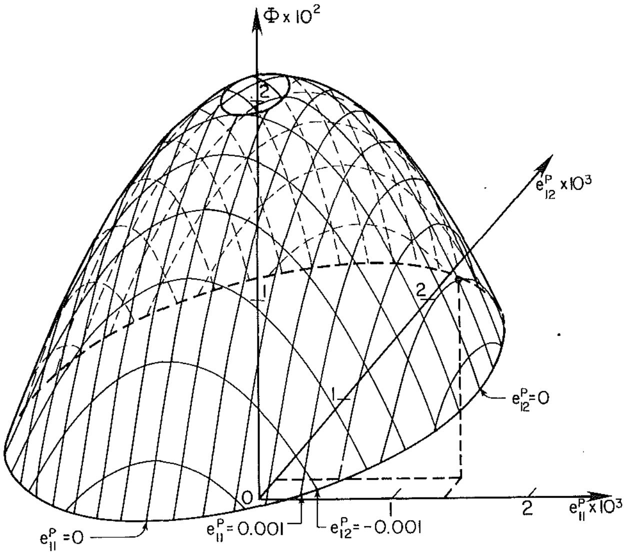

Fig. 4 A geometrical representation of the function Φ (which characterizes strain-hardening) as a surface exhibiting its dependence on the plastic strain components e^p_{11} and e^p_{12}, plotted for fixed values of the total strains (in this figure taken to be $e_{11} = e_{12} = 0$) for OFHC copper having the material constants specified in equation (4.1). For different values of e_{11} and e_{12}, the surface merely translates parallel to the plane of (e^p_{11}, e^p_{12}) but does not change its shape. An example of how the value of Φ may be determined from this plot is also indicated: At a typical point on the surface, the values of the plastic strains e^p_{11}, e^p_{12} are known (the coordinate curves on the surface are drawn at plastic strain intervals of 0.0002) and the corresponding point in the $e^p_{11} - e^p_{12}$ plane is located. Then, the value of Φ is measured by comparing the vertical distance between the point on the plane and the point on the surface with the scale on the Φ axis.

tion of the yield surface is linear in the deviatoric plastic strain and is also linear in κ through the coefficient $\hat{\alpha}$ defined by (2.3). Also, the coefficient functions $\hat{\beta}(\kappa)$ and $\hat{\eta}(\kappa)$ which occur in (2.5) are linear in κ, they assume the respective values β and η at initial yield when $\kappa = \kappa_o$, and both vanish at saturation, i.e., when $\kappa = \kappa_s$, $\dot{\kappa} = 0$.

We also recall here that the strain-hardening behavior may be characterized by means of a rate-independent scalar quantity denoted here by Φ (Casey and Naghdi, 1981, 1983).[10] During loading the quantity Φ has the same value as $\hat{f}/\hat{g}$, where $\hat{f} \equiv (\partial f/\partial s_{KL})\dot{s}_{KL}$ and $\hat{g}$ is defined by $(2.7)_1$. With the particular constitutive equations (i.e., generalized Hooke's law) used here and the work assumption of Naghdi and Trapp (1975b), Φ can be expressed as

$$\Phi = \frac{\Gamma}{\Gamma + \Lambda}, \tag{2.10}$$

and in fact since $\Gamma + \Lambda > 0$, Γ alone may be used to characterize the strain-hardening behavior (Casey and Naghdi 1984b, equations (4.50) and (4.51)).

3 Equations for a Two-Dimensional State of Stress

Consider now the homogeneous deformation of an elastic-plastic material sustained by a biaxial state of stress (one normal component and one shearing component) in which the corresponding two components of strain are prescribed functions of time. Lamba and Sidebottom (1978a,b) modelled this experimentally by performing a strain-controlled combined tension-torsion test of a thin-walled circular cylinder in which the axial strain and the shear strain were prescribed functions of time. With the notation $s_{11}(t)$ for the axial stress and $s_{12}(t)$ for the shear stress, the two-dimensional state of stress can be represented in matrix notation as

$$\|\tau_{KL}\| = \frac{1}{3}\, s_{11} \|b_{KL}\| + s_{12} \|a_{KL}\|, \quad \bar{s} = \frac{1}{3}\, s_{11}, \tag{3.1}$$

where the constant matrices a_{KL} and b_{KL} defined by

$$\|a_{KL}\| = \left\| \begin{matrix} 0 & 1 & 0 \\ 1 & 0 & 0 \\ 0 & 0 & 0 \end{matrix} \right\|, \quad \|b_{KL}\| = \left\| \begin{matrix} 2 & 0 & 0 \\ 0 & -1 & 0 \\ 0 & 0 & -1 \end{matrix} \right\| \tag{3.2}$$

are introduced for convenience.

The intended calculations require prescribing e_{11} and e_{12} parametrically as particular functions of time (which specify a path in the $e_{11} - e_{12}$ plane), while the other two components of normal strain (e_{22} and e_{33}) remain so far unspecified and hence unknowns. Since $\dot{e}^p_{22} = \dot{e}^p_{33} = -1/2\, \dot{e}^p_{11}$ and $\dot{e}^p_{13} = \dot{e}^p_{23} = 0$ by equations (2.4) and (3.1), it follows that the plastic strain tensor can be expressed in the form

$$\|e^p_{KL}\| = \|\gamma^p_{KL}\| = \frac{1}{2}\, e^p_{11} \|b_{KL}\| + e^p_{12} \|a_{KL}\|, \tag{3.3}$$

where e^p_{11} and e^p_{12} depend only on time. From the stress response (generalized Hooke's law) we have

$$s_{11} = E(e_{11} - e^p_{11}), \quad s_{12} = 2\mu(e_{12} - e^p_{12}), \tag{3.4}$$

where E is Young's modulus. From the inverted form of the stress response, as well as (3.3) and $(3.4)_1$, and after adopting the notation $e_r \equiv e_{22} = e_{33}$ we obtain

$$\|e_{KL}\| = \left\| \begin{matrix} e_{11} & e_{12} & 0 \\ e_{12} & e_r & 0 \\ 0 & 0 & e_r \end{matrix} \right\| \tag{3.5}$$

where

$$e_r = -\frac{\nu}{E}\, s_{11} - \frac{1}{2}\, e^p_{11} = -\nu\, e_{11} - \frac{1}{2}(1 - 2\nu) e^p_{11} \tag{3.6}$$

and where $\nu = (E - 2\mu)/2\mu$ is Poisson's ratio. Equation (3.6) relates the unspecified components of strain to the axial strain (which is known) and the axial component of plastic strain. But e_r is still unknown, inasmuch as e^p_{11} remains unknown until all of the constitutive equations pertaining to a particular two-dimensional strain path have been integrated.

In order to simplify some of the expressions that follow, we introduce the abbreviations

$$M = s_{11} - \frac{3}{4}\, \hat{\alpha}(\kappa) e^p_{11}, \quad N = s_{12} - \frac{1}{2}\, \hat{\alpha}(\kappa) e^p_{12}. \tag{3.7}$$

Then, with the use of equations (3.1) to (3.6), the loading functions in (2.2) now assume the simplified forms

$$g = \frac{2}{3}\, E^2 \left[e_{11} - \left(1 + \frac{3}{4}\, \frac{\hat{\alpha}}{E} \right) e^p_{11} \right]^2$$

$$+ 8\mu^2 \left[e_{12} - \left(1 + \frac{\hat{\alpha}}{4\mu} \right) e^p_{12} \right]^2 - \kappa,$$

$$f = \frac{2}{3}\, M^2 + 2N^2 - \kappa. \tag{3.8}$$

For the two-dimensional state of stress defined by equation (3.1), Λ is still given by equation (2.8); but, on the yield surface, Γ in equation (2.9) now assumes the special form

---

[10] It was demonstrated recently by Casey and Naghdi (1984a, equation (3.8)) that the quantity Φ is equal to the determinant of a certain rate-independent fourth-order tensor which plays a fundamental role in the theory of plasticity and which arises naturally in relating the time rate of stress to the time rate of strain.

$$\Gamma = 2\hat{\alpha}\kappa + \frac{4}{3}\left[1 + \left(\frac{\alpha_o - \alpha_s}{\kappa_o - \kappa_s}\right)\left(Me^p_{11} + 2Ne^p_{12}\right)\right]\left[M\left(\hat{\beta}s_{11} + \frac{3}{2}\,\hat{\eta}e^p_{11}\right) + 3N\left(\hat{\beta}\,s_{12} + \hat{\eta}\,e^p_{12}\right)\right]. \tag{3.9}$$

In view of equations (3.1), (3.3), and (3.5), from (2.7) the quantity $\hat{g}$ occurring in the loading criteria in strain space is given by

$$\begin{aligned}\hat{g} &= \frac{8}{3}\,\mu M\dot{e}_{11} + 8\mu N\dot{e}_{12} - \frac{8}{3}\,\mu M\dot{e}_r \\ &= \frac{4}{3}\,EM\dot{e}_{11} + 8\mu N\dot{e}_{12} + \frac{4}{3}(3\mu - E)M\dot{e}^p_{11},\end{aligned} \tag{3.10a,b}$$

and the corresponding quantity $\hat{f}$ in stress space is

$$\hat{f} = \frac{4}{3}\,M\dot{s}_{11} + 4N\dot{s}_{12}, \tag{3.11}$$

where in obtaining (3.10*b*) the time derivative of equation (3.6) has been used. It should be noted that $\hat{g}$ depends on the unspecified strain rate $\dot{e}_r$ (or the unknown axial plastic strain rate $\dot{e}^p_{11}$); and hence the determination of whether the state of strain at an elastic-plastic state is undergoing *loading*, *neutral loading*, or *unloading* cannot in general be ascertained directly from (3.10).

Since during loading the constitutive equation (2.4*b*) for the plastic strain rate contains $\hat{g}$ on its right-hand side, in view of equation (3.10*b*) it is at once obvious that $\dot{e}^p_{11}$ occurs on both sides of the equation in the case of axial plastic strain rate. After solving this equation, a new form of the constitutive equation results which dependes only on the specified strain rates $\dot{e}_{11}$ and $\dot{e}_{12}$. This equation then enables the constitutive equations for the other components of plastic strain rate to be expressed in terms of only $\dot{e}_{11}$ and $\dot{e}_{12}$ also. This procedure along with equations (3.1) and (3.3) leads to the following expressions for the nonzero plastic strain rates during loading ($g = 0$, $\hat{g} > 0$)

$$\dot{e}^p_{11} = \frac{4}{3}\,\frac{M}{Q}\,\tilde{g},\ \dot{e}^p_{12} = \frac{2N}{Q}\,\tilde{g},\ \dot{e}^p_{22} = \dot{e}^p_{33} = -\frac{1}{2}\,\dot{e}^p_{11}, \tag{3.12}$$

where we have introduced the quantities Q and $\tilde{g}$ defined by

$$Q = \Gamma + \Lambda - \frac{16}{9}(3\mu - E)M^2 \tag{3.13}$$

and

$$\tilde{g} = \hat{g} - \frac{4}{3}(3\mu - E)M\dot{e}^p_{11} = \frac{4}{3}\,EM\dot{e}_{11} + 8\mu N\dot{e}_{12}. \tag{3.14}$$

It is shown in Appendix A under the assumption that $Q > 0$ always, which represents a range of strain-hardening behavior sufficiently general for our present purposes, that a knowledge of only the prescribed strain rates $\dot{e}_{11}$ and $\dot{e}_{12}$ is sufficient to determine whether the materal at an elastic-plastic state is undergoing *loading, neutral loading*, or *unloading*. In fact, with $Q > 0$ the quantity $\tilde{g}$ may be used in special loading criteria appropriate for the particular problem under discussion. Thus, with $Q > 0$, the constitutive equations for the plastic strain rate and the rate of work-hardening may alternatively be expressed as[11]

$$\dot{e}^p_{KL} = \begin{cases} 0 & ,\ \text{if } g < 0, & (a) \\ 0 & ,\ \text{if } g = 0 \text{ and } \tilde{g} < 0, & (b) \\ 0 & ,\ \text{if } g = 0 \text{ and } \tilde{g} = 0, & (c) \\ \text{eq. (3.12)} & ,\ \text{if } g = 0 \text{ and } \tilde{g} > 0, & (d) \end{cases} \tag{3.15}$$

and

$$\dot{\kappa} = \left(\hat{\beta}s_{11} + \frac{3}{2}\,\hat{\eta}e^p_{11}\right)\dot{e}^p_{11} + 2\left(\hat{\beta}s_{12} + \hat{\eta}e^p_{12}\right)\dot{e}^p_{12}, \tag{3.16}$$

where the loading criteria in (3.15*a*,*b*,*c*,*d*) correspond, respectively, to an elastic state, unloading from an elastic-plastic state, neutral loading at an elastic-plastic state, and loading at an elastic-plastic state. We note that during unloading and neutral loading it follows from equations (2.4*a*), (3.4), (3.10*b*), and (3.11) that $\tilde{g} = \hat{g} = \hat{f}$, while during loading from equations (3.4) and (3.11) to (3.14) we have

$$\hat{f} = \frac{\Gamma}{Q}\,\tilde{g} = \frac{\Gamma}{\Gamma + \Lambda}\,\hat{g},\ (g = 0, \hat{g} > 0). \tag{3.17}$$

Results from the general theory similar to these and those obtained in Appendix A are summarized in Table 1 of Casey and Naghdi (1984c).

Before closing this section, we need to comment further on the restriction $Q > 0$ which bears on the loading criteria in equation (3.15). With reference to equation (3.13), since Γ may be used to characterize the strain-hardening behavior, with equations (2.8) and (3.8) the condition $Q > 0$ may be seen to include hardening behavior ($\Phi > 0$) and perfectly plastic behavior ($\Phi = 0$), but at first sight may appear to exclude a small range of softening behavior.[12] However, it can be shown (Appendix A) *that at an elastic-plastic state with* $Q \le 0$, the applied strain rates $\dot{e}_{11}$ and $\dot{e}_{12}$ can only be such that $\tilde{g} \le 0$. But the expression $(3.14)_2$ which occurs in the loading criteria (3.15) must be capable of admitting all possible choices of $\dot{e}_{11}$ and $\dot{e}_{12}$ (and hence capable of taking both positive and negative values) for all physically realistic tests. Since a state corresponding to $Q \le 0$ is unnecessarily restrictive, it will be excluded from consideration in the present development.

4 Determination of Material Constants. Details of Calculations.

Previously a procedure was suggested for determining the material coefficients in the constitutive equations from the experimental data in a uniaxial cyclic loading test (Naghdi and Nikkel, 1984). This procedure is by no means unique; and, in fact, for data obtained from one-dimensional tests, other than uniaxial cyclic tests, it may be desirable to use a different procedure. Such alternative procedures are likely to be more advantageous in two or three dimensional tests. With reference to their experimental results for OFHC copper, Lamba and Sidebottom (1978a) note that the peak axial stress attained after the material has been cycled along a strain path such as that in Fig. 1(*a*) is significantly higher than the peak axial stress attained after simple uniaxial cycling. They go on to state that this difference indicates that ". . . material properties obtained from tensile tests or even uniaxial cyclic tests will not give accurate predictions of cyclic deformation under nonproportional or out-of-phase conditions."[13] A conclusion of this kind cannot be made independent of a particular theory used and does not follow from the knowledge of only a part of the experimental measurements (e.g., a part of the measurements that leads to the calculated s_{11}). Rather, it requires a detailed examination of the entire experimental data in conjunction with the relevant constitutive equations.

---

[11] We emphasize that the loading criteria in equation (3.15) are derived from the general form of the strain space loading criteria, and not postulated in an *ad hoc* fashion.

[12] This is because the condition $Q > 0$ places a greater restriction on Γ than does the more general result $\Gamma + \Lambda > 0$ (which is a consequence of the work assumption of Naghdi and Trapp, 1975b).

[13] The term out-of-phase refers to the specification of e_{11} and e_{12} as sinusoidal functions of time with the 90 degree phase difference between them, resulting in an elliptic path in the $e_{11} - e_{12}$ plane.

As can be seen from equation $(3.7)_{1,2}$ and $(3.8)_2$ with $\kappa=\kappa_s$, $\hat{\alpha}(\kappa) = \alpha_s$ and with $f=0$, the expression for κ_s in a two-dimensional cycling test depends on s_{11}, s_{12}, e^p_{11}, e^p_{12} as well as $\hat{\alpha}=\alpha_s$. However, the expression for κ_s in the case of a "peak" axial stress (i.e., the value of s_{11} when $s_{12} = 0$) will depend only on the axial stress s_{11} in addition to other parameters such as α_s and the plastic strains. We further observe that in the biaxial tests under discussion the value of the parameter κ_s, which represents the size of the loading surface in two dimensions, is particularly sensitive to the values of the stresses but much less so to the values of α_s and the plastic strains. In view of the experimental result of Lamba and Sidebottom (1978a) mentioned in the previous paragraph, if κ_s is determined from uniaxial cycling data alone, then the theoretical prediction for the two-dimensional cycling experiments may not be as accurate as when κ_s is determined from the entire experimental data of a two-dimensional strain cycling test.

We keep the foregoing discussion in mind when describing the alternative procedure for determining the material coefficients in the constitutive equations. A value for κ_s will be determined from two-dimensional strain cycling experiments. For our present purpose, it will suffice to determine the other constants from uniaxial cycling data as before.[14] Thus, a value for κ_o follows from $f=0$ and the yield stress in uniaxial tension, and a value for α_s can be determined from the slope of the uniaxial stress-strain curve at saturation. By selecting a point at saturation from the experimental data for a two-dimensional cycling experiment, similar to points Q, R, S, or T shown in the calculated results in Figs. 1(*a-c*) and with the values of stress and plastic strain at such a point the value for κ_s may be determined from $f=0$. We took the value κ_s to be the average of the values obtained from points R and T, in order to have the best overall prediction for all loading paths in the $e_{11}-e_{12}$ plane. The remaining constants may then be determined from the uniaxial cycling data by the procedure described previously (Naghdi and Nikkel, 1984). Using the above procedure with the experimental data of Lamba and Sidebottom (1978a, Figs. 2 and 3(*a-d*)) for the OFHC copper the material constants were determined to be

$$\frac{\alpha_o}{E}=\frac{\alpha_s}{E}=8.14\times10^{-3},$$

$$\frac{\beta}{E}=2.30\times10^{-2},\ \frac{\eta}{E^2}=-9.38\times10^{-5},$$

$$\frac{\kappa_o}{E^2}=4.03\times10^{-8},\ \frac{\kappa_s}{E^2}=1.93\times10^{-6},\ \frac{\mu}{E}=0.374, \qquad (4.1)$$

$$E=115\ \text{GPa}.$$

In the course of identifying values for the coefficients α_o and α_s, it was found that their values differed only by less than 0.3 percent. This suggests that if this difference can be neglected, we could set $\alpha_o=\alpha_s$ approximately and then the coefficient η in equations (2.5) and (2.6) will no longer require an independent identification. This would make the task of determination of the coefficients much easier; and, in fact, with $\alpha_o=\alpha_s$ the coefficient η can be determined in terms of α_o and β. To see this, we recall that in the special case in which $\alpha_o=\alpha_s\equiv\alpha$ (say) the constitutive equations used here reduce to a special case of those employed previously by Caulk and Naghdi (1978, equations (40), (56), and $(70)_1$). For their equations, they obtained the restriction $\eta=-\alpha\beta/2$ (see equation $(70)_2$ in Caulk and Naghdi, 1978). In view of the fact that the values determined for α_o and α_s are essentially the same, for the purpose of comparison with the experimental data of Lamba and Sidebottom (1978a,b) for OFHC copper, it will suffice to take $\alpha_o = \alpha_s$ and $\eta=-\alpha_o\beta/2$.

The calculations summarized in Section 1 were carried out by first parametrically specifying the strains e_{11} and e_{12} as functions of time, corresponding to a particular path in the $e_{11}-e_{12}$ plane. The constitutive equations (3.15) and (3.16) were then integrated numerically with the values (4.1) for the coefficients. Finally, the stresses were calculated using equation (3.4).

To calculate Φ in equation (2.10), a knowledge of Λ in equation (2.8) and Γ in equation (3.9) is needed. The particular representation of Γ in equation (3.9) depends on the stresses, as well as the quantities M and N which also involve the stresses s_{11} and s_{12}. Then, in view of equation (3.4), Γ may be expressed in terms of the total and plastic strains. It follows that Φ depends on total and plastic strains, as well as on κ. But, from the fact that on the yield surface $g = 0$ with the function g given by $(3.8)_1$, it is possible to solve for κ in terms of the other quantities so that Φ may be represented as a function of only e_{11}, e_{12}, e^p_{11}, and e^p_{12}. It is of interest to plot the variation of Φ with plastic strains for fixed values of e_{11} and e_{12}. After making the substitutions indicated above, the dependence of Φ on the total and plastic strains may be expressed in the form

$$\Phi=\hat{\Phi}\left(e^p_{11}-\left(1+\frac{3}{4}\frac{\alpha_o}{E}\right)^{-1}e_{11},\ e^p_{12}-\left(1+\frac{\alpha_o}{4\mu}\right)^{-1}e_{12}\right). \qquad (4.2)$$

For definiteness, we specify $e_{11} = e_{12} = 0$ and then calculate the value of Φ for each e^p_{11}, e^p_{12} pair. The resulting plot using the values (4.1) is shown in Fig. 4. It is clear from the arguments of the function $\hat{\Phi}$ in equation (4.2) that this single calculation provides all of the relevant information on the variation of Φ; and, for any other specified values of e_{11} and e_{12}, the surface plotted in Fig. 4 will not change in shape but will simply translate parallel to the $e^p_{11} - e^p_{12}$ plane by the constant amounts

$$\left(1+\frac{3}{4}\frac{\alpha_o}{E}\right)^{-1}e_{11},\ \left(1+\frac{\alpha_o}{4\mu}\right)^{-1}e_{12} \qquad (4.3)$$

in the e^p_{11} and e^p_{12} directions, respectively. It must be kept in mind that the domain in the $e^p_{11}-e^p_{12}$ plane must be such that the value of κ corresponding to the values of e_{11}, e_{12}, e^p_{11} and e^p_{12} is between κ_o and κ_s. In Fig. 4, the outer boundary (with the smallest value of Φ) corresponds to $\kappa=\kappa_s$ and the inner boundary (with the largest value of Φ) corresponds to $\kappa=\kappa_o$. It should be mentioned that some elastic-plastic states corresponding to points on the surface may not be reached by any path. For example, on the inner boundary in Fig. 4, where $\kappa = \kappa_o$, the plastic strain is nonzero indicating some plastic deformation must occur to reach an elastic-plastic state corresponding to this edge of the surface. However, after plastic deformation has taken place κ cannot have the value κ_o (the value of κ at initial yield) while the material exhibits hardening behavior except in the special case of purely kinematic hardening. Thus, for the plot displayed in Fig. 4, no acutal elastic-plastic state corresponding to the inner boundary of the surface can be reached.

5 Concluding Remarks

In summary, a relatively simple set of constitutive equations is used to predict various phenomena occurring in two-dimensional strain cycling in the range of small deformation. The calculated predictions are compared with corresponding experimental results of Lamba and Sidebottom (1978a,b) with good qualitative agreements. It is noteworthy that even during the post-saturation behavior of the material, the constitutive

---

[14] In contrast to κ_s, for the relatively simple constitutive equations used here the determination of the other constants from the uniaxial tests seems to be adequate.

equations used have adequate predictive capabilities as demonstrated by the results in Figs. 2(*a*–*c*) and Figs. 3(*a*–*c*). Furthermore, it may be emphasized that the theoretical calculations successfully predict the erasure of memory phenomenon which has significant practical utility in two-dimensional, post-saturation strain cycling experiments. Clearly, by exploiting this phenomenon, the response of a material to strain cyclng along strain paths in different directions can be determined by performing experiments on one specimen if a large cycle which erases the material's memory of the preceding smaller cycle is traversed after each smaller cycle.

The main differences between the present calculations and the experimental results can be attributed primarily to the manner of identification of two of the material constants at saturation, namely κ_s and α_s. These values can be chosen to be the same as those identified either from experiments in simple tension ($e_{12} = 0$) or experiments in simple shear ($e_{11} = 0$). The values resulting from experiments in simple tension can lead to discrepancies in matching experiments involving mainly simple shear (such as those in Figs. 2(*a*–*c*) and 3(*a*–*c*)), and likewise values chosen from experiments in simple shear will affect the agreements between the theoretical and experimental results in simple tension. The choice for the value of the constant κ_s used in the calculations (for details see Section 4) was motivated by a desire to obtian the best overall agreement with experimental results for all directions of the strain paths in the $e_{11} - e_{12}$ plane. Similarly, as noted in the last section, α_s was chosen to be equal to α_o in order to simplify the identification of the material coefficients for OFHC copper. The slope of the calculated response curve in the $s_{12} - e_{12}$ plane at saturation can be shown to depend to some degree on α_s, so that if a more accurate prediction of the slope of the curve during loading along FB in Fig. 2(*c*) is desired an alternative procedure for determination of α_s could be used.

The plot displayed in Fig. 4 contains detailed information pertaining to strain-hardening behavior for the particular material used in the experiments of Lamba and Sidebottom (1978a,b). Accessibility to such information or the data representing Φ for all values of total and plastic strains in the domain of interest is clearly of value in analyses and computations. It should be possible in principle to determine the value of Φ directly from experiments. Casey and Naghdi (1984b, equation (4.29)) have previously shown that the function Φ can be interpreted in terms of the ratio of the outward normal velocities of the yield surfaces in stress space and in strain space. It is suggested that future experimenters provide direct measurements concerning the yield surfaces in both stress space and strain space and also consider the possibility of obtaining the values of Φ directly in the course of their experiments.

We close this section with some remarks concerning additional experimental data on two-dimensional cycling that have become available very recently. McDowell (1985) has reported experimental results for two-dimensional strain cycling of a type similar to those of Lamba and Sidebottom (1978a,b); and in principle, similar comparisons can be made with his data. However, the data provided in McDowell's paper are insufficient for the identification of all of the material constants appearing in the constitutive equations used here.[16] Also, it should be noted that our approach for theoretical predictions differs from the "two surface stress space model" used by McDowell (1985) for comparison with his experiments.

Ohashi et al. (1985) have reported some experimental data for two-dimensional stress cycling. They do not discuss any theoretical predictions for comparison with their experiments. While in principle, there should be no difficulty in making such comparisons, the data provided is again insufficient for the identification of all of the material constants appearing in the constitutive equations used here.[17]

Acknowledgment

The results reported here were obtained in the course of research supported by the Solid Mechanics Program of the U.S. Office of Naval Research under Contract N00014-84-K-0264, Project NR 064-436 with the University of California, Berkeley.

References

Casey, J., and Lin, H. H., 1983, "Strain-Hardening Topography of Elastic-Plastic Materials," ASME JOURNAL OF APPLIED MECHANICS, Vol. 50, pp. 795–801.

Casey, J., and Naghdi, P. M., 1981, "On the Characterization of Strain-Hardening in Plasticity," ASME JOURNAL OF APPLIED MECHANICS, Vol. 48, pp. 285–296.

Casey, J., and Naghdi, P. M., 1983, "A Remark on the Definition of Hardening, Softening and Perfectly Plastic Behavior," *Acta Mechanica*, Vol. 48, pp. 91–94.

Casey, J., and Naghdi, P. M., 1984a, "Further Constitutive Results in Finite Plasticity," *Quarterly Journal of Mechanics and Applied Mathematics*, Vol. 37, pp. 231–259.

Casey, J., and Naghdi, P. M., 1984b, "Strain-Hardening Response of Elastic-Plastic Materials," presented at a Conference on "Constitutive Laws for Engineering Materials: Theory and Application," Tuscon, AZ., Jan. 10–14, 1983. In *Mechanics of Engineering Materials*, Desai, C. S., and Gallagher, R. H., eds., Chapt. 4, Wiley.

Casey, J., and Naghdi, P. M., 1984c, "Constitutive Results for Finitely Deforming Elastic-Plastic Materials," in *Constitutive Equations: Macro and Computational Aspects*, Willam, K. J., ed., The American Society of Mechanical Engineers, New York, pp. 53–71.

Caulk, D. A., and Naghdi, P. M., 1978, "On the Hardening Response in Small Deformation of Metals," ASME JOURNAL OF APPLIED MECHANICS, Vol. 45, pp. 755–764.

Green, A. E., and Naghdi, P. M., 1965, "A General Theory of an Elastic-Plastic Continuum," *Archive for Rational Mechanics and Analysis*, Vol. 18, pp. 251–281.

Green, A. E., and Naghdi, P. M., 1966, "A Thermodynamic Development of Elastic-Plastic Continua," *Proceedings of the IUTAM Symposium on Irreversible Aspects of Continuum Mechanics and Transfer of Physical Characteristics in Moving Fluids*, Parkus, H., and Sedov, L. I., eds., Springer-Verlag, New York, pp. 117–131.

Lamba, H. S., and Sidebottom, O. M., 1978a, "Cyclic Plasticity for Nonproportional Paths: Part 1—Cyclic Hardening, Erasure of Memory, and Subsequent Strain Hardening Experiments," *ASME Journal of Engineering Materials and Technology*, Vol. 100, pp. 96–103.

Lamba, H. S., and Sidebottom, O. M., 1978b, "Cyclic Plasticity for Nonproportional Paths: Part 2—Comparison With Predictions of Three Incremental Plasticity Models," *ASME Journal of Engineering Materials and Technology*, Vol. 100, pp. 104–111.

McDowell, D. L., 1985, "A Two Surface Model for Transient Nonproportional Cyclic Plasticity: Part 2 Comparison of Theory with Experiments," ASME JOURNAL OF APPLIED MECHANICS, Vol. 52, pp. 303–308.

Naghdi, P. M., and Nikkel, D. J., Jr., 1984, "Calculations for Uniaxial Stress and Strain Cycling in Plasticity," ASME JOURNAL OF APPLIED MECHANICS, Vol. 51, pp. 487–493.

Naghdi, P. M., and Trapp, J. A., 1975a, "The Significance of Formulating Plasticity Theory With Reference to Loading Surfaces in Strain Space," *International Journal of Engineering Science*, Vol. 13, pp. 785–797.

---

[15] In addition to the two elastic constants, there are six material constants (α_o, α_s, β, η, κ_o, κ_s) which must be determined from experimental results. However, for the special case in which $\alpha_o = \alpha_s$ as utilized in Section 4, an additional restriction obtained by Caulk and Naghdi (1978) can also be invoked and this reduces the number of independent constants to be determined to the four (α_o, β, κ_o, κ_s). With $\alpha_o \neq \alpha_s$, the calculations will involve more complex expressions and plots (for different values of e_{11}, e_{12}) of the function Φ will exhibit changes in shape and will not simply represent translations of the surface parallel to the $e^p_{11} - e^p_{12}$ plane as in the case when $\alpha_o = \alpha_s$.

[16] McDowell's paper (1985) does not include the data for uniaxial strain cycling needed for the identification of material constants in the context of the procedure used here.

[17] Ohashi et al. (1985) do not perform any uniaxial strain cycling tests. The data from such tests are necessary for identification of most of the material constants using the procedure summarized in Section 4.

Naghdi, P. M., and Trapp, J. A., 1975b, "Restrictions on Constitutive Equations of Finitely Deformed Elastic-Plastic Materials," *Quarterly Journal of Mechanics and Applied Mathematics*, Vol. 28, pp. 25–46.

Ohashi, Y., Kawai, M., and Kaito, T., 1985, "Inelastic Behavior of Type 316 Stainless Steel Under Multiaxial Nonproportional Cyclic Stressings at Elevated Temperature," *ASME Journal of Engineering Materials and Technology*, Vol. 107, pp. 101–109.

APPENDIX A

We include here the details of the arguments which demonstrate that the special loading criteria in equation (3.15) with $\tilde{g}$ (rather than $\hat{g}$) are consistent with the loading criteria of the strain-space formulation, i.e., at an elastic-plastic state with $Q > 0$ we establish the correspondence

$$\begin{aligned} \tilde{g}<0 &\Leftrightarrow \hat{g}<0 \ , \ \text{(unloading)}, \\ \tilde{g}=0 &\Leftrightarrow \hat{g}=0 \ , \ \text{(neutral loading)}, \\ \tilde{g}>0 &\Leftrightarrow \hat{g}>0 \ , \ \text{(loading)}. \end{aligned}$$

We first prove that at an elastic-plastic state with $Q \neq 0$, $\hat{g} = 0$ if and only if $\tilde{g} = 0$. Sufficiency follows equation (3.12), where if $\tilde{g} = 0$ so is $\dot{e}^{p}_{KL} = 0$ and then from equation (3.14) $\hat{g} = 0$ also. To establish necessity suppose that $\hat{g} = 0$. It then follows from equations (2.4) and (3.14) that $\tilde{g} = 0$.

In view of the result of the previous paragraph note that at an elastic-plastic state with $Q \neq 0$, $\hat{g} \neq 0$ if and only if $\tilde{g} \neq 0$. We now prove that at an elastic-plastic state with $Q > 0$, $\hat{g} > 0$ if and only if $\tilde{g} > 0$. To establish sufficiency suppose that $\tilde{g} > 0$. If $\hat{g} < 0$, then $\dot{e}^{p}_{KL} = 0$ by equation (2.4) and (3.14) implies $\hat{g} = \tilde{g}$, which is a contradiction and hence we must have $\hat{g} > 0$. To establish necessity, we suppose that $\hat{g} > 0$, and this implies that $\hat{g} = \tilde{g}(\Gamma + \Lambda)/Q$ from equation (3.17). In view of the fact that $\Gamma + \Lambda > 0$ (Casey and Naghdi, 1984b, equation (4.50)) and the fact that we are considering only the case in which $Q > 0$ this implies $\tilde{g} > 0$.

As a consequence of the results of the preceding two paragraphs, it follows that at an elastic-plastic state with $Q > 0$, $\hat{g} < 0$ if and only if $\tilde{g} < 0$.

In the remainder of this appendix we demonstrate that if Q in equation (3.13) is nonpositive at an elastic-plastic state, i.e., if $Q \leq 0$, then the applied strain rates $\dot{e}_{11}$ and $\dot{e}_{12}$ can only be such that $\tilde{g} \leq 0$.

We first prove that with $Q < 0$ we can only have $\tilde{g} \leq 0$. Suppose $\tilde{g} > 0$. If $\hat{g} \leq 0$, then equations (2.4) and (3.14) imply $\tilde{g} = \hat{g}$ which is a contradiction. Alternatively if $\hat{g} > 0$, then $\hat{g} = \tilde{g}(\Gamma + \Lambda)/Q$ from equation (3.17). In view of the fact that $\Gamma + \Lambda > 0$ (Casey and Naghdi, 1984b, equation (4.50)) and that we are considering the case in which $Q < 0$, it follows that $\tilde{g} < 0$ which is also a contradiction. Hence, we can only have $\tilde{g} \leq 0$ if $Q < 0$.

Next, we prove that if $Q = 0$, we can only have $\tilde{g} \leq 0$. Again, suppose that $\tilde{g} > 0$. If $\hat{g} \leq 0$, then equations (2.4) and (3.14) imply $\tilde{g} = \hat{g}$ which is a contradiction. Alternatively if $\hat{g} > 0$, with the use of the expression for $\hat{g}$ resulting from equation $(3.14)_1$ and the identity resulting from equation (3.13) after setting its left-hand side equal to zero, the constitutive equation for the axial plastic strain rate from equation (2.4b) implies $\tilde{g} = 0$ which is also concontradiction. Hence we can only have $\tilde{g} \leq 0$ if $Q = 0$.

Asymptotic Fields of a Perfectly-Plastic, Plane-Stress Mode II Growing Crack

P. Ponte Castañeda
Division of Applied Sciences,
Harvard University,
Cambridge, Mass. 02138

The asymptotic near-tip stress and velocity fields are presented for a plane-stress Mode II crack propagating quasi-statically in an elastic-perfectly plastic Mises solid. The solution is found to have fully continuous stress and velocity fields, and a configuration similar to that of the anti-plane strain problem: a singular centered fan plastic sector ahead of the crack, followed by an elastic unloading sector and a constant stress plastic sector extending to the crack flank. The impossibility of a plane-stress Mode I crack solution having these properties is also discussed.

1 Introduction

Rice (1982) presented a complete analysis of the asymptotic structure of the near-tip stress and deformation fields of a crack growing quasi-statically in an elastic-perfectly plastic solid. There, all possible solutions to the governing equations in the plastic and elastic sectors are given for anti-plane strain, plane strain, and plane stress. Drugan and Rice (1984) presented a general study of the continuity conditions across quasi-statically moving surfaces such as the interfaces between these sectors.

In anti-plane strain, Chitaley and McClintock (1971) gave the first successful assembly of sectors for the Mises material. In plane strain, Slepyan (1974) presented the corresponding assembly of sectors for the Tresca material in both Modes I and II. Independently, Gao (1980) and Rice et al. (1980) produced results for the Mises material in Mode I ($\nu = 1/2$), and Drugan et al. (1982) generalised these results to the case of $\nu \neq 1/2$.

Although the plane-stress Mode II problem does not have the practical importance of the corresponding Mode I problem, it has theoretical importance. It also has special significance because no complete solution has yet been found to the Mode I problem. In this paper we present a solution to the plane-stress Mode II problem and throw some light on the Mode I problem.

2 Formulation

With reference to Fig. 1, let $x_i (i = 1,2,3)$ be a Cartesian coordinate system of fixed orientation travelling with the crack tip such that the x_3 axis coincides with the straight crack front. Furthermore, let $\mathbf{e}_i$ be the unit vector corresponding to the x_i direction. Similarly, let r, θ be polar coordinates corresponding to $x_\alpha (\alpha = 1,2)$ and $\mathbf{e}_r$, $\mathbf{e}_\theta$ be the corresponding unit vectors. The crack tip moves quasi-statically with velocity $\mathbf{V} = V e_1$ with respect to the stationary coordinate system X_i. Thus in asymptotic analysis the material derivative is given by

$$(\ )^{\cdot} = -V(\ )_{,1} \tag{1}$$

The dependent variables of the problem are the in-plane components of the stress tensor $\boldsymbol{\sigma}$, and the velocity vector $\mathbf{v}$ (v_3 does not enter the formulation). The governing equations are equilibrium with the inertia term neglected

$$\nabla \cdot \boldsymbol{\sigma} = \mathbf{0} \tag{2}$$

and the constitutive relations corresponding to an isotropic Mises material satisfying the Prandtl-Reuss flow rule

$$\mathbf{D} = (1/E)(1+\nu)\boldsymbol{\Sigma} - (\nu/E)\,Tr(\boldsymbol{\Sigma})\mathbf{I} + \Lambda^{\cdot}\mathbf{S} \tag{3}$$

Here E is the modulus of elasticity, ν is the Poisson's ratio, $\mathbf{I} = \mathbf{e}_i\mathbf{e}_i$ is the identity tensor, $\mathbf{S} = \boldsymbol{\sigma} - (1/3)\,Tr(\boldsymbol{\sigma})\mathbf{I}$ is the stress-deviator tensor, $\mathbf{D} = (1/2)[\nabla\mathbf{v} + (\nabla\mathbf{v})^t]$ is the strain-rate tensor, $\boldsymbol{\Sigma} = \boldsymbol{\sigma}^{\cdot}$ is the stress-rate tensor, and $\Lambda^{\cdot}$ is a scalar such that: (*i*) $\Lambda^{\cdot} = 0$ for elastic response, (*ii*) $\Lambda^{\cdot} \geq 0$ for plastic loading. In the second case the equations are supplemented by the Mises yield condition

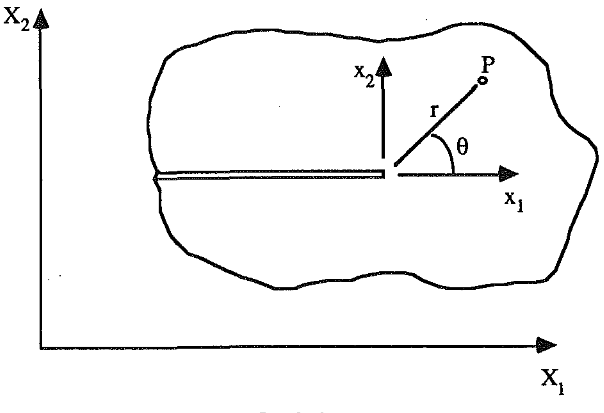

Fig. 1 Crack tip geometry

Contributed by the Applied Mechanics Division for publication in the JOURNAL OF APPLIED MECHANICS.

Discussion on this paper should be addressed to the Editorial Department, ASME, United Engineering Center, 345 East 47th Street, New York, N.Y. 10017, and will be acepted until two months after final publication of the paper itself in the JOURNAL OF APPLIED MECHANICS. Manuscript received by ASME Applied Mechanics Division, October 9, 1985; final revision, January 23, 1986.

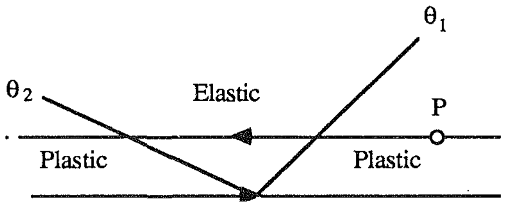

Fig. 2 Loading history of particle *P*

$$\sigma_e = [(3/2)\mathbf{S}:\mathbf{S}]^{1/2} = \sqrt{3}\,\tau_o \tag{4}$$

where τ_o denotes the yield stress in shear.

The boundary conditions of the problem are

$$\sigma_{rr}(r,0) = \sigma_{\theta\theta}(r,0) = v_r(r,0) = 0 \tag{5}$$

as required by Mode II symmetry, and

$$\sigma_{r\theta}(r,\pi) = \sigma_{\theta\theta}(r,\pi) = 0 \tag{6}$$

because the crack faces are traction-free.

Rice (1982) has shown that the governing equations admit only three types of asymptotic solutions. Thus near the crack tip we can only have three types of sectors: elastic sectors, and plastic sectors of either the constant stress or centered fan type. Here we will look for a solution with a centered fan sector ahead of the crack ($0 < \theta < \theta_1$), followed by an elastic sector ($\theta_1 < \theta < \theta_2$) and a constant stress sector extending to the crack face ($\theta_2 < \theta < \pi$). This configuration is schematically depicted in Fig. 2.

According to Pan (1984) we need to impose continuity of all the components of the stress tensor across each elastic-plastic boundary

$$[\sigma_{r\theta}] = [\sigma_{rr}] = [\sigma_{\theta\theta}] = 0 \tag{7}$$

where [ ] denotes the jump in a quantity as θ increases infinitesimally. He also shows that we can impose continuity of the velocity vector, unless the stress state at the interface meets certain specific conditions, in which case discontinuities in the velocities cannot be ruled out. Here we will look for a solution with a continuous velocity so that we impose

$$[v_r] = [v_\theta] = 0 \tag{8}$$

3 Solution

The leading order terms in the asymptotic expansion of the stress and deformation fields in the three sectors can easily be calculated and are given below. Note that the boundary conditions have already been imposed in these expressions.

(*i*) *Centered fan sector*

$$\sigma_{r\theta} = \tau_o \cos\theta \quad \sigma_{rr} = -\tau_o \sin\theta \quad \sigma_{\theta\theta} = -2\tau_o \sin\theta \tag{9}$$

$$\begin{aligned} v_r &= -(3/2)V(\tau_o/E)\sin 2\theta\, ln(r/R) \\ v_\theta &= 3V(\tau_o/E)[1-(4/5)\cos^2\theta + B(\cos\theta)^{-1/2}]\, ln(r/R) \end{aligned} \tag{10}$$

$$\Lambda^\bullet = -(3/2)(V/E)[(6/5)\cos\theta + B(\cos\theta)^{-3/2}]\, ln(r/R)/r \tag{11}$$

(*ii*) *Elastic sector*

$$\begin{aligned} \sigma_{12} &= (\tau_o/4)[A_1(2\theta + \sin 2\theta) - A_2\cos 2\theta + C_{12}] \\ \sigma_{11} &= (\tau_o/4)[4A_1 ln|\sin\theta| + A_1\cos 2\theta + A_2(2\theta + \sin 2\theta) + C_{11}] \\ \sigma_{22} &= (\tau_o/4)[-A_1\cos 2\theta + A_2(2\theta - \sin 2\theta) + C_{22}] \end{aligned} \tag{12}$$

$$\begin{aligned} v_1 &= V(\tau_o/E)A_1 ln(r/R) \\ v_2 &= V(\tau_o/E)A_2 ln(r/R) \end{aligned} \tag{13}$$

(*iii*) *Constant stress sector*

$$\sigma_{12} = 0 \quad \sigma_{11} = \sqrt{3}\,\tau_o \quad \sigma_{22} = 0 \tag{14}$$

$$\begin{aligned} v_1 &= V(\tau_o/E)D_1 ln(r/R) \\ v_2 &= V(\tau_o/E)D_2 ln/r/R) \end{aligned} \tag{15}$$

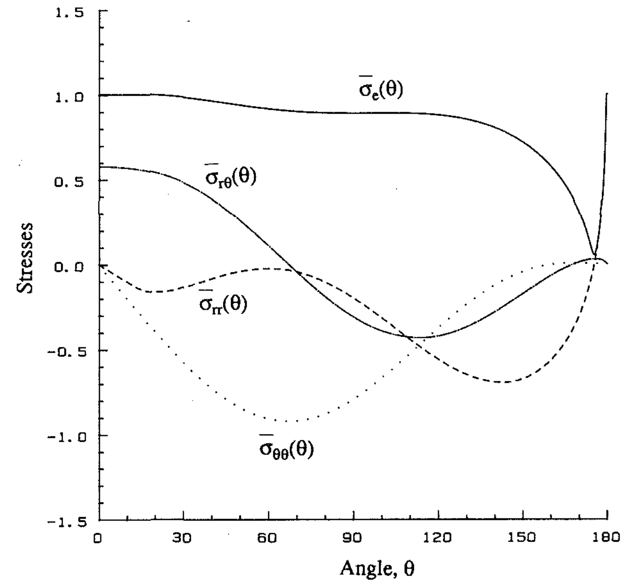

Fig. 3 Stress distribution

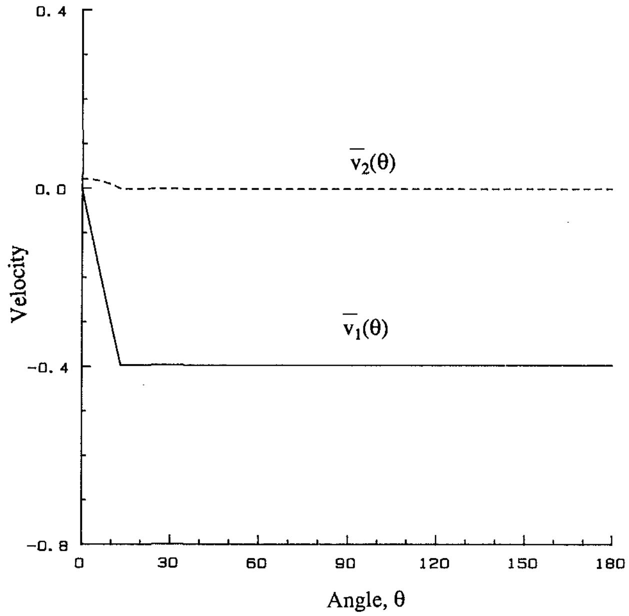

Fig. 4 Velocity distribution

$$\Lambda^\bullet = (1/\sqrt{3})(V/E)[\cos\theta - 1/(3\cos\theta)]^{-1}(D_1 + D_2\tan\theta)/r \tag{16}$$

These fields involve ten unknown constants ($A_1, A_2, B, C_{12}, C_{11}, C_{22}, D_1, D_2, \theta_1$, and θ_2), and must be subjected to the five continuity conditions given by equations (7) and (8) across the two boundaries for a total of ten conditions. A solution to this nonlinear algebraic system was found with

$$\begin{array}{ll} \theta_1 \approx 13.31383 \text{ deg} & \theta_2 \approx 179.61254 \text{ deg} \\ A_1 = D_1 \approx -0.68994 & A_2 = D_2 \approx -0.00387 \\ B \approx -0.18814 & C_{12} \approx 0.26953 \\ C_{11} \approx -0.38413 & C_{22} \approx -0.04160 \end{array} \tag{17}$$

and the associated stress and velocity fields are depicted in Figs. 3 and 4. Note that the yield condition is nowhere violated, and in particular that $\sigma_e < \sigma_o$ for $\theta_1 < \theta < \theta_2$. Also note that $\Lambda^\bullet > 0$ near the crack tip in both plastic sectors.

4 Concluding Remarks

The results of this problem agree in form with those of the other two anti-symmetric cases, anti-plane strain Mode III and plane-strain Mode II. Thus it is found that in all these cases the solution has continuous stress and velocity fields, and the same configuration: a plastic sector ahead of the crack which produces singular strains, followed by an elastic unloading sector and a reverse plastic flow sector on the crack flank which produce no additional singular straining beyond the unloading level.

Vis-à-vis the plane-stress Mode I problem, we find that assuming a similar assembly of sectors does not yield a solution with continuous stresses and velocities. To see this, we remark that the velocities in the centered fan sector would be (Rice, 1982)

$$v_r = -3V(\tau_o/E)\sin^2\theta \, ln(r/R)$$
$$v_\theta = -3V(\tau_o/E)(\sin\theta)^{-1/2}\left[\int_0^\theta (\sin\phi)^{1/2}\cos 2\phi \, d\phi + B\right] ln(r/R) \qquad (18)$$

Mode I symmetry would then require

$$v_\theta(r,0) = 0 \qquad (19)$$

This would make B vanish, which in the context of the previous formulation would leave only nine unknowns to satisfy ten conditions. Hence, it is impossible to find a continuous asymptotic solution to the plane-stress Mode I problem with the given configuration of sectors.

A somewhat similar situation appeared in the plane-strain Mode I problem where a discontinuity in the tangential component of the velocity, consistent with the material model, had to be admitted. Thus it is conceivable that discontinuities in the velocity may have to be introduced in the solution of the plane-stress Mode I problem. Pan (1984) has considered such discontinuities.

Finally, we point out that in addition to the plane-stress Mode I problem, the Mises plane-strain Mode II problem with $\nu \neq 1/2$ remains to be solved. For $\nu = 1/2$ the solution obtained by Slepyan (1974) for the Tresca material also holds for the Mises material.

Acknowledgments

This work was supported in part by the Office of Naval Research under Contract N00014-84-K-0510, and by the Division of Applied Sciences, Harvard University. The author is grateful to B. Budiansky and J. R. Rice for helpful discussions.

References

Chitaley, A. D., and McClintock, F. A., 1971, "Elastic-Plastic Mechanics of Steady Crack Growth Under Anti-Plane Shear," *J. Mech. Phys. Solids*, Vol. 19, pp. 147–163.

Drugan, W. J., Rice, J. R., and Sham, T. L., 1982, "Asymptotic Analysis of Growing Plane Strain Tensile Cracks in Elastic-Ideally Plastic Solids," *J. Mech. Phys. Solids*, Vol. 30, pp. 447–473.

Drugan, W. J., and Rice, J. R., 1984, "Restrictions on Quasi-Statically Moving Surfaces of Strong Discontinuity in Elastic-Plastic Solids," *Mechanics of Material Behavior*, Dvorak, G. J., and Shield, R. T., eds., Elsevier Science Publishers, Amsterdam, pp. 59–73.

Gao, Y.-C., 1980, "Elastic-Plastic Field at the Tip of a Crack Growing Steadily in Perfectly-Plastic Medium," in Chinese, *Acta Mechanica Sinica*, Vol. 1, pp. 48–56.

Pan, H., 1980, "Some Discussion on Moving Strong Discontinuity Under Plane-Stress Condition," *Mechanics of Materials*, Vol. 1, pp. 325–329.

Rice, J. R., Drugan, W. J., and Sham, T. L., 1980, "Elastic-Plastic Analysis of Growing Cracks," *Fracture Mechanics: Twelfth Conference*, ASTM-STP 700, pp. 189–219.

Rice, J. R., 1982, "Elastic-Plastic Crack Growth," *Mechanics of Solids: The Rodney Hill 60th Anniversary Volume*, Hopkins, H. G., and Sewell, M. J., eds., Pergamon Press, Oxford, pp. 539–562.

Slepyan, L. I., 1974, "Growing Crack During Plane Deformation of an Elastic-Plastic Body," *Mekhanika Tverdogo Tela*, Vol. 9, pp. 57–67.

G. J. Rodin[2]

D. M. Parks

Department of Mechanical Engineering,
Massachusetts Institute of Technology,
Cambridge, Mass. 02139

On Consistency Relations in Nonlinear Fracture Mechanics[1]

A simple form of consistency relations between generalized forces and displacements for systems exhibiting power-law behavior is presented. The later discussion focuses on certain details regarding applications of the relations to nonlinear fracture mechanics, emphasizing the finite element analysis of a single edge-cracked strip subjected to remote tension under plane strain conditions.

Introduction

Within the last decade there has been a serious computational effort towards obtaining numerical solutions to problems of nonlinear fracture mechanics. The handbook formatted reference (Kumar et al., 1981) gives extensive tabulations of important parameters (J-integral, CTOD, etc.) for various configurations, loadings, and material behaviors, which makes it useful for engineering analysis, and the review of prior work in the field permits its use as a good starting point for further research. The later work of Shih and Needleman (1984) exposes some quantitative discrepancies between the two results. These discrepancies cause confusion and implicitly raise the legitimate question, "who is right?" The purpose of this work is to help resolve the matter of quality of reported data.

There are three parts in this paper. The first one focuses on the derivation of consistency relations between generalized forces and displacements in fairly general types of nonlinear systems, including the class of traction prescribed boundary-value problems for power-law isotropic materials, exhibiting in pure tension stress-strain behavior

$$\frac{\epsilon}{\epsilon_0}=\left(\frac{\sigma}{\sigma_0}\right)^n, \qquad (1)$$

where ϵ_0 and σ_0 are reference strain and stress values, and n is a material exponent varying from one for the linear material to infinity for the rigid plastic material.

The second section discusses some specific features of solutions for fracture mechanics configurations, stressing both the validity of the application of the consistency relations in principle and their potential use in the detection of errors.

The paper is concluded with a numerical example to which the consistency conditions are applied – the single edge-cracked strip subjected to remote tension under plane-strain conditions. The results are compared against the data reported by Kumar et al. (1981) and Shih and Needleman (1984).

Throughout the paper we use boldface letters for vectors, matrices, and tensors. Dot stands for an appropriate inner product. All computations reported herein have been performed using the ABAQUS finite element program on a DATA GENERAL MV-10000 computer.

Consistency Relations

Let us consider some body loaded by a set of generalized forces $\mathbf{Q}$. The set of generalized displacements is taken as derivable from the constitutive potential F, which depends on the overall geometry, material properties and the forces:

$$\mathbf{q}=\frac{\partial F}{\partial \mathbf{Q}}. \qquad (2)$$

We confine our attention to the class of potentials which are both convex and homogeneous functions of $\mathbf{Q}$ degree $(n+1)$:

$$F(\alpha\mathbf{Q}_1+(1-\alpha)\mathbf{Q}_2)\le\alpha F(\mathbf{Q}_1)+(1-\alpha)F(\mathbf{Q}_2), \qquad (3)$$

$$\frac{\partial F}{\partial \mathbf{Q}}\cdot\mathbf{Q}=(n+1)F. \qquad (4)$$

In equation (3) it is understood that $\mathbf{Q}_1$, $\mathbf{Q}_2$ are arbitrary sets of generalized forces and $0\le\alpha\le 1$. In the relation (4), we adopt Euler's Theorem on homogeneous functions as a definition. One of the important properties of convex functions is the positive semidefiniteness of the Hessian matrix $\mathbf{\Gamma}$ (tangent compliance in the force-displacement framework):

$$\mathbf{\Gamma}=\frac{\partial^2 F}{\partial \mathbf{Q}^2}. \qquad (5)$$

The inner product of $\mathbf{\Gamma}$ with $\mathbf{Q}\otimes\mathbf{Q}$ leads to an important conclusion that the potential functions F defined above are nonnegative.

The alternative definition of a homogeneous function allows us to reduce the effective number of independent variables by one; the most general representation serving our purposes is:

$$F(\mathbf{Q})=f(\mathbf{x})[r(\mathbf{Q})]^{n+1}, \qquad (6)$$

where $f(\mathbf{x})$ is a nonnegative function of the reduced set $\mathbf{x}$, which dimension is one less than that of $\mathbf{Q}$, and $r(\mathbf{Q})$ is an arbitrarily defined positive function in the $\mathbf{Q}$ space. The key point of the forthcoming derivation is that the generalized

---

[1] This work was supported in part by EPRI under contract RP1237-3 and in part by ONR/Solid Mechanics under grant N00014-80-C-0706.

[2] Present Address: Department of Aerospace Engineering and Engineering Mechanics, University of Texas at Austin, Austin, Texas 78712.

Contributed by the Applied Mechanics Division for publication in the JOURNAL OF APPLIED MECHANICS.

Discussion on this paper should be addressed to the Editorial Department, ASME, United Engineering Center, 345 East 47th Street, New York, N.Y. 10017, and will be accepted until two months after final publication of the paper itself in the JOURNAL OF APPLIED MECHANICS. Manuscript received by ASME Applied Mechanics Division, February 10, 1986.

displacements in equation (2) are the partial derivatives of the same function and, therefore, should be related. We limit our demonstration to the case of two generalized forces. The extension to a multidimensional set is transparent and will not be considered here. In this case equation (6) may be reduced to

$$F=\frac{1}{n+1}f(x)Q^{n+1},\ Q:=Q_1>0,\ x:=\frac{Q_2}{Q_1}. \qquad (7)$$

Straightforward differentiation leads to the following expressions for $\mathbf{q}$ and $\mathbf{\Gamma}$:

$$\mathbf{q}=\begin{Bmatrix}(n+1)f-xf' \\ f'\end{Bmatrix}\frac{Q^n}{n+1}, \qquad (8)$$

$$\mathbf{\Gamma}=\begin{bmatrix}(n+1)nf-2nxf'+x^2f'' & \text{symmetry} \\ nf'-xf'' & f''\end{bmatrix}\frac{Q^{n-1}}{n+1}, \qquad (9)$$

where prime denotes differentiation with respect to x. To enforce positive semidefiniteness of $\mathbf{\Gamma}$ we require both Γ_{22} and the determinant of $\mathbf{\Gamma}$ to be nonnegative, which gives

$$f''\geq 0, \qquad (10)$$

$$ff''-\frac{n}{n+1}f'^2\geq 0. \qquad (11)$$

But since the function $f(x)$ is nonnegative, condition (11) is sufficient to guarantee positive semidefiniteness.

Introduction of an auxiliary function y, in a way a conjugate of x, and given by

$$y:=\frac{q_2}{q_1}=\frac{f'}{(n+1)f-xf'}, \qquad (12)$$

permits the rewriting of condition (11) in a simpler form:

$$y'\geq 0. \qquad (13)$$

Now, instead of considering the related pair of functions $f(x)$ and $f'(x)$ to describe the generalized displacements, we can use the pair $f(x)$ and $y(x)$ related via (12). If values of $f(x)$ and $y(x)$ are given at some point, say $x=x_0$, $f(x_0)=f_0$, $y(x_0)=y_0$, then integration of (12) leads to

$$f(x)=f_0\exp\left((n+1)\int_{x_0}^{x}\frac{y(t)dt}{1+ty(t)}\right). \qquad (14)$$

But for any value of $x\geq x_0$ with $x_0\leq t\leq x$ we may write the following inequality

$$\frac{y_0}{1+ty_0}\leq\frac{y(t)}{1+ty(t)}\leq\frac{y(x)}{1+ty(x)}, \qquad (15)$$

which, after the integration gives us the main result of this section:

$$\frac{1+xy_0}{1+x_0y_0}\leq\left(\frac{f}{f_0}\right)^{\frac{1}{n+1}}\leq\frac{1+xy(x)}{1+x_0y(x)} \qquad (16)$$

It is important to mention that (11) and (13) are equivalent only if $q_1>0$ for all the points within the interval $[x_0, x]$, which implicitly imposes conditions on both x_0 and x.

Application to Fracture Mechanics

A broad class of problems of fracture mechanics can be described by a generic problem – one is given a configuration containing a crack, loaded by forces $\mathbf{Q}$, and is asked to determine the value of the J integral (Rice, 1968) to characterize the local fields (Hutchinson, 1968; Rice and Rosengren, 1968) and $\mathbf{q}$ – displacements, at the remote distances, due to the introduction of the crack,

$$\mathbf{q}=\mathbf{q}^t-\mathbf{q}^h, \qquad (17)$$

where $\mathbf{q}^t$ and $\mathbf{q}^h$ stand for generalized displacements in two auxiliary problems. The first one is a prescribed traction boundary-value problem for the given configuration. The second one is identical, but there is no crack.

The constitutive potential $F(\mathbf{Q})$ becomes equal to the difference in the complementary energies of the auxiliary problems:

$$F(\mathbf{Q})=\frac{1}{n+1}\int_V(\mathbf{E}^t\cdot\mathbf{T}^t-\mathbf{E}^h\cdot\mathbf{T}^h)dV, \qquad (18)$$

where $\mathbf{T}$ and $\mathbf{E}$ stand for the stress and strain tensors, respectively.

The connection between this class of problems and the one described in the first section is obvious but, nevertheless, there are some important details to be considered both due to the necessity to perform numerical analysis and the special features of the fracture mechanics problems *per se*.

At first, we would like to address the matter of the possible loss of the homogeneous structure of $F(\mathbf{Q})$. In principle, the linearity of equilibrium, compatibility equations, and boundary conditions, combined with the constitutive law, requires an analytical solution to the problem to be homogeneous. But if we have to model an incompressible material and, therefore, employ a penalty procedure in numerical analysis, we can encounter deviations from homogeneity. The simplest way to introduce a penalty is by linear relations between isotropic components of the stress and strain tensors:

$$tr\mathbf{T}=\frac{K\sigma_0}{3\epsilon_0}\,tr\mathbf{E}. \qquad (19)$$

We argue, heuristically at best, that as K tends to infinity, the influence of the hydrostatic stress diminishes, and material response tends toward incompressibility. An attempt to conserve homogeneity by using a power-law penalty may easily lead to numerical problems as we operate with large numbers. Therefore, we can claim that degree of compressibility and deviation from the homogeneous structure are implicitly related, and in the limiting case of a large K, material tends towards both homogeneous and incompressible response. The straightforward application of (16) may be of use in detecting errors in interpretation of penalty term for sophisticated variational formulations combining both regular displacement-based and hybrid (displacement and pressure) formulations of the finite element method, as implemented, for example, in ABAQUS. Later on we present a numerical example for this relation.

The question of convexity is especially interesting for the fracture mechanics problems. The difficulty here is that there is no single boundary-value problem which may be directly analyzed to determine $F(\mathbf{Q})$, but rather two auxiliary problems. Convexity of each problem is guaranteed by the monotonicity of the stress-strain curve or, more precisely, by the convexity of the strain energy density function (Marsden and Hughes, 1983). The function F is nonnegative (Rice, 1968), but is not necessarily convex. The straightforward mathematical example is $F(Q_1, Q_2)=|Q_1\ Q_2|^{(n+1)/2}$.

In order to demonstrate the possible loss of convexity in a physical problem, we address the case of a penny-shaped crack embedded in an infinite isotropic power-law matrix subjected to axisymmetric remote loading, characterized by the axial and radial stresses Q_1 and Q_2, respectively. We consider three materials which can be generated from (1) as tensorial extensions. The first one is the incompressible material given by

$$\mathbf{E} = \frac{3}{2}\epsilon_0\left(\frac{\bar{\sigma}}{\sigma_0}\right)^{n-1}\frac{\mathbf{S}}{\sigma_0}, \tag{20}$$

$$\bar{\sigma} = \left(\frac{3}{2}\mathbf{S}\cdot\mathbf{S}\right)^{\frac{1}{2}}, \tag{21}$$

where $\mathbf{S}$ is the stress deviator and we take $n=3$. The second material is linear elastic ($n=1$) with Young's modulus $E=\sigma_0/\epsilon_0$ and Poisson's ratio ν. The last case is an isotropic, power-law material, *compressible* material, whose constitutive equations are derived from (20), (21) by substitution of the tensor $\mathbf{T}$ itself for the stress deviator $\mathbf{S}$. The values of σ_0, ϵ_0, and ν are not important because they appear as constant multipliers.

The first example is treated in detail by He and Hutchinson (1981), for the case $Q_1>0$, $Q_1>Q_2$. The suggested functional fit to the numerical solution is given by

$$F(\mathbf{Q}) = 4\sigma_0\epsilon_0 a^3\left(1+\frac{3}{n}\right)^{-\frac{1}{2}}\cdot\left(\frac{Q_1-Q_2}{\sigma_0}\right)^{n-1}\cdot\left(\frac{Q_1}{\sigma_0}\right)^2, \tag{22}$$

where a is the crack radius. The above expression gives us concave $F(\mathbf{Q})$, which can be seen directly from deriving the Hessian matrix. The formula is derived from a perturbation technique, agrees well with numerical solutions providing $x<0.6$, and for larger x it fails to give an accurate estimate (He and Hutchinson, 1981). The finite element analysis of the problem, which we have conducted, shows that at approximately the same point ($x\approx 0.6$) the complete numerical solution gains convexity; therefore, we may conclude that there is conditional convexity in this case.

The well-known solution (Sneddon, 1964) for the isotropic linear material coincides with (22) for $n=1$ and $\nu=1/2$, and is given by

$$F(\mathbf{Q}) = \frac{8(1-\nu^2)}{3E}a^3Q_1^2. \tag{23}$$

This expression gives only one nonzero component, Γ_{11}, of the Hessian matrix, which, of course, retains positive semidefiniteness, but relations (16) degenerate to triviality.

By performing a finite element analysis we find that the third material gives us an unconditionally convex potential, and the main result of the first section is of use.

In the above examples we have encountered three possible situations for two-dimensional $\mathbf{Q}$ space; namely, relations (16) are relevant at some points in the domain, they are relevant throughout the $\mathbf{Q}$ space, or they cannot be applied at all. The heuristic conclusion may be drawn if we consider the dimensions of the $\mathbf{Q}$ space of the two auxiliary and the main problem for all three materials. In the first example the solution of the problem without the crack depends only on the applied equivalent Mises stress $\bar{\sigma}$. If we introduce a new set of generalized forces, namely

$$Q_1' = \frac{Q_1+2Q_2}{3} \quad Q_2' = Q_1 - Q_2, \tag{24}$$

where the first equation of (24) defines the applied hydrostatic pressure and the second equation defines the equivalent Mises stress, then the dimension of $\mathbf{Q}'$-space is one in the context of the problem without the crack. The main and the other auxiliary problem, on the other hand, exhibit two-dimensional load space. It is clear from (23) that an analogous situation occurs with the linear elastic material, except that the main problem is the one which has the reduced space. The potential due to the introduction of the crack does depend on the single force Q_1, but, by superposition, is independent of Q_2. Only for the last example is there a truly two-dimensional $\mathbf{Q}$ space for all three problems.

It is clear that in the first two examples there exists some set $\mathbf{Q}$, which essentially forms the null-space of $F(\mathbf{Q})$ for the main or the auxiliary problem. Obviously, it is hydrostatic pressure for the incompressible material and stressing parallel to the crack plane for the main problem in the linear case. The loosely defined induction is that, in order to employ (16), all three problems must have the two-dimensional $\mathbf{Q}$ space. A more rigorous statement would, perhaps, require the definition of F on the complement of the null-space.

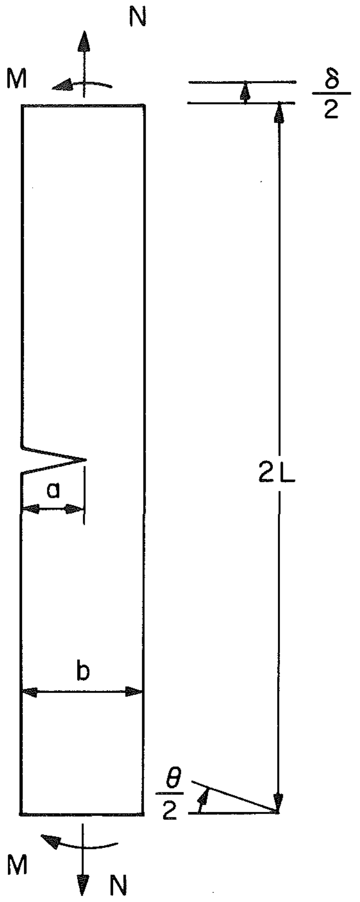

Fig. 1 Single edge-cracked strip

The conclusion is heuristic but, nevertheless, seems to rehabilitate the "misbehavior" of the otherwise mathematically "loyal" equations.

It is important to note that this conclusion does not put any question marks on the substantial body of theoretical and computational effort (Budiansky et al., 1981; Rafalsky, 1985) in terms of the derivations and the implementation of a variational principle for determination of F directly, because here we deal only with the generalized force space of boundary tractions, rather than with a function space of Ritz procedure.

To conclude this section we would like to mention the possibility of including the J integral into a gradient structure analogous to (2), which leads to the correlation between near and far fields and, of course, to another group of consistency relations. The procedure that was initially suggested by Parks et al. (1983) and later was applied by Shih and Needleman (1984) is essentially based on finite difference approximation of the gradient scheme for planar and axisymmetric problems.

Numerical Example

A single edge-cracked strip, Fig. 1, subjected to a remote loading under plane-strain conditions is considered. The dimensions are:

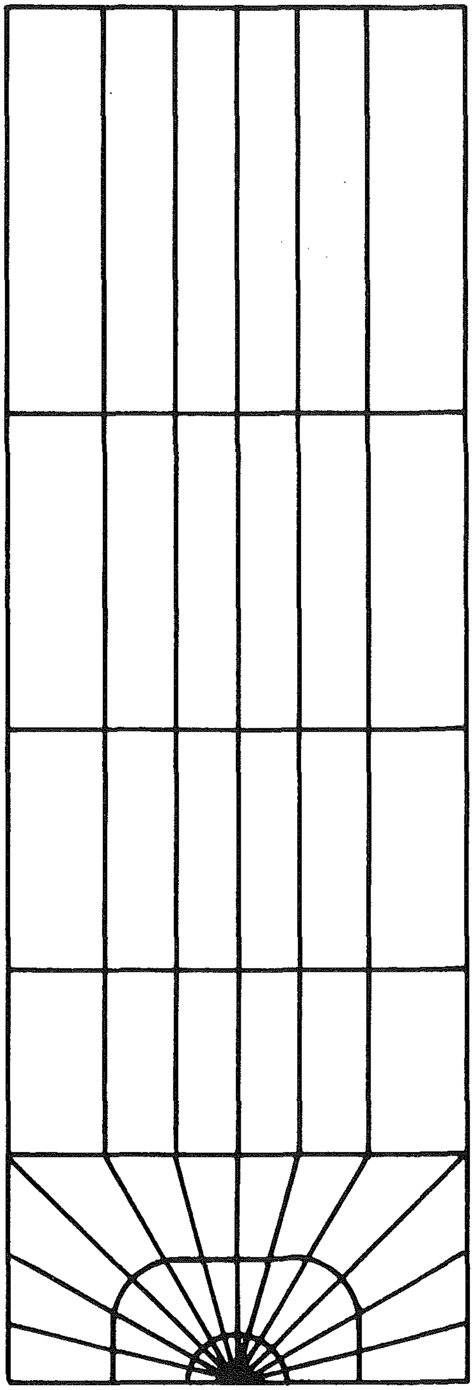

Fig. 2 Finite element mesh

Table 1 Pure tension data, $n = 5$, $K = 10^6$, $a/b = 1/2$

Reference	f	y	h
Kumar et al.	83.90	−2.393	309.9
Shih and Needleman	113.1	−2.430	407.4
current	99.00	−2.677	390.2

Table 2 Combined loading data, $K = 10^6$, $n = 5$, $a/b = 1/2$†

x	f	y	Lower Bound	Intermediate Value	Upper Bound
.0000	99.039237	-2.677448	–	–	–
.0001	98.881223	-2.676500	1.000268	1.000266	1.000268
.0002	98.720673	-2.675612	1.000535	1.000537	1.000536
.0003	98.564139	-2.674622	1.000803	1.000802	1.000804
.0004	98.405337	-2.673701	1.001071	1.001071	1.001072
.0005	98.247815	-2.672751	1.001338	1.001338	1.001341
.0006	98.090018	-2.671816	1.001606	1.001606	1.001609
.0007	97.929625	-2.670958	1.001873	1.001880	1.001878
.0008	97.776636	-2.669905	1.002140	1.002141	1.002147
.0009	97.618779	-2.668991	1.002408	1.002411	1.002416
.0010	97.461915	-2.668057	1.002675	1.002679	1.002685

Table 3 Pure tension data for variable penalty term, $x = 0$, $n = 5$, $a/b = 1/2$

$\log K$	h	f	y	x_{min}
0	393.7	101.8	-2.644	.0060
1	390.5	99.30	-2.674	.0012
2	390.3	99.05	-2.676	.0008
4	390.2	99.05	-2.677	.0008
6	390.2	99.04	-2.677	.0008

$$a = 10, \quad b = 20, \quad L = 60.$$

The constitutive behavior is modeled by (19)-(21) with numerical values of material constants:

$$\sigma_0 = 1, \quad \epsilon_0 = 1, \quad K = 10^6, \quad n = 5.$$

The values of σ_0 and ϵ_0 do not correspond to any real material, but as long as we are able to scale solutions, the idea of operating with more computationally convenient numbers is rather helpful. The finite element discretization is given in Fig. 2. The plane strain eight-node hybrid element with nine integration points and a bilinear interpolation for pressure is employed.

The remote forces per unit thickness are tensile load $N = 20$ and varying *positive* bending moment M, tending to close the crack. We are interested in the pure tension solution and apply bending only for the purpose of simulation of conditions (16). The generalized forces are identified as $Q_1 := N$, $Q_2 := M/b$ with corresponding pair of generalized displacements $q_1 := \delta$ and $q_2 := \theta b$. It is understood that the generalized displacements refer to the contribution due to the crack, as discussed in the previous section.

The potential $F(\mathbf{Q})$ and the J integral are taken in convenient dimensional forms

$$F(\mathbf{Q}) = \frac{1}{n+1}\,\sigma_0\epsilon_0 b^2 f(x)\left(\frac{N}{\sigma_0 b}\right)^{n+1}, \tag{25}$$

$$J = \sigma_0\epsilon_0 b h(x)\left(\frac{N}{\sigma_0 b}\right)^{n+1}. \tag{26}$$

The results of the computations are given in Table 1. We conclude that the current analysis gives results close to those of Shih and Needleman (1984) for the values of the rotation and the J integral; the displacement is somewhere between the earlier reported data. It is worth mentioning that the main point of discrepancy between the previous data is in the near field quantities; therefore, our results rather support the data reported by Shih and Needleman (1984).

The next part of our analysis is concerned with the simulation of data for relations (16). It is obvious that in this example problem, consistency relations can be of importance. But

---

† In the upper block of the table, relations (16) are not valid, in the next block they should be valid according to (27), (28), and in the last part relations (16) are unconditionally valid.

on the other hand, if values of x and x_0 are sufficiently close we expect the interference of the numerical noise in the tabulated data to be substantial; therefore, we have to decide on a minimum value, $x_{\min}$; such that for all $x - x_0 \geq x_{\min}$, consistency relations give us reasonable conclusions.

We adopt a very simplified estimate. The difference between bounding terms in (16) at the pure tension limit $x_0 = 0$ is $(x - x_0)(y - y_0)$, and this should remain positive in the most unfavorable case. As we have four kinematical data entries in the above formula, then we require

$$y - y_0 \geq 4e_{\mathbf{q}}, \tag{27}$$

where $e_{\mathbf{q}}$ is the relative error in $\mathbf{q}$. From the homogeneity and dimensional considerations we can take:

$$e_{\mathbf{q}} = ne_{\mathbf{R}}, \tag{28}$$

where $e_{\mathbf{R}}$ is the relative error in nodal reaction force in the virtual work sense, and in the analysis with the ABAQUS program, the maximum value of this error has been set at 10^{-4}. In expression (28), we have neglected a dimensionless constant multiplier expected to be of order unity. Relations (27), (28) form the implicit conditions on $x_{\min}$. The results of computations are given in Table 2 and give $x_{\min} = 8.10^{-4}$, which is in a fair agreement with conditions (27), (28) which give the value of $x_{\min} = 3.10^{-4}$. Therefore, we *may* claim that our data is *probably acceptable*.

The section is concluded by the consideration of the penalty term as a possibility for the loss of homogeneity. In this set of computations we take K varying from 1 to 10^6, keeping the rest of the material constants to be the same.

The results of Table 3 show that the maximum difference for various $K \geq 100$, in $x_{\min}$, J integral, and $\mathbf{q}$, only appears in the fourth digit. These results suggest that one might be able to use moderate values of the penalty K. There are clear advantages to such a procedure because the computations converge more rapidly and there is less chance to encounter numerical difficulties. For small values of K (below 100) the most sensitive parameter turns out to be $x_{\min}$, though the physical quantities remain within an acceptable variation.

Acknowledgments

Special gratitude is expressed to the Data General Corporation for the major donation of computer hardware and software. The manuscript was typed by Masha Rodin.

References

Budiansky, B., Hutchinson, J. W., Slutsky, S., 1981, "Void Growth and Collapse in Viscous Solids," *Mechanics of Solids, The Rodney Hill 60th Anniversary Volume*, Hopkins, H. G., and Sewell, M. J., eds., Pergamon Press, Oxford, pp. 13-45.

He, M. Y., Hutchinson, J. W., 1981, "The Penny-Shaped Crack and the Plane Strain Crack in an Infinite Body of Power-Law Material," ASME JOURNAL OF APPLIED MECHANICS, Vol. 48, pp. 830-840.

Hutchinson, J. W., 1968, "Singular Behavior at the End of a Tensile Crack in a Hardening Material," *Journal of the Mechanics and Physics of Solids*, Vol. 16, No. 1, pp. 13-31.

Hutchinson, J. W., 1968, "Singular Behavior at End of Tensile Crack in Hardening Material," *Journal of the Mechanics and Physics of Solids*, Vol. 16, No. 1, pp. 13-31.

Kumar, V., German, M. D., Shih, C. F., 1981, "An Engineering Approach for Elastic-Plastic Fracture Analysis," EPRI Topical Report NP-1931, Electric Power Research Institute, Palo Alto.

Marsden, J. E., Hughes, T. J. R., 1983, *Mathematical Foundations of Elasticity*, Prentice-Hall, Englewood Cliffs, New Jersey.

Parks, D. M., Kumar, V., and Shih, C. F., 1983, "Consistency Checks for Power-Law Calibration Functions," *Elastic-Plastic Fracture: Second Symposium, Vol. 1—Inelastic Crack Analysis*, ASTM STP 803, Shih, C. F., and Gudas, J. P., eds., American Society for Testing and Materials, Philadelphia, pp. I-370-I-383.

Rice, J. R., 1968, "Mathematical Analysis in the Mechanics of Fracture," in *Fracture*, Vol. II, Liebowitz, H., ed., Academic Press, New York, pp. 191-311.

Rice, J. R., Rosengren, G. F., 1968, "Plane Strain Deformation Near a Crack Tip in Power-Law Hardening Material," *Journal of the Mechanics and Physics of Solids*, Vol. 16, No. 1, pp. 1-12.

Rafalski, P., 1985, "Extremum Principles for Crack Energy-Release in Elastic Body," *International Journal of Solids and Structures*, Vol. 21, No. 3, pp. 225-234.

Shih, C. F., Needleman, A., 1984, "Fully Plastic Crack Problems: Solutions by a Penalty Method That Pass the Consistency Check," JOURNAL OF APPLIED MECHANICS, Vol. 51, No. 1, pp. 48-64.

Sneddon, I. N., 1964, "The Distribution of Stress in the Neighbourhood of a Crack in an Elastic Solid," *Proceedings of the Royal Society*, London, A 187, pp. 229-260.

H. M. Koh
Research Associate.

R. B. Haber
Associate Professor of Civil Engineering.

Department of Civil Engineering,
University of Illinois at Urbana-Champaign,
Urbana, Ill. 61801

Elastodynamic Formulation of the Eulerian-Lagrangian Kinematic Description

An extension of the Eulerian-Lagrangian kinematic description (Haber, 1984) to elastodynamic problems is presented. Expressions are derived for field variables and material time derivatives using the new kinematic description. The variational equation of motion is written in a weak form suitable for use with isoparametric finite elements. The new kinematic model allows a finite element mesh to continuously adjust for changes in the structural geometry, material interfaces, or the domain of the boundary conditions without a discrete remeshing process. Applications of the new model to mode I dynamic crack propagation demonstrates its advantages over moving mesh methods based on conventional Lagrangian kinematic models. Numerical results show excellent agreement with analytic predictions.

Introduction

Dynamic analysis in solid mechanics is usually based on a Lagrangian kinematic description in which the motion of particles is measured from a known material configuration. In finite element analysis, this implies that the material geometric discretizaton is selected a priori and the finite element mesh is required to follow the material motion.

There are certain problems that require frequent or continuous remeshing if the mesh is forced to follow the material motion. These include situations in which either the structural geometry, material interfaces, or the domain of the boundary conditions change with time; and may pertain to either large or small-deformation behavior. For example, in dynamic crack propagation the material particle associated with the crack tip changes as the crack propagates, and it would be impossible to describe correctly the crack-tip motion without a remeshing process. The displacement and velocity fields need to be updated correctly for the new material discretization to accomplish the remeshing. This is usually done approximately in a conventional Lagrangian description using interpolation techniques (Nishioka and Atluri, 1980a). Incremental contact behavior is another example that calls for some form of remeshing (Haber and Hariandja, 1985). Bazant et al. (1978) have applied a special form of an Eulerian description to mode I dynamic crack propagation problems using a moving coordinate system centered at the crack tip. The finite element mesh is translated as a rigid body to follow the crack-tip motion. This procedure is restricted to semi-infinite strips whose surfaces are parallel to the direction of crack growth. Also, appropriate dynamic boundary conditions must be determined for the leading and trailing edges of the finite element mesh.

The mixed Eulerian-Lagrangian kinematic description (ELD) (Haber, 1984; Haber and Hariandja, 1985) provides an alternative to conventional remeshing procedures to overcome these problems. Haber (1984) presents a general development of the ELD for large-deformation analysis. The ELD shares a similar basic concept with the arbitrary Lagrangian-Eulerian (ALE) descriptions used in fluid mechanics (Donea et al., 1977; Belytschko and Kennedy, 1978; Hughes et al., 1981). However, the displacement-based ELD is appropriate for analysis in solid mechanics, and is distinct from the ALE models that use material velocity as the primary unknown. A specialization of the ELD to small-deformation behavior is the basis of explicit expressions for energy release rates used to analyze mixed-mode crack problems (Haber and Koh, 1984; Haber and Koh, 1985). To date, the ELD has been applied primarily to static problems.

In this paper the ELD is extended to the analysis of dynamic problems. A convenient fixed domain, defined in a special reference coordinate system, is selected as the spatial reference configuration. The mapping of the reference configuration to an actual material domain, defined in the global coordinate system, varies with time. The motion of material particles, other field variables, and the field equations are all expressed in the reference coordinate system. Expressions for material and spatial time derivatives in the ELD are presented and applied to the variational equations of motion. A special weak form of the variational equations of motion is presented for implementing the dynamic ELD in isoparametric finite element procedures. Here, the variation of the mapping between the reference and material configurations constitutes motion of the finite element mesh. Example analyses of dynamic crack propagation problems are presented to demonstrate the new model. Advantages of the dynamic ELD over conventional kinematic models are noted. Further applications of the

---

Contributed by the Applied Mechanics Division for publication in the JOURNAL OF APPLIED MECHANICS.

Discussion on this paper should be addressed to the Editorial Department, ASME, United Engineering Center, 345 East 47th Street, New York, N.Y. 10017, and will be accepted until two months after final publication of the paper itself in the JOURNAL OF APPLIED MECHANICS. Manuscript received by ASME Applied Mechanics Division, October 7, 1985; final revision, March 17, 1986.

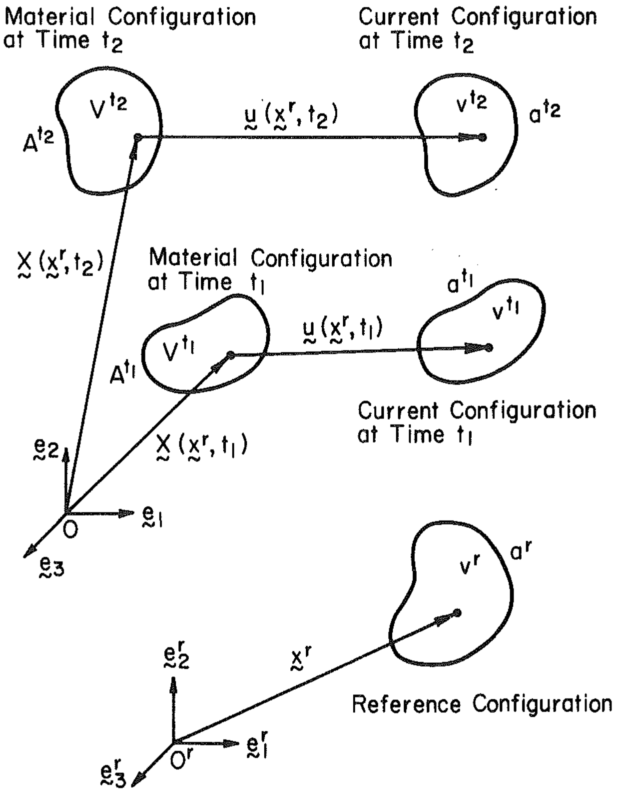

Fig. 1 Eulerian-Lagrangian kinematic model

ELD to dynamic crack propagation problems will be reported in a later paper.

Kinematics

The ELD kinematic model is illustrated in Fig. 1. A fixed Cartesian coordinate system is used to describe the material and current configurations, denoted by volumes V and v. Superscripts t_1 and t_2 are used to refer to two distinct times. An independent spatial reference configuration v^r is selected which is invariant in time. A location on the reference configuration is denoted by its position vector $\mathbf{x}^r$ defined in a separate reference coordinate system. At any time t a reference vector $\mathbf{x}^r$ is mapped onto a material particle identified by its position vector $\mathbf{X}^t$ in the material configuration. This mapping varies with time, so the material volume associated with v^r changes. Changes in the material particle associated with a fixed coordinate $\mathbf{x}^r$ are the Eulerian part of the kinematic model; the displacement of a particle $\mathbf{u}^t$ is the Lagrangian part. The reference coordinates $\mathbf{x}^r$ are the only independent spatial variables and both the displacement field and the mapping to the material configuration change with time.

$$\mathbf{u} = \mathbf{u}(\mathbf{x}^r, t) \tag{1}$$

$$\mathbf{X} = \mathbf{X}(\mathbf{x}^r, t) \tag{2}$$

Hereafter the superscript denoting time is omitted for brevity.

The following notation for differential operators is used.

$$\frac{\partial(\ )}{\partial X_i} = (\ )_{;i}, \qquad \frac{\partial(\ )}{\partial x^r_i} = (\ )_{,i} \tag{3}$$

The Jacobian of the mapping between $\mathbf{X}$ and $\mathbf{x}^r$ has components $\tilde{J}_{ij} = X_{i,j}$ and the inverse, or Eulerian, Jacobian components are $\bar{J}_{ij} = x^r_{i;j} = \tilde{J}^{-1}_{ij}$. Differential volumes dV and dv^r in the material and reference configuration, respectively, are related by $dV = \tilde{J} dv^r$, where $\tilde{J}$ is the determinant of the Jacobian components $\tilde{J}_{ij}$. It is assumed that the determinant of the Jacobian is positive at all points in the structure. Differential areas dA and da^r in the material and reference configuration, respectively, are related by $dA = K_a da^r$; where K_a is an area metric between two configurations.

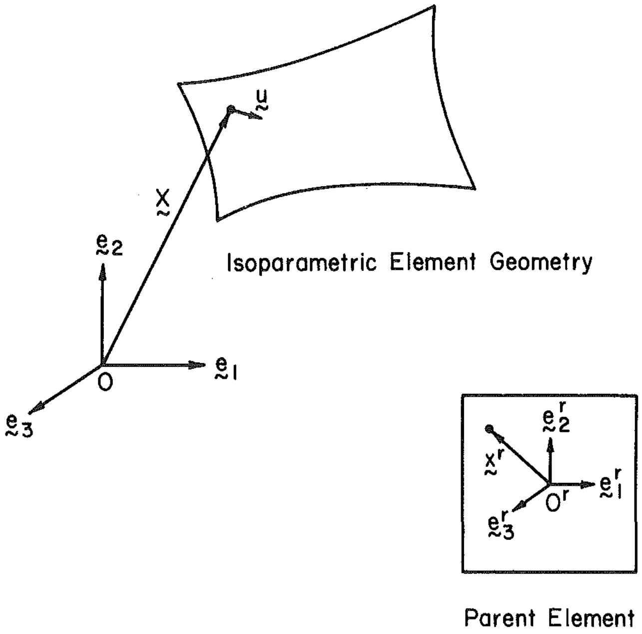

Fig. 2 Specialization of the ELD model to isoparametric finite elements

In the following, it is assumed that the deformations at all times can be adequately described by the engineering strain tensor; but that finite changes in the mapping $\mathbf{X}(\mathbf{x}^r, t)$ are possible. The use of large-deformation strain measures in the ELD is addressed by Haber (1984) for static problems, and has no effect on the dynamic part of the formulation. The components of the small-deformation strain tensor are

$$e_{ij} = \frac{1}{2}\,(u_{i,k}\bar{J}_{kj} + u_{j,k}\bar{J}_{ki}) \tag{4}$$

Time derivatives in the two coordinate systems are written as

$$\left.\frac{\partial(\ )}{\partial t}\right|_{\mathbf{X}\text{fixed}} = (\overset{*}{\ }); \quad \text{Material time derivatives} \tag{5}$$

$$\left.\frac{\partial(\ )}{\partial t}\right|_{\mathbf{x}^r\text{fixed}} = (\dot{\ }); \quad \text{Spatial time derivatives} \tag{6}$$

The material and spatial time derivatives are related by

$$(\overset{*}{\ }) = (\dot{\ }) - (\ )_{;j}\dot{X}_j = (\dot{\ }) - (\ )_{,k}\bar{J}_{kj}\dot{X}_j \tag{7}$$

and the spatial time derivative of the inverse Jacobian is expressed as (see equation (25) in Haber, 1984),

$$\dot{\bar{J}}^t_{ij} = \lim_{\Delta t \to 0} \frac{1}{\Delta t}\,(\bar{J}^{t+\Delta t}_{ij} - \bar{J}^t_{ij}) = -\bar{J}^t_{ik}\dot{X}^t_{k,l}\bar{J}^t_{lj} \tag{8}$$

Then the velocity and acceleration of a material particle are

$$\overset{*}{u}_i = \dot{u}_i - u_{i;j}\dot{X}_j = \dot{u}_i - u_{i,k}\bar{J}_{kj}\dot{X}_j \tag{9}$$

$$\overset{**}{u}_i = \ddot{u}_i - 2\dot{u}_{i;j}\dot{X}_j + 2u_{i;j}\dot{X}_{j;k}\dot{X}_k - u_{i;j}\ddot{X}_j + u_{i;jk}\dot{X}_j\dot{X}_k \tag{10}$$

Variational Equations of Motion

In this section the governing equations for an elastodynamic problem are formulated in the reference coordinate system. The equilibrium and constitutive relations, written in the material configuration, are

$$\sigma_{ij;j} + F_i = \rho\,\overset{**}{u}_i \tag{11}$$

$$\sigma_{ij} = C_{ijkl}e_{kl} \tag{12}$$

where F_i are components of body force per unit volume, σ_{ij} are components of the Cauchy stress tensor, and C_{ijkl} are components of the elasticity tensor. The mass density ρ is assumed to be uniform over the volume V. The strain-displacement relations are defined in equation (4). The displacement and traction boundary conditions are

$$u_i = \bar{u}_i(\mathbf{x}^r, t) \quad \text{on } A_u \tag{13}$$

$$\sigma_{ij} n_j = T_i = \bar{T}_i(\mathbf{x}^r, t) \quad \text{on } A_T \tag{14}$$

in which $\bar{u}_i$ and $\bar{T}_i$ are prescribed displacements and surface tractions, A_u and A_T are surface regions in the material configuration on which displacements and tractions are prescribed, and n_j are the direction cosines of the surface normal vector.

Let δu_i denote a kinematically admissible variation of the displacements at time t and let $\delta e_{ij} = 1/2(\delta u_{i;\,j} + \delta u_{j;i})$. After substitution of equation (10) into the variational equations of motion we obtain

$$\begin{aligned}
&\int_V \sigma_{ij}\delta e_{ij} dV - \int_V F_i \delta u_i dV - \int_{A_T} \bar{T}_i \delta u_i dA + \int_V \rho \ddot{u}_i \delta u_i dV \\
&- \int_V 2\rho \dot{u}_{i;\,j} \dot{X}_j \delta u_i dV + \int_V 2\rho u_{i;\,j} \dot{X}_{j;k} \dot{X}_k \delta u_i dV \\
&- \int_V \rho u_{i;\,j} \ddot{X}_j \delta u_i dV + \int_V \rho u_{i;\,jk} \dot{X}_j \dot{X}_k \delta u_i dV = 0
\end{aligned} \tag{15}$$

The last integral in equation (15) includes a second-order spatial derivative of the displacements, which would require the trial functions in an assumed-displacment solution procedure to be C_1 continuous. This requirement can be inconvenient in finite element solutions, so the Gauss theorem is applied to the last integral to relax the continuity requirement. Finally, the variational equations are rewritten in the reference coordinate system;

$$\begin{aligned}
&\int_{v^r} \sigma_{ij}\delta e_{ij} \tilde{J} dv^r - \int_{v^r} F_i \delta u_i \tilde{J} dv^r - \int_{a^r_T} \bar{T}_i \delta u_i K_a da^r \\
&+ \int_{v^r} \rho \ddot{u}_i \delta u_i \tilde{J} dv^r - \int_{v^r} 2\rho \dot{u}_{i,k} \bar{J}_{kj} \dot{X}_j \delta u_i \tilde{J} dv^r \\
&+ \int_{v^r} \rho u_{i,k} \bar{J}_{kl} \dot{X}_{l,m} \bar{J}_{mj} \dot{X}_j \delta u_i \tilde{J} dv^r \\
&- \int_{v^r} \rho u_{i,k} \bar{J}_{kj} \ddot{X}_j \delta u_i \tilde{J} dv^r \\
&+ \int_{a^r} \rho u_{i,k} \bar{J}_{kj} \dot{X}_j \dot{X}_l n_l \delta u_i K_a da^r \\
&- \int_{v^r} \rho u_{i,k} \bar{J}_{kj} \dot{X}_j \dot{X}_{l,m} \bar{J}_{ml} \delta u_i \tilde{J} dv^r \\
&- \int_{v^r} \rho u_{i,k} \bar{J}_{kj} \dot{X}_j \dot{X}_l \delta u_{i,m} \bar{J}_{ml} \tilde{J} dv^r = 0
\end{aligned} \tag{16}$$

where a^r_T is a surface area in the reference configuration corresponding to A_T. Equation (16) can serve as the basis of weak formulations of general, linearly elastic dynamic problems.

Equation (16) can be simplified for certain special cases. The surfaces of a finite body are constrained by $\dot{\mathbf{X}} \cdot \mathbf{n} = 0$ to prevent material motion across the physical boundaries of the structure. In this case the second surface integral in equation (16) vanishes. Note that the constraint does not hold when the reference configuration is mapped onto a subdomain of a large structure as in Bazant et al. (1978). In this case, some portions of a^r do not represent physical structure boundaries. When the mapping changes only in the X_1 direction, as in the analysis of mode I dynamic fracture problems, equation (16) reduces to

$$\begin{aligned}
&\int_{v^r} \sigma_{ij}\delta e_{ij} \tilde{J} dv^r - \int_{v^r} F_i \delta u_i \tilde{J} dv^r \\
&- \int_{a^r_T} \bar{T}_i \delta u_i K_a da^r + \int_{v^r} \rho \ddot{u}_i \delta u_i \tilde{J} dv^r \\
&- \int_{v^r} 2\rho \dot{u}_{i,k} \bar{J}_{k1} \dot{X}_1 \delta u_i \tilde{J} dv^r \\
&- \int_{v^r} \rho u_{i,k} \bar{J}_{k1} \ddot{X}_1 \delta u_i \tilde{J} dv^r \\
&- \int_{v^r} \rho u_{i,k} \bar{J}_{k1} (\dot{X}_1)^2 \delta u_{i,m} \bar{J}_{m1} \tilde{J} dv^r = 0
\end{aligned} \tag{17}$$

It is easily verified that the variational equation of motion by Bazant et al. (1978) for uniform ρ is equivalent to equation (17) if a moving spatial domain centered at the crack tip is chosen as the reference configuration in the dynamic ELD formulation. It should be noted that this equivalence is only valid for the special case of constant-velocity, uniform motion of the spatial domain. In fact, Bazant's equation is not valid for general nonuniform motions.[1]

Isoparametric Finite Element Model

This section presents a specialization of the dynamic ELD kinematic model to isoparametric finite element formulations. Finite element expressions are written for a general three-dimensional linear elastodynamic problem using equation (16). In general, the motion of a spatial domain can be either known or unknown in advance. In this paper the finite element formulation is only developed explicitly for a known mesh motion, but it can be extended to the case of unknown motion, as will be discussed later.

In the isoparametic specialization of the ELD a mapping is established between a mesh of isoparametric elements and an actual material domain. The kinematic model is depicted in Fig. 2. The parent element geometry is selected as the spatial reference configuration for each element. A local natural coordinate system is used as the reference coordinate system in each parent element. Motion of the finite element mesh is represented by changes in the isoparametric mapping. The displacement field, the element geometry and other field variables are interpolated using isoparametric shape functions as,

$$u_i = h_\alpha u_{i\alpha} \quad , \quad \mathbf{u} = \mathbf{H}\mathbf{U}_e \tag{18a}$$

$$\dot{u}_i = h_\alpha \dot{u}_{i\alpha} \quad , \quad \dot{\mathbf{u}} = \mathbf{H}\dot{\mathbf{U}}_e \tag{18b}$$

$$\ddot{u}_i = h_\alpha \ddot{u}_{i\alpha} \quad , \quad \ddot{\mathbf{u}} = \mathbf{H}\ddot{\mathbf{U}}_e \tag{18c}$$

$$\delta u_i = h_\alpha \delta u_{i\alpha} \quad , \quad \delta\mathbf{u} = \mathbf{H}\delta\mathbf{U}_e \tag{18d}$$

$$X_i = h_\alpha X_{i\alpha} \quad , \quad \mathbf{X} = \mathbf{H}\mathbf{X}_e \tag{18e}$$

$$\dot{X}_i = h_\alpha \dot{X}_{i\alpha} \quad , \quad \dot{\mathbf{X}} = \mathbf{H}\dot{\mathbf{X}}_e \tag{18f}$$

$$\ddot{X}_i = h_\alpha \ddot{X}_{i\alpha} \quad , \quad \ddot{\mathbf{X}} = \mathbf{H}\ddot{\mathbf{X}}_e \tag{18g}$$

where h_α are element shape functions, the subscripts $i\alpha$ indicate the component in direction i at node α ranging from 1 to the number of nodes in the element. The matrix **H** is the usual interpolation matrix containing the element shape func-

---

[1] The left-hand side of equation (20) in Bazant et al. (1978) is missing the term $\int_V \rho c \; \partial c/\partial x_1 \; \partial u_i/\partial x_1 \; \delta u_i dV$ which arises from a convective term in the spatial time derivative of $\partial u_i/\partial x_i$ for the case of general nonuniform motion. This integral cancels with the corresponding right-hand side term. For uniform motion these terms are zero, and have no effect.

tions, and column matrices with subscript e contain quantities measured in the global coordinate system, but evaluated at the element nodes.

Equations (18) are used to obtain a discrete form of equation (16),

$$\begin{aligned}
&\delta\mathbf{U}^T\Sigma\Big(\Big(\int_{v_e^r}\mathbf{B}^T\mathbf{E}\mathbf{B}\tilde{J}dv_e^r+\int_{v_e^r}\rho\mathbf{H}^T\mathbf{D}\mathbf{G}\tilde{J}dv_e^r\\
&\quad-\int_{v_e^r}\rho\mathbf{H}^T\ddot{\mathbf{A}}\mathbf{G}\tilde{J}dv_e^r+\int_{a_e^r}\rho\mathbf{H}^T\dot{\mathbf{A}}\mathbf{G}A_1K_a da_e^r\\
&\quad-\int_{v_e^r}\rho\mathbf{H}^T\mathbf{S}\mathbf{G}\tilde{J}dv_e^r-\int_{v_e^r}\rho\mathbf{G}^T\dot{\mathbf{A}}^T\dot{\mathbf{A}}\mathbf{G}\tilde{J}dv_e^r)\mathbf{U}\\
&\quad+\delta\mathbf{U}^T\Sigma\Big(\int_{v_e^r}\rho\mathbf{H}^T\mathbf{H}\tilde{J}dv_e^r\Big)\ddot{\mathbf{U}}\\
&\quad+\delta\mathbf{U}^T\Sigma\Big(-\int_{v_e^r}2\rho\mathbf{H}^T\dot{\mathbf{A}}\mathbf{G}\tilde{J}dv_e^r\Big)\dot{\mathbf{U}}\\
&\quad=\delta\mathbf{U}^T\Sigma\Big(\int_{v_e^r}\mathbf{H}^T\mathbf{F}_e\tilde{J}dv_e^r+\int_{a_T^r}\mathbf{H}^T\bar{\mathbf{T}}_eK_a da_e^r\Big)
\end{aligned}\tag{19}$$

in which the summation symbol indicates assembly over the number of elements, and v_e^r and a_e^r are volume and area in the parent element geometry. The column matrices $\mathbf{U}$, $\dot{\mathbf{U}}$, and $\ddot{\mathbf{U}}$ are assembled forms of the corresponding element matrices. $\mathbf{B}$ and $\mathbf{E}$ are the strain-displacement transformation and elasticity matrices. Other matrices and the scalar quantity A_1 are defined in Appendix 1. The reader is cautioned that $\dot{\mathbf{U}}$ and $\ddot{\mathbf{U}}$ do not contain material velocities and accelerations, but rather first and second-order spatial time derivatives of displacement at the finite element nodes.

The finite element equations obtained from equation (19) are

$$\mathbf{M}\ddot{\mathbf{U}}+\mathbf{C}\dot{\mathbf{U}}+\mathbf{K}\mathbf{U}=\mathbf{P}\tag{20}$$

where $\mathbf{M}$ is a consistent mass matrix, $\mathbf{C}$ and $\mathbf{K}$ are nonsymmetric "effective damping" and stiffness matrices, and $\mathbf{P}$ is a load vector. Such nonsymmetric matrices are common in moving mesh procedures (Nishioka and Atluri, 1980a; Bazant et al., 1978). Matrix expressions for $\mathbf{M}$, $\mathbf{C}$, $\mathbf{K}$, and $\mathbf{P}$ are presented in Appendix I. The solution to equation (20) can be obtained by either implicit or explicit time integration methods.

The matrices in equation (20) are evaluated based on the geometry at time $t + \Delta t$ when implicit integration is used. This presents no problem for cases in which the history of mesh motion is known. For cases where the element mesh motion is not known (e.g., crack propagation prediction, free surface and moving boundary problems), the variational equation (16) can be rewritten using incremental expressions for both the displacement and the mapping. This renders equation (16) nonlinear with two sets of unknown variables: increments in the displacements $\Delta\mathbf{u}$ and in the mapping $\Delta\mathbf{X}$. One way of solving the problem is to approximate $\Delta\mathbf{X}$ based on conditions at time t, and then treat the problem as a known mesh motion problem. Iteration might improve the prediction of the mesh motion. Another way is to add $\Delta\mathbf{X}$ as unknown solution variables and solve a linearized form of equation (16). This procedure requires additional constraint equations, derived from appropriate criteria (e.g., crack propagation criteria or moving boundary definitions), to determine the mesh motion. Explicit integration methods, based on known geometry at time t, produce simpler finite element expressions. Further study and tests are needed to demonstrate the practicality of the method for problems with unknown mesh motion.

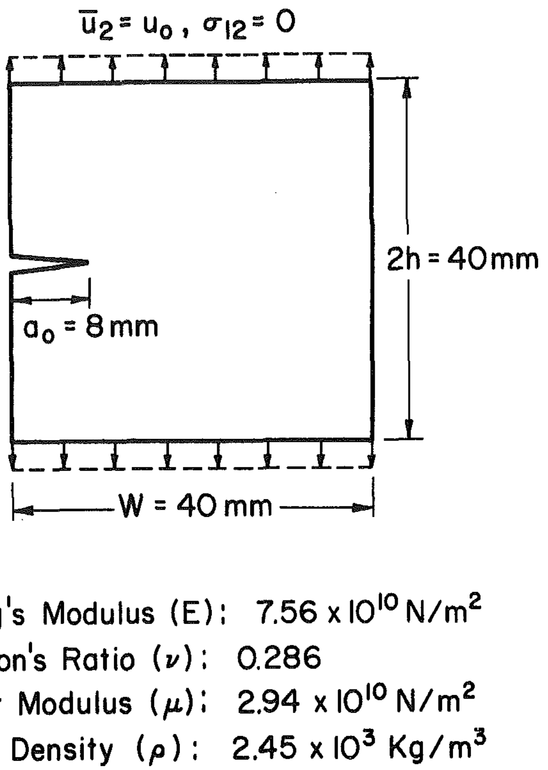

Fig. 3 Dimensions and material properties of a mode I dynamic crack propagation problem

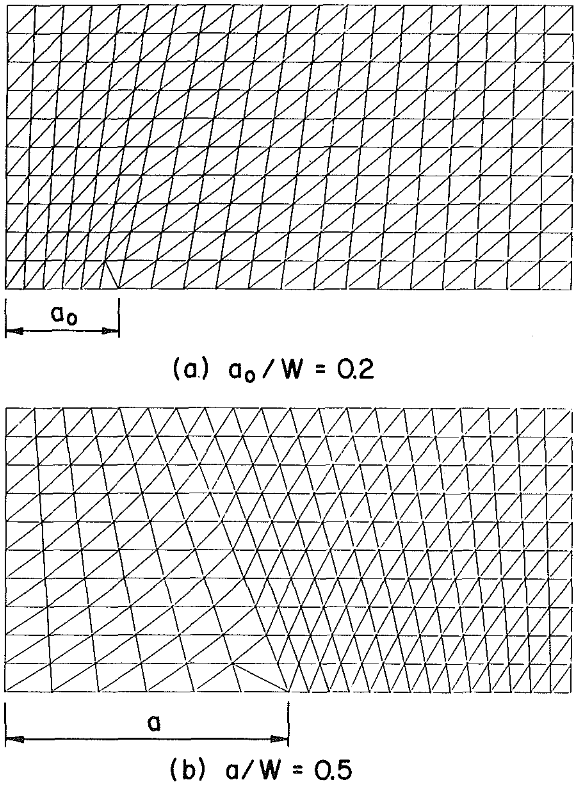

Fig. 4 Finite element mesh for a mode I dynamic crack propagatin problem ($v = 0.4\ C_s$): *a*) initial crack geometry; *b*) final mesh geometry

Numerical Examples of Mode I Dynamic Crack Propagation

In this section the dynamic ELD formulation is applied to the analysis of a mode I dynamic crack propagation problem.

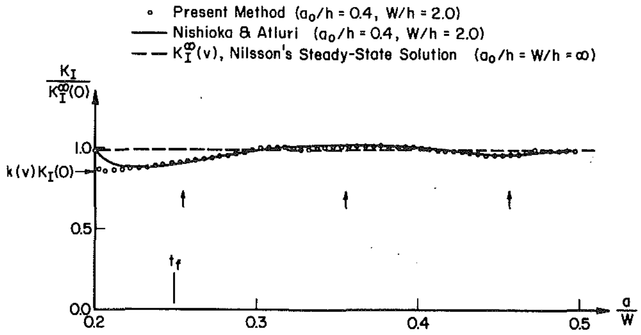

Fig. 5 Normalized stress intensity factor for a mode I dynamic crack propagation problem ($v = 0.2\ C_s$)

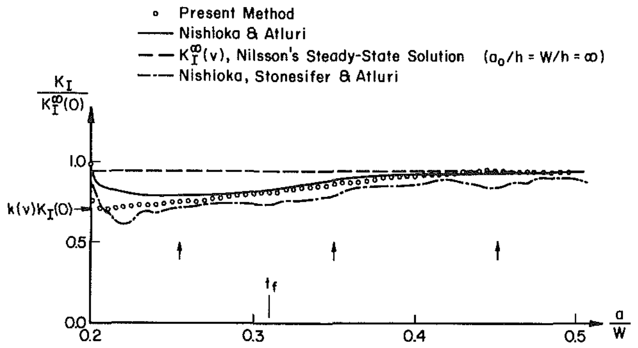

Fig. 6 Normalized stress intensity factor for a mode I dynamic crack propagation problem ($v = 0.4\ C_s$)

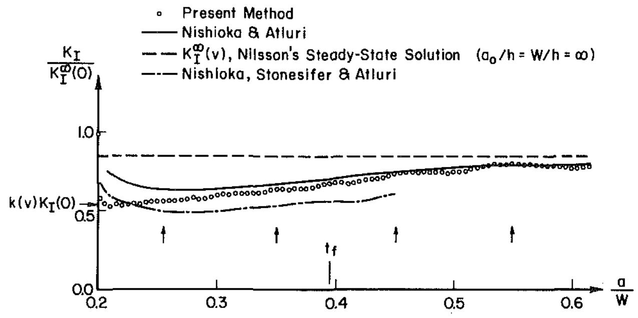

Fig. 7 Normalized stress intensity factor for a mode I dynamic crack propagation problem ($v = 0.6\ C_s$)

Results of finite element solutions are presented, and comparison is made with analytic predictions and other numerical results using conventional kinematic descriptions.

A square plate with an edge crack of length a_0 is subjected to statically applied prescribed displacements under plane strain conditions. After a given time the crack propagates with constant velocity, while the prescribed displacements are maintained. The dimensions and material properties are described in Fig. 3. Three different crack velocities are considered: $v = 0.2$, 0.4, and 0.6 C_s, where C_s is the shear wave speed. This problem is similar to the problem solved by Nilsson (1972), involving steady-state solutions for the problem of a semi-infinite crack propagating with constant velocity in an infinite strip.

A mesh of linear strain triangle (LST) isoparametric elements is used to model the upper half of the structure. Four quarter-point singular LST isoparametric elements (Barsoum, 1976) are used to model the crack-tip elements. Quarter-point isoparametric elements are often used to model the singular strain field near the crack tip in stationary crack problems because they are simple to implement and available in most finite element programs. However, in a conventional Lagrangian kinematic description, the use of quarter-point elements does not generate the desired singularity of order $r^{-1/2}$ in the material velocity field for a dynamically propagating crack. The convective term in equation (9) in the dynamic ELD does introduce the appropriate singularity if quarter-point isoparametric elements are used. The singularity vanishes for a stationary crack. Thus, there is no need to use special singular elements, as in Nishioka and Atluri (1980a), which introduce compatibility problems at the interfaces between the singular and conventional elements. The finite element mesh used in the present study for $v = 0.4\ C_s$ is shown in Fig. 4. The mesh in Fig. 4(*a*) represents the initial crack geometry. As the crack propagates, the mesh changes continuously to model the crack growth. The final mesh at $a/W = 0.5$ is shown in Fig. 4(*b*).

The finite element solutions were obtained using implicit integration with Newmark's parameters $\delta = 0.5$ and $\beta = 0.25$. The initial crack length a_0 is 8 mm, and the change in crack length per integration time step is $\Delta t \cdot v = 0.2$ mm. The dynamic energy release rate for the propagating crack was obtained by considering the increments in global external work and internal energy during a time step. The stress intensity factor (SIF) was computed from the energy release rate using the relation given by Freund (1973). The SIF values plotted in Figs. 5–7 are normalized by the SIF of a stationary, semi-infinite crack in an infinite strip, $K_I^\infty(0) = u_0 E/h^{1/2}(1-\nu^2)$. To indicate the expected long-term behavior, normalized values of Nilsson's steady-state solution are plotted as dashed lines.

Correct tracking of the SIF is critical in the study of crack initiation, propagation, and arrest in brittle materials. The dynamic SIF for a running crack in a half plane can be expressed as the product of a universal function of crack-tip velocity $k(v)$ and the SIF of the equivalent stationary crack (Freund, 1973). Thus, the SIF immediately after the crack starts propagating should be $k(v)K_I(0)$, where $K_I(0)$ is the SIF for a stationary crack of length a_0. This implies a negative jump in the SIF when the crack begins to propagate; because $k(v) < 1.0$ for $v > 0$. Normalized values of $k(v)K_I(0)$ using finite element solutions for $K_I(0)$ are marked on the vertical axes in Figs. 5–7. Previous finite element solutions have not been able to reproduce the expected SIF jump. For all crack-tip velocities studied, the present method predicts values of SIF virtually identical to $k(v)K_I(0)$ immediately after the crack starts propagating, and a steadily increasing SIF until the time t_f when the first reflected waves arrive at the crack tip. In the long term, the SIF approaches Nilsson's steady-state solution.

Numerical results obtained with moving singular elements implemented in a conventional Lagrangian mesh (Nishioka and Atluri, 1980b; Nishioka et al., 1981) are presented for comparison. This method requires frequent remeshing with interpolation of field variables to the new node locations. Results are shown in Figs. 5–7 for a special singular element with propagation-eigen-functions (Nishioka and Atluri, 1980b) and the usual quarter-point isoparametric elements with a global energy balance computation (Nishioka et al., 1981). Upward arrows indicate the times at which a remeshing process is performed in the moving singular element procedure. For $v = 0.2\ C_s$, the results obtained with the quarter-point and propagation-eigen-function singular elements are nearly identical, so only the results of the latter method are plotted. Unlike the results obtained with the dynamic ELD, the propagation-eigen-function results do not match the analytic prediction of an instantaneous drop in the SIF as the crack begins to propagate. The SIF values are overestimated, and the error is larger for higher crack-tip velocities. A disturbance in the SIF is reported in (Nishioka et al., 1981) for the quarter-point isoparametric element procedure at higher crack-tip velocities each time remeshing is performed. This might be an artifact of the displacement discontinuities (in time) that are produced by remeshing operations in a conventional Lagrangian description. In the dynamic ELD formulation the displacement field evolves continuously as the mesh moves, and no disturbance of the SIF is observed.

Conclusions

A version of the Eulerian-Lagrangian kinematic model for the analysis of elastodynamic problems has been developed. Variational equations of motion, suitable for finite element formulations, were derived using the new kinematic model. The new formulation is particularly effective for analyzing problems in which the structural geometry or the domain of the boundary conditions change with time. The ELD allows the finite element mesh to change continuously without a discrete remeshing process, so the displacement and velocity field remain continuous in the time domain. In applications to mode I dynamic crack propagation problems, the new kinematic description correctly models the singularities in both the displacement and material velocity fields when combined with singular quarter-point isoparametric elements. Numerical examples demonstrate the advantages of the ELD with respect to conventional kinematic descriptions and show excellent agreement with analytic predictions. The ability to correctly predict the jump in the SIF at the onset of crack propagation is a significant indication of the reliability and accuracy of the dynamic ELD. Further details of implementation and analysis results for dynamic crack propagation problems will be reported in a later paper.

In the present work the consistent mass matrix is used and the nonsymmetric equations are solved directly. Whether it is possible to improve the accuracy or numerical efficiency of the solution by using a lumped mass matrix (Bazant et al., 1976), symmetric approximations to the stiffness and effective damping matrices or indirect equation solvers (Nishioka and Atluri, 1980a); Bazant et al., 1978) has not yet been studied.

Acknowledgments

This research was supported in part by National Science Foundation grant No. MEA 84-00654. Transient computations were performed on the Boeing Computer Services Cray X-MP with the support of the National Science Foundation Office of Advanced Scientific Computation. Pre and post-processing of the numerical data was carried out on the VAX and Image Processing System, University of Illinois at Urbana-Champaign.

References

Barsoum, R. S., 1976, "On the Use of Isoparametric Finite Elements in Linear Fracture Mechanics," *International Journal of Numerical Methods in Engineering*, Vol. 10, pp. 25–37.

Bazant, Z. P., Glazik, J. L., and Achenbach, D., 1978, "Elastodynamic Fields Near Running Cracks by Finite Elements," *Computers and Structures*, Vol. 8, pp. 193–198.

Bazant, Z. P., Glazik, J. L., and Achenbach, D., 1976, "Finite Element Analysis of Wave Diffraction by a Crack," ASCE, *Journal of the Engineering Mechanics Division*, Vol. 102, No. EM3, pp. 479–496.

Belytschko, T. B., and Kennedy, J. M., 1978, "Computer Models for Subassembly Simulation," *Nuclear Engineering and Design*, Vol. 49, pp. 17–38.

Donea, J., Fasoli-Stella, P., and Giuliani, S., 1977, "Lagrangian and Eulerian Finite Element Techniques for Transient Fluid-Structure Interaction Problems," *4th International Conference on Structural Mechanics in Reactor Technology*, San Francisco, paper B1/2.

Freund, L. B., 1973, "Crack Propagation in an Elastic Solid Subjected to General Loading—III. Stress Wave Loading," *Journal of the Mechanics and Physics of Solids*, Vol. 21, pp. 47–61.

Haber, R. B., 1984, "A Mixed Eulerian-Lagrangian Displacement Model for Large-Deformation Analysis in Solid Mechanics," *Computer Methods in Applied Mechanics and Engineering*, Vol. 43, pp. 277–292.

Haber, R. B., and Hariandja, B. H., 1985, "An Eulerian-Lagrangian Finite Element Approach to Large-Deformation Frictional Contact," *Computers and Structures*, Vol. 20, pp. 193–201.

Haber, R. B., and Koh, H. M., 1985, "Explicit Expressions for Energy Release Rates Using Virtual Crack Extension," *International Journal for Numerical Methods in Engineering*, Vol. 21, pp. 301–315.

Haber, R. B., and Koh, H. M., 1984, "An Eulerian-Lagrangian Virtual Crack Extension Method for Mixed-Mode Fracture Problems," *Proceedings of the 25th Structures, Structural Dynamics and Materials Conference*, AIAA/ASME/ASCE/AHS, Part I, Palm Springs, CA., pp. 116–122.

Hughes, T. J. R., Liu, W. K., and Zimmermann, T. K., 1981, "Lagrangian-Eulerian Finite Element Formulation for Incompressible Viscous Flows," *Computer Methods in Applied Mechanics and Engineering*, Vol. 29, pp. 329–349.

Nilsson, F., 1972, "Dynamic Stress-Intensity Factors for Finite Strip Problems," *International Journal of Fracture Mechancis*, Vol. 8, No. 4, pp. 403–411.

Nishioka, T., and Atluri, S. N., 1980a, "Numerical Modeling of Dynamic Crack Propagation in Finite Bodies, by Moving Singular Elements—Part 1: Formulation," ASME JOURNAL OF APPLIED MECHANICS, Vol. 47, pp. 570–576.

Nishioka, T., and Atluri, S. N., 1980b, "Numerical Modeling of Dynamic Crack Propagation in Finite Bodies, by Moving Singular Elements—Part 2: Results," ASME JOURNAL OF APPLIED MECHANICS, Vol. 47, pp. 577–582.

Nishioka, T., Stonesifer, R. B., and Atluri, S. N., 1981, "An Evaluation of Several Moving Singularity Finite Element Models for Fast Fracture Analysis," *Engineering Fracture Mechanics*, Vol. 15, pp. 205–218.

APPENDIX I

Finite Element Matrices

This appendix presents matrices for general three-dimensional isoparametric finite element analysis based on the dynamic ELD kinematic model. As before, the summation symbol indicates assembly over the number of elements. The consistent mass matrix in equation (20) is

$$\mathbf{M}=\Sigma\int_{v_e^r}\rho\mathbf{H}^T\mathbf{H}\tilde{J}dv_e^r \tag{21}$$

and the effective damping matrix is

$$\mathbf{C}=\Sigma\left(-\int_{v_e^r}2\rho\mathbf{H}^T\dot{\mathbf{A}}\mathbf{G}\tilde{J}dv_e^r\right) \tag{22}$$

where matrices $\dot{\mathbf{A}}$ and $\mathbf{G}$ are

$$\dot{\mathbf{A}}=\begin{bmatrix} \bar{J}_{1j}\dot{X}_j & \bar{J}_{2j}\dot{X}_j & \bar{J}_{3j}\dot{X}_j & 0 & 0 & 0 & 0 & 0 & 0 \\ 0 & 0 & 0 & \bar{J}_{1j}\dot{X}_j & \bar{J}_{2j}\dot{X}_j & \bar{J}_{3j}\dot{X}_j & 0 & 0 & 0 \\ 0 & 0 & 0 & 0 & 0 & 0 & \bar{J}_{1j}\dot{X}_j & \bar{J}_{2j}\dot{X}_j & \bar{J}_{3j}\dot{X}_j \end{bmatrix} \tag{23}$$

$$\mathbf{G}=\begin{bmatrix} \mathbf{g} & \mathbf{O} & \mathbf{O} \\ \mathbf{O} & \mathbf{g} & \mathbf{O} \\ \mathbf{O} & \mathbf{O} & \mathbf{g} \end{bmatrix}\mathbf{H} \tag{24}$$

and

$$\mathbf{g}=\{\partial/\partial x_1^r\partial/\partial x_2^r\partial/\partial x_3^r\}^T \tag{25}$$

The stiffness matrix is defined as

$$\begin{aligned}\mathbf{K}=\Sigma\Bigg(&\int_{v_e^r}\mathbf{B}^T\mathbf{E}\mathbf{B}\tilde{J}dv_e^r+\int_{v_e^r}\rho\mathbf{H}^T\mathbf{D}\mathbf{G}\tilde{J}dv_e^r-\int_{v_e^r}\rho\mathbf{H}^T\ddot{\mathbf{A}}\mathbf{G}\tilde{J}dv_e^r\\ &+\int_{a_e^r}\rho\mathbf{H}^T\dot{\mathbf{A}}\mathbf{G}A_1K_a da_e^r-\int_{v_e^r}\rho\mathbf{H}^T\mathbf{S}\mathbf{G}\tilde{J}dv_e^r\\ &-\int_{v_e^r}\rho\mathbf{G}^T\dot{\mathbf{A}}^T\dot{\mathbf{A}}\mathbf{G}\tilde{J}dv_e^r\Bigg)\end{aligned} \tag{26}$$

Here, matrix $\ddot{\mathbf{A}}$ has the same form as $\dot{\mathbf{A}}$ with $\dot{X}$ being replaced by $\ddot{X}$. $\mathbf{D}$ and $\mathbf{S}$ are defined by introducing the following two vectors:

$$\mathbf{b}=\dot{\mathbf{A}}\bullet\mathbf{G}\bullet\dot{\mathbf{X}}_e,\ \mathbf{q}=a\mathbf{H}\bullet\dot{\mathbf{X}}_e \tag{27}$$

where $a = \dot{X}_{l,m}\bar{J}_{ml}$. Then

$$\mathbf{D}=\begin{bmatrix} b_i\bar{J}_{1i} & b_i\bar{J}_{2i} & b_i\bar{J}_{3i} & 0 & 0 & 0 & 0 & 0 & 0 \\ 0 & 0 & 0 & b_i\bar{J}_{1i} & b_i\bar{J}_{2i} & b_i\bar{J}_{3i} & 0 & 0 & 0 \\ 0 & 0 & 0 & 0 & 0 & 0 & b_i\bar{J}_{1i} & b_i\bar{J}_{2i} & b_i\bar{J}_{3i} \end{bmatrix} \tag{28}$$

and matrix $\mathbf{S}$ is obtained by replacing b_i in $\mathbf{D}$ by q_i. When the mapping changes in the X_1 direction only, matrices $\mathbf{D}$ and $\mathbf{S}$ are identical, and the corresponding integrals in equation (26) cancel.

The scalar A_1K_a in equation (26), where $A_1 = \dot{X}_i n_i$, is expressed as,

$$A_1K_a=\dot{\mathbf{X}}_e{}^T\bullet\mathbf{H}^T\bullet\begin{Bmatrix} \tilde{J}_{22}\tilde{J}_{33} & - & \tilde{J}_{32}\tilde{J}_{23} \\ \tilde{J}_{32}\tilde{J}_{13} & - & \tilde{J}_{12}\tilde{J}_{33} \\ \tilde{J}_{12}\tilde{J}_{23} & - & \tilde{J}_{22}\tilde{J}_{13} \end{Bmatrix} \tag{29}$$

Note that the surface integral in equation (26) will vanish for finite bodies.

The load vector in equation (20) is

$$\mathbf{P}=\Sigma\left(\int_{v_e^r}\mathbf{H}^T\mathbf{F}_e\tilde{J}dv_e^r+\int_{a_T^r}H^T\bar{\mathbf{T}}_eK_a da_e^r\right) \tag{30}$$

where $\mathbf{F}_e$ and $\bar{\mathbf{T}}_e$ are vectors containing nodal intensities of body force and surface traction for each element.

Torsional Wave Sensor—A Theory

H. H. Bau
Department of Mechanical Engineering
and Applied Mechanics,
University of Pennsylvania,
Philadelphia, PA 19104
Assoc. Mem. ASME

Experimental observations suggest that the speed of propagation of torsional waves in a solid, elastic wave guide with a noncircular cross section is inversely proportional to the density of the fluid adjacent to the waveguide. Thus, by measuring the speed of propagation of the torsional wave, one can infer the density of the fluid. Additionally, the above procedure may be utilized to measure, among other things, liquid level and the composition of binary solutions. A simple theory is derived to correlate the torsional wave speed and the fluid density; the theoretical results are also compared with experiments.

1 Introduction

The effect of adjacent fluid on the transmission of stress waves in solids may be utilized to measure various fluid characteristics. For example, since the speed of propagation of torsional stress waves in a rod with a noncircular cross section decreases as the density of the adjacent fluid increases, one can determine the fluid's density by measuring the wave's speed of propagation. A device which operates on the aforementioned principle (hereafter referred to as the "torsional wave sensor") can be installed permanently, in line, to monitor continuously the density and other fluid characteristics such as liquid level, composition of binary suspensions, etc.

Prototypes of torsional wave sensors were manufactured by L. C. Lynnworth (1978). Experiments were conducted with these sensors being used for the measurement of fluid density (Lynnworth, 1977), liquid level (Miller et al., 1980) and void fraction of wet steam (Arave et al., 1978). Based on his experimental data, Lynnworth (1077) derived an empirical correlation between the speed of the stress wave in the wave guide and the adjacent fluid's density. It appears, however, that a quantitative predictive theory for the torsional wave sensor has not been derived yet. In this paper, I derive such a theory and then compare its predictions with the experimental data.

2 Theory

An elastic rod of length L and density ρ_s with a uniform noncircular cross section is submerged in a fluid of density ρ_f and subjected to a torsion pulse. z is a coordinate along the rod axis. The angle of rotation (ϕ) per unit length of the rod is $\partial\phi/\partial z$. Accordingly, the elastic energy in the rod is

$$E_1=\frac{1}{2}\int_o^L GD\left(\frac{\partial\phi}{\partial z}\right)^2 dz, \tag{1}$$

where D is the torsional rigidity and G is the shear modulus. The rate of deformation is $\partial\phi/\partial t$, and the corresponding kinetic energy of the rod is

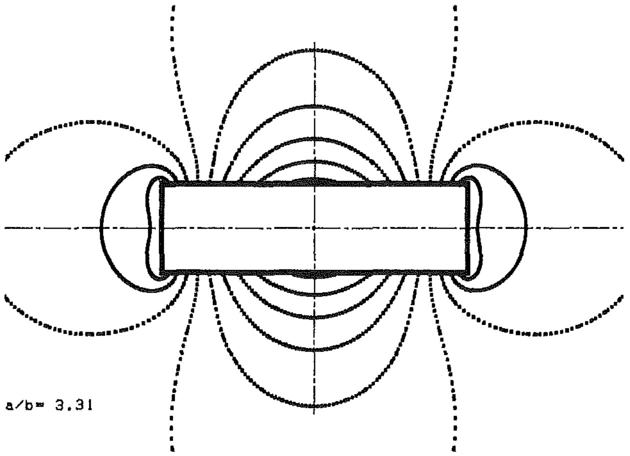

Fig. 1 The flow field (stream lines) around a rotating prism with a rectangular cross section (aspect ratio a/b 3.31)

$$E_2=\frac{1}{2}\int_o^L \rho_s I_s\left(\frac{\partial\phi}{\partial t}\right)^2 dz, \tag{2}$$

where I_s denotes the polar moment of inertia of the rod's cross section.

As the torsional wave passes through the waveguide, acceleration and deceleration of the fluid occurs. To the first approximation, I assume that the fluid motion is two-dimensional and inviscid. To illustrate the effect of the waveguide's deformation on the adjacent fluid, I reproduce in Fig. 1 a description of the flow field (streamlines) around a rectangular prism, of aspect ratio 3.31, rotating in an inviscid fluid.

The corresponding kinetic energy (E_3) of the fluid is

$$E_3=\frac{1}{2}\int_o^L \rho_f I_f\left(\frac{\partial\phi}{\partial t}\right)^2 dz, \tag{3}$$

where I_f denotes the fluid's "apparent" polar inertia.

The assumption of inviscid fluid behavior can be justified on the grounds that the thickness of the viscous boundary layer is much smaller than the dimensions of the waveguide's cross section. The thickness of the viscous boundary layer is of the order $(\nu T)^{1/2}$, where ν is the fluid's kinematic viscosity and T is the wave's period. For example, for a waveguide operating at a frequency of 50 kHz in water, $(\nu T)^{1/2}\sim 10^{-5}$m,

---

Contributed by the Applied Mechanics Division for publication in the JOURNAL OF APPLIED MECHANICS.

Discussion on this paper should be addressed to the Editorial Department, ASME, United Engineering Center, 345 East 47th Street, New York, N.Y. 10017, and will be accepted until two months after final publication of the paper itself in the JOURNAL OF APPLIED MECHANICS. Manuscript received by ASME Applied Mechanics Division, January 29, 1985; final revision March 31, 1986.

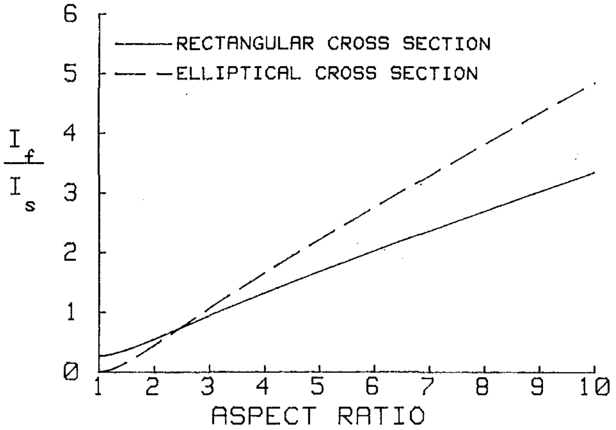

Fig. 2 The ratio between the fluid's apparent inertia (I_f) and the cross section's polar inertia (I_s) as a function of the aspect ratio (a/b) for rectangular and elliptical cross sections

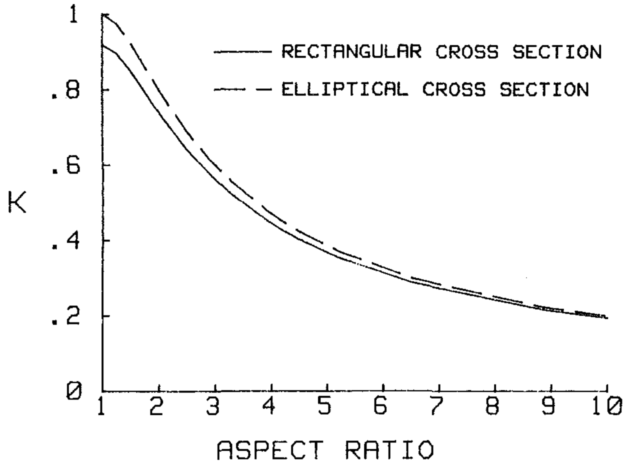

Fig. 3 The K factor (the ratio of the speed of propagation of torsional waves in a waveguide with a rectangular or elliptical cross section and that in a waveguide with a circular cross section) as a function of the aspect ratio a/b

while the waveguide's cross-sectional dimensions are of the order of 10^{-3}m.

Given the assumptions stated above, it follows that D, I_s and I_f are not functions of z. Consequently, the corresponding Lagrange equation is

$$\frac{\partial^2\phi}{\partial t^2}=c^2\frac{\partial^2\phi}{\partial z^2}, \tag{4}$$

where

$$c=K\sqrt{\frac{G}{\rho_s}}\left(1+\frac{I_f\rho_f}{I_s\rho_s}\right)^{-1/2} \tag{5}$$

and $K=\sqrt{D/I_s}\le 1$. In order to obtain a quantitative relationship between c and the ratio of fluid-solid densities (ρ_f/ρ_s), one needs to obtain explicit expressions for K, I_f, and I_s, which depend on the shape of the cross section alone. Here, two different cross-sectional geometries are considered: an ellipse and a rectangle. The former was chosen since the corresponding parameters (K, I_f, and I_s) are readily available and the latter was used to facilitate comparison with Lynnworth's (1977) experiments.

Elliptical Cross-Section. For an elliptical cross section of axes $2a\times 2b$, Milne-Thompson (1968, p. 260) and Sokolnikoff (1983, p. 122) have, respectively, reported that

$$\frac{I_f}{I_s}=\frac{(a^2-b^2)^2}{2ab(a^2+b^2)},\ \text{and}\ K=\frac{2ab}{a^2+b^2}. \tag{6}$$

I_f/I_s and K are depicted as functions of the aspect ratio a/b, where $a>b$, in Figs. 2 and 3, respectively.

Rectangular Cross Section. To obtain I_f/I_s for a rectangular cross section of dimensions $2a\times 2b$, I follow a procedure devised by Bickley (1934). The derivation is lengthy and therefore is not reproduced here. I note in passing that Bickley's paper contains a few misprints. (Corrections are available from me upon request). Calculated values of the ratio I_f/I_s are depicted in Fig. 2 for aspect ratios $1\le a/b\le 10$.

As the ratio $a/b\to\infty$, the apparent inertias around the rectangle and the ellipse approach the same limit of $\pi a^4/8$. In the case of the ellipse, I_f approaches the limit from below while, in the case of the rectangle, the approach is from above. The limit corresponds to the apparent inertia of fluid adjacent to a flat plate of length $2a$. The same is not true, however, with regard to the cross-sections' polar moments of inertia. The ratio here is

$$\frac{(I_s)_{\text{rectangle}}}{(I_s)_{\text{ellipse}}}=\frac{16}{3\pi}$$

for all a/b, which suggests that for $a/b>2.5$ sensors with elliptical cross sections are likely to be more sensitive than their rectangular counterparts.

According to Sokolnikoff (1983, pp. 128–132) the K value for rectangular cross section is

$$K^2=\frac{4}{1+(a/b)^2}\left[1-\frac{192}{\pi^5}\left(\frac{b}{a}\right)\sum_{n=0}^{\infty}\frac{\tanh\frac{(2n+1)\pi}{2}\frac{a}{b}}{(2n+1)^5}\right] \tag{7}$$

where $a>b$. This infinite series converges rapidly and it is sufficient, for any practical purpose, to retain only the first term in the series. The variation of K as a function of the aspect ratio a/b is depicted in Fig. 3.

3 Comparison With Experiments

A few experiments involving the torsional wave sensor have been carried out by Lynnworth (1977). In these experiments, wave guides with rectangular cross sections were submerged in various fluids and torsional pulses were induced at one end of each rod, using a magnetostrictive transducer. The resulting waves were reflected from the rod's other end and intercepted by the original transducer which alternatively operated as a transmitter and as a receiver. The time span between transmission and reception was then measured. Lynnworth documented the ratio between Dt (the difference between transmission time in a waveguide submerged in fluid and in air) and the transmission time t for waveguides surrounded by air.

According to equation (5)

$$\frac{Dt}{t}=\left(1+\frac{I_f}{I_s}\frac{\rho_f}{\rho_s}\right)^{1/2}-1 \tag{8}$$

when the transmission time in air is assumed to be about the same as in a vacuum.

For $I_f/I_s\ \ \rho_f/\rho_s<<1$, this expression can be approximated as

$$\frac{Dt}{t}\sim\frac{1}{2}\frac{I_f}{I_s}\frac{\rho_f}{\rho_s} \tag{9}$$

to yield a linear relationship between Dt/t and ρ_f/ρ_s.

In Fig. 4, the ratio Dt/t is depicted as a function of the density ratio (ρ_f/ρ_s) for rods of various cross sections ($a/b=1.05$, 2.46, 2.93, and 3.75). The curves represent the theoretical results (equation (9)) where the ratio I_f/I_s is obtained from Fig. 2. The crosses correspond to Lynnworth's experimental data. The sensor material was stainless steel (SS 304). The fluids used were: n-Pentane, Ethyl alcohol, Benzene, Water,

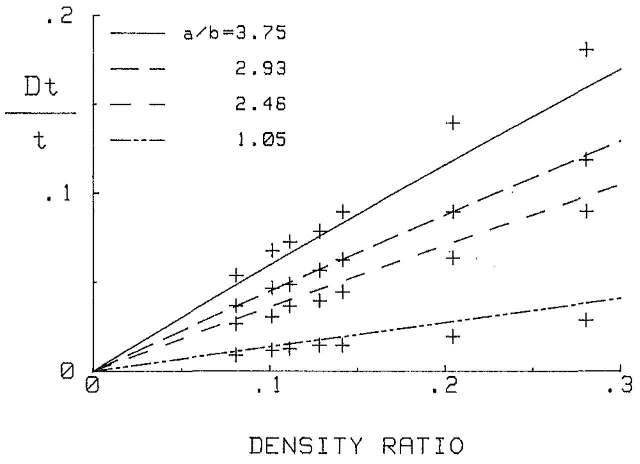

Fig. 4 The ratio Dt/t is depicted as a function of the density ratio ρ_f/ρ_s for stainless steel waveguides with rectangular cross sections of various aspect ratios. Dt denotes the difference in the transmission time in a waveguide submerged in fluid of density ρ_f and the same waveguide in air. t is the transmission time in air.

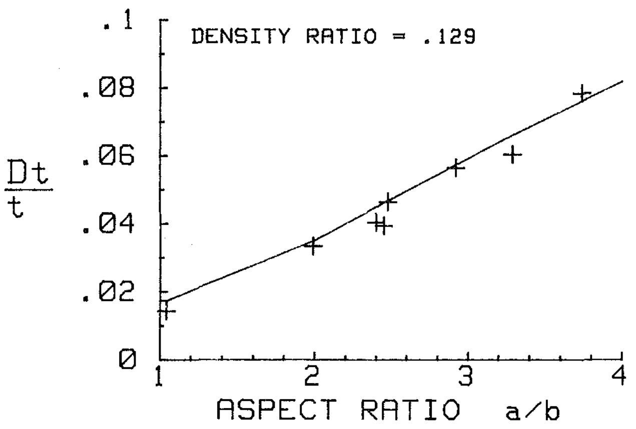

Fig. 5 The ratio Dt/t is depicted as a function of the aspect ratio a/b for stainless steel waveguides with various rectangular cross sections. The waveguides are submerged in water.

Chlorobenzene, Carbon-tetrachloride, and Ethylene-bromide. The deviation in Fig. 4 between the theoretical predictions and the experimental data is typically well below 20 percent. Since Lynnworth (1977) did not report the experimental uncertainty of his experiments, it is impossible to comment whether the above difference is within the experimental error.

In Fig. 5, the ratio Dt/t is depicted as a function of the aspect ratio (a/b) for stainless steel sensors ($a/b = 1.05$, 2, 2.41, 2.46, 2.49, 2.93, 3.3, and 3.75) submerged in water. The density ratio ρ_f/ρ_s is maintained constant. The solid lines and the crosses correspond, respectively, to theory and experiment. The disagreement between theory and experiment is smaller than 12 percent.

In Fig. 6, Dt/t is again depicted as a function of the density ratio ρ_f/ρ_s for sensors of aspect ratio $a/b = 2$. The crosses and stars correspond to Lynnworth's experimental results and the solid lines, to the theoretical predictions. The stars relate to a sensor made of fused silica submerged in the same fluids detailed in Fig. 4, and the crosses correspond to sensors made of graphite, Magnesium, Aluminum, Titanium, stainless steel, copper 129, and Tungsten and submerged in water. The deviation between theory and the experiments is smaller than 25 percent.

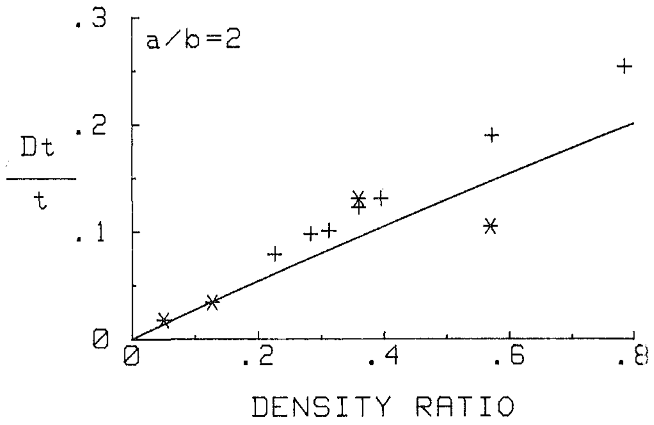

Fig. 6 The ratio Dt/t is depicted as a function of the density ratio ρ_f/ρ_s for waveguides made out of a variety of materials

4 Conclusions

A simple theory has been advanced to predict the performance of a torsional wave sensor. Despite the simplicity of the theory which neglects three dimensional and viscous effects, a favorable agreement with experiments is obtained.

The importance of the theory is that it enables one to optimize sensor performance. To improve sensor sensitivity, one must maximize the ratio I_f/I_s while minimize the density of the wave guide (ρ_s). For both the rectangular and elliptical cross sections, I_f/I_s increases monotonically as the aspect ratio (a/b) increases. However, for practical reasons, the aspect ratio a/b cannot be increased without limit. A minimum value must be set for (b) to assure structural integrity and the value of (a) should be well below the wave length of the torsional wave in order to minimize dispersion. Conceivably, I_f/I_s might be maximized more effectively with cross sections other than those investigated here. A search for the optimal cross section would probably be accomplished most efficiently using numerical techniques rather than the analytical approach taken in this note.

Acknowledgment

This work has been supported, in part, by the Electric Power Research Institute (contract RP2515-03), the National Science Foundation (Grant CBT 8351658), and the National Science Foundation – MRL program at the University of Pennsylvania.

References

Arave, A., Eickas, E., Shurtliff, W., 1978, "Ultrasonic Density Detector for In-Core Dynamic Measurements," ISA, *Instrumentation in the Aerospace Industry*, Vol. 24, Kissell, K. E., ed., pp. 609–620.

Bickley, W. G., 1934, "Two-Dimensional Potential Problems or the Space Outside a Rectangle," *London Math. Soc. Proceedings* (*2*), Vol. 37, pp. 82–105.

Lynnworth, L. C., 1977, "Slow Torsional Wave Sensors," *Ultrasonic Symposium Proceedings*, IEEE, 77 CH 1264-ISU.

Lynnworth, L. C., 1978, "New Designs for Magnetostrictive Probes Using Extensional, Torsional and Flexural Waves," *Ultrasonic Symposium Proceedings*, IEEE, 78 CH 1344-ISU.

Miller, G. N., Anderson, R. L., Rogers, S. C. Lynnworth, L. C., Studley, W. B., and Wade, W. R., 1980, High Temperature, High Pressure, Water Level Sensor, *Ultrasonic Symposium Proceedings*, IEEE 0090-5007/80, pp. 877–881.

Milne-Thomson, L. M., 1968, *Theoretical Hydrodynamics*, Macmillan, London.

Sokolnikoff, I. S., 1983, *Mathematical Theory of Elasticity*, R. E. Krieger, Malabar, Fla.

On the Dynamics of Flexible Beams Under Large Overall Motions—The Plane Case: Part I

J. C. Simo[1]
Applied Mechanics Division,
Stanford University,
Stanford, CA 94305

L. Vu-Quoc
Structural Engineering and
Structural Mechanics Division,
University of California,
Berkeley, CA 94720

The dynamic response of a flexible beam subject to large overall motions is traditionally formulated relative to a floating frame, sometimes referred to as the shadow beam. *This type of formulation leads to equations of motion of the form* $\tilde{\mathbf{g}}(\dot{\mathbf{y}}, \mathbf{y}, t) = \mathbf{0}$, *that are implicit, nonlinear and highly coupled in the inertia terms. An alternative approach is proposed whereby all quantities are referred to the* inertial *frame. As a result, the inertia term enters linearly in the formulation simply as mass times acceleration. Crucial to this formulation is the use of* finite strain rod theories *capable of treating finite rotations. Numerical examples that involve finite vibrations coupled with large overall motions are presented in Part II of this paper.*

Introduction

The dynamics of a flexible beam undergoing large overall motions is typically formulated relative to a coordinate system that follows the rigid body motion of the beam, sometimes referred to as the shadow beam (Laskin, Likins, and Longman, 1983). The introduction of this floating frame, relative to which the strains in the beam are measured, is motivated by the assumption of infinitesimal strains. This assumption has been used by several authors, such as, to name a few, Ashley (1967), Grotte et al. (1971), de Veubeke (1976), Canavin and Likins (1977), Kumar and Bainum (1980), Kane and Levinson (1981a,b), and Kane et al. (1983). With the assumption of small strains, the use of a floating frame allows a simple expression for the total potential energy of the beam. By contrast, the expression of the kinetic energy of the system takes a rather cumbersome form. The resulting equations of motion, although restricted to small strains, are nonlinear and *highly coupled in the inertia terms* due to the presence of Coriolis and centrifugal effects as well as inertia due to rotation of the shadow beam. Moreover, the Galerkin discretization in space variables, leads to a system of implicit coupled nonlinear differential equations in time of the form $\tilde{\mathbf{g}}(\dot{\mathbf{y}}, \mathbf{y}, t) = 0$ (e.g., Song and Haug, 1980). An essential characteristic of this system is that it cannot be transformed to a standard explicit form $\dot{\mathbf{y}} = \mathbf{g}(\mathbf{y}, t)$, without appending an algebraic constraint.[2] Thus, use of the mode shapes of the structure as a Galerkin basis, a procedure often employed (see, e.g., Likins, 1974) appears to be of little value in the general case due to the highly coupled nature of the resulting semi-discrete equations. Moreover, the complex nature of these equations has often led to simplifying assumptions; see, e.g., Winfrey (1971), Erdman and Sandor (1972), and Baghat and Willmert (1973). We refer to Song and Haug (1980) for a review of several approaches in the dynamic analysis of mechanisms and machines.

In this paper, we propose an approach based on a philosophy opposite to that outlined above. The kinetic energy of the system is reduced to a quadratic uncoupled form simply by referring the motion of the system to the *inertial frame*. This results in a drastic simplification of the inertia operator, which now becomes *linear and uncoupled*, while the stiffness operator emanating from the potential energy functional becomes nonlinear. Conceptually, the essential step needed in developing this alternative approach is the use of rod theories capable of accounting for large rotations of the beam. It is important to note that the basic characteristic of the appropriate strain measures in these theories—as discussed by Reissner (1972, 1973), Antman (1972, 1974), Simo (1985), and Simo and Vu-Quoc (1985)—is their invariance under superposed rigid body motions.

From a computational standpoint, the substantial advantage of the proposed approach over the traditional shadow beam approach lies in the much simpler structure of the resulting equations. As shown in Part II of this paper, by introducing a Galerkin semi-discretization in the space variables, one obtains the standard nonlinear system of ODE's that typically arises in nonlinear structural dynamics: $\mathbf{M}\,\ddot{\mathbf{q}} + \mathbf{D}\,\dot{\mathbf{q}} + \mathbf{P}(\mathbf{q}) = \mathbf{F}$ (see, e.g., Belytschko and Hughes, 1983). In addition, this approach has the advantage of automatically accounting for large strains. Within the present context, there is little to be gained by introducing at the outset the additional small strain assumption.

As a basis for our discussion, we choose a specific problem

---

[1] Formerly at the University of California, Berkeley.

[2] One can always set $\dot{\mathbf{y}} = \mathbf{z}$, and append the *algebraic constraint* $\mathbf{g}(\mathbf{z}, \mathbf{y}, t) = \mathbf{0}$. This is a DAE system, and not a standard ODE system (Petzold, 1982).

Contributed by the Applied Mechanics Division for presentation at the Winter Annual Meeting, Anaheim, CA, December 7–12, 1986, of the American Society of Mechanical Engineers.

Discussion on this paper should be addressed to the Editorial Department, ASME, United Engineering Center, 345 East 47th Street, New York, N.Y. 10017, and will be accepted until two months after final publication of the paper itself in the JOURNAL OF APPLIED MECHANICS. Manuscript received by ASME Applied Mechanics Division, September 23, 1985; final revision, May 7, 1986. Paper No. 86-WA/APM-41.

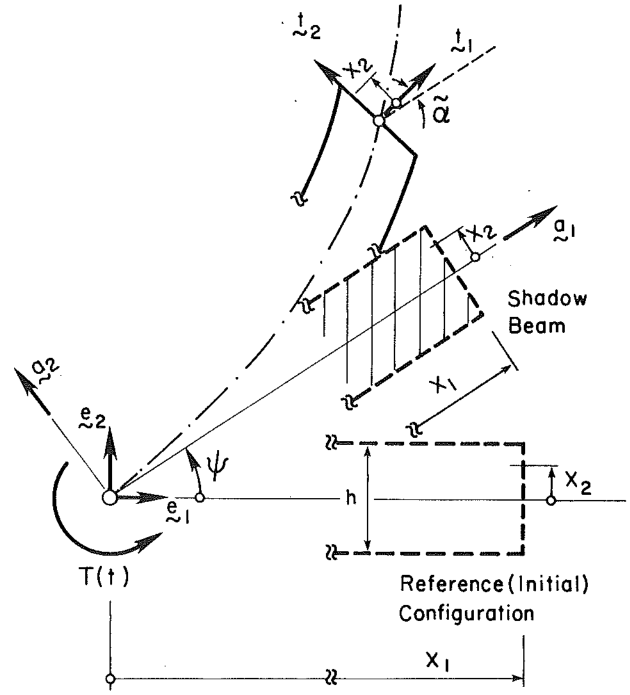

Fig. 2.1 Basic kinematics. Floating and inertial frames.

to introduce our formulation: the dynamics of a flexible robot arm. This model problem consists of a flexible beam with one end at the origin of the inertial frame $\{\mathbf{e}_1, \mathbf{e}_2, \mathbf{e}_3\}$ (see Fig. 2.1). The robot arm is allowed to rotate about the axis $\mathbf{e}_3$, but the entire motion of the arm is restrained to the plane $\{\mathbf{e}_1, \mathbf{e}_2\}$. It will become clear, however, that our formulation can be applied to a more general setting of flexible plane beams subject to large overall motions. We shall also show through numerical examples that our formulation can be employed directly in the analysis of a system of flexible beams connected by hinges, i.e., the multibody dynamics problem.

2 Classical Approach Based on Small Strains: Floating Frame

In this section we summarize the equations of motion for a rotating flexible beam using the shadow beam approach and assuming small strains superposed onto large rigid body rotations. Our purpose is to exhibit the main drawback of this approach. Use of the floating frame, although allowing a simple expression for the potential energy, leads to a cumbersome expression for the kinetic energy of the system. This results in equations of motion with highly coupled nonlinear terms involving the time derivatives of the state variables. From a computational standpoint, the numerical integration of these equations is a nontrivial task.

2.1 Basic Kinematic Assumption. Consider the rotating beam shown in Fig. 2.1. Let ϕ be the position vector of a material particle initially located at $\mathbf{X} = X_1\mathbf{e}_1 + X_2\mathbf{e}_2$ in the *undeformed* (reference) configuration. Here $\{\mathbf{e}_1, \mathbf{e}_2\}$ is the inertial frame attached to the fixed undeformed configuration. In addition, we introduce a floating frame $\{\mathbf{a}_1(t), \mathbf{a}_2(t)\}$ that follows the rigid body motion of the beam, i.e., the shadow beam. The basic kinematic assumption is that plane sections remain plane after deformation. Accordingly, we set

$$\phi(X_1,X_2,t) := \tilde{\phi}_0(X_1,t) + X_2\mathbf{t}_2(X_1,t)\ , \qquad (2.1a)$$

where

$$\begin{aligned}
\tilde{\phi}_0(X_1,t) &:= [X_1 + \tilde{u}_1(X_1,t)]\mathbf{a}_1(t) + \tilde{u}_2(X_1,t)\mathbf{a}_2(t),\\
\mathbf{t}_1(X_1,t) &:= \cos\tilde{\alpha}(X_1,t)\mathbf{a}_1(t) + \sin\tilde{\alpha}(X_1,t)\mathbf{a}_2(t), \qquad (2.1b)\\
\mathbf{t}_2(X_1,t) &:= -\sin\tilde{\alpha}(X_1,t)\mathbf{a}_1(t) + \cos\tilde{\alpha}(X_1,t)\mathbf{a}_2(t).
\end{aligned}$$

For notational simplicity, explicit indication of the arguments X_1, X_2, and t will often be omitted. Since the motion is planar, $\mathbf{e}_3 \equiv \mathbf{t}_3 \equiv \mathbf{a}_3$. Note that $\{\mathbf{t}_1, \mathbf{t}_2\}$ defines a moving frame that follows the deformation of the beam with $\mathbf{t}_2$ always contained in the deformed cross section and $\mathbf{t}_1$ perpendicular to the cross section. Using matrix notation, relations $(2.1b)_{2,3}$ may be expressed as

$$\begin{Bmatrix} \mathbf{t}_1 \\ \mathbf{t}_2 \end{Bmatrix} = \tilde{\Lambda}^t \begin{Bmatrix} \mathbf{a}_1 \\ \mathbf{a}_2 \end{Bmatrix}, \quad \text{where } \tilde{\Lambda} := \begin{bmatrix} \cos\tilde{\alpha} & -\sin\tilde{\alpha} \\ \sin\tilde{\alpha} & \cos\tilde{\alpha} \end{bmatrix}. \qquad (2.2)$$

Although it is possible to develop the formulation without introducing any restriction on the size of the strain field, the assumption of small strains is typically introduced *ab-initio*, as discussed below.

2.2 Motivation: Total Potential Energy. By introducing the floating frame $\{\mathbf{a}_1, \mathbf{a}_2\}$ one can enforce at the outset the following infinitesimal strain assumption:

$$\tilde{\alpha} \textbf{ small } (\leq 10^o) \Leftrightarrow \tilde{\Lambda} \cong \begin{bmatrix} 1 & -\tilde{\alpha} \\ \tilde{\alpha} & 1 \end{bmatrix}$$

$$\tilde{\mathbf{u}}_1, \text{ and } \tilde{\mathbf{u}}_2 \textbf{ small} \qquad (2.3)$$

The strain $\tilde{\gamma}$ and the curvature $\tilde{\kappa}$ relative to the floating frame $\{\mathbf{a}_1, \mathbf{a}_2\}$ are then defined as

$$\tilde{\gamma} = \tilde{\phi}_0' - \mathbf{t}_1, \quad \kappa = \tilde{\alpha}'\mathbf{t}_3, \qquad (2.4a)$$

where $(\bullet)' := d(\bullet)/dX_1$. In component form, $\tilde{\gamma}$ is expressed as

$$\tilde{\gamma} = \tilde{\gamma}_1\mathbf{a}_1 + \tilde{\gamma}_2\mathbf{a}_2 \qquad (2.4b)$$

where

$$\tilde{\gamma}_1 = \tilde{u}_1', \quad \tilde{\gamma}_2 = \tilde{u}_2' - \tilde{\alpha} \qquad (2.4c)$$

One refers to $\tilde{\gamma}_1$ and $\tilde{\gamma}_2$ as the *axial* strain and the *shearing* strain, respectively. Denoting by EA, GA_s, and EI the axial, shear, and flexural stiffnesses of the beam (relative to the floating frame $\{\mathbf{a}_1, \mathbf{a}_2\}$), the potential energy is expressed as

$$\Pi := \frac{1}{2}\int_{[0,L]} \{EA\tilde{\gamma}_1^2 + GA_s\tilde{\gamma}_2^2 + EI(\tilde{\alpha}')^2\}dS + \Pi_{EXT} - T(t)\psi(t) \qquad (2.5)$$

where Π_{EXT} is the potential energy of the external loading acting on the beam and $T(t)\mathbf{e}_3$ is an applied torque at the axis of rotation $\mathbf{e}_3$ of the robot arm.

2.3 Kinetic Energy. The kinetic energy of the system takes a rather cumbersome form compared with the simplicity of (2.5). To obtain the appropriate expression, we introduce the time derivative relative to an observer attached to the floating frame. Accordingly, we define

$$\overset{\nabla}{\phi} := \frac{\partial \phi}{\partial t}\bigg|_{a_i = fixed} \qquad (2.6)$$

The following expression for the material time derivative, denoted by a superposed "dot", is standard in rigid body mechanics (Goldstein, 1980),

$$\dot{\phi} = \overset{\nabla}{\phi} + \mathbf{w} \times \phi, \qquad (2.7)$$

where $\mathbf{w}$ is the angular velocity of the floating frame. For the plane case under consideration, the angular velocity $\mathbf{w}$ is given as

$$\mathbf{w} = \frac{d\psi}{dt}\,\mathbf{a}_3 \equiv \dot{\psi}\mathbf{a}_3, \qquad (2.8)$$

where $\mathbf{a}_3 := \mathbf{a}_1 \times \mathbf{a}_2$ is *fixed*. Since the time derivative of the floating basis is

$$\dot{\mathbf{a}}_1 = \dot{\psi}\mathbf{a}_2, \quad \dot{\mathbf{a}}_2 = -\dot{\psi}\mathbf{a}_1, \tag{2.9}$$

it follows from expressions (2.1*b*) that

$$\dot{\mathbf{t}}_1 = (\dot{\tilde{\alpha}} + \dot{\psi})\mathbf{t}_2, \quad \dot{\mathbf{t}}_2 = -(\dot{\tilde{\alpha}} + \dot{\psi})\mathbf{t}_1. \tag{2.10}$$

Thus, we arrive at the following expression for the time derivative of the position vector $\boldsymbol{\phi}$

$$\dot{\boldsymbol{\phi}} = \overset{\nabla}{\tilde{\boldsymbol{\phi}}}_0 + \dot{\psi}[-\tilde{u}_2\mathbf{a}_1 + (X_1 + \tilde{u}_1)\mathbf{a}_2] - X_2(\dot{\tilde{\alpha}} + \dot{\psi})\mathbf{t}_1, \tag{2.11a}$$

$$\overset{\nabla}{\tilde{\boldsymbol{\phi}}}_0 = \dot{\tilde{u}}_1\mathbf{a}_1 + \dot{\tilde{u}}_2\mathbf{a}_2. \tag{2.11b}$$

The kinetic energy of the system obtained from the expression

$$K := \int_{[0,L]\times\left[-\frac{h}{2}, \frac{h}{2}\right]} \rho(X_1, X_2)\|\dot{\boldsymbol{\phi}}\|^2 dX_1 dX_2, \tag{2.12}$$

where $\rho(X_1, X_2)$ is the density and $\|\dot{\boldsymbol{\phi}}\|^2 := \dot{\phi}_1^2 + \dot{\phi}_2^2$. By substituting (2.11) into (2.12) we obtain

$$K \equiv \frac{1}{2}\int_{[0,L]} [A_\rho(\dot{\tilde{u}}_1^2 + \dot{\tilde{u}}_2^2) + I_\rho(\dot{\tilde{\alpha}} + \dot{\psi})^2]dX_1$$

$$+ \frac{1}{2}\int_{[0,L]} A_\rho\{2\dot{\psi}[-\tilde{u}_2\dot{\tilde{u}}_1 + (X_1 + \tilde{u}_1)\dot{\tilde{u}}_2]$$

$$+ \dot{\psi}^2[(X_1 + \tilde{u}_1)^2 + \tilde{u}_2^2]\}dX_1 \tag{2.13}$$

Here, the inertia constants A_ρ and I_ρ are defined as

$$A_\rho := \int_{\left[-\frac{h}{2}, \frac{h}{2}\right]} \rho(X_1, X_2)dX_2,$$

$$I_\rho := \int_{\left[-\frac{h}{2}, \frac{h}{2}\right]} \rho(X_1, X_2)X_2^2 dX_2 \tag{2.14}$$

2.4 Equations of Motion: Coupled Inertia Terms. The equations of motion may be systematically derived by means of Hamilton's principle. Accordingly, we require that the action

$$L := \int_{[t_1, t_2]} (K - \Pi)dt \quad \text{be stationary,} \tag{2.15}$$

for arbitrary paths connecting two points at time t_1 and t_2 in the configuration space. Substituting expressions (2.5) and (2.13) into (2.15) and making use of standard arguments involving integration by parts, we arrive at the following equations governing the extensional and flexural motion of the beam

$$A_\rho[\ddot{\tilde{u}}_1 - \ddot{\psi}\tilde{u}_2 - 2\dot{\psi}\dot{\tilde{u}}_2 - \dot{\psi}^2(X_1 + \tilde{u}_1)] - EA\tilde{u}_1'' = 0,$$

$$A_\rho[\ddot{\tilde{u}}_2 + \ddot{\psi}(X_1 + \tilde{u}_1) + 2\dot{\psi}\dot{\tilde{u}}_1 - \dot{\psi}^2\tilde{u}_2)] - GA_s(\tilde{u}_2' - \tilde{\alpha}) = 0, \tag{2.16}$$

$$I_\rho(\ddot{\tilde{\alpha}} + \ddot{\psi}) - EI\tilde{\alpha}'' - GA_s(\tilde{u}_2' - \tilde{\alpha}) = 0.$$

Appropriate boundary conditions automatically follow from the stationarity condition (Fung, 1965). In addition to equations (2.16), one obtains the following constraint equation expressing the overall balance of angular momentum of the system

$$\ddot{\psi}\int_{[0,L]} \{A_\rho[(X_1 + \tilde{u}_1)^2 + \tilde{u}_2^2] + I_\rho\}dX_1$$

$$+ 2\dot{\psi}\int_{[0,L]} A_\rho\{(X_1 + \tilde{u}_1)\dot{\tilde{u}}_1 + \tilde{u}_2\dot{\tilde{u}}_2\}dX_1$$

$$+ \int_{[0,L]} A_\rho\{(X_1 + \tilde{u}_1)\ddot{\tilde{u}}_2 - \tilde{u}_2\ddot{\tilde{u}}_1\}dX_1 + \int_{[0,L]} I_\rho\ddot{\tilde{\alpha}}dX_1 = T(t) \tag{2.17}$$

The highly nonlinear nature of the coupled system (2.16)–(2.17) involving the variables $\{\tilde{u}_1, \tilde{u}_2, \tilde{\alpha}, \psi\}$ should be noted.

Remark 2.1. The Euler-Bernoulli formulation is obtained form the above equations by assuming that shear deformation is negligible. Accordingly, we let $(\tilde{u}_2' - \tilde{\alpha}) \to 0$, and $GA_s \to \infty$ so that $GA_s(\tilde{u}_2' - \tilde{\alpha}) \to V$ where V is the shear force acting on the cross section of the beam. Equations $(2.16)_{2,3}$ governing the transverse and flexural vibrations of the beam may be combined to obtain

$$A_\rho\ddot{\tilde{u}}_2 + EI\tilde{u}_2'''' - I_\rho\ddot{\tilde{u}}_2'' + A_\rho[\ddot{\psi}(X_1 + \tilde{u}_1) + 2\dot{\psi}\dot{\tilde{u}}_1 - \dot{\psi}^2\tilde{u}_2)] = 0 \tag{2.18}$$

The first two terms in (2.18) correspond to the standard linear Euler-Bernoulli beam theory. This equation is often attributed to Rayleigh (e.g., Fung, 1965, p. 321) who accounted for the contribution of section rotary inertia to the transverse vibration of the beam. The third one gives the contribution of the rotatory inertia and is often neglected in structural applications. The last three terms within brackets arise as a result of coupling between deformation and rigid body motion. These terms represent the inertia due to rotation of the shadow beam, the Coriolis and the centrifugal effects, respectively. The crucial role of the term $\dot{\psi}^2\tilde{u}_2$ related to centrifugal force in (2.18) with regard to the stability of a rapidly rotating beam is discussed in detail in Simo and Vu-Quoc (1986).

3 Proposed Approach Based on Finite Strains: Inertial Frame

By contrast with the formulation outlined above, we propose an alternative approach whereby the structure of the inertia operator becomes *linear and uncoupled*. This is achieved by referring the basic equations of motion to the *inertial* frame. As a result, drastic simplification of the inertia (temporal) part is obtained by shifting the nonlinearity of the problem to the stiffness (spatial) part of the equations of motion. Conceptually, the essential step needed to develop this approach is the use of finite strain rod theories capable of accounting for large rotations. In section 3.3, we summarize from a physical standpoint the appropriate finite strain measures. We refer to Reissner for the plane case, and Reissner (1973, 1981), Antman (1974), Simo (1985), and Simo and Vu-Quoc (1985) for the three-dimensional case. An essential characteristic of these strain measures is their invariance under superposed rigid body motions.

From a computational standpoint, the substantial advantage of the proposed approach over the shadow beam approach discussed in Section 2 lies in a much simpler structure of the resulting equations. This structure corresponds to the standard nonlinear system of ODE's that typically arises in structural dynamics. In addition, we automatically account for large strains.

3.1 Basic Kinematic Assumption. As in Section 2, the basic kinematic assumption is the condition that plane sections normal to the axis of the beam in the undeformed configuration remain plane, i.e.,

$$\boldsymbol{\phi}(X_1, X_2, t) := \boldsymbol{\phi}_0(X_1, t) + X_2\mathbf{t}_2(X_1, t) \tag{3.1a}$$

The difference between assumptions (2.1*a*) and (3.1*a*) is that the position vector $\boldsymbol{\phi}_0$ and the moving vectors $\{\mathbf{t}_1, \mathbf{t}_2\}$ following the deformation of the beam are now expressed relative to the *inertial frame* $\{\mathbf{e}_1, \mathbf{e}_2\}$. Accordingly, we set

$$\boldsymbol{\phi}_0(X_1, t) := [X_1 + u_1(X_1, t)]\mathbf{e}_1 + u_2(X_1, t)\mathbf{e}_2,$$

$$\mathbf{t}_1(X_1, t) := \cos\theta(X_1, t)\mathbf{e}_1 + \sin\theta(X_1, t)\mathbf{e}_2, \tag{3.1b}$$

$$\mathbf{t}_2(X_1, t) := -\sin\theta(X_1, t)\mathbf{e}_1 + \cos\theta(X_1, t)\mathbf{e}_2.$$

As in equation (2.2), we shall use matrix notation and express relations $(3.1b)_{2,3}$ as

$$\begin{Bmatrix} \mathbf{t}_1 \\ \mathbf{t}_2 \end{Bmatrix} = \Lambda^t \begin{Bmatrix} \mathbf{e}_1 \\ \mathbf{e}_2 \end{Bmatrix}, \quad \text{where } \Lambda := \begin{bmatrix} \cos\theta & -\sin\theta \\ \sin\theta & \cos\theta \end{bmatrix}. \tag{3.2}$$

Note that the floating basis $\{\mathbf{a}_1, \mathbf{a}_2\}$ plays no rôle in the present formulation.

3.2 Motivation: Kinetic Energy. We show that the kinetic energy of the system relative to the inertial basis reduces to the standard quadratic uncoupled form. To see this, note that from equation (3.2) the rate of change of the moving vectors $\{\mathbf{t}_1, \mathbf{t}_2\}$ is given by

$$\dot{\mathbf{t}}_1 = \dot{\theta}\mathbf{t}_2, \quad \dot{\mathbf{t}}_2 = -\dot{\theta}\mathbf{t}_1. \tag{3.4}$$

Hence, the time derivative $\dot{\boldsymbol{\phi}}$ of the position vector $\boldsymbol{\phi}$ is obtained as

$$\begin{aligned} \dot{\boldsymbol{\phi}} &= \dot{\boldsymbol{\phi}}_0 - X_2\dot{\theta}\mathbf{t}_1, \\ \dot{\boldsymbol{\phi}}_0 &= \dot{u}_1\mathbf{e}_1 + \dot{u}_2\mathbf{e}_2. \end{aligned} \tag{3.5}$$

It follows from equation (3.5) that $\|\dot{\boldsymbol{\phi}}\|^2 := \dot{\phi}_1^2 + \dot{\phi}_2^2$ has the expression

$$\|\dot{\boldsymbol{\phi}}\|^2 = [\dot{u}_1^2 + \dot{u}_2^2] + X_2^2\dot{\theta}^2 - 2\dot{\theta}X_2(\cos\theta\dot{u}_1 + \sin\theta\dot{u}_2). \tag{3.6}$$

Upon integrating $\rho(X_1, X_2)\|\dot{\boldsymbol{\phi}}\|^2$ over $[0, L] \times [-(h/2), h/2]$, we arrive at the following expression for the kinetic energy of the system

$$K \equiv \frac{1}{2}\int_{[0,L]} [A_\rho(\dot{u}_1^2 + \dot{u}_2^2) + I_\rho\dot{\theta}^2]dX_1. \tag{3.7a}$$

Here, as in equation (2.13), the inertia coefficients A_ρ and I_ρ are given by equation (2.14).

Remark 3.1. The case of a flexible beam attached to a rigid body considered in Levinson and Kane (1981) can be readily accommodated within the present formulation by modifying expression (3.7*a*) for the kinetic energy. Let m_R be the mass of the rigid body, and I_R its inertia relative to an axis parallel to $\mathbf{e}_3 \equiv \mathbf{t}_3$ and passing through the connecting point with the beam. The kinetic energy of the composite system, then, is given by

$$K_{\text{total}} = K + \frac{1}{2}m_R\|\dot{\boldsymbol{\phi}}_0(0,t)\|^2 + \frac{1}{2}I_R\dot{\theta}^2(0,t) \tag{3.7b}$$

where K is given by (3.7*a*).

Remark 3.2. It is noted that expression (2.13) for the kinetic energy in the shadow beam approach may be exactly recovered from equation (3.7) simply by employing the coordinate transformation

$$\begin{Bmatrix} X_1 + u_1 \\ u_2 \end{Bmatrix} = \begin{bmatrix} \cos\psi & -\sin\psi \\ \sin\psi & \cos\psi \end{bmatrix} \begin{Bmatrix} X_1 + \tilde{u}_1 \\ \tilde{u}_2 \end{Bmatrix} \tag{3.8}$$

That is, the expression for the kinetic energy of the system is independent of any particular assumption on the magnitude of the strain field.

3.3 Potential Energy: Invariant Strain Measures. Within the context of large strains, a physically reasonable definition of the strain field in the beam is also provided in vectorial form by expression (2.4)

$$\boldsymbol{\gamma} := \boldsymbol{\phi}_0' - \mathbf{t}_1, \quad \boldsymbol{\kappa} := \theta'\mathbf{t}_3. \tag{3.9a}$$

The physical interpretation of $\boldsymbol{\gamma}$ is clear as shown in Fig. 3.1. $\boldsymbol{\gamma}$ measures the difference between the slope of the deformed axis of the beam and the normal to the cross section defined by $\mathbf{t}_1$, and $\boldsymbol{\kappa}$ is the rate of rotation of the cross section along the undeformed length of the beam. In component form, relative to the inertial frame we have from equation (3.1*b*) the following expression for $\boldsymbol{\gamma}$

$$\boldsymbol{\gamma} = \gamma_1\mathbf{e}_1 + \gamma_2\mathbf{e}_2 \equiv [(1 + u_1') - \cos\theta]\mathbf{e}_1 + [u_2' - \sin\theta]\mathbf{e}_2 \tag{3.9b}$$

Alternatively, relative to the *moving vectors* $\{\mathbf{t}_1, \mathbf{t}_2\}$, from relation (3.2) we have the following expression

$$\boldsymbol{\gamma} = \Gamma_1\mathbf{t}_1 + \Gamma_2\mathbf{t}_2, \tag{3.10a}$$

where

$$\begin{Bmatrix} \Gamma_1 \\ \Gamma_2 \end{Bmatrix} = \Lambda^t \begin{Bmatrix} 1 + u_1' - \cos\theta \\ u_2' - \sin\theta \end{Bmatrix}. \tag{3.10b}$$

The analogy between expressions (2.4*a,b,c*) and (3.9*a*)-(3.9*b*) should be noted. We now assume the same expression for the potential energy, relative to the moving frame $\{\mathbf{t}_1, \mathbf{t}_2\}$, as the one considered in the small strain shadow beam approach discussed in Section 2. Accordingly, we set

$$\begin{aligned} \Pi := \frac{1}{2}\int_{[0,L]} & \{EA\Gamma_1^2 + GA_s\Gamma_2^2 + EI(\theta')^2\}dS \\ & + \Pi_{EXT} - T(t)\theta(0,t) \end{aligned} \tag{3.11}$$

Remark 3.3. The components of the strain $\boldsymbol{\gamma}$ in the basis $\{\mathbf{t}_1, \mathbf{t}_2\}$ denoted by $[\Gamma_1 \ \Gamma_2]^t$ are invariant under superposed rigid body motions on the beam. One can see this by considering the rigid body motion composed of a superposed translation $\mathbf{c}(t)$, and a superposed rotation $\beta(t)$ represented by the orthogonal transformation matrix

$$\mathbf{Q}(t) := \begin{bmatrix} \cos\beta & -\sin\beta \\ \sin\beta & \cos\beta \end{bmatrix}. \tag{3.12a}$$

The transformed quantities in the expression of Γ_i in equations (3.10) above are as follows

$$\begin{aligned} \boldsymbol{\phi}_o^+(X_1,t) &= \mathbf{c}(t) + \mathbf{Q}(t)\boldsymbol{\phi}_o(X_1,t), \\ \boldsymbol{\phi}_o^{+\prime} &:= \phi_{o1}^{+\prime}\mathbf{e}_1 + \phi_{o2}^{+\prime}\mathbf{e}_2 = \mathbf{Q}\boldsymbol{\phi}_o', \end{aligned} \tag{3.12b}$$

$$\text{i.e.,} \begin{Bmatrix} \phi_{o1}^{+\prime} \\ \phi_{o2}^{+\prime} \end{Bmatrix} = \mathbf{Q}\begin{Bmatrix} 1 + u_1' \\ u_2' \end{Bmatrix}, \tag{3.12c}$$

$$\boldsymbol{\Lambda}^+ = \mathbf{Q}\boldsymbol{\Lambda}, \tag{3.12d}$$

Since $\mathbf{t}_1^+ = \cos(\beta + \theta)\mathbf{e}_1 + \sin(\beta + \theta)\mathbf{e}_2$, it follows that

$$\boldsymbol{\gamma}^+ := \Gamma_1^+\mathbf{t}_1^+ + \Gamma_2^+\mathbf{t}_2^+ = \boldsymbol{\phi}_o^{+\prime} - \mathbf{t}_1^+, \tag{3.13a}$$

where

$$\begin{Bmatrix} \Gamma_1^+ \\ \Gamma_2^+ \end{Bmatrix} = \boldsymbol{\Lambda}^{+t}\left[\begin{Bmatrix} \phi_{o1}^{+\prime} \\ \phi_{o2}^{+\prime} \end{Bmatrix} - \begin{Bmatrix} \cos(\beta + \theta) \\ \sin(\beta + \theta) \end{Bmatrix}\right] \equiv \begin{Bmatrix} \Gamma_2 \\ \Gamma_1 \end{Bmatrix}. \tag{3.13b}$$

The invariance under superposed rigid body motions of the *curvature* $\boldsymbol{\kappa}$ follows at once in the plane case from expression (3.9*a*). This invariance property of the strain measures is essential for the success of the proposed approach.

Remark 3.4. It can be shown that definition (3.9*a*) and expressions (3.9*b*), (3.10) follow from a rigorous argument based on the equivalence of the stress power for the general three dimensional theory with the reduced stress power of the (finite strain) beam theory; see Antman (1972, 1974) and Simo (1985).

Remark 3.5. We shall be concerned only with spatially fixed loads, which do not depend on the deformed configuration, as opposed to follower loads that are configuration dependent. Simo and Vu-Quoc (1985) give a treatment of follower loads in the general context of the three-dimensional finite strain beam. Accordingly, the potential of the distributed loading in (0, L) is given by

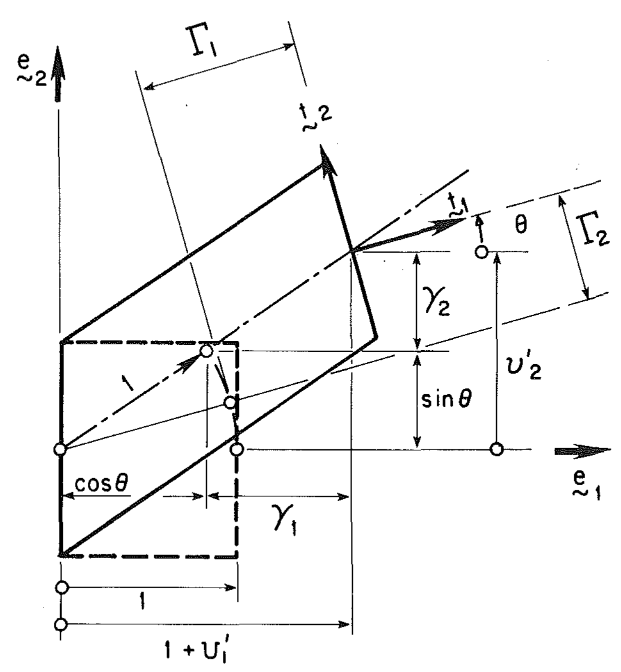

Fig. 3.1 Physical interpretation of the strain components of a beam in the finite strain case

$$\Pi_{EXT} = \int_{[0,L]} [\bar{\mathbf{m}}\cdot\theta\mathbf{e}_3 + \bar{\mathbf{n}}\cdot\boldsymbol{\phi}_0]dX_1 \tag{3.14}$$

Here, $\bar{\mathbf{n}}(X_1,\ t) := \bar{n}_1(X_1,\ t)\mathbf{e}_1\ +\ \bar{n}_2(X_1,\ t)\mathbf{e}_2$ and $\bar{\mathbf{m}}(X_1,\ t) := \bar{m}(X_1,\ t)\mathbf{e}_3$ are the external force and torque per unit of reference length acting on the beam.

Remark 3.6. Dissipative mechanisms with viscous force proportional to the velocity can be readily accommodated in the formulation. To this end, the first variation of equation (2.15) is augmented by a velocity dependent dissipative term W_D defined by

$$W_D := -\int_{[t_1,t_2]}\int_{[0,L]} [\mathbf{n}_D\cdot\delta\boldsymbol{\phi}_0 + \mathbf{m}_D\cdot\delta\theta\mathbf{e}_3]dX_1dt, \tag{3.15}$$

where $\delta\boldsymbol{\phi}_0$ and $\delta\theta\mathbf{e}_3$ denote arbitrary variations, and $\mathbf{n}_D$ and $\mathbf{m}_D$ are the velocity proportional viscous force and torque. For simplicity, we assume the expressions

$$\mathbf{n}_D := \mu A_\rho\dot{\boldsymbol{\phi}}_0, \quad \mathbf{m}_D := \mu I_\rho\dot{\theta}\mathbf{e}_3. \tag{3.16}$$

In the linear case this dissipative mechanism is often referred to as mass proportional damping, and becomes progressively ineffective in the high frequency range of the response. Alternative dissipative mechanisms typically involve inelastic constitutive behavior, e.g., viscoelastic response.

3.4 Equations of Motion: Uncoupled Inertia Terms. As in Section 2, the equations of motion governing the evolution of the system may be systematically obtained from Hamilton's principle. Standard manipulations yield the final result

$$A_\rho\ddot{\boldsymbol{\phi}}_0 + \mu A_\rho\dot{\boldsymbol{\phi}}_0 - \left[\boldsymbol{\Lambda}\mathbf{C}\boldsymbol{\Lambda}^t \begin{Bmatrix} 1+u_1'-\cos\theta \\ u_2'-\sin\theta \end{Bmatrix}\right]' - \bar{n} = 0, \tag{3.17a}$$

$$I_\rho\ddot{\theta} + \mu I_\rho\dot{\theta} - EI\theta'' - \begin{Bmatrix} -u_2' \\ 1+u_1' \end{Bmatrix}^t \boldsymbol{\Lambda}\mathbf{C}\boldsymbol{\Lambda}^t \begin{Bmatrix} 1+u_1'-\cos\theta \\ u_2'-\sin\theta \end{Bmatrix} - \bar{m} = 0. \tag{3.17b}$$

We recall that $\boldsymbol{\Lambda}$ and $\mathbf{C}$ are given by

$$\mathbf{C} := \begin{bmatrix} EA & 0 \\ 0 & GA_s \end{bmatrix}, \quad \boldsymbol{\Lambda} := \begin{bmatrix} \cos\theta & -\sin\theta \\ \sin\theta & \cos\theta \end{bmatrix}. \tag{3.17c}$$

Equations (3.17*a*,*b*) comprise the system of nonlinear partial differential equations governing the response of the system. Note that these nonlinear equations are linear in the time derivative terms.

To define the natural boundary conditions, and for subsequent developments, we introduce the notation

$$\begin{Bmatrix} n_1 \\ n_2 \end{Bmatrix} := \boldsymbol{\Lambda}\mathbf{C}\boldsymbol{\Lambda}^t \begin{Bmatrix} 1+u_1'-\cos\theta \\ u_2'-\sin\theta \end{Bmatrix}, \quad m := EI\theta'. \tag{3.18}$$

Here, $\mathbf{n}(X_1,\ t) := n_1(X_1,\ t)\mathbf{e}_1\ +\ n_2(X_1,\ t)\mathbf{e}_2$ and $\mathbf{m}(X_1,\ t) := m(X_1,\ t)\mathbf{e}_3$ represent the internal force and internal moment acting on a deformed cross section of the beam. For the robot arm in Fig. 3.1 we have the following natural boundary conditions

$$\mathbf{m}(0,t) = T(t)\mathbf{e}_3, \quad \mathbf{m}(L,t) \equiv \mathbf{n}(L,t) \equiv \mathbf{0}. \tag{3.19}$$

These boundary conditions follow automatically from Hamilton's principle and the appropriate expression for Π_{EXT}.

3.5 Conservation of Global Momenta. Within the proposed approach *global* linear and angular momenta are automatically satisfied, and do not provide an additional constraint. This is in contrast with the shadow beam approach in which the basic equations of motion (2.16) must be supplemented by the global angular momentum condition (2.17) for the evolution of the system to be completely determined. To verify conservation of global linear and angular momenta we rewrite equations (3.17*a*,*b*) with the aid of equation (3.19) as

$$\dot{\mathbf{L}} - \mathbf{n}' - \bar{\mathbf{n}}' = \mathbf{0}, \quad \dot{\mathbf{H}} - \mathbf{m}' - \boldsymbol{\phi}_0' \times \mathbf{n} - \bar{\mathbf{m}} = \mathbf{0}. \tag{3.20a}$$

Here $\mathbf{L}(X_1,\ t)$ denotes the linear momentum per unit length, and $\mathbf{H}(X_1,\ t)$ the angular momentum per unit length relative to the centroid of the deformed cross section. Using equation (3.1) we have

$$\mathbf{L} := \int_{\left[-\frac{h}{2},\frac{h}{2}\right]} \rho\dot{\boldsymbol{\phi}}dX_2 = A_\rho\dot{\boldsymbol{\phi}}_0,$$

$$\mathbf{H} := \int_{\left[-\frac{h}{2},\frac{h}{2}\right]} \rho[\boldsymbol{\phi} - \boldsymbol{\phi}_0] \times \dot{\boldsymbol{\phi}}dX_2 = I_\rho\dot{\theta}\mathbf{e}_3, \tag{3.20b}$$

where $\mathbf{e}_3 := \mathbf{e}_1\ \times\ \mathbf{e}_2$. The global linear and angular momentum of the system denoted by $\mathbb{L}(t)$ and $\mathbb{H}(t)$, respectively, are defined as

$$\mathbb{L}(t) := \int_{[0,L]\times\left[-\frac{h}{2},\frac{h}{2}\right]} \rho\dot{\boldsymbol{\phi}}\ dX_1dX_2,$$

$$\mathbb{H}(t) := \int_{[0,L]\times\left[-\frac{h}{2},\frac{h}{2}\right]} \rho\boldsymbol{\phi} \times \dot{\boldsymbol{\phi}}\ dX_1dX_2. \tag{3.21}$$

Making use of the identity $\boldsymbol{\phi}\times\dot{\boldsymbol{\phi}}\ =\ (\boldsymbol{\phi}-\boldsymbol{\phi}_0)\times\dot{\boldsymbol{\phi}}\ +\ \boldsymbol{\phi}_0\times\dot{\boldsymbol{\phi}}$ the global angular momentum is expressed as

$$\mathbb{H}(t) = \int_{[0,L]} [\mathbf{H} + \boldsymbol{\phi}_0 \times \mathbf{L}]dX_1, \tag{3.22}$$

where $\mathbf{L}(X_1,t)$ and $\mathbf{H}(X_1,t)$ are given in equation (3.20*b*). Differentiating equation (3.22) and using equation (3.20*a*), we obtain the following condition involving the applied load and boundary conditions

$$\dot{\mathbb{H}} = [\mathbf{m} + \boldsymbol{\phi}_0 \times \mathbf{n}]\Big|_{X_1=0}^{X_1=L} + \int_{[0,L]} [\bar{\mathbf{m}} + \boldsymbol{\phi}_0 \times \bar{\mathbf{n}}]dX_1. \tag{3.23}$$

Condition (3.23) states that the resultant torque of the applied loading equals the rate of change of the total angular momentum. Similarly, for the global linear momentum we obtain

$$\dot{\mathbb{L}} = \mathbf{n} \Big|_{X_1=0}^{X_1=L} + \int_{[0,L]} \bar{\mathbf{n}} dX_1, \tag{3.24}$$

which states that the resultant force of the applied loads equals the rate of change of the global linear momentum. Equations of motion (3.20*a*) along with definitions (3.20*b*) are general, and remain valid in the three dimensional theory. Thus, the foregoing discussion leading to expressions (3.23) and (3.24) is not only restricted to the plane case.

4 Concluding Remarks

In this paper, we have presented a new approach to the dynamics of a plane beam under large overall motions. The essence of this approach is the fully nonlinear plane beam theory that can account for finite rotations as well as finite strains. The appropriate strain measures in the beam theory are invariant under superposed rigid body motion; such invariance is the necessary ingredient to the success of the present approach. The motion of the beam is completely referred to the inertial frame. We thus obtain the expression of the inertia term in the equations of motion simply as mass times acceleration. By contrast, in the shadow beam approach, one obtains a nonlinear and highly coupled inertia operator; hence a special computer code must be devised to solve the resulting system. In our approach, the inherent nonlinear character of the problem is transferred to the stiffness part of the equations of motion; this results in equations of motion that arise typically in nonlinear structural dynamics. As demonstrated in Part II of this paper, the dynamics of flexible beams under large overall motions can be analyzed in any existing nonlinear finite element program. Without alteration in the formulation, one can apply this approach to the dynamics of a system of flexible beams connected by hinges, as shown by our numerical examples. In addition, the approach proposed in this paper can be readily extended to accommodate inelastic constitutive behavior, and can be used to treat a wide range of problems including the dynamic analysis of an earth-orbiting satellite composed of beam elements. Finally we note that, conceptually, the proposed approach readily carries over to the fully three dimensional case. Further comments on possible extensions of the proposed methodology are given in part II of this paper.

Acknowledgments

We thank Professor R. L. Taylor, the developer of FEAP, for his helpful discussions. This work was performed under the auspices of the Air Force Office of Scientific Research, grant No. AFOSR-83-0361. This support as well as the encouragement provided by Professors K. S. Pister and E. Polak are gratefully acknowledged.

References

Antman, S. S., 1972, "The Theory of Rod," *Handbuch der Physics*, Vol. VIa/2, Springer, Berlin.

Antman, S. S., 1974, "Kirchhoff's Problem for Nonlinearly Elastic Rods," *Quart. J. of Appl. Math.*, Vol. 32, pp. 221–240.

Ashley, H., 1967, "Observation of the Dynamic Behavior of Flexible Bodies in Orbit," *AIAA J.*, Vol. 5, No. 3, pp. 460–469.

Baghat, B. M., and Willmert, K. D., 1973, "Finite Element Vibrational Analysis of Planar Mechanism," *Mechanisms and Machine Theory*, Vol. 8, pp. 497–516.

Belytschko, T., and Hughes, T. J. R., 1983, *Computational Methods For Transient Analysis*, Elsevier Science Publishers.

Canavin, J. R., and Likins, P. W., 1977, "Floating Reference Frames for Flexible Spacecrafts," *J. of Spacecraft*, Vol. 14, No. 12, pp. 724–732.

de Veubeke, B. J., 1976, "The Dynamics of Flexible Bodies," *Int. J. of Engineering Sciences*, Vol. 14, pp. 895–913.

Erdman, A. G., and Sandor, G. N., 1972, "Kineto-Elastodynamics—A Review of the State of the Art and Trends," *Mechanisms and Machine Theory*, Vol. 7, pp. 19–33.

Fung, Y. C., 1965, *Foundations of Solid Mechanics*, Prentice-Hall, Englewood Cliffs, NJ.

Goldstein, H., 1980, *Classical Mechanics*, Second Ed., Addison Wesley, Reading, Massachusetts.

Grotte, P. B., McMunn, J. C., and Gluck, R., 1971, "Equations of Motion of Flexible Spacecraft," *J. of Spacecraft and Rockets*, Vol. 8, No. 6, pp. 561–567.

Kane, T. R., and Levinson, D. A., 1981, "Simulation of Large Motions of Nonuniform Beams in Orbit: Part II—The Unrestrained Beam," *The J. of the Astronautical Sciences*, Vol. 29, No. 3, pp. 213–244.

Kane, T. R., Likins, P. W., and Levinson, D. A., 1983, *Spacecraft Dynamics*, McGraw-Hill, New York.

Kumar, V. K., and Bainum, P. M., 1980, "Dynamics of a Flexible Body in Orbit," *J. of Guidance and Control*, Vol. 3, No. 1, pp. 90–91.

Laskin, R. A., Likins, P. W., and Longman, R. W., 1983, "Dynamical Equations of a Free-Free Beam Subject to Large Overall Motions," *The J. of the Astronautical Sciences*, Vol. 31, No. 4, pp. 507–528.

Levinson, D. A., and Kane, T. R., 1981, "Simulation of Large Motions of Nonuniform Beams in Orbit: Part I—The Cantilever Beam," *The J. of the Astronautical Sciences*, Vol. 29, No. 3, pp. 245–276.

Likins, P. W., 1974, "Analytical Dynamics and Nonrigid Spacecraft Simulation," *Jet Propulsion Laboratory, Technical Report 32-1593*, California Institute of Technology.

Petzold, L. R., 1982, "Differential/Algebraic Equations are Not ODE's," *SIAM J. Sci. Stat. Comput.*, Vol. 3, No. 3, pp. 367–384.

Reissner, E., 1972, "On a One Dimensional Finite Strain Beam: The Plane Problem," *J. Appl. Math. Phys.*, Vol. 23, pp. 795–804.

Reissner, E., 1973, "On a One-Dimensional Large-Displacement, Finite-Strain Beam Theory," *Studies in Applied Math*, Vol. 52, pp. 87–95.

Reissner, E., 1981, "On Finite Deformations of Space-Curved Beams," ZAMP, Vol. 32, pp. 734–744.

Simo, J. C., 1985, "A Finite Strain Beam Formulation. The Three Dimensional Dynamic Problem. Part I," *Comp. Meth. Appl. Mech. Engrg.*, Vol. 49, pp. 55–70.

Simo, J. C., and Vu-Quoc, L., 1985, "Three Dimensional Finite Strain Rod Model. Part II: Computational Aspects," *Electronics Research Laboratory Memorandum No. UCB/ERL M85/31*, University of California, Berkeley, April. (Submitted for publication.)

Simo, J. C., and Vu-Quoc, L., 1986, *The Role of Nonlinear Theories in the Dynamics Analysis of Rotating Structures*, Electronics Research Laboratory Memorandum UCB/ERL M86/10, University of California, Berkeley, January.

Song, J. O., and Huag, E. J., 1980, "Dynamic Analysis of Planar Flexible Mechanism," *Comp. Meth. Appl. Mech. Engrg.*, Vol. 24, pp. 359–381.

Winfrey, R. C., 1971, "Elastic Link Mechanism Dynamics," *ASME J. of Engineering for Industry*, Vol. 93, No. 1, pp. 268–272.

J. C. Simo[1]
Applied Mechanics Division,
Stanford University,
Stanford, CA 94305

L. Vu-Quoc
Structural Engineering and Structural
Mechanics Division,
University of California,
Berkeley, CA 94720

On the Dynamics of Flexible Beams Under Large Overall Motions—The Plane Case: Part II

The numerical treatment of the methodology proposed in Part I of this paper is considered in detail. Unlike traditional approaches, a Galerkin spatial discretization of the equations of motion, now referred to the inertial frame, yields the standard form of nonlinear structural dynamics: $\mathbf{M}\ddot{\mathbf{q}} + \mathbf{D}\dot{\mathbf{q}} + \mathbf{P}(\mathbf{q}) = \mathbf{F}$, *with* $\mathbf{M}$ *and* $\mathbf{D}$ constant *matrices. Numerical examples that involve finite vibrations coupled with large overall motions are presented. These simulations also demonstrate the capability of the present formulation in handling* multibody dynamics.

1 Numerical Approximation: Galerkin Method

In this section we discuss the numerical treatment of the nonlinear partial differential equations developed in Section 3 of Part I. The basic strategy is to perform a Galerkin discretization in the spatial variable leading to the standard system of ODE's in the time variable characteristic of nonlinear structural dynamics. This system may then be solved discretely using standard time stepping algorithms (e.g., the Newmark family). The finite element method provides an established technique for constructing the (spatial) basis functions necessary to perform the Galerkin discretization. Expressions of the matrices resulting from the application of this procedure are given in the appendix.

1.1 Weak Form of Equations of Motion—Spatial Discretization. The equations of motion (3.14) of Part I may be put in the following form

$$\mathbf{I}\ddot{\mathbf{d}}(X_1,t)+\boldsymbol{\Delta}\dot{\mathbf{d}}(X_1,t)+\mathbf{P}[\mathbf{d}(X_1,t)=\mathbf{f}(X_1,t), \qquad (1.1a)$$

where

$$\mathbf{I}:=\mathrm{Diag}[A_\rho,A_\rho,I_\rho],\ \boldsymbol{\Delta}:=\mathrm{Diag}[\mu A_\rho,\mu A_\rho,\mu I_\rho], \qquad (1.1b)$$

$$\mathbf{d}(X_1,t):=\begin{Bmatrix} X_1+u_1(X_1,t) \\ u_2(X_1,t) \\ \theta(X_1,t) \end{Bmatrix},\quad \mathbf{f}(X_1,t):=\begin{Bmatrix} \bar{n}_1(X_1,t) \\ \bar{n}_2(X_1,t) \\ \bar{m}(X_1,t) \end{Bmatrix}$$

Equation (1.1*a*) is a nonlinear partial differential equation in the generalized vector $\mathbf{d}(X_1, t) \in V_1$, where V_1 is the space of admissible (generalized) displacements.[2] This equation is linear in the terms involving time derivatives, i.e., the acceleration $\ddot{\mathbf{d}}$ in the first term and the velocity $\dot{\mathbf{d}}$ in the second term. The third term $\mathbf{P}[\mathbf{d}]$, on the other hand, is a nonlinear differential operator in the space variable $X_1 \in (0,L)$. This nonlinearity results from the coupling between large overall motions and (finite) strain deformations in the beam. Concerning the applied load $\bar{\mathbf{n}}$ and $\bar{m}$, see remark 3.5. The weak form $G(\mathbf{d},\eta)$ of equation (1.1*a*) is obtained by integrating over the spatial domain $(0,L) \subset \mathbf{R}$ the dot product of this equation with an arbitrary weighting function $\eta \in V_2$.[3] That is

$$G(\mathbf{d},\eta):=\int_{[0,L]}\eta^t[\mathbf{I}\ddot{\mathbf{d}}+\boldsymbol{\Delta}\dot{\mathbf{d}}+\mathbf{P}[\mathbf{d}]-\mathbf{f}]dX_1\equiv 0,\forall\eta\in V_2 \qquad (1.2)$$

The final expression is obtained from (1.2) by integration by parts on the spatial derivatives entering $\mathbf{P}[\mathbf{d}]$, so that only *first order spatial derivatives* are involved in $G(\mathbf{d},\eta)$. We refer to the appendix for the details. The displacements $\mathbf{d}(X_1,t)$ and the weighting function $\eta(X_1)$ are then interpolated in the spatial variable X_1 according to

$$\mathbf{d}(X_1,t)\cong\sum_{I=1}^{N}\boldsymbol{\Psi}_I(X_1)\mathbf{q}_I(t),$$

$$\eta(X_1)\cong\sum_{I=1}^{N}\boldsymbol{\Psi}_I(X_1)\eta_I^h \qquad (1.3)$$

Upon introducing the spatial discretization (1.3) of $\mathbf{d}(X_1,t)$ and of $\eta(X_1)$ into the weak form (1.2), we obtain the semidiscrete equation of motion in matrix form

$$\mathbf{M}\ddot{\mathbf{q}}(t)+\mathbf{D}\dot{\mathbf{d}}(t)+\mathbf{P}(\mathbf{q}(t))=\mathbf{F}(t) \qquad (1.4)$$

---

[1] Formerly at the University of California, Berkeley.

Contributed by the Applied Mechanics Division for presentation at the Winter Annual Meeting, Anaheim, CA, December 7-12, 1986, of The American Society of Mechanical Engineers.

Discussion on this paper should be addressed to the Editorial Department, ASME, United Engineering Center, 345 East 47th Street, New York, N.Y. 10017, and will be accepted until two months after final publication of the paper itself in the JOURNAL OF APPLIED MECHANICS. Manuscript received by ASME Applied Mechanics Division, September 23, 1985; final revision, May 7, 1986. Paper No. 86-WA/APM-42.

[2] A possible choice for V_1 could be $V_1:=\{\mathbf{d}\in[H^1(0,L)\times C^\infty(0,\infty)]^3 \mid u_1|_{x_1=0}=u_2|_{x_1=0}=0$, and Ⓗ $|_{x_1=0}\psi\}$

[3] V_2 could be chosen to be $V_2:=\{\eta\in\bar{H}^1(0,L)]^3 \mid$ with appropriate boundary conditions for η such that $\eta_1 n_1+\eta_2 n_2+\eta_3 m=0$ at the boundaries$\}$

where **M** and **D** are constant mass and damping matrices, respectively, $\mathbf{q}(t) := [\mathbf{q}_1(t), \ldots, \mathbf{q}_N(t)]^t$ denotes the generalized displacement vector, $\mathbf{P}(\mathbf{q}(t))$ the vector of internal forces depending on $\mathbf{q}(t)$, and $\mathbf{F}(t)$ the applied load vector. Details of the expressions of $\mathbf{M}$, $\mathbf{D}$, $\mathbf{P}(\mathbf{q}(t))$, and $\mathbf{F}(t)$ can be found in the appendix.

Remark 1.1. In the absence of dissipative mechanisms (e.g., damping) the system has a well defined energy function $H = K + \mathbf{\Pi}$. The Galerkin procedure outlined above is then equivalent to a standard Raleigh-Ritz approximation based on $(1.3)_1$. See, e.g., Meirovitch (1970).

Remark 1.2. In the shadow beam approach restricted to small-strains, one may also use the modal superposition method to discretize spatially the displacements $[\tilde{u}_1, \tilde{u}_2]$ as in (1.3). For this purpose, consider equations (2.16) of Part I. One first eliminates $\tilde{\alpha}$ from equation (2.16) using $(2.16)_2$. The semi-discrete equation of motion of the system is then obtained by projecting the resulting equations (2.16) onto the orthogonal basis of mode-shapes of the Euler-Bernoulli cantilever beam. However, no matter which discretization procedure is used, the resulting semi-discrete equations of motion system constitute a system of highly *coupled nonlinear differential algebraic equations* (DAE). The solution of this complete system of DAE's is not a trivial task, and requires a specially designed computer code (Benson and Hallquist, 1985). Numerical integration methods for DAE systems may be found in Gear (1971a,b), Petzold (1982), and Gear and Petzold (1984). The solution of the standard nonlinear structural dynamics equation (1.4), on the other hand, is much simpler and may be carried out using any nonlinear structural finite element code. A time stepping algorithm solution procedure will be outlined in the next section.

Remark 1.3. Multibody Dynamics. In Section 5, we will show through numerical examples that the proposed approach can be applied without alteration in the formulation to study the dynamics of a system of flexible bodies connected through hinges. It is indeed a simple matter to model such a system in a finite element program. The shadow beam approach, on the other hand, leads to a much more involved formulation, e.g., as in Hughes (1979), Likins (1974), Song and Haug (1980), and Sunada and Dubowsky (1980).

1.2 Time Stepping Scheme—Temporal Discretization. The semi-discrete equations of motion (1.4) can be trivially rephrased into the standard form of a system of nonlinear ODE's, $\dot{\mathbf{y}} = \mathbf{g}(\mathbf{y}, t)$, by setting $\mathbf{y} := \{\mathbf{q}, \dot{\mathbf{q}}\}$. This standard ODE system can be integrated by a variety of time stepping algorithms (Gear, 1971), which must be *consistent* with (1.4) and *stable* for some range of the time step. We refer to standard textbooks such as Gear (1971) and Richtmyer and Morton (1967) for precise definitions of these concepts. Two basic strategies in devising algorithms for (1.4) may be adopted:

(*a*) *Explicit schemes:* Typically, high accuracy may be achieved by employng high order methods. A classical example is furnished by the family of Runge-Kutta methods. It is well-known that the main drawback of explicit schemes is the severe limitation on the time step imposed by their restrictive stability characteristics.

(*b*) *Implicit scheme* typically possess very robust stability characteristics. Classical examples are the trapezoidal rule, which is the highest order A-stable method possible (Dahlquist, 1963), the stiffly stable methods of Gear (1971b), and the family of algorithms devised by Newmark (1959) and widely used in nonlinear structural dynamics (Belytschko and Hughes, 1983).

Here, motivated by stability considerations, attention is focused on the Newmark family of algorithms for solving (1.4), which includes the trapezoidal rule as a special case. The behavior and stability characteristics of the Newmark algorithm applied to *linear* problems is well established, e.g., see the analysis of Goudreau and Taylor (1973), and Hilber (1976). For completeness, we shall outline the basic steps involved in the numerical solution of (1.4) by the Newmark algorithm.

Let $\mathbf{q}_n$ denote the approximate solution to $\mathbf{q}(t_n)$ at time t_n. Similarly, $\mathbf{v}_n \cong \dot{\mathbf{q}}(t_n)$ and $\mathbf{r}_n \cong \ddot{\mathbf{q}}(t_n)$ represent the approximate velocity and acceleration at time t_n, respectively. Assume that the solution $\{\mathbf{q}_n, \mathbf{v}_n, \mathbf{r}_n\}$ at time t_n has already been obtained, i.e., the momentum equation (1.4) is satisfied at time t_n

$$\mathbf{M}\mathbf{r}_n + \mathbf{D}\mathbf{v}_n + \mathbf{P}(\mathbf{q}_n) = \mathbf{F}_n \tag{1.5}$$

where $\mathbf{F}_n \equiv \mathbf{F}(t_n)$. We now aim at satisfying the momentum equation (1.4) at time t_{n+1}, i.e.,

$$\mathbf{M}\mathbf{r}_{n+1} + \mathbf{D}\mathbf{v}_{n+1} + \mathbf{P}(\mathbf{q}_{n+1}) = \mathbf{F}_{n+1} \tag{1.6}$$

The Newmark time stepping algorithm defines the relationship between $\{\mathbf{q}_{n+1}, \mathbf{v}_{n+1}, \mathbf{r}_{n+1}\}$ according to the following formulae

$$\mathbf{r}_{n+1} = \frac{\mathbf{q}_{n+1} - \mathbf{q}_n}{h^2\beta} - \frac{\mathbf{v}_n}{h\beta} - \frac{\dfrac{1}{2} - \beta}{\beta}\mathbf{r}_n \tag{1.7a}$$

$$\mathbf{v}_{n+1} = \mathbf{v}_n + h[(1-\tau)\mathbf{r}_n + \tau\mathbf{r}_{n+1}], \tag{1.7b}$$

where $h := t_{n+1} - t_n$ denotes the time step size, and (β, τ) are the parameters of the Newmark algorithm. We note that $\beta = 0.25$ and $\tau = 0.5$ correspond to the trapezoidal rule; this choice of the parameters β and τ renders the algorithm *unconditionally stable* in the linear case,[4] and second order accurate. Substitution of equation (1.7*a*) into (1.6) yields a system of nonlinear algebraic equations in terms of $\mathbf{q}_{n+1}$.

The resulting nonlinear algebraic system may then be solved employing the classical Newton-Raphson method. Let $\mathbf{q}_{n+1}^{(i)}$ denote the value of $\mathbf{q}_{n+1}$ at iteration (i) of the Newton-Raphson algorithm, and $\Delta\mathbf{q}_{n+1}^{(i+1)}$ the incremental displacements. As an initial guess for $\{\mathbf{q}_{n+1}, \mathbf{v}_{n+1}, \mathbf{r}_{n+1}\}$, one may choose the starting value $\mathbf{q}_{n+1}^{(0)}$ to be the same as the converged value in the previous time increment, i.e., $\mathbf{q}_n$; the initial values $\mathbf{v}_{n+1}^{(0)}$ and $\mathbf{r}_{n+1}^{(0)}$ follow from the Newmark scheme (1.7):

$$\mathbf{q}_{n+1}^{(0)} = \mathbf{q}_n \tag{1.8a}$$

$$\mathbf{r}_{n+1}^{(0)} = -\left[\frac{\mathbf{v}_n}{h\beta} + \frac{\dfrac{1}{2} - \beta}{\beta}\mathbf{r}_n\right] \tag{1.8b}$$

$$\mathbf{v}_{n+1}^{(0)} = \mathbf{v}_n + h[(1-\tau)\mathbf{r}_n + \tau\mathbf{r}_{n+1}^{(0)}] \tag{1.8c}$$

At iteration (i) of the Newton-Raphson scheme, the linearization about $\mathbf{q}_{n+1}^{(i)}$ of the system of nonlinear algebraic equations yields

$$\left[\frac{1}{h^2\beta}\mathbf{M} + \frac{\tau}{h\beta}\mathbf{D} + \mathbf{K}_T(\mathbf{q}_{n+1}^{(i)})\right]\Delta\mathbf{q}_{n+1}^{(i+1)} = \mathbf{F}_{n+1} - \mathbf{M}\mathbf{r}_{n+1}^{(i)} - \mathbf{D}\mathbf{v}_{n+1}^{(i)} - \mathbf{P}(\mathbf{q}_{n+1}^{(i)}) \tag{1.9}$$

It should be noted here that while the mass matrix **M** is positive definite, the tangent stiffness matrix $\mathbf{K}_T(\mathbf{q}_{n+1}^{(i)})$ may be positive semi-definite. The system of equations (1.9) is of

---

[4] Roughly, the notion of stability corresponds to well-posedness of the semi-discrete problem. In the nonlinear case the appropriate concept of stability remains unsettled, and several notions of stability have been proposed (A-stability, spectral stability, stability in the energy sense, etc. . .). See, e.g., Belytschko and Hughes (1983), Gear (1971b), Chorin et al. (1978).

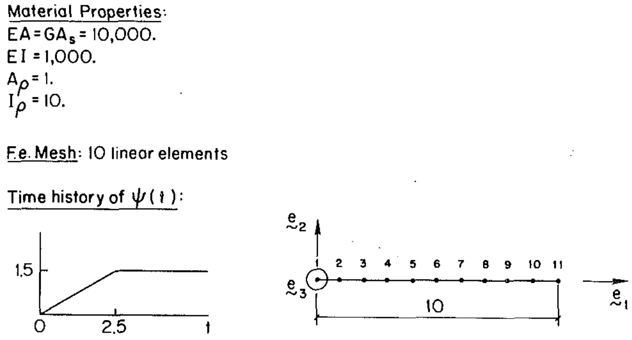

Fig. 1(*a*) **Displacement driven flexible robot arm; problem data**

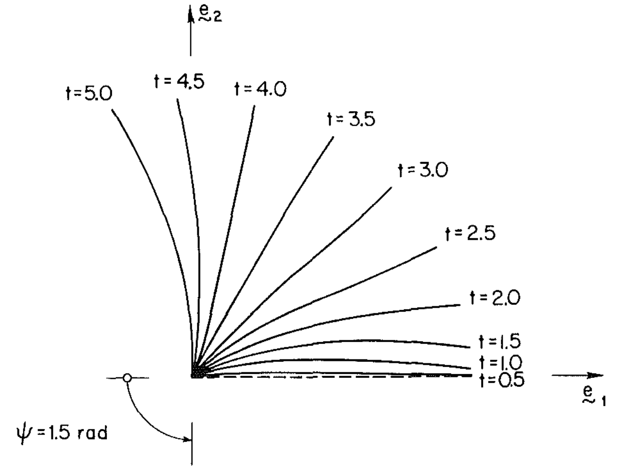

Fig. 1(*b*) Displacement driven flexible robot arm. Repositioning sequence to stop angle $\psi = 1.5$ rad. Time step size $h = 0.5$.

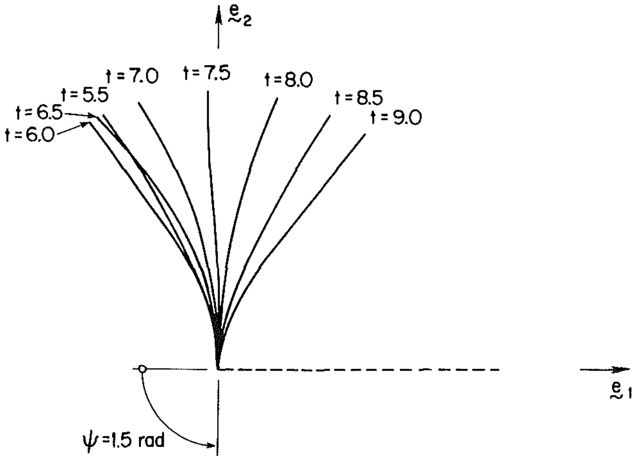

Fig. 1(c) Displacement driven flexible robot arm. Free vibration about $\psi = 1.5$ rad. Time step size $h = 0.5$.

the form $\hat{\mathbf{K}}\Delta\mathbf{q}_{n+1}^{(i+1)} = \hat{\mathbf{F}}$ where the matrix $\hat{\mathbf{K}}$ is banded, symmetric, and positive definite. Solving for $\Delta\mathbf{q}_{n+1}^{(i+1)}$, and updating $(\mathbf{q}_{n+1}^{(i)}, \mathbf{v}_{n+1}^{(i)}, \mathbf{r}_{n+1}^{(i)})$, we obtain the value of $\{\mathbf{q}_{n+1}, \mathbf{v}_{n+1}, \mathbf{r}_{n+1}\}$ at iteration $(i+1)$ as follows

$$\mathbf{q}_{n+1}^{(i+1)} = \mathbf{q}_{n+1}^{(i)} + \Delta\mathbf{q}_{n+1}^{(i+1)} \tag{1.10a}$$

$$\mathbf{v}_{n+1}^{(i+1)} = \mathbf{v}_{n+1}^{(i)} + \frac{\tau}{h\beta}\,\Delta\mathbf{q}_{n+1}^{(i+1)} \tag{1.10b}$$

$$\mathbf{r}_{n+1}^{(i+1)} = \mathbf{r}_{n+1}^{(i)} + \frac{1}{h^2\beta}\,\Delta\mathbf{q}_{n+1}^{(i+1)} \tag{1.10c}$$

The iterations are continued until convergence is attained within certain tolerance. A basic characteristic of Newton's iterative method is that the asymptotic rate of convergence is quadratic.

2 Numerical Simulations

In this section we present a series of numerical simulations that illustrate the formulation and numerical procedure discussed in Sections 3 of Part I. Our purpose is to exhibit:

(*a*) The simplicity of the numerical procedure. Essentially any existing nonlinear structural finite element dynamics code could be employed. Here we employ an extended version of the computer program FEAP developed by R. L. Taylor and documented in Zienkiewicz (1977), chapter 24.

(*b*) The capability of the proposed formulation to automatically handle *finite strains* superposed onto large overall rigid body motions. This includes flexible bodies in free flight. Viscous effects can also be accounted for easily in the formulation.

(*c*) The immediate applicability of the proposed approach to the dynamics of a system of interconnected flexible bodies without alteration of the formulation.

It is emphasized that no simplification is made in the simulations that follow in the sense that Coriolis and centrifugal effects as well as the inertia effect due to rotation are automatically accounted for. The deformed shapes in all figures reported in this paper are given at the *same* scale as the geometry of the beam, i.e., there is no magnification of the structural deformations.

In all simulations reported herein, the trapezoidal rule (Newmark algorithm with $\tau = 0.5$ and $\beta = 0.25$) was employed. Numerical operations were performed in double precision in a VAX 11/780 under the Berkeley UNIX 4.2 BSD operating system.

Example 2.1. Flexible Robot Arm. This simulation is concerned with the repositioning of a flexible beam rotating horizontally about a vertical axis passing through one end. The finite element mesh consists of 10 elements with linear isoparametric interpolation functions for both displacement and rotation. To avoid the well known "shear locking" phenomenon (Zienkiewicz, 1977), a uniformly reduced one-point Gauss quadrature is employed to integrate the tangent stiffness and residual. The mass matrix, however, is integrated exactly with two-point Gauss quadrature. Two cases are considered.

2.1.1. Displacement Driven Flexible Robot Arm. The geometry, material properties, finite element mesh, as well as the time step size used in the integration are given in Fig. 1(*a*). The robot arm is first repositioned to an angle of 1.5 *radians* from its initial position. This is achieved by prescribing the rotation angle $\psi(t) \equiv \theta(0, t)$ as a linear function of time, as shown in Fig. 1(*a*); the sequence of motion during this repositioning stage is depicted in Fig. 1(*b*). Once the rotation angle $\psi(t)$ is fixed at 1.5 rad for all time $t \geq 2.5$, the robot arm then undergoes finite vibrations as shown in Fig. 1(*c*).

2.1.2. Force Driven Flexible Robot Arm. The robot arm is now driven by a prescribed torque $T(t)$ applied at the axis of rotation $\mathbf{e}_3$, as shown in Fig. 2(*a*). The applied torque is removed at time $t = 2.5$; the robot arm then undergoes a torque-free motion. The simulation is terminated after completion of one revolution, as shown in Figs. 2(*b*) and 2(*c*).

Example 2.2. Flying Flexible Rod. A flexible rod with free ends, initially placed in an inclined position, is subject to a force and a torque applied simultaneously at one end, see Fig. 3(*a*). The applied force and torque are removed at the same time $t = 2.5$, so that the subsequent free flight of the rod exhibits a periodic tumbling pattern. It should be noted here that

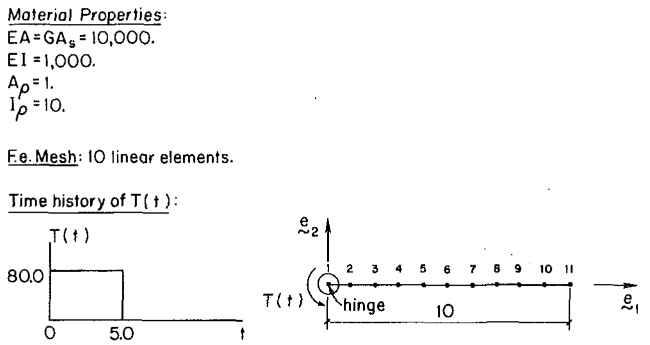

Fig. 2(*a*) Force driven flexible robot arm; problem data

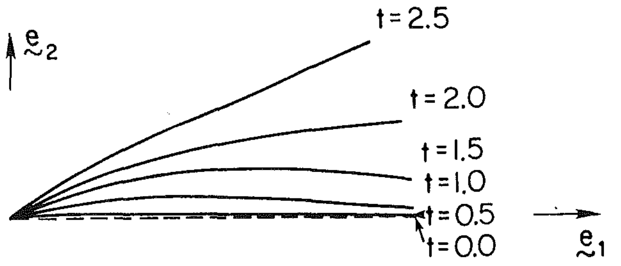

Fig. 2(*b*) Force driven flexible robot arm. Sequence of motion during application of torque. Time step size $h = 0.5$.

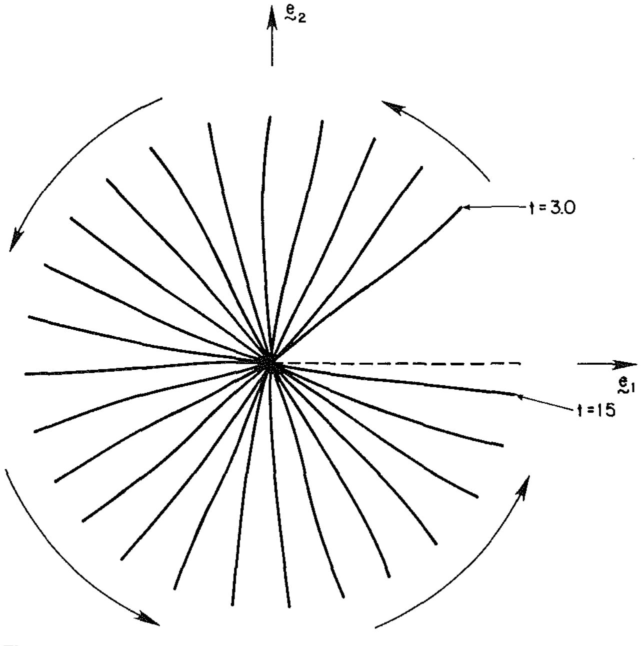

Fig. 2(*c*) Force driven flexible robot arm. Sequence of motion after removal of applied torque.

the boundary conditions (3.19) of Part I now become $\mathbf{m}(0,t) = \mathbf{m}(L,t) = \mathbf{n}(0,t) = \mathbf{n}(L,t) \equiv 0$ during the free flight stage. Two cases are considered.

2.2.1. Flexible Beam in Free Flight. The motion of the rod during application of loading is shown in Fig. 3(*b*). The stiffness of the rod is low enough to exhibit finite deformations. A close-up of the first two revolutions is shown in Fig. 3(*c*) while the entire sequence of motion is depicted in Fig. 3(*d*).

2.2.2. The "Flying Spaghetti." The bending stiffness *EI* of the rod is lowered by a factor of 5 relative to the simulation in 2.2.1. This dramatic reduction in stiffness results in the sequence of motions depicted in Fig. 4.

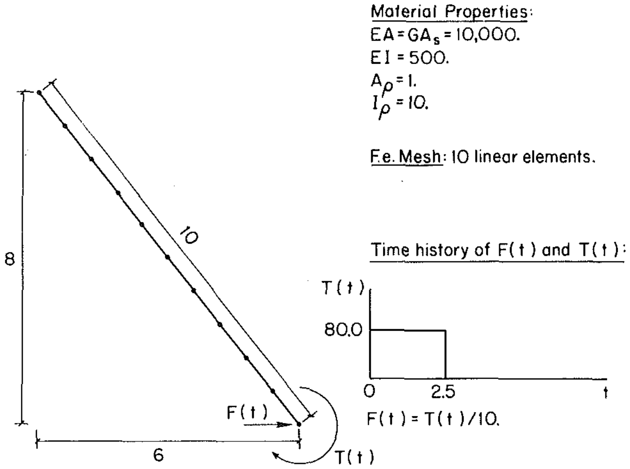

Fig. 3(*a*) Flexible beam in free flight; problem data.

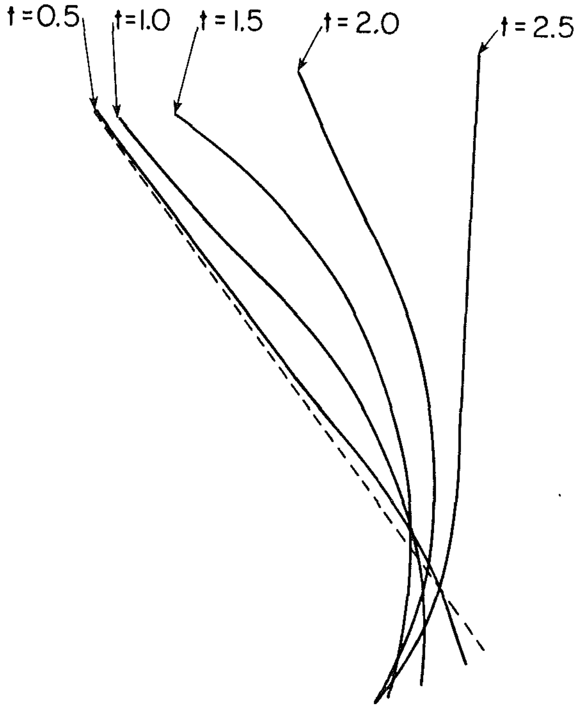

Fig. 3(*b*) Flexible beam in free flight. Sequence of motions during application of loading. Time step size $h = 0.1$, plot after each 5 time increments

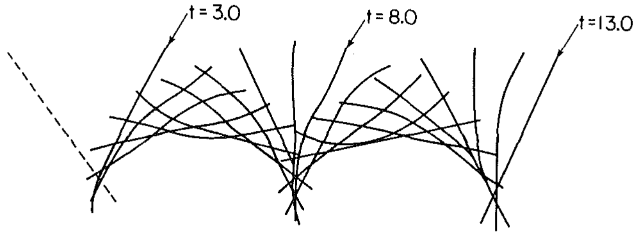

Fig. 3(*c*) Flexible beam in free flight. Free flight of the beam after removal of loading—close-up on the first 2 revolutions. Time step size $h = 0.1$, plot after each 5 time increments

Fig. 3(*d*) Flexible beam in free flight. Free flight—entire sequence.

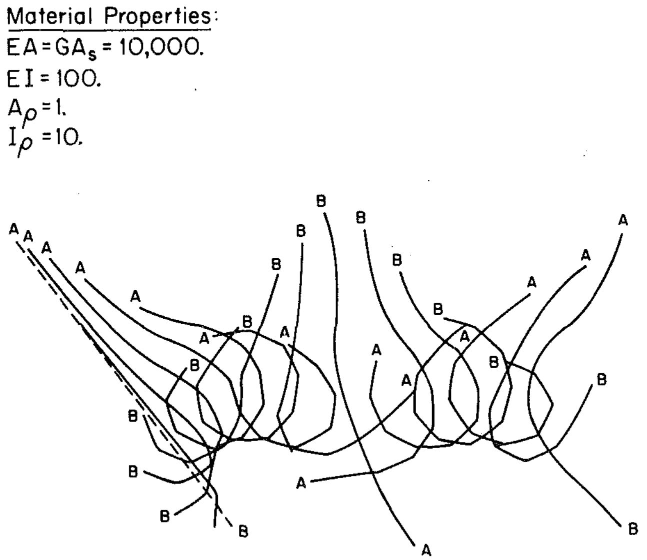

Fig. 4 The "flying spaghetti." Time step size $h = 0.1$, plot after each 5 time increments.

Example 2.3. Multi-Body Dynamics. Two examples will be considered to illustrate the applicability of the present formulation to the dynamics of multibody systems.

2.3.1. Multi-Component Robot Arm. The robot arm considered in Example 2.1.1 is in this example stiffer by a factor of 100, and consists now of two flexible components connected together by a hinge at midlength. The two-component robot arm is subjected to the same prescribe rotation $\psi(t) \equiv \theta(0, t)$ as in Example 2.1.1. The problem data are summarized in Fig. 5(*a*). The sequence of motions is shown in Figs. 5(*b*) and 5(*c*). Note that while the first component vibrates about the stop angle $\psi(t) = 1.5$ rad for $t \geq 2.5$, the second one undergoes a complete revolution about the connecting hinge at midlength.

2.3.2. Multibody System in Free Flight. A two-body system consisting of two flexible links connected by a hinge, is initially at an inclined position. The system is set into motion by applying a force and a torque at one end of the lower link, as shown in Fig. 6. The applied loads are subsequently removed at time $t = 0.5$, so that subsequently the articulated beam undergoes free flight. The lower link, indicated by the letter *A* in the figure, then moves in the same clockwise direction as the applied torque, whereas the upper link, indicated by the letter *B*, moves in the opposite counter clockwise direction.

Example 2.4. Spin-Up Maneuver. The flexible robot arm considered in Example 2.1.1 is now subject to a "spin-up" maneuver by prescribing the angle $\psi(t) \equiv \theta(0,t)$ for $t \in \mathbf{R}_+$ as follows

$$\psi(t) = \begin{cases} \dfrac{6}{15}\left[\dfrac{t^2}{2} + \left(\dfrac{15}{2\pi}\right)^2 \left(\cos\dfrac{2\pi t}{15} - 1\right)\right] \text{rad} & 0 \leq t \leq 15 \quad \text{sec} \\ (6t - 45)\ \text{rad} & t > 15 \quad \text{sec} \end{cases} \tag{2.1}$$

This type of motion was proposed in Kane et al. (1985) to illustrate how naive linearized approximations may lead to grossly inaccurate results, i.e., instability of a physically stable system. The motion is also of practical interest in applications such as helicopter rotor blades or aircraft propellers. The material properties and time history of $\psi(t)$ are shown in Fig.

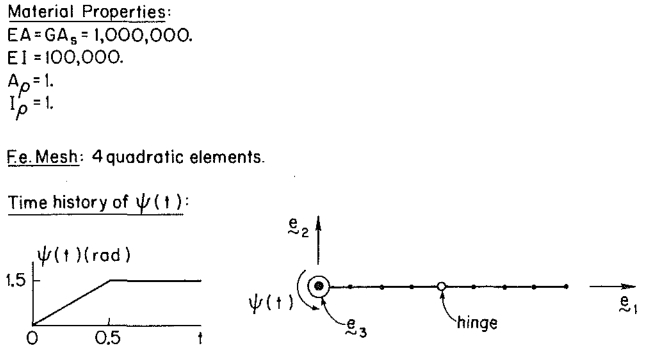

Fig. 5(*a*) Multibody dynamics: displacement driven, multi-component robot arm; problem data

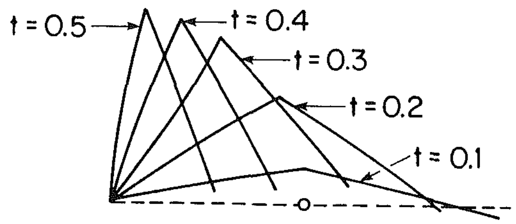

Fig. 5(*b*) Multibody dynamics: displacement driven, multi-component robot arm. Repositioning sequence to stop angle $\psi = 1.5$ rad. Time step size $h = 0.1$.

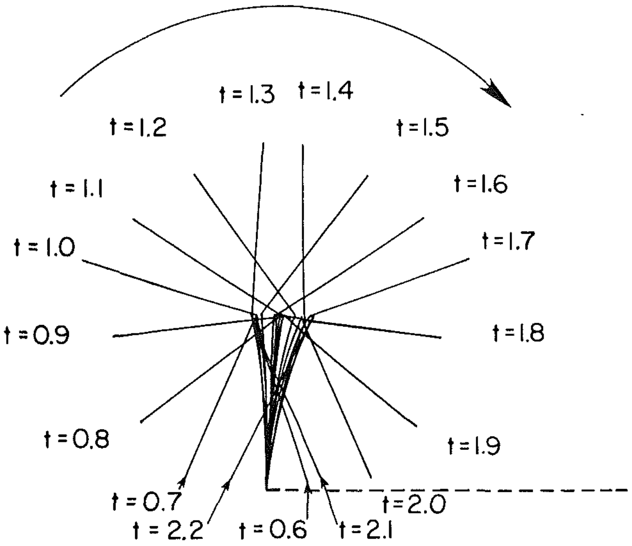

Fig. 5(*c*) Multibody dynamics: displacement driven of multi-component robot arm. Vibration of robot arm about stop angle, and revolution of flexible appendage about connecting hinge. Time step size $h = 0.01$, plot after each 10 time increments.

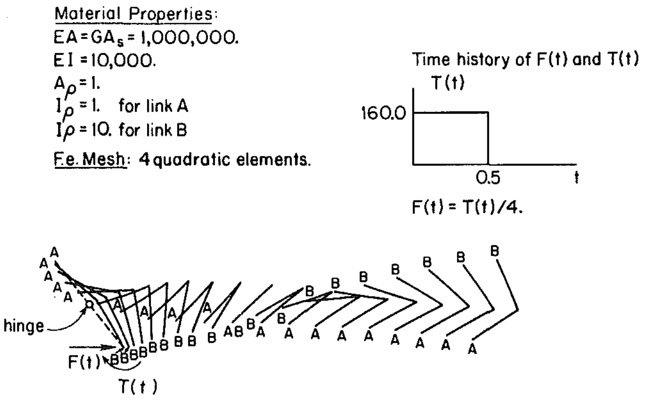

Fig. 6 Multibody dynamics: articulated beam in free flight. Time step size $h = 0.05$, plot after each 5 time increments.

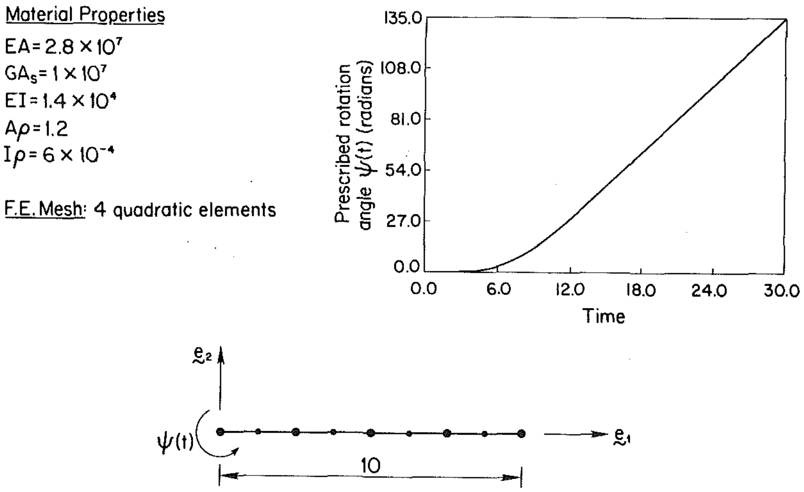

Fig. 7 Spin-up maneuver; problem data

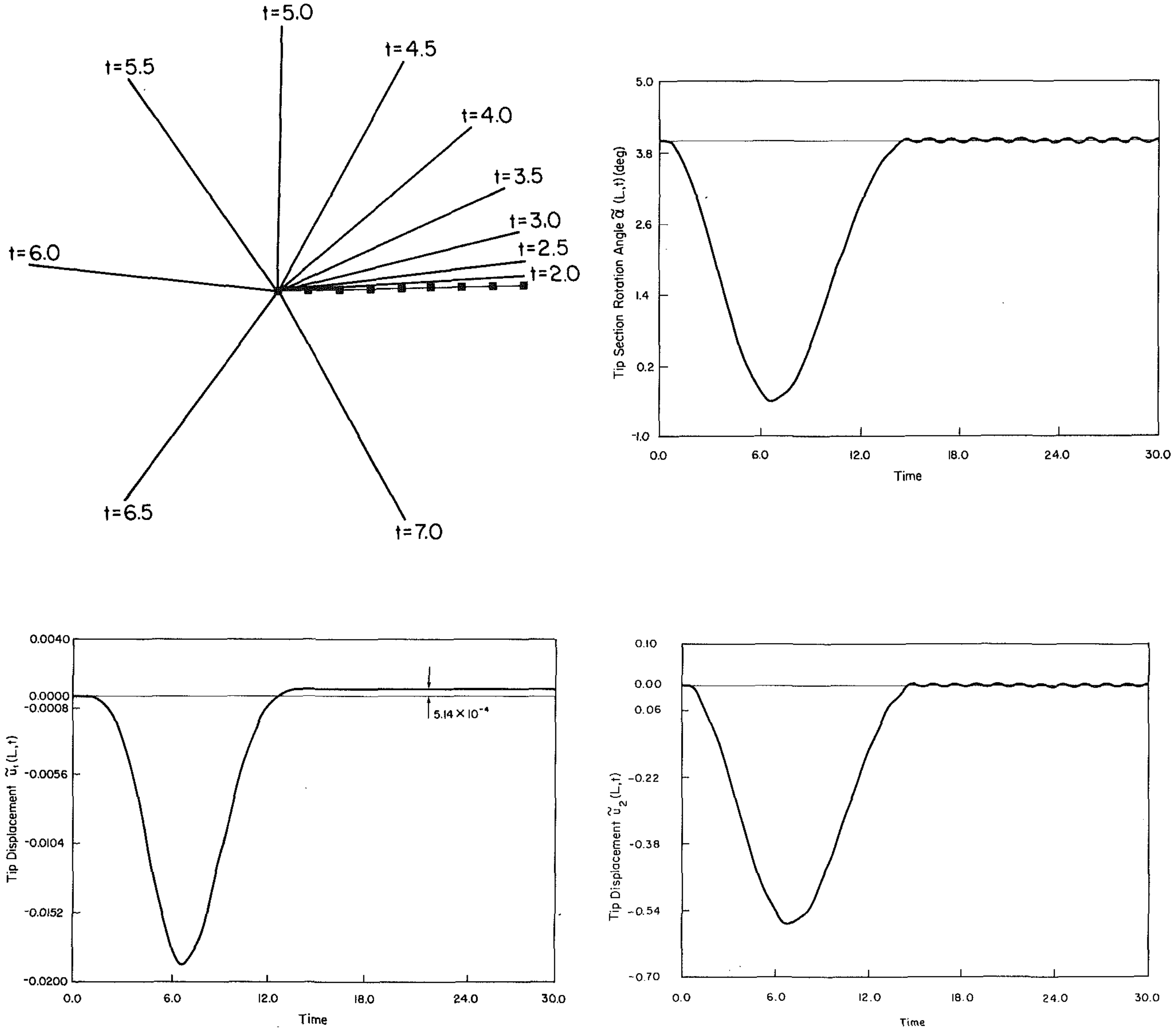

Fig. 8(*a*)-(*d*) Spin-up maneuver. Several deflected shapes during first revolution. Time histories for displacement components and section rotation relative to the shadow beam. Time step size $h = 0.005$.

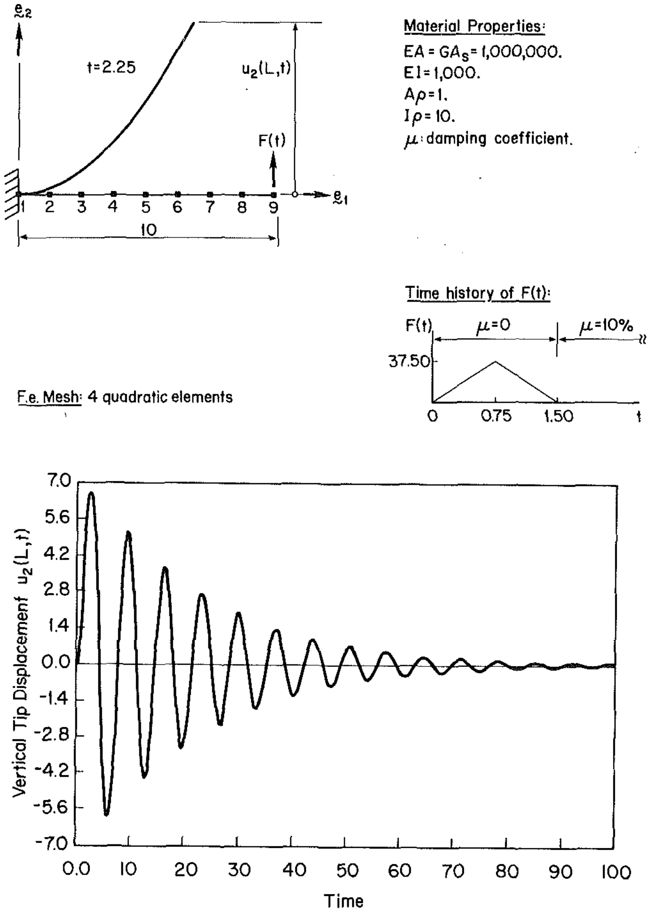

Fig. 9(*a*), 9(*b*) Damped vibration: cantilever beam. Velocity proportional viscous force; problem data; maximum deflected shape; time history of vertical tip displacement.

7. Deflected shapes for several values of t during the first revolution are depicted in Fig. 8. Also shown in this figure are the time histories of the displacements $\tilde{u}_1(L,t)$, $\tilde{u}_2(L,t)$ relative to the shadow beam, and the section rotation $\tilde{\alpha}(L,t)$. The results of Fig. 8 clearly exhibit the *centrifugal stiffening* effect: after an initial deflection during the acceleration phase, $t\in[0,15]$, the centrifugal force straightens the robot arm in the constant angular velocity phase, $t > 15$. The exact solution for the steady state extension of a pinned-free beam with length L, axial stiffness EA and mass per unit length ρA, spinning with constant angular velocity ω can be easily shown to be

$$\tilde{u}_1(X,t) = L\left[\frac{\tan aL}{aL} - 1\right]; \text{ where } a = \sqrt{\frac{\rho A}{EA}}\,\omega \qquad (2.2)$$

For this particular example $\omega = 6\text{rad/sec}$, $L = 10$ and $\rho A/EA = 3/7 \times 10^{-7}$. Expression (2.2) then leads to a steady state extension at the free end of $\tilde{u}_1(L,t) = 5.14 \times 10^{-4}$. This result is in complete agreement with the computed solution (see Fig. 8). The small periodic vibration of the beam about the floating frame during this steady state phase is noted.

Example 2.5. Damped Finite Vibration of a Cantilever Beam. This example illustrates how simply viscous effect can be included in our formulation. A cantilever beam is initially subject to a concentrated end load. Subsequently, the load is removed, and the beam undergoes free vibration. Figure 9 shows the material properties, the maximum deflected shape, and the time history of the vertical tip displacement. Only *velocity* proportional damping is considered here; more general dissipative mechanisms warrant a separate treatment.

3 Concluding Remarks

We recall that in the proposed approach the inherent nonlinear character of the problem is transferred to the stiffness part of the equations of motion. This approach results in equations of motion that arise typically in nonlinear structural dynamics. Consequently, the dynamics of flexible beams under large overall motions can be analyzed in any existing nonlinear finite element program, as demonstrated through several numerical examples. Without alteration in the formulation, one can apply this approach to the dynamics of a system of flexible beams connected by hinges, as shown in examples 2.3.1 and 2.3.2. Further, we will address the following points in forthcoming publications:

(*i*) The approach proposed in this paper can be readily extended to accommodate inelastic constitutive behavior. In particular, general viscoelastic response that extends classical linear models such as the Kelvin and standard linear solids to finite strains. In many applications, this is of practical importance since, as noted in Remark 3.6 of Part I, velocity proportional damping is ineffective at high frequencies.

(*ii*) It will be shown that the algorithmic treatment proposed in Section 4 remains essentially unchanged if generalized viscoelastic models are considered. Only a modified stress update is necessary. This applies to more sophisticated models accounting for damage effects.

(*iii*) The methodology presented in this paper can be employed for the dynamic analysis of an earth-orbiting satellite composed of beam elements. However, one must carefully treat separately the far field and the near field to avoid ill-conditioning. The gravitational force field as well as satellite control actuator forces are configuration dependent and require special treatment.

iv) Conceptually, the proposed approach readily carries over to the fully three dimensional case. This extension relies on a proper treatment of three dimensional finite rotations in both the structural deformations of the beam and in the overall motions. For the static case, such a treatment is available in Kane et al. (1985). The dynamic case, however, warrants a separate treatment.

Acknowledgments

We thank Prof. R. L. Taylor, the developer of FEAP, for his helpful discussions. This work was performed under the auspices of the Air Force Office of Scientific Research, grant No. AFOSR-83-0361. This support as well as the encouragement provided by Profs. K. S. Pister and E. Polak are gratefully acknowledged.

References

Belytschko, T., and Hughes, T. J. R., 1983, *Computational Methods for Transient Analysis*, Elsevier Science Publishers.

Benson, D. J., and Hallquist, J. O., 1985, "A Simple Rigid Body Algorithm for Structural Dynamics Program. Part I," *Proc. of the Int. Conf. on Numerical Methods in Engineering Theory and Applications, Swansea*, Middleton, J., and Pande, G. N., eds., A. A. Balkema Publishers, Netherlands.

Chorin, A. J., Hughes, T. J. R., McCracken, M. F., and Marsden, J. E., 1978, "Product Formulas and Numerical Algorithms," *Communications on Pure and Applied Mathematics*, Vol. 31, pp. 205-256.

Dalhquist, G., 1963, "A Special Stability Problem for Linear Multistep Methods," *BIT*, Vol. 3, pp. 27-43.

Gear, C. W., 1971a, "Simultaneous Numerical Solution of Differential-Algebraic Equations," *IEEE Transaction on Circuit Theory*, Vol. CT-18, No. 1, pp. 89-95.

Gear, C. W., 1971b, *Numerical Initial Value Problems in Ordinary Differential Equations*, Prentice-Hall, New Jersey.

Gear, C. W., and Petzold, L. R., 1984, "ODE Methods for the Solution of Differential/Algebraic Systems," *SIAM J. Numerical Analysis*, Vol. 21, No. 4, pp. 716-728.

Goodreau, G. L., and Taylor, R. L., 1973, "Evaluation of Numerical Methods in Elastodynamics," *Comp. Meth. Appl. Mech. Engrg.*, Vol. 2, pp. 69-97.

Hilber, H. M., 1976, "Analysis and Design of Numerical Integration Methods in Structural Dynamics," Earthquake Engineering Research Center, EERC Report No. 76-29, University of California, Berkeley.
Hughes, P. C., 1979, "Dynamics of a Chain of Flexible Bodies," *The J. of the Astronautical Sciences*, Vol. 27, pp. 359-380.
Kane, T. R., Ryan, R. R., and Banerjee, A. K., 1985, "Dynamics of a Beam Attached to a Moving Base," *AAS/AIAA Astrodynamics Specialist Conference*, Paper AAS 85-390, Vail, Colorado, August 12-15.
Likins, P. W., 1974, "Dynamic Analysis of a System of Hinge Connected Rigid Bodies With Nonrigid Appendages," NASA Technical Report 32-1576.
Meirovitch, L., 1970, *Analytical Methods in Vibrations*, MacMillan, Toronto, Canada.
Newmark, N. M., 1959, "A Method of Computation for Structural Dynamics," *ASCE J. of the Engineering Mechanics Division*, pp. 67-94.
Petzold, L. R., 1982, "Differential/Algebraic Equations are not ODE's," *SIAM J. Sci. Stat. Comput.*, Vol. 3, No. 3, pp. 367-384.
Richtmyer, D., and Morton, K. W., 1967, *Difference Methods for Initial Value Problems*, Second edition, Interscience, New York, 1967.
Song, J. O., and Haug, E. J., 1980, "Dynamic Analysis of Planar Flexible Mechanism," *Comp. Meth. Appl. Mech. Engrg.*, Vol. 24, pp. 359-381.
Sunada, W., and Dubowsky, S., 1980, "The Application of Finite Element Method to the Dynamic Analysis of Flexible Spatial and Co-Planar Linkage Systems," *J. of Mechanical Design*, Vol. 103, pp. 643-651.
Zienkiewicz, O. C., 1977, *The Finite Element Method*, third edition, McGraw-Hill, New York.

APPENDIX

Finite Element Matrices

In this appendix, we shall give the expressions of the relevant matrices discussed in Section 1; namely, the mass matrix **M**, the damping matrix **D**, the internal forces vector **P**(**d**), the tangent stiffness matrix $\mathbf{K}_T(\mathbf{d})$, and the applied forces vector $\mathbf{F}(t)$.

Using the spatial discretization (1.3) in the first term of the weak form of the equations of motion (1.2), i.e., the inertia term, the mass matrix is obtained at once as

$$\mathbf{M} = \int_{[0,L]} \boldsymbol{\Psi}^t(X_1)\mathbf{I}\boldsymbol{\Psi}(X_1)dX_1 \qquad (A.1a)$$

with

$$\boldsymbol{\Psi}(X_1) := [\boldsymbol{\Psi}_1(X_1), \ldots, \boldsymbol{\Psi}_N(X_1)] \qquad (A.1b)$$

The damping matrix **D** is obtained exactly as in (A.1a), but with **Δ** in the place of **I**.

Next, by making use of (3.17) and (3.18) of Part I, we may rephrase the third term in the weak form (1.2) as follows

$$\begin{aligned} &\boldsymbol{\eta} := \eta_1\mathbf{e}_1 + \eta_2\mathbf{e}_2 + \eta_3\mathbf{e}_3, \\ &\int_{[0,L]} \boldsymbol{\eta}\cdot\mathbf{P}[\mathbf{d}]dX_1 = -\int_{[0,L]} [\eta_1 n_1' + \eta_2 n_2' + \eta_3 m' \\ &\qquad + \eta_3\{(1+u_1')n_2 - u_2' n_1\}]dX_1 \end{aligned} \qquad (A.2)$$

Integrate by parts $(A.2)_2$, and recall that $\eta_1 n_1 + \eta_2 n_2 + \eta_3 m = 0$ at the boundaries. There results

$$\int_{[0,L]} \boldsymbol{\eta}\cdot\mathbf{P}[\mathbf{d}]dX_1 = \int_{[0,L]} \mathbf{D}_1(\mathbf{d})\boldsymbol{\eta}\cdot \begin{Bmatrix} n_1(\mathbf{d}) \\ n_2(\mathbf{d}) \\ m(\mathbf{d}) \end{Bmatrix} dX_1 \qquad (A.3a)$$

with $\mathbf{D}_1(\mathbf{d})$ denoting the following differential operator

$$\mathbf{D}_1(\mathbf{d}) := \begin{bmatrix} \frac{d}{dX_1} & 0 & u_2' \\ 0 & \frac{d}{dX_1} & -(1+u_1') \\ 0 & 0 & \frac{d}{dX_1} \end{bmatrix} \qquad (A.3b)$$

Introducing the discretization $(1.3)_2$ into (A.3a), we obtain the expression for the discrete internal forces

$$\mathbf{P}(\mathbf{d}^h) = \int_{[0,L]} [\mathbf{D}_1(\mathbf{d}^h)\boldsymbol{\Psi}(X_1)]^t \begin{Bmatrix} n_1(\mathbf{d}^h) \\ n_2(\mathbf{d}^h) \\ m(\mathbf{d}^h) \end{Bmatrix} dX_1 \qquad (A.4)$$

In (A.4), the superscript h in $\mathbf{d}^h$ is used to designate the spatial approximation to $\mathbf{d}(X_1,t)$ according to $(1.3)_1$. The same notation will be used throughout in this appendix.

We now undertake the linearization of $\int_{[0,L]} \boldsymbol{\eta}\cdot\mathbf{P}[\mathbf{d}]dX_1$ about a fixed configuration $\mathbf{d} \equiv \overset{*}{\mathbf{d}}$. This linearization procedure and the spatial discretization (1.3), lead to the expression for the tangent stiffness matrix $\mathbf{K}_T(\overset{*}{\mathbf{d}})$ appearing in (1.9). For the developments that follow, it proves convenient to rewrite equation (3.18) of Part I as

$$\begin{Bmatrix} N_1(\mathbf{d}) \\ N_2(\mathbf{d}) \\ M(\mathbf{d}) \end{Bmatrix} := \mathbf{C} \left[\boldsymbol{\Lambda}^t(\overset{*}{\mathbf{d}}) \begin{Bmatrix} 1+u_1' \\ u_2' \\ \theta' \end{Bmatrix} - \begin{Bmatrix} 1 \\ 0 \\ 0 \end{Bmatrix} \right],$$

$$\begin{Bmatrix} n_1(\mathbf{d}) \\ n_2(\mathbf{d}) \\ m(\mathbf{q}) \end{Bmatrix} = \boldsymbol{\Lambda}(\overset{*}{\mathbf{d}}) \begin{Bmatrix} N_1(\mathbf{d}) \\ N_2(\mathbf{d}) \\ M(\mathbf{d}) \end{Bmatrix} \qquad (A.5a)$$

where

$$\mathbf{C} := \mathrm{Diag}[EA, GA_S, EI],\ \boldsymbol{\Lambda}(\overset{*}{\mathbf{d}}) := \begin{bmatrix} \cos\theta & -\sin\theta & 0 \\ \sin\theta & \cos\theta & 0 \\ 0 & 0 & 1 \end{bmatrix} \qquad (A.5b)$$

The linearization about $\overset{*}{\mathbf{d}}$ is based on the notion of directional derivative at $\overset{*}{\mathbf{d}}$ in the direction $\Delta\mathbf{d} := [\Delta u_1, \Delta u_2, \Delta\theta]^t$. The following linearized quantities are needed:

$$\left.\frac{d}{d\epsilon}\right|_{\epsilon=0} \boldsymbol{\Lambda}\ [\dot{\mathbf{d}} + \epsilon\Delta\mathbf{d}) = \begin{bmatrix} 0 & -\Delta\theta & 0 \\ \Delta\theta & 0 & 0 \\ 0 & 0 & 0 \end{bmatrix} \boldsymbol{\Lambda}(\overset{*}{\mathbf{d}}), \qquad (A.6a)$$

$$\left.\frac{d}{d\epsilon}\right|_{\epsilon=0} \begin{Bmatrix} N_1 \\ N_2 \\ M \end{Bmatrix} (\overset{*}{\mathbf{d}} + \epsilon\Delta\mathbf{d}) = \mathbf{C}\boldsymbol{\Lambda}(\overset{*}{\mathbf{d}})\mathbf{D}_1(\overset{*}{\mathbf{d}})\Delta\mathbf{d}, \qquad (A.6b)$$

$$\left.\frac{d}{d\epsilon}\right|_{\epsilon=0} \mathbf{D}_1(\overset{*}{\mathbf{d}} + \epsilon\Delta\mathbf{d})\boldsymbol{\eta} = \begin{bmatrix} 0 & 0 & \Delta u_2' \\ 0 & 0 & -\Delta u_1' \\ 0 & 0 & 0 \end{bmatrix} \boldsymbol{\eta}. \qquad (A.6c)$$

The linearization of the second term in the weak form (1.2) then follows at once

$$\begin{aligned} &\left.\frac{d}{d\epsilon}\right|_{\epsilon=0} \left\{ \int_{[0,L]} \boldsymbol{\eta}\cdot\mathbf{P}[\overset{*}{\mathbf{d}} + \epsilon\Delta\mathbf{d}]dX_1 \right\} = \\ &\int_{[0,L]} \mathbf{D}_1(\overset{*}{\mathbf{d}})\boldsymbol{\eta}\cdot\boldsymbol{\Lambda}\ (\overset{*}{\mathbf{d}})\mathbf{C}\boldsymbol{\Lambda}^t(\overset{*}{\mathbf{d}})\mathbf{D}_1(\overset{*}{\mathbf{d}})\Delta\mathbf{d}dX_1. \\ &+ \int_{[0,L]} \mathbf{D}_2\boldsymbol{\eta}\cdot\mathbf{G}(\overset{*}{\mathbf{d}})\mathbf{D}_2\Delta\mathbf{d}dX_1 \end{aligned} \qquad (A.7)$$

in which the differential operator $\mathbf{D}_2$ and the matrix $\mathbf{G}(\overset{*}{\mathbf{d}})$ are defined below

$$\mathbf{D}_2 := \mathrm{Diag}\left[\frac{d}{dX_1}, \frac{d}{dX_1}, 1\right],$$

$$\mathbf{G}(\overset{*}{\mathbf{d}}) := \begin{bmatrix} 0 & 0 & -n_2(\overset{*}{\mathbf{d}}) \\ 0 & 0 & n_1(\overset{*}{\mathbf{d}}) \\ -n_2(\overset{*}{\mathbf{d}}) & n_1(\overset{*}{\mathbf{d}}) & -[(1+\overset{*}{u}{}_1')n_1(\overset{*}{\mathbf{d}}) + \overset{*}{u}{}_2' n_2(\overset{*}{\mathbf{d}})] \end{bmatrix} \qquad (A.8)$$

Let us now introduce the spatial discretization of $\Delta\mathbf{d}(X_1)$ in the same manner as in $(1.3)_1$

$$\Delta\mathbf{d}(X_1) \cong \sum_{I=1}^{N} \mathbf{\Psi}(X_1)\Delta\mathbf{q}_I \qquad (A.9)$$

Using (1.3) together with (*A*.9), we finally arrive at the expression for the tangent stiffness matrix at $\overset{*}{\mathbf{d}}{}^h \cong \overset{*}{\mathbf{d}}$

$$\mathbf{K}_T(\overset{*}{\mathbf{d}}{}^h) = \mathbf{K}(\overset{*}{\mathbf{d}}{}^h) + \mathbf{K}_G(\overset{*}{\mathbf{d}}{}^h) \qquad (A.10a)$$

where $\mathbf{K}(\overset{*}{\mathbf{d}}{}^h)$ represents the *material* part of the tangent stiffness,

$$\mathbf{K}(\overset{*}{\mathbf{d}}{}^h) := \int_{[0,L]} [\mathbf{D}_1(\overset{*}{\mathbf{d}}{}^h)\mathbf{\Psi}(X_1)]^t \mathbf{\Lambda}(\overset{*}{\mathbf{d}}{}^h)\mathbf{C}\mathbf{\Lambda}^t(\overset{*}{\mathbf{d}}{}^h)\mathbf{D}_1(\overset{*}{\mathbf{d}}{}^h)\mathbf{\Psi}(X_1)dX_1 \qquad (A.10b)$$

and $\mathbf{K}_G(\overset{*}{\mathbf{d}}{}^h)$ the *geometric* part,

$$\mathbf{K}_G(\overset{*}{\mathbf{d}}{}^h) := \int_{[0,L]} [\mathbf{D}_2\mathbf{\Psi}(X_1)]^t \mathbf{G}(\overset{*}{\mathbf{d}}{}^h)\mathbf{D}_2\mathbf{\Psi}(X_1)dX_1 \qquad (A.10c)$$

It is clear that the applied load vector $\mathbf{F}(t)$ is given by

$$\mathbf{F}(t) = \int_{[0,L]} \mathbf{\Psi}^t(X_1) \begin{Bmatrix} \bar{n}_1(X_1,t) \\ \bar{n}_2(X_1,t) \\ \bar{m}(X_1,t) \end{Bmatrix} dX_1 \qquad (A.11)$$

The integration in all of the above matrices may be performed numerically using Gauss quadrature. For the tangent stiffness matrix $\mathbf{K}_T$, we use uniform reduced integration to avoid shear locking.

Free Rotation of an Elastic Rod With an End Mass

C. Y. Wang
Professor,
Michigan State University,
East Lansing, Mich. 48824
Mem. ASME

This paper models a rotating space satellite with a long flexible antenna. Large deformations of the elastic rod are caused by the centrifugal forces. Bifurcation analysis shows the effect of end mass on the critical rotation speeds above which sinuous equilibrium configurations occur. The nonlinear governing equations are then integrated numerically. We find a class of solutions with a looped configuration whose existence requires a certain minimum total energy and minimum angular momentum. Catastrophic changes are possible.

Introduction

Space structures often rotate due to necessity. This type of motion is called "free rotation" since the system is not influenced by outside forces and moments. When the structure is flexible, large deformations may occur due to centrifugal forces. Previous work on free rotation includes only two sources: the rotation of an elastic rod (Wang, 1982) and the rotation of an elastic ring along a diameter (Wang, 1983).

The present paper studies the elastic deformations due to the free rotation of a long, thin, elastic rod with an end mass. This situation occurs in the case of an artificial satellite with a long appendage or antenna. For example, the Radio Astronomy Explorer Satellite (Stone, 1965) used a 460 m antenna for detecting low-frequency signals. These antennas are very flexible due to weight considerations and due to ease of storage during launching. We wish to determine the possible equilibrium configurations and the conditions under which they may occur.

Formulation

Consider a spherical satellite of mass m with an originally straight antenna (slender elastic rod) of length ℓ and density ρ. Figure 1 shows one possible configuration of the system which is in steady rotation with angular velocity Ω. We shall put Cartesian axes (x', y'), rotating with the system, at the center of mass, where x' coincides with the axis of rotation. For $\Omega \neq 0$ the rod may remain straight if it coincides with the axis x' (Case I) or coincides with the axis y' (Case II). There may be other curved equilibrium configurations as well.

If the rod is slender enough, the local moment M is proportional to the local curvature:

$$M = EI \frac{d\theta}{ds'} . \tag{1}$$

Here EI is the flexural rigidity, s' is the arc length from the mass, and θ is the local angle of inclination. The coordinates (x', y') and (s', θ) are related by

$$\frac{dx'}{ds'} = \cos\theta, \quad \frac{dy'}{ds'} = \sin\theta \tag{2}$$

Consider an elemental length ds' of the rod. A local moment balance gives

$$M + dM = M - ds' \cos\theta \int_{s'}^{l} \rho\Omega^2 y' \, ds' \tag{3}$$

If we normalize all lengths by ℓ, and drop primes, equations (1)–(3) yield

$$\frac{d^2\theta}{ds^2} = J^4 u \cos\theta \tag{4}$$

$$\frac{d^2 u}{ds^2} = \sin\theta \tag{5}$$

where

$$u \equiv \int_1^s y \, ds \tag{6}$$

and $J \equiv \ell \rho^{1/4} \Omega^{1/2} (EI)^{-1/4}$ is an important nondimensional parameter representing the relative importance of length and rotation to flexural rigidity. Since other parameters are generally constant, J is a measure of rotation rate Ω. At $s = 0$ we expect the centrifugal force of the rod to balance the centrifugal force of the end mass:

$$m\Omega^2 y'(0) + \int_0^{\ell} \rho\Omega^2 y' \, ds' = 0 \tag{7}$$

or

$$u(0) = \alpha \frac{du}{ds}(0). \tag{8}$$

Here α is the ratio between the end mass and the rod mass, $\alpha \equiv m/(\rho\ell)$. The other boundary conditions are

$$u(1) = 0, \quad \frac{d\theta}{ds}(0) = \frac{d\theta}{ds}(1) = 0. \tag{9}$$

Equations (4), (5), (8), (9) are extremely nonlinear. There are two trivial solutions resulting in a straight rod:

$$\theta = u = 0 \tag{10}$$

Contributed by the Applied Mechanics Division for publication in the Journal of Applied Mechanics.

Discussion on this paper should be addressed to the Editorial Department, ASME, United Engineering Center, 345 East 47th Street, New York, N.Y. 10017, and will be accepted until two months after final publication of the paper itself in the Journal of Applied Mechanics. Manuscript received by ASME Applied Mechanics Division, October 21, 1985; final revision March 18, 1986.

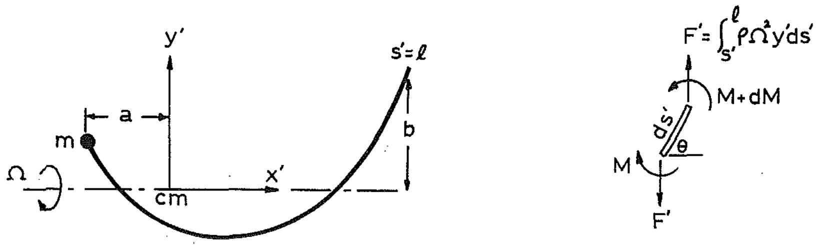

Fig. 1 The coordinate system

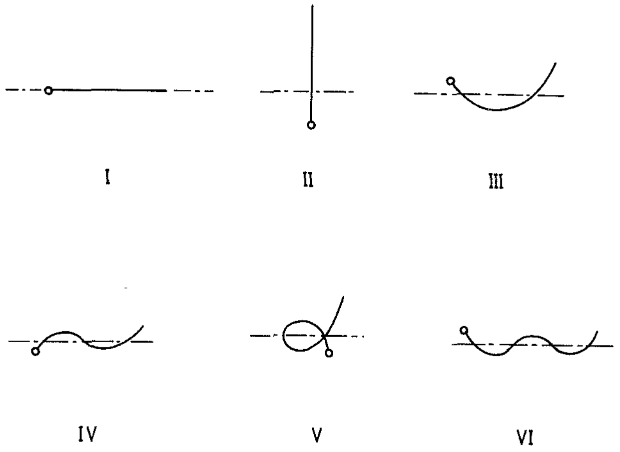

Fig. 2 The six different Cases

Table 1

α	J_1	J_2	J_3
0	4.73004	7.85321	10.99561
0.2	4.29292	7.31747	10.40160
1	4.04183	7.13384	10.25663
∞	3.92660	7.06858	10.21018

which is a rotation along the axis of the rod, and

$$\theta=\frac{\pi}{2}, \quad u=\frac{s^2}{2}-\frac{(s+\alpha)}{2(1+\alpha)} \tag{11}$$

representing rotation perpendicular to the rod. In what follows, we shall investigate the cases where the antenna may be curved.

Bifurcation

As rotation speed, and thus centrifugal force, is increased by some means, the state represented by equation (11) remains invariant. However, the rotation along the axis, equation (10), may lead to curved equilibrium states. The bifurcation properties are studied by a perturbation about small θ and u. The governing equations linearize to

$$\frac{d^2\theta}{ds^2}=J^4u, \quad \frac{d^2u}{ds^2}=\theta. \tag{12}$$

The general solution is

$$\theta=c_1\sinh Js+c_2\cosh Js+c_3\sin Js+c_4\cos Js \tag{13}$$

$$u=J^{-2}(c_1\sinh Js+c_2\cosh Js-c_3\sin Js-c_4\cos Js). \tag{14}$$

The boundary conditions, equations (8) and (9), yield the condition for a nontrivial solution:

$$\alpha J(\cos J\sinh J-\sin J\cosh J)+\cos J\cosh J-1=0. \tag{15}$$

For given α, equation (15) is solved numerically for the eigenvalues J. The results for nontrivial J are given in Table 1. The rod would remain straight if the rotation speed is so small such that $J \leq J_1$. When $J > J_1$, the first bifurcation occurs and the configuration shown in Fig. 2 (Case III) is possible. When $J > J_2$, the second bifurcation, an S-shaped configuration (Case IV), may occur. The higher bifurcations correspond to higher J. See Fig. 2.

When the end mass is absent, $\alpha = 0$. The bifurcation values agree with those of the rotation of a single flexible rod studied by Wang (1982). The effect of increased end mass is to decrease the bifurcation value J_n, or the critical rotation speed.

Numerical Integration

For large deflections, equations (4), (5), (8), (9) must be integrated numerically. It is better to turn the two-point boundary value problem into an initial value problem as follows. Set

$$t\equiv(l-s)J, \; v\equiv J^2u. \tag{16}$$

The original equations become

$$\frac{d^2\theta}{dt^2}=v\cos\theta, \quad \frac{d^2v}{dt^2}=\sin\theta. \tag{17}$$

The initial conditions are

$$v\Big|_{t=0}=0, \quad \frac{d\theta}{dt}\Big|_{t=0}=0. \tag{18}$$

Given $\theta|_{t=0}$ and any $dv/dt|_{t=0}$ we integrate equations (17) and (18) by the fifth order Runge-Kutta-Fehlberg algorithm until $d\theta/dt$ is zero again, say at $t=t^*$. Then

$$J=t^*, \quad \alpha=\frac{-\;v(t^*)}{t^*\,\dfrac{dv}{dt}(t^*)}>0. \tag{19}$$

We see that J and α are obtained inversely. By adjusting $dv/d\theta|_{t=0}$ one can obtain the results for a specific α. We find

$$u(0)=\frac{1}{J^2}\,v(J), \quad \frac{du}{ds}(0)=\frac{1}{\alpha J^2}\,v(J)$$
$$\theta(0)=\theta|_{t=t^*}, \quad \frac{d\theta}{ds}(0)=0. \tag{20}$$

In order to determine the equilibrium configuration of the system, we set

$$\bar{x}=x+a \tag{21}$$

where a is the unknown axial distance from the end mass to the center of mass. Then

$$\frac{d\bar{x}}{ds}=\cos\theta, \quad \bar{x}(0)=0 \tag{22}$$

Equations (4), (5), (20), (22) are integrated numerically. The shape is obtained by

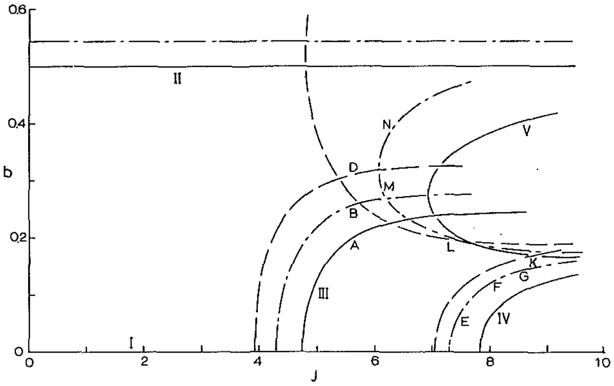

Fig. 3 Maximum amplitude. Letters correspond to States in Figs. (6—8): —— $\alpha = 0$; —•— • $\alpha = 0.2$; — — — $\alpha = \infty$.

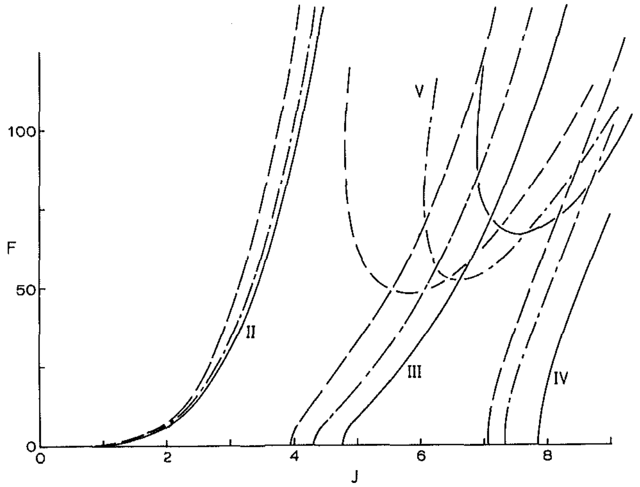

Fig. 4 Maximum force: —— $\alpha = 0$; —•— $\alpha = 0.2$; — — — $\alpha = \infty$

$$x=\bar{x}-a, \quad y=\frac{du}{ds}. \tag{23}$$

The location of the center of mass is found by

$$a=\frac{1}{\alpha+1}\int_0^1 \bar{x}\, ds \tag{24}$$

Figure 2 shows schematically the equilibrium configurations of some of the lowest modes. As rotation rate is increased while other parameters are fixed, Case II is stable, while Case I may become unstable and bifurcate into Cases III, IV, VI, when the critical rotation speeds J_1, J_2, J_3 are reached. Case V, however, does not bifurcate from a trivial state and, thus, cannot be predicted from the linearized equations. Only by numerical integration of the nonlinear equations can we determine the configurations of Case V. Higher rotation rates may lead to more complicated equilibrium states.

Figure 3 shows the maximum amplitude $y(1) \equiv b$ as function of normalized rotation rate J. For Case II, the maximum amplitude is

$$b=\frac{1+\alpha}{2+\alpha}. \tag{25}$$

The value of b ranges from 1/2 for $\alpha = 0$ to 1 for $\alpha = \infty$. The amplitude of Case I, of course, is zero. As rotation rates are increased, Case III solutions bifurcate at J_1, and Case IV solutions bifurcate at J_2. Of interest are the Case V solutions which do not bifurcate from zero. In general, the amplitudes of Case V solutions may increase or decrease with J. There is a minimum rotation rate below which Case V solutions do not exist ($J_{\min} = 6.9, 6.1, 4.8$, for $\alpha = 0, 0.2, \infty$, respectively). The above mentioned Cases are the only ones found below $J = 10$.

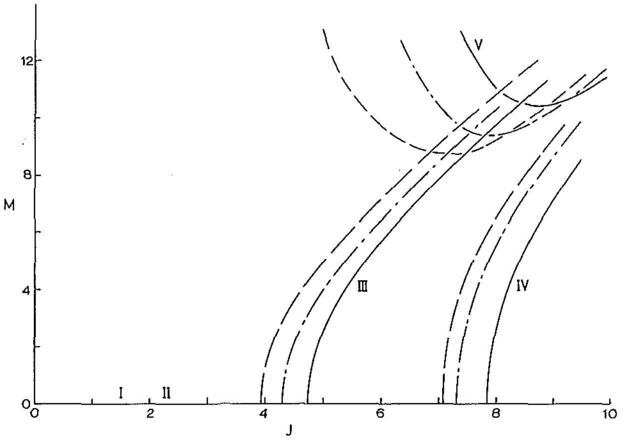

Fig. 5 Maximum local moment: —— $\alpha = 0$; —•— $\alpha = 0.2$; — — — $\alpha = \infty$

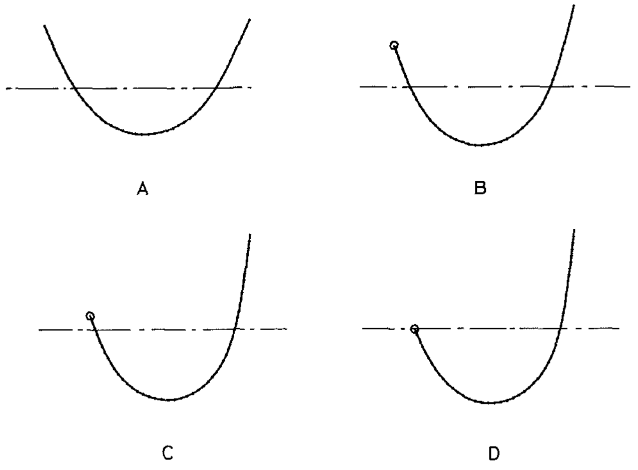

Fig. 6 Configurations for Case III. $J = 5.6$; A: $\alpha = 0$; B: $\alpha = 0.2$; C: $\alpha = 1.0$; D: $\alpha = \infty$.

Figure 4 shows the maximum force experienced, occurring at the first intersection of the rod with the rotation axis. This force, normalized by EI/ℓ^2, is calculated from

$$F=\frac{F'}{EI/\ell^2}=J^4 u|_{\max}. \tag{26}$$

Unlike the amplitude, the force increases without bound as J is increased. Case V curves show a characteristic minimum due to nonbifurcation. For Case II, a simple formula can be obtained:

$$F=\frac{J^4}{2}\left[1-\left(\frac{1+\alpha}{2+\alpha}\right)^2\right] \tag{27}$$

Figure 5 shows the maximum normalized moment, represented by the curvature $d\theta/ds$. For both Cases I and II the moment is identically zero. For the other Cases, the maximum moment occurs at some interior point. The effect of the mass ratio α is to shift the curves towards the left. Figures 4 and 5 are important in the design of satellites with long antennas.

Figure 6 shows some equilibrium configurations for Case II at the same rotation rate J. As α is increased, the location of the end mass becomes closer to the rotation axis. Figure 7 depicts Case IV configurations for fixed $\alpha = 0.2$. The elastic rod becomes more sinuous with increased rotation. Case V, not studied before, has a characteristic looped shape (Fig. 8). The conditions for its existence will be discussed in the next

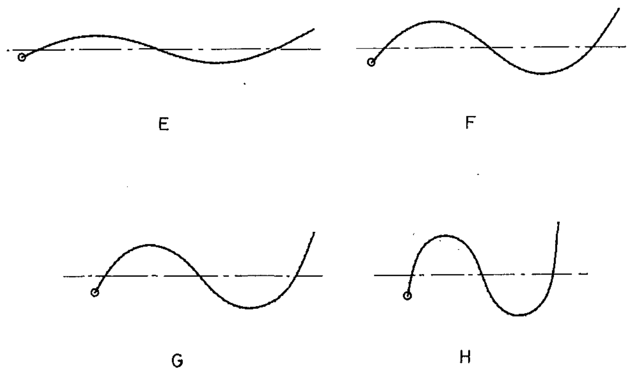

Fig. 7 Configurations for Case IV. $\alpha = 0.2$; E: $J = 7.48$; F: $J = 8.08$; G: $J = 8.56$; H: $J = 10.41$.

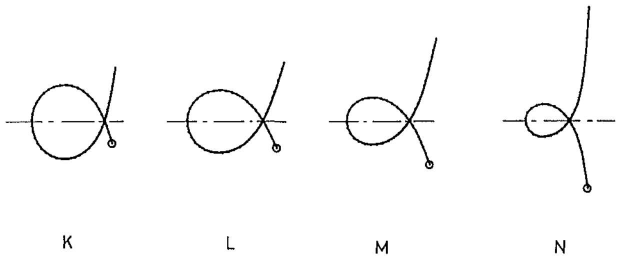

Fig. 8 Configurations for Case V. $\alpha = 0.2$; K: $J = 8.77$; L: $J = 7.29$; M: $J = 6.2$; N: $J = 6.2$.

section. We note (e.g., from Fig. 3) that for given J, the solution is not unique. The States M and N in Fig. 8 have the same rotation rate.

Energy and Angular Momentum

The total energy of a freely rotating elastic system consists of two parts, the kinetic energy and the strain energy. The elastic rod has both kinetic and strain energies while the end mass has kinetic energy only. Thus, total energy is

$$\epsilon' = \frac{1}{2}\rho\Omega^2\ell^3\int_0^1 y^2 ds + \frac{EI}{2\ell}\int_0^1\left(\frac{d\theta}{ds}\right)^2 ds + \frac{1}{2}m\Omega^2\ell^2 y^2(0). \tag{28}$$

Normalizing with $EI/2\ell$ we obtain

$$\epsilon = \int_0^1\left(\frac{d\theta}{ds}\right)^2 ds + J^4\left[\int_0^1 y^2 ds + \alpha y^2(0)\right]. \tag{29}$$

The total energy can be integrated numerically since $\theta(s)$ and $y(s)$ have been determined previously. Figure 9 shows ϵ plotted against J. The total energy of Case I is zero for our idealized infinitesimally thin rod and point mass. For Case II the energy is entirely kinetic and increases rapidly from $J = 0$:

$$\epsilon = J^4\left[\frac{1}{3} - \frac{1}{(2+\alpha)^2}\right]. \tag{31}$$

For Cases III and IV the total energy bifurcates from zero at J_1 and J_2. It is interesting to note that the Case V solutions not only require a minimum rotation rate J but also a minimum total energy in order to exist. The minimum energy requirements are $\epsilon_{\min} = 76$, 64, and 51 for $\alpha = 0$, 0.2, and ∞, respectively. For example, when a satellite system is disturbed by an impact from a meteor, if the sum of the energies of the meteor and satellite is less than $\epsilon_{\min}$, then Case V will not occur.

Another characteristic of free rotation is the total angular momentum which, after normalizing with $\ell\sqrt{\rho EI}$, can be expressed as

$$\mathfrak{M} = J^2\left[\int_0^1 y^2 ds + \alpha y^2(0)\right]. \tag{32}$$

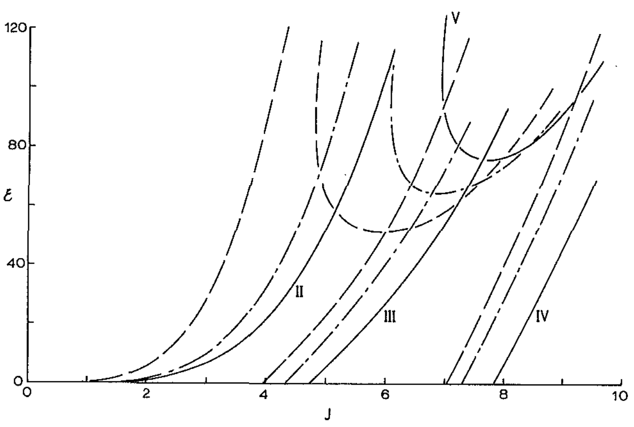

Fig. 9 The total energy ϵ as a function of J

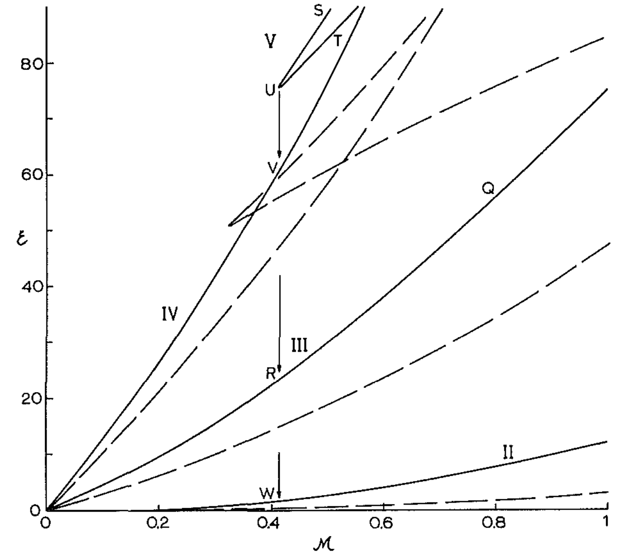

Fig. 10 Total energy and total angular momentum: —— $\alpha = 0$; — — — $\alpha = \infty$

Similar to total energy, the angular momentum also shows a minimum for Case V, $\mathfrak{M}_{\min} = 0.41$, 0.40, 0.32 for $\alpha = 0$, 02, ∞, respectively. Thus $\mathfrak{M}_{\min}$ is an additional necessary criterion for the existence of Case V.

For sufficiently large values of J, ϵ, and $\mathfrak{M}$, the system may rotate in one of the several admissible configurations. Which final equilibrium state actually occurs depends on its dynamical history (not studied here). All cases presented in this paper are locally stable except Case I when $J > J_1$. In general, for small changes in energy or momentum, the state of the system tends to adjust slightly but remains close to its previous state unless a catastrophe happens.

In Fig. 10, the total energy is plotted against total angular momentum. If an ideal free rotating system is in equilibrium at State Q of Case III, say, it would remain there due to conservation of momentum and energy. However, minute irreversible friction would gradually decrease both energy and angular momentum such that the State moves slowly from Q to R and eventually into the origin. The situation is different for Case V. With a gradual loss of energy and momentum both States S and T (on different branches) move toward State U, where a further minute decrease causes large changes (a catastrophe). We would expect that angular momentum $\mathfrak{M}$ will be conserved while total energy ϵ drops abruptly toward another Case at States V, R, or W. This sudden transformation may cause large amplitude transient oscillations of the elastic rod which may eventually dissipate the excess energy through internal heating.

Discussion

Space structures are becoming increasingly larger and more flexible. Structural problems unique to space are not found on earth. Free rotation is one of the examples. In this paper, we found many characteristics of nonlinear mechanics: bifurcation, nonuniqueness, nonexistence, catastrophic change, etc. Further work, especially in the dynamical area, should be investigated.

References

Stone, R. G., 1965, "RAE– 1500 ft. Antenna Satellite," *Astronautics and Aeronautics*, Vol. 3, pp. 46–49.

Wang, C. Y., 1982, "Rotation of a Free Elastic Rod," ASME JOURNAL OF APPLIED MECHANICS, Vol. 49, pp. 225–227.

Wang, C. Y., 1983, "Free Rotation of a Circular Ring about a Diameter," *Journal of Applied Mathematics and Physics* (ZAMP), Vol. 34, pp. 13–24.

N. G. Stephen
Lecturer.

P. J. Wang[1]
Department of Mechanical Engineering,
University of Southampton,
Southampton, England S09 5NH

Stretching and Bending of Rotating Beam

The effect of uniform high-speed rotation on the simplest representation of a rotating blade is analyzed according to the linear theory of elasticity. The blade is modeled as a uniform prismatic beam of general cross section rotating about a principal section axis perpendicular to the centroidal axis. This quasi-elastostatic three-dimensional problem is reduced to a two-dimensional boundary value problem to which solutions for the amenable circular and elliptic cross sections are given. For sections not possessing two axes of cross-sectional symmetry, the theory predicts curvature of the blade center line.

1 Introduction

The determination of stress and strain fields in prismatic rods of arbitrary cross section due to forces applied at the ends of the rod only, is known as Saint-Venant's Problem. Solutions have been obtained for tension, pure bending, torsion, and bending due to a terminal shearing force (Sokolnikoff, 1956); apart from their direct application, these solutions provide justification and limitations to the technical theories used in "strength of materials". Exact solutions have also been obtained for body force gravity loadings of rods and beams producing longitudinal extension (Sokolnikoff, 1956) and bending (Love, 1944). In principle, exact solutions can be obtained for any case in which the forces applied to the beam along its length can be represented by rational integral functions of the beam axial coordinate (Almansi, 1901).

In the present paper the authors give the solution for a beam rotating about a principal axis perpendicular to its centroidal axis, as shown in Fig. 1. Such a centrifugal body force loading is of obvious importance in the design of turbine blades, where a knowledge of the deformed shape of the blade due to rotation and thermal effects is required before subsequent vibration analysis. The physical model analyzed here is the simplest representation of a rotating blade, having no pretwist or taper, and a "setting angle" fixed by cross-sectional shape; the coincidence of the x axis of rotation with a cross section principal axis precludes twisting of the blade which would otherwise arise due to asymmetric "body force loading" in the y direction. Apart from classical interest, the solution should provide a test for approximate methods of analysis.

2 Blade Model

The problem to be solved is the determination of stress, strain, and displacements of the prismatic isotropic beam shown in Fig. 1; the z axis coincides with the beam centroidal axis and the x and y axes are principal. The beam is assumed to rotate in a horizontal plane about a vertical axis through the end $z=0$ with constant angular velocity Ω rad/sec. The surface generators of the beam are assumed free of traction, and no specific constraint is placed on the displacements at the end $z=0$.

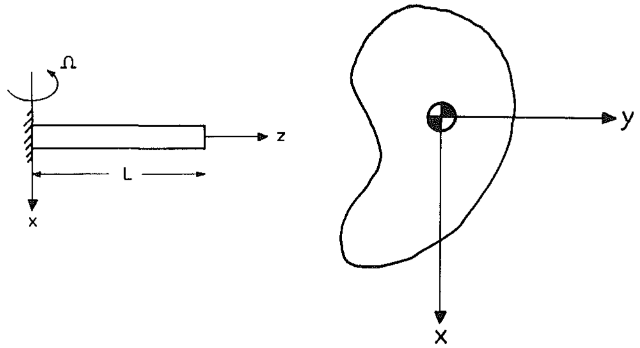

Fig. 1 Rotating blade model

3.1 Elasticity Equations

We have to satisfy the equilibrium equations

$$\left.\begin{aligned}\frac{\partial \sigma_x}{\partial x}+\frac{\partial \tau_{xy}}{\partial y}+\frac{\partial \tau_{xz}}{\partial z}=0\\ \frac{\partial \tau_{yx}}{\partial x}+\frac{\partial \sigma_y}{\partial y}+\frac{\partial \tau_{yz}}{\partial z}+\rho\Omega^2 y=0\\ \frac{\partial \tau_{zx}}{\partial x}+\frac{\partial \tau_{zy}}{\partial y}+\frac{\partial \sigma_z}{\partial z}+\rho\Omega^2 z=0\end{aligned}\right\} \qquad (1a,b,c)$$

subject to the boundary conditions on the surface generators

$$\left.\begin{aligned}\sigma_x \cdot \ell+\tau_{xy} m=0\\ \tau_{yx}\cdot \ell+\sigma_y m=0\\ \tau_{zx}\cdot \ell+\tau_{zy} m=0\end{aligned}\right\} \qquad (2a,b,c)$$

where ℓ and m are the direction cosines.

---

[1] Visiting Research Fellow from the Maritime Transportation Institute of Shanghai, The People's Republic of China.

Contributed by the Applied Mechanics Division for publication in the JOURNAL OF APPLIED MECHANICS.

Discussion on this paper should be addressed to the Editorial Department, ASME, United Engineering Center, 345 East 47th Street, New York, N.Y. 10017, and will be accepted until two months after final publication of the paper itself in the JOURNAL OF APPLIED MECHANICS. Manuscript received by ASME Applied Mechanics Division, July 24, 1984; final revision, February 12, 1986.

The conditions at the free end $z=L$ are not specified except insofar as all the stress resultants are required to be zero. Additionally, the following equations of compatibility must be satisfied:

$$\left.\begin{aligned} \frac{\partial^2\epsilon_x}{\partial y^2}+\frac{\partial^2\epsilon_y}{\partial x^2}&=\frac{\partial^2\gamma_{xy}}{\partial x\partial y}\\ \frac{\partial^2\epsilon_y}{\partial z^2}+\frac{\partial^2\epsilon_z}{\partial y^2}&=\frac{\partial^2\gamma_{yz}}{\partial y\partial z}\\ \frac{\partial^2\epsilon_z}{\partial x^2}+\frac{\partial^2\epsilon_x}{\partial z^2}&=\frac{\partial^2\gamma_{xz}}{\partial x\partial z} \end{aligned}\right\} \qquad (3a,b,c)$$

$$\left.\begin{aligned} \frac{2\partial^2\epsilon_x}{\partial y\partial z}&=\frac{\partial}{\partial x}\left(-\frac{\partial\gamma_{yz}}{\partial x}+\frac{\partial\gamma_{xz}}{\partial y}+\frac{\partial\gamma_{xy}}{\partial z}\right)\\ \frac{2\partial^2\epsilon_y}{\partial x\partial z}&=\frac{\partial}{\partial y}\left(\frac{\partial\gamma_{yz}}{\partial x}-\frac{\partial\gamma_{xz}}{\partial y}+\frac{\partial\gamma_{xy}}{\partial z}\right)\\ \frac{2\partial^2\epsilon_z}{\partial x\partial y}&=\frac{\partial}{\partial z}\left(\frac{\partial\gamma_{yz}}{\partial x}+\frac{\partial\gamma_{xz}}{\partial y}-\frac{\partial\gamma_{xy}}{\partial z}\right) \end{aligned}\right\} \qquad (4a,b,c)$$

3.2 Semi-Inverse Solution

The solution was originally obtained by assuming stress and strain components to be quadratic functions of the axial coordinate z, i.e.,

$$\begin{aligned} \sigma_x&=\sigma_x^{(2)}z^2+\sigma_x^{(1)}z+\sigma_x^{(0)}\\ \epsilon_x&=\epsilon_x^{(2)}z^2+\epsilon_x^{(1)}z+\epsilon_x^{(0)} \end{aligned} \qquad (5)$$

etc.

and by adopting a procedure very similar to that employed by Love (1944) for the consideration of a beam subjected to distributed transverse loading.

We now employ a semi-inverse procedure and assume the following:

(a) $\tau_{xz}=\tau_{yz}=\gamma_{xz}=\gamma_{yz}=0$,

(b) planar stresses and strain σ_x, τ_{xy}, σ_y, and γ_{xy} to be independent of z, and

(c) longitudinal strain given by

$$\epsilon_z=\epsilon_o+\frac{\rho\Omega^2}{2E}\ (L^2-z^2)-\kappa_o x-\kappa_o' y+\epsilon_1(x^2+y^2) \qquad (6)$$

where ϵ_o, ϵ_1, κ_o, and κ_o' are constants to be determined.

The first two terms in equation (6) are consistent with the elementary longitudinal strain expected, the second two terms allow bending, while the final term allows distortion of the cross section into a paraboloid of revolution and is suggested by the known solution for longitudinal loading in a beam due to self weight.

The equilibrium equations (1*a*, *b*, *c*) reduce to

$$\left.\begin{aligned} &\frac{\partial\sigma_x}{\partial x}+\frac{\partial\tau_{xy}}{\partial y}=0\\ &\frac{\partial\tau_{xy}}{\partial x}+\frac{\partial\sigma_y}{\partial y}+\rho\Omega^2 y=0\\ &\frac{\partial\sigma_z}{\partial z}+\rho\Omega^2 z=0 \end{aligned}\right\} \qquad (7a,b,c)$$

the compatibility equations (3*a*,*b*,*c*) become

$$\left.\begin{aligned} \frac{\partial^2\epsilon_x}{\partial y^2}+\frac{\partial^2\epsilon_y}{\partial x^2}&=\frac{\partial^2\gamma_{xy}}{\partial x\partial y}\\ \frac{\partial^2\epsilon_y}{\partial z^2}+\frac{\partial^2\epsilon_z}{\partial y^2}&=0\\ \frac{\partial^2\epsilon_z}{\partial x^2}+\frac{\partial^2\epsilon_x}{\partial z^2}&=0 \end{aligned}\right\} \qquad (8a,b,c)$$

and equations (4*a*,*b*,*c*) become

$$\left.\begin{aligned} \frac{\partial^2\epsilon_x}{\partial y\partial z}&=0\\ \frac{\partial^2\epsilon_y}{\partial x\partial z}&=0\\ \frac{\partial^2\epsilon_z}{\partial x\partial y}&=0 \end{aligned}\right\} \qquad (9a,b,c)$$

We note that (9*c*) is immediately satisfied by the choice of ϵ_z. The equilibrium equations (7*a*,*b*) are satified by introducing the stress function $\Phi(x,y)$ such that

$$\sigma_x=\frac{\partial^2\Phi}{\partial y^2}\ ,\ \tau_{xy}=\frac{-\partial^2\phi\Phi}{\partial x\partial y}\ ,\ \sigma_y=\frac{\partial^2\Phi}{\partial x^2}-\frac{\rho\Omega^2y^2}{2}\ . \qquad (10a,b,c)$$

Now from the Hookes' Laws

$$\left.\begin{aligned} \epsilon_x&=\frac{\sigma_x}{E}-\frac{\nu}{E}\ (\sigma_y+\sigma_z)\\ \epsilon_y&=\frac{\sigma_y}{E}-\frac{\nu}{E}\ (\sigma_z+\sigma_x)\\ \epsilon_z&=\frac{\sigma_z}{E}-\frac{\nu}{E}\ (\sigma_x+\sigma_y) \end{aligned}\right\} \qquad (11a,b,c)$$

the first two when differentiated twice with respect to z give

$$\frac{\partial^2\epsilon_x}{\partial z^2}=\frac{\partial^2\epsilon_y}{\partial z^2}=-\frac{\nu}{E}\,\frac{\partial^2\sigma_z}{\partial z^2}=\frac{\nu\rho\Omega^2}{E}$$

by virtue of equation (7*c*). The compatibility equations (8*b*,*c*) thus require

$$\frac{\partial^2\epsilon_z}{\partial x^2}=\frac{\partial^2\epsilon_z}{\partial y^2}=\frac{-\nu\rho\Omega^2}{E}$$

which enables the constant ϵ_1 to be evaluated as $\epsilon_1=-\nu\rho\Omega^2/2E$. The direct longitudinal stress σ_z may be constructed from (11*c*) as

$$\begin{aligned} \sigma_z=E\epsilon_o+\frac{\rho\Omega^2}{2}\ (L^2-z^2)-E\kappa_o x-E\kappa_o' y\\ -\frac{\nu\rho\Omega^2}{2}\ (x^2+y^2)+\nu(\sigma_x+\sigma_y) \end{aligned}$$

and integrating over the cross section gives the tensile force resultant as

$$\begin{aligned} T=\int\int\sigma_z dxdy=EA\epsilon_o+\frac{\rho A\Omega^2}{2}\ (L^2-z^2)\\ -\frac{\nu\rho\Omega^2}{2}\ (I_y+I_x)+\nu\int\int(\sigma_x+\sigma_y)dxdy \end{aligned}$$

where $I_y=\int\int x^2dxdy$, $I_x=\int\int y^2dxdy$.

The area integral $\int\int(\sigma_x+\sigma_y)\ dxdy$ may be expressed as

$$\int\int (\sigma_x+\sigma_y)\ dxdy=\int\int\left\{\frac{\partial}{\partial x}\ (x\sigma_x+y\tau_{xy})+\frac{\partial}{\partial y}\ (x\tau_{xy}+y\sigma_y)\right\}dxdy$$

$$-\int\int\left\{x\left(\frac{\partial\sigma_x}{\partial x}+\frac{\partial\tau_{xy}}{\partial y}\right)+y\left(\frac{\partial\tau_{xy}}{\partial x}+\frac{\partial\sigma_y}{\partial y}\right)\right\}dxdy$$

The first integral transforms to the line integral

$$\int_c \{x(\sigma_x l+\tau_{xy}m)+y(\tau_{xy}l+\sigma_y m)\}ds$$

which is zero by virtue of the boundary conditions (2*a*,*b*), while the second integral reduces to

$$\int\int \rho\Omega^2 y^2\ dxdy,$$

by virtue of the equilibrium equations (7*a*,*b*).

Thus we find, $\nu\int\int(\sigma_x+\sigma_y)\ dxdy=\nu\rho\Omega^2 I_x$, and the tensile force becomes

$$T=EA\epsilon_o+\frac{\rho A\Omega^2}{2}\ (L^2-z^2)+\frac{\nu\rho\Omega^2}{2}\ (I_x-I_y).$$

To evaluate the constant ϵ_o, we require the tensile force T to be zero at the free end $z=L$, giving

$$\epsilon_o=\frac{\nu\rho\Omega^2}{2EA}\ (I_y-I_x)$$

from which

$$T=\frac{\rho A\Omega^2}{2}\ (L^2-z^2), \tag{12}$$

as expected from the elementary theory.

To evaluate the constants κ_o and κ_o' we construct the bending moments

$$M_x=\int\int y\sigma_z dxdy \text{ and } M_y=-\int\int x\sigma_z dxdy.$$

Firstly

$$M_x=\int\int\left\{E\epsilon_o y+\frac{\rho\Omega^2}{2}\ (L^2-z^2)y-E\kappa_o xy-E\kappa_o' y^2-\frac{\nu\rho\Omega^2}{2}\ (x^2+y^2)y+\nu(\sigma_x+\sigma_y)y\right\}dxdy,$$

and the first three terms become zero, as the centroidal x and y axes are also principal, giving

$$M_x=-E\kappa_o' I_x-\frac{\nu\rho\Omega^2}{2}\int\int (x^2+y^2)y\ dxdy+\nu\int\int(\sigma_x+\sigma_y)y\ dxdy.$$

Now the area integral may be expressed as

$$\int\int(\sigma_x+\sigma_y)y\ dxdy=\int\int\left\{\frac{\partial}{\partial y}\left(\left(\frac{y^2-x^2}{2}\right)\sigma_y+xy\tau_{xy}\right)+\frac{\partial}{\partial x}\ \left(xy\sigma_x+\left(\frac{y^2-x^2}{2}\right)\tau_{xy}\right)\right\}dxdy$$

$$-\int\int\left\{xy\left(\frac{\partial\sigma_x}{\partial x}+\frac{\partial\tau_{xy}}{\partial y}\right)+\left(\frac{y^2-x^2}{2}\right)\left(\frac{\partial\tau_{xy}}{\partial x}+\frac{\partial\sigma_y}{\partial y}\right)\right\}dxdy.$$

The first integral transforms to the line integral

$$\int_c\left\{xy(\sigma_x l+\tau_{xy}m)+\left(\frac{y^2-x^2}{2}\right)(\tau_{xy}l+\sigma_y m)\right\}ds$$

which is zero by virtue of the boundary conditions (2*a*,*b*), while the second integral reduces to

$$\frac{\rho\Omega^2}{2}\int\int(y^2-x^2)y\ dxdy$$

and hence the bending moment M_x becomes

$$M_x=-EI_x\kappa_o'-\nu\rho\Omega^2\int\int x^2y\ dxdy.$$

Similarly we find

$$M_y=EI_y\kappa_o-\frac{\nu\rho\Omega^2}{2}\int\int(y^2-x^2)x\ dxdy.$$

Now since these bending moments are independent of z and are required to be zero at the tip $z=L$, the constants (curvatures in the xz and yz planes, respectively) are found to be

$$\left.\begin{aligned}\kappa_o&=\frac{\nu\rho\Omega^2}{2EI_y}\int\int(y^2-x^2)x\ dxdy\\ \kappa_o'&=-\frac{\nu\rho\Omega^2}{EI_x}\int\int x^2y\ dxdy\end{aligned}\right\} \tag{13}$$

Before considering in detail the two-dimensional problem and determination of the stress function Φ, the remaining unknown strains ϵ_x and ϵ_y may be readily calculated from the Hooke's Laws (11*a*,*b*), and the stress and strain components listed as

$$\left.\begin{aligned}
\sigma_x&=\frac{\partial^2\Phi}{\partial y^2}\\
\sigma_y&=\frac{\partial^2\Phi}{\partial x^2}-\frac{\rho\Omega^2y^2}{2}\\
\sigma_z&=\frac{\rho\Omega^2}{2}\ (L^2-z^2)-E\kappa_o x-E\kappa_o' y\\
&\quad+\frac{\nu\rho\Omega^2}{2}\left[\frac{(I_y-I_x)}{A}-(x^2+y^2)\right]\\
&\quad+\nu\left(\frac{\partial^2\Phi}{\partial x^2}+\frac{\partial^2\Phi}{\partial y^2}-\frac{\rho\Omega^2y^2}{2}\right)\\
\tau_{xy}&=-\frac{\partial^2\Phi}{\partial x\partial y}\ ,\ \tau_{xz}=\tau_{yz}=0\\
\epsilon_x&=-\frac{\nu\rho\Omega^2}{2E}\ (L^2-z^2)+\nu\kappa_o x+\nu\kappa_o' y\\
&\quad-\frac{\nu^2\rho\Omega^2}{2E}\left[\frac{(I_y-I_x)}{A}-(x^2+y^2)\right]\\
&\quad+\frac{(1-\nu^2)}{E}\ \frac{\partial^2\Phi}{\partial y^2}-\frac{\nu(1+\nu)}{E}\ \left(\frac{\partial^2\Phi}{\partial x^2}-\frac{\rho\Omega^2y^2}{2}\right)\\
\epsilon_y&=-\frac{\nu\rho\Omega^2}{2E}\ (L^2-z^2)+\nu\kappa_o x+\nu\kappa_o' y\\
&\quad-\frac{\nu^2\rho\Omega^2}{2E}\left[\frac{(I_y-I_x)}{A}-(x^2+y^2)\right]\\
&\quad+\left(\frac{1-\nu^2}{E}\right)\left(\frac{\partial^2\Phi}{\partial x^2}-\frac{\rho\Omega^2y^2}{2}\right)-\frac{\nu(1+\nu)}{E}\ \frac{\partial^2\Phi}{\partial y^2}\\
\epsilon_z&=\frac{\rho\Omega^2}{2E}\ (L^2-z^2)-\kappa_o x-\kappa_o' y\\
&\quad+\frac{\nu\rho\Omega^2}{2E}\left[\frac{(I_y-I_x)}{A}-(x^2+y^2)\right]\\
\gamma_{xy}&=-\frac{1}{G}\ \frac{\partial^2\Phi}{\partial x\partial y}\ ,\ \gamma_{xz}=\gamma_{yz}=0.
\end{aligned}\right\} \tag{14}$$

3.3 Two-Dimensional Problem

The equilibrium equations (7*a*,*b*) have been satisfied by introduction of the stress function Φ, through equations (10*a*,*b*,*c*). From the calculated strain components in equation (14), compatibility equation (8*a*) requires

$$\nabla^4\Phi=-\left(\frac{\nu+3\nu^2}{1-\nu^2}\right)\rho\Omega^2 \tag{15}$$

while the remainder (8*b*,*c*, 9*a*,*b*,*c*) are seen to be satisfied.

The boundary conditions for Φ become, from equations (2*a*,*b*) and (14),

$$\left.\begin{aligned}&\frac{d}{ds}\left(\frac{\partial\Phi}{\partial y}\right)=0\\&\frac{d}{ds}\left(\frac{\partial\Phi}{\partial x}\right)=\frac{\rho\Omega^2y^2}{2}\frac{dx}{ds}\end{aligned}\right\} \tag{16}$$

3.4 Solution to Two Dimensional Problem

3.4.1 Circular Cross Section. For the boundary $x^2+y^2-R^2=0$, we find

$$\begin{aligned}\Phi=&-\left(\frac{\nu+3\nu^2}{1-\nu^2}\right)\frac{\rho\Omega^2}{64}(x^2+y^2-R^2)^2\\&+\frac{\rho\Omega^2}{64}\left(y^4-\frac{5}{3}x^4+2x^2y^2+14R^2x^2-2R^2y^2\right),\end{aligned} \tag{17}$$

curvatures κ_o and κ_o' are both zero, and hence stresses are:

$$\left.\begin{aligned}&\quad+\frac{\rho\Omega^2}{2}(R^2-x^2-y^2)\\&\sigma_z=\frac{\rho\Omega^2}{2}(L^2-z^2)\\&\quad+\frac{\nu(3+\nu)}{8(1-\nu^2)}\rho\Omega^2(R^2-2x^2-2y^2)\\&\tau_{xy}=-\frac{(1-\nu-4\nu^2)}{8(1-\nu^2)}\rho\Omega^2xy\\&\tau_{xz}=\tau_{yz}=0\end{aligned}\right\} \tag{18}$$

3.4.2 Elliptic Cross Section. For the boundary $x^2/a^2+y^2/b^2-1=0$, we find

$$\Phi=\frac{\Lambda}{8}a^2b^2\left(\frac{x^2}{a^2}+\frac{y^2}{b^2}-1\right)^2-\frac{\rho\Omega^2}{24}\frac{b^2}{a^2}x^4+\frac{\rho\Omega^2}{4}b^2x^2, \tag{19}$$

curvatures κ_o and κ_o' are both zero, and hence stresses

$$\left.\begin{aligned}&\sigma_x=\frac{\Lambda}{2}a^2\left(\frac{x^2}{a^2}+\frac{3y^2}{b^2}-1\right)\\&\sigma_y=\frac{\Lambda}{2}b^2\left(\frac{3x^2}{a^2}+\frac{y^2}{b^2}-1\right)\\&\quad-\frac{\rho\Omega^2b^2}{2}\left(\frac{x^2}{a^2}+\frac{y^2}{b^2}-1\right)\\&\sigma_z=\frac{\rho\Omega^2}{2}(L^2-z^2)\\&\quad+\frac{\nu\rho\Omega^2}{2}\left\{\left(\frac{a^2-b^2}{4}\right)-(x^2+y^2)\right\}\\&\quad+\frac{\nu\Lambda}{2}\left\{\left(1+\frac{3b^2}{a^2}\right)x^2\right.\\&\quad\left.+\left(1+\frac{3a^2}{b^2}\right)y^2-(a^2+b^2)\right\}\\&\quad-\frac{\nu\rho\Omega^2b^2}{2}\left(\frac{x^2}{a^2}+\frac{y^2}{b^2}-1\right)\\&\tau_{xy}=-\Lambda xy,\quad\tau_{xz}=\tau_{yz}=0,\end{aligned}\right\} \tag{20}$$

where

$$\Lambda=\rho\Omega^2\left[\frac{b^2}{a^2}-\left(\frac{\nu+3\nu^2}{1-\nu^2}\right)\right]\frac{a^2b^2}{3a^4+2a^2b^2+3b^4}.$$

References

Almansi, E., 1901, "Sopra la Deformazione dei Cilindri Sollecitati Lateralmente," *Atti della Reale Accademia dei Lincei, Rendiconti*, Series 5, Vol. 10, p. 333-338, pp. 400-408.

Love, A. E. H., 1944, *A Treatise on the Mathematical Theory of Elasticity*, Fourth Edition, Dover Publications, New York, Chapter 16.

Sokolnikoff, I. S., 1956, *Mathematical Theory of Elasticity*, Second Edition, McGraw-Hill, New York, Chapter 4.

S. Im[1]

R. T. Shield
Fellow ASME

Department of Theoretical and
Applied Mechanics,
University of Illinois at Urbana-Champaign,
Urbana, Ill. 61801

Elastic Deformations of Strips and Circular Plates Under Uniform Pressure

A consistent theory for linear elastic behavior in which the strains are small but in which the displacements and rotations can be large is applied to the bending of a long rectangular plate and of a circular plate by uniform pressure. Within the range of small-strain, linear elastic behavior, the theory provides solutions for all slenderness ratios of the plates and magnitudes of the loading. Thus the theory bridges the gap between the classical theory and the nonlinear structural theory of Föppl and von Kármán. The results show that the von Kármán equations provide accurate solutions for thin plates for which deflections are not small.

1 Introduction

The classical theory of elasticity treats deformations in which the displacements, strains, and rotations are small, and uses linear stress-strain relations which are suitable for the description of materials such as metals in the elastic range. The difficulties involved in the solution of the equations of the classical theory has led to the development of technical theories for elastic deformations of beams, plates, and shells, and there is now an extensive literature on applications and refinements and modifications to the theories (see, for example, the classical books by Love, 1927, and Timoshenko and Woinowsky-Krieger, 1959, and survey articles by Nagdhi, 1972, and Koiter and Simmonds, 1973). For a body slender in one or more dimensions, such as a thin beam or plate, a large deflection or rotation of one part of the body relative to another is possible although the strains remain small and within the linear elastic range over the entire body. Technical or structural theories for large deflections, such as Kirchhoff's theory of rods and the theory of Föppl and von Kármán for plates, mainly rely upon the kinematics of the deformations and overall equilibrium equations, and apply to very thin rods and plates (see Love, 1927). Some writers have used finite elasticity theory together with asymptotic expansions based upon small parameters such as a depth-to-length ratio or a strain measure (see Parker, 1984 and the references cited therein) to justify structural theories. Here we use a consistent theory for linear elastic behavior with small strains which was developed by Shield (1984). In this theory the strains are small enough that second order terms in the stress-strain relation can be neglected, but there is no restriction on the magnitude of rotations and displacements. The theory bridges the gap between the infinitesimal theory and structural theories for slender bodies, and it can provide results for geometries and loadings for which neither of the theories applies.

Shield (1984) applied the theory to pure torsion of a very long cylinder and to the bending of a cantilever beam by an end load about a principal axis of the cross section. Other successful applications of the theory include the analysis of the deformation of a rod or beam by end loads and the bending of a beam by its own weight (Im, 1985; Shield and Im, 1986).

Here we treat the bending of a long strip and of a circular plate by uniform pressure. The basic formulas and equations in the theory are reviewed briefly in Section 2. Section 3 deals with the bending of an infinitely long strip loaded by pressure on its upper surface with support conditions on its long sides. For small deflections, the plane strain modification of the generalized plane stress solution (see Love, 1927, pp. 363-364) provides the solution, and for a very thin strip, the von Kármán equations have been used (see Love, 1927, pp. 559-564). In the present approach, the deformation is considered to consist of small displacements which distort cross sections relative to the middle surface of the strip, together with rotations and translations of the cross sections which vary along the span. The infinitesimal solution is used to guide the form taken for the deformation relative to the midsurface of the strip and this approach leads to a solution valid for all values of the span-to-depth ratio of the strip. Because of the pressure loading, the expressions for the bending moment and axial force resultants contain constant terms; these terms become second order and negligible for a thin strip experiencing deflections comparable to its thickness. For thin plates with depth-to-span ratios not greater than $0(\epsilon^{1/2})$, where ϵ is a measure of the maximum strain in the plates, the predictions of the von Kármán theory are confirmed, and accurate results are obtained for the transition range in which the pressure is carried by the bending moment as well as by tension in the plate. The bending of a circular plate by uniform pressure supported on its edge is examined in a similar manner in Section 4. The classical theory for a moderately thick plate again guides the choice of the displacement field, and gives the solu-

---

[1] Presently at the Center for the Advancement of Computational Mechanics, Georgia Institute of Technology, Atlanta, Ga. 30332.

Contributed by the Applied Mechanics Division for publication in the JOURNAL OF APPLIED MECHANICS.

Discussion on this paper should be addressed to the Editorial Department, ASME, United Engineering Center, 345 East 47th Street, New York, N.Y. 10017, and will be accepted until two months after final publication of the paper itself in the JOURNAL OF APPLIED MECHANICS. Manuscript received by ASME Applied Mechanics Division, December 5, 1985.

tion when the deflections are small (see Love, 1927, p. 481). For large deflections, on the other hand, nonlinear plate theory has been applied (see Stoker, 1968, for example). As in the case of the long strip, the von Kármán equations are found to give accurate results for thin circular plates when thickness-to-diameter ratios are $0(\epsilon^{1/2})$ or less.

2 Basic Formulas

We suppose that a body occupies a region V of space in its reference state B. In a deformation of B, a typical particle initially at the point x_i moves to the point y_i referred to a fixed rectangular Cartesian coordinate system. The Cauchy strains C_{ik} are given by

$$C_{ik} = y_{r,i} y_{r,k}. \tag{1}$$

A repeated Latin index implies summation over the values 1,2,3 and a comma is used to denote partial differentiation with respect to x_i. For deformations with small strains, the Green strain tensor e_{ik} is written as

$$e_{ik} = \frac{1}{2}(C_{ik} - \delta_{ik}) = 0(\epsilon), \tag{2}$$

where "0" denotes order of magnitude, ϵ is a dimensionless loading parameter representing the amount of strain induced in the body, and δ_{ik} is the Kronecker delta. From the polar decomposition theorem (Truesdell and Noll, 1965) we have

$$y_{i,k} = r_{im} s_{mk}. \tag{3}$$

Here r_{im} is a proper orthogonal (rotation) tensor, and the right stretch tensor s_{mk} is the positive definite square root of C_{ik},

$$s_{im} s_{mk} = C_{ik}. \tag{4}$$

Using equations (2), (3), (4), we find that

$$s_{ik} = \delta_{ik} + e_{ik} + 0(\epsilon^2), \quad r_{ik} = y_{i,k} + 0(\epsilon). \tag{5}$$

We assume that the first partial derivatives of e_{ik} are $0(\epsilon)/h$, where h is a reference length involved in the description of a body and the loading causing the deformation. It can then be shown that (see Shield, 1984)

$$r_{ik,j} = 0(\epsilon)/h, \; y_{i,k\ell} = 0(\epsilon)/h. \tag{6}$$

The equilibrium equations in terms of the Lagrangian stress tensor T_{ik} are given by

$$\frac{\partial T_{ki}}{\partial x_k} + F_i = 0, \tag{7}$$

where F_i are the components of the body force measured per unit volume of the reference state B.

An elastic material has a strain energy W per unit volume of the reference state which is a function of the deformation gradient $y_{i,k}$ only through the strains C_{ik} or e_{ik}. When the strain energy W is written symmetrically in e_{ik} and e_{ki}, the Lagrangian stress tensor T_{ik} and the Kirchhoff stress tensor σ_{ik} are given by

$$T_{ki} = \frac{\partial W}{\partial y_{i,k}} = \frac{\partial y_i}{\partial x_r} \frac{\partial W}{\partial e_{rk}}, \quad \sigma_{ik} = T_{kr} \frac{\partial x_i}{\partial y_r} = \frac{\partial W}{\partial e_{ik}}. \tag{8}$$

To $0(\epsilon)$, σ_{ik} are true stresses associated with directions in the deformed state of line elements which were initially parallel to the coordinate axes. Substituting for T_{ki} in (7) and multiplying by $\partial x_r/\partial y_i$, we find that the equilibrium equations can be written as

$$\frac{\partial \sigma_{ik}}{\partial x_k} + \sigma_{rk} \Gamma^i_{rk} + F_k \frac{\partial x_i}{\partial y_k} = 0, \tag{9}$$

where the Christoffel symbol is given by

$$\Gamma^i_{rk} = \frac{\partial^2 y_m}{\partial x_r \partial x_k} \frac{\partial x_i}{\partial y_m} = C^{-1}_{im}(e_{rm,k} + e_{km,r} - e_{rk,m}).$$

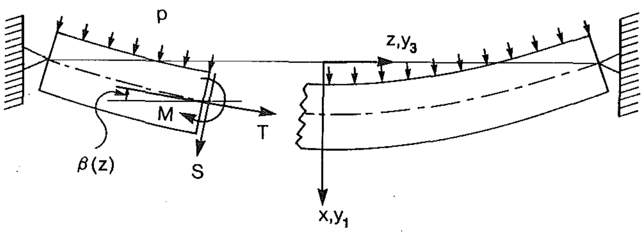

Fig. 1 Force and moment resultants for a long strip under uniform pressure

For linear elastic behavior for small strain deformations, it is sufficient to take W to be

$$W = \frac{1}{2} c_{ikmn} e_{ik} e_{mn}, \quad c_{ikmn} = c_{mnik} = c_{kimn},$$

where c_{ikmn} are the usual elastic moduli for small strains. The stresses σ_{ik} are then given by

$$\sigma_{ik} = c_{ikmn} e_{mn}. \tag{10}$$

Consistent with the accuracy of the assumption of linear behavior for small strains, second order terms are ignored in calculating the strains e_{ik} from equation (2). With $e_{ik,\ell} = 0(\epsilon)/h$ as assumed earlier, the Christoffel symbols in equation (9) will be $0(\epsilon)/h$. Thus neglecting terms of the order of $E\epsilon^2/h$, where E is a typical elastic modulus of the material, the equations of equilibrium become

$$\frac{\partial \sigma_{ik}}{\partial x_k} + F_k \frac{\partial x_i}{\partial y_k} = 0, \tag{11}$$

in which $\partial x_i/\partial y_k$ is evaluated to 0(1). To our order of accuracy, it is only necessary to satisfy equation (11) to $0(\epsilon)$.

If the tractions are prescribed on a portion S_T of the surface S of V, then

$$T_{ki} n_k = \sigma_{rk} y_{i,r} n_k = \hat{T}_i \quad \text{on} \quad S_T,$$

where $\hat{T}_i$ are the applied tractions of order $E\epsilon$ and n_i is the unit outward normal to S. Equivalently we have

$$\sigma_{ik} n_k = \hat{T}_k \frac{\partial x_i}{\partial y_k} = \hat{\tau}_i \quad \text{on} \quad S_T. \tag{12}$$

To the present order of approximation $\partial x_i/\partial y_k$ in equation (12) need only be evaluated to 0(1) and $\hat{\tau}_i$ are then the components of the applied traction in the directions of line elements that were originally parallel to the coordinate axes. For zero surface tractions $\sigma_{ik} n_k$ must vanish to $0(\epsilon)$ on S_T.

3 Bending of an Infinitely Long Strip by Uniform Pressure

In this section we consider the bending of an infinitely long strip by uniform pressure. The strip is initially horizontal and supported on its long edges. The upper surface is subject to uniform pressure p, while the lower surface is free from traction. The weight of the strip is neglected but it could be included as in the beam treated in Im (1985), and Shield and Im (1986). The support conditions and the loading do not vary along the length of the strip so that we have a plane strain problem. For small deflections, the plane strain modification of the generalized plane stress solution (see Love, 1927, pp. 363–364) provides the classical linear theory solution, and for a very thin strip, which can have deflections comparable to the thickness of the strip, the von Kármán equations have been used (see Love, 1927, pp. 559–564). Here we obtain solutions for all values of the span-to-depth ratio.

A rectangular Cartesian coordinate system is taken with origin at the center of the cross section and with the x axis vertically downward and the z axis along the span-direction. The ends of the span are at $z=\pm\ell$, and the lower and upper surfaces of the strip at $x=\pm h$. The coordinates of the deformed middle plane are denoted by $X(z)$ and $Z(z)$, and then the extension e of the middle plane is given by

$$X'^2+Z'^2=(1+e)^2,$$

where a prime denotes differentiation with respect to z. We use $\beta(z)$ for the inclination to the horizontal of the tangent to the deformed middle plane along the z coordinate (Fig. 1). Then we have the relations

$$\sin\beta=X'/(1+e), \quad \cos\beta=Z'/(1+e), \tag{13}$$

and we can take

$$y_1=X(z)+u_3\sin\beta+(x+u_1)\cos\beta,$$
$$y_3=Z(z)+u_3\cos\beta-(x+u_1)\sin\beta,$$

where u_1, u_3 are small displacements which vanish with x. For small strains and small strain derivatives, the first and second partial derivatives of u_1, u_3 with respect to x and z are required to be $0(\epsilon)$ and $0(\epsilon)/h$ at most, respectively. Guided by the classical infinitesimal solution, we assume that

$$u_1(x,z)=-\frac{\nu ex}{(1-\nu)}+\frac{\nu}{2(1-\nu)}\beta' x^2$$
$$-\frac{p}{D}\left\{\frac{1+\nu}{24(1-\nu)}x^4-\frac{h^2x^2}{4(1-\nu)^2}-\frac{2\nu-1}{3(1-\nu)^2}h^3x\right\},$$
$$u_3(x,z)=-\frac{\beta''}{6(1-\nu)}\{(\nu-2)x^3+6h^2x\},$$

where $D=2Eh^3/3(1-\nu^2)$ is the flexural rigidity of the strip and E, ν are Young's modulus and Poisson's ratio. We can calculate the Green strains for the deformation using equations (1), (2), and from the stress-strain law for an isotropic material we obtain the components of the Kirchhoff stress tensor to $0(\epsilon)$,

$$\sigma_{xx}=-p\left\{\frac{1}{4}\left(\frac{x}{h}\right)^3-\frac{3}{4}\frac{x}{h}+\frac{1}{2}\right\},$$
$$\sigma_{xz}=\frac{E}{2(1-\nu^2)}\beta''(x^2-h^2),$$
$$\sigma_{zz}=\frac{E}{1-\nu^2}(e-\beta' x)+p\left\{\frac{1}{2}\left(\frac{x}{h}\right)^3\right.$$
$$\left.-\frac{3(2-\nu)}{4(1-\nu)}\frac{x}{h}-\frac{\nu}{2(1-\nu)}\right\},$$

provided that to $0(\epsilon)$

$$\beta'''=\frac{p}{D}, \quad e'=0. \tag{14}$$

These assumptions will be verified later. The traction boundary conditions (12) on the upper and lower surfaces are now seen to be satisfied to $0(\epsilon)$, and the equilibrium equations $\sigma_{ik,k}=0$ are also satisfied to $0(\epsilon)$ (β^{iv} and e'' are assumed to be zero to $0(\epsilon)$, in agreement with equation (14)).

The resultant of the traction on the surface which was initially the cross section $z=$constant is statically equivalent to transverse and longitudinal forces $S(z)$ and $T(z)$ per unit length acting at the deformed position of the middle plane together with a moment $M(z)$ per unit length (Fig. 1). We then have

$$S\cos\beta+T\sin\beta=\int_A T_{31}dA, \; -S\sin\beta+T\cos\beta=\int_A T_{33}dA,$$
$$M=\int_A \{(y_3-Z)T_{31}-(y_1-X)T_{33}\}dA,$$

where A denotes the cross-sectional area. Using the relation between σ_{ik} and T_{ik} in equation (8) together with the expressions for σ_{ik}, we find that to $0(\epsilon)$

$$S=-D\beta'', \; T=\frac{2Eeh}{1-\nu^2}-\frac{\nu}{1-\nu}ph,$$
$$M=D\beta'+\frac{8-3\nu}{10(1-\nu)}h^2p. \tag{15}$$

The geometry of the strip and loading are symmetric with respect to the x axis, and consideration of overall balance of force and moment between $z=0$ and $z=\ell$ leads to

$$S\cos\beta+T\sin\beta+py_3(-h,z)=0,$$
$$T\cos\beta-S\sin\beta-T_o+p\{y_1(-h,0)-y_1(-h,z)\}=0, \tag{16}$$
$$M-M_o+p\{y_3(-h,z)\}^2/2+pX_o\{y_1(-h,0)-y_1(-h,z)\}$$
$$-\frac{p}{2}[\{y_1(-h,0)\}^2-\{y_1(-h,z)\}^2]+(T\cos\beta$$
$$-S\sin\beta)(X_o-X)+(T\sin\beta+S\cos\beta)Z=0,$$

where the subscript o indicates values at $z=0$. Differentiating these equations and manipulating the resulting equations with neglect of higher order terms, consistent with the present order of accuracy, we obtain

$$S'+\beta' T+p=0, \quad T'-\beta' S=0, \quad M'+S=0. \tag{17}$$

A term $-p\,\partial u_1(-h,z)/\partial z$ neglected in the second equation represents the effect of the difference in the orientations of the middle surface and the upper surface, and can be shown to produce only negligible corrections within the accuracy of the present theory. Thus it is sufficient to assume that the pressure p acts on the middle surface in formulating the overall equilibrium equations.

We first assume that both edges are supported so that the displacements of the middle plane at $z=\pm\ell$ are constrained to be zero but there is no constraint on the rotation of the edges. (The case of clamped edges is treated later.) The deformation is then symmetric about $z=0$ and we have the conditions

$$\beta_o=\beta(0)=0, \quad S_o=S(0)=0, \quad M(\ell)=0,$$
$$Z(\ell)=\ell, \quad Z(0)=0, \quad X(\ell)=0. \tag{18}$$

The bending moment is largest at $z=0$, and we take

$$\epsilon_b=h|\beta_o'|, \quad \epsilon_m=|e|_{\max}, \quad \epsilon=\epsilon_b+\epsilon_m, \tag{19}$$

where ϵ_b, ϵ_m represent measures for the bending strain and the membrane strain, respectively. For a fixed value of ϵ, as h/ℓ decreases the rotation β increases and the flexural strain ϵ_b eventually becomes small compared with the membrane strain ϵ_m. For very thin strips, the membrane solution ultimately applies with the strip deformed into a circular arc. The curvature β' then has the constant value $-p/T$ and the extension e is constant so that

$$\beta(\ell)=(1+e)\sin\beta(\ell), \quad X_o/\ell=-(1+e)\{1-\cos\beta(\ell)\}/\beta(\ell),$$
$$p\ell/Eh=4eX_o/\ell(1-\nu^2).$$

From these relations, it follows that for the membrane solution

$$|\beta(\ell)|\sim\sqrt{6e}=0(\epsilon^{1/2}), \; X_o/\ell\sim-\frac{1}{2}\beta(\ell)$$
$$=0(\epsilon^{1/2}), \quad p\ell/Eh=0(\epsilon^{3/2}). \tag{20}$$

The first relation above implies that the rotation is $0(\epsilon^{1/2})$ at most for the present problem. This may be compared with the basic assumption involved in the von Kármán equations (see Stoker, 1968, p. 45) that the derivatives of the horizontal displacements are of the same order of magnitude as the squares of the derivatives of the normal displacements.

The orders of magnitude of the derivatives of β and e can be

Table 1 Comparison of results for long strips under pressure with supported edges and with the maximum strain approximately 0.50×10^{-3}

			Central Deflection $X_o/2h$		
h/ℓ	p/E	$\bar{k}$	Present Theory	Classical Theory	von Kármán Equations
1/10	6.950×10^{-6}	4.887×10^{-2}	1.041×10^{-2}	1.042×10^{-2}	1.018×10^{-2}
1/20	1.740×10^{-6}	1.958×10^{-1}	4.081×10^{-2}	4.102×10^{-2}	4.058×10^{-2}
1/30	7.730×10^{-7}	4.402×10^{-1}	8.976×10^{-2}	9.195×10^{-2}	8.954×10^{-2}
1/45	3.560×10^{-7}	1.026	1.924×10^{-1}	2.141×10^{-1}	1.923×10^{-1}
1/60	2.248×10^{-7}	2.048	3.238×10^{-1}	4.270×10^{-1}	3.236×10^{-1}
1/80	1.640×10^{-7}	4.723	5.297×10^{-1}	9.844×10^{-1}	5.296×10^{-1}

Table 2 Comparison of results for long strips under pressure with clamped edges and with the maximum strain approximately 0.50×10^{-3}

			Central Deflection $X_o/2h$		
h/ℓ	p/E	$\bar{k}$	Present Theory	Classical Theory	von Kármán Equations
1/10	1.066×10^{-5}	7.495×10^{-2}	3.123×10^{-3}	3.123×10^{-3}	3.123×10^{-3}
1/20	2.660×10^{-6}	2.993×10^{-1}	1.247×10^{-2}	1.247×10^{-2}	1.247×10^{-2}
1/30	1.180×10^{-6}	6.720×10^{-1}	2.799×10^{-2}	2.800×10^{-2}	2.799×10^{-2}
1/45	5.240×10^{-7}	1.511	6.277×10^{-2}	6.295×10^{-2}	6.277×10^{-2}
1/60	2.932×10^{-7}	2.672	1.103×10^{-1}	1.113×10^{-1}	1.103×10^{-1}
1/80	1.653×10^{-7}	4.761	1.931×10^{-1}	1.984×10^{-1}	1.931×10^{-1}
1/160	4.613×10^{-8}	2.126×10	6.682×10^{-1}	8.857×10^{-1}	6.682×10^{-1}

estimated using the overall equilibrium equations. Taking $z=\ell$ in equations (16) and using the last two equations of (15), for deformations in which the bending strain dominates the membrane strain we can show that

$$\frac{p\ell h^2}{2D}=\frac{h}{\ell}0(\epsilon). \tag{21}$$

In order to estimate the order of magnitude of S, it is sufficient to examine the case for thick strips, in which the membrane strain is negligible compared with the bending strain, because S decreases as h/ℓ becomes smaller for a fixed value of strain measure ϵ. Manipulation of the first two equations of (16) in conjunction with equation (21) leads to

$$S=\frac{h}{\ell}Eh0(\epsilon) \leqq Eh0(\epsilon).$$

Combining the last two equations of (15) with (17), and using the above result, we find that at most

$$\beta''=\frac{1}{\ell h}0(\epsilon) \leqq 0(\epsilon)/h^2, \quad T'=Eh0(\epsilon^2)/\ell \leqq E0(\epsilon^2),$$

$$e'=0(\epsilon^2)/\ell \leqq 0(\epsilon^2)/h.$$

Differentiating equations (17), we can show that $\beta'''=p/D$ to $0(\epsilon)/h^3$, and β^{iv} and e'' are second order as assumed earlier.

The overall equilibrium equations (17) provide equations for β and T given by

$$\beta'''-T\beta'/D-p/D=0, \quad T'+D\beta''\beta'=0. \tag{22}$$

The first five of equation (18) provide the associated end conditions, and from the first three we have

$$\beta(0)=0, \quad \beta'(\ell)=-\frac{8-3\nu}{10(1-\nu)}h^2\frac{p}{D}, \quad \beta''(0)=0. \tag{23}$$

With the aid of the second equations of (13) and (15), we find that the conditions $Z(0)=0$ and $Z(\ell)=\ell$ require

$$\int_o^\ell \left\{\frac{h^3}{3D}\left(\frac{T}{h}+\frac{\nu}{1-\nu}p\right)-\frac{1}{2}\beta^2\right\}dz=0. \tag{24}$$

For thick strips for which h/ℓ is not too small, the infinitesimal solution applies. In this case T is compressive, but the term $T\beta'/D$ is negligible in the first of equations (22) and the term involving e can be neglected in the second relation of (15). For decreasing h/ℓ, e increases and T becomes tensile until for very thin strips, the β''' and β'' terms in equations (22) become negligible. The moment M then becomes second order and the third relation in equation (15) does not apply.

When the geometry and loading are such that the bending and membrane strain measures ϵ_b and ϵ_m are both $0(\epsilon)$, β varies from zero at the center to $0(\epsilon^{1/2})$ at the ends and $\beta'=0(\epsilon^{1/2})/\ell$. Because $\beta'=0(\epsilon_b)/h$, we see that h/ℓ must be $0(\epsilon^{1/2})$. From equations (22), T is constant to $0(\epsilon)$ and p/D is second order so that for h/ℓ of $0(\epsilon^{1/2})$ or less we can take

$$\beta'''-T\beta'/D-p/D=0, \quad T'=0, \tag{25}$$

and

$$\beta(0)=0, \quad \beta'(\ell)=0, \quad \beta''(0)=0, \quad \frac{Th^2}{3D}=\frac{1}{2\ell}\int_o^\ell \beta^2 dz. \tag{26}$$

The von Kármán equations also lead to equations (25) and the solution can be easily obtained (see Love, 1927, pp. 559–562).

Equations (22) under conditions (23) and (24) were solved by numerical integration to compare the results with the solution for the von Kármán equations. The central deflection $X_o/2h$ for various values of h/ℓ from 1/10 to 1/80 is tabulated for comparison in Table 1. The pressure was chosen so that the maximum strain is approximately 0.5×10^{-3} in each case, and Poisson's ratio ν was taken to be 0.25. As shown in the table, the classical linear theory breaks down as h/ℓ decreases; on the other hand there is a slight discrepancy between the present theory and the solution from the von Kármán equations when h/ℓ is not too small. When $h/\ell=1/45$, h^2/ℓ^2 is close to the value for ϵ used in Table 1, and the table shows that the von Kármán solution is very accurate for $h/\ell=1/45$ or smaller. This is in agreement with the previous paragraph which showed that the von Kármán equations will apply for this problem when h/ℓ is $0(\epsilon^{1/2})$ or smaller.

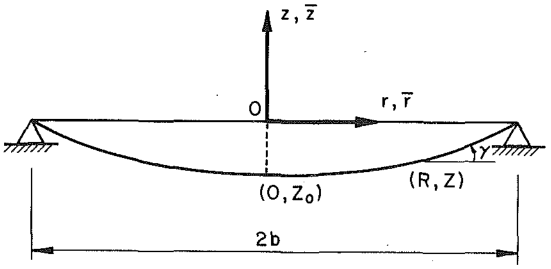

Fig. 2 Deformation of the middle plane of a circular plate under pressure

When both edges are clamped so that the displacements and rotation of the middle plane at $z = \pm\ell$ are constrained to be zero, the end conditions on β become

$$\beta(0)=0, \quad \beta(\ell)=0, \quad \beta''(0)=0, \tag{27}$$

while the conditions $Z(0)=Z(\ell)=0$ again require condition (24). Together with the last condition of (26), conditions (27) constitute the end conditions for the von Kármán equations also. The solution for the von Kármán equations in this case is also given in Love (1927, pp. 563-564). For comparison, Table 2 shows the central deflection $X_0/2h$ for various values of h/ℓ from 1/10 to 1/160 as predicted by the present theory, the von Kármán equations and the classical theory. The pressure was chosen so that the maximum strain, which occurs at the edges, is approximately 0.5×10^{-3} in each case. The table shows that the von Kármán equations and the present theory give the same results for the values used for h/ℓ, in contrast with the simply supported case (Table 1) in which there was a slight inaccuracy in the von Kármán solution for values of h/ℓ which are not too small. For the present case of clamped edges, the end conditions on β are given by equation (27) for both of the approaches, and the bending strain is much larger than the membrane strain (in fact the ratio of ϵ_b to ϵ_m tends to a finite limit $3\sqrt{2}$ as h/ℓ goes to zero, (see Love, 1927, pp. 563-564). Thus the differences between the two theories, occurring in the second equation of (22) and the condition (24), are insignificant, and the two approaches predict the same results. We note that the classical theory gives better approximations for smaller values of h/ℓ compared with the previous case because the bending strain is more dominant for the clamped-end conditions.

4 Bending of a Circular Plate by Uniform Pressure

In this section we consider the axisymmetric bending of a circular plate. The plate is initially horizontal and supported on its edge so that the edge displacements of the middle plane are constrained to be zero but there is no constraint on rotation of the edge. The upper surface is subject to uniform pressure p, while the lower surface is free from traction. A plate with a clampled edge can be treated in a similar manner.

The classical theory gives the small deflection solution for a thick plate (see Love, 1927, p. 481). For a thin plate, the deflection can be comparable to the thickness of the plate and the von Kármán equations have been used for this case (see Stoker, 1968). As in the preceding section, we obtain solutions for all values of the radius-to-thickness ratio.

A cylindrical coordinate system is taken with the origin at the center of the middle plane, and with z axis vertically upward. The radius of the plate is denoted by b and the thickness by $2h$. The coordinates of points on the deformed middle plane are denoted by $R(r)$ and $Z(r)$, and the radial and circumferential extensions e_r and e_θ are then given by

$$R'^2+Z'^2=(1+e_r)^2, \; R=(1+e_\theta)r. \tag{28}$$

We use $\gamma(z)$ for the inclination to the horizontal of the tangent to the deformed middle plane along the radial direction, Fig. 2, and we have (c.f. equation (13))

$$R'=(1+e_r)\cos\gamma, \; Z'=(1+e_r)\sin\gamma. \tag{29}$$

We denote by κ_r and κ_θ the curvatures along the radial and circumferential directions, respectively, and in terms of γ they are given by

$$\kappa_r=\gamma'/(1+e_r), \;\; \kappa_\theta=\sin\gamma/R=\sin\gamma/r(1+e_\theta).$$

Because e_r and e_θ will be $0(\epsilon)$ at most, for our purposes we take

$$\kappa_r=\gamma', \;\; \kappa_\theta=\sin\gamma/r. \tag{30}$$

For strain measures we can take

$$\epsilon_b=\max(|\kappa_r h|,|\kappa_\theta h|), \;\; \epsilon_m=\max(|e_r|,|e_\theta|),$$
$$\epsilon=\epsilon_b+\epsilon_m, \tag{31}$$

where ϵ_b, ϵ_m represent measures for the bending strain and the membrane strain, respectively. Combining the second of equation (28) with the first of equation (29), we have

$$1+e_\theta+re_\theta'=(1+e_r)\cos\gamma=1+e_r-\frac{1}{2}\gamma^2+\ \ldots\ , \tag{32}$$

and assuming that re_θ' is $0(\epsilon)$ it follows that at most

$$\gamma=0(\epsilon^{1/2}), \;\; \cos\gamma=1-\frac{1}{2}\gamma^2+0(\epsilon^2). \tag{33}$$

The curvatures κ_r and κ_θ are not independent but they satisfy the Codazzi relation $\kappa_r = \kappa_\theta + Rd\kappa_\theta/dR$, so that to $0(\epsilon)$ we have

$$\kappa_r=\kappa_\theta+r\kappa_\theta'. \tag{34}$$

Let (r, θ, z) and $(\bar r, \bar\theta, \bar z)$ denote the coordinates of a particle before and after the deformation. For this axisymmetric problem we take

$$\bar r=R+u_r\cos\gamma-(z+u_z)\sin\gamma,$$
$$\bar z=Z+u_r\sin\gamma+(z+u_z)\cos\gamma, \tag{35}$$

where u_r, u_z are small displacements which vanish with z. Expressions (35) may be compared to the corresponding expressions in the previous section. The square of the length of a material line element in the deformed state is related to the physical components of the Green strain tensor for the cylindrical coordinates through

$$d\bar r^2+\bar r^2d\theta^2+d\bar z^2=(1+2e_{rr})dr^2+(1+2e_{\theta\theta})r^2d\theta^2$$
$$+(1+2e_{zz})dz^2+4e_{r\theta}rdrd\theta+4e_{\theta z}rd\theta dz+4e_{rz}drdz. \tag{36}$$

Guided by the classical infinitesimal solution, we take

$$u_r=(\kappa_r'+\kappa_\theta')\left\{\frac{2-\nu}{6(1-\nu)}z^3-\frac{1}{1-\nu}h^2z\right\}$$
$$+\frac{\nu}{2(1-\nu)}(e_r'+e_\theta')z^2,$$
$$u_z=\frac{-\nu}{1-\nu}(e_r+e_\theta)z+\frac{\nu}{2(1-\nu)}(\kappa_r+\kappa_\theta)z^2$$
$$+\frac{p}{D}\left\{\frac{(1+\nu)z^4}{24(1-\nu)}-\frac{h^2z^2}{4(1-\nu)^2}+\frac{(1-2\nu)h^3z}{3(1-\nu)^2}\right\}. \tag{37}$$

Substituting equations (37) into (35), and the resulting expressions into the left-hand side of (36), we can obtain the strain components to $0(\epsilon)$. Using the stress-strain law for linear isotropic materials, the Kirchhoff stress components σ_{rr}, $\sigma_{\theta\theta}$, σ_{zz}, σ_{rz}, which are true stresses associated with directions in the deformed state of line elements which were initially in the

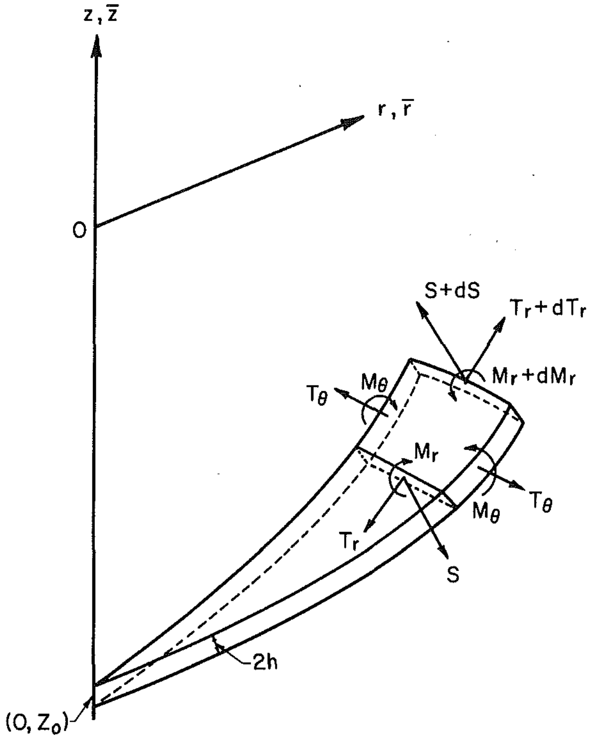

Fig. 3 Force and moment resultants for a circular plate

radial, circumferential and axial directions, are then found to be $0(\epsilon)$

$$\sigma_{rr}=\frac{E}{1-\nu^2}\ \{e_r-\kappa_r z+\nu(e_\theta-\kappa_\theta z)\}$$

$$+p\Big\{-\frac{\nu+2}{8}\Big(\frac{z}{h}\Big)^3+\frac{3}{4(1-\nu)}\ \frac{z}{h}-\frac{\nu}{2(1-\nu)}\Big\},$$

$$\sigma_{\theta\theta}=\frac{E}{1-\nu^2}\ \{e_\theta-\kappa_\theta z+\nu(e_r-\kappa_r z)\}$$

$$+p\Big\{-\frac{\nu+2}{8}\Big(\frac{z}{h}\Big)^3+\frac{3}{4(1-\nu)}\ \frac{z}{h}-\frac{\nu}{2(1-\nu)}\Big\},$$

$$\sigma_{zz}=p\Big\{\frac{1}{4}\Big(\frac{z}{h}\Big)^3-\frac{3}{4}\ \frac{z}{h}-\frac{1}{2}\Big\},$$

$$\sigma_{rz}=\frac{E}{2(1-\nu^2)}\ (\kappa_r'+\kappa_\theta')\,(z^2-h^2), \tag{38}$$

provided that

$$\kappa_r''=3\kappa_\theta''=\kappa_r'/r=3\kappa_\theta'/r=-3p/8D \text{ to } 0(\epsilon)/h^3,$$

$$e_r''+e_\theta''=0(\epsilon^2)/h^2,\ (e_r'+e_\theta')/r=0(\epsilon^2)/h^2. \tag{39}$$

(In equation (38) we have neglected contributions from second order terms involving $u_r e_\theta/r$ and $u_r\kappa_\theta z/r$, which are bounded around $r = 0$ because $u_r(0,z) = 0$ by symmetry.) The traction boundary conditions (12) on the upper and lower surfaces are now seen to be satisfied to $0(\epsilon)$, and the local equilibrium equations are also satisfied to $0(\epsilon)$ provided that

$$e_r'+\nu e_\theta'+(e_r-e_\theta)(1-\nu)/r=0(\epsilon^2)/h. \tag{40}$$

which will be verified using overall equilibrium equations. To $0(\epsilon)$, the local equilibrium equations in terms of σ_{rr}, $\sigma_{\theta\theta}$, σ_{zz}, σ_{rz}, and the independent variables r and z have the same form as those in the infinitesimal theory for a cylindrical coordinate system.

Stress and moment resultants associated with surfaces which were initally the surfaces r = constant, θ = constant will be denoted by $S(r)$, $T_r(r)$, $M_r(r)$, measured per unit length along the circumferential direction, and $T_\theta(r)$ and $M_\theta(r)$, measured per unit length along the radial direction. These resultants act through the deformed position of the middle plane, Fig. 3. With an approach similar to that leading to equations (15) of the preceding section, we obtain the following expressions, which are correct to $0(\epsilon)$,

$$T_r=2Eh(e_r+\nu e_\theta)/(1-\nu^2)-\nu ph/(1-\nu),$$

$$T_\theta=2Eh(e_\theta+\nu e_r)/(1-\nu^2)-\nu ph/(1-\nu),$$

$$S=-D(\kappa_r'+\kappa_\theta'),\ M_r=D(\kappa_r+\nu\kappa_\theta)$$

$$-(\nu^2+\nu+8)ph^2/20(1-\nu),$$

$$M_\theta=D(\kappa_\theta+\nu\kappa_r)-(\nu^2+\nu+8)ph^2/20(1-\nu). \tag{41}$$

As in the previous section, when considering overall balance of force and moment in terms of these resultants, it is sufficient to assume that the pressure p acts on the central surface of the deformed plate. From equilibrium of a sector of the plate, we obtain

$$r(T_r\sin\gamma+S\cos\gamma)-pR^2/2=0,$$

$$r(T_r\cos\gamma-S\sin\gamma)-\int_o^r T_\theta dr+p\int_o^r R(1+e_r)\sin\gamma dr=0,$$

$$rM_r-\int_o^r M_\theta dr+Rr(S\cos\gamma+T_r\sin\gamma)$$

$$+r(Z-Z_o)(S\sin\gamma-T_r\cos\gamma)-pR^3/3$$

$$-p\int_o^r (Z-Z_o)R(1+e_r)\sin\gamma dr+\int_o^r T_\theta(Z-Z_o)dr=0, \tag{42}$$

where the subscript o indicates values at $r = 0$. Differentiation of (42) and manipulation of the resulting equations gives

$$(rT_r)'-\gamma' rS-T_\theta\cos\gamma=0,\ (rS)'+\gamma' rT_r+T_\theta\sin\gamma-pR=0,$$

$$(M_r r)'-M_\theta+rS=0, \tag{43}$$

where higher order terms have been discarded for consistency. Since the edge displacements of the middle plane are constrained to be zero while there is no constraint on rotations of the ridge, we have

$$Z(b)=0,\ R(b)=b,\ M_r(b)=0. \tag{44}$$

At $r = 0$, we have

$$R(0)=0,\ \gamma(0)=0, \tag{45}$$

and we expect that κ_θ' and e_θ' are bounded at $r = 0$ because there is no concentrated load at the center. Equations (32), (34), (43) can then be used to show that

$$e_r(0)=e_\theta(0),\ \kappa_\theta(0)=\kappa_r(0),\ M_\theta=M_r(0),$$

$$T_r(0)=T_\theta(0),\ S(0)=0.$$

For a fixed value of ϵ, as h/b decreases the flexural strain ϵ_b eventually becomes small compared with ϵ_m, and the pressure loading p and the shear force S also will be correspondingly smaller. Therefore, for conservative estimates of the order of magnitude of p and S, it is sufficient to examine the case for thick plates. Using equations (42), we find that

$$p=E\Big(\frac{h}{b}\Big)^2 0(\epsilon_b)=E\Big(\frac{h}{b}\Big)^2 0(\epsilon)\leqq E0(\epsilon)$$

and

$$S=Eh\Big(\frac{h}{b}\Big)0(\epsilon_b)=Eh\frac{h}{b}\ 0(\epsilon)\leqq Eh0(\epsilon). \tag{46}$$

Table 3 Maximum numerical values for the strains and derivatives of the strains and curvatures for a circular plate under pressure; ϵ_m is the maximum extensional strain of the middle surface and ϵ_b is the maximum bending strain

	h/b	1/20	1/50	1/100	1/200
	p/E	1.1×10^{-5}	2.06×10^{-6}	1.36×10^{-6}	1.15×10^{-6}
	$\mathrm{Max}\lvert e_{1k}\rvert$	9.855×10^{-4}	9.934×10^{-4}	9.923×10^{-4}	9.925×10^{-4}
	ε_m	3.700×10^{-5}	1.791×10^{-4}	4.427×10^{-4}	7.001×10^{-4}
	ε_b	9.485×10^{-4}	8.143×10^{-4}	5.524×10^{-4}	3.827×10^{-4}
$\frac{h}{b}\,0(\varepsilon_m)$	$e_r'h$	6.334×10^{-7}	1.188×10^{-6}	1.235×10^{-6}	5.541×10^{-7}
	$e_\theta'h$	2.555×10^{-6}	5.017×10^{-6}	6.877×10^{-6}	6.795×10^{-6}
$\frac{h}{b}\,0(\varepsilon_b)$	$\kappa_r'h$	1.119×10^{-4}	4.473×10^{-5}	3.317×10^{-5}	2.751×10^{-5}
	$\kappa_\theta'h$	3.714×10^{-5}	1.334×10^{-5}	5.681×10^{-6}	2.008×10^{-6}
$h^2 0(\varepsilon_b)/b^2$	$\kappa_r''h^3$	5.684×10^{-6}	1.289×10^{-6}	1.249×10^{-6}	1.303×10^{-6}
$0(\varepsilon^2)$ or less	$(\kappa'' + \frac{3p}{8D})h^3$	2.7×10^{-7}	4.6×10^{-7}	7.0×10^{-7}	7.0×10^{-7}
	$(\kappa_r'' - 3\kappa_\theta'')h^3$	4.5×10^{-8}	2.1×10^{-7}	4.5×10^{-7}	9.5×10^{-7}
	$(\kappa_r'' - \kappa_r'/r)h^3$	9.0×10^{-8}	3.9×10^{-7}	7.2×10^{-7}	1.2×10^{-6}
	$(\kappa_\theta'' - \kappa_\theta'/r)h^3$	2.2×10^{-8}	9.4×10^{-8}	1.6×10^{-7}	1.1×10^{-7}
	$\kappa_r'''h^4$	1.1×10^{-8}	1.8×10^{-8}	3.3×10^{-8}	5.2×10^{-8}
	$\kappa_\theta'''rh^3$	4.0×10^{-8}	2.1×10^{-7}	5.9×10^{-7}	9.5×10^{-7}

Combining the last two equations in (43) and using the last two relations of (41) and equation (34), we reach the equation

$$D(3\kappa_\theta' + 5r\kappa_\theta'' + r^2\kappa_\theta''') = \gamma' rT_r + T_\theta\gamma - pr, \qquad (47)$$

where γ and r have been used for $\sin\gamma$ and R for consistency. In the classical theory the three terms containing κ_θ''', T_r, T_θ in the above equation do not appear and κ_θ'' has the constant value $-p/8D$. From equation (47) and its derivatives in conjuction with the first equation of (46) and equation (34), for thick plates in which the bending strain dominates the membrane strain we can expect

$$\kappa_\theta',\ \kappa_r' = \frac{1}{hb}\,0(\epsilon),\ 3\kappa_\theta'' = 3\kappa_\theta'/r = \kappa_r'' = \kappa_r'/r$$
$$= -3p/8D \text{ to } 0(\epsilon)/h^3,\ r\kappa_\theta''' = 0(\epsilon^2)/h^3, \qquad (48)$$

The third derivative of κ_r will be of second order to be consistent with the second of (48). The terms containing κ_θ''', T_r, T_θ in equation (47), which can be neglected for thick plates, become significant as ϵ_m increases, and for the complete verification of the orders of magnitude of κ_r', κ_θ' and their derivatives for smaller values of h/b, numerical results, given in Table 3, are used. The assumption (40) can be confirmed by using the first equation of (43) and the relation between the stress resultants and the extensions to give

$$(e_r - e_\theta)(1-\nu)/r + e_r' + \nu e_\theta' = (1-\nu^2)\gamma' S/2Eh \leqq 0(\epsilon^2)/h, \qquad (49)$$

in which the inequality follows because $S = Eh\,0(\epsilon)$ is a conservative estimate for all values of h/b. Combination of equation (49) with (32) provides

$$e_r' + e_\theta' = (\nu - 1)\gamma^2/2r \text{ to } 0(\epsilon)/h,$$

and manipulating this equation we can verify that

$$(e_r' + e_\theta')/r = 0(\epsilon^2)/h^2,\ e_r'' + e_\theta'' = 0(\epsilon^2)/h^2.$$

Thus the assumptions on the orders of magnitude have been verified.

The equations governing the deformd shape of the middle plane are given by the twelve equations in (29), (30), (43), the second equation of (28), and the first two and the last two in equations (41). To simplify these equations, we use the expansions $\cos\gamma = 1 - \gamma^2/2 + \ldots$, $\sin\gamma = \gamma(1 - \gamma^2/6 + \ldots)$ in conjunction with the first of (33) and retain only leading order terms in the resulting equations, consistent with the present order of accuracy. Then the governing equations are reduced to two equations in γ, T_r as

Table 4 Comparison of results for a circular plate under pressure with a supported edge and with the maximum strain approximately 10^{-3} for various thickness to radius ratios

h/b	p/E	Central Deflection $-Z_0/2h$		
		Present Theory	Classical Theory	von Kármán Equations
1/10	4.4×10^{-5}	1.981×10^{-2}	1.982×10^{-2}	1.912×10^{-2}
1/20	1.1×10^{-5}	7.636×10^{-2}	7.772×10^{-2}	7.570×10^{-2}
1/50	2.06×10^{-6}	4.190×10^{-1}	5.606×10^{-1}	4.186×10^{-1}
1/100	1.36×10^{-6}	1.299	5.915	1.299
1/200	1.15×10^{-6}	3.192	8.000×10	3.192

$$r\gamma'' + \gamma' - \gamma/r - r\gamma T_r/D + pr^2/2D = 0,$$
$$r(3T_r' + rT_r'') + Eh\Big[\gamma^2 + \frac{2h^2}{3(1-\nu^2)}\{(4+\nu)r\gamma'\gamma'' + \nu\gamma'^2$$
$$- \nu\gamma'\gamma/r + r^2\gamma''^2 - \gamma\gamma'' + r^2\gamma'\gamma'''\}\Big] = 0. \qquad (50)$$

We note that the terms containing γ'', γ''' in the second equation can be eliminated by using the first equation so that equations (50) involve a fourth order system. Using the second relation of (28), the first and last equations of (43) together with the force-extension and moment-curvature relations, we find that the last two conditions of (44) require

$$(1-\nu)T_r + rT_r' + \nu ph + Dr\gamma'(\gamma'' + \gamma'/r - \gamma/r^2) = 0,$$
$$\gamma' + \nu\gamma/r - \frac{\nu^2 + \nu + 8}{20(1-\nu)D}ph^2 = 0 \text{ at } r = b. \qquad (51)$$

With the aid of the governing equation (50), the regularity of γ and R at $r = 0$ requires

$$T_r'(0) = 0. \qquad (52)$$

Thus the boundary conditions for the nonlinear equations (50) are given by equations (51), (52) and the second condition of (45). Introducing the radial displacement $U = R - r$, we can formulate the boundary value problem in terms of U and γ (see Im, 1985).

For thick plates under small pressure loading, T_r is compressive but the term $r\gamma T_r/D$ in the first of the govening equations (50) is negligible and the second governing equation can be neglected. We then reach the following equation for the classical theory,

$$r\gamma'' + \gamma' - \gamma/r + pr^2/2D = 0,$$

and the boundary conditions are given by the second of (51) and the second of (45). The solution for the infinitesimal case is obtained as (c.f. Love, 1927, pp. 481)

$$\gamma = \frac{pr}{4D}\left\{-r^2/4 + \frac{3+\nu}{4(1-\nu)}b^2 + \frac{\nu^2+\nu+8}{5(1-\nu^2)}h^2\right\}.$$

For thin plates for which h/b is very small, the load is primarily sustained by the membrane stresses, and ϵ_b is negligible compared with ϵ_m over the entire plate. Although a boundary layer is developed in this case near the edge where γ'' and its higher derivatives change abruptly [12], their numerical values remain very small and the present theory is not affected by the existence of this boundary layer. When ϵ_b is negligible compared with ϵ_m, so is S compared with T_r, T_θ, and the first three terms in the first equation of (50), which are related to ϵ_b, can be neglected compared with the other terms. The terms multiplied by $2h^2/3(1-\nu^2)$ in the second equation of (50), which are $h^2 0(\gamma^2)/b^2$, are also negligible compared with γ^2 in this case. Hence we reach the governing equations for the membrane solution (see Stoker, 1968, pp. 22-27)

$$\gamma T_r - \frac{1}{2}pr = 0,\quad 3rT_r' + r^2 T_r'' + Eh\gamma^2 = 0. \tag{53}$$

The boundary conditions are obtained from equation (52), and the first condition of (51) by neglecting higher order terms,

$$T_r' = 0 \text{ at } r = 0,\ (1-\nu)T_r + rT_r' = 0 \text{ at } r = b.$$

The membrane theory leads to the first order interior solution in a perturbation approach by Bromberg (1956) and the solution can be given in terms of a power series in r/b (see Stoker, 1968). In conjunction with the first of (33), the first equation of (53) suggests that for the membrane solution

$$p/E = h0(\epsilon^{3/2})/b,$$

which agrees with the result for the strip (20) as expected (and justifies the neglect of the term νph in the first condition of equation (51) for the membrane theory).

We have discussed the two extremes, the classical theory and the membrane theory. They cover the geometries and loadings for which one of ϵ_b and ϵ_m dominates the other. When ϵ_b, ϵ_m are comparble to each other, both $0(\epsilon)$, γ varies from zero at the center to $0(\epsilon^{1/2})$ at the edge and then $\gamma' = 0(\epsilon^{1/2})/b$. Combining this with $h\gamma' = 0(\epsilon_b) = 0(\epsilon)$, we expect h^2/b^2 to be $0(\epsilon)$ when ϵ_b, ϵ_m are comparable in magnitude. It then follows that the terms multiplied by $2h^2/3(1-\nu^2)$ in the second equation of (50), which are $h^2 0(\gamma^2)/b^2$, become $0(\epsilon^2)$ and negligible compared with γ^2 and the terms containing the pressure p and the term $Dr\gamma'(\gamma'' + \gamma'/r - \gamma/r^2)$ in the boundary conditions (51) become second order compared with the other terms. For the loading and geometry such that h/b is $0(\epsilon^{1/2})$ or less, we therefore obtain the governing equations

$$\begin{aligned} &r\gamma'' + \gamma' - \gamma/r - r\gamma T_r/D + pr^2/2D = 0,\\ &r(3T_r' + rT_r'') + Eh\gamma^2 = 0, \end{aligned} \tag{54}$$

and the boundary conditions

$$\begin{aligned} &(1-\nu)T_r + rT_r' = 0,\ \gamma' + \nu\gamma/r = 0 \text{ at } r = b,\\ &\gamma = 0,\ T_r' = 0 \text{ at } r = 0. \end{aligned} \tag{55}$$

These agree with the von Kármán equations for large deflections of a circular plate. The solution for these equations can be given in terms of a power series in r/b (see Timoshenko and Woinowsky-Krieger, 1959, pp. 408-409). For comparison of the von Kármán equations with the present theory, however, we use numerical integration together with a shooting method, and the results are shown in Table 4. Here the equations in terms of U and γ were used for the present theory with Poisson's ratio $= 0.3$, and the pressure was chosen so that the maximum strain is approximately 10^{-3} for each case. As expected, the table shows that for values of h/b which are not very small, the classical theory agrees well with the present theory, but breaks down as h/b becomes smaller; for very small values of h/b, on the other hand, the results from the von Kármán equations are in an excellent agreement with those from the present theory. We note that the von Kármán equations give good approximations even for values of h/b which are not very small.

References

Bromberg, E., 1956, "Nonlinear Bending of a Circular Plate under Normal Pressure," *Comm. Pure Appl. Math.*, Vol. 9, pp. 633-659.

Im, S., 1985, "Large Deflections of Structures with Small Elastic Strains," Ph.D. Thesis, University of Illinois at Urbana-Champaign, October 1985. T.&A.M. Report No. 474.

Koiter, W. T., and Simmonds, J. G., 1973, "Foundation of Shell Theory," in *Applied Mechanics: Proceedings of the 13th International Congress of Theoretical and Applied Mechanics, Moscow, 1972*, Becker, E., and Mikhailov, G. K., eds., Springer-Verlag, Berlin, pp. 150-176.

Love, A. E. H., 1927, A Treatise on the Mathematical Theory of Elasticity, Cambridge Univ., 4th ed., Reprinted by Dover, New York, 1944.

Nagdhi, P. M., 1972, "The Theory of Shells and Plates," in *Hand. Phys.*, Vol. VIa/2, Springer-Verlag, Berlin, pp. 425-640.

Parker, D. F., 1984, "On the Derivation of Nonlinear Rod Theories from Three-Dimensional Elasticity," *J. Appl. Math. Phys.* (ZAMP), Vol. 35, pp. 833-847.

Shield, R. T., 1984, "A Consistent Theory for Elastic Deformations with Small Strains," ASME JOURNAL APPLIED MECHANICS, Vol. 51, pp. 717-723.

Shield, R. T., and Im, S., 1986, "Small Strain Deformations of Elastic Beams and Rods Including Large Deflections," *J. Appl. Math. Phys.* (ZAMP), Vol. 37, pp. 491-513.

Stoker, J. J., 1968, *Nonlinear Elasticity*, Nelson, London.

Timoshenko, S., and Woinowsky-Krieger, S., 1959, *The Theory of Plates and Shells*, 2nd Ed., McGraw-Hill, New York.

Truesdell, C., and Noll, W., 1965, "The Nonlinear Field Theory of Mechanics," *Hand. Phys.*, Vol. III/3, Springer, Berlin.

A General Theory of Shells and the Complementary Potentials

G. Wempner
Georgia Institute of Technology,
Atlanta, GA 30332

This theory incorporates the attributes which are essential to the approximation of shells by finite elements. It is limited only by one assumption: Displacement is a linear function of distance along the normal to a reference surface. Deformation is decomposed into rotation and strain; the rotation carries elements of the reference surface to the same surface in any subsequent state. Transverse-shear deformations accommodate simple elements. The theory is couched in the potential P_{v} *and in the complementary potential* P_{c}*; these have the property,* $\mathrm{P}_{\mathrm{v}} + \mathrm{P}_{\mathrm{c}} = 0$ *for all admissible (equilibrated) states. The theory is also cast in the complementary functional* $\bar{\mathrm{P}}_{\mathrm{c}}$ *of stress and displacement, and the functional* $\bar{\mathrm{P}}_{\mathrm{v}}$ *of displacement, strain and stress;* $\bar{\mathrm{P}}_{\mathrm{c}}$ *and* $\bar{\mathrm{P}}_{\mathrm{v}}$ *are akin to the functionals of Hellinger-Reissner and Hu-Washizu. These alternate functionals provide the means to develop various hybrid elements.*

Introduction

The role of thin shells in modern structures is evident. Increasingly, we turn to numerical methods, often based on finite elements, to predict the response of shells. When the strains are small, then the analysis of an element entails only small relative rotations; large rotations in the assembly are accommodated by the decomposition of rigid rotation and strain. To avoid complicated elemental approximations, the theory of the shell must admit transverse shear strains; then kinks are admissible along the continguous edges of elements. The foregoing observations and a theory for "finite elements, finite rotations and small strains" were presented previously (Wempner, 1969).

Before and after the earlier work (Wempner, 1969) many contributions have been made to the subject of shells. Intrinsically, most theories admit finite rotations. These include the important works of Koiter (1960, 1966, 1973), Sanders (1963), Leonard (1961), Naghdi (1972), and Reissner (1974). Simmonds and Danielson (1970) and Pietraszkiewicz (1980) have explicitly addressed the decomposition and alternative representations of the finite rotation. The works of Reissner (1974), Pietraszkiewicz (1980), Libai and Simmonds (1983) also accommodate transverse shear deformations. The literature is vast; the works cited include many additional references, beginning with the early work of Aron (1874) and Love (1927).

The foundations of structural mechanics were recently fortified by Fraeijs de Veubeke's formulation (1972) of the complementary potential. Independently, Koiter (1973) arrived at similar results: These demonstrate the roles of the rotation and the use of the tensors of stretch, engineering strain and the associated stress in the formulation of general complementary potentials. The author has given interpretations (1980) which reveal the complementary character of those potentials and also the physical significance of the associated stress.

Here we present a general theory which is drawn from the three-dimensional theory with one underlying assumption: The displacement varies linearly through the thickness. Our decomposition of rotation and strain differs from the usual decomposition of three-dimensions: Our rotation is more natural for shells because it carries elements of the reference surface to the same surface in any subsequent state. With no restrictions upon the magnitudes of rotations or strains, the theory is expressed by the complementary functionals which are analogous to the functionals of three dimensions. Some basic equations (kinematics and dynamics) apply to any continuous shell; all results apply to any continuous elastic shell.

Since our theory is given by any of four functionals, accommodates finite deformations and transverse shear strain, it provides a vehicle for a variety of approximations and, specifically, hybrid elements.

Three-Dimensional Theory

In a previous paper (Wempner, 1980) we began with a primitive functional P of a stress vector $\mathbf{T}^i$ and the position vector $\mathbf{R}$ of a deformed state

$$P \equiv \int_v [\mathbf{T}^i \cdot \mathbf{R}_{,i} - \mathbf{f} \cdot \mathbf{R}] dv - \int_a \mathbf{t} \cdot \mathbf{R}\, da - \int_{a_v} \mathbf{t} \cdot (\mathbf{R} - \tilde{\mathbf{R}}) da \tag{1}$$

Here $\mathbf{f}$ is body force (per unit of initial volume v), $\mathbf{t}$ is the traction (per unit of the initial bounding surface a) and $\tilde{\mathbf{R}}$ is the prescribed position on a portion a_v of the boundary surface. The variation of $\mathbf{R}$ in v and on surface a_t (where tractions are prescribed) provides the equilibrium conditions for the stress $\mathbf{T}^i$ in v and on a_t. The variations of $\mathbf{T}^i$ in v and $\mathbf{t}$ on a are subject to the conditions of equilibrium; then the variation of the

---

Contributed by the Applied Mechanics Division for publication in the JOURNAL OF APPLIED MECHANICS.

Discussion on this paper should be addressed to the Editorial Department, ASME, United Engineering Center, 345 East 47th Street, New York, N.Y. 10017, and will be accepted until two months after final publication of the paper itself in the JOURNAL OF APPLIED MECHANICS. Manuscript received by ASME Applied Mechanics Division, *December 1, 1985; final revision May 21, 1986.*

functional vanishes for kinematically admissible displacements. In short, the functional includes the potential $P_v(\mathbf{R})$ and the complementary functional $P_c(\mathbf{T}^i)$. To appreciate this fully we introduce the strain, stress and complementary energy densities:

As before (Wempner, 1980), let $r^j_{.i}$ denote components of rigid rotation which carries the initial tangent vectors, $\mathbf{g}_i \equiv \mathbf{r}_{,i}$ to an intermediate system

$$\mathbf{g}_i' \equiv r^j_{.i}\mathbf{g}_j \tag{2}$$

A stretch with components C_i^j carries the intermediate triad $\mathbf{g}_i'$ to the current system:

$$\mathbf{R}_{,i} \equiv \mathbf{g}_i = C_i^j \mathbf{g}_j' \tag{3}$$

Here the component of stretch, $C_{ij} = C_{ji}$, is related to the component of engineering strain:

$$h_{ij} = h_{ji} = C_{ij} - g_{ij}, \tag{4}$$

where

$$g_{ij} = \mathbf{g}_i \bullet \mathbf{g}_j = \mathbf{g}_i' \bullet \mathbf{g}_j'$$

The internal power is

$$\dot{W} = \mathbf{T}^i \bullet \dot{\mathbf{R}}_{,i} = \mathbf{T}^i \bullet (C_i^j \mathbf{g}_j')^{\boldsymbol\cdot} \tag{5a}$$

$$\dot{W} = \mathbf{T}^i \bullet (\dot{C}_i^j \mathbf{g}_j' + C_i^j \dot{\boldsymbol\Omega}\; x\; \mathbf{g}_j') \tag{5b}$$

Here $\dot{\boldsymbol\Omega}$ is the spin of the triad $\mathbf{g}_i'$ and $\dot{C}_i^j = \dot{h}_i^j$. In another form,

$$\dot{W} = (\mathbf{T}^i \bullet \mathbf{g}'^j)\dot{h}_{ij} + (T^{ik}C_i^j)(\mathbf{g}_g'\; x\; \mathbf{g}_k') \bullet \dot{\boldsymbol\Omega} \tag{5c}$$

The final sum of (5*c*) is the power expended in the rigid spin; it must vanish. The first term is the work expended in strain:

$$\dot{W} = T^{\langle ij \rangle}\dot{h}_{ij} \tag{5d}$$

where $T^{\langle ij \rangle}$ signifies the symmetric part of the stress component

$$T^{ij} = \mathbf{g}'^j \bullet \mathbf{T}^i \tag{6}$$

If $W_v(h_{ij})$ and $W_c(T^{\langle ij \rangle})$ denote the complementary densities, then

$$\mathbf{T}^i \bullet \mathbf{R}_{,i} = T^{ij}(h_{ij} + g_{ij}) \tag{7a}$$

$$= W_v + W_c + T^{ij}g_{ij} \tag{7b}$$

Upon substituting (7*b*) into (1), we obtain

$$P = P_v + P_c \tag{8}$$

where

$$P_v \equiv \int_v [W_v - \mathbf{f} \bullet \mathbf{R}]dv - \int_{a_t} \mathbf{t} \bullet \mathbf{R}\, da \tag{9a}$$

$$P_c \equiv \int_v [W_c + T^{ij}g_{ij}]dv - \int_{a_v} \mathbf{t} \bullet \mathbf{R}\, da \tag{9b}$$

$$- \int_{a_v} \mathbf{t} \bullet (\mathbf{R} - \tilde{\mathbf{R}})da$$

$P_v(\mathbf{R})$ is the potential when **f** and **t** are dead loads. $P_c(\mathbf{T}^i)$ is subject to variations $\dot{\mathbf{T}}^i$ which fulfill equilibrium and $\dot{\mathbf{t}} = 0$ on a_t; therefore, in (9*b*)

$$\int_{a_v} \dot{\mathbf{t}} \bullet \mathbf{R}\, da = \int_a \dot{\mathbf{t}} \bullet \mathbf{R}\, da = \int_v \dot{\mathbf{T}}^i \bullet \mathbf{R}_{,i} dv$$

In view of the foregoing, functional P_c can be rewritten:

$$\bar{P}_c = \int_v [W_c - T^{ij}\mathbf{g}_j' \bullet (\mathbf{G}_i - \mathbf{g}_i')]dv - \int_{a_v} \mathbf{t} \bullet (\mathbf{R} - \tilde{\mathbf{R}})da \tag{9c}$$

It is important to note that the variation $\dot{\mathbf{T}}^i$ requires the variation of the components $\dot{T}^{ij}$, and the vector $\dot{\mathbf{g}}'$, i.e., the rotation $\dot{\boldsymbol\Omega}$, which leads to the conditions for equilibrium of moment:

$$(T^{ik}C_i^j)(\epsilon_{jk\ell})\mathbf{g}'^{\ell} = 0 \tag{10}$$

Reduction to Two-Dimensions

Our theory of the shell is founded upon the assumption:

$$\mathbf{R} = \mathbf{R}^o + \theta^3 \mathbf{A}_3 \tag{11}$$

Here we follow the conventions: θ^α denotes an arbitrary coordinate of the reference surface ($\alpha = 1, 2$) and θ^3 denotes distance along the initial normal **n**. Also,

$$\mathbf{A}_\alpha \equiv \mathbf{R}^o_{,\alpha}$$

Top and bottom surfaces lie at $\theta^3 = h_+, -h_-$; *s* denotes the reference surface; *c* denotes the bounding edge. If *h* and *k* denote the mean and Gaussian curvatures of the initial reference surface, then

$$dv = \mu(\theta^3)ds$$

$$\mu \equiv 1 - 2h\theta^3 + k(\theta^3)^2$$

With these notations and the assumption (11), the functional (1) is integrated with respect to the coordinate θ^3, to obtain

$$P = \int_s [\mathbf{N}^\alpha \bullet \mathbf{R}^o_{,\alpha} - \mathbf{F} \bullet \mathbf{R}^o + \mathbf{M}^\alpha \bullet \mathbf{A}_{3,\alpha} + \mathbf{T} \bullet \mathbf{A}_3 - \mathbf{C} \bullet \mathbf{A}_3]ds \tag{12}$$

$$- \int_c \mathbf{N} \bullet \mathbf{R}^o dc - \int_c \mathbf{M} \bullet \mathbf{A}_3 dc$$

$$- \int_{c_v} \mathbf{N} \bullet (\mathbf{R}^o - \tilde{\mathbf{R}})dc - \int_{c_v} \mathbf{M} \bullet (\mathbf{A}_3 - \tilde{\mathbf{A}}_3)dc$$

Instead of the one vector $\mathbf{R}(\theta^1, \theta^2, \theta^3)$ of three dimensions, we have two vectors, $\mathbf{R}^o(\theta^1, \theta^2)$ and $\mathbf{A}_3(\theta^1, \theta^2)$, which fully define the configuration. **F** and **C** are net external force and "couple", which include body force and surface tractions. The "stresses" are

$$\mathbf{N}^\alpha \equiv \int_{-h_-}^{h_+} \mathbf{T}^\alpha \mu d\theta^3 \tag{13a}$$

$$\mathbf{M}^\alpha \equiv \int_{-h_-}^{h_+} \mathbf{T}^\alpha \theta^3 \mu d\theta^3 \tag{13b}$$

$$\mathbf{T} \equiv \int_{-h_-}^{h_+} \mathbf{T}^3 \mu d\theta^3 \tag{13c}$$

N and **M** are the edge tractions (force and "couple"); $\tilde{\mathbf{N}}$ and $\tilde{\mathbf{M}}$ are prescribed on part c_t of the edge.

The variation of vectors $\mathbf{R}^o$ and $\mathbf{A}_3$ provides a variation of *P* (the virtual work) and the stationary conditions are the equilibrium equations in *s* and on c_t. With the customary notation, $ds = \sqrt{a}\, d\theta^1\, d\theta^2$, and the usual integration-by-parts, we obtain

$$\frac{1}{\sqrt{a}}(\sqrt{a}\,\mathbf{N}^\alpha)_{,\alpha} + \mathbf{F} = 0 \qquad \text{in } s \tag{14a}$$

$$\frac{1}{\sqrt{a}}(\sqrt{a}\,\mathbf{M}^\alpha)_{,\alpha} - \mathbf{T} + \mathbf{C} = 0 \qquad \text{in } s \tag{14b}$$

$$\mathbf{N}^\alpha n_\alpha = \tilde{\mathbf{N}}, \; \mathbf{M}^\alpha n_\alpha = \tilde{\mathbf{M}} \qquad \text{on } c_t \tag{15a,b}$$

Again, the variation of stresses $\mathbf{N}^\alpha$, $\mathbf{M}^\alpha$ and **T** produces meaningful results only when their components are referred to a suitable basis.

Natural Basis for the Shell

With the presence of transverse shear strain the usual rotation (which carries $\mathbf{g}_i$ to $\mathbf{g}_i'$) would rotate the (initial) tangent vector ($\mathbf{a}_\alpha \equiv \mathbf{r}^o_{,\alpha}$) out of the (deformed) surface. Therefore, it is more natural to employ a rotation which carries the initial triad ($\mathbf{a}_1, \mathbf{a}_2, \mathbf{a}_3 \equiv \mathbf{n}$) to a triad ($\mathbf{b}_1, \mathbf{b}_2, \mathbf{b}_3 \equiv \mathbf{N}$) such that $\mathbf{b}_\alpha$ are tangent and **N** is normal to the deformed reference surface. With this new meaning, we have

$$\mathbf{b}_i = r^j_{.i}\mathbf{a}_j \tag{16}$$

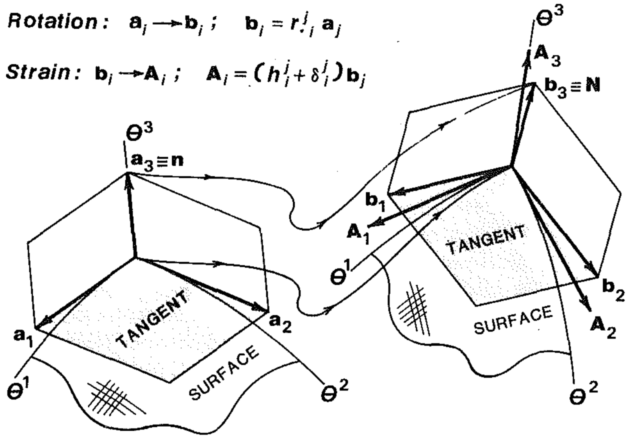

Fig. 1 Decompositon of motion

The orientation of $\mathbf{b}_\alpha$ is such that the stretch *of the surface* is given by a symmetrical tensor:

$$C_{\alpha\beta} \equiv \mathbf{b}_\alpha \cdot \mathbf{A}_\beta = \mathbf{b}_\beta \cdot \mathbf{A}_\alpha \tag{17a}$$

$$\mathbf{A}_\alpha \equiv \mathbf{R}^o_{,\alpha}$$

The deformation also carries the vector $\mathbf{N}$ to the vector $\mathbf{A}_3$ via transverse extension and shear:

$$C_{3i} = \mathbf{b}_i \cdot \mathbf{A}_3 \tag{17b}$$

Note that $\mathbf{b}_3 \cdot \mathbf{A}_\alpha = 0$.

All components of stress are referred to the natural basis:

$$N^{\alpha i} \equiv \mathbf{b}^i \cdot \mathbf{N}^\alpha,\ M^{\alpha i} \equiv \mathbf{b}^i \cdot \mathbf{M}^\alpha \tag{18a,b}$$

$$T^i \equiv \mathbf{b}^i \cdot \mathbf{T}$$

To illustrate the basis, the initial triad $(\mathbf{a}_i)$, the reference triad $(\mathbf{b}_i)$ and the current (deformed) triad $(\mathbf{A}_i)$ are depicted in Fig. 1.

Internal Power

The internal power of the stresses (per unit area) is

$$\dot{W} = \mathbf{N}^\alpha \cdot \dot{\mathbf{R}}^o_{,\alpha} + \mathbf{M}^\alpha \cdot \dot{\mathbf{A}}_{3,\alpha} + \mathbf{T} \cdot \dot{\mathbf{A}}_3 \tag{19a}$$

After much algebra, we obtain

$$\begin{aligned} \dot{W} = {} & N^{\alpha\beta}\dot{C}_{\alpha\beta} + M^{\alpha\beta}\dot{D}_{\alpha\beta} \\ & + T^\alpha \dot{C}_{3\alpha} + T^3\dot{C}_{33} + M^{\alpha 3}\dot{D}_{\alpha 3} \\ & + [(N^{\alpha 3} - K^\alpha_\eta M^{\eta 3})C^\mu_\alpha - T^\mu C_{33} + T^3 C^\mu_3 - M^{\alpha\mu}D_{\alpha 3}]\dot{\omega}_{3\mu} \\ & + [(N^{\alpha\gamma} - K^\alpha_\beta M^{\beta\gamma})C^\mu_\alpha + T^\gamma C^\mu_3]\dot{\omega}_{\gamma\mu} \end{aligned} \tag{19b}$$

Here a component of spin $\dot{\mathbf{\Omega}}$ is expressed by

$$\dot{\Omega}^i \equiv \mathbf{b}^i \cdot \dot{\mathbf{\Omega}} = \frac{1}{2}\,\epsilon^{ikj}\dot{\omega}_{jk}$$

Spin components about the normal $\mathbf{b}^3 \equiv \mathbf{N}$, tangents $\mathbf{b}^1$ and $\mathbf{b}^2$ are, respectively, $\dot{\omega}_{21}/\sqrt{a}$, $\dot{\omega}_{32}/\sqrt{a}$, and $\dot{\omega}_{13}/\sqrt{a}$. The flexure K^α_β is defined as follows:

$$K^\alpha_\beta \equiv -\mathbf{A}^\alpha \cdot \mathbf{A}_{3,\beta} \tag{20a}$$

$$= C^3_3 B^\alpha_\beta - (C^\eta_3 c^\alpha_\eta)|_\beta \tag{20b}$$

Here B^α_β and $B_{\alpha\beta}$ are components of curvature:

$$B^\alpha_\beta \equiv \mathbf{A}^\alpha_{,\beta} \cdot \mathbf{N},\ B_{\alpha\beta} = \mathbf{A}_{\alpha,\beta} \cdot \mathbf{N}$$

Also, in (19*b*),

$$D_{\alpha\beta} \equiv \mathbf{b}_\beta \cdot \mathbf{A}_{3,\alpha} = -K^\mu_\alpha C_{\mu\beta} \tag{21a,b}$$

$$D_{\alpha 3} \equiv \mathbf{N} \cdot \mathbf{A}_{3,\alpha} = C^3_{3,\alpha} + C^\beta_3 c^\mu_\beta B_{\mu\alpha} \tag{22a,b}$$

The expression (19*b*) serves to identify the strains associated with each of the stresses, $N^{\alpha\beta}$, $M^{\alpha i}$, T^α and T^3, respectively:

$$h_{\alpha\beta} \equiv C_{\alpha\beta} - a_{\alpha\beta} \tag{23a}$$

$$k_{\alpha\beta} \equiv D_{\alpha\beta} + b_{\alpha\beta},\ k_{\alpha 3} = D_{\alpha 3} \tag{23b,c}$$

$$h_{3\alpha} \equiv C_{3\alpha},\ h_{33} = C_{33} - 1 \tag{23d,e}$$

Since the stretch $(C_{\alpha\beta})$ and strain $(h_{\alpha\beta})$ of the surface are symmetric, only the symmetrical part of the membrane stress $(N^{\alpha\beta})$ plays a role in the power, in a potential or dissipation. Also, the shear stresses $N^{\alpha 3}$ are merely reactive.

In addition, the power (19*b*) serves to identify three conditions of equilibrium: Since no power is expended in the spin, each bracketed term vanishes. These three equations serve to determine, or eliminate,the skew-symmetric part of the stress $N^{\alpha\beta}$ and the reactive stresses $N^{\alpha 3}$.

Complementary Potentials of the Shell

With the identification of strains and the associated stresses, we can formulate the two-dimensional counterparts of the potentials (9*a*) and (9*b*). The potential is analogous to (9*a*) and follows from (12).

$$\begin{aligned} P_v = {} & \int_s [W_v(h_{\alpha\beta}, k_{\alpha\beta}, h_{3i}, k_{\alpha 3}) \\ & -\mathbf{F} \cdot \mathbf{R}^o - \mathbf{C} \cdot \mathbf{A}_3]ds \\ & -\int_{c_t} [\mathbf{N} \cdot \mathbf{R}^o + \mathbf{M} \cdot \mathbf{A}_3]dc \end{aligned} \tag{24}$$

Here the strains are implicit functions of the displacements ($\mathbf{R}_o$ and $\mathbf{A}_3$), so that the potential (24) is implicitly a functional of displacement.

The complementary "potential" is analogous to (9*b*) and follows from equations (12) and (24); $P_c = P - P_v$:

$$\begin{aligned} P_c = {} & \int_s [W_c(N^{\alpha\beta}, M^{\alpha\beta}, T^i., M^{\alpha 3}) + N^{\alpha\beta}a_{\alpha\beta} \\ & \qquad -M^{\alpha\beta}b_{\alpha\beta} + T^3]ds \\ & -\int_{c_v} [\mathbf{N} \cdot \mathbf{R}^o + \mathbf{M} \cdot \mathbf{A}_3]dc \\ & -\int_{c_v} [\mathbf{N} \cdot (\mathbf{R}^o - \tilde{\mathbf{R}}^o) + \mathbf{M} \cdot (\mathbf{A}_3 - \tilde{\mathbf{A}}_3)]dc \end{aligned} \tag{25}$$

The complementary density is defined, as in equation (7*b*), by the Legendre transformation:

$$W_c \equiv N^{\alpha\beta}h_{\alpha\beta} + M^{\alpha\beta}k_{\alpha\beta} + M^{\alpha 3}k_{\alpha 3} + T^i h_{3i} - W_v \tag{26}$$

The sum of equations (24) and (25) is the functional (12):

$$P = P_v + P_c \tag{27}$$

Verification requires the definition of the complementary density (26), the stresses (18) and strains (23).

The stationary conditions for P_v ($\mathbf{R}^o$, $\mathbf{A}_3$) provide six equilibrium equations (14*a*,*b*) and edge conditions (15*a*,*b*), consistent with the potential W_v (dependent upon the elasticity).

The functional P_c of equation (25) depends on the stresses ($N^{\alpha i}$, $M^{\alpha i}$, T^i) *and* rotation of the triad $(\mathbf{b}_i)$ just as it's three-dimensional counterpart (9*b*). Admissible variations of stress must satisfy the equilibrium equations; in particular, variations vanish on c_t. Therefore, enforcing (14*a*,*b*) in P_c of equation (25), we obtain

$$\int_{c_v} [\mathbf{N} \cdot \mathbf{R}^o + \mathbf{M} \cdot \mathbf{A}_3]dc = \int_c [\quad]dc - \int_{c_t} [\quad]dc \tag{28a}$$

$$\begin{aligned} = \int_s [& N^{\alpha i}\mathbf{b}_i \cdot \mathbf{R}^o_{,\alpha} + M^{\alpha i}\mathbf{b}_i \cdot \mathbf{A}_{3,\alpha} + \mathbf{T} \cdot \mathbf{A}_3 \\ & -\mathbf{F} \cdot \mathbf{R}^o - \mathbf{C} \cdot \mathbf{A}_3]ds - \int_{c_t} [\quad]dc \end{aligned} \tag{28b}$$

Then, by employing equation (28*b*) in (25), we obtain the two-dimensional counterpart of (9*c*):

$$\begin{aligned}\bar{P}_c = \int_s & [W_c - N^{\alpha\beta}(\mathbf{b}_\beta \bullet \mathbf{R}^o_{,\alpha} - a_{\alpha\beta}) - N^{\alpha 3}\mathbf{N}\bullet\mathbf{R}^o_{,\alpha} \\ & - M^{\alpha\beta}(\mathbf{b}_\beta \bullet \mathbf{A}_{3,\alpha} + b_{\alpha\beta}) - M^{\alpha 3}\mathbf{N}\bullet\mathbf{A}_{3,\alpha} \\ & - T^\alpha \mathbf{b}_\alpha \bullet \mathbf{A}_3 - T^3\mathbf{N}\bullet(\mathbf{A}_3 - \mathbf{N}) + \mathbf{F}\bullet\mathbf{R}^o + \mathbf{C}\bullet\mathbf{A}_3]ds \\ & - \int_{c_v}[\mathbf{N}\bullet(\mathbf{R}^o - \tilde{\mathbf{R}}^o) + \mathbf{M}\bullet(\mathbf{A}_3 - \tilde{\mathbf{A}}_3)]dc \\ & + \int_{c_t}[\mathbf{N}\bullet\mathbf{R}^o + \mathbf{M}\bullet\mathbf{A}_3]dc\end{aligned} \tag{29}$$

The latter form of P_c is akin to the Hellinger-Reissner functional (Hellinger, 1914; Reissner, 1950). The functional is stationary under varations of stress provided that the displacement-stress conditions are satisfied, e.g.,

$$\mathbf{b}_\beta \bullet (\mathbf{R}^o_{,\alpha} - \mathbf{b}_\alpha) = \frac{\partial W_c}{\partial N^{\alpha\beta}}$$

In addition, the functional (29) can be regarded as a functional of displacements ($\mathbf{R}_o$, $\mathbf{A}_3$). The functional is stationary under variations of displacements provided that the equilibrium equations (14*a,b*) are satisfied in s and equations (15*a,b*) are satisfied on c_t. Finally, the functional (29), like (25) is dependent on the rotation of the triad ($\mathbf{b}_i$). Both are stationary under variations of rotation provided that the three conditions of equilibrium (of moments) are satisfied; these are the conditions that the bracketed terms of (19*b*) vanish.

If we employ the transformation (26) to eliminate W_c in equation (29), we obtain

$$\bar{P}_v(= -\bar{P}_c) =$$

$$\begin{aligned}\bar{P}_v = \int_s & \{W_v - N^{\alpha\beta}[h_{\alpha\beta} - \mathbf{b}_\beta \bullet (\mathbf{R}^o_{,\alpha} - \mathbf{b}_\alpha)] \\ & - M^{\alpha\beta}[k_{\alpha\beta} - \mathbf{b}_\beta \bullet (\mathbf{A}_{3,\alpha} + b^\mu_\alpha \mathbf{b}_\mu)] \\ & + N^{\alpha 3}[\mathbf{N}\bullet R^o_{,\alpha}] - M^{\alpha 3}[k_{\alpha 3} - \mathbf{N}\bullet\mathbf{A}_{3,\alpha}] - T^\alpha[h_{3\alpha} - \mathbf{b}_\alpha \bullet \mathbf{A}_3] \\ & - T^3[h_{33} - \mathbf{N}\bullet(\mathbf{A}_3 - \mathbf{N})] - \mathbf{F}\bullet\mathbf{R}^o - \mathbf{C}\bullet\mathbf{A}_3\}ds \\ & + \int_{c_v}[\mathbf{N}\bullet(\mathbf{R}^o - \tilde{\mathbf{R}}^o) + \mathbf{M}\bullet(\mathbf{A}_3 - \mathbf{A}_3)]dc \\ & - \int_{c_t}[\mathbf{N}\bullet\mathbf{R}^o + \mathbf{M}\bullet\mathbf{A}]dc\end{aligned} \tag{30}$$

The functional $\bar{P}_v$ is dependent on all variables, displacements ($\mathbf{R}_o$, $\mathbf{A}_3$), strains (h_{ij}, $k_{\alpha i}$), stresses ($N^{\alpha i}$, T^i, $M^{\alpha i}$) *and* rotations (of $\mathbf{b}_i$). The latter is a two-dimensional counterpart of the Hu-Washizu functional (Hu, 1955; Washizu, 1955) cast in terms of the rotated system ($\mathbf{b}_i$) and the engineering strains (h_{ij}, $k_{\alpha i}$). The stationary conditions are all equilibrium conditions, stress-strain relations, and the strain-displacement relations.

Correlation with Classical Theory

Alternative choices of strains and stresses are always possible. From equation (20*a*), we could adopt the flexural strain

$$k^\alpha_\beta \equiv \mathbf{A}^\alpha \bullet \mathbf{A}_{3,\beta} + b^\alpha_\beta = -K^\alpha_\beta + b^\alpha_\beta$$

Then, from equation (21*b*)

$$\dot{D}_{\alpha\beta} = \dot{k}^\mu_\alpha C_{\mu\beta} - K^\mu_\alpha \dot{C}_{\mu\beta}$$

The first terms of (19*b*) assume the form:

$$\dot{W} = (N^{\alpha\beta} - K^\alpha_\mu M^{\mu\beta})\dot{C}_{\alpha\beta} + M^{\alpha\mu}C_{\beta\mu}\dot{k}^\beta_\alpha$$

This suggest that we adopt, as membrane and flexural stresses, respectively,

$$\begin{aligned} n^{\alpha\beta} &= N^{\alpha\beta} - K^\alpha_\mu M^{\mu\beta} \\ m^\alpha_{.\beta} &= M^{\alpha\mu}C_{\beta\mu}\end{aligned}$$

The latter are the usual choices (c.f. Koiter, 1966, 1973; Sanders, 1963; Leonard, 1961; Naghdi, 1972). Under the Kirchhoff-Love hypothesis, $K^\alpha_\beta = B^\alpha_\beta$. If products of strains and stresses are also dismissed, then

$$\begin{aligned} n^{\alpha\beta} &\doteq N^{\alpha\beta} - b^\alpha_\mu M^{\mu\beta} \\ m^\alpha_{.\beta} &\doteq M^\alpha_{.\beta}\end{aligned}$$

Under these circumstances the latter choices pose no difficulties; however in the general nonlinear theory, we need the separation of stresses and strains, and the unambiguous transformation (26). Though unconventional, our strains ($h_{\alpha i}$, $k_{\alpha i}$) and stresses ($N^{\alpha\beta}$, $M^{\alpha i}$, T^i) provide a precise theory under the one hypothesis (11).

If transverse strains are neglected, and surface strains are small, then (19*b*) assumes the usual form:

$$\begin{aligned}\dot{W} = {} & n^{\alpha\beta}\dot{h}_{\alpha\beta} + m^{\alpha\beta}\dot{k}_{\alpha\beta} \\ & + (N^{\alpha 3} - T^\alpha)\dot{\omega}_{3\alpha} + n^{\alpha\beta}\dot{\omega}_{\beta\alpha}\end{aligned} \tag{31}$$

From equation (31) we can draw the anticipated conclusions: Since $k_{\alpha\beta} = k_{\beta\alpha}$, only the symmetrical part of $m^{\alpha\beta}$ plays a role. Equilibrium requires that the stress $T^\alpha = N^{\alpha 3}$, the transverse shear force. Also, we note the equilibrium requirement $n^{\alpha\beta} = n^{\beta\alpha}$.

On Application of the Nonlinear Theory

In general, "solutions" (actually approximations) of the nonlinear equations (differential equations of the continuous shell or algebraic equations of a discrete model) must be obtained by successive solutions of linear systems which govern increments (Wempner, 1971). In particular, we record the linear relations between incremental rotations ($\dot{\omega}_{ji} = \mathbf{b}_j \bullet \mathbf{b}_i$), strains ($\dot{C}_{i\alpha}$) and displacements ($\dot{\mathbf{R}}^o$, $\dot{\mathbf{A}}_3$):

$$\begin{aligned}\dot{\omega}_{i\alpha} &= c^\phi_\alpha(\mathbf{b}_i \bullet \dot{\mathbf{A}}_\phi - \dot{C}_{\phi i}) \\ \dot{C}_{ij} &= \mathbf{b}_j \bullet \dot{\mathbf{A}}_i - \dot{\omega}_{jk}C^k_i\end{aligned}$$

Recall that $C_{\alpha 3} = C^3_\alpha = 0$ and

$$\mathbf{A}_\phi \equiv \frac{\partial \mathbf{R}^o}{\partial \theta^\phi}.$$

Note that the rotation ($\dot{\omega}_{i\alpha}$) is determined entirely by the displacement ($\mathbf{R}^o$) of the reference surface. Also, increments of the rotation tensor are given by

$$\dot{r}^j_{.i} = \dot{\omega}^k_{.i} r^j_{.k}$$

The displacement of the "normal" ($\dot{\mathbf{A}}_3$) enters only in the determination of transverse shear ($\dot{C}_{3\alpha}$).

Conclusion

A theory of shells is founded on the one assumption: The normal remains straight or, equivalently, the displacement is a linear function of the normal coordinate. The theory is otherwise general: Finite rotations, finite strains and transverse shear strains are admitted without additional approximations. The theory is expressed by the potential and the complementary potential, in the manner of Fraeijs de Veubeke (1972). These functionals are expressed in terms of a rotated system and engineering components of strain. The theory is also expressed by a functional of displacement and stress in the manner of Reissner (1950) and by a functional of displacement, strain and stress in the manner of Washizu (1955). All are precisely consistent with the one underlying assumption. The theory encompasses the more restrictive versions based upon the hypothesis of Kirchhoff-Love; all incorporating the decomposition of rotation and strain. This provides a general basis for the approximations, via finite elements, without the limitations of earlier work (Wempner, 1969). As noted then, approximations of small rotations within discrete elements involve only small rotations relative to the rotated basis ($\mathbf{b}_i$); such elemental models are nonetheless applicable to finite rotations in the assembly.

Acknowledgment

The author is indebted to the National Science Foundation which supported his studies under auspices of the Structures and Building-Systems Program, Directed by Gifford H. Albright of the Division of Mechanics, Structures and Materials Engineering, Grant MSM-8411757.

References

Aron, H., 1874, "Das Gleichgewicht und die Bewegung einer Unendlich Dünnen Beliebig Gekrümten, Elastischen Schale," *Zeitschrift für Reine und Angewandte Mathematik*, Vol. 78, pp. 136–173.

Fraeijs de Veubeke, B., 1972, "A New Variational Principle for Finite Elastic Displacements," *International Journal of Engineering Sciences*, Vol. 10, pp. 745–763.

Hellinger, E., 1914, "Die Algemeinen Ansätze der Mechanik der Continua," in *Encklopädie der Mathematischen Wissenschaften*, Vol. 4, No. 4.

Hu, H. C., 1955, "On Some Variational Principles in the Theory of Elasticity and Plasticity," *Scientia Sinica*, Vol. 4.

Koiter, W. T., 1960, "A Consistent First Approximation in the General Theory of Thin Elastic Shells," *Proceedings IUTAM Symposium*, North-Holland, Delft, pp. 12–33.

Koiter, W. T., 1966, "On the Nonlinear Theory of Thin Elastic Shells," *Proc. Koninklijke Nederlandse Akademie Van Wetenschappen*, 69B, pp. 1–54.

Koiter, W. T., and Simmonds, J. G., 1973, "Foundations of Shell Theory," *Proceedings of the Thirteenth Congress of Theoretical and Applied Mechanics*, Becker, E., and Mikhailov, G. K., eds., Springer Verlag, pp. 150–176.

Koiter, W. T., 1973, "On the Principle of Stationary Complementary Energy in the Nonlinear Theory of Elasticity," *SIAM Journal of Applied Mathematics*, Vol. 25, pp. 424–434.

Leonard, R. W., 1961, Nonlinear First-Approximation Thin Shell and Membrane Theory, Thesis, Virginia Polytechnic Institute.

Libai, A., and Simmonds, J. G., 1983, "Nonlinear Elastic Shell Theory," in *Advances in Applied Mechanics*, Hutchinson and Wu, eds., Academic Press, pp. 271–371.

Love, A. E. H., 1927, *Mathematical Theory of Elasticity*, 4th Ed., Cambridge University Press, Chap. 24.

Naghdi, P. M., 1972, "The Theory of Plates and Shells," in *Encyclopedia of Physics*, 2nd Ed., VIa/2, Flugge, S., ed., Springer Verlag, pp. 425–640.

Pietraskiewicz, W., 1980, "Finite Rotations in Shells," in *Theory of Shells*, Becker, E., and Mikhailov, G. K., eds., North-Holland, pp. 445–471.

Pietraszkiewicz, W., 1980, "Finite Rotations in the Nonlinear Theory of Thin Elastic Shells," in *Thin Shell Theory: New Trends and Applications*, Olszak, W., ed., Springer-Verlag, pp. 155–208.

Reissner, E., 1950, "On a Variational Theorem in Elasticity," *Journal of Mathematics and Physics*, Vol. 25.

Reissner, E., 1974, "Linear and Nonlinear Theory of Shells," in *Thin-Shell Structures*, Fung, Y. C., and Sechler, E. E., eds., Prentice-Hall, pp. 29–44.

Sanders, J. L., Jr., 1963, "Nonlinear Theories for Thin Shells," *Quarterly Journal of Applied Mathematics*, Vol. 21, pp. 21–36.

Simmonds, J. G., and Danielson, D. A., 1970, "Nonlinear Shell Theory with a Finite Rotation Vector," *Koninklijke Nederlandse Akademie Van Wetenschappen*, Vol. 73B, pp. 460–478.

Washizu, K., 1955, "On the Variational Principles in the Theory of Elasticity and Plasticity," Technical Report 25-18, Massachusetts Institute of Technology.

Wempner, G., 1969, "Finite Elements, Finite Rotations and Small Strains of Flexible Shells," *International Journal of Solids and Structures*, Vol. 5, pp. 117–153.

Wempner, G., 1971, Discrete Approximations Related to Nonlinear Theories of Solids, *International Journal of Solids and Structures*, Vol. 7, pp. 1581–1599.

Wempner, G., 1980, Complementary Theorems of Solid Mechanics, in *Variational Methods in the Mechanics of Solids*, Nemat-Nasser, S., ed., Pergamon Press, Oxford, pp. 127–135.

APPENDIX

Some Differential Geometry and Notations

Where possible, minuscules signify variables of the initial state and majuscules signify variables of the current (deformed state). Unless specifically noted, components are associated via the metric of the initial state.

The basis of the initial state is the triad ($\mathbf{a}_i$) and reciprocal triad ($\mathbf{a}^i$):

$$\mathbf{a}_\alpha \equiv \mathbf{r}^o_{,\alpha},\ \mathbf{a}_3 \equiv \mathbf{n},\ \mathbf{a}^i \cdot \mathbf{a}_j = \delta^i_j$$

The rigidly rotated triad ($\mathbf{b}_i$) and reciprocal triad ($\mathbf{b}^i$) also form the components of the initial metric:

$$a_{\alpha\beta} \equiv \mathbf{a}_\alpha \cdot \mathbf{a}_\beta = \mathbf{b}_\alpha \cdot \mathbf{b}_\beta$$

$$a^{\alpha\beta} \equiv \mathbf{a}^\alpha \cdot \mathbf{a}^\beta = \mathbf{b}^\alpha \cdot \mathbf{b}^\beta$$

The triad ($\mathbf{A}_i$) and the reciprocal triad ($\mathbf{A}^i$) are defined by the equations:

$$\mathbf{A}_\alpha = \mathbf{R}^o_{,\alpha},\ \mathbf{A}_3 = \mathbf{R}_{,3}(\theta^1,\ \theta^2,\ 0),\ \mathbf{A}_i \cdot \mathbf{A}^j = \delta^j_i$$

The stretch is defined by (17*a*); the inverse (or contraction) is denoted by the minuscule c^α_β and defined by

$$c^\alpha_\beta C^\beta_\gamma = \delta^\alpha_\gamma,$$

Relations between the triads, ($\mathbf{b}_i$, $\mathbf{b}^j$) and ($\mathbf{A}_i$, $\mathbf{A}^j$) follow:

$$\begin{aligned} \mathbf{A}_\alpha &= C^\beta_\alpha \mathbf{b}_\beta = C_{\alpha\beta} \mathbf{b}^\beta \\ \mathbf{A}^\alpha &= c^\alpha_\beta \mathbf{b}^\beta \\ \mathbf{b}_\alpha &= c^\beta_\alpha \mathbf{A}_\beta = C_{\alpha\beta} \mathbf{A}^\beta \\ \mathbf{b}^\alpha &= C^\alpha_\beta \mathbf{A}^\beta \end{aligned}$$

The shear is defined by (17*b*); the mixed components follow:

$$C^i_3 = \mathbf{b}^i \cdot \mathbf{A}_3 = a^{ij} C_{3j}$$

Numerical Solution to an Inextensible Plate Theory With Experimental Results

P. Darmon[1]
Assoc. Mem. ASME

R. C. Benson
Mem. ASME

Department of Mechanical Engineering,
The University of Rochester,
Rochester, New York 14627

A numerical and experimental study of the Simmonds-Libai (1979) plate theory is presented in this paper. This concerns the large, inextensional, noncylindrical bending of cantilevered plates.

Introduction

Presented in this paper is a comparison between numerical and experimental results for the large, inextensional, deflections of cantilevered plates. To the authors' knowledge, this is the first numerical solution to a nonlinear plate theory first put forth by Simmonds and Libai (1979), and later modified by Darmon and Benson (1985). To briefly review, the Simmonds-Libai (S-L) plate theory represents an extension of Euler's elastica to noncylindrical bending, with the principal kinematic feature that a line of zero curvature, called a "generator," exists at any point in the deformed plate. See Fig. 1. A curve $\mathcal{B}$ passes perpendicularly through all of the generators. Knowledge of the normal curvature, $k(\xi)$, and the geodesic curvature, $g(\xi)$, of this curve, permits one to construct the deformed geometry of the plate (ξ is the curvilinear coordinate along $\mathcal{B}$, as measured from the "loaded edge"). Reduction to cylindrical bending brings great simplification as $g(\xi)$ becomes identically zero and the parallel orientation of the generators is known a priori. The modifications of Darmon and Benson were to include orthotropic, elastic properties and to admit distributed loading in the Simmonds-Libai equilibrium equations. This was motivated by the desire to better model such flexible, fibrous materials as paper and cloth. Readers desiring additional information on this inextensional plate theory are referred to Libai and Simmonds (1983), Darmon (1985), and the two previously cited works.

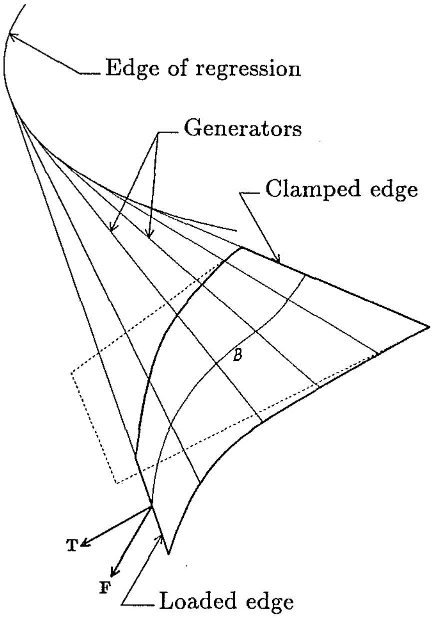

Fig. 1 Geometry of the plate

In the Numerical Solution Section we describe the techniques used to integrate the differential equations of the theory, and take note of alternative techniques which proved less useful. We also examine some numerical problems that arise when the normal curvature of the plate vanishes. At such inflection points in the plate the local generators are ambiguously defined and the basic kinematic tool of the S-L theory is lost. Techniques to bridge these points of vanishing curvature will be presented. To test the utility of the S-L theory, and the validity of the present solution, experiments were performed on steel plates. "Short plate" results, little influenced by gravity, and "long plate" results, much influenced by gravity, are reported in the Experiments Section. The closeness of the match between the numerical results and the experimental measurements is considered in the Discussion Section. We find the match to be quite good.

Notation follows Simmonds and Libai (1979). References on the numerical study may be found in Carnahan et al. (1969).

Numerical Solution

The S-L equations of equilibrium, as modified by Darmon and Benson (1985) for orthotropism and distributed loading, comprise a set of sixteen differential equations, three integral equations, and various algebraic constraints. The integral equations are of the form:

---

[1] Presently at IBM Corporation, Thomas J. Watson Research Center, Yorktown Heights, NY 10598.

Contributed by the Applied Mechanics Division for publication in the Journal of Applied Mechanics.

Discussion on this paper should be addressed to the Editorial Department, ASME, United Engineering Center, 345 East 47th Street, New York, N.Y. 10017, and will be accepted until two months after final publication of the paper itself in the Journal of Applied Mechanics. Manuscript received by ASME Applied Mechanics Division, March 24, 1986.

$$\mathbf{Q}(\xi)=\int_0^{\xi}\mathbf{q}(t)dt, \qquad (1)$$

where $\mathbf{q}(t)$ is the resultant of the distributed load acting along a single generator at t, and $\mathbf{Q}(\xi)$ is the resultant of all distributed loading between the loaded edge at $t=0$ and an intermediate generator at $t=\xi$. For the present purpose of numerical solution, we find it preferable to differentiate vector equation (1) so that the integro-differential system becomes a purely differential system. The three scalar components of $\mathbf{Q}$ are then incorporated as additional unknowns so that the eventual formulation appears as:

$$\frac{d\mathbf{y}}{d\xi}=\mathbf{f}(\xi,\mathbf{y}) \quad \mathbf{y}(0)=\mathbf{y}_0, \qquad (2)$$

where $\mathbf{y}$ is a vector unknown, $\mathbf{y}_0$ is a vector boundary condition, and $\mathbf{f}$ is a vector function, all of dimension nineteen. See the Appendix for a complete list of these equations.

Of the various numerical techniques that might be used for the integration of (2), two main categories can be identified: a simultaneous, finite-difference, matrix method; and a "shooting" method. The matrix method consists of replacing the differential equations with a system of $19 \times N$ algebraic equations where N is the number of points at which the solution is desired. The problem is then reduced to the inversion of a $19 \times N$ by $19 \times N$ matrix. Although experience has proven that this method can be more stable than some shooting techniques, it requires far more computation time and is fairly complicated to implement. For that reason, it has been discarded after some trials.

Shooting methods are of two kinds: explicit or implicit (also known as open and closed formulas, respectively). Implicit schemes, although a bit slower, are numerically more stable than explicit schemes (Carnahan et al., 1969). An explicit fourth-order Runge-Kutta scheme was first tried with no success, due to a lack of stability. A fourth-order and then a six-order Milne predictor-corrector method, both implicit schemes, gave unacceptable results as well. Finally, the Hamming predictor-corrector method was tried, and was retained for it gave satisfactory and stable answers to our problem. It is based on the Milne method, but its stabilty is improved at the expense of an increased truncation error. The subroutine DHPCG (Double precision Hamming Predictor Corrector for General differential equations), from the Scientific Subroutine Package by IBM, has been used.

The Simmonds-Libai equations require iteration on the unknown initial geodesic curvature $g(0)$ so that the final generator aligns properly with the clamp. There are two other unknown quantities which require iteration: the direction of the distributed load in the frame attached to the plate, and the final value of the independent variable ξ. The iteration on the maximum value of ξ is necessary as the curve $\mathcal{B}$ is not a material line and therefore its length is not known a priori. The present results were obtained by the Newton-Raphson method.

Singularities and Implementation

When the normal curvature $k(\xi)$ of the plate vanishes, a numerical singularity arises. In the neighborhood of such inflection points of the curve $\mathcal{B}$, the plate is practically undeformed and it follows that the bending strains are so small as to become of the same order of magnitude as the stretching strains. This contradicts the basic assumption of the inextensible plate theory, which stipulates that the stretching strains are negligible in comparison to the bending strains. In the limit, a zero normal curvature causes a numerical singularity as the derivative of the geodesic curvature, $g'(\xi)$, becomes infinite. The singularity has been treated by the present authors in two separate cases depending whether it occurs at the loaded edge of the plate (as occurs when no bending moment applied), or at an interior generator (plate deformed into an "S" shape). In the case of vanishing curvature at the loaded edge, experiment has shown that if a small bending moment is applied, the numerical solution still behaves nicely, but the determination of the unknown initial geodesic curvature remains delicate (Darmon, 1985). If the guess for $g(0)$ is poor, the numerical singularity that ensues (negative argument of a logarithm) can be physically interpreted as follows: $1/|g|$, which represents the distance between the curve $\mathcal{B}$ and the edge of regression of the developable surface, becomes smaller than or equal to the actual dimension of the plate along the generator. Hence the edge of regression falls into the plate. Theoretically, this means that the plate should be represented with the two branches of a developable surface which connect on the edge of regression. Physically, this is not possible without folding or in some cases tearing the plate.

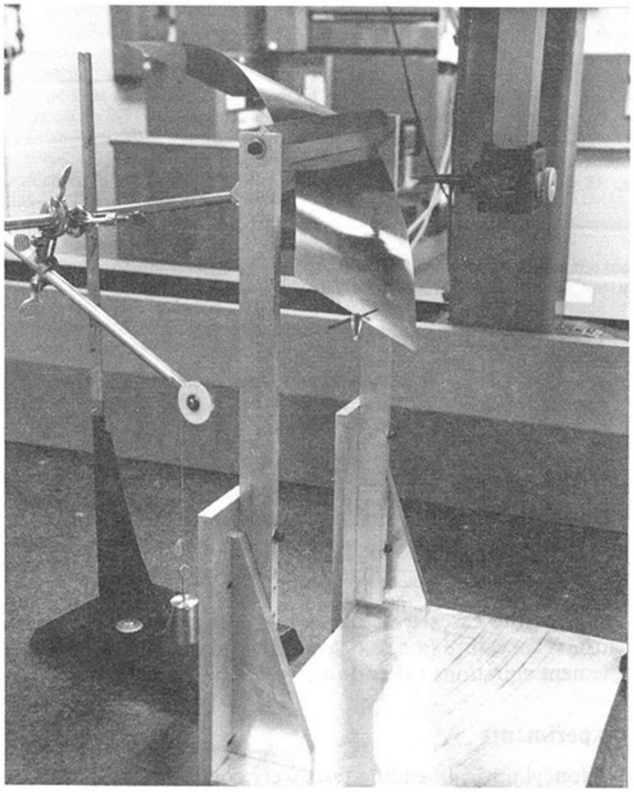

Fig. 2 Experimental apparatus

Applying a small, fictitious bending moment to the edge of the plate provides a simplistic means for avoiding the singularity, however it is not computationally efficient and an alternative solution has been sought. It consists of assuming that a small area close to the tip of the plate behaves like a wide elastica (no twist). This removes the singularity as g is identically zero for an elastica. After a short distance, k will be small but nonzero, and normal integration with the S-L equations may be resumed. We found the elastica-patch to be very simple and very accurate.

A configuration in which the normal curvature vanishes at an interior generator of the plates requires the integration of the geodesic curvature g on an interval where it is infinite. Although such a configuration can sometimes be unstable (see Love's 1944 statements with regards to the elastica), it is nevertheless worth studying. Since, physically, the plate deforms in a continuous manner, the mathematical analog ought to have a solution, i.e., the singularity should be integrable. Thus, in that interval, g' should be of the approximate form:

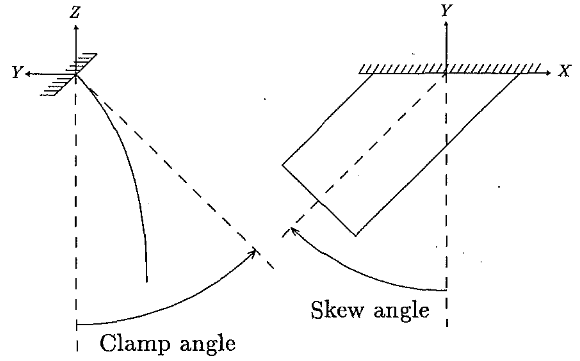

Fig. 3 Clamp and skew angles

$$g'(\xi)=\frac{a}{|\xi-\xi^*|^n},\quad 0<n<1,\quad \xi<\xi^*, \tag{3}$$

$$g'(\xi)=\frac{-a}{|\xi-\xi^*|^n},\quad 0<n<1,\quad \xi>\xi^*. \tag{4}$$

As all the cases we studied had monotonically increasing normal curvature (see next section), we never had cause to implement equations (3) and (4).

Experiments

Noncylindrical bending tests were conducted on a thin, rectangular, stainless steel plate, which we felt provided a reasonable faithfulness to the assumptions of perfectly homogeneous, isotropic, elastic behavior in the Simmonds-Libai plate theory. The plate measured 635 mm (25 in.) long, 152 mm (6 in.) wide, and 0.305 mm (0.012 in.) thick, and had a mass of 235 g (0.0161 slug). Through a simple cylindrical (i.e., elastica) deflection test, the bending rigidity was measured to be 0.477 Nm (4.23 lb-in.). To minimize the experimental error from the original curl of the plate, all tests were performed twice, and averages were taken of the "curl-up" and the "curl-down" values. The plate was sufficiently stiff so that extraneous effects such as the weight of strings, air currents, etc., could be safely neglected.

The clamping fixture was composed of an aluminum base plate on which two vertical beams were mounted. See Fig. 2. These beams supported, along a horizontal straight line, a slope-adjustable clamp. The adjustability of the clamp allowed for the rotation of the test plate in the gravity field so that its effect could be enhanced or diminished. It was also possible to skew the plate within the plane of the clamp in order to enhance or diminish the noncylindrical nature of the deformation. Figure 3 depicts these angles more precisely. The plate shown in Fig. 2 has a clamp angle of 50 deg and a skew angle of 45 deg.

A follower load at the edge of the plate is provided by accurately calibrated weights hung on a light string passed over a pulley. The pulley is fixed on a bar supported by a chemistry stand. Small pointers, centered on the loaded edge of the plate, help to adjust the position of the pulley so that the applied load is perpendicular to the tangent plane of the plate.

The deflection of the plate was measured along the two parallel, unloaded sides. (Recall that the clamped edge and loaded edge are part of the set of straight line generators.) Small, evenly spaced marks were scribed on the sides of the plate where measurements were to be taken. The spacing was set at one tenth of the plate width (15.2 mm), and the marks were made very short and shallow so that there would be no measurable effect on the bending rigidity of the plate. A three-dimensional digitizer with a cone-shaped probe was used to measure the deflection. The probe is visible in Fig. 2. The digitizer had a capability of recording Cartesian XYZ coordinates to within 0.001 mm (0.0004 in.). We defined the coordinate axes such that **X** lay in the line of the clamp, and **Z** aligned with gravity. See Fig. 3.

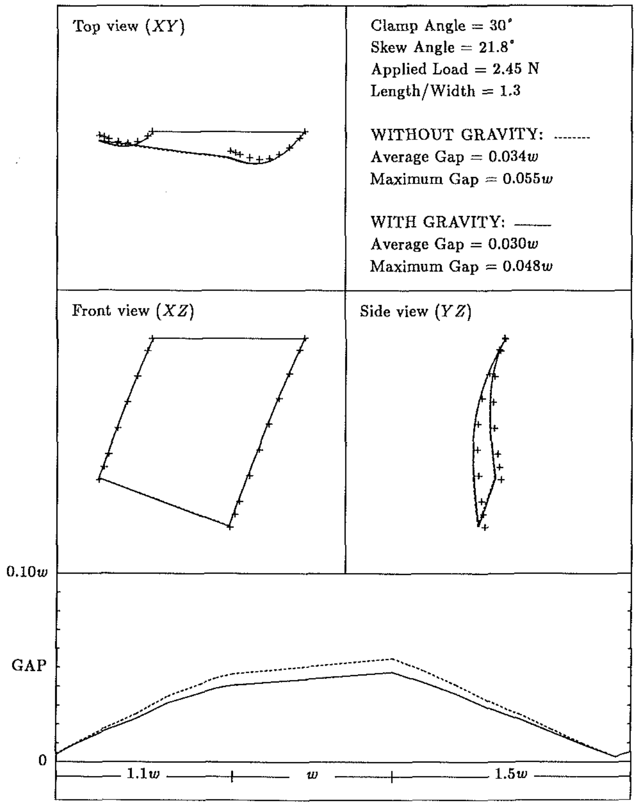

Fig. 4 Short plate results

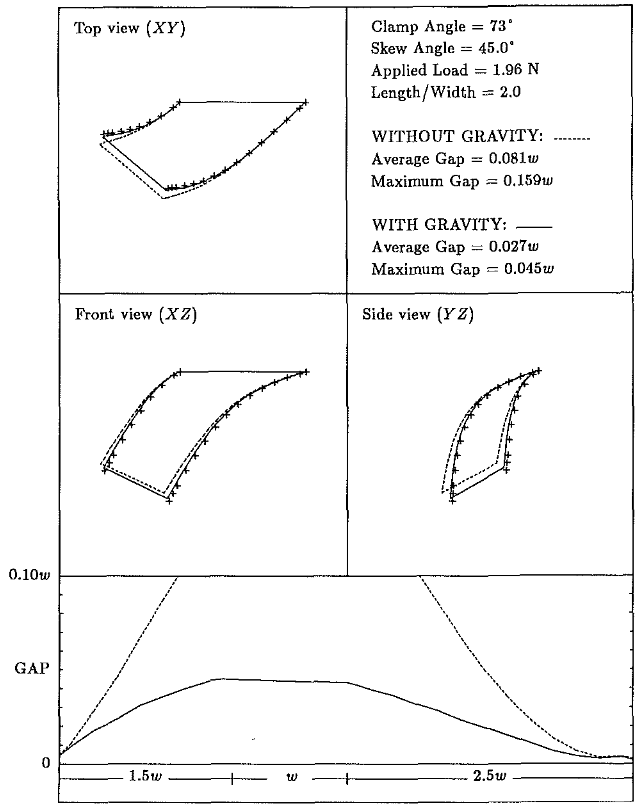

Fig. 5 Long plate results

Two test configurations will be described:

1. A "short plate" with a centerline length of 198 mm (7.8 in.), clamp angle of 30 deg, skew angle of 22 deg, and a normal follower force of 2.45 N (0.55 lb).
2. A "long plate" with a centerline length of 304 mm (12.0 in.), clamp angle of 73 deg, skew angle of 45 deg, and a normal follower force of 1.96 N (0.44 lb).

The short plate configuration was chosen to deemphasize the influence of gravity, thereby to provide a fairer test of the original Simmonds-Libai (1979) plate theory which discounted distributed loading in the overall equilibrium equations. The long plate configuration was chosen to emphasize the contribution of gravity, thus to serve as a check on the modifications made to the S-L theory by Darmon and Benson (1985).

Experimental results for the short plate and long plate are compared with numerical results in Figs. 4 and 5, respectively. Three orthogonal views are shown. In the figures, a solid curve denotes a numerically predicted plate perimeter, taking into account gravity. A dashed line shows the same plate perimeter when gravity is neglected. Small crosses mark the experimentally obtained perimeter points from the three-dimensional digitizer.

The plot of the "gap" at the bottom of Figs. 4 and 5 is a measure of the discrepancy between the numerical and experimental results. The gap is defined to be the distance separating the experimentally measured and numerically predicted locations of the same material point on the perimeter of the plate. This value is then nondimensionalized by dividing by the width of the plate (152 mm in both test cases). The gap is plotted as a function of the perimeter distance around the three nonclamped sides of the plate. As before, a solid line takes into account gravity, and a dashed line does not.

Discussion

The short plate and long plate results that are presented here are the *least* favorable comparisons that the authors obtained in 10 experiments. Nevertheless the "gap" between the experimental measurements and the corresponding theoretical/numerical prediction is at no point greater than 5 percent of the width of the plate. The authors believe that most of this error is due to experimental inaccuracy, particularly in the measurement of the clamp angle. Indeed a rigid-body rotation of 1 deg or 2 deg of the plate around the clamp line can reduce the maximum gap down to about 1 percent. Further statistical analysis of the experimental results leads to the same conclusion (Darmon, 1985).

It ought to be noted that incorporation of gravity in the model does not significantly reduce the gap for the short plate. This was expected as the effect of gravity was deliberately minimized. For the long plate however, the inclusion of gravity is a substantial improvement over the original S-L theory.

In the opinion of the authors, the Simmonds-Libai theory, with the addition of distributed loading, has met its potential as a model for lightweight structures such as webs, film, paper, and thin metal plates. Comparison with experimental measurements has shown that the model is very accurate when applied to nearly inextensible plates. A worthwhile activity for future study would be a similar numerical/experimental comparison of *orthotropic*, inextensible plates.

Acknowledgment

The authors thank the Xerox Corporation which sponsored this work.

References

Carnahan, B., Luther, H. A., and Wilkes, J. O., 1969, *Applied Numerical Methods*, Wiley, New York.

Darmon, P., 1985, "Large Inextensional Deformation of Thin Orthotropic Inhomogeneous Cantilevered Plates with Distributed Loads," Ph.D. thesis, University of Rochester, Rochester, New York.

Darmon, P., and Benson, R. C., June 1985, "Large Inextensional Deformation of Thin Orthotropic Cantilevered Plates with Distributed Loads," ASME JOURNAL OF APPLIED MECHANICS, Vol. 52, pp. 385–388.

Frish-Fray, 1962, *Flexible Bars*, Butterworth and Co., LTD, Washington.

Libai, A., and Simmonds, J. G., 1983, "Nonlinear Elastic Shell Theory," *Advances in Applied Mechanics*, Academic Press, New York, Vol. 23, pp. 335–337.

Love, A. E. H., 1944, *A Treatise on the Mathematical Theory of Elasticity*, Dover Publications, Inc.

Simmonds, J. G., and Libai, A., Sept. 1979, "Exact Equations for the Inextensional Deformation of Cantilevered Plates," ASME JOURNAL OF APPLIED MECHANICS, Vol. 46, pp. 631–636.

"System/360 Scientific Subroutine Package," Version III Programmer's Manual, 360A-CM-03X, IBM Corporation.

APPENDIX

Following is a list of equations needed for the extended S-L theory. Notation follows Darmon and Benson (1985).

Angle of the generators:

$$\alpha' = g, \quad \alpha(0) = 0. \tag{5}$$

Cartesian coordinates of a point on the curve $\mathcal{B}$ in the undeformed plate:

$$u' = \cos\alpha, \qquad u(0) = 0, \tag{6}$$

$$v' = \sin\alpha, \qquad v(0) = 0. \tag{7}$$

Components of the torque **T**:

$$T_t' = gT_u + kT_m - l_m, \qquad T_t(0) = T\mathbf{a}\cdot\mathbf{i}, \tag{8}$$

$$T_u' = -gT_t + Pc_m - Q_m, \qquad T_u(0) = T\mathbf{a}\cdot\mathbf{j}, \tag{9}$$

$$T_m' = -kT_t - Pc_u + Q_u + l_t, \qquad T_m(0) = T\mathbf{a}\cdot\mathbf{k}. \tag{10}$$

Geodesic curvature g:

$$g' = \frac{1}{A_0A_2 - A_1^2}\left[\left(\frac{\eta\tan\theta}{1-\eta g}\Big|_-^+ - \frac{T_t}{D_\xi k}\right)D_\xi A_0 - \left(\frac{gT_t - Pc_m + Q_m}{D_\xi k} + \tan\theta\Big|_-^+\right)D_\xi A_1\right],$$

$$g(0) = ?. \tag{11}$$

Angles needed to locate the direction of the force P:

$$\phi' = k\cos\gamma, \qquad \phi(0) = \phi_0, \tag{12}$$

$$\gamma' = -g - k\cot\phi\sin\gamma, \qquad \gamma(0) = \gamma_0. \tag{13}$$

Euler parameters:

$$\beta_1' = \frac{1}{2}(k\beta_3 + g\beta_2), \qquad \beta_1(0) = 0, \tag{14}$$

$$\beta_2' = -\frac{1}{2}(k\mu + g\beta_1), \qquad \beta_2(0) = 0, \tag{15}$$

$$\beta_3' = \frac{1}{2}(g\mu - k\beta_1), \qquad \beta_3(0) = 0, \tag{16}$$

$$\mu' = \frac{1}{2}(k\beta_2 - g\beta_3), \qquad \mu(0) = 1. \tag{17}$$

Integrals of the distributed load:

$$Q_x' \equiv \frac{dQ_x}{d\xi} = q_x, \qquad Q_x(0) = 0, \tag{18}$$

$$Q_y' \equiv \frac{dQ_y}{d\xi} = q_y, \qquad Q_y(0) = 0, \tag{19}$$

$$Q_z' \equiv \frac{dQ_z}{d\xi} = q_z, \qquad Q_z(0) = 0. \tag{20}$$

Curve $\mathcal{B}$:

$$\mathbf{x}' = \mathbf{t}, \qquad \mathbf{x}(0) = \mathbf{0}. \tag{21}$$

Angles θ_+ and θ_-:

$$\theta_\pm = \alpha - \beta_\pm, \tag{22}$$

$$\tan \beta_\pm = \frac{df_\pm}{dx}. \tag{23}$$

Relation for the $\mathbf{u}_i$'s in terms of the $\mathbf{e}_i$'s:

$$\mathbf{u}_i = \mathbf{e}_i + 2\mu\beta \times \mathbf{e}_i + 2(\beta \bullet \mathbf{e}_i)\beta - 2(\beta \bullet \beta)\mathbf{e}_i. \tag{24}$$

Distances along a generator from the curve $\mathcal{B}$ to the free edges, η_+ and η_-:

$$\eta_\pm \cos\alpha + v = f_\pm\,(u - \eta_\pm \sin\alpha). \tag{25}$$

Normal curvature k in terms of the bending moment T_u:

$$k = -\frac{T_u}{A_0}. \tag{26}$$

Direction cosines of the force P:

$$c_u = \sin\phi \sin\gamma, \tag{27}$$

$$c_m = \cos\phi. \tag{28}$$

Integrals along a generator:

$$A_j(\xi) = \int_{\eta_-}^{\eta_+} \frac{D_\xi \eta^j d\eta}{(1-\eta g)^{j+1}}, \tag{29}$$

$$B_j(\xi) = \int_{\eta_-}^{\eta_+} \frac{D_{\xi,\xi} \eta^j d\eta}{(1-\eta g)^{j+1}}, \tag{30}$$

$$\mathbf{l}(\xi) = \int_{\eta_-}^{\eta_+} \eta(1-\eta g)\mathbf{p}\,d\eta, \tag{31}$$

$$\mathbf{q}(\xi) = \int_{\eta_-}^{\eta_+} (1-\eta g)\mathbf{p}\,d\eta. \tag{32}$$

Rigidities:

$$D_\xi = c^4 D_x + 2c^2 s^2 (D_{xy} + 2G_{xy}) + s^4 D_y, \tag{33}$$

$$D_{\xi\eta} = (c^4 + s^4) D_{xy} + c^2 s^2 (D_x + D_y - 4G_{xy}). \tag{34}$$

Derivatives of the rigidities:

$$\begin{aligned} D_{\xi,\xi} = {} & -4csg[c^2 D_x - (c^2 - s^2)(D_{xy} + 2G_{xy}) - s^2 D_y] \\ & + (1-\eta g)\left[c^4\left(\cos\alpha \frac{\partial D_x}{\partial x} + \sin\alpha \frac{\partial D_x}{\partial y}\right)\right. \\ & + 2c^2 s^2\left(\cos\alpha \frac{\partial (D_{xy} + 2G_{xy})}{\partial x} + \sin\alpha \frac{\partial (D_{xy} + 2G_{xy})}{\partial y}\right) \\ & \left. + s^4\left(\cos\alpha \frac{\partial D_y}{\partial x} + \sin\alpha \frac{\partial D_y}{\partial y}\right)\right], \end{aligned} \tag{35}$$

$$\begin{aligned} D_{\xi,\eta} = {} & c^4\left[-\sin\alpha \frac{\partial D_x}{\partial x} + \cos\alpha \frac{\partial D_x}{\partial y}\right] \\ & + 2c^2 s^2\left[-\sin\alpha \frac{\partial (D_{xy} + 2G_{xy})}{\partial x} + \cos\alpha \frac{\partial (D_{xy} + 2G_{xy})}{\partial y}\right] \\ & + s^4\left[-\sin\alpha \frac{\partial D_y}{\partial x} + \cos\alpha \frac{\partial D_y}{\partial y}\right], \end{aligned} \tag{36}$$

$$\begin{aligned} D_{\xi\eta,\xi} = {} & -4csg\left[(c^2 - s^2)D_{xy} - \frac{1}{2}(c^2 - s^2)(D_x + D_y - 4G_{xy})\right] \\ & + (c^4 + s^4)\left[\cos\alpha \frac{\partial D_{xy}}{\partial x} + \sin\alpha \frac{\partial D_{xy}}{\partial y}\right] \\ & + c^2 s^2\left[\cos\alpha \frac{\partial (D_x + D_y - 4G_{xy})}{\partial x}\right. \\ & \left. + \sin\alpha \frac{\partial (D_x + D_y - 4G_{xy})}{\partial y}\right], \end{aligned} \tag{37}$$

$$\begin{aligned} D_{\xi\eta,\eta} = {} & (c^4 + s^4)\left[-\sin\alpha \frac{\partial D_{xy}}{\partial x} + \cos\alpha \frac{\partial D_{xy}}{\partial y}\right] \\ & + c^2 s^2\left[-\sin\alpha \frac{\partial (D_x + D_y - 4G_{xy})}{\partial x}\right. \\ & \left. + \cos\alpha \frac{\partial (D_x + D_y - 4G_{xy})}{\partial y}\right]. \end{aligned} \tag{38}$$

Kinetoelastostatics of Axisymmetric Nets

E. N. Kuznetsov
Professor,
Department of General Engineering,
University of Illinois,
Urbana, IL 61801
Mem. ASME

Intricately interrelated external loads, internal forces and equilibrium shapes of axisymmetric nets are studied. After developing the basic equations in a generic form, the most important particular types of nets are investigated—geodesic, Chebyshev, and orthogonal nets. Closed-form statical-geometric relations are obtained for each type of net and, as a by-product, for a wrinkling axisymmetric membrane. These allow a comprehensive investigation into the equilibrium configurations of the above systems and their evolution in the course of loading. Load combinations studied involved edge loads and normal surface loads such as net-solid contact pressure, pneumatic pressure or pressure induced by an axial gas flow.

Introduction

A net is an underconstrained, multidegree-of-freedom structural system with intricately interrelated statics and geometry: the equilibrium shape of a net is uniquely determined by the applied load whereas, for a given geometry, equilibrium is possible under a whole class of loads (equilibrium loads). A systematic study of nets within the general framework of structural mechanics began about three decades ago [1, 7–9] although a few works on the analysis of simple shallow nets appeared long before. In a comprehensive work by Rivlin [9], an inextensible Chebyshev net is subjected to a large axisymmetric deformation followed by a small cyclic deformation. Read [8] found in numerical form the feasible shapes of axisymmetric geodesic nets under uniform pressure. The problem statement in Pipkin and Rivlin [7] was much more general and, in fact, reversed: sought was a layout with uniformly stressed fibers (an isotensoid design) for a given convex surface of revolution. For the case of geodesic isotensoid, the problem was reduced to an integral equation in the unknown distribution of the wound fiber inclinations to a reference parallel. Closed-form solutions were obtained for a sphere, cone, and ellipsoid of revolution. Interestingly, Pipkin and Rivlin [7], apparently unaware that their geodesic isotensoid design is the exhaustive solution to the problem, mentioned a nongeodesic isotensoid system. The latter, however, is impossible by virtue of the following proposition [3].

If, under a normal surface load and an edge load, the cable net meets *one* of the three conditions: 1) the net is geodesic; 2) cable intersections do not transfer tangential forces; 3) cable forces do not vary along the length; then *all* of the three conditions are met.

Thus, any isotensoid net under the above type of load is geodesic. For example, a yielding ideally plastic net is geodesic; in particular, if it is flat (edge loads only) all the cables are straight regardless of the initial geometry of the net.

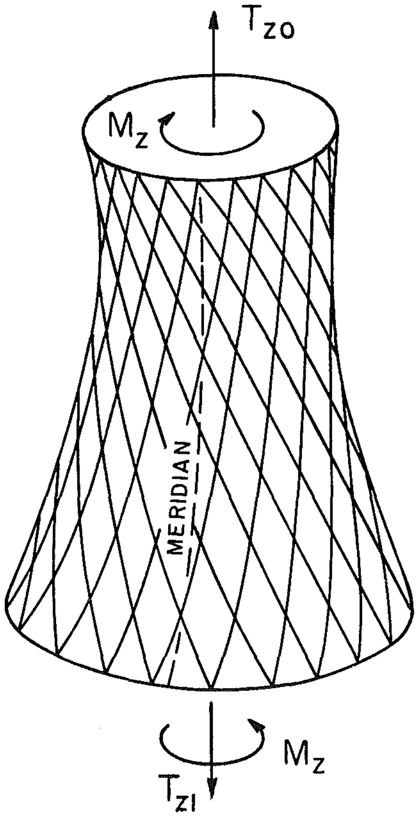

Fig. 1 Skew axisymmetric net

The object of this paper is an axisymmetric net generally lacking reflection symmetry relative to a meridian plane, i.e., a skew axisymmetric net (Fig. 1). The homogeneous problem for such a net (edge loads only) has been solved in [4] where the feasible equilibrium shapes of prestressed nets were established. The present study deals primarily with statical-geometric interrelations for nets supporting normal surface loads. Such relations are necessary for determining the equilibrium shape for a given load, or, conversely, for finding

---

Contributed by the Applied Mechanics Division for publication in the JOURNAL OF APPLIED MECHANICS.

Discussion on this paper should be addressed to the Editorial Department, ASME, United Engineering Center, 345 East 47th Street, New York, N.Y. 10017, and will be accepted until two months after final publication of the paper itself in the JOURNAL OF APPLIED MECHANICS. Manuscript received by ASME Applied Mechanics Division, March 24, 1986; final revision May 12, 1986.

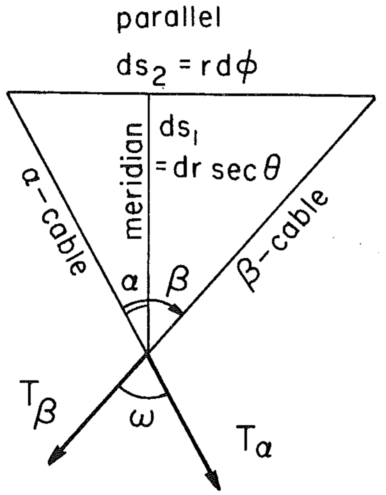

Fig. 2 Net angles and forces

the equilibrium loads for a given shape. The latter alternative underlies the concept of statically controlled geometry whereby a desired configuration of an underconstrained system is obtained by statical means and is subsequently fixed (by imposing additional constraints) or actively controlled (using some kind of feedback).

Material properties are usually brought into the analysis after establishing the equilibrium shape attained kinematically. However, prestressed nets represent an exception: they lack kinematic mobility, hence, in their analysis constitutive relations cannot be decoupled.

Generic Statical-Geometric Relations

For a continuous model of an axisymmetric net with a meridian $r = r(z)$, the equilibrium condition in the normal direction is the same as the one for a membrane shell of revolution

$$T_1\sigma_1 + T_2\sigma_2 = P \qquad (1)$$

Here T_1 and T_2 are the meridional and hoop forces (per unit lengths $ds_2 = 1$ and $ds_1 = 1$, respectively), σ_1 and σ_2 are the principal curvatures, and P is the normal surface load.

When introducing the net forces, T_α and T_β, it is convenient to refer them to a unit polar angle, $d\phi = 1$, since it contains a certain constant number of cables from each array. Let α and β be the respective cable inclinations to the meridian with the positive direction shown in Fig. 2. Then the three membrane forces are related to the cable forces as follows:

$$rT_1 = T_\alpha cos\alpha + T_\beta \cos\beta \qquad (2)$$

$$rT_{12} = T_\alpha \sin\alpha + T_\beta \sin\beta \qquad (3)$$

and, by virtue of

$$d\phi/ds_1\,|_\alpha = \tan\alpha/r,\ d\phi/ds_1\,|_\beta = \tan\beta/r \qquad (4)$$

the hoop force

$$rT_2 = T_\alpha \sin\alpha\ \tan\alpha + T_\beta \sin\beta\ \tan\beta \qquad (5)$$

After introducing the axial force resultant, T_z, and torque moment, M_z,

$$T_z = 2\pi r T_1 \sin\theta,\ M_z = 2\pi r^2 T_{12} \qquad (6)$$

the cable forces are evaluated from equations (2) and (3) as follows

$$2\pi r\ \sin\omega\ T_\alpha = rT_z \sin\beta/\sin\theta - M_z \cos\beta \qquad (7)$$

$$2\pi r\ \sin\omega\ T_\beta = M_z \cos\alpha - rT_z \sin\alpha/\sin\theta \qquad (8)$$

Here θ and ω are, respectively, the slope of the meridian and the net angle:

$$ctn\theta = dr/dz,\ \omega = \beta - \alpha \qquad (9)$$

Note that torque M_z is constant throughout the net while the axial force T_z, in the presence of a surface pressure, varies along the z axis.

The three membrane forces produced by a net are mutually dependent which allows the hoop force to be expressed in terms of the meridional and shearing forces

$$T_2 = T_{12}(\tan\alpha + \tan\beta) - T_1 \tan\alpha\ \tan\beta \qquad (10)$$

Upon the substitution of equations (6) and (10), equation (1) becomes

$$T_z(\sigma_1 - \sigma_2 \tan\alpha\ \tan\beta)/\sin\theta + M_z\sigma_2(\tan\alpha + \tan\beta)/r = 2\pi r P \qquad (11)$$

Presenting the principal curvatures as

$$\sigma_1 = d\sin\theta/dr,\ \sigma_2 = \sin\theta/r \qquad (12)$$

and employing the condition of axial equilibrium

$$2\pi r P = dT_z/dr \qquad (13)$$

enables equation (11) to be transformed into a first-order differential equation

$$\frac{d}{dr}\,\frac{T_z}{\sin\theta} + \frac{T_z \tan\alpha\ \tan\beta}{r\sin\theta} - \frac{M_z(\tan\alpha + \tan\beta)}{r^2} = 0 \qquad (14)$$

The above equations interrelate the statical and geometric variables describing an axisymmetric net in equilibrium. In the absence of torque, $M_z = T_{12} = 0$, it follows from equations (11) and (12) that

$$\sigma_1/\sigma_2 = 2\pi r^2 P/T_z + \tan\alpha\ \tan\beta \qquad (15)$$

where, as is seen from equation (3),

$$\tan\alpha\ \tan\beta < 0 \qquad (16)$$

provided that both of the cable arrays are in tension. Accordingly, in the state of prestress and under an external pressure ($P < 0$) the meridian is always concave. Under an internal pressure, σ_1 reduces in absolute value, and a point where it first reaches zero becomes an inflection point with

$$2\pi r^2 P = -T_z \tan\alpha\ \tan\beta \qquad (17)$$

The axial force is given by

$$T_z = T_{zo} + 2\pi \int_{z_o}^{z_1} P(z)\ ctn\theta\ dz = T_{zo} + 2\pi \int_{r_o}^{r_1} P(r)dr \qquad (18)$$

where T_{zo} is the axial force at the parallel $z = z_o$. If pressure P is known as a function of r, the second alternative of equation (18) leads to an explicit expression for $T_z(r)$. Such is the case, for example, of an incompressible gas flow (the normal pressure is proportional to r^{-4}). For a uniform pressure,

$$T_z = T_{zo}[1 + p(r^2/r_o^2 - 1)] \qquad (19)$$

where p is the normalized pressure

$$p = \pi r_o^2 P/T_{zo} \qquad (20)$$

There exist three invariant parameters associated with a segment of an axisymmetric net contained between the edge parallels, z_o and z_1. The first two invariants are the natural (unstretched) cable lengths:

$$L_\alpha = \int_{z_o}^{z_1} \frac{dz}{\sin\theta\ \cos\alpha},\ L_\beta = \int_{z_o}^{z_1} \frac{dz}{\sin\theta\ \cos\beta} \qquad (21)$$

The third invariant is the angular distance, Φ, (Fig. 3) at the terminal parallel, z_1, between an α line and a β line originating at one and the same point A at the initial parallel, z_o. Φ is evaluated via the respective cable winding angles, ϕ_α and ϕ_β. Although both ϕ_α and ϕ_β change in the net deformations, their difference preserves:

$$\Phi = \phi_\beta - \phi_\alpha = \int_{z_o}^{z_1} \frac{\tan\beta - \tan\alpha}{r\ \sin\theta}\,dz \qquad (22)$$

L_α, L_β and Φ are the only geometric invariants of a net; all

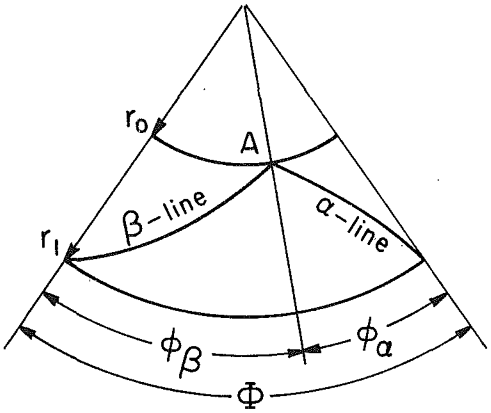

Fig. 3 Cable winding angles and angular invariant

other parameters, including the axial length $L_z = z_1 - z_o$ and the radii of the edge parallels can, and generally do, change in the net deformations.

Further investigation requires knowledge of the intrinsic geometric properties of the net obtainable only upon specifying the net type. In what follows, the three most important particular types of nets are studied—geodesic, Chebyshev, and orthogonal nets.

Geodesic Nets

A geodesic net with the member intersections not fixed remains geodesic in both kinematic (inextensible) and elastic deformations under any normal surface load and edge load. This is in spite of the fact that the form of an elementary cell as well as the overall shape of the net surface change in both deformations. An axisymmetric geodesic net on a given surface of revolution $r = r(z)$ is uniquely defined by specifying the constants a and b in the Clairaut formula [2]

$$r \sin\alpha = a,\ r \sin\beta = b \tag{23}$$

After these formulas and their differential versions

$$d\alpha\ ctn\alpha = d\beta\ ctn\beta = -dr/r \tag{24}$$

are introduced into equation (14) the latter admits an integrating factor leading to the solution

$$T_z/\sin\theta - M_z(\cos\alpha + \cos\beta)/(a+b) = Cr \sin\omega \tag{25}$$

where C is an arbitrary constant. By subtracting equation (8) from (7) and comparing the result with solution (25) it is found that

$$C = 2\pi(T_\alpha - T_\beta)/(a+b) \tag{26}$$

Furthermore, expressing the cable forces in terms of the constants C and M_z confirms that the forces do not vary along the cable lengths:

$$2\pi T_\alpha = M_z/(a+b) + Cb,\ 2\pi T_\beta = M_z/(a+b) - Ca \tag{27}$$

The obtained equations allow some observations to be made on the evolution of the meridian shape for a geodesic net under a uniform pressure. As with any axisymmetric net, in the state of prestress or under an external pressure, the meridian is concave. In accordance with equations (17) and (23), under a uniform internal pressure, inflection first sets in at the larger of the edge rings and gradually propagates toward the smaller ring. At this stage the meridian is S shaped and stays this way until the inflection reaches the smaller ring, whereupon the meridian becomes convex. A conical shape is not feasible, but a cylindrical one is possible if $r_o = r_1$ and occurs when

$$p = -(\tan\alpha\ \tan\beta)/2 \tag{28}$$

Curiously, a geodesic net is one of the few objects in structural mechanics where the applicability of conventional analytical means, including the finite element method, is not obvious. One of the reasons is the necessity to satisfy the three preservation requirements (21)-(22).

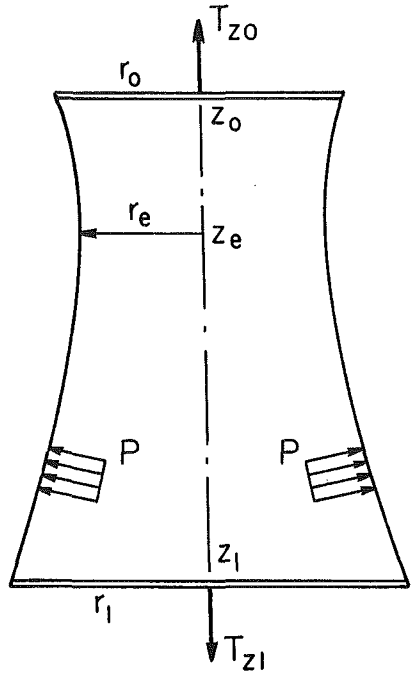

Fig. 4 Geometric parameters and loads on net

The following example is an analysis of a skew geodesic net for a 250 m high cooling tower [5] with two rigid edge rings of radii $r_o = 75$ m and $r_1 = 100$ m (Fig. 4). The net is torque free, i.e., no external torque is applied and the edge rings are not constrained against mutual rotation about the z axis. With $M_z = 0$, solution (25) yields

$$ctn\theta \equiv dr/dz = \sqrt{(Cr \sin\omega/T_z)^2 - 1} \tag{29}$$

whereupon the equilibrium configuration of a net is obtained explicitly by forward integration employing equations (9), (13), and (23).

The analysis [6] starts with determining the prestressed state. In this case, $P = 0$, $T_z = T^*$ and only three initial parameters are needed for forward integration: a, b, and C/T^*. These are selected and then adjusted by trial-and-error until a satisfactory prestressed state (net shape and forces) is obtained. At this stage the invariants L_α, L_β and Φ are evaluated. In particular,

$$L_\alpha = L^*_\alpha - T^*_\alpha/EA_\alpha,\ L_\beta = L^*_\beta - T^*_\beta/EA_\beta \tag{30}$$

where L^*_α and L^*_β are the pretensioned cable lengths obtained by integration, EA_α and EA_β are the cable stiffnesses.

The deformed state of the net under an applied pressure P is determined by a set of four parameters, say, a, b, T_α, and T_β, all of them yet unknown. Their values must be such that the sought state is consistent with the three net invariants and the preservation of L_z, which is equivalent to

$$r_1 = r_o + \int_{z_o}^{z_1} ctn\theta\ dz \tag{31}$$

and is treated as a fourth invariant. This gives rise to a system of four simultaneous equations of the form (21), (22), and (31) in which the left hand side values are already known while the four unknown parameters figure implicitly under the sign of a definite integral.

In solving this system of equations for several pressure levels, a shooting technique has been employed in conjunction with a fourth-order Runge-Kutta integration scheme. Using

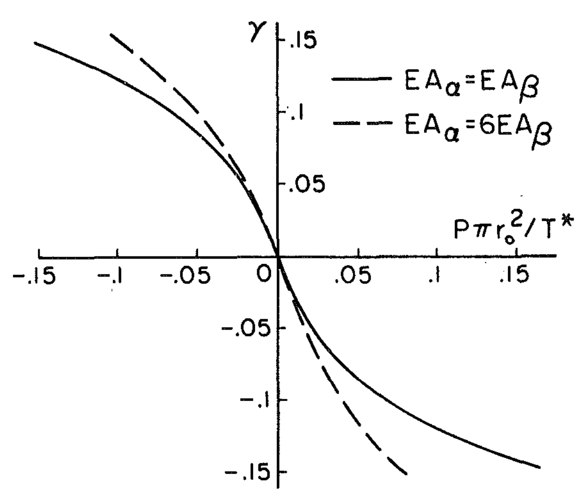

Fig. 5 Rotation of edge ring under uniform surface pressure

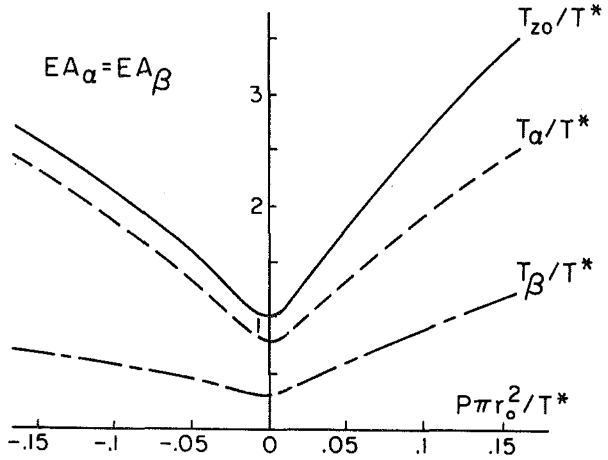

Fig. 6 Axial force and cable forces in geodesic net

trial values of the unknown parameters, approximations for the four invariants are obtained. The errors in the invariants are then used to refine the unknowns iteratively. With pressure increments sufficiently small, the net forces and geometry change gradually so that the unknown parameters for each pressure level are fairly accurately predicted by extrapolation thus reducing the required number of iterations. To further the investigation, unlimited elasticity was assumed and the analysis was carried out beyond the realistic load levels using two different ratios of the elastic stiffnesses of the cables.

The edge rings of a skew net mutually rotate under axisymmetric loads including a uniform pressure. The effect is strongly nonlinear (Fig. 5) and in the absence of prestress the graph would have a vertical tangent at the onset of pressure loading. On the other hand, because of the polar symmetry of the net, there must be no edge ring rotation under any polar-cyclic load.

Under a uniform external pressure, the net equator shrinks, shifts downward and, for both ratios of cable stiffnesses, asymptotically approaches almost the same location at about $0.4L_z$ from the upper ring. Under an internal pressure, the equator expands, shifts toward the smaller ring, reaches it and leaves the net.

Quite unexpected was the evolution of the cable forces in loading. In conventional prestressed cable systems under a transverse load, the elastic deformation always causes tension to increase in one array of cables and to decrease in the other. The only way of preventing the unloading cables from disengagement is to increase the prestress, but this is counterproductive for the load-carrying cables. Surprisingly, the geodesic net in consideration does not behave this way; under a uniform pressure, either internal or external, tension increases in both cable arrays (Fig. 6). The explanation lies in the mutual rotation of the edge rings required by torsional equilibrium. Although very small, this kinematic displacement has a strong force-leveling effect offsetting the above unfavorable outcome of the elastic deformation. As a result, both arrays share in supporting the applied load and the prestress requirement is appreciably reduced.

Chebyshev Nets

A Chebyshev net is one with rhombic cells. To preserve this characteristic property, all the intersections must be fixed which reduces the kinematic mobility of the net as compared with a geodesic net. It was proved by Chebyshev that due to the variability of the net angle the net is applicable to any smooth surface. The net is widely used as an analytical model of woven fabrics although fabrics usually allow some fiber slippage and ultimately, with unrestrained slippage, would become geodesic.

A skew axisymmetric Chebyshev net is characterized by

$$r \cos\beta/\sin\omega = a, \; r \cos\alpha/\sin\omega = b \tag{32}$$

so that

$$d\alpha \; ctn\beta = d\beta \; ctn\alpha = -dr/r \tag{33}$$

and

$$r = b \sin\beta - a \sin\alpha \tag{34}$$

It is assumed that parameters a and b are such that $b > a > 0$.

Taking advantage of these formulas in treating equation (14) results in the following closed-form solution:

$$T_z/\sin\theta - M_z(a^2\tan\beta - b^2\tan\alpha)/r(b^2-a^2) = Cr/\sin\omega \tag{35}$$

From here, the equilibrium shape of a Chebyshev net under a given load can be determined explicitly by forward integration. Eliminating T_z and M_z from equation (35) with the aid of equations (7) and (8) shows that

$$2\pi r(T_\alpha \sin\beta + T_\beta \sin\alpha)/(b^2-a^2) = C \tag{36}$$

Finally, the net forces can be expressed in terms of constants C and M_z:

$$2\pi T_\alpha = \frac{r}{\sin^2\omega}\left(C\sin\beta - \frac{M_z\sin\alpha}{b^2-a^2}\right) \tag{37}$$

$$2\pi T_\beta = \frac{r}{\sin^2\omega}\left(\frac{M_z\sin\beta}{b^2-a^2} - C\sin\alpha\right) \tag{38}$$

wherefrom it is seen that these forces, unlike forces in a geodesic net, vary along the cable lengths.

The evolution of the shape of a Chebyshev net in loading is also different from that of a geodesic net. According to equations (17) and (32), in a Chebyshev net subjected to a uniform internal pressure, meridian inflection first sets in at the smaller edge ring and then propagates toward the larger ring. Once again, a conical shape is infeasible while a cylindrical shape occurs under condition (28). In the latter case the net is simultaneously geodesic and Chebyshev which is possible only on developable surfaces.

In contrast to geodesic nets, Chebyshev nets can be analyzed by conventional means, including an appropriately modified finite element method. As to the foregoing statical-kinematic equations, they are valid only in inextensional deformations, in which the net cells remain rhombic with unchanged side lengths. The following example is typical of the kind of a problem where these equations are useful. A long segment of a Chebyshev net suspended from a ring of radius r_3 (Fig. 7) is under tension T_{zo} and supports an axisymmetric solid being

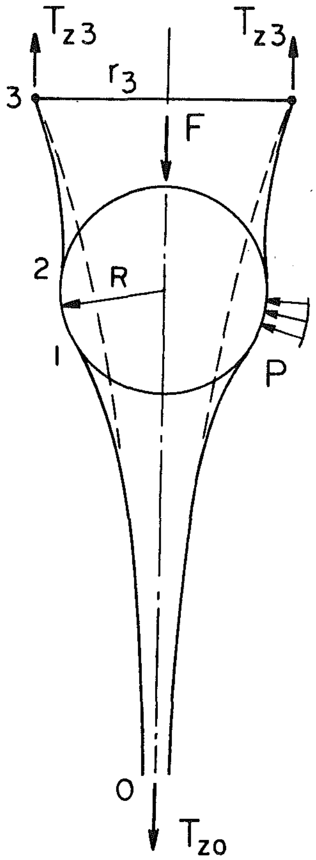

Fig. 7 Axisymmetric solid pushed through prestressed net

pushed through. The net is reflection-symmetric ($\alpha = -\beta = -\omega/2$, $a = b$) so that, according to equations (34) and (35),

$$r = 2b\ \sin\beta,\ 2b = r_3/\sin\beta_3 \tag{39}$$

and

$$T_z\ \cos\beta/\sin\theta = \text{const.} \tag{40}$$

Treating the net as infinitely long implies that initially the net has the form of a parabolic pseudosphere [4] whereby

$$\sin\theta = \cos\beta \tag{41}$$

with $\theta_o = \pi/2$ and $\beta_o = 0$ at $z \to \infty$. Moreover, these are also the properties of the bottom segment (0-1) of the deformed net. As a result,

$$T_z = T_{zo}\ \sin\theta/\cos\beta \tag{42}$$

for the entire net, regardless of its deformed shape and load pattern. Thus, in a contact problem with a solid of a known shape, the axial force is obtained explicitly from equations (42) and (39). For example, for a spherical solid,

$$r = R\ \sin\theta \tag{43}$$

and the force F_p required for equilibrium is

$$F_p = T_{z2} - T_{z1} = T_{zo}\,(c\ \tan\beta_2 - 1) \tag{44}$$

where

$$c = \tan\theta_1 = ctn\beta_1 = 2b/R \tag{45}$$

The resultant F_p of the normal contact pressure P at the net-solid interface does not account for friction. Since the contact zone geometry is known and fixed, the friction force, F_f, is not difficult to evaluate using formulas (13), (39), and (42). With f denoting the coefficient of friction,

$$F_f = 2\pi f \int_{r_1}^{r_2} P\ \tan\theta\ r dr = f T_{zo}\ \frac{c}{c^2-1} + \left(1 - c\,\frac{\cos\theta_2}{\cos\beta_2}\right) \tag{46}$$

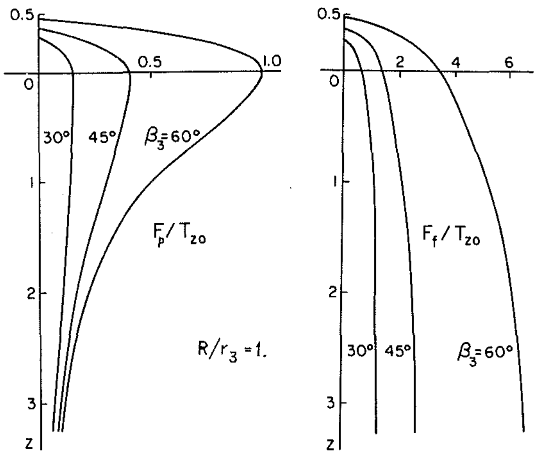

Fig. 8 Resistance forces due to contact pressure and friction

Finally, the axial distance, z_s, between the support ring and the center of the sphere is evaluated as a function of net geometry

$$z_s = -R\cos\theta_2 + \int_{r_2}^{r_3} dr\ \tan\theta = -R\ \cos\theta_2 + 2bk^2 \int_{\theta_2}^{\theta_3} \frac{\sin^2\theta d\theta}{\sqrt{1-k^2\sin^2\theta}} \tag{47}$$

where

$$k^2 = (\tan\beta_1/\tan\beta_2)^2 = 1 + ctn^2\theta_2 - ctn^2\theta_1 \tag{48}$$

Unlike F_p and F_f found in a closed form, the distance z_s is obtainable only numerically. The normalized axial forces due, respectively, to the contact pressure and to the corresponding friction are plotted versus z_s in Fig. 8.

Orthogonal Nets

The generic equation (14) is specified for an orthogonal net by letting $\beta - \alpha = \pi/2$ as follows

$$\frac{d}{dr}\ \frac{T_z}{\sin\theta} - \frac{T_z}{r\ \sin\theta} + \frac{2}{r^2}\ M_z\ ctn\ 2\beta = 0 \tag{49}$$

In contrast to geodesic and Chebyshev nets, further specification of the intrinsic geometric properties of an orthgonal net is required in order to advance the investigation. An important subclass is a semigeodesic net, where one of the arrays (say, β) is geodesic. After substituting $r\ \sin\beta = b$, equation (49) yields

$$bT_z/\sin\theta - M_z\ \cos\beta = C/\sin\beta \tag{50}$$

and, according to equations (7) and (8),

$$2\pi bT_\alpha = C,\ 2\pi bT_\beta = C\ ctn\beta + M_z \tag{51}$$

Thus, in a semigeodesic net under a normal surface load the nongeodesic array is isotensoid. It can be shown that the converse is also true: an orthogonal net with an isotensoid array is semigeodesic.

Orthogonality generally does not preserve in either kinematic or elastic deformations of the net. The significance of this class of nets lies in the obvious analogy between a material orthogonal net and a net of the principal stress trajectories of a membrane. For a given membrane shape and surface pressure, the axial force T_z is readily obtainable, allowing the angle β to be evaluated from equation (49), and the principal forces in the membrane—from equations (7) and (8). The most interesting situation arises when one of the principal forces turns out to be compressive while the membrane is incapable of supporting any compression (a wrinkling membrane). A condition for biaxial tension is obtained by setting $T_\alpha > 0$ in equation (7) which leads to

$$\tan \beta > M_z \sigma_2 / T_z \tag{52}$$

If this inequality is not satisfied by the value of $\tan \beta$ found from equation (49), the stress state of the membrane is uniaxial. Then $T_\alpha = 0 = C$ and, as is seen from equation (51), the force in the geodesic array, which is also the nonzero principal force in a wrinkling membrane, is constant:

$$T_\beta = M_z / 2\pi b \tag{53}$$

The statical-geometric relation (50) now acquires the form

$$\sin\theta \cos\beta = b T_z / M_z \tag{54}$$

from which the shape of the wrinkling membrane is obtainable by forward integration. Note that the foregoing equations are valid for an arbitrary normal surface load. It is also assumed that $\beta \neq 0$; a comprehensive treatment of reflection-symmetric membranes ($\beta = 0$) under a uniform pressure is given in [10].

In the absence of surface loads, T_z = const and equation (54) describes a one-sheet hyperboloid of revolution with the β-array as linear generators. Although this is the generic shape of a wrinkling axisymmetric membrane under edge loads [11], parameters of a particular hyperboloid depend on the original membrane geometry in a complicated way. The fact is that a linear generator is formed by one of the original membrane geodesics connecting the two edge rings. For a given magnitude of the mutual rotation of the edge rings, this geodesic is unique in that its length equals the distance between its end points after torsion; the lengths of all other geodesics exceed the respective distances between their termination points.

References

1 Hanging roofs, 1963, *Proc. of 1962 IASS Colloquim in Paris*, North Holland, Amsterdam.

2 Kreyszig, E., 1968, *Introduction to Differential Geometry*, Univesity of Toronto Press.

3 Kuznetsov, E. N., 1966, "On the Problem of Rational Design of Cable Systems," *Proc. of IASS Congress in Lengingrad.*

4 Kuznetsov, E. N., 1982, "Axisymmetric Static Nets," *Int. J. of Solids Structures*, Vol. 18, pp. 1103–1112.

5 Kuznetsov, E. N., and Groom, J. J., 1984, "Prestressed Cooling Tower," U.S. Patent 4,473, 976.

6 Landmann, A. E., 1985, "Analysis of Axisymmetric Geodesic Nets," Thesis, Dept. of General Engineering, Univ. of Illinois/Urbana.

7 Pipkin, A. C., and Rivlin, R. S., 1963, "Minimum-Weight Design for Pressure Vessels Reinforced with Inextensible Fibers," ASME JOURNAL OF APPLIED MECHANICS, Vol. 30, pp. 103–108.

8 Read, W. S., 1963, "Equilibrium Shapes for Pressurized Fiberglass Domes," *J. of Engineering for Industry*, Vol. 85, pp. 115–118.

9 Rivlin, R. S., 1959, "The Deformation of a Membrane Formed by Inextensible Cords," *Arch. Rat. Mech. Anal.*, Vol. 2, pp. 447–476.

10 Wu, C. H., 1974, "The Wrinkled Axisymmetric Air Bags Made of Inextensible Membrane," ASME JOURNAL OF APPLIED MECHANICS, Vol. 41, pp. 963–968.

11 Zak, M., 1982, "Statics of Wrinkling Films," *J. of Elasticity*, Vol. 12, pp. 51–63.

J. Cagan[1]
Assoc. Mem. ASME

L. A. Taber
Assoc. Mem. ASME

Department of Mechanical Engineering,
University of Rochester,
Rochester, NY 14627

Large Deflection Stability of Spherical Shells With Ring Loads

Large deflections of shallow and deep spherical shells under ring loads are studied. The axisymmetric problem is solved through a Newton-Raphson technique on discretized nonlinear shell equations. Comparison of computed load-deflection curves to experimental data from both thick and thin shells generally shows good agreement in peak loads and the type of instability. For a point load, the load increases monotonically with deflection; as the ring radius increases, transition-type (snap-through) and then local buckling occurs. In addition, the pre- and post-buckled mechanical behaviors of the shell are examined.

Introduction

Previous work pertaining to the deformation of spherical shells under ring loads has been rather limited. Experimental work was done by Evan-Iwanowski et al. (1963), who investigated buckling of thin, shallow, spherical shells with this type of loading. They found that if the ring diameter is less than some minimum value, the shell does not buckle. Otherwise, the shell either snap-buckles or, for large rings, buckles locally (Fig. 1). Snap-through, or transition buckling (Fig. 1*a*), implies that past a critical point of a load versus deflection curve, a smooth, continuous transition takes place from relatively stiff ring-type to a softer point-load-type behavior, as a dimple of reversed curvature forms gradually. On the other hand, with ring deflection specified, local buckling (Fig. 1*b*) exhibits a discontinuity at a critical point as the load jumps suddenly to a much smaller value, with the dimple forming abruptly. Since local buckling curves also include a deflection snap (for a specified load), we will refer to "snap-through" buckling as "transition" buckling herein.

Taber (1983) presented experimental results for the deflection of both fluid-filled and empty hemispherical rubber shells due to solid cylindrical indenters. As the deflection increases, the load-deflection curves for an empty shell initially resemble those due to a flat plate but eventually fall back toward the point-load curve as the indenter becomes immersed within a dimple of reversed curvature, with the indenter now applying essentially a ring load. The deformation can occur with or without a peak in load, depending on the indenter radius. As found by Evan-Iwanowski et al. (1963), there is a minimum radius below which no peak occurs; yet this is a different situation in that the indenter acts as a ring load only after it is immersed within the dimple.

Pieces of the ring load problem have been studied analytically. Using an energy method, Chien and Hu (1956) computed the critical load for "oil canning," or transition buckling, of a thin spherical cap due to a ring load. With an implicit numerical technique, which involved a Newton-Raphson scheme on integral matrices, Parnell (1984) solved Reissner's (1950) nonlinear shell equations for moderate rotation. Limited application to shallow spherical caps deformed by ring loads showed only transition-type buckling. In other work, Wan (1984) constructed asymptotic solutions to study the fundamental behavior for polar dimpling of spherical shells with ring and other similar loadings, while Updike and Kalnins (1970, 1972) examined the related problem of a spherical shell compressed between rigid plates.

In this paper, we will apply Parnell's (1984) method to steep and shallow, thin and thick, spherical shells. Both local and transition buckling will be studied, along with the mechanical

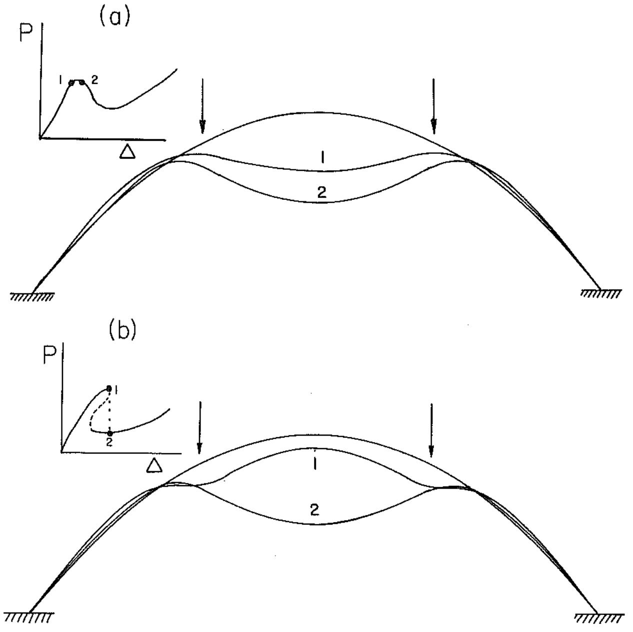

Fig. 1 Typical load-deflection curves and corresponding deflection shapes for ring load on spherical shell: (*a*) transition buckling; (*b*) local buckling

---

[1] Presently at the Eastman Kodak Company, Engineering Technology Laboratory, Rochester, NY 14650.

Contributed by the Applied Mechanics Division for publication in the JOURNAL OF APPLIED MECHANICS.

Discussion on this paper should be addressed to the Editorial Department, ASME, United Engineering Center, 345 East 47th Street, New York, N.Y. 10017, and will be accepted until two months after final publication of the paper itself in the JOURNAL OF APPLIED MECHANICS. Manuscript received by ASME Applied Mechanics Division, October 31, 1985; final revision April 24, 1986.

behavior of the shell around the critical points. Comparison with experimental data from Evan-Iwanowski et al. (1963) demonstrates the accuracy of the analytical solution. In addition, computed results are compared to new data from experiments on deep shells deflected by solid indenters.

Solution Technique

In state-vector form, the nonlinear equations of Reissner (1950) for moderate rotation of a thin shell of revolution are (Parnell, 1984)

$$\frac{d\mathbf{y}}{ds} = \mathbf{A}\cdot\mathbf{y} + \mathbf{N}(\mathbf{y}) \tag{1}$$

where the solution vector is

$$\mathbf{y}^T = [rM_\phi, rH, rV, \chi, h, v], \tag{2}$$

the linear terms are given by

$$\mathbf{A} = \begin{bmatrix} \nu\cos\phi & \sin\phi & -\cos\phi & \frac{Et^3}{12}\frac{\cos^2\phi}{r} & 0 & 0 \\ 0 & \frac{\nu}{r}\cos\phi & -\frac{\nu}{r}\sin\phi & 0 & \frac{Et}{r} & 0 \\ 0 & 0 & 0 & 0 & 0 & 0 \\ (rEtc^2)^{-1} & 0 & 0 & -\frac{\nu}{r}\cos\phi & 0 & 0 \\ 0 & \frac{1-\nu^2}{rEt}\cos^2\phi & \frac{1-\nu^2}{rEt}\sin\phi\cos\phi & -\sin\phi & -\frac{\nu}{r}\cos\phi & 0 \\ 0 & \frac{1-\nu^2}{rEt}\sin\phi\cos\phi & \frac{1-\nu^2}{rEt}\sin^2\phi & \cos\phi & -\frac{\nu}{r}\sin\phi & 0 \end{bmatrix}, \tag{3}$$

the nonlinear contribution is

$$\mathbf{N}(\mathbf{y}) = \begin{bmatrix} \chi(rH\cos\phi + rV\sin\phi) \\ 0 \\ 0 \\ 0 \\ -\chi^2\cos\phi/2 \\ -\chi^2\sin\phi/2 \end{bmatrix}, \tag{4}$$

and surface load terms are deleted.

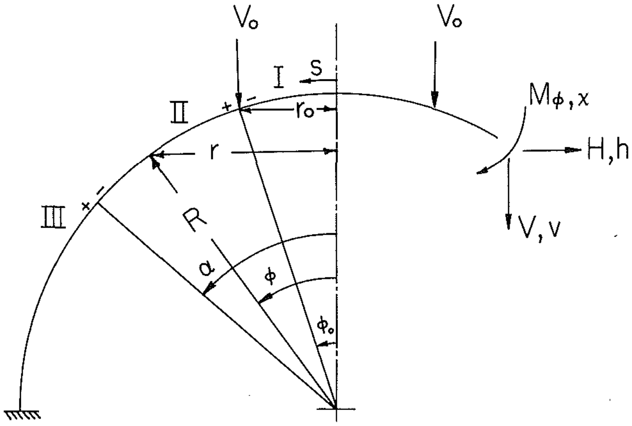

Fig. 2 Geometry and force system for spherical shell with ring load

In these equations M_ϕ, H, V, χ, h, v are the meridional bending moment, horizontal and vertical force resultants, rotation, and horizontal and vertical displacements, respectively (Fig. 2). Also, ν is Poisson's ratio, E is Young's modulus, and t is the shell thickness.

Consider now a vertical ring load of radius r_0 and magnitude $P = 2\pi r_0 V_0$ on a clamped spherical shell of radius R (Fig. 2). The appropriate regularity and boundary conditions are

$$rV = \chi = h = 0 \quad \text{at} \quad \phi = 0, \tag{5}$$

$$\chi = h = v = 0 \quad \text{at} \quad \phi = \phi_e, \tag{6}$$

where ϕ_e is the edge angle. The numerical solution to equation (1) is obtained by splitting the shell into two regions separated by the ring load and enforcing the continuity conditions

$$\mathbf{y}^+ = \mathbf{y}^- + [0, 0, P/2\pi, 0, 0, 0]^T \quad \text{at} \quad \phi = \phi_0 \tag{7}$$

where + and − denote the regions outside and inside the load, respectively. With the deflection $v^+ = v^- = \Delta$ specified at $\phi = \phi_0$, the corresponding load P is computed.

Each region is divided into N subintervals, and an initial solution is guessed. With a first-order polynomial employed to integrate the discretized shell equation (1), a Newton-Raphson method is used to converge on the correct solution. See Parnell (1984) or Cagan (1985) for more detail.

Care must be taken to include an adequate number of subintervals within the boundary layers near the load, the dimple edge, and the shell edge, where bending stresses change rapidly. Thus, the shell is actually divided into three regions (Fig. 2); regions I and II join at $\phi = \phi_0$, and, since the location of the dimple edge is not known *a priori*, regions II and III meet at some user-defined point $\phi = \alpha$ to allow for high accuracy within the decaying boundary layers. The decay angle is approximated as

$$\phi_{\text{dec}} = \pi\left(\frac{2c}{R}\right)^{1/2}, \tag{8}$$

where

$$c^2 = \frac{t^2}{12(1-\nu^2)}. \tag{9}$$

Load-deflection curves were found by starting at zero load with $\mathbf{y} = \mathbf{0}$ and incrementing the deflection a small amount. After convergence, this solution became the initial guess at the next deflection, and so on. Based on the energy quantity

$$\|\mathbf{y}^{(k)}(s)\|_E = (|rM_\phi\cdot\chi| + |rH\cdot h| + |rV\cdot v|), \tag{10}$$

convergence at each point of the shell is obtained when the relative difference between the new and old solutions

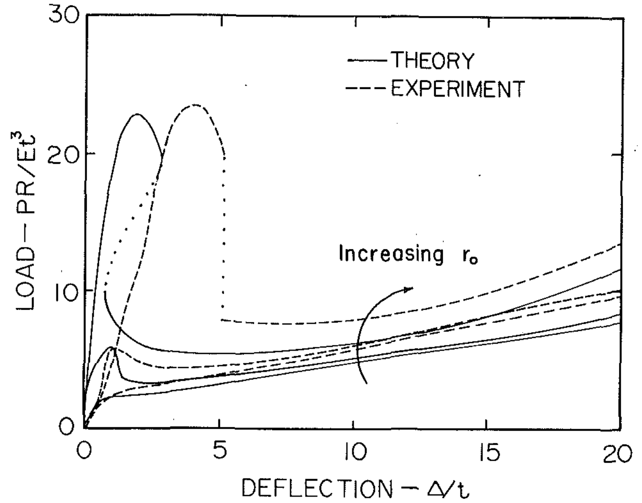

Fig. 3 **Comparison of calculated load-deflection curves with experimental data of Evan-Iwanowski et al. (1963): R = 254 mm; R/t = 666.7; r_0 = 6.35, 12.7, 25.4 mm**

$$\epsilon = \frac{\|\mathbf{y}^{(k+1)}(s)\|_E - \|\mathbf{y}^{(k)}(s)\|_E}{\|\mathbf{y}^{(k+1)}(s)\|_E} \tag{11}$$

is less than a prescribed amount.

Shallow Shell

Evan-Iwanowski et al. (1963) presented experimental data for ring loads on die-pressed, plastic, shallow spherical shells. Figure 3 compares their experimental and our analytical results for a clamped shell of radius $R = 254$ mm.

As shown in Fig. 3, the load versus deflection curves for the smallest ring ($r_0 = 6.35$ mm) agree in general with no instabilities. Meanwhile, the experimental and theoretical results for the larger rings show similar trends, but the computed curves are steeper before the peaks. In addition, the calculated results peak at somewhat lower values of deflection than do the experimental results. This discrepancy is because the present model does not allow for slippage under the load; thus, the arc length of the shell inside the ring is assumed to remain constant. In reality there is not enough friction to maintain this constant contact and slippage does occur. Therefore, our model is slightly stiffer and buckles before the experimental shells.

While the second smallest ring ($r_0 = 12.7$ mm) demonstrates transition buckling, the largest ring ($r_0 = 25.4$ mm) illustrates local buckling with a discontinuity in the load. The analysis shows that these latter curves possess multiple equilibria over certain regions of deflection similar to the buckling of circular cylinders with axial load (Timoshenko and Gere, 1961). In order to obtain the section of the curve past the peak, the point-load solution at $\Delta/t = 8.2$ was used as an initial guess for larger diameters at nearby deflections. Then the deflection was incremented (decremented) as before to obtain the remainder of the curve.

Figure 4 shows the changing shape of the shell for the largest ring load ($r_0 = 25.4$ mm). At $\Delta/t = 2.88$, there is an abrupt change in shape. The dimple of reversed curvature forms suddenly during local buckling as the shell moves to a lower strain energy configuration. On the other hand, in transition buckling, the dimple forms gradually (see Fig. 1*a*).

Figure 5 shows the nondimensional bending stress ($\sigma R/2cE$; $\sigma = 6M_\phi/t^2$) versus meridional angle for the same shell and deflections. The bending stresses for the first two deflections (curves 1 and 2), which occur before buckling, peak under the load and then decay to zero in both directions. After the dimple forms during buckling, however, relatively constant bending stress develops inside the ring (curves 3 and 4). This behavior agrees with the finding of Ashwell (1960), who studied the point-load solution to this problem and showed that a constant bending moment is necessary to hold the dimple in a state of reversed curvature, i.e., as an applicable surface.

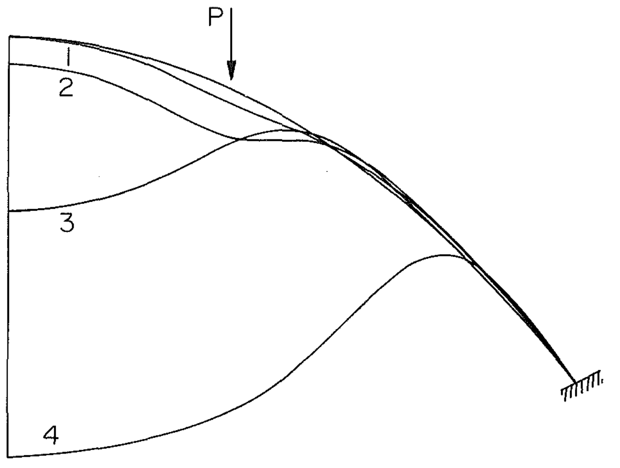

Fig. 4 **Computed deformed configurations for shallow shell under ring load (r_0/R = 0.1; R/t = 666.7) for Δ/t = 0, 0.967, 2.88, 19.5. Local buckling occurs from configurations 2 to 3 at Δ/t = 2.88.**

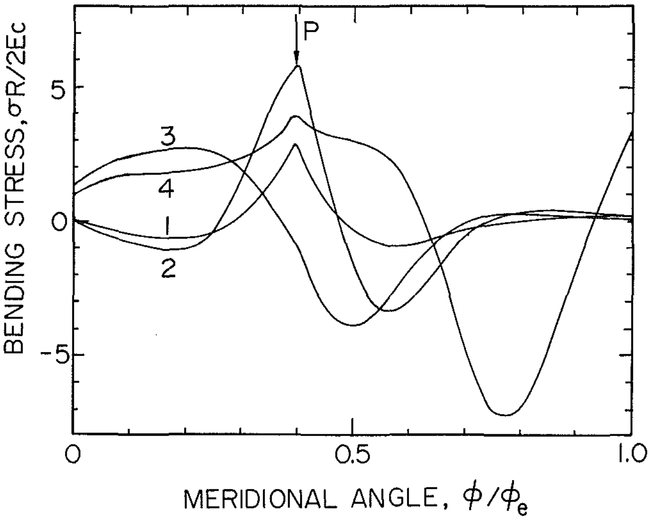

Fig. 5 **Bending stress distribuitons along shallow shell with ring load (r_0/R = 0.1; R/t = 666.7). Curve numbers correspond to configurations of Fig. 4.**

The largest deflection (curve 4) shows peaks in stress under the load, at the dimple edge, and at the clamped shell edge. Just after buckling (curve 3) the trends are different; the peak at the dimple edge occurs, but the stress under the load is quite small. Here, the unstable shell transfers from a high energy state to a low energy condition, and so the load sees minimal restraint. The stress relaxes under the load until the shell stabilizes after buckling, and then additional load is applied.

Deep Shell

The behavior of deep shells under ring loads is similar to that of shallow shells. Taber (1983) presented experimental results for solid, cylindrical indenter loads on clamped, hemispherical rubber shells ($R \simeq 25$ mm). Although the present analysis is actually for pure ring loads, some conclusions can be made by comparing the results of the two problems. In Figs. 6(*a*)-6(*c*), new data is presented from those experiments,

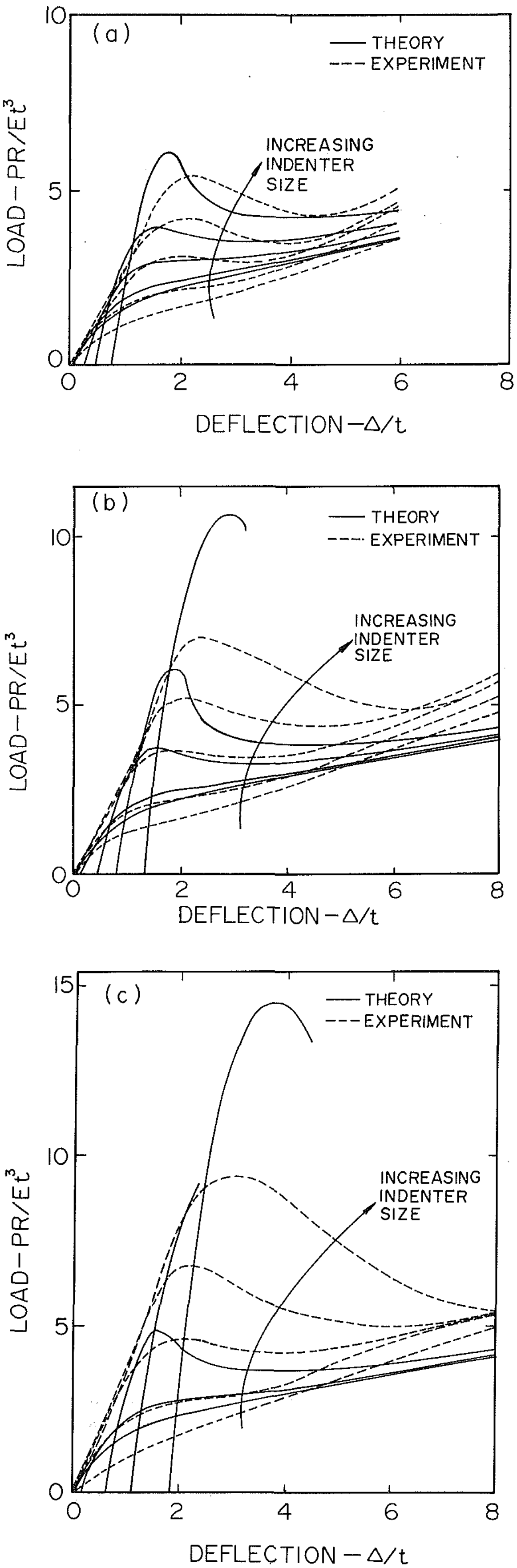

Fig. 6 Comparison of calculated load-deflection curves with experimental data from hemispherical shells with indenter loads: $R \simeq 25$ mm; $r_0 = 1.25, 3.75, 7.5, 10.0, 12.7$ mm; (*a*) $R/t = 6.0$; (*b*) $R/t = 9.6$; (*c*) $R/t = 12.9$

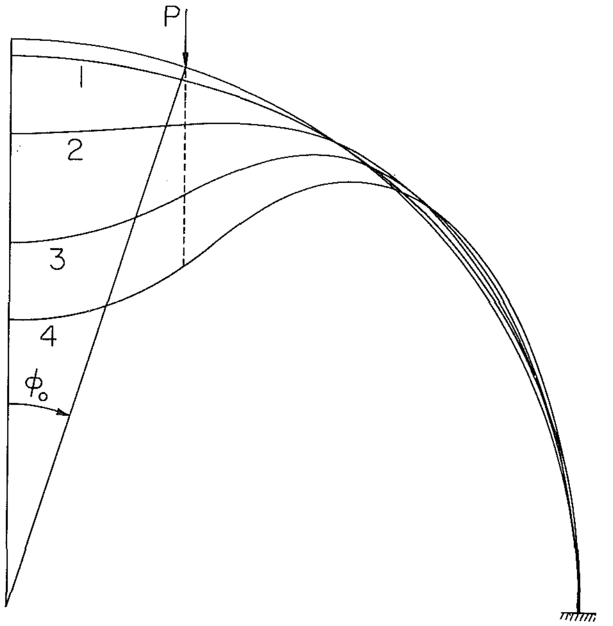

Fig. 7 Computed deformed configurations for hemispherical shell under ring load ($r_0/R = 0.3$; $R/t = 12.9$) for $\Delta/t = 0, 0.945, 2.27, 3.91, 5.55$

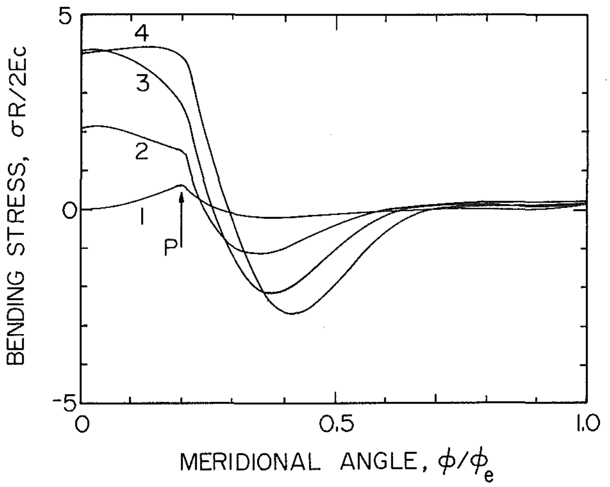

Fig. 8 Bending stress distribution along hemispherical shell with ring load ($r_0/R = 0.3$; $R/t = 12.9$). Curve numbers correspond to configurations of Fig. 7.

along with calculations from our model. Relatively thick to thin shells (R/t = 6.0, 9.6, 12.9) deformed by indenters of various radii are considered. As with the shallow shell, small indenters show no buckling. The discrepancy in load magnitude may be due to shear deformation, which was not included in the analysis. As the indenter size increases, transition buckling appears; the curves initially follow the relatively stiff behavior of a flat plate and then approach the limiting point load case.

Note that the computed solution does not begin at the origin. When the ring load forms, its point of zero deflection occurs at $\Delta = R\ (1 - \cos\phi_0)$ as measured from the apex, which was taken as the experimental reference point. Thus, the load initially is lower analytically than experimentally. But after the indenter makes full contact with the shell, forming a ring load, the solution approaches the experimental data.

Figure 7 shows the ring load representation for the indenter. Physically, a ring allows the shell inside the load ($\phi < \phi_0$) to penetrate above the point of load application. The solid indenter, however, obstructs this penetration and forces the entire area within the indenter radius to form a dimple from the start. Thus, the experimental results show transition-buckling at smaller loads than do the analytic results, and local buckling does not occur under solid indenters.

The theoretical results from the thinner shells show local buckling for the larger indenters (Figs. 6*b*, *c*). For the thickest shell, however, this type of instability does not occur (Fig. 6*a*); due to the high bending stiffness, the ring forces the dimple to form from an early deflection, similar to the solid indenter case. The sharpness of the peaks during the transition buckling is also lost as the shell becomes thicker, approaching a three-dimensional solid, which does not buckle. As the deflection increases to large values, the theoretical and experimental curves diverge. The calculations are limited to moderate rotations and small strains, but at very large deflections, the physical shells undergo large rotations and large bending strains. In addition, the effects of material nonlinearity (Taber, 1985) may contribute to the difference.

Figure 7 demonstrates the calculated deflected shape of the thinnest shell ($R/t = 12.9$) with a 7.5 mm radius indenter. Since this indenter shows only transition buckling, these results illustrate a smooth formation of the dimple, unlike the abrupt change found in local buckling (Fig. 4).

Figure 8 displays the bending stress for the same shell and deflections. A negative peak forms at the dimple edge and then the stress decays toward zero before increasing slightly near the clamped edge ($\phi_e = \pi/2$). An abrupt change in slope occurs under the load. Again, as in Fig. 5, a relatively constant stress forms inside the dimple as the deflection increases.

Conclusions

The results of this study show that, for a given value of R/t for a spherical shell with a ring load of radius r_0, there exist characteristic ring load radii r_1 and r_2 with $r_1 < r_2 < R$ such that:

(1) For $r_0 < r_1$, no buckling occurs and the solution resembles that for a point load.

(2) For $r_1 < r_0 < r_2$, transition buckling takes place in which the load rises to a peak and then drops off toward the point-load curve.

(3) For $r_2 < r_0 < R$, the shell buckles locally, with an abrupt change in shape and load at a critical deflection.

In addition, the values of r_1 and r_2 increase as the shell thickness increases. These conclusions apply to both shallow and deep shells with clamped edges. For a solid, cylindrical indenter, the behavior is similar, but local buckling does not occur.

References

Ashwell, D. G., 1960, "On the Large Deflection of a Spherical Shell with an Inward Point Load," *Proceedings of the IUTAM Symposium on the Theory of Thin Elastic Shells*, Koiter, W. T., ed., North Holland, Amsterdam, pp. 43–63.

Cagan, J., 1985, "Large Deflection of a Deep Spherical Shell Due to Rigid Indenters of Various Radii," Master's Thesis, University of Rochester.

Chien, W. Z., and Hu, H. C., 1956, "On the Snapping of a Thin Spherical Cap," *Proceedings of the 9th International Congress of Applied Mechanics*, Brussels, Belgium, pp. 309–320.

Evan-Iwanowski, R. M., Loo, T. C., and Tierney, D. W., 1963, "Local Buckling of Shells," *Developments in Mechanics*, Vol. 2, Ostrach, S., and Scanlan, R. H., eds., Pergamon, New York, pp. 221–251.

Parnell, T. K., 1984, "Numerical Improvement of Asymptotic Solutions and Nonlinear Shell Analysis," Ph.D. Thesis, Stanford University.

Reissner, E., 1950, "On Axisymmetrical Deformations of Thin Shells of Revolution," *Proceedings of the Third Symposium in Applied Mathematics*, McGraw-Hill, New York, pp. 27–52.

Taber, L. A., 1983, "Compression of Fluid-Filled Spherical Shells by Rigid Indenters," ASME JOURNAL OF APPLIED MECHANICS, Vol. 50, pp. 717–722.

Taber, L. A., 1985, "On Approximate Large Strain Relations for a Shell of Revolution," *International Journal of Nonlinear Mechanics*, Vol. 20, pp. 27–39.

Timoshenko, S. P., and Gere, J. M., 1961, *Theory of Elastic Stability*, McGraw-Hill, New York.

Updike, D. P., and Kalnins, A., 1970, "Axisymmetric Behavior of an Elastic Spherical Shell Compressed Between Rigid Plates," ASME JOURNAL OF APPLIED MECHANICS, Vol. 37, pp. 635–640.

Updike, D. P., and Kalnins, A., 1972, "Axisymmetric Postbuckling and Nonsymmetric Buckling of a Spherical Shell Compressed Between Rigid Plates," ASME JOURNAL OF APPLIED MECHANICS, Vol. 39, pp. 172–178.

Wan, F. Y. M., 1984, "Shallow Caps with a Localized Pressure Distribution Centered at the Apex," *Flexible Shells, Theory and Applications*, Axelrad, E. L., and Emmerling, F. A., eds., Springer-Verlag, New York, pp. 124–145.

M. El-Raheb

P. Wagner

Technical Staff,
Jet Propulsion Laboratory,
California Institute of Technology,
Pasadena, Calif. 91109

Damped Response of Shells by a Constrained Viscoelastic Layer

Vibration absorbers are introduced into an asymmetric configuration of thin cylinders and tori enclosing an acoustic medium. The absorbers consist of thin axial strips bonded to the cylinder with a thin viscoelastic layer. The constrained layer dissipates the energy of relative motions between strip and cylinder. The absorber is most effective on response modes with two or more circumferential waves. The use of transfer matrices is extended to the coupled cylinder-absorber system.

Introduction

Constrained viscoelastic layers have been used to dissipate vibrational energy in beams (Kerwin, 1959, and DiToranto et al., 1965), thin rings (D. Toranto et al., 1973), and thin cylinders (Lu, 1977). The idea relies on deforming a thin viscoelastic layer sandwiched between the structure to be damped and a secondary oscillator with prescribed dynamic characteristics. In the case of the cylinder, thin strips of metal are bonded along generators at equal angular intervals about the circumference. Relative motions between strip and cylinder wall are reduced by a dissipation of vibrational energy. Most of the energy is lost by shear of the constrained layer.

A viscoelastic material exhibits maximum damping when subjected to strain rates that fall within the transition regime between glassy and rubbery states. Its thickness can be optimized to produce this state for a given operating frequency and response amplitude. In some cases, however, the need for a thicker layer to optimize damping is opposed by the need for a thinner layer in order to raise the critical frequency of the single degree-of-freedom oscillator defined by the strip's mass and the layer's stiffness. Above the critical frequency, elastic waves propagate along the strip amplifying the response in resonance. The two requirements can be met by judiciously tuning the inertial properties of the strip.

Previous work by Lu (1977) analyzed simply supported, thin cylinders where discrete absorbers are distributed along generators of each cylinder. The work described here extends a more general analysis to asymmetric configurations composed of thin cylinders and tori. This method requires the derivation of new transfer matrices of the damped system with vibration absorbers formed by strips bonded to a cylinder by a thin viscoelastic layer. Transfer matrices of the bare shells have been derived by El-Raheb and Wagner (1985a). Since the layer is sufficiently thin to be uniaxially stressed, forces at each point on its boundary are proportional to displacement of the same point relative to the opposite boundary. Each strip is approximated as a Euler beam.

Computations proceed more quickly by assuming that each strip is free from tractions at the two ends which reduces the size of the transfer matrix through partial elimination. Another step which accelerates computations is to treat the round-off error that arises with very long segments. A numerical method termed selective abbreviation is faster than the alternative of using more and shorter segments (El-Raheb and Wagner, 1985a, 1985b), especially for long systems with length to radius ratio greater than 50.

Shell walls are coupled to an internal fluid through a low frequency approximation to the acoustic pressure and added mass. This approximation is acceptable for frequencies below cut-off of the first transverse acoustic wave in a cylinder with rigid walls. Finally, the effects on response of a damped absorber are studied for a symmetric L-shaped configuration made of two cylinders joined by a torus and excited mechanically.

I Analysis

Figure 1 illustrates the coupled system of cylinder-layer-strip, and Fig. 2 establishes the convention on displacements and forces acting on an element. Subscripts s, c, and b denote strip, cylinder, and viscoelastic layer variables, respectively. In

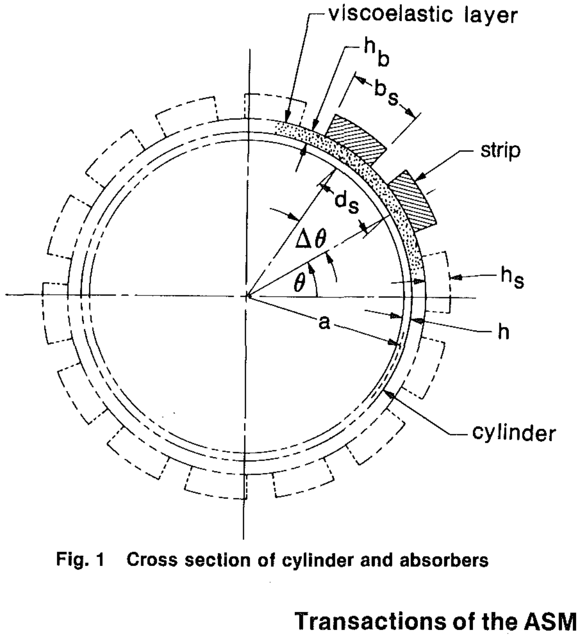

Fig. 1 Cross section of cylinder and absorbers

Contributed by the Applied Mechanics Division for publication in the JOURNAL OF APPLIED MECHANICS.

Discussion on this paper should be addressed to the Editorial Department, ASME, United Engineering Center, 345 East 47th Street, New York, N.Y. 10017, and will be accepted until two months after final publication of the paper itself in the JOURNAL OF APPLIED MECHANICS. Manuscript received by ASME Applied Mechanics Division, October 7, 1985.

order to show how equations for cylinders and strips, which are topologically very unlike, can be combined into a consistent, general system, a skeleton of the derivation is now out lined. Details of the operators and variables must await specific treatments in the section on transfer matrices.

Let $\mathbf{D}_c$ be the matrix of partial differential operators governing the cylinder's motion and $\mathbf{g}_c = \{u_c, v_c, w_c, w_c'\}^T$ the cylinder's displacement vector. Also let $\mathbf{p}_c$ be the jth vector of surface tractions applied on the cylinder. Then dynamic equilibrium requires

$$\mathbf{D}_c\mathbf{g}_c = \sum_j \mathbf{p}_{cj} \tag{1}$$

Furthermore let the reaction from the strip to the cylinder be concentrated as a line load $\mathbf{F}_{cj}$ acting midway of the strip's width at angular position θ_j. The line load is equal to the stress in the layer

$$\mathbf{F}_{cj} = \mathbf{k}_{b1}\mathbf{g}_c(\theta_j) - \mathbf{k}_{b2}\mathbf{g}_{sj} \tag{2}$$

where $\mathbf{g}_{sj} = \{u_s, v_s, w_s, \theta_{xs}, \theta_{ys}, \theta_{zs}\}_j^T$ is the displacement vector of the jth strip and $\mathbf{k}_{b1}$, $\mathbf{k}_{b2}$ are matrices with coefficients that depend on bond geometric and material properties. Expanding (2) in Fourier series about θ gives a correspondence between the coefficients of $\mathbf{F}_{cj}$ and $\mathbf{p}_{cj}$

$$\mathbf{p}_{cj} = \frac{1}{\pi a} \sum_{n'} (\mathbf{k}_{b1}\mathbf{g}_{cn'} \cos n'\theta_j$$

$$-\mathbf{k}_{b2}\mathbf{g}_{sn'} \cos n'\theta_j) \sum_n \cos n\theta \cos n'\theta_j \tag{3}$$

where $\mathbf{g}_{cn}$ and $\mathbf{g}_{sn}$ are the displacement vectors in harmonic space. Expanding $\mathbf{D}_c$ in terms of its harmonics $\mathbf{D}_{cn}$, substituting equation (3) in (1) and using orthogonality of cos $n\theta$ yields

$$\mathbf{D}_{cn}\mathbf{g}_{cn} = \frac{1}{\pi a} \sum_{n'} (\mathbf{k}_{b1}\mathbf{g}_{cn'} - \mathbf{k}_{b2}\mathbf{g}_{sn'}) \sum_j \cos n'\theta_j \cos n\theta_j \tag{4}$$

Note that variable inter-strip spacing d_{sj} couples the different harmonics as indicated by equation (4). If the strips are evenly spaced about the circumference, i.e., d_{sj} and $\Delta\theta_j$ are held constant for all j, then

$$\sum_j \cos n'\theta_j \cos n\theta_j = \frac{N_s}{2}(\delta_{nn'} + \delta_{0n}\delta_{0n'}) \tag{5}$$

where N_s is the total number of strips and δ is the Kronecker delta function. Noting that $N_s/(2\pi a) = 1/d_s$, equation (4) simplifies and uncouples as

$$\mathbf{D}_{cn}\mathbf{g}_{cn} = \frac{1}{d_s}(\mathbf{k}_{b1}\mathbf{g}_{cn} - \mathbf{k}_{b2}\mathbf{g}_{sn}) \tag{6}$$

Furthermore the equation of the jth strip forced by the reaction from the cylinder is

$$\mathbf{D}_s\mathbf{g}_{sj} = \mathbf{k}_{b2}\mathbf{g}_{sj} - \mathbf{k}_{b1}\mathbf{g}_c(\theta_j) \tag{7}$$

where $\mathbf{D}_s$ is the matrix of ordinary differential operators governing the motion of the strip. $\mathbf{D}_s$ applies to all θ_j. Expanding $\mathbf{g}_{sj}$ and $\mathbf{g}_c(\theta_j)$ in harmonic components

$$\mathbf{g}_{sj} = \sum_n \mathbf{g}_{sn} \cos n\theta_j,\ \mathbf{g}_c(\theta_j) = \sum_n \mathbf{g}_{cn} \cos n\theta_j$$

then substituting in equation (7) yields

$$\sum_n \mathbf{D}_s\mathbf{g}_{sn} \cos n\theta_j = \sum_n (\mathbf{k}_{b2}\mathbf{g}_{sn} - \mathbf{k}_{b1}\mathbf{g}_{cn}) \cos n\theta_j \tag{8}$$

Since equation (8) is valid for all θ_j then

$$\mathbf{D}_s\mathbf{g}_{sn} = \mathbf{k}_{b2}\mathbf{g}_{sn} - k_{b1}\mathbf{g}_{cn} \tag{9}$$

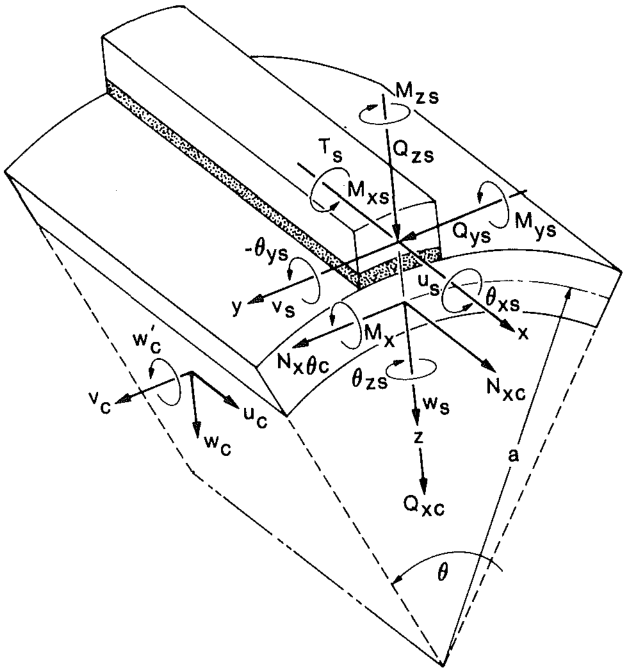

Fig. 2 **Elemental forces and displacements**

Equations (6) and (9) constitute a complete set in harmonic space with components $\mathbf{g}_{sn}$ and $\mathbf{g}_{cn} \forall\ n \geq 0$.

A Transfer Matrix of Damped Cylinder. The different terms (6) and (9) are now derived for the damped cylinder. In this section, all equations and variables are in harmonic space where subscript n has been omitted for shortness.

The strip and layer are modeled by an Euler beam on visco-elastic foundation. As expressed by equation (9) the stress in the layer is proportional to the relative displacement between cylinder and strip. For periodic motions in time, the 12th order set of equations is

$$E_sA_su_s'' = -\rho_sA_s\omega^2u_s - k_{bs}^*\left(u_c - u_s + \frac{h}{2}w_c' - \frac{h_s}{2}w_s'\right) \tag{10a}$$

$$E_sI_{zs}v_s'''' = \rho_sA_s\omega^2v_s + k_{bs}^*\left(v_c - v_s + \frac{h}{2}\frac{n}{a}w_c + \frac{h_s}{2}\theta_{xs}\right) \tag{10b}$$

$$E_sI_{ys}w_s'''' = \rho_sA_s\omega^2w_s + k_{be}^*(w_c - w_s) \tag{10c}$$

$$G_sJ_s\theta_{xs}'' = -\rho_sI_{xs}\omega^2\theta_{xs} + k_{bs}^*\frac{h_s}{2}\left(v_c - v_s + \frac{h}{2}\frac{n}{a}w_c\right.$$

$$\left.+\frac{h_s}{2}\theta_{xs}\right) + k_{be}^*\left(-\frac{n}{a}w_c + \theta_{xs}\right)\frac{b_s^2}{12} \tag{10d}$$

where ( )′ is the derivative with respect to the axial coordinate x, n is the circumferential wave number of the cylinder; (E_s, G_s) are the Young's and shear moduli; (I_{xs}, I_{ys}, I_{zs}) are the cross-section moments of inertia about local orthogonal axes x,y,z; ρ_s,A_s,J_s are the mass density, cross-sectional area and torsional rigidity; and (k_{be}^*, k_{bs}^*) are the extensional and shear stiffness of the layer

$$k_{be}^* = E_b^*b_s/h_b,\ k_{bs}^* = G_b^*b_s/h_b$$

where now (E_b^*, G_b^*) are the complex moduli of the viscoelastic material for periodic motions in time and are functions of frequency and temperature. All other parameters and dependent variables are depicted in Figs. 1 and 2. Since the viscoelastic layer is thin compared to the strip width, i.e., $h_b/b_s < < 1$, the approximation of uniaxial strain applies. Therefore the equivalent extensional modulus of elasticity $E_b^* \simeq (2(1-\nu_b)/(1-2\nu_b))\ G_b^*$ where $\nu_b \simeq 0.49$ for a typical viscoelastic material.

Equations (10) can be rewritten as a first-order system

$$\mathbf{S}_s' = \mathbf{B}_s \mathbf{S}_s + \mathbf{B}_{sc} \tag{11}$$

where $\mathbf{S}_s = \{T, Q_y, Q_z, M_x, M_y, M_z, u, v, w, \theta_x, \theta_y, \theta_z\}_s^T$ is the vector of forces and displacements of the strip. $\mathbf{B}_s$ is a matrix of constant coefficients and $\mathbf{B}_{sc}$ is a vector coupling cylinder variables to the strip and is a function of $\mathbf{g}_c$, $\mathbf{g}_s$ and the layer properties. Similarly the cylinder equations can be written as a first-order system

$$\mathbf{S}_c' = \mathbf{B}_c \mathbf{S}_c + \mathbf{B}_{cs} \tag{12}$$

where $\mathbf{S}_c = \{N_{xx}, N_{x\theta}, Q_x, M_x, u, v, w, w'\}_c^T$ is the vector of forces and displacements of the cylinder. $\mathbf{B}_c$ is the matrix derived by Cohen (1964), and $\mathbf{B}_{cs}$ is a vector coupling strip variables to the cylinder. The components of $\mathbf{B}_{cs}$ are listed below

$$\begin{aligned}
B_{cs1} &= \frac{k_{bs}^*}{d_s}\left(u_c - u_s + \frac{h}{2}\ w_c' + \frac{h_s}{2}\ w_s'\right) \\
B_{cs2} &= \frac{k_{bs}^*}{d_s}\left(v_c - v_s + \frac{h}{2a}\ n\ w_c + \frac{h_s}{2}\ \theta_{xs}\right) + \frac{B_{cs\theta}}{a} \\
B_{cs3} &= \frac{k_{be}^*}{d_s}(w_c - w_s) + \frac{n}{a}\ B_{cs\theta} \\
B_{cs4} &= \frac{k_{bs}^*}{d_s}\ \frac{h}{2}\left(\frac{h}{2}\ w_c' + \frac{h_s}{2}\ w_s' + u_c - u_s\right) \\
B_{csj} &= 0 \text{ for } j = 5,6,7,8 \\
B_{cs\theta} &= \frac{k_{be}^*}{d_s}\ \frac{b_s^2}{12}\left(\frac{n}{a}\ w_c - \theta_{xs}\right) + \frac{k_{bs}^*}{d_s}\ \frac{h}{2}\left(v_c - v_s \right. \\
&\quad \left. + \frac{h}{2a}\ nw_c + \frac{h_s}{2}\ \theta_{xs}\right)
\end{aligned} \tag{13}$$

The derivation of the transfer matrix proceeds by the steps in El-Raheb and Wagner (1985b). The combined homogeneous set (11) and (12) can be expressed as

$$\mathbf{S}' = \mathbf{B}\ \mathbf{S} \tag{14}$$

where $\mathbf{S} = \{\mathbf{S}_c, \mathbf{S}_s\}^T$ is a vector of 20th order in each harmonic n and $\mathbf{B}$ is formed of $\mathbf{B}_c$, $\mathbf{B}_{cs}$, $\mathbf{B}_{sc}$ and $\mathbf{B}_s$. Since equation (14) has constant coefficients, a solution exists in terms of exponentials $e^{\lambda x}$ where the λ's are determined from the eigenvalue problem:

$$(\mathbf{B} - \lambda \mathbf{I})\mathbf{S} = 0 \tag{15}$$

where $\mathbf{I}$ is the unit matrix. Corresponding to each λ_i there exists an eigenvector $\mathbf{A}_i$ satisfying equation (15). The 20 columns of distinct eigenvectors produce the matrix $\mathbf{A}$. The general solution of $\mathbf{S}$ can now be expressed as

$$\mathbf{S}(x) = \mathbf{A}\mathbf{e}^{\Lambda x}\mathbf{A}^{-1}\mathbf{S}(0) \tag{16}$$

where Λ is a diagonal matrix with coefficients $(\lambda_1, \lambda_2, \ldots, \lambda_{20})$. Therefore

$$\mathbf{S}(l) = \mathbf{T}(l)\mathbf{S}(0), \mathbf{T}(l) = \mathbf{A}e^{\Lambda l}\mathbf{A}^{-1} \tag{17}$$

B Condensation. Since for each harmonic, $\mathbf{T}(l)$ of the damped cylinder is 20 × 20 while for the bare cylinder it is only 8 × 8, its inversion requires computational effort greater by a factor of $(20/8)^3 = 15.6$. This onerous increase motivates restricting attention to the case where strips are free from tractions at their ends which permits condensing $\mathbf{T}(l)$ back to an 8 × 8 size. Fortunately, this case describes best what occurs in practice. Furthermore the contribution to cylinder stiffness from bending rigidity of the strip from its ends is minor beyond certain length of strip. Specifically, the effect on resonance and response of freeing the strip at its ends diminishes with strip length and becomes vanishingly small for lengths exceeding a characteristic size which depends on a/h_s and axial wave length of the response mode. To demonstrate this sensitivity, computations were carried out for a steel cylinder with $a/h = 11$, $l/a = 67$, damped by 105 steel strips spanning the full length of the cylinder and distributed evenly along the circumference with $h_s/h = b_s/h = 0.67$ bonded to the cylinder by a layer with $h_b/h = 0.02$ and $|G_b^*|/E_c = 3 \times 10^{-5}$. Results at $\omega^* = 300$ Hz with 2, 4, and 8 equal divisions of the strips showed less than 2 percent difference on response amplitude between the first two cases and 17 percent difference between the last two cases. This observation suggests that for strip lengths having $l/a \geq 15$, freeing the ends is without consequence.

Let $\{\mathbf{f}_c, \mathbf{g}_c\}$ and $\{\mathbf{f}_s, \mathbf{g}_s\}$ be the force and displacement vector dyads of the cylinder and strip, respectively. From equations (17)

$$\begin{Bmatrix} \mathbf{f}_c \\ \mathbf{g}_c \\ \mathbf{f}_s \\ \mathbf{g}_s \end{Bmatrix}_l = \begin{bmatrix} \mathbf{t}_{11} & \mathbf{t}_{12} & \mathbf{t}_{13} & \mathbf{t}_{14} \\ \mathbf{t}_{21} & \mathbf{t}_{22} & \mathbf{t}_{23} & \mathbf{t}_{24} \\ \mathbf{t}_{31} & \mathbf{t}_{32} & \mathbf{t}_{33} & \mathbf{t}_{34} \\ \mathbf{t}_{41} & \mathbf{t}_{42} & \mathbf{t}_{43} & \mathbf{t}_{44} \end{bmatrix} \begin{Bmatrix} \mathbf{f}_c \\ \mathbf{g}_c \\ \mathbf{f}_s \\ \mathbf{g}_s \end{Bmatrix}_0 \tag{18}$$

where $\mathbf{t}_{ij}$ are submatrices of $\mathbf{T}$. When strips are free at both ends of the segment $\mathbf{f}_{sl} = \mathbf{f}_{s0} = 0$. The third equation in (18) can now be used to eliminate $\mathbf{g}_{s0}$ from the first two equations in (18). A condensed transfer matrix for $\{\mathbf{f}_c, \mathbf{g}_c\}$ can now be written as

$$\begin{Bmatrix} \mathbf{f}_c \\ \mathbf{g}_c \end{Bmatrix}_l = \begin{bmatrix} \mathbf{t}_{11} - \mathbf{t}_{14}\mathbf{t}_{34}^{-1}\mathbf{t}_{31} & \mathbf{t}_{12} - \mathbf{t}_{14}\mathbf{t}_{34}^{-1}\mathbf{t}_{32} \\ \mathbf{t}_{21} - \mathbf{t}_{24}\mathbf{t}_{34}^{-1}\mathbf{t}_{31} & \mathbf{t}_{22} - \mathbf{t}_{24}\mathbf{t}_{34}^{-1}\mathbf{t}_{32} \end{bmatrix} \begin{Bmatrix} \mathbf{f}_c \\ \mathbf{g}_c \end{Bmatrix}_0 \tag{19}$$

which is 8 × 8 and incorporates the effects of the damped absorber.

C Selective Abbreviation. A drawback of the transfer matrix approach when applied to thin cylinders is the requirement that segment length be comparable to mean radius. This requirement is set by the emergence of complex roots λ with large magnitudes when solving the dispersion relation. The exponential solutions $e^{\lambda x}$ lead to round-off error in the transfer matrix when $|\lambda l|$ is large.

Approximate expressions of the nondimensional roots $\tilde{\lambda} = \lambda a$ are now derived for both axisymmetric and asymmetric motions of the bare cylinder. For axisymmetric motions, the coupled equations in the normalized axial and radial displacements $(\tilde{u}, \tilde{w})$ take the form:

$$\tilde{u}'' + \tilde{\omega}^2 \tilde{u} = \nu \tilde{w}' \tag{20a}$$

$$\tilde{r}^2 \tilde{w}'''' + (1 - \tilde{\omega}^2)\tilde{w} = \nu \tilde{u}' \tag{20b}$$

where $(\quad)'$ is the derivative with respect to $\tilde{x} = x/a$, $\tilde{\omega} = \omega/\omega_o$, $\omega_o = [E/\rho(1-\nu^2)a^2]^{1/2}$ is the axisymmetric breathing frequency, $\tilde{r} = h/(\sqrt{12}\ a)$ is the nondimensional radius of gyration of the cylinder wall. When $n = 0$, the eigenvalue problem in equation (15) gives

$$\tilde{r}^2\tilde{\lambda}^6 + \tilde{r}^2\tilde{\omega}^2\tilde{\lambda}^4 + (1 - \nu^2 - \tilde{\omega}^2)\tilde{\lambda}^2 + \tilde{\omega}^2(1 - \tilde{\omega}^2) = 0 \tag{21}$$

For $|\tilde{\lambda}| = 0(1)$ and $\tilde{\omega} < < 1$, the first two terms in equation (21) can be neglected leading to:

$$\tilde{\lambda}_{1,2} \simeq \pm \alpha i,\ \alpha = \frac{\tilde{\omega}(1 - \tilde{\omega}^2)^{1/2}}{(1 - \nu^2 - \tilde{\omega}^2)^{1/2}} \tag{22}$$

where $i = \sqrt{-1}$. The roots in equation (22) describe the axial wave number of extensional waves along the axis of the cylinder as determined approximately from equation (20a) when $\nu\tilde{w}'$ is neglected. For large $|\tilde{\lambda}| = 0(\tilde{r}^{-1/2})$ and $\tilde{\omega} < < 1$, four complex conjugates are found when terms of $0(\tilde{\lambda}^2)$ are retained in equation (21).

$$\tilde{\lambda}_{3,4,5,6} \simeq \pm\beta(1 \pm i),\ \beta = \frac{(1-\nu^2-\tilde{\omega}^2)^{1/4}}{(2\tilde{r})^{1/2}} \tag{23}$$

The roots in equation (23) describe the axial wave number of bending waves of a strip of cylinder along the generator, supported by hoop stress serving as an elastic foundation. An axisymmetric radial ring excitation at one end of the cylinder segment influences only a short span of cylinder which is $0(\tilde{r}^{1/2})$ near that end. This region is known as the bending boundary layer. Far from this region the cylinder's response decays exponentially with distance.

For asymmetric motions, a simplified dispersion relation can be derived for $\tilde{\omega} << 1$:

$$\tilde{\lambda}^8 - 4n^2\tilde{\lambda}^6 + \left[6n^4 + \frac{1-\nu^2-\tilde{\omega}^2}{\tilde{r}^2}\right]\tilde{\lambda}^4$$

$$-\left[4n^6 - \frac{\tilde{\omega}^2(2n^2+3+2\nu)}{\tilde{r}^2}\right]\tilde{\lambda}^2 + \left[n^8 - \frac{\tilde{\omega}^2 n^2(n^2-1)}{\tilde{r}^2}\right] = 0 \tag{24}$$

For $\tilde{\lambda} = 0(1)$, the first two terms in equation (24) can be neglected leading to the quadratic whose roots are

$$\tilde{\lambda}^2 \simeq \frac{n^2\left(2n^4 - \frac{\tilde{\omega}^2}{\tilde{r}^2}\right) \pm \left\{n^4\left(2n^4 - \frac{\tilde{\omega}^2}{\tilde{r}^2}\right) + \left(-n^8 + \frac{n^2(n^2+1)\tilde{\omega}^2}{\tilde{r}^2}\right)\left(6n^4 + \frac{1-\nu-\tilde{\omega}^2}{\tilde{r}^2}\right)\right\}^{1/2}}{\left(6n^4 + \frac{(1-\nu^2-\tilde{\omega}^2)}{\tilde{r}^2}\right)} \tag{25}$$

When $n=1$, further approximation yields

$$\tilde{\lambda}_{1,2} \simeq \pm\alpha,\ \tilde{\lambda}_{3,4} \simeq \pm i\alpha,\ \alpha = \frac{2^{1/4}\tilde{\omega}^{1/2}}{\sqrt{1-\nu^2}} \tag{26}$$

The roots in equation (26) are proportional to $\tilde{\omega}^{1/2}$ and independent of $\tilde{r}$ and can also be derived from the dispersion relation of a Euler beam having the same cross-section as the cylinder's. Below the ring frequency, that is $\tilde{\omega} < \tilde{r}n^2$, and for $n \geq 2$, (25) reduces to two complex pairs:

$$\tilde{\lambda}_{1,2,3,4} \simeq \pm\alpha(1 \pm i),\ \alpha = \frac{\tilde{r}^{1/2} n^2}{\sqrt{2}(1-\nu^2-\tilde{\omega}^2)^{1/4}} \tag{27}$$

Also, when $n \geq 2$ and $\tilde{\omega} > \tilde{r}n^2$, (25) reduces to

$$\tilde{\lambda}^2 \simeq \left\{n^2\left(2n^4 - \frac{\tilde{\omega}^2}{\tilde{r}^2}\right) \pm \left(\frac{n^2(n^2+1)\tilde{\omega}^2}{\tilde{r}^2}\right.\right.$$

$$\left.\left. - n^8\right)^{1/2} \left(\frac{1-\nu^2-\tilde{\omega}^2}{\tilde{r}^2}\right)^{1/2}\right\} \Big/ \frac{(1-\nu^2-\tilde{\omega}^2)}{\tilde{r}^2} \tag{28}$$

(28) determines a pair of real roots $\tilde{\lambda}_{1,2}$ and a pair of imaginary roots $\tilde{\lambda}_{3,4}$. The imaginary pair represents the axial wave number of propagating waves and contains a part proportional to $\tilde{r}$ which accounts for bending and a part independent of $\tilde{r}$ which accounts for extension. When $\tilde{\lambda}$ is large and of order $0(\tilde{r}^{-1/2})$, retaining the first three terms in equation (24) yields

$$\tilde{\lambda}_{5,6,7,8} \simeq \beta e^{i(\psi + m\pi)/2},\ m = 0,1,2,3$$

$$\beta = \left(6n^4 + \frac{1-\nu^2-\tilde{\omega}^2}{\tilde{r}^2}\right)^{1/4},\ \psi = \tan^{-1}\left(\frac{1}{2} + \frac{1-\nu^2-\tilde{\omega}^2}{4\tilde{r}^2 n^4}\right)^{1/2} \tag{29}$$

The complex conjugates in equation (29) are comparable to those in equation (23) and describe wave numbers in the bending boundary layer.

Consider the expression for transfer matrix given by equation (17)

$$\mathbf{S}(\mathrm{l}) = \mathbf{A}\mathbf{e}^{\Lambda \mathrm{l}}\mathbf{A}^{-1}\mathbf{S}(0) = \mathbf{T}(\mathrm{l})\mathbf{S}(0) \tag{17}$$

Then for some large number M, it is convenient to classify and sort the column vectors $\mathbf{A}_k$ into

$$\{\mathbf{A}_1^-, \mathbf{A}_2^-, \ldots, \mathbf{A}_1^o, \mathbf{A}_2^o, \ldots, \mathbf{A}_1^+, \mathbf{A}_2^+, \ldots\} \tag{30a}$$

as well as the corresponding Λ into

$$\{\lambda_1^-, \lambda_2^-, \ldots, \lambda_1^o, \lambda_2^o, \ldots, \lambda_1^+, \lambda_2^+, \ldots\} \tag{30b}$$

according to the following rules:

(*i*) $\mathrm{Re}(\lambda_k^-) < 0$ and $\mathrm{Re}(\lambda_k^-) < \mathrm{Re}(\lambda_{k+1}^-)$

(*ii*) $|\mathrm{Re}(\lambda_k^o)| < (\ln M)/\mathrm{l}$

(*iii*) $\mathrm{Re}(\lambda_k^+) > 0$ and $\mathrm{Re}(\lambda_k^+) > \mathrm{Re}(\lambda_{k+1}^+)$

When $\mathrm{Re}(\lambda_1^+ \mathrm{l})$ is sufficiently large, the usual procedure for computing $\mathbf{T}(\mathrm{l})$ fails for the purely numerical reason of round-off error. The usual recourse has been to further divide the interval $(0,\mathrm{l})$ into a sequence $\{0, x_1, x_2, \ldots, x_j, \ldots, \mathrm{l}\}$ so that for each j, evaluation of a term such as $[1 - \exp(-2\lambda_1^+(x_{j+1} - x_j))]$ does not suffer from round-off error (Kalnins, 1964).

An alternate procedure succeeds in computing $\mathbf{T}(\mathrm{l})$ because it is insensitive to the round-off even for large $|\lambda_1^+ \mathrm{l}|$. Its conceptual rationale lies in the fact that contributions to $\mathbf{S}(x)$ from sets of eigenfunctions $\{\mathbf{A}_k^-\}$ and $\{\mathbf{A}_k^+\}$ are small outside narrow regions near $x=0$ and $x=\mathrm{l}$, respectively, containing boundary layers. The procedure simply approximates these contributions as zero outside the boundary layers. The validity of this approximation is backed by the requirement that $\mathbf{S}(x)$ remain bounded within $0 \leq x \leq \mathrm{l}$. To be specific, first define the transformed vector

$$\boldsymbol{\sigma}(x) = \mathbf{A}^{-1}\mathbf{S}(x) \tag{31a}$$

in which set the redefined transfer matrix $\tau(x)$ is now diagonal

$$\boldsymbol{\sigma}(x) = \boldsymbol{\tau}(x)\boldsymbol{\sigma}(0),\ \boldsymbol{\tau}(x) = \mathbf{e}^{\Lambda \mathbf{x}} \tag{31b}$$

The vector $\boldsymbol{\sigma}$ has components $\{\sigma_1^-, \sigma_2^-, \ldots, \sigma_1^o, \sigma_2^o, \ldots, \sigma_1^+, \sigma_2^+, \ldots\}$. To mark the selective boundary depths, define the set of x-coordinates $\{x_1^-, x_2^-, \ldots, \mathrm{l}, \mathrm{l}, \ldots, x_1^+, x_2^+, \ldots\}$ such that

$$\mathrm{Re}(-\lambda_k^- x_k^-) = \mathrm{Re}(\lambda_k(\mathrm{l} - x_k^+)) = \ln M \tag{32a}$$

These values are selected because based on (31*b*)

$$|\sigma_k^-(x)| < |\sigma_k^-(0)|/M \text{ for } x > x_k^-$$

$$|\sigma_k^+(x)| < |\sigma_k^+(\mathrm{l})|/M \text{ for } x < x_k^+ \tag{32b}$$

The approximation then consists of setting $\sigma_k^-(x) \simeq 0$ when $x > x_k^-$ and setting $\sigma_k^+(x) \simeq 0$ when $x < x_k^+$. The procedure therefore yields a different transfer matrix for $\boldsymbol{\sigma}(x)$

$$\boldsymbol{\tau}_{sa}(x) = \mathbf{e}^{\Lambda_{sa}} \tag{33}$$

where Λ_{sa} is the diagonal matrix with components $(\lambda_1^- x_1^-, \lambda_2^- x_2^-, \ldots, \lambda_1^o \mathrm{l}, \lambda_2^o \mathrm{l}, \ldots, \lambda_1^+ x_1^+, \lambda_2^+ x_2^+, \ldots)$ and hence a different transfer matrix as well for $\mathbf{S}$

$$\mathbf{T}_{sa}(\mathrm{l}) = \mathbf{A}\mathbf{e}^{\Lambda_{sa}}\mathbf{A}^{-1} \tag{34}$$

which is now insensitive to round-off. The shortening of the lengths factoring some of the λ_k's suggests the name "selective abbreviation" for this procedure.

The choice of M will be motivated by two contrary considerations. First, M must be small enough to ensure accuracy against round-off error. In other words, for calculations with L digits of precision, $M < 10^L$. In fact, $M \simeq 10^{L/2}$ proved quite successful. Second, M must be large enough so that the actual boundary layers are contained in $[0, x_1^-] \cup [x_1^+, \mathrm{l}]$.

This approximation may also be applied to the case of the damped cylinder where $|\tilde{\lambda}_s|$ becomes significantly larger. An estimate of this root is made by solving the characteristic equation after neglecting w_c in (10c). Where $\tilde{r}_s$ is the radius of gyration of the strip's cross-section normalized by a, and $\tilde{\omega}_{bc}$ is the critical frequency of the layer

$$\tilde{\omega}_{bc} = \frac{a}{\sqrt{h_s h_b}} \left(\frac{E_b}{E_s} \right)^{1/2} > 1$$

then

$$\tilde{\lambda}_s \simeq \pm \frac{(\tilde{\omega}_{bc}^2 - \tilde{\omega}^2)^{1/4}}{(2\tilde{r}_s)^{1/2}} (1 \pm i) \tag{35}$$

As an example, let $a/h = 10$, $a/h_s = 20$, $a/h_b = 600$, and $E_b/E_s = 3 \times 10^{-3}$. This yields $\tilde{\omega}_{bc}^2 \simeq 36$. Comparing $|\tilde{\lambda}|$ in (23) with $|\tilde{\lambda}|$ in (35) reveals that $|\tilde{\lambda}_s| \simeq 2.5\ |\tilde{\lambda}|$.

D Acoustic Fluid. An acoustic fluid within an oscillating cylinder responds by exerting pressure against the walls. The same effect may be accomplished by adding a suitable mass to the cylinder. The method of added mass is quite accurate when the cylinder is driven mechanically while its terminations are free from acoustic excitation. The acoustic pressure $p(r,\theta,x)$ is governed by the Helmholtz equation which in cylindrical coordinates gives

$$\left(\partial_{rr} + \frac{1}{r}\,\partial_r + \frac{1}{r^2}\,\partial_{\theta\theta} + \partial_{xx} + k_f^2\right) p(r,\theta,x) = 0 \tag{36}$$

where (r,θ,x) are the radial, circumferential, and axial coordinates, $k_f = \omega/c_f$ and c_f is the speed of sound in the fluid. The boundary conditions at the terminations and continuity of acoustic and elastic accelerations at the cylinder-fluid interface are

$$p(r,\theta,0) = p(r,\theta,l) = 0 \tag{37a}$$

$$\partial_r p(a_i,\theta,x) = -\rho_f \omega^2 w_c(\theta,x) \tag{37b}$$

where ρ_f is the mass density of the fluid and a_i is the inner radius of the cylinder. Decomposing p and w_c into circumferential harmonics and solving for p in equation (36) with use made of equation (37b) yields

$$\begin{aligned} p_n(r,x) &= A_n J_n(\gamma r/a) e^{\eta x/a} \\ A_n e^{\eta x/a} &= -\rho_f a_i \omega^2 w_{cn}(x)/(\gamma J_n'(\gamma)) \end{aligned} \tag{38}$$

where ( )′ is the derivative with respect to the argument and

$$\gamma^2 = \kappa_f^2 + \eta^2,\ \kappa_f = k_f a$$

$$J_n(\gamma) = \begin{cases} J_n(\tilde{\gamma}) \text{ if } \gamma^2 > 0 \\ I_n(\tilde{\gamma}) \text{ if } \gamma^2 < 0 \end{cases}$$

J_n and I_n are Bessel functions and $\tilde{\gamma}^2 = |\gamma^2|$. If A_n is a constant, p_n and w_{cn} must have the same dependence in x. For propagating waves and $n \geq 1$, η assumes the largest imaginary root $\tilde{\lambda}_3$ in equations (26) and (28). Consequently

$$\begin{aligned} p_n(a_i,x) &\simeq -\rho_f a_i \omega^2 w_{cn} \frac{J_n(\gamma)}{\gamma J_n'(\gamma)} \\ \gamma^2 &\simeq \kappa_f^2 - |\tilde{\lambda}_3^2| \end{aligned} \tag{39}$$

The expression for p_n in equation (39) is approximate because it fails to satisfy the pressure conditions (37a) when w_{cn} is finite. This approximation is acceptable when the configuration is much longer than the radius beause end-effects lose importance. When p_n in equation (39) forces the cylinder, it adds to radial inertia $\mathcal{I}_n$ in the form of a mass factor $\mu_n(\gamma)$

$$\begin{aligned} \mathcal{I}_n &= \mu_n(\gamma) \rho_c h \omega^2 w_{cn}(x) \\ \mu_n(\gamma) &= 1 + \frac{J_n(\gamma)}{\gamma J_n'(\gamma)} \frac{\rho_f a_i}{\rho_c h} \end{aligned} \tag{40}$$

The second term in $\mu_n(\gamma)$ is the ratio of mass added by the fluid to the mass of the cylinder.

An approximation to $\mu_n(\gamma)$ can be made for $\gamma << 1$. From the Bessel equality

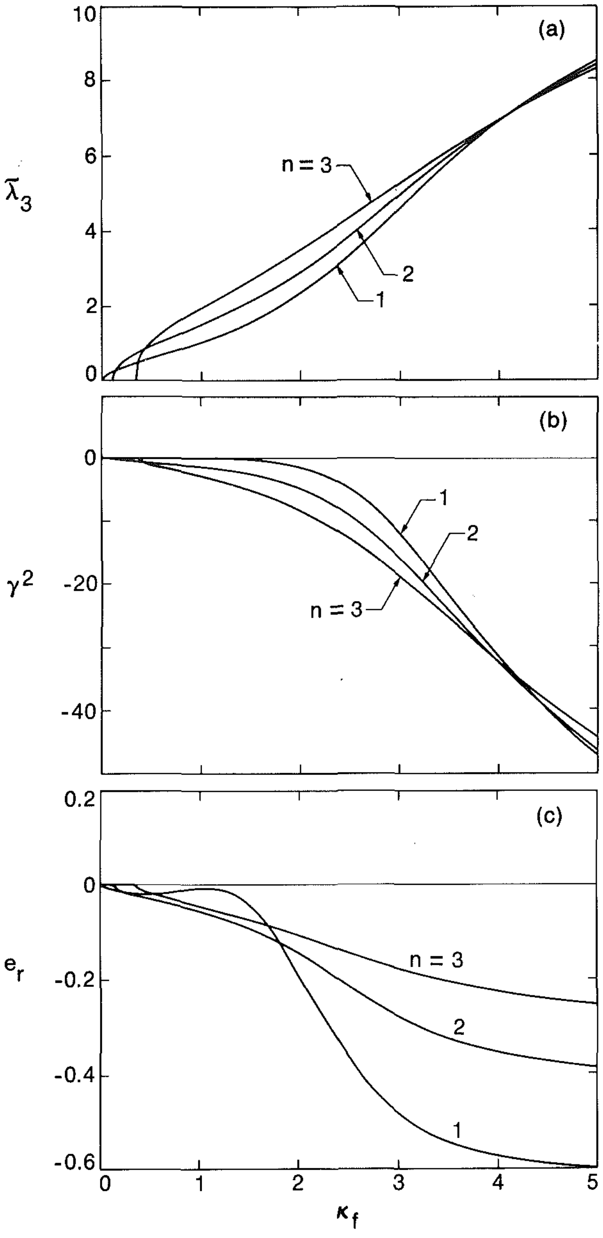

Fig. 3 Variation of $\tilde{\lambda}_3$, γ^2, and e_r with κ_f

$$\gamma J_n'(\gamma) = n J_n(\gamma) - \gamma J_{n+1}(\gamma)$$

in the limit as $\gamma \to 0$ and $n \geq 1$, $J_n(\gamma) \propto \gamma^n$ and $\gamma J_n'(\gamma) \simeq n J_n(\gamma)$. Using this, equations (40) become

$$\mu_n(\gamma) \simeq 1 + \frac{1}{n} \frac{\rho_f a_i}{\rho_c h} = \mu_{0n},\ n \geq 1 \tag{41}$$

The error committed by the approximation in equation (41) is defined by

$$e_\mu = \mu_n(\gamma)/\mu_{0n} - 1$$

To compute the exact $\mu_n(\gamma)$, in equation (24) modify radial inertia using mass added by the fluid as given by equation (40). The root $\tilde{\lambda}_3$ is determined by iteration on the transcendental equation.

Figures 3a, b, c trace $\tilde{\lambda}_3$, γ^2, and e_μ with κ_f for a cylinder with $a/h = 20$, $\rho_c/\rho_f = 8.14$ and $c_c/c_f = 4$ where $c_c = (E_c/\rho_c)^{1/2}$. For $n = 1$, $\tilde{\lambda}_3$ is finite for $\kappa_f > 0$ which is consistent with propagation of bending waves for all frequencies. As predicted by equation (26), $\tilde{\lambda}_3$ varies as $\kappa_f^{1/2}$ for small κ_f then becomes proportional to κ_f for $\kappa_f > 1$. However, for $n \geq 2$, $\tilde{\lambda}_3$ is finite only when $\kappa_f > \kappa_{fr}$ where $\kappa_{fr} = \omega_{rn}\, a/c_f$ and ω_{rn} is the ring

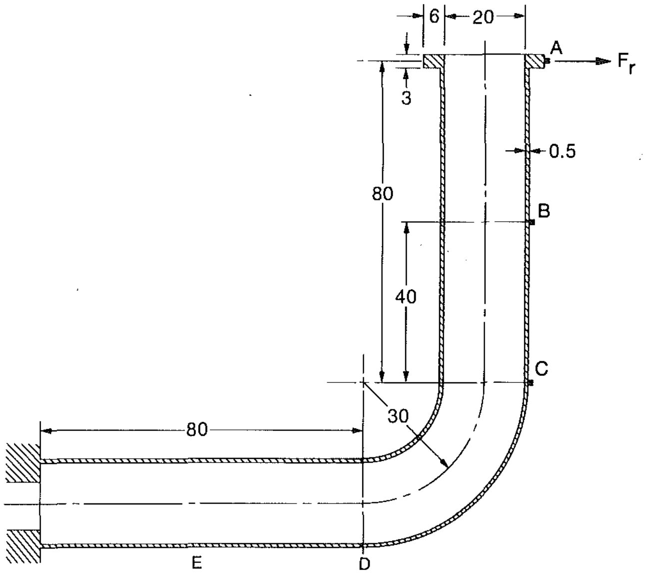

Fig. 4 ***L*-shaped configuration**

frequency. When $n=1$, γ^2 is vanishingly small up to $\kappa_f=2$ then drops sharply to negative values. When $n\geq 2$, γ varies linearly with κ_f for $\kappa_f>\kappa_{fr}$, then drops to zero and takes on imaginary values for $\kappa_f>\kappa_{fr}$. Negative γ^2 for $\kappa_f>\kappa_{fr}$ implies that transverse acoustic resonances for $n\geq 1$ disappear when the acoustic fluid is excited only by the cylinder walls. This is because J_n' (γ) in the denominator of equation (39) has no purely imaginary roots. As the cylinder thickens, κ_{fr} rises. Transverse resonances reappear once κ_{fr} increases above cutoff of the transverse acoustic waves in the rigid cylinder. For $n=1$, e_μ remains near zero for $\kappa_f<1.5$ then drops sharply at the stage when $\tilde{\lambda}_3$ changes its dependence on κ_f. For $n\geq 2$, e_μ falls smoothly with κ_f for $\kappa_f>\kappa_{fr}$. Since e_μ is negative for all $\kappa_f>\kappa_{fr}$, μ_{0n} serves as an upper bound on mass factor. Its use overestimates the mass added by the fluid for frequencies higher than the ring frequency.

II Results

The effect of vibration absorbers is studied using the L-shaped configuration shown in Fig. 4. The material properties were carefully selected in order to be as close to practice as possible. The configuration consists of two steel cylinders each 80 cm long connected by a 90 deg elbow with center line radius of 30 cm. The average radius of the cross section is 10 cm and the wall thickness is 0.5 cm. The vibration absorbers consist of 120 steel strips each 80 cm long, evenly distributed about the circumference of the cylinders. Strips are rectangular in cross section with $b_s=0.5$ cm and $h_s=0.4$ cm. They are bonded to the cylinders by a visco-elastic layer 0.01 cm thick. This thickness was selected without regard to optimization. The matter of optimization with regard to this quantity in the case of beams has been treated by Plunkett and Lee (1970). The properties of this layer are taken from Roscoe et al. (1966). Another source of properties as well as further information is Jones (1980). The configuration is clamped at one end and connected to a free ring at the other end. It is excited by a concentrated force F_r with periodic time dependence acting radially on the cylinder wall at point A. The two terminations are free from acoustic excitation while the interior is filled with water. Radial response is computed at points A,B,C as shown in Fig. 4. For frequencies up to 2000 Hz an expression for G_b^* that fits experimental data is

$$G_b^*=1.6\times 10^6(\omega^*)^{0.64}[1+i\ 2(\omega^*)^{-0.12}]dyn/\text{cm}^2$$

Relative to a local cylindrical coordinate system let F_r act at some point $(x_F,\ \theta_F)$ on the wall of a segment. Then F_r can be decomposed into its harmonic components such that

$$F_r=\int_0^{2\pi}p_r(\theta)ad\theta$$

where the equivalent harmonic line load $p_r(\theta)=p_{ro}\ \delta(\theta-\theta_F)$, and $\delta(\theta-\theta_F)$ is the Dirac delta function. Expanding $p_r(\theta)$ in Fourier series and truncating at N terms results in

$$p_r(\theta)=\frac{F_r}{2\pi a}\left\{1+2\sum_{n=1}^{N}\cos n(\theta-\theta_F)\right\}$$

This expansion decomposes F_r into a set of harmonic line loads about the circumference at $x=x_F$.

Mobility at A, B, C and acoustic pressure at B, C were calculated for both the undamped and damped configurations. The definitions of mobility M_j and pressure P_j are

$$M_j=|(w_{cj}\omega)/F_r|,\ P_j=|p_j/F_r|$$

where w_{cj} and p_j are radial displacement and acoustic pressure at sensor j caused by F_r at A. Figures 5*a*, *b*, *c* plot M_j as a logarithm relative to 1 cm/*s*/*dyn* versus ω^* in the range $10\leq\omega^*\leq 2000$ Hz at 10 Hz intervals. Comparison between the undamped M_j (dashed lines) and the damped M_j (solid lines) reveals that the amplitude of the fundamental resonance with $n=1$ at 20 Hz remains unaffected by damping. Vibration absorbers reduce only those motions dominated by modes with $n\geq 2$. In this case, these modes appear starting at 300 Hz for $n=2$, 1000 Hz for $n=3$, and 2000 Hz for $n=4$. Graphic evidence for these modes can be found in the cross sections in Fig. 6. The drop in M_j due to damping is larger within the cylinder (Fig. 5*b*) than at junctions (Figs. 5*a*,*c*). Although resonant peaks have shrunk, antiresonances remain sharp. This might be caused by the absence of damping in the elbow.

Figures 7*a*,*b* plot P_j as a logarithm relative to 1 *dyn*/cm^2/*dyn* versus ω^*. The effect on P_j of damping is small for motions dominated by $n=1$ modes. This agrees with the proportionality between p_j and w_{cj}. However, the harmonic component of p_j is inversely proportional to n. This means that $n=1$ modes dominate p_j up to frequencies even higher than they dominate w_{cj}. Therefore damping begins to affect p_j only when modes with $n\geq 2$ already dominate the response, and for this configuration that means $\omega^*>1000$ Hz.

A simple explanation exists for why the vibration absorbers damp with relatively greater efficacy when: (1) $n>1$, or more generally, (2) at higher frequencies. In this model damping arises solely by deforming the visco-elastic layer. One class of deformations, $\partial_\theta w_c$, is proportional to n which explains observation (1). Another class, $\partial_x w_c$, is proportional to axial wave number m and only higher frequencies bring about higher n and m which can explain observation (2). Damping then seems to rely mainly on these two rotations, an exclusivity which is itself a subject for investigation.

Conclusion

The effect of vibration absorbers on damping response is studied on a general configuration of shells composed of cylinders and tori containing an acoustic fluid. Absorbers are applied to cylindrical segments only. Transfer matrices were derived that include coupling of cylinder and strip bonded to a visco-elastic layer. The method of selective abbreviation extends segment length beyond $l/a=1$. The diminution in stiffness from segmenting the strips has little effect on resonant frequency and response amplitude. Analysis proceeds to an L-shaped configuration excited mechanically over a frequency range that includes modes with $n\leq 4$. Damping affects only those motions with modes having $n\geq 2$ dominant, while beam-type motions remain unaltered. Independent of whether vibration dampers have been added, some further findings apply to any acoustic fluid contained within an elastic shell in responding to an excitation of the shell. Under these conditions the fluid is indirectly excited and does not display any of the

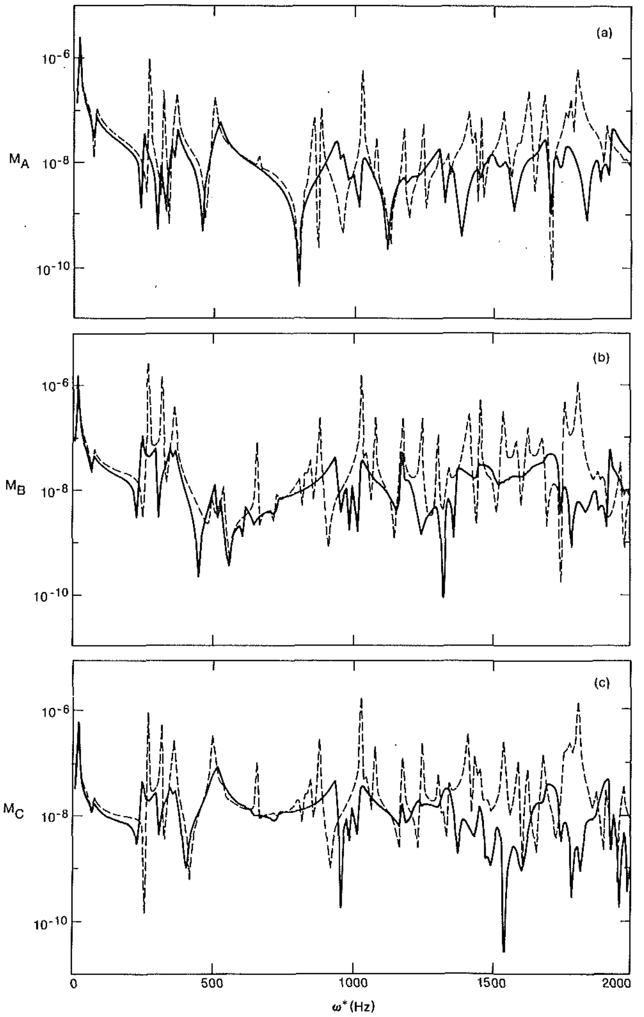

Fig. 5 Mobilities of *L*-shaped configuration: (_ _ _ _ _) undamped; (__________) damped

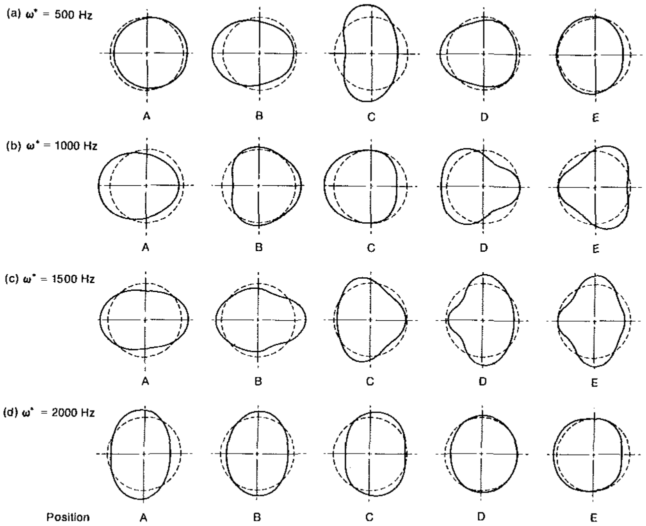

Fig. 6 Deformed cross sections of damped configuration

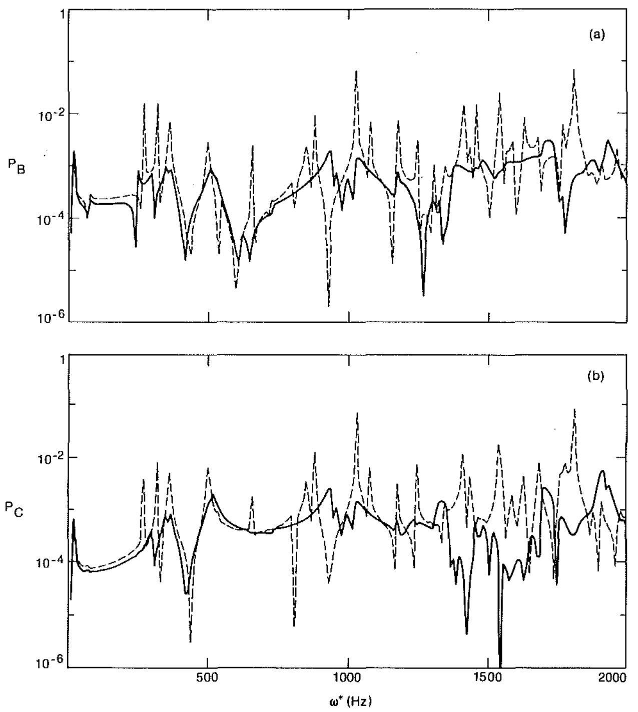

Fig. 7 Acoustic pressure in *L*-shaped configuration: (_ _ _ _ _) undamped; (__________) damped

acoustic resonances it would have displayed if excited acoustically. Also its acoustic pressure is inversely proportional to n.

References

Cohen, G., 1964, "Computer Analysis of Asymmetrical Deformation of Orthotropic Shells of Revolution," *American Institute of Aeronautics and Astronautics Journal*, Vol. 2, pp. 932–934.

Di Toranto, R., 1965, "Theory of Vibratory Bending for Elastic and Viscoelastic Layered Finite-Length Beams," ASME JOURNAL OF APPLIED MECHANICS, Vol. 32, pp. 881–886.

Di Toranto, R., Lu, Y. P., Douglas, B., 1973," Forced Response of a Discontinuously Constrained Damped Ring," *Journal of the Acoustical Society of America*, Vol. 54, pp. 74–79.

El-Raheb, M., Wagner, P., 1985a, "Harmonic Response of Cylindrical and Toroidal Shells Enclosing an Acoustic Medium, Part I: Theory," *Journal of the Acoustical Society of America*, Vol. 78, pp. 738–746.

El-Raheb, M., Wagner, P., 1985b, "Harmonic Response of Cylindrical and Toroidal Shells Enclosing an Acoustic Medium, Part II: Results," *Journal of the Acoustical Society of America*, Vol. 78, pp. 747–757.

Jones, D., 1980, *Damping Applications for Vibration Control*, AMD Vol. 38, ASME, pp. 27–52.

Kalnins, A., 1964, "Free Vibration of Rotationally Symmetric Shells," *Journal of the Acoustical Society of America*, Vol. 36, pp. 1355–1365.

Kerwin, E., 1959, "Damping of Flexural Waves by a Constrained Viscoelastic Layer," *Journal of the Acoustical Society of America*, Vol. 31, pp. 952–962.

Lu, Y. P., 1977, "Forced Vibration of Damped Cylindrical Shells Filled with Pressurized Liquid," *American Institute of Aeronautics and Astronautics Journal*, Vol. 15, pp. 1242–1249.

Plunkett, R., Lee, C., 1970, "Length Optimization for Constrained Viscoelastic Layer," *Journal of the Acoustical Society of America*, Vol. 48, pp. 150–161.

Roscoe III, A., Thomas, E., Blasingame, W., 1966, "Measurement of Complex Shear Modulus of Viscoelastic Materials by Mechanical Impedance Methods," *Shock and Vibration Bulletin*, Vol. 35, Pt. 7, pp. 267–274.

J. T. Katsikadelis
Associate Professor of
Structural Analysis,
Department of Civil Engineering,
National Technical University of Athens,
Athens, Greece 147

L. F. Kallivokas
Graduating Student,
Department of Civil Engineering,
National Technical University of Athens,
Athens, Greece 147

Clamped Plates on Pasternak-Type Elastic Foundation by the Boundary Element Method

A boundary element solution is developed for the analysis of thin elastic clamped plates of any shape resting on a Pasternak-type elastic foundation. The plate may have holes and it is subjected to concentrated loads, line loads, and distributed loads. The analysis is complete, i.e., deflections, stress resultants, subgrade reactions, and reactions on the boundary are evaluated. Several numerical examples are worked out and the results are compared with those available from analytical solutions. The efficiency of the BEM is demonstrated and discussed.

1 Introduction

Biparametric elastic foundation models have been developed to overcome the inadequacy of Winkler's model in describing the real soil response and the mathematical complexity of the three-dimensional continuum. They are characterized by two independent elastic constants and they are derived either as an extension of the Winkler model by assuming interaction between the spring elements (Filonenko-Borodich, 1940; Hetenyi, 1946; Pasternak, 1954; Kerr, 1964) or by simplifying the three-dimensional continuum (Reissner, 1958; Vlasov and Leontiev, 1966). Among them, the Pasternak-type foundation model is the most natural extension of the Winkler model for homogeneous soil deposit and the next higher approximation to the foundation response (Kerr, 1964). Although this foundation model can adequately approximate the soil-structure interaction, the analysis of plates resting on it must overcome practically insurmountable mathematical difficulties when a general analytical solution to the governing boundary value problem is sought. Thus, only plates with simple geometry and loading have been treated analytically, such as circular plates with axisymmetric loading or rectangular plates with uniform loading. On the other hand approximate methods (Galerkin's, Ritz's) and numerical methods (finite difference, finite element) have also been used. However, the application of these methods has been restricted to simple geometries. An extensive and lucid literature on the subject at hand is found in Vlasov and Leontiev (1966) and Selvadurai (1979). Recently (Balas et al., 1984), a boundary integral equation formulation of the problem has been presented with application to a circular plate under a concentrated force at the center.

In this investigation a boundary element solution to the problem of thin elastic clamped plates resting on a Pasternak-type elastic foundation is developed. The shape of the plate is arbitrary and it may have holes while its boundary may have corners. The plate may be subjected to any kind of loading (concentrated loads, line loads, distributed loads). The analysis is complete in the sense that deflections, stress resultants, and subgrade reactions at interior points as well as reaction forces and moments on the boundary are fully evaluated. The numerical technique presented herein for the solution of the coupled boundary singular integral equations and for the computation of all the field quantities is very efficient. In case of linearly varying loading, the efficiency of the method is improved by converting the domain integrals into line integrals, thus reducing drastically the required computer time. Numerical results are obtained for circular plates, rectangular plates, and plates with a composite shape. They are compared with those obtained from existing analytical solutions. The accuracy of the results is very good, notwithstanding the complexity of the kernel functions, which, in this case, are real and imaginary parts of Hankel functions with complex argument. Finally, the solution to plates resting on a Winkler foundation as well as to plates not resting on a subgrade are obtained as special cases for appropriate values of the elastic constants.

2 Formulation of the Boundary Value Problem

Consider a thin elastic plate of thickness h, occupying the two-dimensional multiply-connected region R of the plane, bounded by the $M+1$ curves $C_0, C_1, C_2, \ldots, C_M$ and resting on a Pasternak-type elastic foundation with subgrade reaction modulus k and shear modulus G. The curves C_i ($i=0, 1, 2, \ldots M$) may be piecewise smooth, i.e., the boundary of the plate may have a finite number of corners (Fig. 1).

Assuming that the plate maintains contact with the subgrade and that there are no friction forces at the interface, its deflection $w(P)$ at any point $P \epsilon R$ satisfies the following differential equation (Kerr, 1964)

$$Lw = f(P)/D \tag{1}$$

where $f(P)$ is the transverse loading, D is the flexural rigidity $[D = Eh^3/12(1-\nu^2)]$ of the plate and L is an operator defined as

---

Contributed by the Applied Mechanics Division for publication in the Journal of Applied Mechanics.

Discussion on this paper should be addressed to the Editorial Department, ASME, United Engineering Center, 345 East 47th Street, New York, N.Y. 10017, and will be accepted until two months after final publication of the paper itself in the Journal of Applied Mechanics. Manuscript received by ASME Applied Mechanics Division September 9, 1985; final revision February 20, 1986.

$$L=\nabla^4-\frac{G}{D}\nabla^2+\frac{k}{D},\quad \nabla^2=\frac{\partial^2}{\partial x^2}+\frac{\partial^2}{\partial y^2},\quad \nabla^4=(\nabla^2)^2 \tag{2}$$

In this case the interaction pressure p between plate and subgrade is given as

$$p=kw-G\nabla^2 w \tag{3}$$

Moreover, the deflection of the plate must satisfy the following conditions on the boundary $C=\bigcup_{i=0}^{M} C_i$ of the plate

$$w=0,\quad \frac{\partial w}{\partial n}=0 \tag{4a,b}$$

where $\partial w/\partial n$ denotes the directional derivative along the outward normal to the boundary.

The bending moments M_n and M_t, the twisting moment M_{nt}, and the effective shear force V_n acting on the boundary of the plate are related to the deflection w by the following relations (Katsikadelis and Armenakas, 1984a).

$$M_n=-D\nabla^2 w \qquad M_t=-\nu D\nabla^2 w \tag{5a,b}$$

$$M_{nt}=0 \qquad V_n=-D\frac{\partial}{\partial n}\nabla^2 w \tag{5c,d}$$

3 Integral Representation of the Solution

The integral representation of the solution can be obtained by using the Green identity for the operator L and the fundamental solution to equation (1).

The Green identity for the self-adjoint operator L is:

$$\iint_R (vLw-wLv)d\sigma=\int_C\left[v\frac{\partial}{\partial n}\nabla^2 w-\frac{\partial v}{\partial n}\nabla^2 w\right.$$
$$\left.-w\frac{\partial}{\partial n}\nabla^2 v+\frac{\partial w}{\partial n}\nabla^2 v-\frac{G}{D}v\frac{\partial w}{\partial n}+\frac{G}{D}w\frac{\partial v}{\partial n}\right]ds \tag{6}$$

where $\partial/\partial n$ denotes the outward normal derivative.

Relation (6) is readily obtained by combining the Rayleigh-Green identity (Katsikadelis, 1982) for the biharmonic operator with the classical Green identity for the harmonic operator (equation ($A7$) in the Appendix). Relation (6) is valid for any two functions w and v, which are four times continuously differentiable inside the region R and three times continuously differentiable on its boundary C.

The fundamental solution to equation (1) is a singular particular solution of the following differential equation

$$Lv=\delta(Q-P)/D \tag{7}$$

in which $\delta(Q-P)$ is the Dirac δ-function, Q is the field point, and P is the source point. The nature of the solution to equation (7) depends on the quantity $\mu=G^2/4kD$. In this investigation only the case $\mu<1$ is considered which seems to be valid for usual foundation materials (Kerr, 1964). For these values of μ the solution to equation (7) is given as (Vlasov and Leontiev, 1966):

$$v=v(P,Q)=v(Q,P)=\frac{\ell^2}{4D\sin 2\theta}\mathrm{Re}[H_o^{(1)}(\beta\rho)] \tag{8}$$

where

$$\ell=\sqrt[4]{D/k},\quad \rho=r/\ell \tag{9a,b}$$

$$\beta=\cos\theta+i\sin\theta,\quad 2\theta=\arctan(-\sqrt{1/\mu-1}) \tag{9c,d}$$

$r=|P-Q|$ is the distance between the points P, Q and $\mathrm{Re}[H_o^{(1)}(\beta\rho)]$ denotes the real part of the zero order Hankel function of the first kind. Notice that when G approaches 0, it can be shown that $v(P,Q)$ reduces to $-(\ell^2/2\pi D)kei(\rho)$ which is the fundamental solution to the equation governing the plate resting on a Winkler-type elastic foundation (Katsikadelis and Armenakas, 1984a, 1984b).

From equation (8) it can be shown that

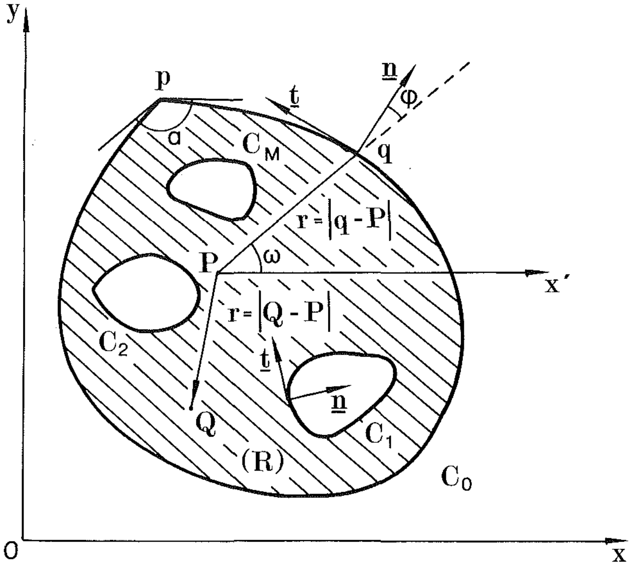

Fig. 1 Two dimensional region *R* occupied by the plate

$$\frac{\partial v}{\partial n}=\frac{\ell}{4D\sin 2\theta}V'(\rho)\cos\varphi \tag{10a}$$

$$\nabla^2 v=\frac{1}{4D\sin 2\theta}U(\rho) \tag{10b}$$

$$\frac{\partial}{\partial n}\nabla^2 v=\frac{1}{4\ell D\sin 2\theta}U'(\rho)\cos\varphi \tag{10c}$$

in which ( )′ denotes differentiation with respect to the argument ρ, φ is the angle between **r** and **n** (see Fig. 1), and

$$V(\rho)=\mathrm{Re}[H_o^{(1)}(\beta\rho)] \tag{11a}$$

$$\begin{aligned}V'(\rho)&=\mathrm{Re}[-\beta H_1^{(1)}(\beta\rho)]\\&=-\cos\theta\,\mathrm{Re}[H_1^{(1)}(\beta\rho)]+\sin\theta\,Im[H_1^{(1)}(\beta\rho)]\end{aligned} \tag{11b}$$

$$\begin{aligned}U(\rho)&=\mathrm{Re}[-\beta^2 H_o^{(1)}(\beta\rho)]\\&=-\cos 2\theta\,\mathrm{Re}[H_o^{(1)}(\beta\rho)]+\sin 2\theta\,Im[H_o^{(1)}(\beta\rho)]\end{aligned} \tag{11c}$$

$$\begin{aligned}U'(\rho)&=\mathrm{Re}[\beta^3 H_1^{(1)}(\beta\rho)]\\&=\cos 3\theta\,\mathrm{Re}[H_1^{(1)}(\beta\rho)]-\sin 3\theta\,Im[H_1^{(1)}(\beta\rho)]\end{aligned} \tag{11d}$$

The real valued functions $\mathrm{Re}[H_o^{(1)}(\beta\rho)]$, $Im[H_o^{(1)}(\beta\rho)]$, $\mathrm{Re}[H_1^{(1)}(\beta\rho)]$, $Im[H_1^{(1)}(\beta\rho)]$ involved in the aforegoing relations (11) are evaluated, for both small and large arguments, from their series expressions which are given in Zinke (1959).

It can be shown that for $\rho\to 0$ it is

$$\lim_{\rho\to 0}V(\rho)=1-2\theta/\pi,\qquad \lim_{\rho\to 0}V'(\rho)=0 \tag{12a,b}$$

$$\lim_{\rho\to 0}U(\rho)\sim \ell n\rho,\qquad \lim_{\rho\to 0}U'(\rho)\sim\frac{1}{\rho} \tag{12c,d}$$

$$\lim_{\rho\to 0}[\rho V'(\rho)]=0,\qquad \lim_{\rho\to 0}[\rho U'(\rho)]=2\sin 2\theta/\pi \tag{12e,f}$$

Applying equation (6) for the deflection of the plate w and the fundamental solution v, which satisfy equations (1) and (7), respectively, using relations (8, 10a, 11a) and the boundary conditions (4a, b) the integral representation for the deflection $w(P)$ is obtained as

$$w(P)=\iint_R v(P,Q)f(Q)d\sigma_Q-D\int_C\left[v(P,q)\Psi(q)\right.$$
$$\left.-\frac{\partial v(P,q)}{\partial n_q}\Phi(q)\right]ds_q=\frac{\ell^2}{4\sin 2\theta}[F(P)-J_1(P)+J_2(P)] \tag{13}$$

where the following notation has been introduced for conciseness

$$\Phi(q)=\nabla^2 w(q), \quad \Psi(q)=\frac{\partial}{\partial n_q}\nabla^2 w(q) \qquad (14a,b)$$

$$F(P)=\frac{1}{D}\iint_R V(\rho_{PQ})f(Q)d\sigma_Q \qquad (15)$$

$$J_1(P)=\int_C V(\rho_{Pq})\Psi(q)ds_q,$$

$$J_2(P)=\int_C \rho_{Pq}V'(\rho_{Pq})\Phi(q)d\omega_q \qquad (16a,b)$$

$$\rho_{Pq}=|P-q|/\ell, \qquad \omega=\widehat{\mathbf{x},\mathbf{r}}$$

Notice that in equation (16*b*) the relation $\cos\varphi ds=rd\omega$ has been used (Katsikadelis, 1982). In the aforegoing relations, points inside the region R are denoted by uppercase letters, while points on the boundary C are denoted by lowercase letters. Moreover, the subscript of the elements $d\sigma$, and ds indicates the point that varies during integration. Furthermore, $\partial/\partial n_q$ denotes that the normal derivative is taken with respect to point q.

From relations (5) it is seen that the boundary quantities $\nabla^2 w$ and $\partial/\partial n\nabla^2 w$ appearing in the line integral of equation (13) have a direct physical meaning.

4 Derivation of the Boundary Integral Equations

In equation (13) the loading function $f(Q)$ is given at every point in R. Moreover, the function $v(P,Q)$ and its derivatives are obtained from equations (8) and (10). However, the functions $\Psi(q)$ and $\Phi(q)$ are not known at the points of the boundary C. These two unknown boundary quantities are established from the solution of two coupled boundary integral equations which are derived using the procedure presented in Katsikadelis and Armenakas (1984a). Thus, the first boundary integral equation is established from equation (13) by letting point P approach a point p on the boundary C. The existence of the line integrals in equation (13) for $P\equiv p\epsilon C$ and their continuity as $P\rightarrow p\epsilon C$ can be easily concluded from relations (12*a*,*b*). Consequently, taking into account that $w(p)=0$ the first boundary integral equation is obtained as

$$-\int_C \rho_{pq}V'(\rho_{pq})\Phi(q)d\omega_q+\int_C V(\rho_{pq})\Psi(q)ds_q=F(p) \qquad (17)$$

The second boundary integral equation is obtained by applying the operator ∇^2 on both sides of equation (13) and by letting point P approach a point p on the boundary. Thus

$$\nabla^2 w(p)=\iint_R \nabla^2 v(p,Q)f(Q)d\sigma_Q$$

$$-D\lim_{P\rightarrow p}\int_C \nabla^2 v(P,q)\Psi(q)ds_q$$

$$+D\lim_{P\rightarrow p}\int_C \frac{\partial}{\partial n}\nabla^2 v(P,q)\Phi(q)ds_q \qquad (18)$$

By virtue of equations (10*b*,*c*) and (12*c*,*d*) it is seen that, the first line integral on the right-hand side of equation (18) represents a single layer potential due to a mass distribution $\Psi(q)$, while the second line integral represents a double layer potential due to a mass distribution $\Phi(q)$. Hence, both line integrals exist for $P\equiv p\epsilon C$. Moreover, the first line integral is continuous, while the second line integral exhibits a discontinuity jump as $P\rightarrow p\epsilon C$ (Courant and Hilbert, 1953) which is equal to

$$\lim_{P\rightarrow p}\int_C \frac{\partial}{\partial n}\nabla^2 v(P,q)\Phi(q)ds_q$$

$$-\int_C \frac{\partial}{\partial n}\nabla^2 v(p,q)\Phi(q)ds_q=\frac{2\pi-\alpha}{2\pi D}\Phi(p) \qquad (19)$$

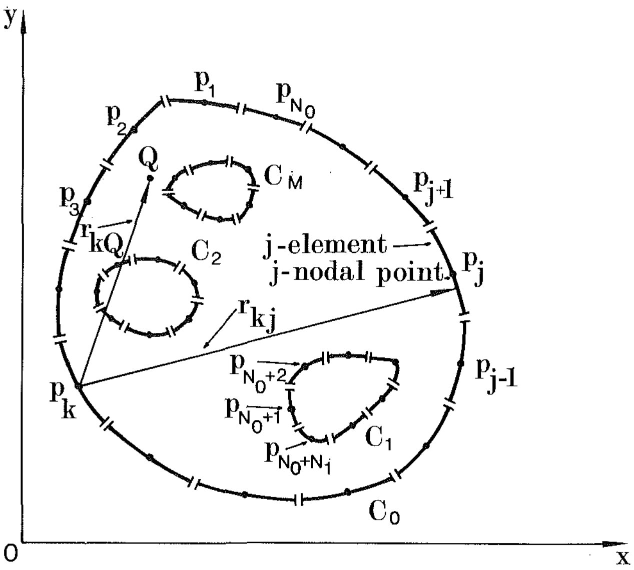

Fig. 2 Discretization of the boundary

where α is the angle between the tangents at point p (see Fig. 1). It is $\alpha=\pi$ when the boundary is smooth at point p. Taking into account equation (19), the second boundary integral equation is obtained from equation (18) as

$$\frac{2\alpha\sin2\theta}{\pi}\Phi(p)+\int_C U(\rho_{pq})\Psi(q)ds_q$$

$$-\int_C \rho_{pq}U'(\rho_{pq})\Phi(q)d\omega_q=G(p) \qquad (20)$$

in which

$$G(p)=\frac{1}{D}\iint_R U(\rho_{pQ})f(Q)d\sigma_Q \qquad (21)$$

For any given geometry of the clamped boundary of the plate, the functions $\Phi(s)$ and $\Psi(s)$ may be obtained from the solution of the coupled boundary integral equations (17) and (20). Once the functions $\Phi(s)$ and $\Psi(s)$ are known, the solution to the boundary value problem (equations (1) and (4)) may be obtained from equation (13).

5 Numerical Analysis

The numerical solution of the coupled boundary singular integral equations (17) and (20) is accomplished using the boundary element approach. In this approach the boundary is divided into N intervals, not necessarily equal, referred to as boundary elements. The end points of each element are referred to as extreme points. Each boundary element is approximated by a given curve (straight line, parabolic arc, etc.) and the unknown boundary functions Φ, Ψ are approximated by a polynomial (constant, linearly varying, parabolically varying, etc.). The points on which the unknown functions are evaluated are referred to as nodal points.

In this investigation each boundary C_i is divided into N_i elements ($i=0, 1, \ldots, M$) not necessarily equal. The center of the elements or other points near them are taken as their nodes. The elements on the external boundary are numbered consecutively counterclockwise while on the internal boundaries clockwise (Fig. 2). The values of Φ and Ψ are assumed constant on each element (step function assumption) and equal to their values at the nodal point of each element. Moreover, the curved elements are approximated by parabolic arcs (Katsikadelis and Sapountzakis, 1985). This approximation reduces appreciably the error due to the approximation of curved boundaries by straight line elements. Denoting by Φ_j and Ψ_j the values of Φ and Ψ at the jth nodal point (i.e., the nodal point of the j element), the integral equations (17) and (20) are transformed into the following system of $2N$ $\left(N=\sum_{i=0}^{M} N_i\right)$ simultaneous algebraic equations

$$\sum_{j=1}^{N} \alpha_{kj}\Phi_j + \sum_{j=1}^{N} b_{kj}\Psi_j = F_k \quad (k=1,2,\ .\ .\ .\ ,N) \tag{22a}$$

$$\sum_{j=1}^{N} \left(C_{kj} + \frac{2\alpha}{\pi}\sin 2\theta\delta_{kj}\right)\Phi_j + \sum_{j=1}^{N} d_{kj}\Psi_j = G_k \quad (k=1,2,\ .\ .\ .\ ,N) \tag{22b}$$

in which δ_{kj} is the Kronecker delta and

$$\alpha_{kj} = -\int_j \rho_{kq} V'(\rho_{kq}) d\omega_q, \quad b_{kj} = \int_j V(\rho_{kq}) ds_q \tag{23a,b}$$

$$c_{kj} = -\int_j \rho_{kq} U'(\rho_{kq}) d\omega_q, \quad d_{kj} = \int_j U(\rho_{kq}) ds_q \tag{23c,d}$$

$$F_k = \frac{1}{D}\iint_R V(\rho_{kQ}) f(Q) d\sigma_Q,$$

$$G_k = \frac{1}{D}\iint_R U(\rho_{kQ}) f(Q) d\sigma_Q \tag{23e,f}$$

$$\rho_{kq} = |p_k - q|/\ell, \quad \rho_{kQ} = |p_k - Q|/\ell, \quad Q \epsilon R, p_k \epsilon C, \quad q \epsilon j\text{-element}$$

In relations (23a, b, c, d), the symbol $\int_j$ denotes integration on the j-element; point p_k is a nodal point.

Evaluation of Line Integrals α_{kj}, $\mathbf{b}_{kj}$, $\mathbf{c}_{kj}$, and $\mathbf{d}_{kj}$. When $k \neq j$ ($\rho \neq 0$), these integrals can be evaluated using any of the known numerical techniques for the evaluation of line integrals. In this investigation the curved boundary element is approximated by a parabolic arc passing through its nodal and extreme points and its value is computed using eight-point Gaussian quadrature. When $k=j$, the argument ρ vanishes for $q=p_k$. From relations (12a), (12e), and (12f) it is seen that the line integrals α_{kk}, b_{kk}, and c_{kk} are not singular and consequently they are evaluated as in the case $k \neq j$. However, as it is seen from relation (12c), the line integral d_{kk} has a logarithmic singularity and it is evaluated using the technique presented in Katsikadelis and Armenakas (1985).

Evaluation of Double Integrals $\mathbf{F}_k$ and $\mathbf{G}_k$. We may distinguish the following four cases:

a) The plate is subjected to a concentrated load P at a point Q_o. In this case, the loading function $f(Q)$ can be represented as

$$f(Q) = P\delta(Q - Q_o) \tag{24}$$

Using relation (24) the values of the integrals (23e,f) are

$$F_k = \frac{P}{D} V(\rho_{kQ_o}), \quad G_k = \frac{P}{D} U(\rho_{kQ_o}) \tag{25a,b}$$

where $\rho_{kQ_o} = |p_k - Q_o|/\ell$.

b) The plate is subjected to a line load $p(s)$ distributed along a curve L^*. In this case the double integrals (23e,f) are evaluated using relations (25a, b) from the following line integrals along the curve L^*

$$F_k = \frac{1}{D}\int_{L^*} p(Q) V(\rho_{kQ}) ds_Q,$$

$$G_k = \frac{1}{D}\int_{L^*} p(Q) U(\rho_{kQ}) ds_Q \tag{26a,b}$$

where $\rho_{kQ} = |p_k - Q|/\ell$, $Q \epsilon L^*$.

c) The plate is subjected to a uniform or a linearly varying load distributed over an area $R^* \subseteq R$ of the plate bounded by a curve C^*. In this case, it is $\nabla^2 f = 0$ and by virtue of relations (A6), (A7), (A8), and (A9) in the Appendix the double integrals (23e, f) can be converted into the following line integrals on the curve C^*.

$$F_k = -\cos 2\theta G_k - \frac{\ell^2 \sin 2\theta}{D}\left[\epsilon f(p_k) + \int_{C^*} \rho_{kq} I'(\rho_{kq}) f(q) d\omega_q - \int_{C^*} I(\rho_{kq}) \frac{\partial f(q)}{\partial n_q} ds_q\right] \tag{27a}$$

$$G_k = \frac{\ell^2}{D}\left[\int_{C^*} \rho_{kq} V'(\rho_{kq}) f(q) d\omega_q - \int_{C^*} V(\rho_{kq}) \frac{\partial f(q)}{\partial n_q} ds_q\right] \tag{27b}$$

where $\rho_{kq} = |p_k - q|/\ell$, $q \epsilon C^*$; $I(\rho) = Im[H_o^{(1)}(\beta\rho)]$; ϵ is given in the Appendix.

The substitution of the domain integrals by line integrals reduces drastically the required computer time. The line integrals (27a, b) as well as (26a, b) are evaluated numerically employing the technique presented in Katsikadelis and Armenakas (1985). Thus, the curve C^*, L^*, respectively, is approximated by a finite number of parabolic elements. On each element the line integral is computed and the resulting partial values are summed.

d) In the general case where $f(Q)$ is an arbitrary function, the domain integrals (23e, f) are evaluated using the method presented in Katsikadelis and Armenakas (1983).

6 Evaluation of the Deflections, Stress Resultants and Subgrade Reactions

When the integrals α_{kj}, b_{kj}, c_{kj}, d_{kj}, F_k, and G_k are established, the system of simultaneous algebraic equations (22a, b) is solved and the values Φ_j and Ψ_j of the functions $\Phi(s)$ and $\Psi(s)$ at the nodal points are obtained. These values can be used to obtain the deflection $w(P)$ and the stress resultants at any point P in the interior of the plate.

The deflections $w(P)$ is obtained from its integral representation (13). The line integrals $J_1(P)$ and $J_2(P)$ are computed from the relations

$$J_1(P) = \sum_{j=1}^{N} \Psi_j \int_j V(\rho_{Pq}) ds_q,$$

$$J_2(P) = \sum_{j=1}^{N} \Phi_j \int_j \rho_{Pq} V'(\rho_{Pq}) d\omega_q \tag{28a,b}$$

For the computation of the double integral $F(P)$ in relation (15) we distinguish again four cases as for the integral F_k in the previous section.

Referring to relations (5) and (14) it is apparent that the bending moments M_n, M_t and the reaction force V_n on the boundary of the plate are readily computed from the values of Φ and Ψ.

The bending moments M_x, M_y, the twisting moment M_{xy} and the shear forces Q_x and Q_y at any point of the plate are equal to

$$M_x = -D\left(\frac{\partial^2 w}{\partial x^2} + \nu\frac{\partial^2 w}{\partial y^2}\right), \quad Q_x = -D\frac{\partial}{\partial x}\nabla^2 w \tag{29a,b}$$

$$M_y = -D\left(\frac{\partial^2 w}{\partial y^2} + \nu\frac{\partial^2 w}{\partial x^2}\right), \quad Q_y = -D\frac{\partial}{\partial y}\nabla^2 w \tag{29c,d}$$

$$M_{xy} = -M_{yx} = D(1-\nu)\frac{\partial^2 w}{\partial x \partial y} \tag{29e}$$

The second and third order derivatives of the deflections in equation (29) may be evaluated from the computed values of the deflections with sufficient accuracy using numerical differentiation. However, the accuracy is increased and the computer time is considerably reduced when they are evaluated by direct differentiation of relation (13) using the following combinations of derivatives.

$$d_i = \frac{1}{4\sin 2\theta}\left[\frac{1}{D}\iint_R K_i(\rho) f d\sigma - \int_C K_i(\rho)\Psi ds + \frac{1}{\ell}\int_C \Lambda_i(\rho)\Phi ds\right] \quad (i=1,2,3,4,5) \tag{30}$$

where

$$d_1 = \frac{\partial^2 w}{\partial x^2} + \frac{\partial^2 w}{\partial y^2},\quad d_2 = \frac{\partial^2 w}{\partial x^2} - \frac{\partial^2 w}{\partial y^2},\quad d_3 = 2\frac{\partial^2 w}{\partial x \partial y}, \tag{31a,b,c}$$

$$d_4 = -\ell\frac{\partial}{\partial x}\nabla^2 w,\quad d_5 = -\ell\frac{\partial}{\partial y}\nabla^2 w \tag{31d,e}$$

$$K_1(\rho) = U(\rho),\quad K_2(\rho) = C(\rho)\cos 2\omega,\quad K_3(\rho) = C(\rho)\sin 2\omega \tag{32a,b,c}$$

$$K_4(\rho) = U'(\rho)\cos\omega,\quad K_5(\rho) = U'(\rho)\sin\omega \tag{32d,e}$$

$$\Lambda_1(\rho) = U'(\rho)\cos\varphi,\quad \Lambda_2(\rho) = U'(\rho)\cos\varphi\cos 2\omega - \frac{2}{\rho}C(\rho)\cos(2\omega-\varphi) \tag{32f,g}$$

$$\Lambda_3(\rho) = U'(\rho)\cos\varphi\sin 2\omega - \frac{2}{\rho}C(\rho)\sin(2\omega-\varphi) \tag{32h}$$

$$\Lambda_4(\rho) = -\left[\frac{1}{\rho}U'(\rho)\cos(\omega-\varphi) + V(\rho)\cos\omega\cos\varphi + 2U(\rho)\cos 2\theta\cos\omega\cos\varphi\right] \tag{32i}$$

$$\Lambda_5(\rho) = -\left[\frac{1}{\rho}U'(\rho)\sin(\omega-\varphi) + V(\rho)\sin\omega\cos\varphi + 2U(\rho)\cos 2\theta\sin\omega\cos\varphi\right] \tag{32j}$$

$$C(\rho) = U(\rho) - \frac{2}{\rho}V'(\rho) \tag{32k}$$

For an arbitrary loading function $f(Q)$ the double integrals in equation (30) may be evaluated using the technique presented in Katsikadelis and Armenakas (1983).

When the loading is due to a concentrated force P at some point Q the double integrals in relation (30) can be directly evaluated from relations analogous to (25). Moreover, when the loading is due to a line load along a curve L^*, the double integrals in relation (30) are reduced to line integrals on the curve L^* and they are computed from relations analogous to (26). Finally, when the plate is loaded by a uniform or a linearly varying load distributed over a region $R^* \subseteq R$ bounded by a curve C^* the double integrals in relation (30) can be converted into line integrals. Thus, using integration by parts and employing relations ($A6$) and ($A8$) in Appendix, we obtain

$$\iint_{R^*} f\left(\frac{\partial^2}{\partial x^2} - \frac{\partial^2}{\partial y^2}\right)V(\rho)d\sigma = \frac{1}{\ell}\int_{C^*} fV'(\rho)\cos(2\omega+\varphi)ds - \int_{C^*}\left[\frac{\partial f}{\partial \xi}\cos(\omega+\varphi) - \frac{\partial f}{\partial \eta}\sin(\omega+\varphi)\right]V(\rho)ds \tag{33a}$$

$$\iint_{R^*} f\frac{\partial^2}{\partial x \partial y}V(\rho)d\sigma = \frac{1}{\ell}\int_{C^*} fV'(\rho)\sin\omega\cos(\omega+\varphi)ds - \int_{C^*}\frac{\partial f}{\partial \xi}V(\rho)\sin(\omega+\varphi)ds \tag{33b}$$

$$\iint_{R^*} f\frac{\partial}{\partial x}\nabla^2 V(\rho)d\sigma = -\frac{1}{\ell^2}\int_{C^*} fU(\rho)\cos(\omega+\varphi)ds + \frac{1}{\ell}\int_{C^*}\frac{\partial f}{\partial \xi}V'(\rho)\cos\varphi ds \tag{33c}$$

$$\iint_{R} f\frac{\partial}{\partial y}\nabla^2 V(\rho)d\sigma = -\frac{1}{\ell^2}\int_{C^*} fU(\rho)\sin(\omega+\varphi)ds + \frac{1}{\ell}\int_{C^*}\frac{\partial f}{\partial n}V'(\rho)\cos\varphi ds \tag{33d}$$

where x, $y \epsilon R$ and ξ, $\eta \epsilon C^*$.

Table 1 Percent error in the deflection w, bending moment M_r, and reaction force V_n in a clamped circular plate with radius a, resting on an elastic foundation ($\lambda = 10$, $s = 13$), and subjected to a uniform load q

Number of BE	Error in w $r=.5a$	Error in M_r $r=.5a$	Error in V_n $r=a$
10	.051	1.056	.836
20	.006	.137	.117
30	.002	.041	.036
40	.001	.017	.015
50	.000	.009	.008
60	.000	.005	.005
70	.000	.003	.003
80	.000	.002	.002

7 Numerical Results

A computer program has been written for the numerical evaluation of the response of clamped plates resting on a Pasternak-type elastic foundation by integrating the boundary integral equations (17) and (20) using the numerical technique described in Section 5. Numerical results have been obtained for circular plates with or without holes, rectangular plates and a plate of composite shape subjected to concentrated loads, uniform, and linearly varying loads. The obtained results are in excellent agreement with those obtained from analytical solutions or other numerical solutions. When $G \rightarrow 0$ the solution for the plate resting on a Winkler-type elastic foundation is obtained, while when both constants, G and k, are small, the solution for the plate not resting on an elastic subgrade is obtained.

For the presentation of the numerical results the following dimensionless parameters are introduced which are established by writing equation (1) in a dimensionless form

$$s = a/\sqrt{D/G},\quad \lambda = a/\sqrt[4]{D/k}$$

where a is a characteristic length of the plate (e.g., the radius of a circular plate, the length of one side of a rectangular plate, etc.). The shear modulus G may vary between 0 to 40MN/m, while the subgrade reaction modulus k may vary from 0 to 200MN/m^3. Thus, for usual engineering applications it is $0 \leq s \leq 30$ and $0 \leq \lambda \leq 20$. In computations, it may be set $s=0$. However, the value $\lambda=0$ must be excluded because it raises computational difficulties. A small value of λ (say $\lambda = 0.1$ to 0.5) and $s=0$ give accurate results for the plate not resting on subgrade.

In Table 1, the percent error in the numerical results obtain-

Table 2 **Deflections $\bar{w} = w/(\mathrm{Pa}^2/D)$ in a clamped circular plate with radius a subjected to a concentrated force P at its center**

	$\lambda = .134,\ s = 0$		$\lambda = 12,\ s = 0$		$\lambda = 12,\ s = 15$	
r/a	analytic	BEM	analytic	BEM	analytic	BEM
0	.19894E-01	.19894E-01	.86806E-03	.86806E-03	.59681E-03	.59681E-03
0.2	.16537E-01	.16537E-01	.13953E-03	.13953E-03	.11590E-03	.11590E-03
0.4	.10878E-01	.10877E-01	-.12264E-04	-.12264E-04	.10507E-04	.10507E-04
0.6	.54154E-02	.54150E-02	-.22695E-05	-.22695E-05	.51292E-06	.51292E-06
0.8	.14797E-02	.14795E-02	.35712E-06	.35711E-06	-.12968E-07	-.12965E-07

Table 3 **Deflections, bending moments and shearing forces in a clamped circular ring-shaped plate with an inner radius b and an outer radius $a = 3b$ subjected to a uniform load q**

	$\lambda = .134,\ s = 0$		$\lambda = 12,\ s = 0$		$\lambda = 12,\ s = 15$	
r/b	analytic	BEM	analytic	BEM	analytic	BEM
			Deflections $\bar{w} = w/(qa^4/D)$			
1.4	.21740E-01	.21741E-01	.54455E-04	.54455E-04	.51193E-04	.51188E-04
1.8	.44073E-01	.44073E-01	.52551E-04	.52551E-04	.52615E-04	.52615E-04
2.1	.40622E-01	.40622E-01	.52518E-04	.52518E-04	.52617E-04	.52617E-04
2.6	.16895E-01	.16894E-01	.54912E-04	.54912E-04	.50906E-04	.50906E-04
			Bending moment $\bar{M}_r = M_r/qa^2$			
1.0	-.44861E+00	-.44861E+00	-.73420E-02	-.73420E-02	-.74249E-02	-.74715E-02
1.4	.80839E-02	.80860E-02	.14935E-03	.14935E-03	.19618E-03	.19677E-03
1.8	.15789E+00	.15789E+00	-.24074E-05	-.24073E-05	.55076E-06	.55478E-06
2.2	.13134E+00	.13134E+00	-.35616E-05	-.35623E-05	.81261E-06	.81279E-06
2.6	-.24062E-01	-.24065E-01	.17698E-03	.17701E-03	.22293E-03	.22296E-03
3.0	-.28612E+00	-.28612E+00	-.68067E-02	-.68074E-02	-.67599E-02	-.67623E-02
			Shearing force $\bar{Q}_r = Q_r/qa$			
1.0	.14684E+01	.14685E+01	.12489E+00	.12489E+00	.16905E+00	.16960E+00
1.4	.70599E+00	.70598E+00	-.34146E-02	-.34146E-02	-.19353E-02	-.19402E-02
1.8	.19355E+00	.19354E+00	.95462E-04	.95463E-04	-.14228E-04	-.14296E-04
2.2	-.20528E+00	-.20528E+00	-.13524E-03	-.13525E-03	.20057E-04	.20061E-04
2.6	-.54293E+00	-.54293E+00	.40313E-02	.40316E-02	.22448E-02	.22451E-02
3.0	-.84387E+00	-.84387E+00	-.11555E+00	-.11556E+00	-.15316E+00	-.15318E+00

Table 4 **Deflection $\bar{w} = w/(qa^4/D)$ and bending moments $\bar{M}_x = M_x/qa^2$ $\bar{M}_y = M_y/qa^2$ in a clamped rectangular ($a \times b$) plate subjected to a hydrostatic load $f = qx/a$, $0 \leq x \leq a$, $0 \leq y \leq b$, for various side ratios b/a ([$\lambda = 0.134$, $s = 0$, $\nu = 0.3$). The analytical results are obtained from Timoshenko and Woinowsky-Krieger (1959)**

	$b/a = 0.5$		$b/a = 1.0$		$b/a = 1.5$	
	analytic	BEM	analytic	BEM	analytic	BEM
$w(a/2,b/2)$	.080E-03	.079E-03	.630E-03	.630E-03	.110E-02	.109E-02
$M_x(a/2,b/2)$	.198E-02	.198E-02	.115E-01	.114E-01	.184E-01	.183E-01
$M_y(a/2,b/2)$	.515E-02	.513E-02	.115E-01	.114E-01	.102E-01	.101E-01
$M_x(a,b/2)$	-.115E-01	-.115E-01	-.334E-01	-.336E-01	-.462E-01	-.463E-01
$M_x(0,b/2)$	-.028E-02	-.028E-01	-.179E-01	-.179E-01	-.295E-01	-.295E-01
$M_y(a/2,b)$	-.104E-01	-.104E-01	-.257E-01	-.257E-01	-.285E-01	-.286E-01

Table 5 **Influence coefficients for a clamped rectangular ($2a \times 2b$) plate with side ratio $b/a = 1.2$ resting on an elastic foundation with $\lambda = 5$, $s = 7$**

Load position			Influence coefficients for $\bar{w} = w/(\mathrm{Pa}^2/D)$ at $x = 0$, $y = 0$		
x/a y/b	0	0.2	0.4	0.6	0.8
0.8	.5162E-04	.4602E-04	.3248E-04	.1727E-04	.5126E-05
0.6	.2121E-03	.1858E-03	.1261E-03	.6504E-04	.1970E-04
0.4	.6331E-03	.5314E-03	.3287E-03	.1558E-03	.4547E-04
0.2	.1664E-02	.1261E-02	.6620E-03	.2796E-03	.7735E-04
0	.3197E-02	.1920E-02	.8765E-03	.3465E-03	.9330E-04
			Influence coefficients for $\bar{M}_x = M_x/P$ at $x = 0$, $y = 0$ ($\nu = 0.3$)		
x/a y/b	0	0.2	0.4	0.6	0.8
0.8	-.2970E-04	-.6935E-04	-.1236E-03	-.1099E-03	-.4193E-04
0.6	.1802E-03	-.1224E-03	-.5151E-03	-.4878E-03	-.1915E-03
0.4	.2578E-02	.3950E-03	-.1750E-02	-.1565E-02	-.5783E-03
0.2	.2081E-01	.2087E-02	-.5684E-02	-.3793E-02	-.1241E-02
0	.1000E+31	-.4089E-02	-.1025E-01	-.5392E-02	-.1641E-02

ed using the BEM as compared with those obtained from analytical solutions (Selvadurai, 1979) is presented versus the number of boundary elements for a clamped circular plate resting on an elastic foundation ($\lambda = 10$ and $s = 13$), subjected to a uniform load. It is apparent that only a few boundary elements (20 to 30) are sufficient to obtain accurate results.

To demonstrate the accuracy of the BEM three more examples are worked out for which results from analytical solutions are available. Thus, in Table 2 the deflections along the radius of a clamped circular plate subjected to a concentrated load P at its center are tabulated. They are obtained on the basis of analytical solutions and also using the BEM with 32 elements. Three characteristic cases are considered: (*a*) plate not resting on an elastic foundation ($\lambda = 0.134$, $s = 0$); (*b*) plate resting on a Winkler-type foundation ($\lambda = 12$, $s = 0$); (*c*) plate resting on a Pasternak-type foundation ($\lambda = 12$, $s = 15$). The analytical solutions are obtained from Timoshenko and Woinowsky-Krieger (1959), Schleicher (1926), and Selvadurai (1979), respectively.

Moreover, in Table 3 the deflection, the bending moment and the shearing force along the radius of a clamped circular ring-shaped plate with an inner radius b and an outer radius $a = 3b$ are presented when it is subjected to a uniform load q. The numerical results are obtained using the BEM with 32 boundary elements on each boundary and they are compared with those obtained from the analytical solutions (as in Table 2). Furthermore, in Table 4 the deflection and bending moments in a clamped rectangular plate ($a \times b$) not resting on an elastic foundation ($\lambda = 0.134$, $s = 0$) and subjected to a hydrostatic load are presented. The results are obtained using 44 boundary elements and they are compared with existing results from the analytical solution (Timoshenko and Woinowsky-Krieger, 1959).

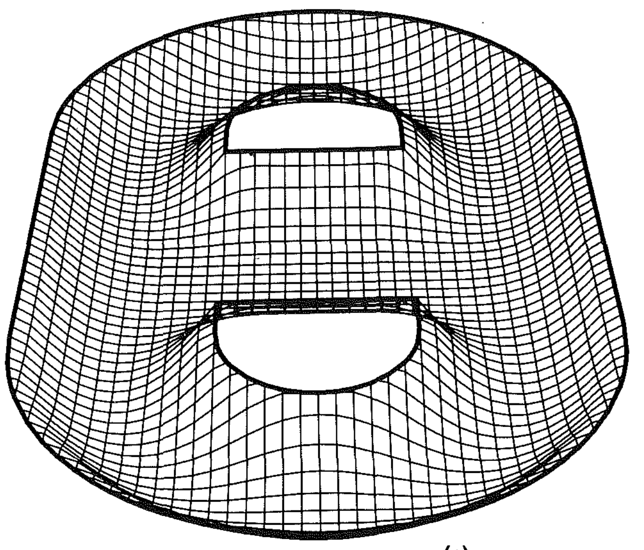
(*a*)

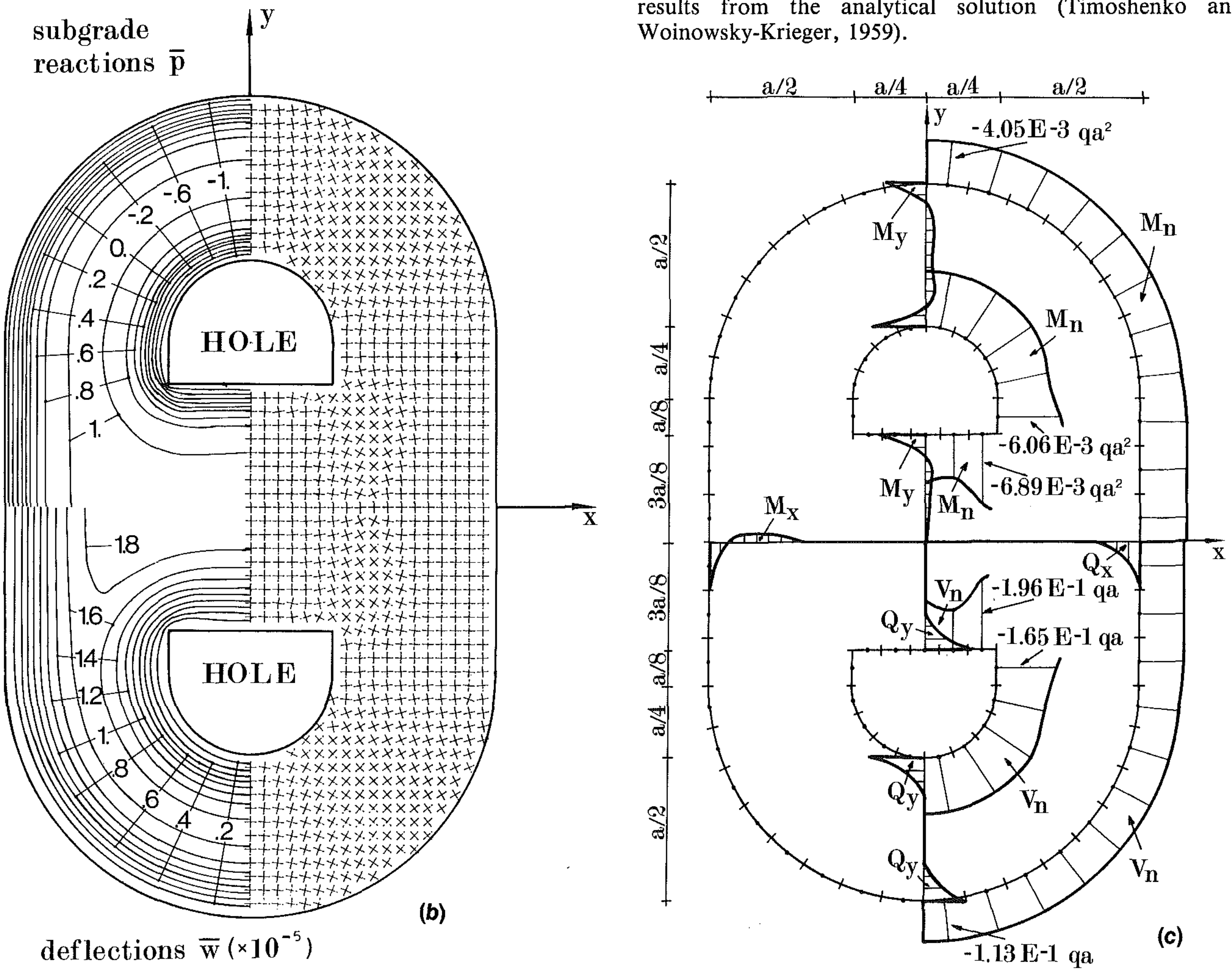

(*b*)

(*c*)

Fig. 3 Uniformly loaded clamped plate of composite geometry resting on a Pasternak-type elastic foundation ($\lambda = 15$, $s = 18$): (*a*) Perspective of the deflection surface of the plate; (*b*) deflections $\bar{w} = w/(qa^4/D)$, subgrade reactions $\bar{p} = p/q$ and directions of principal bending moments; (*c*) boundary reactions and stress resultants

In Table 5, the influence coefficients for the deflection $\bar{w} = w/(Pa^2/D)$ and for the bending moment $\bar{M}_x = M_x/P$ at point $x = y = 0$ of a clamped rectangular plate $(2a \times 2b)$ with side ratio $b/a = 1.2$ for various positions of the concentrated load P are presented ($\lambda = 5$, $s = 7$). The obtained values differ considerably from the corresponding values for a Winkler-type foundation (see Katsikadelis and Armenakas, 1984a).

Finally, in Fig. 3 results obtained on the basis of BEM using 74 boundary elements for a clamped plate of composite shape resting on elastic foundation ($\lambda = 15$, $s = 18$) and subjected to a uniform load q are shown. These results are considered accurate because they differ negligibly from those obtained using twice as many boundary elements.

Conclusions

The following conclusions can be deduced from this investigation:

(*a*) The BEM solution to the problem of bending of thin plates on a biparametric elastic foundation developed herein is well suited for computer-aided analysis.

(*b*) Plates having a composite shape including holes and subjected to any kind of loading are efficiently and completely analyzed; i.e., their deflections, bending, and twisting moments, shearing forces, boundary reactions and subgrade reactions can be established with good accuracy.

(*c*) The conversion of the domain integrals into line integrals reduces drastically the computer time and renders BEM a powerful tool for analyzing difficult plate problems.

(*d*) For plates with relatively smooth boundary the constant element yields good results. The results are considerably improved if curved boundaries are approximated by parabolic arcs.

(*e*) The evaluation of the kernel functions, which are real and imaginary parts of Hankel functions with complex argument, are accurately computed from real valued series expressions.

References

Abramowitz, M., and Stegun, I., eds., 1972, *Handbook of Mathematical Functions*, 10th Ed., Dover, New York.

Balas, J., Sladek, V., and Sladek, J., 1984, "The Boundary Integral Equation Method for Plates Resting on a Two Parameter Foundation," *Zeitschrift für Angewandte Mathematik und Mechanik*, Vol. 51, pp. 574–580.

Courant, R., and Hilbert, D., 1953, *Methods of Mathematical Physics*, Vol. 11, Interscience, New York, Chapt. IV.

Filonenko-Borodich, M. M., 1940, "Some Approximate Theories of the Elastic Foundation," in Russian, *Uchenyie Zapiski Moskovskogo Gosudarstvennogo Universiteta, Mekhanica* (Scientific Notes of the Moscow State University, Mechanics), No. 46, pp. 3–18.

Hetenyi, M., 1946, *Beams on Elastic Foundations*, The University of Michigan Press, Ann Arbor, Mich.

Katsikadelis, J. T., 1982, "The Analysis of Plates on Elastic Foundation by the Boundary Integral Equation Method," Ph.D. Dissertation, Polytechnic Institute of New York.

Katsikadelis, J. T., and Armenakas, A. E., 1983, "Numerical Evaluation of Double Integrals with a Logarithmic or a Cauchy-Type Singularity," ASME JOURNAL OF APPLIED MECHANICS, Vol. 50, pp. 682–684.

Katsikadelis, J. T., and Armenakas, A. E., 1984a, "Analysis of Clamped Plates on Elastic Foundation by the Boundary Integral Equation Method," ASME JOURNAL OF APPLIED MECHANICS, Vol. 51, pp. 574–580.

Katsikadelis, J. T., and Armenakas, A. E., 1984b, "Plates on Elastic Foundation by BIE Method," *Journal of Engineering Mechanics*, ASCE, Vol. 110, No. 7, pp. 1086–1105.

Katsikadelis, J. T., and Armenakas, A. E., 1985, "Numerical Evaluation of Line Integrals with a Logarithmic Singularity," *AIAA Journal*, Vol. 23, pp. 1135–1137.

Katsikadelis, J. T., and Sapountzakis, E. J., 1985, "Torsion of Composite Bars by the Boundary Element Method," *Journal of Engineering Mechanics*, ASCE, Vol. 111, No. 9, pp. 1197–1210.

Kerr, A. D., 1964, "Elastic and Viscoelastic Foundation Models," ASME JOURNAL OF APPLIED MECHANICS, Vol. 31, pp. 491–498.

Pasternak, P. L., 1954, "On a New Method of Analysis of an Elastic Foundation by Means of two Foundation Constants," in Russian, *Gosudarstvennoe Izdatelstvo Literaturi po Stroitelstvu i Arkhitekture*, (State Publications on Construction Literature, Architecture), Moscow, USSR.

Reissner, E., 1958, "A Note on Deflection of Plates on Viscoelastic Foundation," ASME JOURNAL OF APPLIED MECHANICS, Vol. 80, pp. 144–145.

Schleicher, F., 1926, *Kreisplatten auf Elastischer Unterlage*, Springer Verlag, Berlin.

Selvadurai, A. P. S., 1979, *Elastic Analysis of Soil-Foundation Interaction*, Elsevier, Amsterdam-Oxford-New York, Chapt. 2, pp. 27–30, Chapt. 6, pp. 223–244 and pp. 307–313.

Timoshenko, S., and Woinowsky-Krieger, S., 1959, *Theory of Plates and Shells*, 2nd Ed., McGraw-Hill, New York.

Vlasov, V. Z., and Leontiev, N. N., 1966, *Beams, Plates and Shells on Elastic Foundations*, Israel Program for Scientific Translations, Jerusalem, Chapt. IV, pp. 161–183.

Zinke, O., 1959, *Elementare Einführung in die Bessel-, Neumman- und Hankel-Functionen*, S. Hirzel Verlag, Stuttgart, pp. 31–33.

APPENDIX

In this Appendix certain formulae are derived which are used to convert the double integrals (23*e*, *f*) and (33*a*, *b*, *c*, *d*) into line integrals when the loading function $f(Q)$ varies linearly over a region $R^* \subseteq R$ bounded by a curve C^*.

Consider the differential equation

$$\frac{d^2 w}{dz^2} + \frac{1}{z} \frac{dw}{dz} + w = 0 \qquad (A1)$$

When $z = \beta\rho$, with $\rho = |P - Q|/\ell$ and $\beta = e^{i\theta}$ a complex-constant, equation ($A1$) reduces to

$$\frac{d^2 w}{d\rho^2} + \frac{1}{\rho} \frac{dw}{d\rho} + \beta^2 w = 0 \qquad (A2)$$

Equation ($A2$) is satisfied by the Hankel function (Abramowitz and Stegun, 1972)

$$H_o^{(1)}(\beta\rho) = V(\rho) + iI(\rho) \qquad (A3)$$

where $V(\rho)$ and $I(\rho)$ are, respectively, the real and imaginary part of $H_o^{(1)}(\beta\rho)$.

Substituting equation ($A3$) into equation ($A2$) and separating real and imaginary parts, the following two simultaneous differential equations are obtained

$$\nabla^2 V(\rho) = \sin 2\theta I(\rho) - \cos 2\theta V(\rho) \qquad (A4)$$

$$\nabla^2 I(\rho) = -\cos 2\theta I(\rho) - \sin 2\theta V(\rho) \qquad (A5)$$

where $\nabla^2 = \frac{d^2}{d\rho^2} + \frac{1}{\rho} \frac{d}{d\rho}$.

Elimination of $I(\rho)$ from equations ($A4$) and ($A5$) yields

$$V(\rho) = -\cos 2\theta \nabla^2 V(\rho) - \sin 2\theta \nabla^2 I(\rho) \qquad (A6)$$

For any two functions w and v which are two times continuously differentiable in the region R^* and one time continuously differentiable on its boundary C^* it is valid

$$\iint_{R^*} (v\nabla^2 w - w\nabla^2 v) d\sigma = \int_{C^*} \left(v\frac{\partial w}{\partial n} - w\frac{\partial v}{\partial n} \right) ds \qquad (A7)$$

Applying the Green identity ($A7$) for the pair of functions $v = f$, $w = V(\rho)$ and noting that $\nabla^2 f = 0$ we obtain

$$\iint_{R^*} \nabla^2 V(\rho) f(Q) d\sigma_Q$$

$$= \ell^2 \int_{C^*} \left[\frac{\partial V(\rho)}{\partial n_q} f(q) - V(\rho) \frac{\partial f(q)}{\partial n_q} \right] ds_q \qquad (A8)$$

Similarly, applying the same identity for the pair of functions $v = f$ and $w = I(\rho)$ we obtain

$$\iint_{R^*} \nabla^2 I(\rho) f(Q) d\sigma_Q$$

$$= \ell^2 \left\{ \epsilon f(P) + \int_{C^*} \left[f(q) \frac{\partial I(\rho)}{\partial n_q} - I(\rho) \frac{\partial f(q)}{\partial n_q} \right] ds_q \right\} \qquad (A9)$$

where in double integrals it is $\rho = |P - Q|/\ell$, $Q \epsilon R^*$ while in line integrals, it is $\rho = |P - q|/\ell$, $q \epsilon C^*$.

The additional term $\epsilon f(P)$ in equation ($A9$) is due to the fact that the line integral behaves like a double layer potential. The value of the constant is established by a limiting process. Thus, isolating point P by a small circle centered at point P, when P is inside R^*, or by a small circular sector when point P is on C^*, applying Green's identity ($A7$), letting the radius of the small circle or of the circular sector, respectively, shrink to a point and taking into account that for small values of the argument ρ it is

$$\frac{\partial I(\rho)}{\partial n} = \frac{1}{\ell} I'(\rho)\cos\varphi = -\frac{1}{\ell}\{\sin\theta \mathrm{Re}[H_1^{(1)}(\beta\rho)] + \cos\theta Im[H_1^{(1)}(\beta\rho)]\}\cos\varphi \simeq -\frac{1}{\ell}\frac{2}{\pi\rho}\cos\varphi$$

we obtain

$$\epsilon = -4 \qquad \text{when } P \text{ is inside } R^* \qquad (A10a)$$

$$\epsilon = -2(2-\alpha/\pi) \qquad \text{when } P \text{ is on } C^* \qquad (A10b)$$

Note that

$$\epsilon = 0 \qquad \text{when } P \text{ is outside } R^* \qquad (A10c)$$

α is the angle between the tangents at point p of the boundary. For smooth boundaries it is $\alpha = \pi$.

Modal Parameter Analysis of Gyroelastic Continua

P. C. Hughes

G. M. T. D'Eleuterio

Institute for Aerospace Studies,
University of Toronto,
Downsview, Ontario, Canada M3H 5T6

This paper builds on the theory of gyroelastic dynamics presented in a recent paper by the authors. An elastic continuum with a continuous distribution of stored angular momentum (called gyricity*) is considered. We introduce the modal parameters (coefficients) thereof, including integrals of the mode shapes, and show they must satisfy a number of useful identities. In addition to the coefficients* (p_α *and* h_α) *associated with momentum and angular momentum which also arise in the dynamics of a purely elastic body, there is a third coefficient* (g_α) *wholly attributable to the gyricity distribution. The modal parameter analysis presented here is an extension of that for purely elastic continua. The analysis concludes with a simple demonstration of the theoretical results using a spatially discretized model of a cantilevered rod.*

1 Introduction

In a recent paper [1] the authors developed a theory for the dynamics of *gyroelastic* structures—that is, structures represented by a continuous distribution of mass and elasticity and that contain, as well, a continuous distribution of stored angular momentum, or *gyricity*. The equation of motion for such a structure (denoted E in Fig. 1) was shown to be

$$\mathfrak{M}\ddot{\mathbf{u}} + \mathcal{G}\dot{\mathbf{u}} + \mathcal{K}\mathbf{u} = \mathbf{f}_e(\mathbf{r},t) \qquad (1)$$

a form that is suggestive of its better-known discrete counterpart [2]. Here $\mathbf{u}(\mathbf{r},t)$ is the small deformation of E at position $\mathbf{r}$ and time t. The symbol $\mathcal{K}$ denotes a *stiffness operator* (normally a differential operator); it is Hermitian and positive definite [1]. The *mass operator* $\mathfrak{M}$ is just $\sigma(\mathbf{r})\,1$ where σ is the mass density at $\mathbf{r}$ and 1 is the identity operator; clearly $\mathfrak{M}$ is also Hermitian and positive definite. The focus of attention, however, is the *gyric operator* $\mathcal{G}$ given by

$$\mathcal{G} = -\frac{1}{4}\nabla^{\times}\mathbf{h}_s^{\times}\nabla^{\times} \qquad (2)$$

where ∇ is the gradient operator and the gyricity function $\mathbf{h}_s(\mathbf{r})$ represents the angular momentum stored within an element dV of E at $\mathbf{r}$. The notation $\nabla^{\times}$ simply refers to the components of the curl operator, and it can therefore be demonstrated [1] that $\mathcal{G}$ is skew-Hermitian. The only remaining symbol in equation (1), $\mathbf{f}_e$, represents the external force per unit volume at $\mathbf{r}$.

The equation of motion (1) can be derived using the principles of Newton and d'Alembert or, alternatively, from Hamilton's (extended) principle. A third derivation can be obtained from the balance laws of continuum mechanics [3]. This approach uses the concepts developed by Eringen and others [4, 5, for example].

Elastic structures (large space structures, perhaps) containing a very large number of small spinning wheels furnish an excellent example of a system that could profitably be modeled using a partial differential equation of the form (1). Thus systems of the type characterized by equations (1) and (2) are of practical, as well as theoretical interest.

The free motions of continuous gyroelastic systems lead to *gyroelastic modes*, as derived and discussed in [1]. Although each mode is a sinusoidal vibration (as with nongyric elastic systems) one must now associate two mode shapes with each mode (as compared to one mode shape for the nongyric case). These mode shapes can be shown to satisfy certain orthonormality conditions which are, as expected, generalizations of the familiar nongyric conditions.

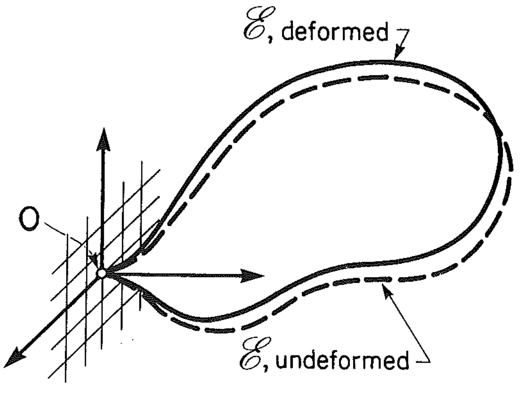

Fig. 1 Constrained elastic body

Contributed by the Applied Mechanics Division for publication in the Journal of Applied Mechanics.

Discussion on this paper should be addressed to the Editorial Department, ASME, United Engineering Center, 345 East 47th Street, New York, N.Y., 10017, and will be accepted until two months after final publication of the paper itself in the Journal of Applied Mechanics. Manuscript received by ASME Applied Mechanics Division, August 20, 1984; final revision October 25, 1985.

The object of this paper is to extend the theory of gyroelastic structures by certain integrals of the mode shapes (these integrals arise naturally in the dynamics) and to state and prove a number of *modal identities* which these modal integrals must satisfy. In addition to their mathematical interest, these identities provide useful checks on analysis. They also provide a rational basis for model order reduction.

2 Gyroelastic Vibration Modes

In some of the following proofs it would be advantageous to write the motion equation (1) in an equivalent first-order form:

$$\mathcal{E}\dot{\chi} + \mathcal{S}\chi = \gamma \tag{3}$$

where

$$\mathcal{E} \triangleq \begin{bmatrix} \mathcal{M} & \mathcal{O} \\ \mathcal{O} & \mathcal{K} \end{bmatrix}; \quad \mathcal{S} \triangleq \begin{bmatrix} \mathcal{G} & \mathcal{K} \\ -\mathcal{K} & \mathcal{O} \end{bmatrix} \tag{4}$$

$$\chi \triangleq \begin{bmatrix} \dot{\mathbf{u}} \\ \mathbf{u} \end{bmatrix}; \quad \gamma \triangleq \begin{bmatrix} \mathbf{f}_e \\ \mathbf{0} \end{bmatrix} \tag{5}$$

and $\mathcal{O}$ is the null operator. It can be shown that $\mathcal{E}$ is Hermitian and positive-definite, and $\mathcal{S}$ skew-Hermitian. The equivalent eigenvalue problem,

$$\lambda_\alpha \mathcal{E}\chi_\alpha + \mathcal{S}\chi_\alpha = \mathbf{0} \tag{6}$$

has the properties that λ_α is purely imaginary (we shall set $\lambda_\alpha = j\omega_\alpha$) and that

$$\chi_\alpha(\mathbf{r}) = \phi_\alpha(\mathbf{r}) + j\psi_\alpha(\mathbf{r}) \tag{7}$$

where the six-tuples ϕ_α and ψ_α are of the form

$$\phi_\alpha = \begin{bmatrix} -\omega_\alpha \mathbf{v}_\alpha \\ \mathbf{u}_\alpha \end{bmatrix}; \quad \psi_\alpha = \begin{bmatrix} \omega_\alpha \mathbf{u}_\alpha \\ \mathbf{v}_\alpha \end{bmatrix} \tag{8}$$

with $\mathbf{u}_\alpha(\mathbf{r})$ and $\mathbf{v}_\alpha(\mathbf{r})$ being the two mode shapes associated with the αth gyroelastic mode. In fact, the motion of that mode is expressed as:

$$\mathbf{u}(\mathbf{r},t) = \mathbf{u}_\alpha(\mathbf{r})\cos\omega_\alpha t - \mathbf{v}_\alpha(\mathbf{r})\sin\omega_\alpha t \tag{9}$$

For nongyric modes, $\mathbf{u}_\alpha$ and $\mathbf{v}_\alpha$ are identical.

It will prove indispensable to associate an *inner product* with the space of real six-tuples. Thus define

$$\phi^\tau \psi = \int_E \phi^T(\mathbf{r})\psi(\mathbf{r})dV$$

The τ-operator may be regarded as a generalization of the transpose operator. For a detailed explanation of the τ-notation as pertaining to both inner and *outer* products, see the Appendix.

In [1] it has been shown that the orthonomality conditions satisfied by the ϕ_α and ψ_α are

$$\phi_\alpha^\tau \mathcal{E}\phi_\beta = 2\omega_\alpha^2 \delta_{\alpha\beta} \tag{10}$$

An additional family of conditions, neither proved nor stated in [1] but needed below, is this

$$\phi_\alpha^\tau \mathcal{E}\psi_\beta = 0 \quad (\text{all } \alpha,\beta) \tag{11}$$

The proof may be found in [6]. The equivalent conditions in terms of the mode shapes $\mathbf{u}_\alpha$ and $\mathbf{v}_\alpha$ are

$$\mathbf{u}_\alpha^\tau \mathcal{K}\mathbf{v}_\beta = \omega_\alpha\omega_\beta \mathbf{v}_\alpha^\tau \mathcal{M}\mathbf{u}_\beta \quad (\text{all } \alpha,\beta) \tag{12}$$

Written without the inner-product notation, equation (12) takes the form

$$\int_E \mathbf{u}_\alpha^T \mathcal{K}\mathbf{v}_\beta dV = \omega_\alpha\omega_\beta \int_E \mathbf{v}_\alpha^T \mathbf{u}_\beta dm \tag{13}$$

Note that without gyricity, in which case

$$\mathbf{u}_\alpha = \mathbf{v}_\alpha \equiv \mathbf{u}_{\alpha o}(\mathbf{r}) \tag{14}$$

both the left and right sides of equation (13) vanish when $\alpha \neq \beta$. When $\alpha = \beta$, equation (13) reduces to $\omega_\alpha^2 = \omega_\beta^2$.

3 Modal Momentum Coefficients

We shall now introduce the *modal momentum coefficients* for the gyroelastic continuum E. The momentum and angular momentum (the latter about O) are given by

$$\mathbf{p}(t) = \int_E \dot{\mathbf{u}}(\mathbf{r},t)dm \tag{15}$$

and

$$\mathbf{h}(t) = \int_E \mathbf{C}(\mathbf{r},t)\mathbf{h}_s(\mathbf{r})dV + \int_E \mathbf{r}^\times \dot{\mathbf{u}}(\mathbf{r},t)dm \tag{16}$$

where

$$\mathbf{C}(\mathbf{r},t) = \mathbf{1} - \theta^\times(\mathbf{r},t) \tag{17}$$

is the (first-order) rotation matrix from a local reference frame at $\mathbf{r}$, in which $\mathbf{h}_s$ is expressed, to an inertial frame. The quantity θ is the column of corresponding (first-order) rotational displacements at $\mathbf{r}$ and may be expressed as

$$\theta(\mathbf{r}) = \frac{1}{2}\nabla^\times \mathbf{u}(\mathbf{r}) \tag{18}$$

Substituting for θ in equation (16) yields

$$\mathbf{h}(t) = \mathbf{h}_T + \frac{1}{2}\int_E \mathbf{h}_s^\times(\mathbf{r})\nabla^\times \mathbf{u}(\mathbf{r},t)dV + \int_E \mathbf{r}^\times \dot{\mathbf{u}}(\mathbf{r},t)dm \tag{19}$$

where

$$\mathbf{h}_T \triangleq \int_E \mathbf{h}_s(\mathbf{r})dV \tag{20}$$

is the total angular momentum stored in E. The general displacement of E may be expanded as follows:

$$\mathbf{u}(\mathbf{r},t) = \sum_\beta [\mathbf{u}_\beta(\mathbf{r})\eta_{u\beta}(t) + \mathbf{v}_\beta(\mathbf{r})\eta_{v\beta}(t)] \tag{21}$$

Upon insertion of this expression, equations (15) and (19) become

$$\mathbf{p}(t) = \sum_\beta [\mathbf{p}_{u\beta}\dot{\eta}_{u\beta} + \mathbf{p}_{v\beta}\dot{\eta}_{v\beta}] \tag{22}$$

and

$$\mathbf{h}(t) = \mathbf{h}_T + \sum_\beta [\mathbf{h}_{u\beta}\dot{\eta}_{u\beta} + \mathbf{h}_{v\beta}\dot{\eta}_{v\beta} - \mathbf{g}_{u\beta}\eta_{u\beta} - \mathbf{g}_{v\beta}\eta_{v\beta}] \tag{23}$$

where

$$\mathbf{p}_{u\beta} \triangleq \int_E \mathbf{u}_\beta dm, \quad \mathbf{p}_{v\beta} \triangleq \int_E \mathbf{v}_\beta dm \tag{24}$$

shall be called the *modal momentum coefficients*,

$$\mathbf{h}_{u\beta} \triangleq \int_E \mathbf{r}^\times \mathbf{u}_\beta dm, \quad \mathbf{h}_{v\beta} \triangleq \int_E \mathbf{r}^\times \mathbf{v}_\beta dm \tag{25}$$

the *modal angular-momentum coefficients* and

$$\mathbf{g}_{u\beta} \triangleq -\frac{1}{2}\int_E \mathbf{h}_s^\times \nabla^\times \mathbf{u}_\beta dV, \quad \mathbf{g}_{v\beta} \triangleq -\frac{1}{2}\int_E \mathbf{h}_s^\times \nabla^\times \mathbf{v}_\beta dV \tag{26}$$

the *modal stored-momentum coefficients*.

The body E is constrained at O and thus its motion must be resisted by a reaction force $\mathbf{F}_R$ and a reaction torque (about O) $\mathbf{G}_R$ on E at O. The reaction force and torque are given by

$$-\mathbf{F}_R(t) = \int_E \mathbf{f}(\mathbf{r},t)dm \tag{27}$$

and

$$-\mathbf{G}_R(t) = \int_E \mathbf{r}^\times \mathbf{f}(\mathbf{r},t)dm \tag{28}$$

where $\mathbf{f}(\mathbf{r},t)$ is the sum of all force fields, inertial, gyric and external, acting on E, that is

$$\mathbf{f}(\mathbf{r},t) = -\mathcal{M}\ddot{\mathbf{u}} - \mathcal{G}\dot{\mathbf{u}} + \mathbf{f}_e(\mathbf{r},t) \tag{29}$$

The expansion for $\dot{\mathbf{u}}$ analogous to equation (21) is

$$\dot{\mathbf{u}}(\mathbf{r},t) = \sum_\beta \omega_\beta [\mathbf{u}_\beta(\mathbf{r})\eta_{v\beta}(t) + \mathbf{v}_\beta(\mathbf{r})\eta_{u\beta}(t)] \tag{30}$$

which may be obtained by considering the general expansion for $\chi(\mathbf{r},t)$ [1]. Substituting equation (30) into equations (27) and (28), and integrating by parts (see [1]) where required, we have

$$-\mathbf{F}_R(t) = \mathbf{F}_e(t) - \sum_\beta \omega_\alpha [\mathbf{p}_{u\alpha}\dot{\eta}_{v\alpha} + \mathbf{p}_{v\alpha}\dot{\eta}_{u\alpha}] \tag{31}$$

$$-\mathbf{G}_R(t) = \mathbf{G}_e(t) - \sum_\beta [\mathbf{h}_{u\alpha}\dot{\eta}_{v\alpha} + \mathbf{h}_{v\alpha}\dot{\eta}_{u\alpha} - \mathbf{g}_{u\alpha}\eta_{v\alpha} - \mathbf{g}_{v\alpha}\eta_{u\alpha}] \tag{32}$$

where

$$\mathbf{F}_e(t) \triangleq \int_E \mathbf{f}(\mathbf{r},t)\,dV, \quad \mathbf{G}_e(t) \triangleq \int_E \mathbf{r}^\times \mathbf{f}(\mathbf{r},t)\,dV \tag{33}$$

are the total external force and torque on E.

Before proceeding onward we note that the modal coefficients can be expressed using the (inner product) τ-notation, namely,

$$\begin{aligned} \mathbf{p}_{u\alpha} &= \mathbf{1}^\tau \mathcal{M}\mathbf{u}_\alpha, & \mathbf{p}_{v\alpha} &= \mathbf{1}^\tau \mathcal{M}\mathbf{v}_\alpha \\ \mathbf{h}_{u\alpha} &= -(\mathbf{r}^\times)^\tau \mathcal{M}\mathbf{u}_\alpha, & \mathbf{h}_{v\alpha} &= -(\mathbf{r}^\times)^\tau \mathcal{M}\mathbf{v}_\alpha \\ \mathbf{g}_{u\alpha} &= -(\mathbf{r}^\times)^\tau \mathcal{G}\mathbf{u}_\alpha, & \mathbf{g}_{v\alpha} &= -(\mathbf{r}^\times)^\tau \mathcal{G}\mathbf{v}_\alpha \end{aligned} \tag{34}$$

These forms will prove useful.

4 Modal Expansion for $\mathcal{E}^{-1}$

The proof of the identities for the modal momentum coefficients, to be presented in the next section, rests on the fundamental result that $\mathcal{E}^{-1}$ can be written as a modal expansion. As stated earlier the operator $\mathcal{E}$ is positive-definite; hence $\mathcal{E}^{-1}$ exists and, in fact, is given by

$$\mathcal{E}^{-1} = \begin{bmatrix} \mathcal{M}^{-1} & \cdot \\ \cdot & \mathcal{K}^{-1} \end{bmatrix} \tag{35}$$

We assert that $\mathcal{E}^{-1}$ can be expanded in forms of the eigenfunctions as follows:

$$\mathcal{E}^{-1} = \frac{1}{2} \sum_\alpha \omega_\alpha^{-2} [\boldsymbol{\phi}_\alpha \boldsymbol{\phi}_\alpha^\tau + \boldsymbol{\psi}_\alpha \boldsymbol{\psi}_\alpha^\tau] \tag{36}$$

(The reader is reminded that the outer-product τ-notation is explained in the Appendix.) One can be convinced of the verisimilitude of this identity by noting that, upon substitution, it satisfies the eigenvalue problem when written in real terms as

$$\begin{aligned} -\omega_\alpha \boldsymbol{\psi}_\alpha + \mathcal{E}^{-1}\mathcal{S}\boldsymbol{\phi}_\alpha &= \mathbf{0} \\ \omega_\alpha \boldsymbol{\phi}_\alpha + \mathcal{E}^{-1}\mathcal{S}\boldsymbol{\psi}_\alpha &= \mathbf{0} \end{aligned} \tag{37}$$

For a rigorous proof, however, consult [6]. Combining equations (35) and (36) with (8) it is clear that

$$\mathcal{M}^{-1} = \frac{1}{2} \sum_\alpha [\mathbf{u}_\alpha \mathbf{u}_\alpha^\tau + \mathbf{v}_\alpha \mathbf{v}_\alpha^\tau] \tag{38}$$

$$\mathcal{O} = \sum_\alpha \omega_\alpha^{-1} [\mathbf{u}_\alpha \mathbf{v}_\alpha^\tau + \mathbf{v}_\alpha \mathbf{u}_\alpha^\tau] \tag{39}$$

$$\mathcal{K}^{-1} = \frac{1}{2} \sum_\alpha \omega_\alpha^{-2} [\mathbf{u}_\alpha \mathbf{u}_\alpha^\tau + \mathbf{v}_\alpha \mathbf{v}_\alpha^\tau] \tag{40}$$

In the interest of completeness, we note that $\mathcal{S}^{-1}$ ($\mathcal{S}$ is nonsingular) can also be expanded in forms of the eigenfunctions:

$$\mathcal{S}^{-1} = \frac{1}{2} \sum_\alpha \omega_\alpha^{-3} [\boldsymbol{\phi}_\alpha \boldsymbol{\psi}_\alpha^\tau + \boldsymbol{\psi}_\alpha \boldsymbol{\phi}_\alpha^\tau] \tag{41}$$

Moreover, it can be shown by induction that

$$(\mathcal{S}^{-1}\mathcal{E})^n \mathcal{E}^{-1} (\mathcal{E}\mathcal{S}^{-1})^n = \frac{(-1)^n}{2} (1)^n \sum_\alpha \omega^{-2}n^{-2} [{}_\alpha \boldsymbol{\phi}_\alpha^\tau \boldsymbol{\phi}_\alpha^\tau + \boldsymbol{\psi}_\alpha \boldsymbol{\psi}_\alpha^\tau] \tag{42}$$

$$(\mathcal{S}^{-1}\mathcal{E})^n \mathcal{S}^{-1} (\mathcal{E}\mathcal{S}^{-1})^n = \frac{1}{2} \sum_\alpha \omega^{-2}n^{-3} [\boldsymbol{\phi}_\alpha \boldsymbol{\psi}_\alpha^\tau + \boldsymbol{\psi}_\alpha \boldsymbol{\phi}_\alpha^\tau] \tag{43}$$

5 Modal Identities

Having established the results (38–40), we can proceed with great facility in proving a series of modal identities which are reminiscent of Parseval. Let us begin with equation (38),

$$\mathcal{M}^{-1} = \frac{1}{2} \sum_\alpha [\mathbf{u}_\alpha \mathbf{u}_\alpha^\tau + \mathbf{v}_\alpha \mathbf{v}_\alpha^\tau]$$

This is an operator equation and so we can operate on $\sigma(\mathbf{r})\mathbf{1}$ to give

$$\mathcal{M}^{-1}(\sigma\mathbf{1}) = \frac{1}{2} \sum_\alpha [\mathbf{u}_\alpha \{\mathbf{u}_\alpha^\tau(\sigma\mathbf{1})\} + \mathbf{u}_\alpha \{\mathbf{v}_\alpha^\tau(\sigma\mathbf{1})\}] \tag{44}$$

Recalling the definition of $\mathcal{M}$, it follows that

$$\mathcal{M}^{-1} \equiv \sigma^{-1} I \tag{45}$$

Hence, the right-hand side of equation (44) reduces to the identity matrix $\mathbf{1}$. Now, taking the inner product of equation (44) with $\sigma(\mathbf{r})\mathbf{1}$ leads to

$$\begin{aligned} (\sigma\mathbf{1})^\tau \mathbf{1} = \frac{1}{2} \sum_\alpha [\{(\sigma\mathbf{1})^\tau \mathbf{u}_\alpha\}\{\mathbf{u}_\alpha^\tau(\sigma\mathbf{1})\} \\ + \{(\sigma\mathbf{1})^\tau \mathbf{v}_\alpha\}\{\mathbf{v}_\alpha^\tau(\sigma\mathbf{1})\}] \end{aligned} \tag{46}$$

But $(\sigma\mathbf{1})^\tau\mathbf{1}$ is just the matrix $m\mathbf{1}$, where m is the mass of E. Finally, upon realizing that

$$(\sigma\mathbf{1})^\tau \mathbf{u}_\alpha = \mathbf{1}^\tau \mathcal{M}\mathbf{u}_\alpha = \mathbf{p}_{u\alpha}, \quad (\sigma\mathbf{1})^\tau \mathbf{v}_\alpha = \mathbf{1}^\tau \mathcal{M}\mathbf{v}_\alpha = \mathbf{p}_{v\alpha}$$

and

$$\mathbf{u}_\alpha^\tau(\sigma\mathbf{1}) = (\mathcal{M}\mathbf{u}_\alpha)^\tau \mathbf{1} = \mathbf{p}_{u\alpha}^T, \; \mathbf{v}_\alpha^\tau(\sigma\mathbf{1}) = (\mathcal{M}\mathbf{v}_\alpha)^\tau \mathbf{1} = \mathbf{p}_{v\alpha}^\tau$$

we achieve the desired result,

$$\frac{1}{2} \sum_\alpha [\mathbf{p}_{u\alpha}\mathbf{p}_{u\alpha}^T + \mathbf{p}_{v\alpha}\mathbf{p}_{v\alpha}^T] = m\mathbf{1} \tag{I,a}$$

(For clarity, new identities will be labeled with Roman numerals as they are cited.) These then are the essential steps in the proof of the modal identities.

In the absence of gyricity recall that [1]

$$\mathbf{u}_\alpha(\mathbf{r}) = \mathbf{v}_\alpha(\mathbf{r}) \equiv \mathbf{u}_{o\alpha}(\mathbf{r}) \quad (h_s \equiv 0) \tag{47}$$

and so

$$\mathbf{p}_{u\alpha} = \mathbf{p}_{v\alpha} \equiv \mathbf{p}_{o\alpha} \quad (h_s \equiv 0) \tag{48}$$

Hence, Identity (I,a) reduces to

$$\sum_\alpha \mathbf{p}_{o\alpha}\mathbf{p}_{o\alpha}^T = m\mathbf{1} \quad (h_s \equiv 0) \tag{49}$$

which is the familiar result for (nongyric) elastic continua [7].

Additional identities for the modal coefficients may be derived by replacing $\sigma(\mathbf{r})\mathbf{1}$ with $\sigma(\mathbf{r})\mathbf{r}^\times$ and/or $\mathcal{G}\mathbf{r}^\times$ in the two appropriate steps, leading to equations (44) and (46) of the foregoing proof. Thus, the complete set of identities born of equation (38) is

$$\frac{1}{2}\sum_{\alpha}[\mathbf{p}_{u\alpha}\mathbf{p}_{u\alpha}^T+\mathbf{p}_{v\alpha}\mathbf{p}_{v\alpha}^T]=m\mathbf{1}$$

$$\frac{1}{2}\sum_{\alpha}[\mathbf{h}_{u\alpha}\mathbf{h}_{u\alpha}^T+\mathbf{h}_{v\alpha}\mathbf{h}_{v\alpha}^T]=\mathbf{J}$$

$$\frac{1}{2}\sum_{\alpha}[\mathbf{g}_{u\alpha}\mathbf{g}_{u\alpha}^T+\mathbf{g}_{v\alpha}\mathbf{g}_{v\alpha}^T]=\frac{1}{4}\int_E(\nabla^{\times}\mathbf{h}_s^{\times})^T(\nabla^{\times}\mathbf{h}_s^{\times})\sigma^{-1}dV$$

$$\frac{1}{2}\sum_{\alpha}[\mathbf{p}_{u\alpha}\mathbf{h}_{u\alpha}^T+\mathbf{p}_{v\alpha}\mathbf{h}_{v\alpha}^T]=-\mathbf{c}^{\times} \qquad (I,a\text{–}f)$$

$$\frac{1}{2}\sum_{\alpha}[\mathbf{h}_{u\alpha}\mathbf{g}_{u\alpha}^T+\mathbf{h}_{v\alpha}\mathbf{g}_{v\alpha}^T]=-\mathbf{h}_T^{\times}$$

$$\frac{1}{2}\sum_{\alpha}[\mathbf{g}_{u\alpha}\mathbf{p}_{u\alpha}^T+\mathbf{g}_{v\alpha}\mathbf{p}_{v\alpha}^T]=\mathbf{O}$$

where

$$m=\int_E dm,\quad \mathbf{c}=\int_E\mathbf{r}dm,\quad \mathbf{J}=-\int_E\mathbf{r}^x\mathbf{r}^x dm$$

are, respectively, the zeroth, first, and second moments of inertia (about O) of E. The proofs of (I,cef) require integration by parts as well as observing, for (I,f), that $\mathbf{h}_s$ vanishes on the surface of E. In the limit as $h_s\to 0$, Identities (I,bd) also reduce to those established for (nongyric) elastic continua [3].

The identities derived above involve the modal coefficients exclusively. We now present six more identities which involve the modal frequencies ω_α as well. These are derived in the same fashion as those above but with the null operator $\mathcal{O}$, as given by equation (39), replacing $\mathcal{M}^{-1}$. Clearly, the value of the sums will be $\mathbf{O}$, the (3×3) zero matrix. The end results are

$$\sum_{\alpha}\omega_\alpha^{-1}[\mathbf{p}_{u\alpha}\mathbf{p}_{v\alpha}^T+\mathbf{p}_{v\alpha}\mathbf{p}_{u\alpha}^T]=\mathbf{O}$$

$$\sum_{\alpha}\omega_\alpha^{-1}[\mathbf{h}_{u\alpha}\mathbf{h}_{v\alpha}^T+\mathbf{h}_{v\alpha}\mathbf{h}_{u\alpha}^T]=\mathbf{O}$$

$$\sum_{\alpha}\omega_\alpha^{-1}[\mathbf{g}_{u\alpha}\mathbf{g}_{v\alpha}^T+\mathbf{g}_{v\alpha}\mathbf{g}_{u\alpha}^T]=\mathbf{O}$$

$$(II,a\text{–}f)$$

$$\sum_{\alpha}\omega_\alpha^{-1}[\mathbf{p}_{u\alpha}\mathbf{h}_{v\alpha}^T+\mathbf{p}_{v\alpha}\mathbf{h}_{u\alpha}^T]=\mathbf{O}$$

$$\sum_{\alpha}\omega_\alpha^{-1}[\mathbf{h}_{u\alpha}\mathbf{g}_{v\alpha}^T+\mathbf{h}_{v\alpha}\mathbf{g}_{u\alpha}^T]=\mathbf{O}$$

$$\sum_{\alpha}\omega_\alpha^{-1}[\mathbf{g}_{u\alpha}\mathbf{p}_{v\alpha}^T+\mathbf{g}_{v\alpha}\mathbf{p}_{u\alpha}^T]=\mathbf{O}$$

All of these identities become trivial when $h_s\equiv 0$.

One may well anticipate by now that another family of identities can be generated by using the modal expansion for $\mathcal{K}^{-1}$, given by equation (40), in the same manner as the $\mathcal{M}^{-1}$ and $\mathcal{O}$ expansions have already been exploited. These identities will have a more attractive form if we can find an interpretation of $\mathcal{K}^{-1}$ that is somewhat analogous to the interpretation (45) for $\mathcal{M}^{-1}$. To this end, we note that, since $\mathcal{K}$ is typically a differential operator, $\mathcal{K}^{-1}$ is typically an integral operator which may be written as

$$\mathcal{K}^{-1}(\bullet)=\int_E\mathbf{F}(\mathbf{r},\xi)(\bullet)dV(\xi) \qquad (50)$$

where $\mathbf{F}(\mathbf{r},\xi)$, a (3×3) matrix function of $\mathbf{r}$ and ξ, is known as the *flexibility kernel*. Note that because $\mathcal{K}$ is symmetric and positive-definite, $\mathbf{F}(\mathbf{r},\xi)$ is symmetric,

$$\mathbf{F}^T(\xi,\mathbf{r})=\mathbf{F}(\mathbf{r},\xi) \qquad (51)$$

and positive-definite

$$\int_E\mathbf{f}^T(\mathbf{r})\mathbf{F}(\mathbf{r},\xi)\mathbf{f}(\xi)dVdV>0 \qquad (52)$$

for $\mathbf{f}(\mathbf{r})$ in the domain of $\mathcal{K}^{-1}$ and not identically zero. Perhaps the best known of the flexibility kernels is that for a slender, uniform cantilevered rod:

$$F(x,\xi)=\begin{cases}x^2(3\xi-x)/6B, & 0\le x\le\xi\le\ell\\ \xi^2(3x-\xi)/6B, & 0\le\xi\le x\le\ell\end{cases} \qquad (53)$$

where B is the rod's flexural stiffness and ℓ is its length.

The identities thus wrought from (40) are

$$\frac{1}{2}\sum_{\alpha}\omega_\alpha^{-2}[\mathbf{p}_{u\alpha}\mathbf{p}_{u\alpha}^T+\mathbf{p}_{v\alpha}\mathbf{p}_{v\alpha}^T]=\int_E\int_E\mathbf{F}(\mathbf{r},\xi)dmdm$$

$$\frac{1}{2}\sum_{\alpha}\omega_\alpha^{-2}[\mathbf{h}_{u\alpha}\mathbf{h}_{u\alpha}^T+\mathbf{h}_{v\alpha}\mathbf{h}_{v\alpha}^T]=-\int_E\int_E\mathbf{r}^{\times}\mathbf{F}(\mathbf{r},\xi)\xi^{\times}dmdm$$

$$\frac{1}{2}\sum_{\alpha}\omega_\alpha^{-2}[\mathbf{g}_{u\alpha}\mathbf{g}_{u\alpha}^T+\mathbf{g}_{v\alpha}\mathbf{g}_{v\alpha}^T]$$

$$=\frac{1}{4}\int_E\int_E[\nabla_r^x\mathbf{h}_s^x(\mathbf{r})]^T\mathbf{F}(\mathbf{r},\xi)[\nabla_g^x\mathbf{h}_s^{\times}(\xi)]dVdV$$

$$(III,a\text{–}f)$$

$$\frac{1}{2}\sum_{\alpha}\omega_\alpha^{-2}[\mathbf{p}_{u\alpha}\mathbf{h}_{u\alpha}^T+\mathbf{p}_{v\alpha}\mathbf{h}_{v\alpha}^T]=-\int_E\int_E\mathbf{F}(\mathbf{r},\xi)\mathbf{r}^{\times}dmdm$$

$$\frac{1}{2}\sum_{\alpha}\omega_\alpha^{-2}[\mathbf{h}_{u\alpha}\mathbf{g}_{u\alpha}^T+\mathbf{h}_{v\alpha}\mathbf{g}_{v\alpha}^T]$$

$$=\frac{1}{2}\int_E\int_E\mathbf{r}^{\times}\mathbf{F}(\mathbf{r},\xi)[\nabla_\xi^{\times}\mathbf{h}_s^{\times}(\xi)]dV(\xi)dm(\mathbf{r})$$

$$\frac{1}{2}\sum_{\alpha}\omega_\alpha^{-2}[\mathbf{g}_{u\alpha}\mathbf{p}_{u\alpha}^T+\mathbf{g}_{v\alpha}\mathbf{p}_{v\alpha}^T]$$

$$=\frac{1}{2}\int_E\int_E[\nabla_r^{\times}\mathbf{h}_s^{\times}(\mathbf{r})]^T\mathbf{F}(\mathbf{r},\xi)dm(\xi)dV(\mathbf{r})$$

Taking advantage of these identities is more challenging than employing the earlier ones since in general they require a sextuple integration (quadruple for two-dimensional structures and double for one-dimensional structures). On the other hand, the weighting coefficients for these identities are ω_α^{-2} and therefore convergence would tend to be much more rapid. There is certainly something to be said for any nontrivial identity that involves the modal frequencies because they are well known to be of the greatest importance.

6 Sum of Squares of Modal Periods

For a nongyric elastic structure, the modal frequencies obey the following identity [7]:

$$\sum_{\alpha}\omega_{o\alpha}^{-2}=tr\int_E\mathbf{F}(\mathbf{r},\mathbf{r})dm \qquad (54)$$

The subscript $(\bullet)_o$ is a reminder that the natural frequency $\omega_{o\alpha}$ is for the same structure as is ω_α but containing no gyricity, i.e., $h_s\equiv 0$. Because the period of Mode α varies inversely with ω_α ($T_\alpha = 2\pi/\omega_\alpha$), identities of the form (54) can be regarded

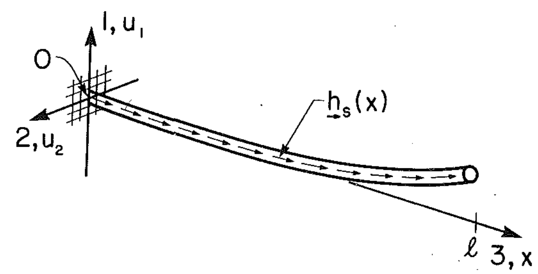

Fig. 2 Slender cantilevered rod

as expressions for the sum of squares of the modal periods.

The generalization of equation (54) to constrained gyroelastic systems may be written as

$$\sum_{\alpha} (\omega_{\alpha}^{-2}-\omega_{o\alpha}^{-2})=\frac{1}{2}\, tr\int_E\int_E [\mathbf{h}_s^{\times}(\mathbf{r})\mathbf{F}_{r\xi}(\xi,\mathbf{r})]^T [\mathbf{F}_{r\xi}(\xi,\mathbf{r})\mathbf{h}_s^{\times}(\xi)]dVdV \qquad (IV)$$

where

$$\mathbf{F}_{r\xi}^T(\xi,\mathbf{r})=\mathbf{F}_{\xi r}(\mathbf{r},\xi)=\frac{1}{2}\,\nabla_{\xi}^{\times}\,\mathbf{F}_r^T(\mathbf{r},\xi)$$
$$\mathbf{F}_r(\mathbf{r},\xi)=\frac{1}{2}\,\nabla_r^{\times}\,\mathbf{F}(\mathbf{r},\xi) \qquad (55)$$

The derivation of (*IV*) is, unfortunately, much longer and more subtle than its nongyric counterpart and thus is not included but is available in [6].

Identity (*IV*) brings to light three new flexibility kernels related to the kernel $\mathbf{F}(\mathbf{r},\xi)$. The physical interpretations of these new kernels are noteworthy: (1) $\mathbf{F}_r(\mathbf{r},\xi)$ is the kernel required to express the local angular deformation caused by a force distribution; (2) $\mathbf{F}_r^T(\mathbf{r},\xi)$ relates the local translational deformation to its corresponding torque distribution; and (3) $\mathbf{F}_{\xi r}(\mathbf{r},\xi)$ is the kernel appropriate for determining the local angular deformation due to a torque distribution.

7 Numerical Example

As an example of the preceding results we return to the slender cantilevered rod (Fig. 2) considered in [1]. The sense of the gyricity is parallel to the rod, everywhere along the rod, thus reducing the problem to two dimensions. The rod is taken to have a constant linear mass density ρ and constant bending stiffnesses B_1 and B_2. Let us choose the gyricity distribution to be

$$h_s(x)=\frac{1}{2}\,h_T\,\frac{\pi}{\ell}\,\sin\left(\frac{\pi}{\ell}\,x\right) \qquad (56)$$

where h_T is the total angular momentum stored in the rod.

For this system, Identities (*I*) are

$$\iota_o(\mathbf{pp})=\rho\mathbf{1}$$
$$\iota_o(\mathbf{hh})=\frac{1}{3}\,\rho\ell^3\mathbf{1}$$
$$\iota_o(\mathbf{gg})=\frac{\pi^4}{8}\,\frac{h_T^2}{\rho\ell^3}\,\mathbf{1}$$
$$\iota_o(\mathbf{ph})=\frac{1}{2}\,\rho\ell^2\begin{bmatrix}0 & 1\\ -1 & 0\end{bmatrix} \qquad (57)$$
$$\iota_o(\mathbf{hg})=h_T\begin{bmatrix}0 & 1\\ -1 & 0\end{bmatrix}$$
$$\iota_o(\mathbf{gp})=\mathbf{O}$$

wherein we have introduced the abridged notation,

$$\iota_n(\mathbf{ab})\triangleq\sum_{\alpha}\omega_{\alpha}^{-n}[\mathbf{a}_{u\alpha}\mathbf{b}_{u\alpha}^T+\mathbf{a}_{v\alpha}\mathbf{b}_{v\alpha}^T]$$

for the left-hand sides of the identities. (The identity matrix **1** and the null matrix **O** above are, of course, 2×2.) Furthermore, noting that the flexibility kernel for the cantilevered rod is

$$\mathbf{F}(\mathbf{x},\xi)=\begin{bmatrix}B_1^{-1} & 0\\ 0 & B_2^{-1}\end{bmatrix}\cdot\begin{cases}x^2(3\xi-x)/6, & 0\le x\le\xi\le\ell\\ \xi^2(3x-\xi)/6, & 0\le\xi\le x\le\ell\end{cases} \qquad (58)$$

and defining

$$B\triangleq(B_1B_2)^{1/2};\ \beta\triangleq(B_1/B_2)^{1/2} \qquad (59)$$

and identities involving ω_{β}^{-2}, (*II*), are calculated to be

$$\iota_2(\mathbf{pp})=\frac{\rho^2\ell^5}{20B}\begin{bmatrix}\beta & 0\\ 0 & -\beta^{-1}\end{bmatrix}$$
$$\iota_2(\mathbf{hh})=\frac{11\rho^2\ell^5}{420B}\begin{bmatrix}\beta^{-1} & 0\\ 0 & \beta\end{bmatrix}$$
$$\iota_2(\mathbf{gg})=\frac{3h_T^2\ell}{8B}\begin{bmatrix}\beta & 0\\ 0 & \beta^{-1}\end{bmatrix}$$
$$\iota_2(\mathbf{ph})=\frac{13\rho^2\ell^6}{360B}\begin{bmatrix}0 & \beta\\ -\beta^{-1} & 0\end{bmatrix} \qquad (60)$$
$$\iota_2(\mathbf{hg})=\left(\frac{1}{16}+\frac{1}{4\pi^2}+\frac{1}{\pi^4}\right)\frac{\rho h_T\ell^4}{B}\begin{bmatrix}0 & \beta\\ -\beta^{-1} & 0\end{bmatrix}$$
$$\iota_2(\mathbf{gp})=-\left(\frac{1}{12}+\frac{1}{2\pi^2}\right)\frac{\rho h_T\ell^3}{B}\begin{bmatrix}\beta & 0\\ 0 & \beta^{-1}\end{bmatrix}$$

Finally, the identity involving only frequencies, namely (*IV*), becomes

$$\sum_{\alpha}(\omega_{\alpha}^{-2}-\omega_{o\alpha}^{-2})=\left(\frac{3}{8}-\frac{2}{\pi^4}\right)\frac{h_T^2\ell^2}{B^2} \qquad (61)$$

To verify the above identities numerically, the vibration frequencies and the gyroelastic modes of the system were determined [1] using a finite element method with 10 elements (40 degrees of freedom). The modal coefficients were then evaluated according to equations (24)-(26). A comparison between the theoretical and numerical results is charted in Table 1. For brevity we shall consider only the numerical coefficients appearing on the right-hand sides of the modal identities. The "discrepancies" in Table 1 are due to the finite number of modes taken in the series and, of course, to numerical error in the finite element approximation. (Calculation of the discrepancy in $\iota_o(\mathbf{gp})$ should be based on $\pi^2/\sqrt{8}$, obtained from the geometric average of $\iota_o(\mathbf{pp})$ and $\iota_o(\mathbf{gg})$, and thus is 4.2 percent. As expected, this lies between the discrepancies for $\iota_o(\mathbf{pp})$ and $\iota_o(\mathbf{gg})$.) Agreement among the second set of identities is much better than among the first set owing to the presence of ω_{α}^{-2}.

It is useful to define a completeness index that measures the degree to which the modal identities are satisfied by a finite number, N, of modes. An *inertial completeness index* has been suggested for nongyric elastic structures [8]. To extend the concept to gyroelastic structures, consider

Table 1 Modal identities: A comparison between theoretical and numerical results

Identity	Coefficient on Right-Hand Side Theoretical	 Numerical	Discrepancy (%)
I			
(*a*) $\iota_o(\mathbf{pp})$	1	0.97060	2.9
(*b*) $\iota_o(\mathbf{hh})$	$\frac{1}{3}$	0.33333	<0.001
(*c*) $\iota_o(\mathbf{gg})$	$\frac{\pi^4}{8}$	11.460	5.9
(*d*) $\iota_o(\mathbf{ph})$	$\frac{1}{2}$	0.49966	<0.003
(*e*) $\iota_o(\mathbf{hg})$	1	1.0017	−0.17
(*f*) $\iota_o(\mathbf{gp})$	0	−0.14509	---
III			
(*a*) $\iota_2(\mathbf{pp})$	$\frac{1}{20}$	0.050000	<0.002
(*b*) $\iota_2(\mathbf{hh})$	$\frac{11}{420}$	0.026190	<0.004
(*c*) $\iota_2(\mathbf{gg})$	$\frac{3}{8}$	0.037500	<0.003
(*d*) $\iota_2(\mathbf{ph})$	$\frac{11}{360}$	0.036111	<0.003
(*e*) $\iota_2(\mathbf{hg})$	$\frac{1}{16}+\frac{1}{4\pi^2}+\frac{1}{\pi^4}$	0.098096	<0.001
(*f*) $\iota_2(\mathbf{gp})$	$\frac{1}{12}+\frac{1}{2\pi^2}$	0.13399	<0.008
IV			
$\Sigma(\omega_\alpha^{-2}-\omega_{o\alpha}^{-2})$	$\frac{3}{8}-\frac{2}{\pi^2}$	0.71236	<0.002

$$\mathbf{M}_N \triangleq \frac{1}{2}\sum_{\alpha=1}^{N}\left\{\begin{bmatrix}\mathbf{p}_{u\alpha}\\ \mathbf{h}_{u\alpha}\\ \mathbf{g}_{u\alpha}\end{bmatrix}\begin{bmatrix}\mathbf{p}_{u\alpha}\\ \mathbf{h}_{u\alpha}\\ \mathbf{g}_{u\alpha}\end{bmatrix}^T+\begin{bmatrix}\mathbf{p}_{v\alpha}\\ \mathbf{h}_{v\alpha}\\ \mathbf{g}_{v\alpha}\end{bmatrix}\begin{bmatrix}\mathbf{p}_{v\alpha}\\ \mathbf{h}_{v\alpha}\\ \mathbf{g}_{v\alpha}\end{bmatrix}^T\right\} \tag{62}$$

and $\mathbf{M}_\infty \triangleq \lim_{N\to\infty} \mathbf{M}_N$. The matrix $\mathbf{M}_\infty$ is positive-definite for nonzero gyricity and therefore we can define

$$I_o(N) \triangleq \frac{1}{n}\Big[\sum_{i=1}^{n} \mu_i^2(\mathbf{M}_\infty^{-1/2}\mathbf{M}_N\mathbf{M}_\infty^{-1/2})\Big]^{1/2} \tag{63}$$

(where n is the dimension of $\mathbf{M}_\infty$ and μ_i are eigenvalues) as a *completeness index* for gyroelastic structures. As $N\to\infty$, $\mu_i \to 1$ and hence $I_o(\infty)=1$, which means the system is "complete". It should be noted that this definition differs from its nongyric counterpart in that equation (63) is a root mean square average of μ_i whereas the inertial completeness index is just the smallest μ_i. The eigenvalues μ_i can be easily solved using the form $(\mu_i\mathbf{M}_\infty - \mathbf{M}_N)\mathbf{x} = \mathbf{0}$, for which many computer algorithms exist.

A similar completeness index for the modal identities involving ω_α^{-2} can be defined as follows:

$$I_2(N) \triangleq \Big[\frac{1}{n}\sum_{i=1}^{n} \mu_i^2(\Xi_\infty^{-1/2}\Xi_N\Xi_\infty^{-1/2})\Big]^{1/2} \tag{64}$$

where

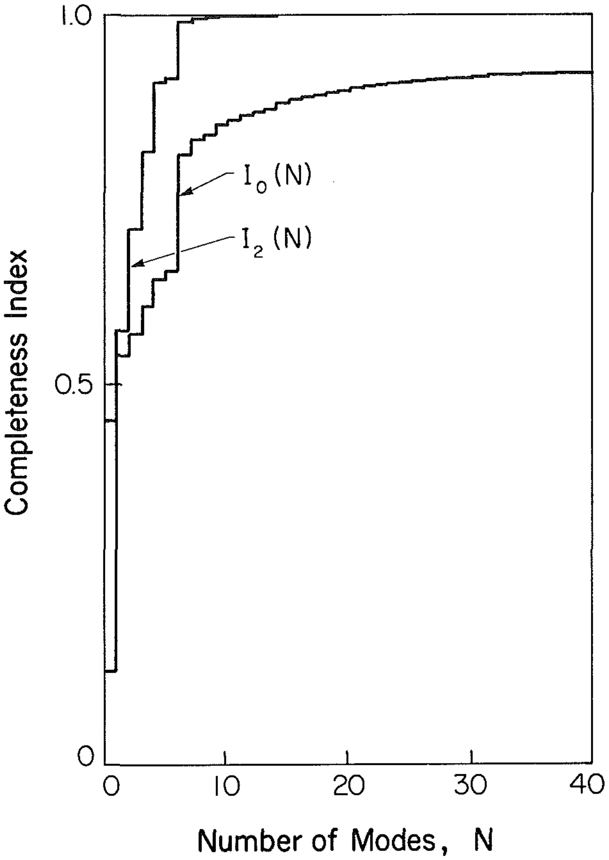

Fig. 3 Completeness indices for the slender cantilevered rod

$$\Xi_N \triangleq \frac{1}{2}\sum_{\alpha=1}^{N}\omega_\alpha^{-2}\left\{\begin{bmatrix}\mathbf{p}_{u\alpha}\\ \mathbf{h}_{u\alpha}\\ \mathbf{g}_{u\alpha}\end{bmatrix}\begin{bmatrix}\mathbf{p}_{u\alpha}\\ \mathbf{h}_{u\alpha}\\ \mathbf{g}_{u\alpha}\end{bmatrix}^T+\begin{bmatrix}\mathbf{p}_{v\alpha}\\ \mathbf{h}_{v\alpha}\\ \mathbf{g}_{v\alpha}\end{bmatrix}\begin{bmatrix}\mathbf{p}_{v\alpha}\\ \mathbf{h}_{v\alpha}\\ \mathbf{g}_{v\alpha}\end{bmatrix}^T\right\}$$

and $\Xi_\infty \triangleq \lim_{N\to\infty} \Xi_N$.

The indices $I_o(N)$ and $I_2(N)$ are plotted in Fig. 3 for the cantilevered rod example. As would be expected, the identities involving ω_α^{-2} as monitored by $I_2(N)$ converge much faster than the others.

8 Concluding Remarks

As the preceding development indicates the concept of modal coefficients is a natural extension of eigenvalue analyses traditionally performed on vibration structures. The practical importance of our analysis lies in the potential efficacy with which gyricity can be used to control very large flexible space vehicles. A dense distribution of momentum wheels and control moment gyros over the structure may be advantageously represented by a continuous gyricity distribution.

The modal coefficients constitute a dynamical description of a gyroelastic body and are known to be of great significance [7]. Apart from their academic appeal, the theoretical results obtained here are very useful in verifying the accuracy of spatially discretized models and, more important, in supplying a rational basis for model-order reduction schemes. It should also be emphasized that while we have focused on an elastic continuum containing a gyricity distribution, the results are in fact applicable with minor modifications to any system which can be described by equation (1).

The equation of motion (1) can be derived using the principles of Newton and d'Alembert or, alternatively, from

Hamilton's (extended) principle. A third, and consistent, derivation can be obtained from the balance laws of continuum mechanics [3]. This approach uses the concepts developed by Eringen and others [4, 5, for example].

Acknowledgments

The figures were prepared by Ida Szalkay. This work was supported by the Natural Sciences and Engineering Research Council (NSERC) of Canada.

References

1 D'Eleuterio, G. M. T., and Hughes, P. C., "Dynamics of Gyroelastic Continua," Journal of Applied Mechanics, Vol. 51, No. 2, June 1984, pp. 415–422.

2 Huseyin, K., "Vibrations and Stability of Multiple Parameter Systems," Sijthoff & Noordhoff, 1978.

3 D'Eleuterio, G. M. T., "On the Theory of Gyroelasticity," submitted to Journal of Applied Mechanics.

4 Eringen, A. C., *Mechanics of Continua*, Wiley, 1967.

5 Eringen, A. C., "Balance Laws of Micromorphic Mechanics," *Int. J. Engng. Sci.*, Vol. 8, pp. 819–828.

6 D'Eleuterio, G. M. T., "Dynamics of Gyroelastic Systems," Ph.D. Dissertation, University of Toronto, Institute for Aerospace Studies, 1984.

7 Hughes, P. C., "Modal Identities for Elastic Bodies, With Application to Vehicle Dynamics and Control," Journal of Applied Mechanics, Vol. 47, No. 1, 1980, pp. 177–184.

8 Hughes, P. C., and Skelton, R. E., "Modal Truncation for Flexible Spacecraft," *J. of Guidance and Control*, Vol. 4, No. 3, 1981, pp. 291–297.

APPENDIX

Inner and Outer Products

We begin with two matrices, $\mathbf{X}(\mathbf{r})$ and $\mathbf{Y}(\mathbf{r})$, whose dimensions are $n_1 \times n_2$ and $n_3 \times n_4$, respectively. The *inner product* (over E) of $\mathbf{X}$ and $\mathbf{Y}$, denoted here by $\mathbf{X}^T\mathbf{Y}$, is defined to be

$$\mathbf{X}^T\mathbf{Y} \equiv \mathbf{X}^T(\mathbf{r})\mathbf{Y}(\mathbf{r}) \triangleq \int_E \mathbf{X}^T(\mathbf{r})\mathbf{Y}(\mathbf{r})\,dV \qquad (A.1)$$

This definition of course requires $n_1 = n_3$. Note that the inner product $\mathbf{X}^T\mathbf{Y}$ is an $n_2 \times n_4$ constant matrix.

The *outer product* over E of $\mathbf{X}$ and $\mathbf{Y}$, denoted here by $\mathbf{X}\mathbf{Y}^T \equiv \mathbf{X}(\mathbf{r})\mathbf{Y}^T(\xi)$ is defined such that, for any $n_5 \times n_6$ matrix $\mathbf{\Psi}(\xi)$.

$$(\mathbf{X}\ \mathbf{Y}^T)\mathbf{\Psi} \triangleq \mathbf{X}(\mathbf{r})(\mathbf{Y}^T\mathbf{\Psi}) \qquad (A.2)$$

This definition of course requires $n_3 = n_5$ and $n_2 = n_4$. Note that the outer product $\mathbf{X}\ \mathbf{Y}^T$ is an $n_1 \times n_3$ matrix operator; thus, in $(A.2)$, $\mathbf{\Psi}(\xi)$ is mapped into $\mathbf{X}(\mathbf{r})$.

As a final observation, we note that if a fourth matrix, $\mathbf{\Phi}(\mathbf{r})$ is introduced ($n_7 \times n_8$, say), then the inner product between $\mathbf{\Phi}$ and $(\mathbf{X}\ \mathbf{Y}^T)\psi$ is given by

$$\mathbf{\Phi}^T(\mathbf{r})[\mathbf{X}(\mathbf{r})\mathbf{Y}^T(\xi)]\mathbf{\Psi}(\xi) \equiv (\mathbf{\Phi}^T\mathbf{X})(\mathbf{Y}^T\mathbf{\Psi}) \qquad (A.3)$$

(One must have $n_2 = n_4$, $n_3 = n_5$, and $n_7 = n_1$.) Note that the result is a $n_8 \times n_6$ constant matrix.

J. Clastornik

M. Eisenberger

D. Z. Yankelevsky

M. A. Adin

Faculty of Civil Engineering,
Technion-Israel Institute of Technology,
Haifa 32000, Israel

Beams on Variable Winkler Elastic Foundation

A stiffness approach is presented for computing the solution of beams on variable Winkler foundation. The solution may be achieved using only a small number of elements along the beam. Accuracy is dependent only on a preset user criterion. A numerical example demonstrates the efficiency and accuracy of the procedure.

Introduction

The analysis of beams on Winkler foundation is very common in engineering. Other foundation models are reviewed by Kerr (1964). The Winkler foundation model consists of an infinite number of closely spaced springs uniformly distributed along the beam. When the spring constant, also called foundation modulus, is constant along the length of the beam, the differential equation of the beam has constant coefficients, and the solution can be given as a linear combination of elementary functions (Hetenyi, 1946). If the foundation stiffness varies along the beam, the differential equation in most of the cases cannot be solved exactly, and numerical methods should be applied. This situation occurs in the case of buried structures, in particular in piles driven into soil.

Exact stiffness matrix for beam member on constant Winkler elastic foundation has been derived previously (Eisenberger & Yankelevsky, 1985). Franklin and Scott (1979) presented a closed-form solution for a linear variation of the foundation modulus, using contour-integrals. For a higher order of variation in x (the coordinate along the beam), they present a partial solution, which is applicable to infinite beams (or piles). Lentini (1979) presented a finite difference method to solve the problem when the foundation stiffness varies along x as a power of x.

In this work we present a solution for finite beams resting on a Winkler elastic foundation with stiffness variation that can be presented as a general polynomial of x. A stiffness formulation for the solution of the deflection curve, moments, and shear is presented and demonstrated in a numerical example.

The Differential Equation

The differential equation for the deflection curve of a beam of constant flexural rigidity EI supported on a variable elastic foundation is:

$$\frac{d^4y}{dx^4}+\frac{k(x)}{EI}y=\frac{p(x)}{EI} \tag{1}$$

If we represent the foundation modulus and loading as two infinite series

$$k(x)=\sum_{i=0}^{\infty} k_i x^i \tag{2}$$

$$p(x)=\sum_{i=0}^{\infty} p_i x^i \tag{3}$$

and introduce a new variable

$$\xi=\frac{x}{L} \tag{4}$$

we get

$$\frac{d^4y}{dx^4}=\frac{1}{L^4}\frac{d^4y}{d\xi^4} \tag{5}$$

$$k(x)=\sum_{i=0}^{\infty} k_i L^i \xi^i \tag{6}$$

$$p(x)=\sum_{i=0}^{\infty} p_i L^i \xi^i \tag{7}$$

Substitution of these expressions into the differential equation, equation (1), yields

$$\frac{d^4y}{d\xi^4}+\left(\sum_{i=0}^{\infty} k_i^* \xi^i\right)y=\sum_{i=0}^{\infty} p_i^* \xi^i \tag{8}$$

where

$$k_i^*=\frac{k_i L^{i+4}}{EI} \tag{9}$$

$$p_i^*=\frac{p_i L^{i+4}}{EI} \tag{10}$$

If we choose the general solution of equation (8) as

$$y=\sum_{i=0}^{\infty} a_i \xi^i \tag{11}$$

Contributed by the Applied Mechanics Division for publication in the JOURNAL OF APPLIED MECHANICS.

Discussion on this paper should be addressed to the Editorial Department, ASME, United Engineering Center, 345 East 47th Street, New York, N.Y. 10017, and will be accepted until two months after final publication of the paper itself in the JOURNAL OF APPLIED MECHANICS. Manuscript received by ASME Applied Mechanics Division, May 24, 1985; final revision December 4, 1985.

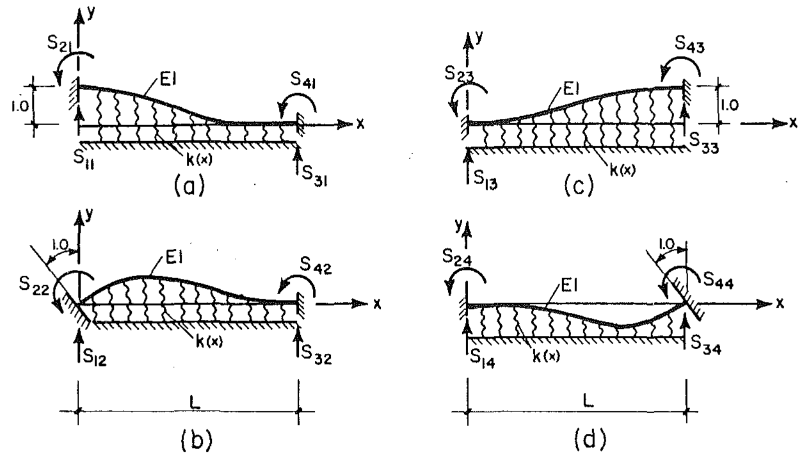

Fig. 1 Beam on elastic foundation: stiffnesses

then

$$\frac{d^4y}{d\xi^4} = \sum_{i=0}^{\infty} i(i-1)(i-2)(i-3)a_i\xi^{i-4}$$

$$= \sum_{i=0}^{\infty} (i+4)(i+3)(i+2)(i+1)a_{i+4}\xi^i \quad (12)$$

which, on substituting into equation (8), gives

$$\sum_{i=0}^{\infty} (i+4)(i+3)(i+2)(i+1)a_{i+4}\xi^i + \left(\sum_{i=0}^{\infty} k_i^*\xi^i\right)\left(\sum_{i=0}^{\infty} a_i\xi^i\right) = \sum_{i=0}^{\infty} p_i^*\xi^i \quad (13)$$

The multiplication of the two series in the second term can be written as

$$\left(\sum_{i=0}^{\infty} k_i^*\xi^i\right)\left(\sum_{i=0}^{\infty} a_i\xi^i\right) = \sum_{i=0}^{\infty}\left(\sum_{j=0}^{\infty} k_j^*a_{i-j}\right)\xi^i \quad (14)$$

and equation (13) becomes

$$\sum_{i=0}^{\infty} (i+4)(i+3)(i+2)(i+1)a_{i+4}\xi^i + \sum_{i=0}^{\infty}\left(\sum_{j=0}^{i} k_j^*a_{i-j}\right)\xi^i = \sum_{i=0}^{\infty} p_i^*\xi^i \quad (15)$$

or

$$\sum_{i=0}^{\infty}\left[(i+4)(i+3)(i+2)(i+1)a_{i+4} + \sum_{j=0}^{i} k_j^*a_{i-j} - p_i^*\right]\xi^i = 0 \quad (16)$$

To satisfy this equation for every value of ξ, we must have

$$a_{i+4} = \frac{p_i^* - \sum_{j=0}^{i} k_j^*a_{i-j}}{(i+4)(i+3)(i+2)(i+1)} \qquad i=0,1,2,\ldots,\infty \quad (17)$$

so that in equation (11) we have all the a_i coefficients, except for the first four, which should be found using the boundary conditions.

Boundary Conditions

All boundary conditions are assumed to be displacement-type because of the intended application of the result in developing a displacement based stiffness matrix. At $\xi=0$ we have

$$y(0) = a_0 \quad (18a)$$

$$\theta(0) = \frac{1}{L}\frac{dy}{d\xi} = \frac{1}{L}a_1 \quad (18b)$$

and the first two a_i are found. The next two a_i are found from the boundary conditions at $x=L$ $(\xi=1)$.

From equations (11) and (17), we can express the deflection y, for each ξ, as a linear combination of the first four a_i's and the terms p_i^*, as all the other coefficients are linearly dependent on them. In particular, for $\xi=1$, we can write:

$$y(x=L,\xi=1) = C_0a_0 + C_1a_1 + C_2a_2 + C_3a_3 + \sum_{i=0}^{\infty} C_{pi}p_i^* \quad (19)$$

$$\theta(x=L,\xi=1) = C_0'a_0 + C_1'a_1 + C_2'a_2 + C_3'a_3 + \sum_{i=0}^{\infty} C_{pi}'p_i^* \quad (20)$$

The C coefficients are functions of the k_i^* terms and can be evaluated using equation (11) and (17). C_0, for example, is the value of the function y (equation (19)) at $\xi=1$, when $a_0=1$ and $a_1=a_2=a_3=p_i^*=0$, and therefore it can be calculated using equations (11) and (17) with the preceding values.

In general we can write all the C coefficients as follows:

$$C_i = y_{\xi=1} = \sum_{j=0}^{\infty} a_j = 1 + \sum_{j=4}^{\infty} a_j \quad (21)$$

$$C_i' = y_{\xi=1}' = \sum_{j=0}^{\infty} ja_j = 1 + \sum_{j=4}^{\infty} ja_j \quad (22)$$

both with a_j (from equation (17)) based on $a_i=1$, $a_{k\neq i}=0$; $p_n^*=0$; $i, k=0, 1, 2, 3, n=0, 1, 2, \ldots\ldots$

$$\sum_{i=0}^{\infty} C_{pi}p_i^* = y_{\xi=1} = \sum_{j=0}^{\infty} a_j = \sum_{j=4}^{\infty} a_j \quad (23)$$

$$\sum_{i=0}^{\infty} C_{pi}'p_i^* = y_{\xi=1}' = \sum_{j=0}^{\infty} ja_j = \sum_{j=4}^{\infty} ja_j \quad (24)$$

both with a_j (from equation (17)) based on $a_0=a_1=a_2=a_3=0$, using the values of p_i^* for the particular loading. Knowing all the terms in equations (21)-(24), the values of a_0 and a_1 (equations (18)), and the boundary conditions at $x=L$ $(\xi=1)$, we can solve equations (19) and (20), for the two unknowns, a_2 and a_3. Thus, for any given variable foundation $k(x)$ and loading $p(x)$ (equations (2), (3)), we can find all the a_i coefficients in the expression for $y(x)$ (equation (11)), from equations (17)-(20).

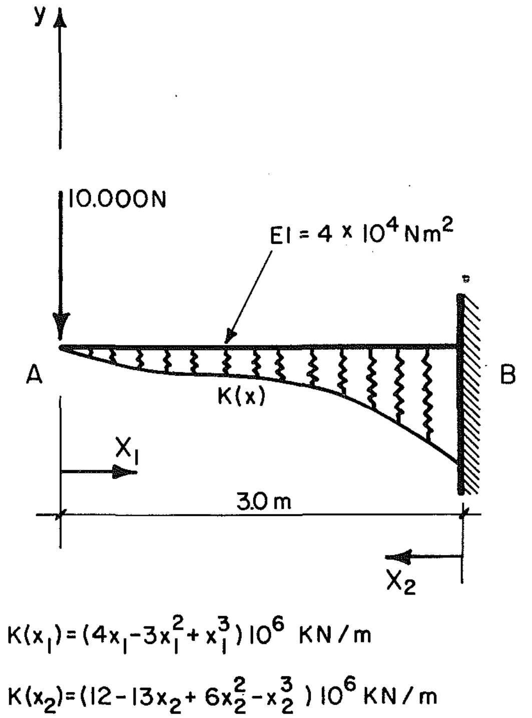

Fig. 2 Example: cantilever beam on variable elastic foundation

Stiffness Matrix and Member End-Actions

The terms in the stiffness matrix are defined as the holding actions at both ends of the beam, due to unit translations and rotations as shown in Fig. 1, where there is no load on the beam (i.e., $p_i = 0$). For the solution y_i, $i = 1, 2, 3, 4$ of the four cases shown in the figure, one can use the boundary conditions and get a_{ji} $(j = 0, 1, 2, \ldots \infty)$.

Then, the terms in the stiffness matrix are:

$$S_{1i} = Q(0) = \frac{EI}{L^3}\frac{d^3y_i}{d\xi^3} = 6\frac{EI}{L^3}a_{3i} \tag{25a}$$

$$S_{2i} = M(0) = -\frac{EI}{L^2}\frac{d^2y_i}{d\xi^2} = -2\frac{EI}{L^2}a_{2i} \tag{25b}$$

$$S_{3i} = Q(1) = -\frac{EI}{L^3}\frac{d^3y_i}{d\xi^3} = -\frac{EI}{L^3}\sum_{j=3}^{\infty} j(j-1)(j-2)a_{ji} \tag{25c}$$

$$S_{4i} = M(1) = \frac{EI}{L^2}\frac{d^2y_i}{d\xi^2} = \frac{EI}{L^2}\sum_{j=2}^{\infty} j(j-1)a_{ji} \tag{25d}$$

As an example, the first column of the matrix is found using the deflection curve y_1, for which the a_{j1} coefficients may be found using the following boundary conditions:

$$y_1(0) = 1 \tag{26a}$$

$$y_1'(0) = y_1(L) = y_1'(L) = 0 \tag{26b}$$

Member end-actions for any loading are found using equations (25), but the solution y is found using the loading data, p_i for fixed-end boundary conditions, i.e.,

$$y(0) = y'(0) = y(L) = y'(L) = 0 \tag{27}$$

Examples

Considering the case of a constant Winkler foundation, $k(x) = k_o$, for $p(x) = 0$, then

$$a_{i+4} = \frac{-k_o^* a_i}{(i+4)(i+3)(i+2)(i+1)} \tag{28}$$

Table 1 Results for example beam

segments	-10Ya[m]	10θa[rad]	Rb[N]	-Mb[Nm]	CPU[s]
1	.11735	.25820	51.65	15.596	0.58
2	.22180	.39362	100.47	26.788	0.67
3	.26558	.44105	145.07	25.577	0.75
5	.33354	.52619	176.00	26.507	0.74
10	.40509	.63440	219.41	32.789	1.10
20	.43212	.67869	235.46	35.201	1.50
40	.43970	.69135	239.93	35.882	2.50
80	.44166	.69464	241.08	36.058	4.49
160	.44215	.69546	241.36	36.102	8.41
320	.44228	.69567	241.44	36.114	17.05
1	.44232	.69574	241.46	36.117	0.77

and, if $i = 4^*n + m$ $(n = 1, 2, \ldots.$ and for each n, $m = 0, 1, 2, 3)$ we get

$$a_i = \frac{(-k_o^*)^n m!}{i!}a_m \tag{29}$$

And considering the case of linearly varying Winkler foundation, $k(x) = k_1 x$, then, for $p(x) = 0$

$$a_{i+4} = \frac{-k_1^* a_{i-1}}{(i+4)(i+3)(i+2)(i+1)} \tag{30}$$

and we get the same series as Hetenyi, (1946, p. 109). In this case, if $i = 5^*\ell + m$ $(\ell = 1, 2, \ldots.$ and for each ℓ, $m = 0, 1, 2, 3)$ then

$$a_i = \frac{(-k_1^*)^\ell \left[\prod_{j=1}^{\ell}(5j-4+m)\right] m!}{i!}a_m \quad m = 0,1,2,3 \tag{31a}$$

$$a_{5\ell-1} = 0 \qquad \ell = 1,2,3,\ldots. \tag{31b}$$

In both cases, y can be expressed as the sum of four series, that correspond, for $\xi = 1$, each one with the C coefficients, in equation (19).

In these two cases convergence is evident. In the general case, the series always converge for finite p and k polynomials. It can be seen easily from the two examples or directly from equation (17) that the number of terms needed to obtain convergency depends only on the values of k^*, for finite p polynomials.

Using the beam stiffness matrix and member end-actions we can solve any general continuous-beam using the direct stiffness method (Weaver and Gere, 1980). A continuous beam program was modified to include the possiblity of variable elastic foundations, and the results are demonstrated in the example.

The cantilever beam shown in Fig. 2 was analyzed using the proposed stiffness formulation. The beam rests on a variable Winkler elastic foundation and was solved using one section. For comparison, the same problem was solved using the exact stiffness matrix for beams on constant Winkler foundation (Eisenberger and Yankelevsky, 1985). The beam was divided into equal segments with constant foundation, in such a way that the total foundation reaction of each segment is equal to that of the original foundation reaction. The results of these cases, and of the proposed solution, are given in Table 1, for the deflections, rotations, and reactions at A and B.

It can be seen that the solution converges to the results obtained using only one section, that obviously required much shorter computation time. In the last column of the table the CPU time for each case is shown, and the big saving in com-

Table 2 Stiffness matrices for example beam

$$K(x_1)=(4x_1-3x_1^2+x_1^3)10^6\ \text{KN/m}$$

$$S_m=\begin{bmatrix} 566095.5645341235 & 216162.5595999291 & -6109.791883247904 & -87.20392055978066 \\ 216162.5595999295 & 137425.1141049063 & -413.7380016882916 & -574.5602670603874 \\ -6109.791883136082 & -413.7380018381857 & 3534622.215303887 & -597666.9091349428 \\ -87.20392045799123 & -574.5602668704000 & -597666.9091349448 & 212550.3891939011 \end{bmatrix}$$

$$K(x_2)=(12-13x_2+6x_2^2-x_2^3)10^6\ \text{KN/m}$$

$$S_m=\begin{bmatrix} 3534622.215303817 & 597666.9091349144 & -6109.791883247865 & 413.7380016883045 \\ 597666.9091349084 & 212550.3891938803 & 87.20392055986304 & -574.5602670603734 \\ -6109.791493126612 & 87.20395761805602 & 566095.5645341776 & -216162.5596000219 \\ 413.7379749021453 & -574.5602715076991 & -216162.6696999461 & 137425.1141048908 \end{bmatrix}$$

Table 3 First column of stiffness matrix

EPS	SM(1,1)	SM(2,1)	SM(3,1)	SM(4,1)	TERMS
1.E-01	585529.2340117421	214335.3658006047	-14263100.18482930	3178262.236744432	37 - 54
1.E-02	567965.7647265322	215176.2682136999	-2362283.943837869	614507.2321755555	43 - 61
1.E-03	565864.6102763164	216284.1708242434	283849.7906181943	-76054.13077739591	47 - 67
1.E-04	566100.1176651456	216153.4255440069	-19505.32424408148	4029.267790100886	51 - 75
1.E-05	566098.6727565474	216162.9297521721	-7725.984763551770	154.7686111965075	54 - 80
1.E-06	566095.4963783332	216162.5327313837	-6095.726269172014	-85.21943796552056	58 - 82
1.E-07	566095.5663392797	216162.5690002106	-6100.261794332094	-90.63444116110341	61 - 85
1.E-08	566095.5642920391	216162.5604174414	-6108.701393869584	-87.55180526012907	64 - 87
1.E-09	566095.5645813759	216162.5597030293	-6109.705358534087	-87.23813728865589	67 - 89
1.E-10	566095.5645343206	216162.5596051972	-6109.786007892238	-87.20594405616216	70 - 92
1.E-11	566095.5645343714	216162.5596000147	-6109.791946368579	-87.20392294721190	73 - 94
1.E-12	566095.5645343474	216162.5595999233	-6109.792037063159	-87.20389003656125	76 - 97
1.E-13	566095.5645341199	216162.5595999275	-6109.791882735090	-87.20392041662683	79 - 99
1.E-14	566095.5645341235	216162.5595999296	-6109.791883347669	-87.20392059598476	81 - 101
1.E-15	566095.5645341235	216162.5595999294	-6109.791883525373	-87.20392043077526	83 - 104
1.E-16	566095.5645341235	216162.5595999295	-6109.791884545353	-87.20392020609712	85 - 106
1.E-17	566095.5645341235	216162.5595999295	-6109.791883136082	-87.20392045799123	88 - 108
1.E-18	566095.5645341235	216162.5595999295	-6109.791883136082	-87.20392045799123	88 - 108

puter time is evident. To check the accuracy, the same problem was solved by introducing the data referred to the new axes x_2 (Fig. 2). The stiffness matrices in both cases are presented in Table 2.

We used the series as an analytical solution of the differential equations. Then, the series were truncated checking that the errors (ratios of a_j to Σa_j equations (21) and (23)), ja_j to Σja_j (equations (22) and (24)), $j(j-1)a_i$ to $\Sigma j(j-1)a_j$ (equation (25*d*)) and $j(j-1)(j-2)a_j$ to $\Sigma j(j-1)(j-2)a_j$ (equation (25*c*)) were less than a fixed value "EPS" (in this example, EPS $=1e-17$).

In Table 3 the values of the first column of the stiffness matrix and the number of terms needed to obtain convergency are presented as a function of the prefixed value EPS. No significant differences in the CPU time were observed. It can be seen that better accuracy is achieved in the first two rows in the stiffness matrix, clearly because these require only coefficients a_3 and a_2 (equations (25*a*,*b*)), rather than a series as given by equations (25*c*,*d*), for the last two rows. The problem is limited to the terms S_{33}, S_{34}, and S_{44} because of the symmetry of the stiffness matrix.

Taking into account symmetry, the 16 series which are needed to calculate the member stiffness matrix (4 for each C_i, C_i', S_{3i}, and S_{4i} in equations (21) (22), (25*a*), and (25*b*)) can be reduced to 11 series, thus saving CPU time. The number of terms which are needed to obtain convergency (the minimum and maximum in the above mentioned 16 series), as a function of EPS are also given in Table 3.

In general, then, just the upper part of the stiffness matrix should be calculated, and eventually, a check program should be incorporated for calculating the matrix by a change of axis, although for the example shown, with EPS $=1.e-17$, there is no practical need for it.

Conclusions

The paper presents a stiffness formulation for the solution of beams on variable Winkler foundation. The accuracy of the solution is dependent only on our computer precision, i.e., better than 10 figures accuracy. The solution may be achieved by using only a small number of elements, thus reducing also the data preparation time. The procedure can be incorporated into a standard beam analysis program. Big savings in computer time are achieved, with even better accuracy.

Acknowledgment

The authors gratefully acknowledge the valuable suggestions of the reviewer.

References

Eisenberger, M., and Yankelevsky, D. Z., 1985, "Exact Stiffness Matrix for Beams on Elastic Foundation," *Computers and Structures*, Vol. 21, pp. 1355-1359.

Franklin, J. N., and Scott, R. F., Oct. 1979, "Beam Equation with Variable Foundation Coefficient," *ASCE Eng. Mech. Div.*, Vol. 105, EM5, pp. 811-827.

Hetenyi, M., 1946, *Beams on Elastic Foundations*, University of Michigan Press, Ann Arbor, Mich.

Kerr, A. D., 1964, "Elastic and Viscoelastic Foundation Models," ASME JOURNAL OF APPLIED MECHANICS, Vol. 31, pp. 491-498.

Lentini, M., 1979, "Numerical Solution of the Beam Equation With Nonuniform Foundation Coefficient," ASME JOURNAL OF APPLIED MECHANICS, Vol. 46, pp. 901-904.

Weaver, W., Jr., and Gere, J. M., 1980, *Matrix Analysis of Framed Structures*, D. Van Nostrand Co.

K. G. Sorenson
Invetech, Inc.,
Houston, Texas 77042
Mem. ASME

J. B. Cheatham, Jr.
Professor,
Department of Mechanical Engineering
and Material Science,
Rice University,
Houston, Texas 77001
Fellow ASME

Post-Buckling Behavior of a Circular Rod Constrained Within a Circular Cylinder

An axially loaded weightless circular rod buckles helically when constrained within a circular cylinder. The effects of pinned and fixed-end conditions are investigated. Both end conditions locate the rod end on the cylinder axis, and are found to perturb the helix in an exponentially decaying manner for a distance of less than one helix pitch length. Far from the end, the rod behaves as an undisturbed constant-pitch helix. The distance from the rod end to the point of initial contact with the cylinder wall is calculated. Closed-form analytical solutions are obtained for the deflected shapes and internal reactions of the end sections. The solution procedure applies to rods of either finite or infinite length.

1.0 Introduction

An analysis by Lubinski et al. (1962) established the helical post-buckled configuration of an axially loaded weightless circular rod constrained in a right circular cylinder. This analysis addressed the post-buckled, torque-free, static rod behavior away from the rod end and assumed frictionless constraint. The relationship between the pitch of the helix, p, and the axial compressive force, W, was found to be

$$p^2 = \frac{8\pi^2 EI}{W} \tag{1.1}$$

where EI is the rod bending stiffness. Analyses by Paslay and Bogy (1964), Dawson and Paslay (1982), and Paslay and Dawson (1982) considered the buckling problem using elastic stability theory, and investigated the effect of rod weight on buckling initiation and behavior.

With the exception of works by Lubinski (1950), Lubinski and Woods (1953), and Woods and Lubinski (1955), which considered planar buckling only, and an investigation by Mitchell (1982), previous buckling analyses have concentrated on rod behavior remote from ends effects. The purpose of this paper is to describe the effect of end conditions on the helical post-buckled configuration of an axially loaded circular rod constrained in a circular cylinder.

This problem has been of interest to the oil industry for many years and applies to the buckling of drill pipe near the drill bit and buckling of tubing at a packer. The post-buckling equilibrium analyses which follow assume that the constant diameter circular rod is weightless and static, and that displacements are small. Contact between the rod and the smooth cylinder wall is frictionless. The effects of torque and axial variation in the axial force are neglected. Results are presented for both a pinned-end case and a fixed-end case.

2.0 Analysis of a Pinned-End Helically Buckled Rod

The deflected centerline of a helically buckled rod with a pinned-end condition is shown schematically in Fig. 1. The pinned-end condition positions the rod end on the cylinder axis and allows axial translation and rotation about all three axes. The effective radius, r, of the circular cylinder on which the rod centerline lies is equal to the difference between the radii of the constraining cylinder and the rod. The centerline of the continuous circular rod is described by three sections: an end section, a transition section, and a contact section. The end section is that portion of the rod from the rod end to the point of initial wall contact at A. The transition section is an intermediate portion of the rod which is not on the cylinder wall and connects the end section at A to the contact section at B. The contact section is on the right circular cylinder wall everywhere along its length.

It is found that the force system which acts on the end section is incompatible with the internal reactions of a rod deformed into a simple helix. This suggests that the end section connects to a perturbed helix with a variable helix angle. Analysis of a helically buckled rod with a variable helix angle, however, results in wall contact forces which act to pull, rather than push, on the rod near the initial contact point at A. This behavior further indicates that an intermediate transition section, which does not contact the wall, is present as shown in Fig. 1.

2.1 Analysis of the Contact Section. The governing differential equations for a three-dimensionally buckled beam-column subject to the assumptions specified above reduce to a set of standard beam-column equations applied in the $x-z$ and $y-z$ planes:

$$EI\frac{d^4\hat{v}_j}{dz^4} + W\frac{d^2\hat{v}_j}{dz^2} - \hat{q}_j = 0 \tag{2.1}$$

Contributed by the Applied Mechanics Division for publication in the JOURNAL OF APPLIED MECHANICS.

Discussion on this paper should be addressed to the Editorial Department, ASME, United Engineering Center, 345 East 47th Street, New York, N.Y. 10017, and will be accepted until two months after final publication of the paper itself in the JOURNAL OF APPLIED MECHANICS. Manuscript received by ASME Applied Mechanics Division, March 15, 1985; final revision, February 10, 1986.

where $\hat{v}_j$ describe the position of the rod centerline with $j = 1$ for the x direction and $j = 2$ for the y direction.

The distributed lateral forces $\hat{q}_1$ and $\hat{q}_2$ which act on the rod are the x and y components of the wall contact force and are

$$\hat{q}_1 = -\hat{w}\cos\theta \qquad (2.2a)$$

and

$$\hat{q}_2 = -\hat{w}\sin\theta \qquad (2.2b)$$

where $\hat{w}$ is the wall contact force per unit length acting radially inward on the rod, and θ is the circumferential position of the rod centerline measured from the x axis as shown in Fig. 1.

Incorporating equation (2.2), equation (2.1) can be rewritten in a nondimensional format as

$$v_1'''' + v_1'' + w\cos\theta = 0 \qquad (2.3a)$$

$$v_2'''' + v_2'' + w\sin\theta = 0, \qquad (2.3b)$$

where $v_j = \hat{v}_j/r$ is the nondimensional position of the rod centerline in the x ($j = 1$) and y ($j = 2$) coordinate directions; $w = \hat{w}/\alpha^2 Wr$ is the nondimensional distributed wall contact force; $\zeta = \alpha z$ is the nondimensional position along the z axis; $\alpha = [W/EI]^{1/2}$; and a prime designates differentiation with respect to the new independent variable ζ.

The equation for a curve lying on the surface of a circular cylinder is written parametrically in the nondimensional format as

$$v_1 = \cos\theta \qquad (2.4a)$$

$$v_2 = \sin\theta \qquad (2.4b)$$

$$\zeta = g(\theta) \qquad (2.4c)$$

Substitution of these relations into equations (2.3) results in two equations for $\theta(\zeta)$:

$$\theta'''' + [1 - 6(\theta')^2]\theta'' = 0 \qquad (2.5)$$

and

$$w + (\theta')^4 - (\theta')^2 - 4\theta'\theta''' - 3(\theta'')^2 = 0 \qquad (2.6)$$

Equation (2.5) is the governing differential equation for $\theta(\zeta)$ in the contact section. Once $\theta(\zeta)$ is determined by solution of equation (2.5), equation (2.6) can be solved separately for the wall contact force $w(\zeta)$.

Note that it is not possible to linearize equation (2.5) by neglecting the $6(\theta')^2$ term relative to unity. The solution for a helically buckled rod away from the end gives values of $0.707 \leq \theta' \leq 1.0$ (Lubinski et al., 1962, and Cheatham and Pattillo, 1984), such that $3 \leq 6(\theta')^2 \leq 6$, which is clearly not small relative to unity.

The internal reactions of the rod in the contact section are expressed in terms of the rod deflections:

$$V_j = -(v_j''' + v_j'), \qquad (2.7)$$

and

$$M_j = v_j'', \qquad (2.8)$$

where $V_j = \hat{V}_j/\alpha Wr$ is the nondimensional internal shear force corresponding to the dimensional shear force $\hat{V}_j$; $M_j = \hat{M}_j/Wr$ is the nondimensional internal bending moment corresponding to the dimensional bending moment $\hat{M}_j$; and $j = 1$ for the x-direction component, and $j = 2$ for the y-direction component.

2.2 Analysis of the End and Transition Sections. Since there is no distributed force acting on the end and transition sections, $w = 0$ and the governing differential equations become

$$u_{ij}'''' + u_{ij}'' = 0 \qquad (2.9)$$

where $u_{ij} = \hat{u}_{ij}/r$ is the nondimensional position of the rod centerline in the end ($i = 1$) and transition ($i = 2$) sections, and $j = 1$ and 2 for the x and y directions as before.

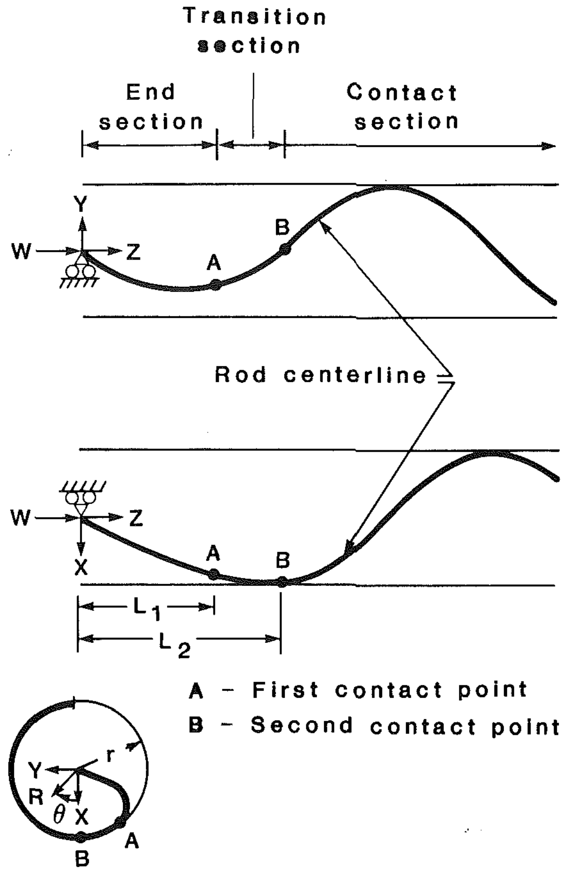

Fig. 1 Pinned-end rod geometry and nomenclature

The general solution of equation (2.9) is

$$u_{ij} = a_{ij} + b_{ij}\zeta + c_{ij}\cos\zeta + d_{ij}\sin\zeta \qquad (2.10)$$

where a_{ij}, b_{ij}, c_{ij}, and d_{ij} are unknown constants.

2.3 Boundary Conditions. Boundary conditions at the rod end are those for a pinned connection in the $x-z$ and $y-z$ planes located on the cylinder axis:

$$u_{1j}(0) = 0 \qquad (2.11)$$

$$u_{1j}''(0) = 0 \qquad (2.12)$$

The boundary conditions at the first contact point, $\zeta = \phi_1 = \alpha L_1$, require the rod to contact the cylinder wall tangent to the wall surface. Continuity of position, slope, curvature, and tangential shear between the end and transition sections is also required:

$$u_{11}(\phi_1) = \cos\theta_1 \qquad (2.13a)$$

$$u_{12}(\phi_1) = \sin\theta_1 \qquad (2.13b)$$

$$u_{11}'(\phi_1) = -\theta_1'\sin\theta_1 \qquad (2.14a)$$

$$u_{12}'(\phi_1) = \theta_1'\cos\theta_1 \qquad (2.14b)$$

$$u_{21}(\phi_1) = \cos\theta_1 \qquad (2.15a)$$

$$u_{22}(\phi_1) = \sin\theta_1 \qquad (2.15b)$$

$$u_{21}'(\phi_1) = -\theta_1'\sin\theta_1 \qquad (2.16a)$$

$$u_{22}'(\phi_1) = \theta_1'\cos\theta_1 \qquad (2.16b)$$

$$u_{11}''(\phi_1) = u_{21}''(\phi_1) \qquad (2.17a)$$

$$u_{12}''(\phi_1) = u_{22}''(\phi_1) \qquad (2.17b)$$

$$\begin{aligned} &u_{11}'''(\phi_1)\sin\theta_1 - u_{12}'''(\phi_1)\cos\theta_1 \\ &\quad = u_{21}'''(\phi_1)\sin\theta_1 - u_{22}'''(\phi_1)\cos\theta_1 \end{aligned} \qquad (2.18)$$

where θ_1 and θ_1' are constants; $\theta_1 = \theta(\phi_1)$, and $\theta_1' = \theta'(\phi_1)$. A discontinuous radial shear force is allowed since a concentrated radial contact force can occur.

The boundary conditions at the second contact point, $\zeta = \phi_2 = \alpha L_2$, require that the rod contact the wall at a position of $\theta(\phi_2) = 0$ and that there be a continuity of position, slope, curvature, and tangential shear between the transition and contact sections:

$$u_{21}(\phi_2) = 1 \tag{2.19a}$$

$$u_{22}(\phi_2) = 0 \tag{2.19b}$$

$$u_{21}'(\phi_2) = 0 \tag{2.20a}$$

$$u_{22}'(\phi_2) = \theta_2' \tag{2.20b}$$

$$u_{21}''(\phi_2) = -(\theta_2')^2 \tag{2.21a}$$

$$u_{22}''(\phi_2) = \theta_2'' \tag{2.21b}$$

$$-(u_{22}''' + u_{22}') = (\theta_2')^3 - \theta_2' - \theta_2''' \tag{2.22}$$

where θ_2', θ_2'', θ_2''' are unknown constants; $\theta_2' = \theta'(\phi_2)$, $\theta_2'' = \theta''(\phi_2)$, and $\theta_2''' = \theta'''(\phi_2)$. The specification of $\theta(\phi_2) = 0$ is arbitrary since the rod is assumed weightless.

An additional boundary condition is necessary in the contact section. The problem being solved is either that of a finite length rod loaded axially at both ends, or that of a semi-infinite rod. For the semi-infinite case it is required that the pitch of the contact section be some constant value far from the rod end; i.e., $\theta''(\infty) = 0$. This requirement is also the midlength condition for the finite length rod. The final boundary condition is, therefore,

$$\theta''(\phi_s) = 0 \tag{2.23}$$

where $\zeta = \phi_s$ is the half-length of the finite length rod, or is infinity for the semi-infinite rod case.

2.4 Solution Method. The solution procedure is comprised of two major parts: 1) solution of the set of simultaneous nonlinear algebraic equations resulting from application of the boundary conditions for the end and transition sections at $\zeta = 0$, $\zeta = \phi_1$, and $\zeta = \phi_2$; and 2) solution of the nonlinear fourth-order differential equation of the contact section such that $\theta''(\phi_s) = 0$. The first part is accomplished by assuming a value for ϕ_1 and using the first 22 boundary conditions, equations (2.11)-(2.22) to solve for the remaining 22 unknowns. This calculation generates values for θ_2', θ_2'', and θ_2''' for a given value of ϕ_1. These are then used in the second part of the solution as initial values, along with $\theta(\phi_2) = 0$, for the numerical integration of the nonlinear equation (2.5). Integration is continued along ζ to $\zeta = \phi_s$, and the results are checked to determine if $\theta''(\phi_s) = 0$. ϕ_1 is adjusted until $\theta''(\phi_s) = 0$ is satisfied. The overall approach is, therefore, a shooting method for the solution of the nonlinear boundary value problem on θ in the contact section. The adjustment of ϕ_1 is performed using an interval halving procedure.

Treating ϕ_1 as known, applications of equations (2.11) and (2.12) shows that

$$a_{1j} = c_{1j} = 0 \tag{2.24}$$

for $j = 1, 2$.

Equations (2.13) and (2.14) give

$$b_{11} = \frac{-\cos\theta_1 \cos\phi_1 - \theta_1' \sin\theta_1 \sin\phi_1}{\sin\phi_1 - \phi_1 \cos\phi_1} \tag{2.25a}$$

$$b_{12} = \frac{-\sin\theta_1 \cos\phi_1 + \theta_1' \cos\theta_1 \sin\phi_1}{\sin\phi_1 - \phi_1 \cos\phi_1} \tag{2.25b}$$

$$d_{11} = \frac{\cos\theta_1 + \phi_1 \theta_1' \sin\theta_1}{\sin\phi_1 - \phi_1 \cos\phi_1} \tag{2.26a}$$

$$d_{12} = \frac{\sin\phi_1 - \phi_1 \theta_1' \cos\theta_1}{\sin\phi_1 - \phi_1 \cos\phi_1} \tag{2.26b}$$

Equations (2.16) through (2.23) require that

$$a_{21} + b_{21}\phi_1 + c_{21}\cos\phi_1 + d_{21}\sin\phi_1 - \cos\theta_1 = 0 \tag{2.27a}$$

$$a_{22} + b_{22}\phi_1 + c_{22}\cos\phi_1 + d_{22}\sin\phi_1 - \sin\theta_1 = 0 \tag{2.27b}$$

$$b_{21} - c_{21}\sin\phi_1 + d_{21}\cos\phi_1 + \theta_1'\sin\theta_1 = 0 \tag{2.27c}$$

$$b_{22} - c_{22}\sin\phi_1 + d_{22}\cos\phi_1 - \theta_1'\cos\theta_1 = 0 \tag{2.27d}$$

$$(\cos\theta_1 - \phi_1\theta_1'\sin\theta_1)\frac{\sin\phi_1}{\sin\phi_1 - \phi_1\cos\phi_1} - c_{21}\cos\phi_1 - d_{21}\sin\phi_1 = 0 \tag{2.27e}$$

$$(\sin\theta_1 - \phi_1\theta_1'\cos\theta_1)\frac{\sin\phi_1}{\sin\phi_1 - \phi_1\cos\phi_1} - c_{22}\cos\phi_1 - d_{22}\sin\phi_1 = 0 \tag{2.27f}$$

$$\theta_1' \frac{\sin\phi_1}{\sin\phi_1 - \phi_1\cos\phi_1} + b_{21}\sin\theta_1 - b_{22}\cos\theta_1 = 0 \tag{2.27g}$$

$$a_{21} + b_{21}\phi_2 + c_{21}\cos\phi_2 + d_{21}\sin\phi_2 - 1 = 0 \tag{2.27h}$$

$$a_{22} + b_{22}\phi_2 + c_{22}\cos\phi_2 + d_{22}\sin\phi_2 = 0 \tag{2.27i}$$

$$b_{21} - c_{21}\sin\phi_2 + d_{21}\cos\phi_2 = 0 \tag{2.27j}$$

$$b_{22} - c_{22}\sin\phi_2 + d_{22}\cos\phi_2 - \theta_2' = 0 \tag{2.27k}$$

$$c_{21}\cos\phi_2 + d_{21}\sin\phi_2 - (\theta_2')^2 = 0 \tag{2.27l}$$

$$\theta_2'' + c_{22}\cos\phi_2 + d_{22}\sin\phi_2 = 0 \tag{2.27m}$$

$$b_{22} + (\theta_2')^3 - \theta_2' - \theta_2''' = 0 \tag{2.27n}$$

Solution for the unknowns of equation (2.27) requires simultaneous solution of the set of 14 nonlinear algebraic equations. This is accomplished numerically using the Modified Quasilinearization Algorithm (MQA) (Miele and Iyer, 1971).

Integration of equation (2.5), once the values of θ_2', θ_2'', and θ_2''' are determined from the solution of equations (2.27), is performed numerically using a fixed-step fourth-order Runge-Kutta integration procedure.

3.0 Analysis of a Fixed-End Helically Buckled Rod

The fixed-end analysis is identical to that for the pinned-end case except that the boundary conditions at the rod end are modified to require the rod end to be tangent to the cylinder axis.

Boundary conditions at the rod end are those for a built-in end in the $x-z$ and $y-z$ planes located on the cylinder axis:

$$u_{1j}(0) = 0 \tag{3.1}$$

$$u_{1j}'(0) = 0 \tag{3.2}$$

All other boundary conditions, equations (2.13)-(2.23), remain the same as for the pinned-end case.

The problem solution procedure of Section 2.4 is also used for the fixed-end case.

Equations (3.1), (3.2), (2.13), and (2.14) require that

$$a_{11} = \frac{\cos\theta_1(1 - \cos\phi_1) + \theta_1'\sin\theta_1(\phi_1 - \sin\phi_1)}{2 - 2\cos\phi_1 - \phi_1\sin\phi_1} \tag{3.3a}$$

$$b_{11} = \frac{-\theta_1'\sin\theta_1(1 - \cos\phi_1) - \sin\phi_1\cos\theta_1}{2 - 2\cos\phi_1 - \phi_1\sin\phi_1} \tag{3.3b}$$

$$c_{11} = -a_{11} \tag{3.3c}$$

$$d_{11} = -b_{11} \tag{3.3d}$$

$$a_{12} = \frac{\sin \theta_1 (1 - \cos \phi_1) - \theta_1' \cos \theta_1 (\phi_1 - \sin \phi_1)}{2 - 2 \cos \phi_1 - \phi_1 \sin \phi_1} \tag{3.4a}$$

$$b_{12} = \frac{\theta_1' \cos \theta_1 (1 - \cos \phi_1) - \sin\theta_1 \sin \phi_1}{2 - 2 \cos \phi_1 - \phi_1 \sin \phi_1} \tag{3.4b}$$

$$c_{12} = -a_{12} \tag{3.4c}$$

$$d_{12} = -b_{12}. \tag{3.4d}$$

Equations (2.15)–(2.21*a*) require

$$a_{21} + b_{21}\phi_1 + c_{21} \cos \phi_1 + d_{21} \sin \phi_1 - \cos \theta_1 = 0 \tag{3.5a}$$

$$a_{22} + b_{22}\phi_1 + c_{22} \cos \phi_1 + d_{22} \sin \phi_1 - \sin \theta_1 = 0 \tag{3.5b}$$

$$b_{21} - c_{21} \sin \phi_1 + d_{21} \cos \phi_1 + \theta_1' \sin \theta_1 = 0 \tag{3.5c}$$

$$b_{22} - c_{22} \sin \phi_1 + d_{22} \cos \phi_1 - \theta_1' \cos \theta_1 = 0 \tag{3.5d}$$

$$c_{21} \cos \phi_1 + d_{21} \sin \phi_1 - \left[\frac{\cos \theta_1 (1 - \cos \phi_1) + \theta_1' \sin \theta_1 (\sin \phi_1 - \phi_1 \cos \phi_1)}{2 - 2\cos \phi_1 - \phi_1 \sin \phi_1} \right] = 0 \tag{3.5e}$$

$$c_{22} \cos \phi_1 + d_{22} \sin \phi_1 - \left[\frac{\sin \phi_1 (1 - \cos \phi_1) - \theta_1' \cos \theta_1 (\sin \phi_1 - \phi_1 \cos \phi_1)}{2 - 2\cos \phi_1 - \phi_1 \sin \phi_1} \right. = 0 \tag{3.5f}$$

$$-(c_{21} \sin \theta_1 - c_{22} \cos \theta_1) \sin \phi_1 + (d_{21} \sin \theta_1 - d_{22} \cos \theta_1) \cos \phi_1 + \theta_1' \frac{(1 - \cos \phi_1 - \phi_1 \sin \phi_1)}{(2 - 2\cos \phi_1 - \phi_1 \sin \phi_1)} = 0 \tag{3.5g}$$

$$a_{21} + b_{21}\phi_2 + c_{21} \cos \phi_2 + d_{21} \sin \phi_2 - 1 = 0 \tag{3.5h}$$

$$a_{22} + b_{22}\phi_2 + c_{22} \cos \phi_2 + d_{22} \sin \phi_2 = 0 \tag{3.5i}$$

$$b_{21} - c_{21} \sin \phi_2 + d_{21} \cos \phi_2 = 0 \tag{3.5j}$$

$$b_{22} - c_{22} \sin \phi_2 + d_{22} \cos \phi_2 - \theta_2' = 0 \tag{3.5k}$$

$$c_{21} \cos \phi_2 + d_{21} \sin \phi_2 - \theta_2'^2 = 0. \tag{3.5l}$$

Equations (2.21*b*) and (2.22) are used to solve directly for θ_2'' and θ_2''':

$$\theta_2'' = -c_{22} \cos \phi_2 - d_{22} \sin \phi_2 \tag{3.6a}$$

$$\theta_2''' = b_{22} + (\theta_2')^3 - \theta_2' \tag{3.6b}$$

Solution for the 12 unknowns of equation (3.5) and integration of equation (2.5) were accomplished with the same techniques as described in Section 2.4.

4.0 Results

Figures 2 through 5 present the key results of both the pinned-end and fixed-end analyses. The geometry of the buckled rod is shown in Fig. 2. For the pinned-end case, initial wall contact occurs at $\zeta = \phi_1 = 2.46867$, and a second contact point occurs at $\zeta = \phi_2 = 4.38105$. The pinned-end rod is in contact with the cylinder wall everywhere along its length for $\zeta \geq 4.38105$. For the fixed-end case, the initial wall contact occurs at $\zeta = \phi_1 = 3.81729$, and a second contact point occurs at $\zeta = \phi_2 = 5.24273$. The fixed-end rod is in contact with the cylinder wall everywhere for $\zeta \geq 5.24273$. The deflected shape of the end section for the pinned-end rod is planar.

In Fig. 2*a*, the radial position of the rod in the transition section for both the pinned and fixed cases appears to be on the wall. The numerical results (Sorenson, 1984) show that the transition sections are actually off the wall by a very small amount. The maximum clearance for the pinned-end case is approximately 0.002 r and for the fixed-end case is 0.0005 r.

Figures 2 and 3 show that away from the rod end, the rod is buckled into a constant pitch helical configuration with $\theta' = 1/\sqrt{2} = 0.70711$. This is the result obtained by Lubinski et al. (1962) for a helically buckled rod away from any end effects. It is interesting to note that while the present analysis does force the contact section solution to a constant value of θ' by requiring that $\theta''(\phi_s) = 0$, it does not force the solution to any particular value of θ'. The fact that the solution converges to the value predicted by Lubinski provides corroboration of these results.

The contact section of the rod can be described by two subsections: a perturbed helix section and a helical section. The perturbed helix section is defined as that portion of the rod from the second contact point at $\zeta = \phi_2$ to the point $\zeta = \phi_h$, defined such that $\theta'(\phi_h) = 0.999/\sqrt{2}$ where the choice of the factor 0.999 is arbitrary. The helical section is defined as the portion of the rod at $\zeta \geq \phi_h$. Using these definitions, the total nonhelical length of rod from the rod end to the beginning of the helical section can be expressed as a fraction of the helix pitch, p, by $(\phi_h/\alpha p)_{\text{pinned}} = 0.760$; $(\phi_h/\alpha p)_{\text{fixed}} = 0.877$.

As shown in Fig. 4, the pinned-end maximum bending moment occurs in the end section at $\zeta\,(M_{\text{max,pinned}}) = \pi/2 = 1.57080$ and is $M_{\text{max,pinned}} = 0.59727$, which is 19.5 percent greater than the bending moment in the helical portion of the rod. The maximum bending moment in the fixed-end rod also occurs in the end section, at $\zeta(M_{\text{max,fixed}}) = 2.99229$, and is $M_{\text{max,fixed}} = 0.50491$, which is only 1 percent greater than in the helical portion. The bending moment at the fixed rod end equals that of the helical portion.

The maximum shear force occurs in the helical portion of the rod and is $V_{\max} = 0.35355$ for both the pinned-end and fixed-end cases.

The wall contact force is shown in Fig. 5. The pinned-end contact force is $w(\phi_2)_{\text{pinned}} = 0.14672$ at the beginning of the contact section. The fixed-end force starts at $w(\phi_2)_{\text{fixed}} = 0.12050$. For both cases, the contact force increases along the length until it reaches a maximum value of $w_{\max} = 0.25$ in the helical portion.

The pinned-end radial force acting at the rod end is $F(0)_{\text{pinned}} = 0.32670$, where $F = \hat{F}/\alpha Wr$ is the nondimensional force corresponding to the dimensional force $\hat{F}$. Concentrated radial contact forces associated with the radial shear discontinuities at the first and second contact points are $F(\phi_1)_{\text{pinned}} = 0.61028$, and $F(\phi_2)_{\text{pinned}} = 0.04726$. The fixed-end rod has an end force and moment of $F(0)_{\text{fixed}} = 0.19187$, and $M(0)_{\text{fixed}} = 0.50000$, and concentrated radial contact forces of $F(\phi_1)_{\text{fixed}} = 0.38202$, and $F(\phi_2)_{\text{fixed}} = 0.02557$.

The analysis of Sections 2 and 3 was formulated to produce closed-form solutions for the deflected shapes of the end and transition sections for both the pinned-end and fixed-end cases. The rod geometry is described by

$$u_{ij} = a_{ij} + b_{ij\zeta} + c_{ij} \cos \zeta + d_{ij} \sin \zeta \tag{2.10}$$

The internal rod reactions are

$$V_{ij} = -(u_{ij}''' + u_{ij}') = -b_{ij}$$

and

$$M_{ij} = u_{ij}'' = -c_{ij} \cos \zeta - d_{ij} \sin \zeta.$$

Parameter values for the pinned-end problem are:

$$\begin{array}{llll}
a_{11} = & 0 & a_{12} = & 0 \\
b_{11} = & 0.22147 & b_{12} = & -0.24017 \\
c_{11} = & 0 & c_{12} = & 0 \\
d_{11} = & -0.26884 & d_{12} = & -0.53335 \\
a_{21} = & 0.57127 & a_{22} = & -1.39407 \\
b_{21} = & -0.00994 & b_{22} = & 0.32454 \\
c_{21} = & -0.14423 & c_{22} = & 0.35197 \\
d_{21} = & -0.44980 & d_{22} = & -0.09174
\end{array}$$

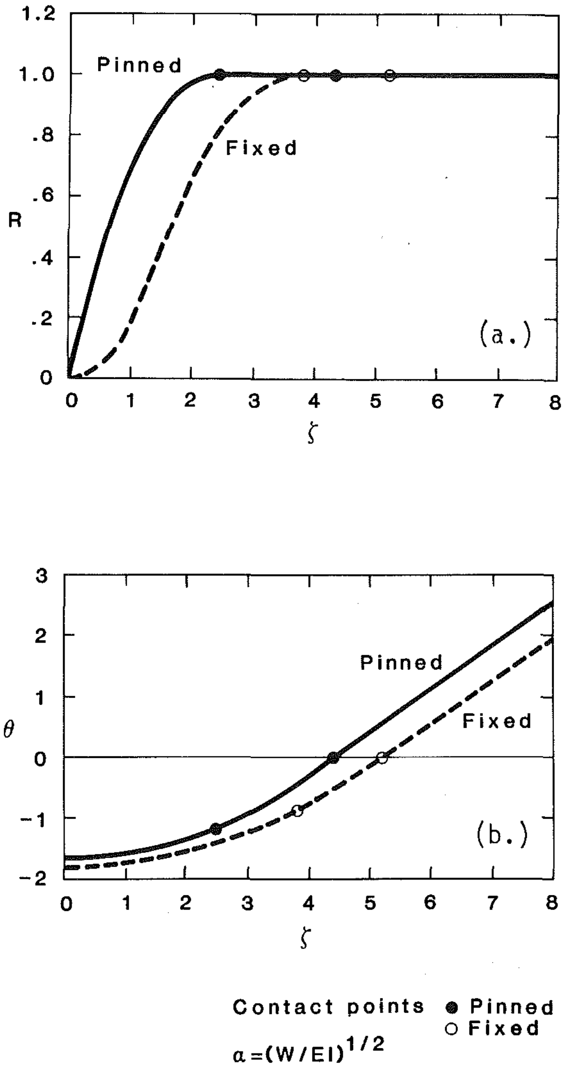

Fig. 2 Rod displacement results in $R-\theta$ Coordinates: (a) Rod centerline dimensionless deflection from hole centerline, $R=\hat{R}/r$, versus dimensionless distance from rod end, $\zeta=\alpha z$; (b) Rod centerline angular deflection from x axis, θ (radians) versus distance from rod end, $\zeta=\alpha x$

Parameter values for the fixed-end problem are:

$a_{11} = -0.12662$ $\quad$ $a_{12} = -0.48370$
$b_{11} = 0.19104$ $\quad$ $b_{12} = 0.01782$
$c_{11} = 0.12662$ $\quad$ $c_{12} = 0.48370$
$d_{11} = -0.19104$ $\quad$ $d_{12} = -0.01782$
$a_{21} = 0.78238$ $\quad$ $a_{22} = -1.62402$
$b_{21} = -0.04708$ $\quad$ $b_{22} = 0.31654$
$c_{21} = 0.27556$ $\quad$ $c_{22} = 0.29687$
$d_{21} = -0.37685$ $\quad$ $d_{22} = 0.21527$

Summary

The effect of pinned and fixed-end conditions on the post-buckling behavior of a circular rod constrained within a circular cylinder has been investigated subject to certain idealizations. The rod is found to buckle into a helical configuration far from the end, with the helix pitch given by Lubinski et al. (1962). Both end conditions are found to perturb the helix near the rod end in an exponentially decaying manner for a distance of less than one helix pitch length. The pinned-end condition is more severe than the fixed-end condition. The maximum bending moment increases by 19.5 percent due to end effects for the pinned-end condition, and increases by less than 1 percent for the fixed-end condition.

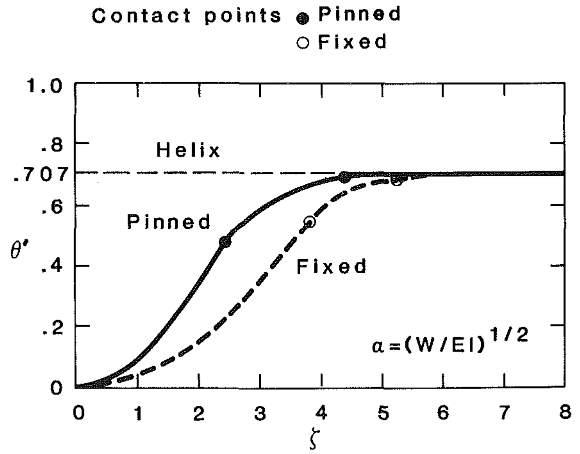

Fig. 3 Local helix angle results: rate of change of angular deflection, $\theta'=\gamma/\alpha r$ versus distance from rod end, $\zeta=\alpha z$, where $\tan\gamma=2\pi r/p$

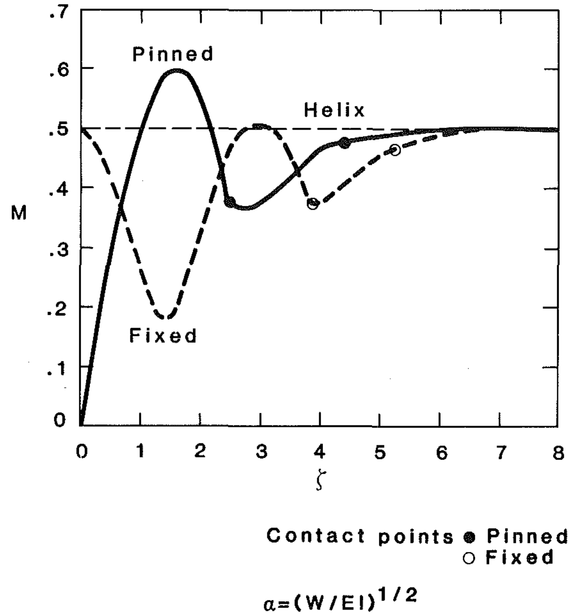

Fig. 4 Bending moment results: dimensionless bending moment, $M=\hat{M}/Wr$ versus dimensionless distance from rod end, $\zeta=\alpha z$

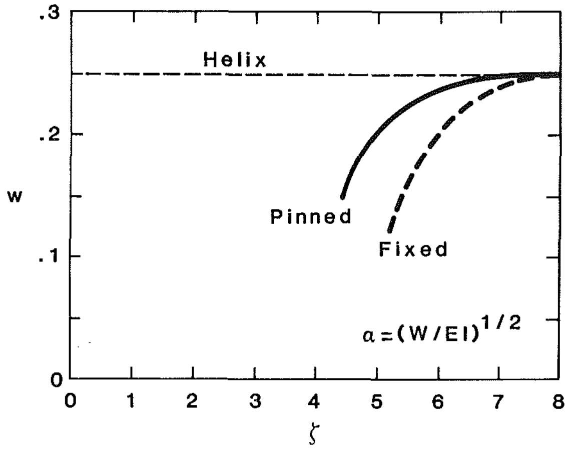

Fig. 5 Wall contact force results: dimensionless contact force, $w=\hat{w}/\alpha^2 Wr$ versus dimensionless distance from rod end, $\zeta=\alpha z$

Comparison of the pinned and fixed-end results shows that the general behavior is very similar for the two cases. Both can be described by an end section, a transition section, and a contact section. Both have the same helix pitch far from the rod end. The rod first contacts the wall farther from the rod end for the fixed-end case, and the transition section is shorter. The distance from the rod end to the beginning of the helical section is longer for the fixed-end case than for the pinned-end case. The magnitudes of the concentrated contact forces for the fixed-end case are approximately 60 percent of those for the pinned-end case. The maximum bending moment occurs in the end section for both cases. The maximum shear force and maximum wall contact force occur in the helical section and are the same for both cases. Closed-form analytical solutions are obtained for the deflected shape of the end portions of the rod.

Acknowledgments

The authors thank Paul R. Paslay for his contributions to this work.

References

Cheatham, Jr., J. B., and Pattillo, P. D., 1984, "Helical Post-Buckling Configuration of a Weightless Column Under the Action of an Axial Load," *SPE Journal*, Vol. 24, pp. 467–472.

Dawson, R., and Paslay, P. R., 1982, "Drill Pipe Buckling in Inclined Holes," SPE paper no. 11167, presented at the 57th Annual Fall Technical Conference of the Society of Petroleum Engineers.

Lubinski, A., 1950, "A Study of the Buckling of Rotary Drilling Strings," *Drilling and Production Practice*, American Petroleum Institute, pp. 178–214.

Lubinski, A., Althouse, W. S., and Logan, J. L., 1962, "Helical Buckling of Tubing Sealed in Packers," *Journal of Petroleum Technology*, Vol. 225, pp. 655–670.

Lubinski, A., and Woods, H. B., 1953, "Factors Affecting the Angle of Inclination and Dog-Legging in Rotary Bore Holes," *Drilling and Production Practice*, American Petroleum Institute, pp. 222–250.

Miele, A., and Iyer, R. R., 1971, "Modified Quasilinearization Algorithm for Solving Non-Linear, Two Point Boundary Value Problems," *Journal of Mathematical Analysis and Application*, Vol. 36, pp. 674–692.

Mitchell, R. F., 1982, "Buckling Behavior of Well Tubing," *SPE Journal*, Vol. 22, pp. 616–624.

Paslay, P. R., and Bogy, D. B., 1964, "The Stability of a Circular Rod Laterally Constrained to be in Contact with an Inclined Circular Cylinder," ASME JOURNAL OF APPLIED MECHANICS, Vol. 31, pp. 605–610.

Paslay, P. R., and Dawson, R., 1982, "Analysis of Drill Pipe and Drill Collar Buckling," *Proceedings of the 9th U.S. National Congress of Applied Mechanics*, ASME, pp. 453–456.

Sorenson, K. G., 1984, "Post-Buckling Behavior of a Circular Rod Constrained Within a Circular Cylinder," Ph.D. Dissertation, Rice University, Houston, Texas.

Woods, H. B., and Lubinski, A., 1955, "Use of Stabilizers in Controlling Hole Deviation," *Drilling and Production Practice*, American Petroleum Institute, pp. 165–182.

K. Craig
Assistant Professor,
Hofstra University,
Hempstead, NY 11550
Mem. ASME

R. H. Buckholz
Associate Professor,
Columbia University,
New York, NY 10027

G. Domoto
Xerox Corporation,
Palo Alto Research Center, M.E.S.,
N. Tarrytown, New York 10591

An Experimental Study of the Rapid Flow of Dry Cohesionless Metal Powders

This paper studies the rapid shearing flow of dry metal powders. To perform this study, we built and used an annular shear cell test apparatus. In this apparatus the dry metal powders are rapidly sheared by rotating one of the shear surfaces while the other shear surface remains fixed. The shear stress and normal stress on the stationary surface were measured as a function of three parameters: the shear-cell gap thickness, the shear-rate and the fractional solids content. Stresses are measured while holding both the fractional-solids content and the gap thickness at prescribed values. The results show the dependence of the normal stress and the shear stress on the shear-rate. Likewise, a significant stress dependence on both the fractional solids content and the shear-cell gap thickness was observed. Our experimental results are compared with the results of other reported experimental studies.

I Introduction

Traditionally, a granular material is defined as an assembly of discrete solid components. When these solid constituents are in static equilibrium, substantial contact with their near neighbors occurs. We examine the flow of such a granular material. In these flows the individual particle motions dominate the dynamics of motion. The material's behavior is governed by interparticle cohesion, friction, and particle collisions. In general, the motion and flow of the individual beads are very complex.

Granular materials form one member of the class of materials known as dispersed two-phase systems. These systems consist of solid and fluid components. An example of one such system is dilute suspension. Granular flows are encountered in industrial situations in the following two examples: mineral and powder processing in both chemical and pharmaceutical industries, and the storage, handling and transport of particulate materials. Granular material flow also occurs in the environment. Two additional related examples are rock slides and debris flows. Likewise, some analogous flows are snow avalances, mud slides, and subaqueous sediment flow. These latter examples have close affinities with the motion of granular materials. An understanding of the mechanics of granular material flow is essential for the understanding and solution of a wide range of technological and scientific problems.

The motivation for this study arose from the process of xerography. In this process a dry powder image is formed upon a xerographic plate by optical and electrostatic mechanisms. Toner, a dry, thermoplastic powder, is used and the powder image is then transferred to a sheet of ordinary paper. This process relies upon the use of both a magnetic field and the use of flow of metal powders to transport the thermoplastic powder. The results reported here are for the rapid flow of carbon steel beads without a magnetic field. The results we obtain for the flow of other metal powders and carbon steel beads with a magnetic field are to be reported in another publication.

The understanding of granular flow situations has evolved over time. Early experimental investigation of granular material by Reynolds (1885) shows that a closely-packed assemblage of solid particles tends to expand when deformed. Later, Hvorslev (1936, 1939) developed the first annular shear cell to consider the behavior of soils. Subsequent to his study, other studies were performed at low strain-rates. Bulk solids are then experimentally considered by: Novosad (1964); Carr and Walker (1968); Scarlett and Todd (1968, 1969); Scarlett et al. (1969, 1970); Mandl et al. (1977); and Stephens and Bridgwater (1978). However, very low rates-of-deformation are used in the above mentioned studies. Consequently, the measured stresses are found to be independent of the shear-rate. However, experiments to test dry, coarse, granular materials at high shear-rates are then developed by Novosad (1964), Bridgwater (1972), Savage and Sayed (1984), and by Hanes and Inman (1985). All of the latter experiments use the annular, shear-cell test apparatus. Novosad (1964) is the first to study departure from quasistatic deformation. He does not observe that the measured stresses depend on shear-rate. In another study, Bridgwater (1972) develops an annular shear cell to operate at shear-rates that are larger than the ones reported by Novosad. Savage and Sayed also developed a shear-cell test apparatus to operate at high shear-rate; they configured their test apparatus to allow a prescribed, fractional solids content. Similar tests are reported by Hanes and Inman. In a theoretical study, a computer simulation of two-

---

Contributed by the Applied Mechanics Division for publication in the JOURNAL OF APPLIED MECHANICS.

Discussion on this paper should be addressed to the Editorial Department, ASME, United Engineering Center, 345 East 47th Street, New York, N.Y. 10017, and will be accepted until two months after final publication of the paper itself in the JOURNAL OF APPLIED MECHANICS. Manuscript received by ASME Applied Mechanics Division, September 5, 1985; final revision February 15, 1986.

dimensional granular flow is presented by Campbell and Brennen (1985). Their two-dimensional results can be extended to three-dimensional shear-flow experiments by using appropriate scale factors. Surveys of granular flows are made by Spencer (1981), by Mroz (1980), and by Savage (1985).

One of the central issues related to the prediction of granular material flow is characterization of its material properties. One view, the one adopted in this paper, is a continuum approach. Another angle of vision could consider the dynamics of the individual particles. The continuum mechanics point-of-view to describe the granular flow involves determining an appropriate constitutive equation. Therefore, we focus on the issue of stress as a function of shear-rate. The purpose of this experiment is to study the stresses associated with the shearing motion of metal powders. The results obtained can guide the theoretical development of constitutive equations for metal powders. Stress measurements are obtained that are analogous to the type obtained in rheological tests of both viscous fluids and solid suspensions.

It is essential to control as many of the independent parameters as possible. One of these independent parameters, the fractional solids content, is maintained at a prescribed constant value for a range of experimental conditions. The average stresses are then measured as functions of shear-rate. The importance of holding the fractional solids content fixed is first pointed out by Savage (1978). Fractional solids content changes because volumetric expansion occurs during the shearing of dry granular materials. Therefore, it is necessary that special care be taken in the design of the shear cell test apparatus. The experimental apparatus used here is designed such that the fractional solids content can be controlled. The first flow data obtained under conditions of fixed fractional solids content for high density metal powders are given.

II Description of Experimental Apparatus

The apparatus, as shown in Fig. 1, has two concentric horizontal aluminum disks that are mounted on a rotating vertical stainless steel shaft. The bottom disk has an annular channel 19.05 mm wide. This channel is 19.05 mm deep at a mean radius of 68.26 mm. The granular material to be tested is contained in this annular channel. The top disk has an annular protrusion that fits into the channel of the bottom disk. The top disk must be free to rotate in order to measure the torque caused by the shearing action of the granular material. It must also be free to translate in the vertical direction, so as to allow for expansion or contraction of the granular material under shear. The translation of the upper shear surface is accomplished by using a linear, ball-bearing mounting. The required tolerances are met and the apparatus performs exceptionally well. The annular protrusion of the top disk does not contact the side walls of the bottom disk channel. The clearance between these two surfaces is approximately 50 microns. A small clearance is needed to prevent the jamming of the granular material being sheared. The top disk is kept from rotating by a torque arm that is connected to a force transducer. The rotation rate of the bottom disk is determined by using an optical tachometer. The displacement of the top disk relative to the bottom disk is measured by using a dial indicator. Thus, the fractional solids content can be determined. The side walls of the annular channel are hard-coated both for abrasion resistance and reduced friction. The top and bottom horizontal surfaces of the annular channel are the shear transmission surfaces. The top surface is stationary, and the bottom one is rotated about the vertical axis. Thus, a nearly simple shearing type flow of metal beads is expected to occur in the annular channel. The beads are driven into motion by contact with the moving surface.

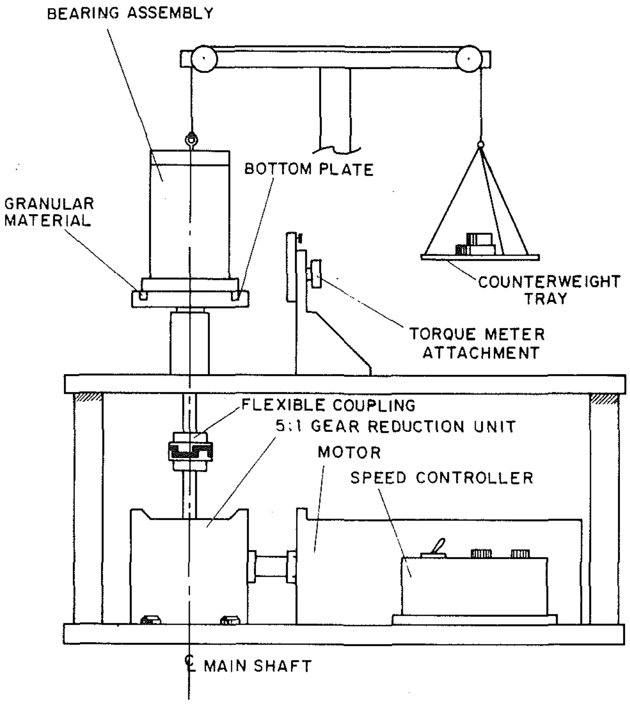

Fig. 1 Sketch of the shear flow test apparatus

Both the moving and stationary surfaces are coated with the carbon steel beads being tested. Spherical particles of the material tested are bonded onto two, thin-aluminum annular rings. A high temperature epoxy is used to attach a dense monolayer of beads to the annular aluminum rings. These aluminum rings are then secured to the top and bottom of the annular channel by very thin, high-shear-strength, double-sided adhesive tape. The rings can be replaced as different materials are tested. During the testing no particles were observed to be dislodged from the shear transmission surfaces. Nor did the rings slip during the tests. Particle jamming in the gap between the side walls of the annular channel and the upper shear transmission surface was avoided. A recess is cut into the top disk so that approximately a half particle diameter layer can protrude from the top disk. Forces are applied to the top disk by using a system of weights and counterweights. This system is used to change the applied normal stresses.

III Metal Powders Tested and Testing Procedure

Several different types of materials and bead sizes are being tested. This study reports the results for carbon-steel 1018 spherical beads. The carbon-steel, bead diameter range tested is 0.85 mm to 0.71 mm, and the bead density is 7.86 gm/cm^3.

The experimental apparatus is designed to study the normal and shear stresses as a function of shear-rate. Prescribed values of both the fractional solids content and shear-cell gap thickness are used. The fractional solids content is measured using the method described below. The top disk is fixed into position and the vertical displacement reading, without powder in the annular channel, is used as a reference. Then, the carbon-steel particles are placed into the annular channel of the bottom disk. The top disk is then placed back into its position. A prescribed normal load is applied to the metal powder. The bottom disk is then placed into rotation. This bottom-disk rotation causes the granular material to expand so as to lift the top disk. The rotation rate is increased until a desired fractional solids content is achieved. The fractional solids content is determined from the total mass of the beads in the annular channel, the density of the beads, and the volume of the annular shear region. The latter is calculated after determining the relative positions of the top and bottom disks from the vertical displacement reading. We measure the

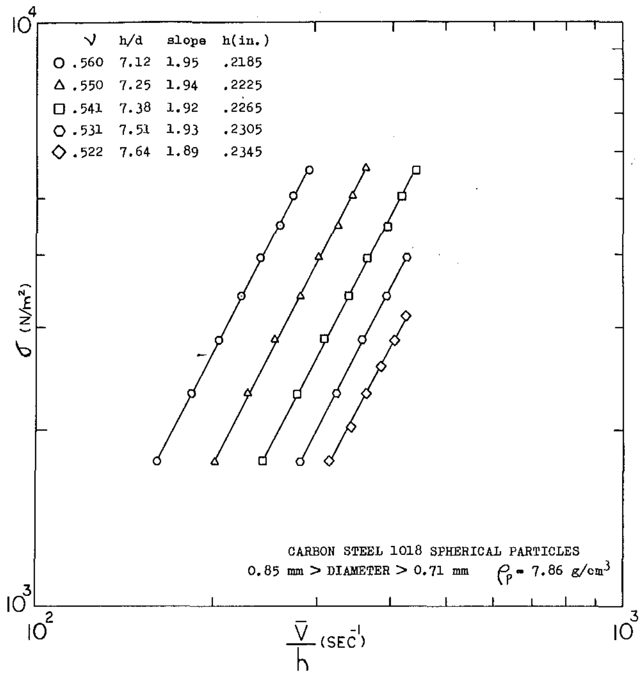

Fig. 2(*a*) **Dimensional plot of average normal stress versus average shear rate for carbon steel beads;** $(h/d)_{\text{avg.}} = 7.38$

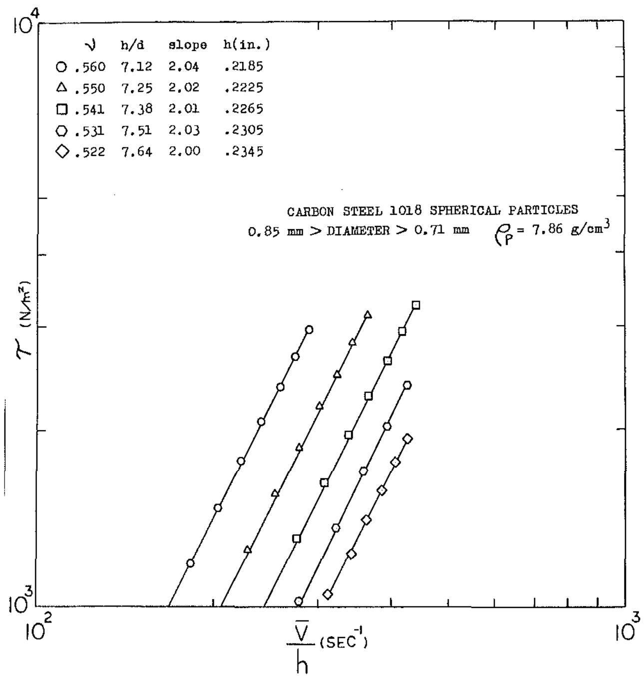

Fig. 2(*b*) **Dimensional plot of average shear stress versus average shear-rate for carbon-steel beads;** $(h/d)_{\text{avg.}} = 7.38$

normal stress, the shear stress, and rotation rate, corresponding to this particular value of the fractional solids content. The maximum normal stress applied is 5535 N/m^2 (0.802 psi). Higher normal stresses can be obtained, but this would cause greater wear on the test apparatus. The minimum normal stress applied is 1725 N/m^2 (0.250 psi). Rotation rates possible for the apparatus are 0-375 RPM. The depth of the powder in the annular channel is controlled so as to study the effect of different shear-cell gap thicknesses.

IV Measurement of Average Stresses, Shear-Rates and Fractional Solids Content

The average shear-rate is determined by dividing the velocity of the lower disk, at the mean radius of the annular channel, by the height of the shear cell gap h (i.e., the distance between the top and bottom disks):

$$\frac{\bar{V}}{h} = N\left(\frac{2\pi}{60}\right)\left(\frac{R_i + R_o}{2h}\right) \tag{1}$$

In the above expression, N is the rotation rate of the bottom disk (RPM), and R_i and R_o are the inner and outer radii of the annular channel. This shear-rate calculation assumes a no-slip velocity boundary condition on both the top and bottom shear surfaces of the test apparatus. Because of gravitational and rotational effects in the shear-cell, the fractional solids content may be nonuniformly distributed in both the radial and axial directions. For example, the value of the fractional solids content can be larger at the lower-outside radius. Likewise, it can be smallest at the upper-inside radius of the annular channel.

The average normal stress applied to the top of the granular material is $\sigma = w/\pi(R_o^2 - R_i^2)$. The applied weight is W. The torque, T, is a result of the shear stresses developed on the upper disk. The torque is calculated from the measured force; this force is multiplied by the radius of the torque arm. The torque is related to the local value of the shear stress τ at the upper surface by:

$$T = \int_{R_i}^{R_o} r\tau(2\pi r)dr \tag{2}$$

If we assume τ is uniform and independent of r, then:

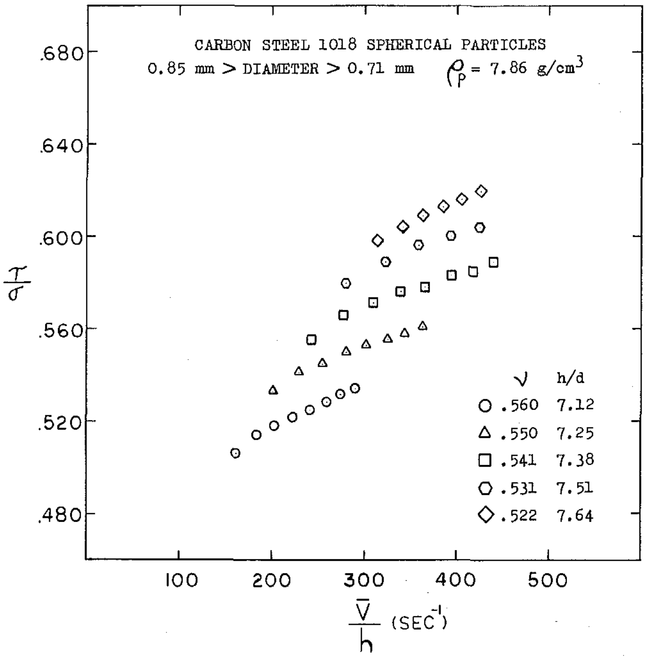

Fig. 2(c) **Dimensional plot of stress ratio versus average shear-rate for carbon-steel beads;** $(h/d)_{\text{avg.}} = 7.38$

$$T = \tau \int_{R_i}^{R_o} 2\pi r^2 dr \tag{3a}$$

and

$$\tau = \frac{3}{2}\,\frac{T}{\pi(R_o^3 - R_i^3)} \tag{3b}$$

The increase in the shear surface speed at an increasing radius will cause the shear stresses on the upper transmission surface to increase with the radius. Therefore, the effective shear force on the upper transmission surface is located at a radius larger than the mean radius of the annular channel. This is because of the nonuniform, shear stress distribution. The largest possible variation will occur for an extreme case, when the shear

Table 1 (A, B) Values of the power-law exponents M and P are given for a range of the fractional solids content and the shear-cell gap thickness-to-bead diameter ratio: Table 1A shows the values for the exponent M, Table 1B shows the values for the exponent P

Table 1A

$\left(\frac{h}{d}\right)_{\text{AVG.}}$		3.70	5.54	7.38	9.23	11.07	12.90
ν	0.559–0.561	1.93	2.02	2.04	2.13	2.24	2.40
	0.549–0.551	1.90	1.99	2.02	2.08	2.13	2.20
	0.539–0.541	1.85	1.96	2.01	2.01	2.06	2.11
	0.530–0.532	1.83	1.94	2.03	2.01	2.02	2.11
	0.521–0.523	1.85	1.98	2.00	1.94	2.04	2.06

Table 1B

$\left(\frac{h}{d}\right)_{\text{AVG.}}$		3.70	5.54	7.38	9.23	11.07	12.90
ν	0.559–0.561	1.78	1.92	1.95	2.13	2.23	2.49
	0.549–0.551	1.75	1.90	1.94	2.10	2.12	2.29
	0.539–0.541	1.71	1.86	1.92	2.03	2.07	2.24
	0.530–0.532	1.69	1.86	1.93	2.01	2.05	2.21
	0.521–0.523	1.71	1.89	1.89	1.98	2.07	2.14

stress is concentrated at the outer radius. The ratio of the extreme to the average shear stress is calculated. The average stress for the extreme case is roughly 12.2 percent lower than the average stress obtained by neglecting this rotational effect. Rotational effects for the test apparatus are thus small. They tend to reduce the average shear stress (i.e., when the shear stress is assumed uniform) by only a few percent. Therefore, no rotational effect corrections are applied to the data reported in this paper.

V Experimental Results and Discussion

Experiments are conducted to measure both the normal and shear stresses averaged over one of the drive surfaces. These stresses are functions of: the shear-rate, the fractional solids content, and the shear-cell gap thickness. The stresses and shear-rate results are presented in their dimensional form; stresses are given in Newtons/meter^2, and shear-rate is given in sec^{-1}. The shear-cell gap thickness is normalized by the average bead diameter. The fractional solids content is dimensionless by definition.

Six experiments for different shear-cell gap thicknesses were done. This was accomplished by using amounts of granular material from 100g to 350g. The average values of the gap thicknesses are 3.70, 5.54, 7.38, 9.23, 11.07, and 12.90 bead diameters. The fractional solids content varies from 0.561 to 0.521. At values of $\nu \gtrsim 0.561$ (i.e., low shear-rates) changing the normal load at a fixed rotation rate had only a small effect on the shear-cell gap thickness. Values of $\nu \lesssim 0.521$ were not tested because of the test apparatus limitations.

First, data is presented in dimensional form for the rapid shearing of 200 grams of carbon steel beads. A shear-cell gap thickness range of $7.12 \leq h/d \leq 7.64$ was used. Figures (2*a*, *b*, *c*) show the normal stress, shear stress and stress ratio as a function of the average shear-rate. The results are parameterized by the fractional solids content. We make the following observations regarding Figs. 2(*a*), 2(*b*), 2(*c*).

The fractional solids content tends to decrease with increasing shear-surface speed for a fixed value of the normal stress. This occurs because more momentum is imparted to the upper surface by the bead collisions. Consequently, the upper surface tends to move upward. This displacement of the upper surface decreases the fractional solids content.

For the range of ν tested and at fixed value of the shear-rate there is a strong increase in stresses with only small increases in fractional solids content. As the fractional solids content increases, multiple collisions and sliding friction between particles play an increasingly significant role in stress generation.

At a constant fractional solids content, the stresses vary as the shear-rate raised to a power. This power law behavior between stress and average shear-rate is paraphrased in Table 1. In this table, M is the power for the shear stress τ,

$$\tau = a\left(\frac{\bar{V}}{h}\right)^{M} \tag{4a}$$

and P is the power for the normal stress σ,

$$\sigma = b\left(\frac{\bar{V}}{h}\right)^{P} \tag{4b}$$

Shear-rate powers for both the normal and shear stress are near a value of two. A simple physical argument for this square shear-rate dependence is given (Bagnold, 1954). The stresses in a rapid granular shear flow are developed as a result of glancing particle collisions when particles in one layer overtake those of an adjacent slower layer. Both the change in momentum during a single collision and the rate at which collisions occur are proportional to the relative velocity of the two layers. Thus, it is not surprising that the stresses are proportional to the square of the shear-rate. Savage and Sayed (1984) point out that departures from this square shear-rate dependence may result from the effects of enduring contacts beween particles, interparticle surface friction, interparticle locking, formation of rigid zones, gravitational effects and finite particle size effects.

The stress ratio, K, is shown to be weakly dependent upon shear-rate for a constant value of the fractional solids content. This weak shear-rate dependence does vary with the depth of the granular material tested. The stress ratio increases with increasing shear rate when the gap thickness to bead diameter ratio is equal to 3.70, 5.54, and 7.38. When the gap thickness to bead diameter is 9.13 and 11.03 the stress ratio is shown to

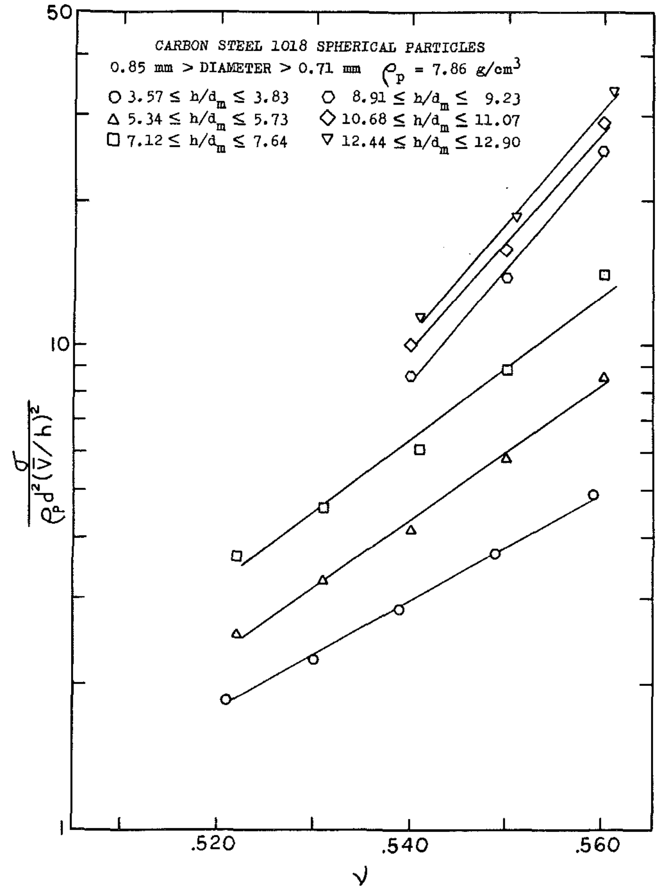

Fig. 3(*a*) Nondimensional normal stress as a function of unscaled fractional solids content

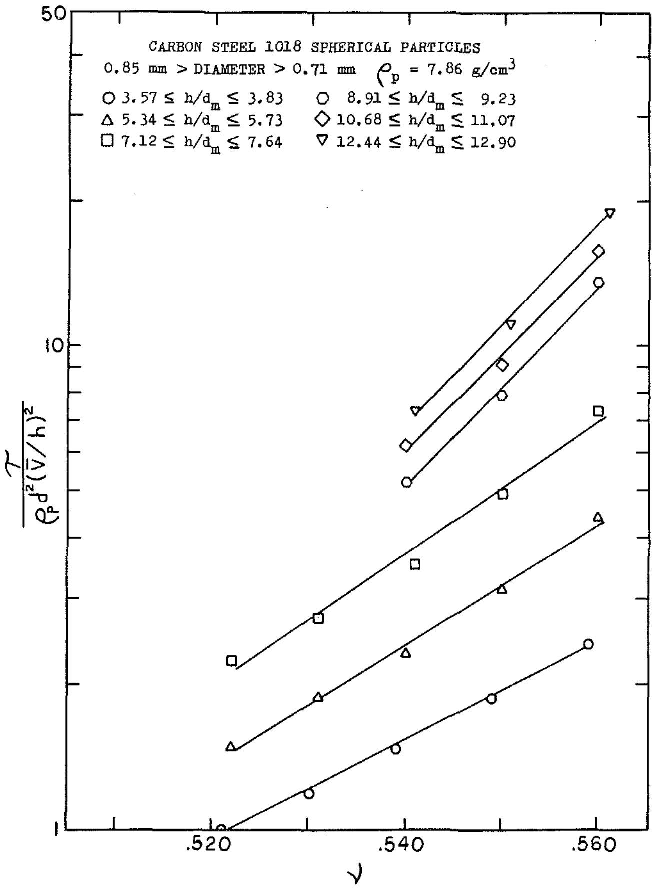

Fig. 3(*b*) Nondimensional shear stress as a function of unscaled fractional solids content

be independent of the shear rate. Finally, when $(h/d)_{\mathrm{AVG.}} = 12.90$ the stress ratio was found to decrease with increasing shear rate. A physical explanation for this relationship between stress ratio and shear-rate is not evident.

For a prescribed amount of test material and prescribed shear-rate, the stress ratio increases slightly with decreasing values of the fractional solids content. This behavior is opposite to that usually observed in quasi-static granular material testing at high stresses. Savage and Sayed (1984) and Campbell and Brennen (1985b) give a physical explanation for the increase in K as ν decreases in continuous fully-developed shear flow experiments.

The dependence of the stresses upon fractional solids content and shear-cell gap thickness is shown in Figs. 3(*a*), 3(*b*). The stresses have been nondimensionalized using the scaling $\rho_p d^2 (\bar{V}/h)^2$ where ρ_p is the mass density of the individual particles. Each data point represents the average of 5 to 8 experimental tests. The stresses are shown to be strongly dependent on ν. This dependence increases with shear-cell gap thickness. At a constant value of ν, the stresses are also shown to increase with increasing shear-cell gap thickness. This observation is contrary to both intuition and the observations of Savage and Sayed (1984). We offer the following explanations. At the conclusion of each test the bottom disk was gradually stopped and the gap thickness recorded. For a constant amount of test material, this gap thickness never varied more than ±0.0005 in. for the entire range of fractional solids content. Table 2 shows the values of the corresponding fractional solids content, ν_c. The precise value of ν_c should only depend on the bead characteristics. The differences are due to the effect of a finite-sized apparatus. The larger the shear-cell gap thickness, the greater the effect of the side walls on the flow field and the larger the reduction in the value of ν_c. We

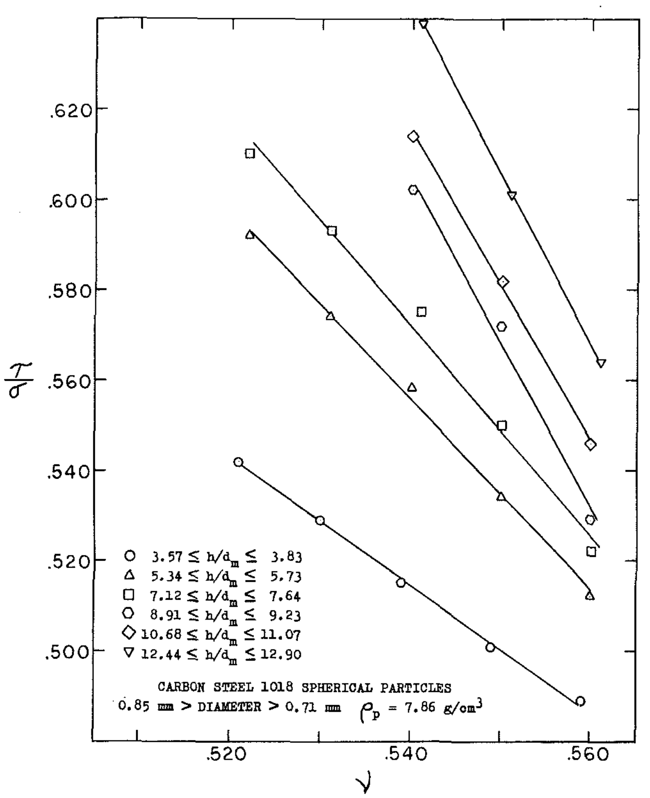

Fig. 3(*c*) Ratio of shear stress to normal stress as a function of unscaled fractional solids content

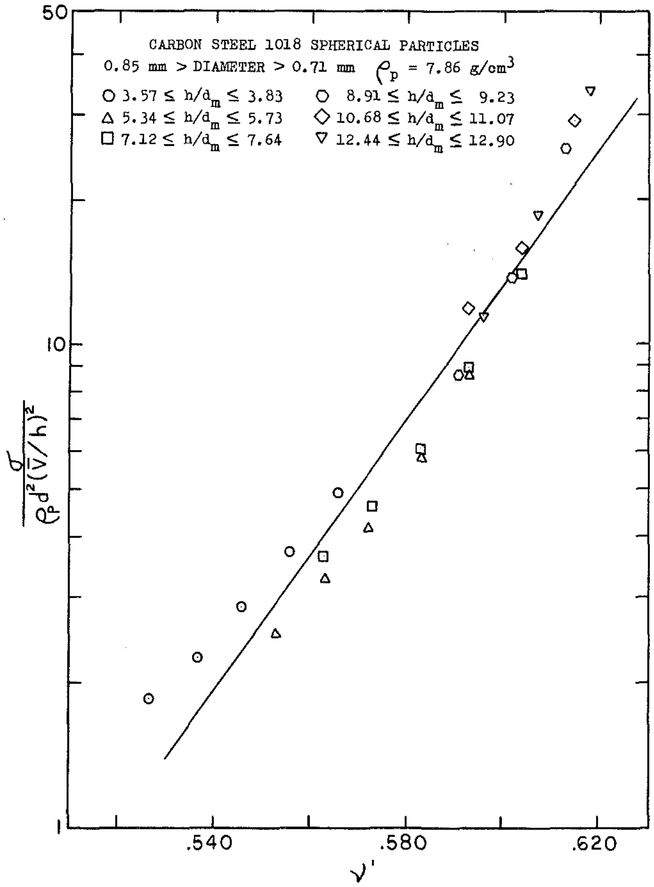

Fig. 4(a) Nondimensional normal stress as a function of scaled fractional solids content

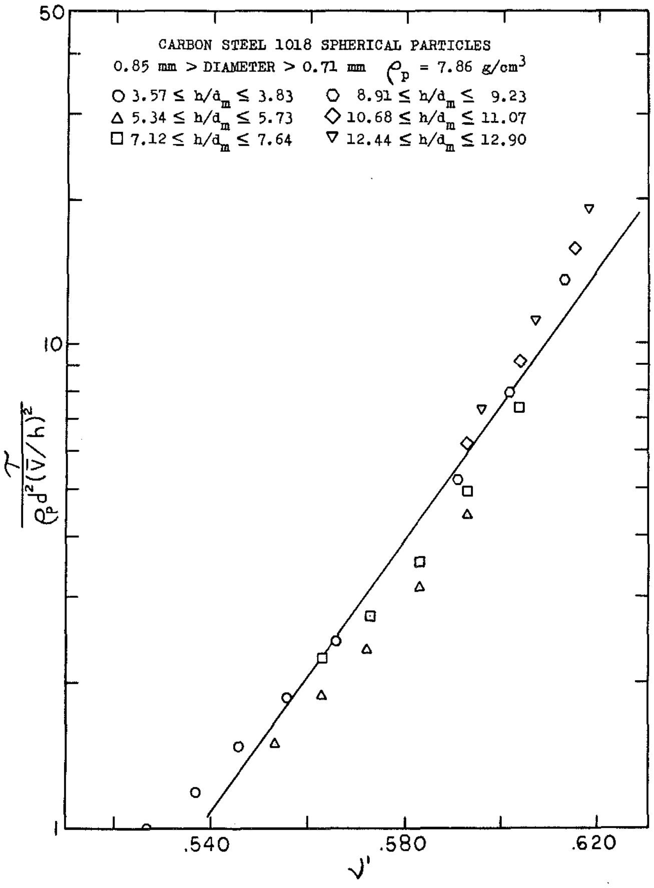

Fig. 4(b) Nondimensional shear stress as a function of scaled fractional solids content

Table 2 Values of the post-test fractional solids content, ν_c, are given for the six different ranges of h/d tested

Mass Tested (Grams)	Test Range of h/d	Post-Test Value of h/d	ν_c
100	3.57–3.83	3.06	0.652
150	5.34–5.73	4.80	0.623
200	7.12–7.64	6.51	0.612
250	8.91–9.23	8.26	0.603
300	10.68–11.07	9.95	0.601
350	12.44–12.90	11.65	0.599

propose that results obtained from testing different amounts of the same material in the same apparatus cannot be directly compared. To compare this data the fractional solids content is scaled as follows:

$$\nu' = \nu \frac{\nu_\infty}{\nu_c} \qquad (5)$$

In this scaling the ν_c is the measured post-test fractional solids content for a prescribed amount of test material and ν_∞ is the value ν_c would have without side-wall effects. We assume ν_∞ to be approximately 0.66. A similar scaling procedure based on the maximum attainable value of ν was used by Hanes and Inman (1985). The data shown in Figs. 3(*a*), 3(*b*) is now replotted as shown in Figs. 4(*a*), 4(*b*). The abscissa is now the scaled fractional solids content. The stresses are now shown to increase with increasing fractional solids content as expected.

Figure 3(*c*) shows the stress-ratio as a function of the unscaled fractional solids content with the shear-cell gap thickness as the parameter. For a prescribed amount of test material, the stress ratio increases slightly as the fractional

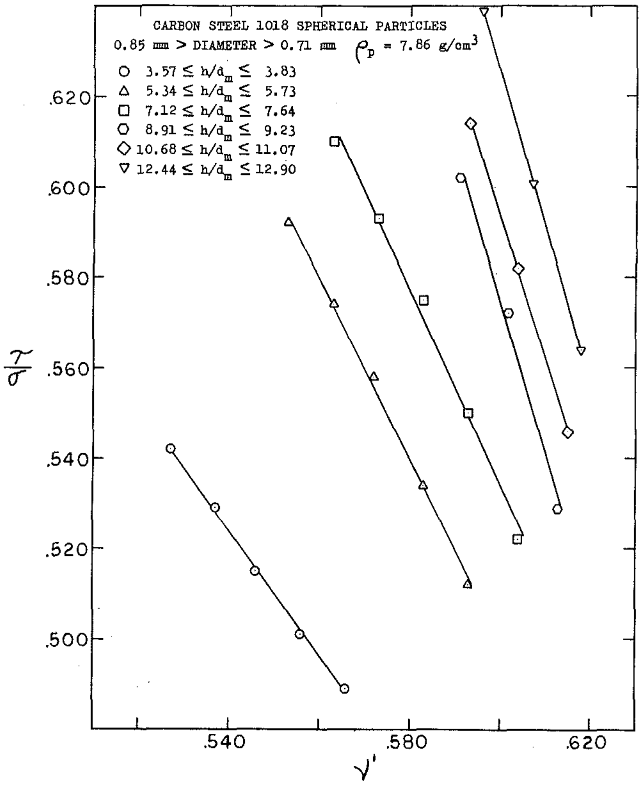

Fig. 4(c) Ratio of shear stress to normal stress as a function of scaled fractional solids content solids content decreases. However when the stress ratio is plotted as a function of the scaled fractional solids content, as done in Fig. 4(*c*), the stress ratio is still seen to increase with increasing shear-cell gap thickness at a prescribed value of ν'. As the shear-cell gap thickness is increased, the influence of the side walls on the material behavior is increased. The effect of the apparatus side walls on the measured fractional solids content has been approximately accounted for by scaling the measured fractional solids content. The side walls also affect the measured normal and shear stresses. Data has not been rescaled to include this latter effect. The side walls are hard-coated for increased hardness and lubricity; the particles in contact with the side walls have a larger velocity than particles which are near the walls. This is especially true at the outer wall where centrifugal forces on the particles cause increased particle-wall friction. The effect of the side wall velocity is to increase the measured normal and shear stresses on the top surface. This effect on the shear stress is larger than on the normal stress. This accounts for the increasing stress ratio with increasing shear-cell gap thickness at a prescribed value of the scaled fractional solids content.

Direct visual observation of the granular material during testing was not possible. Therefore, it is quite possible that as the shear-cell gap thickness increased (i.e., as more material was being tested), an internal boundary, separating a shearing region from a rigid region, is developed. This was directly observed by Hanes and Inman (1985). They deduce this phenomenon to be the result of both a momentum conservation in a gravity field and a Coulomb-type yield criterion. Hanes and Inman (1985) found that the stress ratios for the fully shearing experiments were significantly higher than those resulting from the partially shearing flows. A significant decrease in stress ratio with increasing shear-cell gap thickness was not observed in the present tests; on the contrary, the stress ratio continued to increase. This lends support to the assumption that all experiments reported here involved fully shearing conditions. However, there still remains some question regarding the side-wall effects and the remarkable dependence of stress ratio on shear-rate as the shear-cell gap thickness varies.

Figures 5(*a*), 5(*b*) show comparisons of the nondimensional stresses and stress ratio. Results presented here are compared to those of Savage and Sayed and of Hanes and Inman. Both of the stresses and the stress ratio are shown as a function of unscaled fractional solids content. Savage and Sayed (1984) tested 1.80 mm diameter glass spheres. They used a shear cell with an annular channel 21 beads wide at a mean radius of 12.7 cm. The shear-cell gap thickness for these tests was between 5.90 to 6.45 beads. They used sandpaper for the shear transmission surfaces. Hanes and Inman (1985) tested 1.85 mm diameter glass spheres in a shear cell with an annular channel 24 beads wide at mean radius of 12.4 cm. The shear-cell gap thickness for these tests was approximately 7 beads. The shear transmission surfaces were of the same material being tested, prepared in a manner similar to that of the present tests. The annular channel in the present tests is 25 beads wide at a mean radius of 6.83 cm. The data plotted in Figs. 5(*a*), 5(*b*) from the present tests is for a shear-cell gap thickness range 7.12 to 7.64 beads. In all these tests it is certain that shearing is occurring over the full depth of the test material. The stress levels in the experiments of Hanes and Inman (1985) are greater than the stress levels in the experiments of Savage and Sayed (1984), at equivalent concentrations. Hanes and Inman believe the differences are the result of the following: (*a*) The materials used for the shear transmission surfaces may act as sources or sinks of energy. The rigid bead boundaries of Hanes and Inman may have been more of an energy source than the sandpaper boundaries of Savage and Sayed. (*b*) The frictional nature (i.e., smooth or rough) of the test particles. Recent microstructural theories for rapid granular flow show that the shearing of rough particles generates lower stresses than a similar shearing of smooth particles. The test particles used by Savage and Sayed are believed to have been roughened by the sandpaper shear-transmission surfaces.

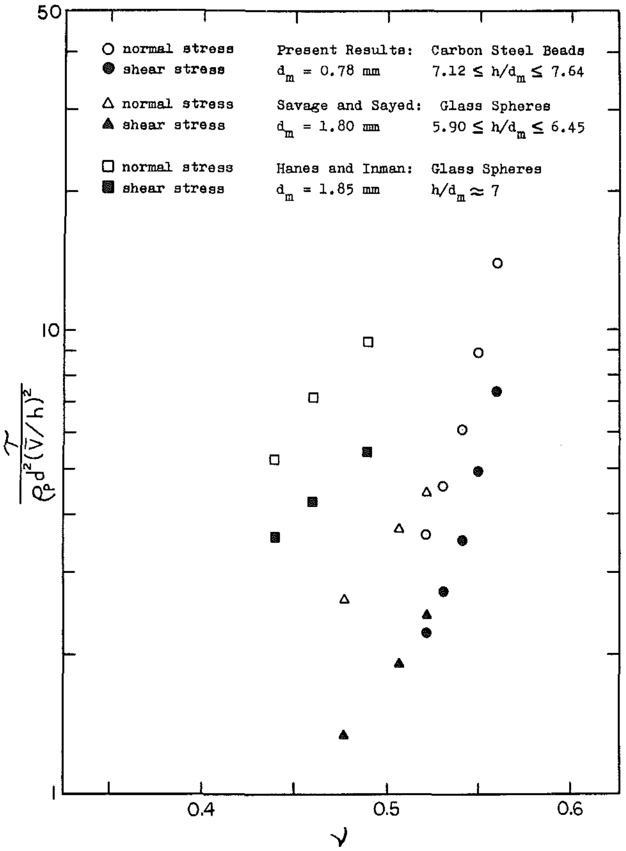

Fig. 5(*a*) Comparison of nondimensional stresses measured by Savage and Sayed (1984) and Hanes and Inman (1985) with present results. Fractional solids content is unscaled.

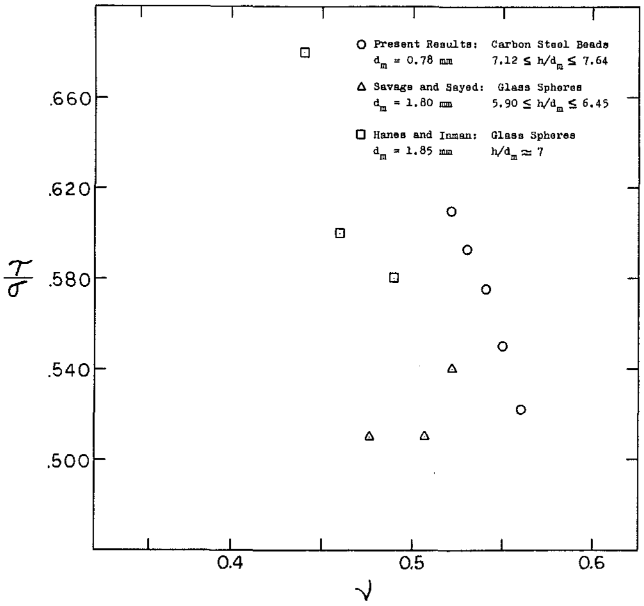

Fig. 5(*b*) Comparison of the ratio of shear stress to normal stress measured by Savage and Sayed (1984) and Hanes and Inman (1985) with present results. Fractional solids content is unscaled.

In addition to the effects of the finite-sized test apparatus, the differences between the boundary material properties and the test material properties will contribute to differences in stress measurements between this paper and other published data.

VI Conclusion

The results presented in this paper show that the stress generated in a rapid shear flow of purely granular carbon-steel beads has a nearly quadratic dependence on the shear-rate. The stresses depend upon the fractional solids content. They increase with increasing values of the fractional solids content, when the shear rate is prescribed.

The general trends observed here are consistent with the results reported by both Savage and Sayed (1984) and Hanes and Inman (1985). Although the general trends are similar the results of these three experiments have some differences. In these three experimental studies a large number of factors affect the generation of stresses: shear-rate; fractional solids content; bead size and shape; bead material properties and the surface coefficient of friction, the bead density, and the bead coefficient of restitution; size of test apparatus; elastic and surface frictional properties of the boundaries of the flow; amount of material being tested and thickness of the shearing layer; oxidation of metal powders; and effects of temperature on the beads and test apparatus. It is often difficult to experimentally isolate each of the above effects. We are currently exploring the effect of different particle sizes and materials in order to better understand material property effects.

Acknowledgments

The authors would like to thank Dr. Juris Pirvics of Xerox M.E.S. for supporting this work and both G. Bay and H. Metternich for their help in fabricating the test apparatus. The authors are indebted to Professor H. Elrod for his encouragement. K. Craig would like to especially thank Professor S. B. Savage of McGill University for his encouragement and generous help throughout this research.

References

Bagnold, R. A., (1954), "Experiments on a Gravity-Free Dispersion of Large Solid Spheres in a Newtonian Fluid Under Shear," *Proceedings of the Royal Society*, London, Vol. 225, Series A, pp. 49–63.

Bridgwater, J., (1972), "Stress-Velocity Relationships for Particulate Solids," ASME Paper No. 72-MH-21.

Campbell, C. S., (1982), Shear Flows of Granular Materials. Ph.D. thesis and Rep. E-200.7, Division of Engineering and Applied Science, California Institute of Technology.

Campbell, C. S., and Brennen, C. E., (1982a), "Computer Simulation of Shear Flows of Granular Materials," *Proc. 2nd US-Japan Seminar on New Models and Constitutive Relations in the Mechanics of Granular Materials*, Ithaca, N.Y., Elsevier.

Campbell, C. S., and Brennen, C. E., (1982b), "Computer Simulation of Chute Glows of Granular Materials," *Proc. IUTAM Symp. on Deformation and Failure of Granular Materials*, Delft, Netherlands, Balkema.

Campbell, C. S., and Brennen, C. E., (1985a), "Chute Flows of Granular Material: Some Computer Simulations," ASME JOURNAL OF APPLIED MECHANICS, Vol. 52, pp. 172–178.

Campbell, C. S., and Brennen, C. E., (1985b), "Computer Simulation of Granular Shear Flows," *J. Fluid Mech.*, Vol. 151, pp. 167–188.

Carr, J. F., and Walker, D. M., (1968), "An Annular Shear Cell for Granular Materials," *Powder Techn.*, Vol. 1, No. 370, pp. 369–373.

Hanes, D. M., and Inman, D. L., (1985), "Observations of Rapidly Flowing Granular-Fluid Materials," *J. Fluid Mech.*, Vol. 150, pp. 357–380.

Hvorslev, M. J., (1936), "A Ring Shearing Apparatus for the Determination of the Shearing Resistance and Plastic Flow of Soil," *Proc. Inter. Conf. Soil Mech. Found. Engrg.*, Cambridge, Mass., Vol. 2, pp. 125–129.

Hvorslev, M. J., (1939), "Torsion Shear Tests and Their Place in the Determination of the Shearing Resistance of Soils," *Proc. ASTM*, Vol. 39, pp. 999–1022.

Mandl, G., de Jong, L. N. J., and Maltha, A., (1977), "Shear Zones in Granular Material," *Rock Mech.*, Vol. 9, pp. 95–144.

Mroz, A., (1980), "On Hypoelasticity and Plasticity Approaches to Constitutive Modeling of the Inelastic Behavior of Soils," *Intl. J. Numer. and Anal. Meth. in Geomech.*, Vol. 4, pp. 45–55.

Novosad, J., (1984), "Apparatus for Measuring the Dynamic Angles of Internal Friction and External Friction of a Granular Material," Collection Czech. Chem. Commun., Vol. 29, pp. 2697–2701.

Reynolds, O., (1885), "On the Dilatancy of Media Composed of Rigid Particles in Contact: With Experimental Illustrations," *Phil. Mag. Series 5*, Vol. 20, pp. 469–481.

Savage, S. B., (1978), "Experiments on Shear Flows of Cohesionless Granular Materials," *Proc. U.S.-Japan Seminar on Continuum-Mechanical and Statistical Approaches in the Mechanics of Granular Material*, pp. 241–254.

Savage, S. B., "The Mechanics of Rapid Granular Flows," *Advances in Applied Mechanics*, Vol. 24, Hutchinson, J. W., Wu, T. Y., eds., Academic Press, 1984.

Savage, S. B., and Sayed, M., (1984), "Stresses Developed by Dry Cohesionless Granular Materials Sheared in an Annular Shear Cell," *J. Fluid Mech.*, Vol. 142, pp. 391–430.

Scarlett, B., Ackers, R. J., Parkinson, J. S., and Todd, A. C., (1969–1970), "Application of Geometrical Probability to Particulate Systems," *Powder Techn. 3*, pp. 299–308.

Scarlett, B., and Todd, A. C., (1968), "A Split Ring Annular Shear Cell for Determination of the Shear Strength of a Powder," *J. Sci. Instr.*, Vol. 1, pp. 655–656.

Scarlett, B., and Todd, A. C., (1969), "The Critical Porosity of Free Flowing Solids," *Trans. ASME*, Ser. B., Vol. 91, pp. 478–488.

Spencer, A. J. M., (1981), "Deformation of an Ideal Granular Material," *Mechanics of Solids*, Rodney Hill 60th Anniversary Volume, (Hopkins, H. G., Sewell, J. J., eds., Pergamon.

Stephens, D. J., and Bridgwater, J., (1978), "The Mixing and Segregation of Cohesionless Particulate Materials; Part I, Failure Zone Formation and Part II, Microscopic Mechanisms for Particles Differing in Size," *Powder Techn.*, Vol. 21, pp. 17–44.

J. A. Tichy
Department of Mechanical Engineering,
Rensselaer Polytechnic Institute,
Troy, NY 12180-3590
Mem. ASME

P. Bourgin
Laboratoire de Mécanique
des Fluides,
Ecole Centrale de Lyon,
Ecully, France 69130
Assoc. Mem. ASME

A Similarity Solution for Flow in a Narrow Channel of Varying Gap

A similarity solution may be obtained for the case of a narrow channel where the gap h *varies, according to* $(a+bx)^m$. *The lower surface may slide in either direction and there may be suction or injection at either surface which must vary as* h^{-1}. *Asymptotic solutions are found for large and small values of a modified Reynolds number which is based on the sliding velocity or the suction/injection rate. Boundary layer behavior may be exhibited at high Reynolds number. The present solution, being "exact" for all Reynolds numbers once the thin film assumptions have been invoked, may be of value to hydrodynamic lubrication workers to test approximations for the fluid inertia effect.*

Introduction

The tribology literature contains many papers which approximately account for fluid inertia forces which are omitted in Reynolds' hydrodynamic lubrication theory. Such papers often use small Reynolds number perturbations, e.g., Reinhardt and Lund (1975) and Tichy and Winer (1970), or various cross-film averaging techniques (Szeri et al., 1983; Constantinescu and Galetuse, 1974), but questions often arise as to their accuracy and range of validity.

Recently, an exact similarity solution for squeeze film flow between disks of long plates if the dimensionless film thickness varies by $h = (a+bt)^{1/2}$ was published (Wang, 1976). The authors have found Wang's paper valuable as a test case of inertia approximations for the simple squeeze film bearing (Tichy and Bourgin, 1986; Bourgin and Tichy, 1985). Further, we have noted the lack of a comparable test for the presumably simpler case of the steady slider bearing.

Fortunately such a similarity solution does exist for steady thin film flows where the film thickness variation is $h = (a+bx)^m$ where a, b and m are constants. The analogy to Wang's solution is obviously strong but there is at least one important difference. Wang's solution is exact in the sense that all terms of the Navier-Stokes equation are retained. In the present case, the thin film lubrication assumptions must be used. The present solution is "exact" for the limiting case of a narrow channel far downstream of the inlet.

The present problem, which may involve suction or injection at the surfaces, is similar to the well-known problem for suction or injection in a straight channel, studied by Berman (1953), Terrill and Shrestha (1965), Terrill (1965), Yuan (1956), and others.

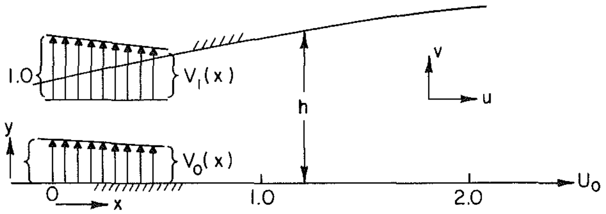

Fig. 1 Channel geometry

Analysis

Consider the steady, two-dimensional, laminar incompressible flow of a Newtonian fluid in a long, narrow channel of slowly varying height as shown in Fig. 1. All symbols represent dimensionless variables. The coordinates x and y as shown are scaled to a reference film thickness, and the velocities u and v are scaled to a reference sliding speed, thus we have $x >> 1$, $y \sim 1$, $u \sim 1$, $v << 1$. The lower surface may slide along its length at varying speed and there may be spatially varying suction or injection at either surface. The channel arbitrarily begins at $x = 0$ but we are concerned with the region $x >> 1$ and $h > 0$.

Under these conditions the Navier Stokes equations can be written in terms of the stream function as

$$\mathrm{Re}(\psi_y \psi_{xyy} - \psi_x \psi_{yyy}) = \psi_{yyyy}. \tag{1}$$

The no-slip boundary conditions are

$$\begin{array}{lll} y=0 & u=U_o(x) & u=V_o(x) \\ y=h(x): & u=0 & v=V_1(x) \end{array} . \tag{2}$$

The Reynolds number Re is the reference sliding velocity times film thickness divided by kinematic viscosity. Introducing the transformation

$$\eta = \frac{y}{h(x)} \quad \xi = x \quad \psi = h^c(\xi) f(\eta) \tag{3}$$

the differential equation (1) becomes

$$f^{iv} + \mathrm{Re} h^c h' [(2\text{-}c) f' f'' + c f f'''] = 0 \tag{4}$$

where the prime (′) superscript represents differentiation with

---

Contributed by the Applied Mechanics Division for publication in the JOURNAL OF APPLIED MECHANICS.

Discussion on this paper should be addressed to the Editorial Department, ASME, United Engineering Center, 345 East 47th Street, New York, N.Y. 10017, and will be accepted until two months after final publication of the paper itself in the JOURNAL OF APPLIED MECHANICS. Manuscript received by ASME Applied Mechanics Division, April 17, 1986.

respect to the appropriate independent variable. An ordinary differential equation is obtained when we set

$$h^c h' = \alpha \tag{5}$$

which gives

$$h = [h_o^{c+1} + \alpha(c+1)x]^{\frac{1}{c+1}} \tag{6}$$

using $h = h_o$ when $x = 0$. The resulting differential equation is

$$f^{iv} + \alpha\mathrm{Re}[f'f''(2-c) + cff'''] = 0 \tag{7}$$

where α is a measure of the slope h' and the parameter $\alpha\mathrm{Re}$ is analogous to the modified or reduced Reynolds number commonly used in lubrication analysis (Szeri, 1980). In this case the velocities become

$$u = h^{c-1}f'(\eta), \quad v = -h'h^{c-1}(cf - \eta f'). \tag{8}$$

We can find a similarity solution if we choose appropriate functions for U_o, V_o, and V_1, namely,

$$U_o(x) = h^{c-1}\bar{U}_o, \quad V_o(x) = -ch'h^{c-1}\bar{V}_o,$$
$$V_1(x) = -ch'h^{c-1}\bar{V}_1. \tag{9}$$

Thus, the boundary conditions on f can be obtained:

$$\begin{array}{ll} f(0) = \bar{V}_o & f(1) = \bar{V}_1 \\ f'(0) = \bar{U}_o & f'(1) = 0. \end{array} \tag{10}$$

Equation (6) can be integrated once to yield

$$f''' + \alpha\mathrm{Re}[(1-c)f'^2 + cff''] = B \tag{11}$$

where B is an integration constant.

The dimensionless flow rate is given by

$$Q = \int_o^h u\,dy = \psi(x,h) - \psi(x,0) = h^c[\bar{V}_1 - \bar{V}_o] \tag{12}$$

while the dimensionless pressure gradient is

$$\frac{dp}{dx} = \frac{\partial^2 u}{\partial y^2} - \mathrm{Re}\left(u\frac{\partial u}{\partial x} + v\frac{\partial u}{\partial y}\right)$$
$$= h^{c-3}\{f''' + \alpha\mathrm{Re}[(1-c)f'^2 + cff'']\} \tag{13}$$

which can be integrated to obtain

$$p = B\ln\frac{1-x}{1-x_f} \quad x >> 1 \tag{14}$$

using $p = 0$ at the film exit $x = x_f$.

The present configuration is not really a bearing in the conventional sense where fluid is drawn into the gap from ambient conditions. Assuming fluid exits the channel at ambient conditions, it must be injected into the channel at a prescribed pressure.

The flow described above is analogous to Falkner-Skan flow (White, 1974), for flow past a wedge for the case $h(x = 0) = h_o = 0$, c.f. equation (6). The solid wedge surface is represented by $\eta = 1$ where $U = V = 0$, while $\eta = 0$ represents a horizontal surface in the flow where $U = bx^m$.

In the calculations and discussion which follow, let us confine ourselves to the case when $h_o = 1$, i.e.,

$$h = (1 + 2\alpha x)^{1/2} \tag{15}$$

and

$$U_o = \bar{U}_o \quad V_o = -h'\bar{V}_o \quad V_1 = -h'\bar{V}_1. \tag{16}$$

The analogy to Wang's problem is now stronger and the flow is more realistic since these are the fluid boundary velocities which would be achieved by a sliding horizontal solid surface and a stationary curved porous surface with a constant (normal) suction or ejection velocity.

Let us confine our further attention to four cases which illustrate many interesting features of this flow. For a widening gap ($\alpha > 0$) with no suction or injection at the lower surface ($\bar{V}_o = 0$) they are:

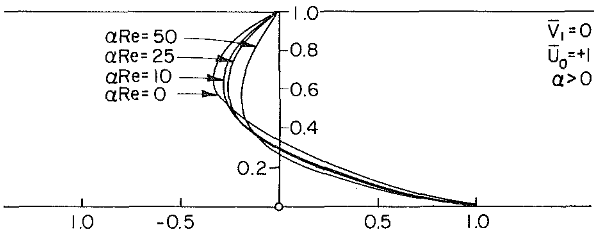

Fig. 2 Velocity profiles, Case (*a*); no suction or injection, sliding toward a widening gap

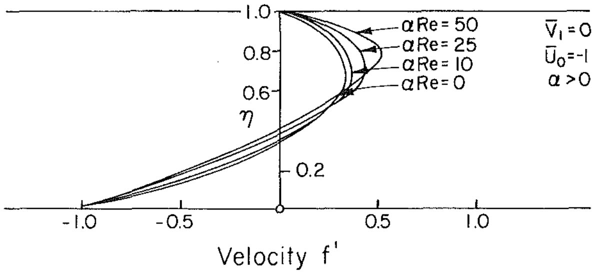

Fig. 3 Velocity profiles, Case (*b*); no suction or injection, sliding toward a widening gap

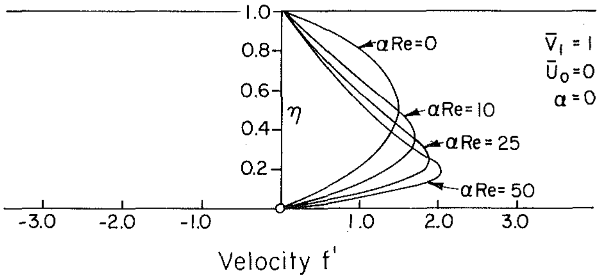

Fig. 4 Velocity profiles, Case (c); net suction, no sliding

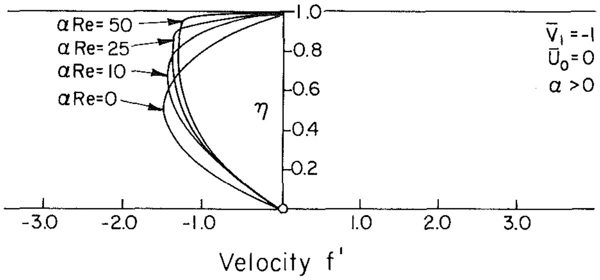

Fig. 5 Velocity profiles, Case (*d*); net suction, no sliding

(*a*),(*b*) Positive/negative sliding with no suction or injection:

$$f(0) = f(1) = f'(1) = 0 \quad f'(0) = \bar{U}_o = \pm 1,$$

(*c*),(*d*) Suction/injection on the upper surface with no sliding:

$$f(0) = f'(0) = f'(1) = 0 \quad f(1) = \bar{V}_1 = \pm 1.$$

Small αRe Solution

We assume a regular perturbation solution of the form

$$\begin{array}{l} f = f_o + \alpha\mathrm{Re}f_1 \\ B = B_o + \alpha\mathrm{Re}B_1 \end{array} \tag{17}$$

and substitute into equations (10) and (11) in the conventional

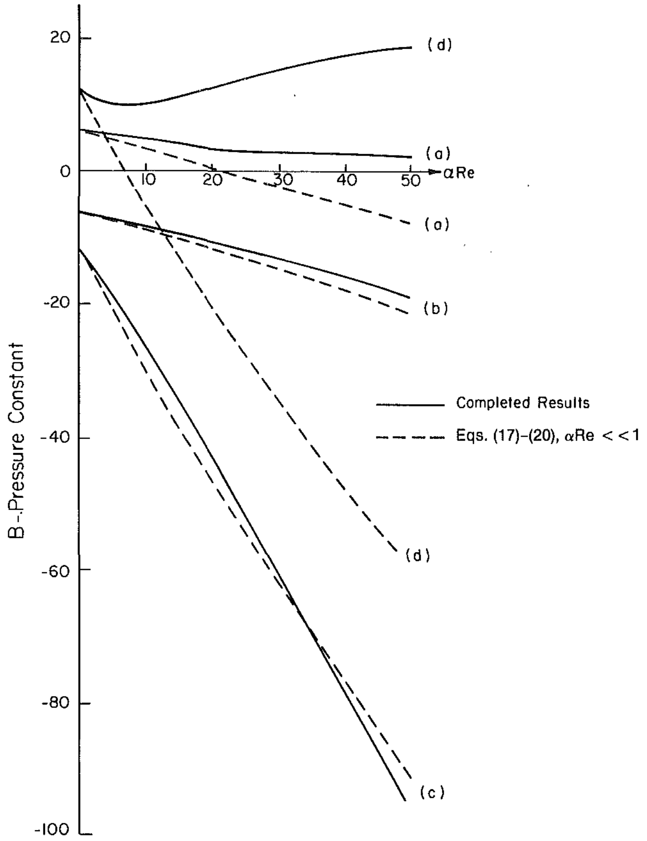

Fig. 6 Pressure constant versus modified Reynolds number

manner. The results are obtained by gathering coefficients $(\alpha R)^o, (\alpha R)^1 \ldots :$

$$f_o = C_a\eta^3 + C_b\eta^2 + C_c\eta + \bar{V}_o$$

$$C_a = (\bar{U}_o - 2\bar{V}_1) \quad C_b = (-2\bar{U}_o + 3\bar{V}_1) \quad C_c = \bar{U}_o \tag{18}$$

$$f_1 = K_7\eta^7 + K_6\eta^6 + \ldots K_2\eta^2$$

$$K_7 = \frac{C_a^2}{35}, \; K_6 = \frac{C_aC_b}{15}, \; K_5 = \frac{C_b^2}{30} + \frac{C_aC_c}{10} \quad K_4 = \frac{C_bC_c}{12} \tag{19}$$

$$K_3 = -5K_7 - 4K_6 - 3K_5 - 2K_4 \quad K_2 = 4K_7 + 3K_6 + 2K_5 + K_4$$

$$B_o = 6C_a \quad B_1 = 6K_3. \tag{20}$$

Computed Results

A NAG, "Numerical Algorithms Group" (1982), FORTRAN Library routine for solving two-point boundary value systems of ordinary differential equations (DO2RAF) was used to obtain the present solution. The DO2RAF subroutine uses a finite difference technique with Newton iteration, including a "continuation" feature where a simple problem solution is provided (αRe = 0) and a sequence of problems is solved leading up to the desired case (αRe = 10, 25, 50). Convergence was obtained in all cases with mesh sizes between $\Delta\eta = 0.02$ and $\Delta\eta \cong 0.002$. The algorithm selects an optimum mesh size at least as fine as the user's initial estimate and distributes errors over the mesh until they are everywhere less than the user's selected tolerance (in this case 0.1%).

Figures 2-5 depict the velocity profiles $f'(\eta)$ of the four cases for different Reynolds numbers.

Figure 6 portrays the variations of the constant B with Reynolds number for the various cases. Recall that B ($= f'''(0)$) is proportional to the pressure and pressure gradient, equations (13) and (14). The small Reynolds number asymptotic behavior is also shown. For cases (b) and (c), the pressure gradient is favorable to the flow direction.

Large αRe Solution

Outer Solution. The large αRe limit of equation (7) is singular because the highest derivative is lost as $\alpha\mathrm{Re} \rightarrow \infty$. The first term outer solution, denoted $f_o(\eta)$, must satisfy (for c = 1)

$$f_o'f_o'' + f_of_o''' = 0, \tag{21}$$

which can be integrated once to yield

$$f_of_o'' = D_1. \tag{22}$$

The first integral of equation (22) is

$$f_o' = \pm[2D_1 \ln f_o + D_2]^{1/2} \tag{23}$$

and the formula for f_o is

$$\int_{f_o(0)}^{f_o} \frac{df}{(2D_1 \ln f + D_2)^{1/2}} = \pm\eta. \tag{24}$$

We drop the boundary condition $f'(0) = \bar{U}_o$ and retain the boundary conditions $f'(1) = 0, f(0) = 0, f(1) = \bar{V}_1$. Using the latter two boundary conditions we obtain

$$\int_o^{\bar{V}_1} \frac{df}{(2D_1 \ln f + D_2)^{1/2}} = \pm 1. \tag{25}$$

To illustrate some interesting properties of this flow, let us confine ourselves to the cases (a) and (b), where $\bar{V}_1 = 0$. Clearly the denominator of the integrand is zero hence $D_1 = D_2 = 0$. From equation (23), $f' = 0$, and therefore f = const. But since $f(0) = f(1) = 0$, therefore

$$f_o = f_o' = 0, \tag{26}$$

which is clearly an inviscid flow.

To match this outer solution, a boundary layer must form on the lower surface where $f_o' = \bar{U}_o = \pm 1$.

Inner Solution. We search for a solution in the form

$$f \sim \epsilon^{1/2}F_1(\zeta) + \epsilon F_2 + \ldots \quad \zeta = \frac{y}{\epsilon^{1/2}} \quad \epsilon = \frac{1}{\alpha\mathrm{Re}} << 1, \tag{27}$$

valid near $y = 0$ where the F's and ζ are $\sigma(1)$. Substituting in equation (11), the leading term in powers of ϵ is

$$2F''' + F_1F_1'' = B, \tag{28}$$

which is the same as the Blasius boundary layer equation.

The matching condition is that the first term inner expansion of f_o must equal the first term outer expansion of F_1, i.e.,

$$f_o(y \rightarrow 0) = F_1(\zeta \rightarrow \infty),$$

from which one obtains

$$\begin{aligned} \zeta &= 0 \quad && F = 0, F' = \bar{U}_o = \pm 1 \\ \zeta &= \infty \quad && F' = 0 \end{aligned} \tag{29}$$

and $B = 0$, i.e., pressure gradient is zero.

It is well known that a solution to equations (28)-(29) results only if $\bar{U}_o = +1$, hence case (b) does not appear to have a large αRe asymptotic solution.

Discussion

Each of the four sets of boundary conditions used seems to generate a separate special case. The flow may be in either or both directions, boundary layers may or may not be present, and the pressure gradient may be positive or negative. Results have been shown for the widening channel only ($\alpha > 0$). For $\alpha < 0$, the solutions are identical other than the fact that case (a) behaves like case (b) (and vice versa) with f and its derivatives multiplied by minus one. Similarly, case (c) behaves like case (d) for $\alpha < 0$.

The present results have some qualitative similarities to those found in squeeze film flow by Wang (1976) and in other references cited. In these cases the flow is symmetric about the midplane. During the fast squeezing case of Wang or injection due to Berman (1953), boundary layers form in both walls and the core becomes inviscid. In Wang's study, for the case of reverse squeezing, complicated flow reversals occur at large Reynolds number and boundary layers do not develop. In the analysis of suction due to Terrill (1965), a singular shear layer occurs at the channel midplane. Thus there exists a boundary layer of sorts, but not at a wall.

As stated above, the authors believe this result will be useful to test approximations used in lubrication to account for fluid inertia. In fact from Fig. 6 we can assess the range of validity of the small Reynolds number perturbation. The approximation may be very good for modified Reynolds numbers (αRe) up to one hundred, or very poor at $\alpha\text{Re} = 10$, depending on the specific case. There is no apparent a priori reason why one approximation is good and the other bad. Strictly speaking, the approximation need only be valid for $|\alpha\text{Re}| << 1$ in all cases.

References

Berman, A. S., 1953, "Laminar Flow in Channels with Porous Walls," *Journal of Applied Physics*, Vol. 24, No. 9, pp. 1232–1235.

Bourgin, P., and Tichy, J. A., 1985, "Lubricating Films of a Viscoelastic Fluid Studied by a Linearization Method," *International Journal of Engineering Science*, pp. 1135–1149.

Constantinescu, V. N., and Galetuse, S., 1974, "On the Possibilities of Improving the Accuracy of the Evaluation of Inertia Forces in Laminar and Turbulent Films," ASME *Journal of Lubrication Technology*, Vol. 96, No. 1, pp. 69–79.

NAG (Numerical Analysis Group), 1982, FORTRAN Library, Vol. 2, Mayfield House, Oxford, England.

Reinhardt, E., and Lund, J. W., 1975, "The Influence of Fluid Inertia on the Dynamic Properties of Journal Bearings," ASME *Journal of Lubrication Technology*, Vol. 97, No. 2, pp. 159–167.

Szeri, A. Z., Raimondi, A. A., and Giron-Duarte, A., 1983, "Linear Force Coefficients for Squeeze Film Dampers," ASME *Journal of Lubrication Technology*, Vol. 105, No. 3, pp. 326–333.

Terrill, R. M., and Shrestha, G. M., 1965, "Laminar Flow Through a Channel with Uniformly Porous Walls of Different Permeability," *Applied Science Research*, Sec. A, Vol. 15, pp. 440–468.

Terrill, R. M., 1965, "Laminar Flow in a Uniformly Porous Channel with Large Injection," *The Aeronautical Quarterly*, Vol. XVI, pp. 323–332.

Tichy, J. A., and Winer, W. O., 1978, "Inertia Considerations in Parallel Circular Squeeze Film Bearings," ASME *Journal of Lubrication Techology*, Vol. 92, No. 4, pp. 588–592.

Tichy, J. A., and Bourgin, P., 1986, "The Effect of Inertia in Lubrication Flow Including Entrance and Initial Conditions," ASME JOURNAL OF APPLIED MECHANICS, Vol. 107, No. 4, pp. 759–765.

Wang, C. Y., 1976, "The Squeezing of a Fluid Between Two Plates," ASME JOURNAL OF APPLIED MECHANICS, Vol. 43, No. 4, pp. 579–583.

White, F. M., 1974, *Viscous Fluid Flow*, McGraw-Hill, New York.

Yuan, S. W., 1956, "Further Investigations of Laminar Flow in Channels with Porous Walls," *Journal of Applied Physics*, Vol. 27, pp. 267–269.

A. Sanz
Laboratorio de Aerodinámica,
E. T. S. I. Aeronáuticos,
Universidad Politécnica,
28040 Madrid, Spain

On the Two-Dimensional Theory of Incompressible Flow Over Inlets

The linearized solution for the two-dimensional flow over an inlet of general form has been derived, assuming incompressible potential flow. With this theory suction forces at sharp inlet lips can be estimated and ideal inlets can be designed.

1 Introduction

The interest of studying the suction forces at the sharp lips of an air inlet has been pointed out by Huang (1982). This kind of inlet is used on supersonic aircraft to reduce the wave drag at supersonic speeds. However, sharp lips produce flow separation at subsonic speeds and that is the reason why rounded noses are preferred in this regime to obtain maximum thrust over the cowl (Donovan and Lawrence, 1957). In the case of an idealized intake of infinite length of general cross section, the thrust F is given by (Kuchemann and Weber, 1953)

$$C_F=\frac{F}{qA_i}=(1-\alpha)^2, \tag{1}$$

where q is the dynamic pressure of the free stream, A_i the inlet duct area, $\alpha=U_i/U_\infty$ the inlet duct to the free stream velocity ratio, and C_F the force coefficient. At a rounded nose this force can be efficiently distributed, e.g., optimum intake contours are designed to obtain an uniform pressure distribution over the suction part of the intake (Ruden, 1941).

In the case of sharp lips, the suction localized just at the lip should substantially contribute the total thrust, but, unfortunately, that force is almost lost due to the flow separation.

It is of interest to estimate the suction force and also to design the so called "ideal" inlets in which there exits smooth flow without separation at the sharp lip, so that the localized force is redistributed avoiding the abovementioned thrust loss.

A simple method to estimate the suction force of a two-dimensional inlet of general shape has recently appeared (Huang, 1982). This author utilizes a conformal mapping which preserves the complex velocity in the transformation. His solution can be considered as the superposition of those of the following two problems: an almost-straight inlet with $\alpha=1$ and a straight inlet with $\alpha\neq 1$. However, the first solution is only valid for $\alpha=0(1)$ because it is obtained by a linearization process with respect to the free stream velocity U_∞, so that no real influence of α in the first problem is considered.

The contribution here presented solves the problem of the inlet flow by linearizing with respect to the solution of the straight inlet with $\alpha\neq 1$, thus the influence of α in the almost-straight inlet problem is retained, avoiding restrictions in the value of α. It should be pointed out that the zone which has more influence in the calculation of the suction force is the neighborhood of the inlet lip, and it is also where boundary conditions are more affected by the flow with respect to which linearizations are made. Furthermore, a different approach conserving the complex potential function is employed. In this way singularities are clearly identified although the relation between boundary conditions in both planes requires some manipulation.

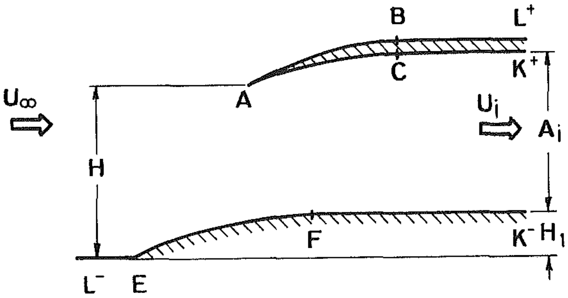

Fig. 1 Typical two-dimensional inlet

In the Huang's approach (derived from Lissaman, 1968) boundary conditions are conserved because they are stated in terms of velocity although appropriate singularities should be added. Anyway, it can be demonstrated that the solutions of the problems derived from both approaches coincide.

One interesting point in this kind of problem is that before linearization is made the boundary condition only gives a relationship between velocity components. Over the inlet contour in the transformed half plane, which is a horizontal straight line, the horizontal component of the velocity can be written as a function of both the vertical component and the velocity generated by a discrete singularity. The combination of both expressions gives raise to an integral equation whose simplification is based on the small slopes of the inlet.

The method followed here, which is applicable to two-dimensional, almost-straight inlets consists mainly of three steps: first, finding a suitable conformal mapping which transforms the "skeleton" of the intake in the real axis; second, identifying and taking into account the singularities of the transformation which occur at the inlet lip and at the infinity inside the inlet; and third, calculating the velocity at the mapped plane. Thus, design criteria for ideal inlets are obtained and validation of the expressions derived is performed by checking against the exact solution of a simple problem ob-

---

Contributed by the Applied Mechanics Division for publication in the JOURNAL OF APPLIED MECHANICS.

Discussion on this paper should be addressed to the Editorial Department, ASME, United Engineering Center, 345 East 47th Street, New York, N.Y. 10017, and will be accepted until two months after final publication of the paper itself in the JOURNAL OF APPLIED MECHANICS. Manuscript received by ASME Applied Mechanics Division August 26, 1985; *final revision March 19, 1986.*

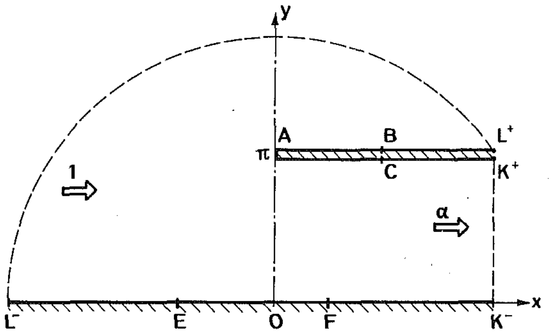

Fig. 2(*a*) Physical plane $z=x+iy$

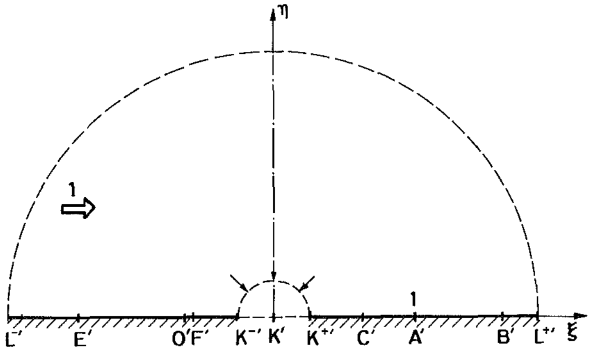

Fig. 2(*b*) Transformed plane, $\tau=\xi+i\eta$

tained by a Schwarz-Christoffel transformation. Finally a comparison is made with Huang's results showing a 20 percent differences although both results match for $\alpha=1$, as expected.

2 Problem Definition

Let us consider a two-dimensional inlet with a ramp as shown in Fig. 1, in which *BL*, *CK*, and *FK* are straight lines parallel to the *x* axis. Assume that the flow is incompressible, inviscid, and irrotational. Thus, the solution can be expressed as an analytical function of a complex variable. Also, the deformations of the inlet with respect to straight horizontal lines are supposed to be so small that the boundary conditions can be transferred to the cut LBACK and *x* axis, as shown in Fig. 2(*a*), where speeds are made dimensionless with U_∞ and lengths with a characteristic length, $L=H/\pi$ (H is the capture height). Boundary conditions are

$$\frac{v}{u}=\frac{dy_c}{dx}=F(x) \qquad \text{on } BAC \text{ and } EF,$$

$$v\ =0 \qquad \text{on } CKF \text{ and } ELB. \tag{2}$$

$W=u-iv$ is the complex velocity in the z plane and $y_c(x)$ is the equation of the nonstraight surfaces of the inlet. Let M be the contour BAC and EF.

3 Conformal Mapping

To solve the problem we use the conformal mapping (Lissaman, 1968; Huang, 1982)

$$z-i\pi=\tau-1-ln\tau \tag{3}$$

which transforms the interior of the region shown in Fig. 2(*a*) in the interior of the transformed boundary (Fig. 2(*b*)). In particular, the boundary of the inlet is defined by $x=\xi-1-ln|\xi|$. $\xi<0$ corresponds to the x axis, $\xi>0$ to the cowl ($\xi>1$, $\xi<1$ the upper and lower surfaces, respectively), as shown in Figs. 2(*a*) and 3. Conserving the complex potential function, we should consider the derivative of equation (3)

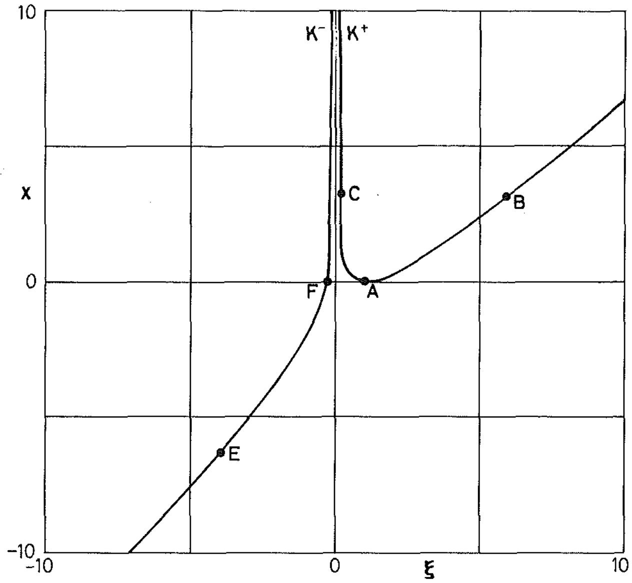

Fig. 3 Mapping of the x coordinate of the inlet contour into the ξ axis in the τ plane. $\xi<0$, x axis; $0<\xi<1$ and $\xi>1$ lower and upper surfaces of the cowl, respectively. Points corresponds to the example in Fig. 4.

$$\frac{dz}{d\tau}=1-\frac{1}{\tau} \tag{4}$$

in order to analyze the characteristics of the transformation. The complex velocity in the τ plane, $W'=u'-iv'$, is related to $W(z)$ by the expression

$$W(z)=W'(\tau)/(1-1/\tau). \tag{5}$$

At the infinity in the τ-plane ($\tau\rightarrow\infty$) which corresponds to the infinity outside of the inlet in z plane, the transformation is an identity. Thus, the free stream velocities are identically in both planes. The critical points of the mapping are $K'(\tau=0)$ and $A'(\tau=1)$, close to which the transformation should be carefully studied. In the neighborhood of K (splitted into K^+ and K^-)

$$\tau\rightarrow 0,\ z\simeq -ln\tau\rightarrow +\infty, \tag{6}$$

which shows that in this region the mapping is similar to the classical one transforming a strip on a half plane. The finite segment K^-K^+ (inlet duct) is transformed in the semicircle $K^{-\prime}K^{+\prime}$, of vanishing radius, centered at the origin K' of the τ-plane. In this region the complex velocities are related by

$$W'\simeq -W/\tau=-\alpha/\tau, \tag{7}$$

where it has been taken into account that in the inlet duct ($\tau\rightarrow 0$) the velocity $W\rightarrow\alpha$. Equation (7) shows that near K' the flow field is like that induced by a sink of strength $2\pi\alpha$, which accounts for the flux through both K^-K^+ and their image in the symmetric half plane.

Concerning the other critical point, let $\tau=1+\epsilon$, $|\epsilon|\rightarrow 0$ in the neighborhood of A'. Then the transformation can be approximated by

$$z-i\pi=\epsilon-ln(1+\epsilon)\simeq\frac{1}{2}\epsilon^2\ , \tag{8}$$

which shows that the arguments of straight lines passing through A' are multiplied by 2. The derivative of the transformation is $dz/d\tau\simeq\epsilon$ and velocities are related through the expression

$$W\simeq\frac{W'(1)}{\epsilon}\simeq\frac{W'(1)}{2^{1/2}(z-i\pi)^{1/2}}. \tag{9}$$

If $W'(1)\neq 0$, ∞, equation (9) represents, as expected, the flat-plate leading edge singularity. In conserving the complex velocity, Huang and Lissaman introduce a singularity in point A' to model the velocity at the leading edge. If the complex potential function is conserved the velocity singularities appear in a straightforward way. However, in this case the correspondence of boundary conditions requires some elaboration.

4 Boundary Conditions

The velocities in both planes are related by the expression (5), that can be written as

$$u - iv = A(\tau)(u' - iv'), \tag{10}$$

where $A(\tau) = d\tau/dz$ is in general complex. Fortunately, in this problem both $\tau = \xi$ and $A(\xi)$ are real-valued over the contour so that the velocity components are decoupled

$$\begin{aligned} u_c &= A(\xi)u'_c \\ v_c &= A(\xi)v'_c, \end{aligned} \tag{11}$$

where subscript c indicates values over the contour. If $A(\xi)$ were complex, u_c and v_c in both planes would appear coupled. In τ plane conditions (2) become

$$\begin{aligned} \frac{v'_c}{u'_c} &= F\,[x(\xi)] \equiv f(\xi) && \text{on } C'A'B' \text{ and } E'F', \\ v'_c &= 0 && \text{on } C'K'F' \text{ and } E'L'B'. \end{aligned} \tag{12}$$

The segments $C'K'F'$ and $E'L'B'$ are streamlines and a relation between v'_c and u'_c is specified over the segments $E'F'$ and $C'A'B'$.

By adding the image of the flow formed in the other half-plane we obtain a problem for the whole τ plane which is symmetrical with respect to the ξ axis. Boundaries $E'F'$ and $C'A'B'$ can be regarded as a distributed array of sources with the appropriate intensity to fulfil the boundary conditions in these segments. Based on the symmetry of the flow, the strength of each source is twice the value of v'_c at that point, as it occurs for instance in the symmetric thin airfoil theory (Ashley and Landahl, 1965), and the condition over $C'K'F'$ and $E'L'B'$ is automatically fulfilled. Therefore, the velocity in the whole τ-plane is generated by superposition of the normalized free stream velocity, a sink at $K'(\tau = 0)$ of strength $2\pi\alpha$ and the source distribution of intensity $2v'_c$ over $E'F'$ and $C'A'B'$. That is

$$W'(\tau) = 1 - \frac{\alpha}{\tau} + \frac{1}{\pi}\int_{M'} \frac{v'_c(\xi_o)}{\tau - \xi_o}\, d\xi_o, \tag{13}$$

where M' represents both the segments $C'A'B'$ and $E'F'$. The Cauchy value of the integral should be taken in the segment where $\xi_o = \tau$. Over the boundary the imaginary part of equation (13) is an identity and the real part expresses u'_c as a function of v'_c. At this stage v'_c is not known because boundary conditions (12) only states a relation between u'_c and v'_c. Calculating u'_c by using equation (13), and substituting in the first of conditions (12) we obtain

$$v'_c(\xi) = f(\xi)\left[1 - \frac{\alpha}{\xi} + \frac{1}{\pi}\int_{M'} \frac{v'_c(\xi_o)}{\xi - \xi_o}\, d\xi_o\right]. \tag{14}$$

This equation relates $f(\xi)$ and $v'_c(\xi)$ over M. Once $v'_c(\xi)$ is calculated, the solution for the complex velocity in the whole τ-plane is given by equation (13).

As in the thin wing section theory, three kinds of problems can be considered. First, the direct problem where the inlet shape $f(\xi)$ is known and we look for the pressure distribution. This problem is easily solved by using Bernoulli's equation, once $v'_c(\xi)$ is obtained from the integral equation (14). The second is the inverse problem in which the pressure distribution $c_p(x)$ is fixed and the shape $f(\xi)$ is sought. In this case

$$c_p[x(\xi)] = 1 - A^2(\xi)v'^2_c\left[1 + \frac{1}{f^2(\xi)}\right]. \tag{15}$$

With equations (14) and (15) the shape of the inlet $f(\xi)$ can be calculated. The third is the mixed problem in which a combination of both previous conditions applies over different parts of the boundary. In what follows we will deal with the direct problem by introducing additional simplifications.

5 Direct Problem

The integral equation (14), which resembles that appearing in the Lanchester – Prandtl finite airfoil theory, has to be solved to determine $v'_c(\xi)$ once $f(\xi)$ is given. However, if $f(\xi)$ is a C^o function as it happens in supersonic inlets (not in subsonic ones) and $f(\xi) << 1$, we can use the expansion

$$\begin{aligned} v'_c(\xi) &= \delta\bar{v}'_c(\xi) + 0(\delta^2), \\ f(\xi) &= \delta\bar{f}(\xi), \end{aligned} \tag{16}$$

where δ is a small parameter of the order of the maximum slope of the inlet shape. Introducing equation (16) into (14) and retaining first order terms we obtain

$$\bar{v}'_c(\xi) = \bar{f}(\xi)\left[1 - \frac{\alpha}{\xi}\right]. \tag{17}$$

This is the approximate solution of integral equation (14). In the following we drop the bars.

6 Forces Over the Inlet

The total thrust over the inlet is given by equation (1). The suction force coefficient C_s is calculated in the same way as the leading edge suction in the thin wing theory (Milne-Thompson, 1952)

$$C_s = \frac{F_s}{qA_i} = \frac{\pi\rho U_\infty^2 LB^2}{2qA_i} = \frac{H}{A_i}\, W'(1)^2, \tag{18}$$

where B is obtained from the approximate expression of W near A in the form $W = 2^{-1/2}B/(z - i\pi)^{1/2}$. From equation (9), $B = W'(1)$. Equation (18) shows that C_s depends on the velocity generated at A' by the singularities.

In the case of a straight inlet $W' = 1 - \alpha/\tau$, so that

$$C_s = (1 - \alpha)^2 \tag{19}$$

since $H = A_i$ and $W'(1) = 1 - \alpha$. Expression (19) compared with equation (1) shows that all the thrust over the inlet is concentrated in the lip suction. The stagnation point position over the cowl is given by $\tau = \alpha$, that is, $z_{sp} - i\pi = \alpha - 1 - ln\alpha \simeq 1/2(\alpha - 1)^2$ in the case $\alpha = 0(1)$.

To calculate the suction in a general case, we bring the value of v'_c given by equation (17) to equation (13) reaching

$$\begin{aligned} W'(1) = 1 - \alpha + \frac{1}{\pi}\int_{M'} \frac{f(\xi_o)}{1 - \xi_o}\left[1 - \frac{\alpha}{\xi_o}\right] d\xi_o = 1 + I_1 \\ - \alpha(1 + I_1 - I_2), \end{aligned} \tag{20}$$

where

$$I_1 = \frac{1}{\pi}\int_{M'} \frac{f(\xi_o)}{1 - \xi_o}\, d\xi_o, \quad I_2 = -\frac{1}{\pi}\int_{M'} \frac{f(\xi_o)}{\xi_o}\, d\xi_o. \tag{21}$$

The main contribution to the suction force is $1 + I_1$ if α is small and I_2 if $\alpha = 0(1)$. I_1 and I_2 are, respectively, the velocities generated at the points A' and K' by the distribution of the physical slopes $f(\xi)$. With this idea, it is easy to estimate the variation of the suction force due to the change of the slope in a given part of the inlet surface. For instance, increasing the slope of the ramp ($E'F'$) or of the cowl ($C'B'$) has opposite influence in I_2, because these segments are symmetrically placed with respect to K'.

The integral I_2 can be transformed in a more convenient expression. To this aim lets write down the differential relationship (4) over the x axis and his transformed ξ axis

$$\frac{dx}{d\xi}=1-\frac{1}{\xi} \tag{22}$$

in the form $d\xi_o/\xi_o=d\xi_o-dx_o$. By substitution of equation (22) in I_2 we obtain

$$I_2=\frac{1}{\pi}\int_M F(x)dx-\frac{1}{\pi}\int_{M'} f(\xi_o)d\xi_o, \tag{23}$$

and thence

$$I_2=\frac{1}{\pi}[y_c(x_F)-y_c(x_E)+y_c(x_B)-y_c(x_C)]-\frac{1}{\pi}\int_{M'} f(\xi_o)d\xi_o. \tag{24}$$

If the lip has not width $y_c(x_B)=y_c(x_C)$.

As in the thin wing section theory, an ideal configuration with smooth flow without separation at the sharp lip is obtained if $W'(1)=0$, or $\alpha=\alpha_i$

$$\alpha_i=\frac{1+I_1}{1+I_1-I_2}\simeq 1+I_2 \tag{25}$$

giving a thrust

$$C_{F_i}=(1-\alpha_i)^2=\frac{I_2^2}{(1+I_1-I_2)^2}\simeq I_2^2. \tag{26}$$

Thus, for a fixed geometry we can determine the ideal velocity ratio and the associated thrust. The approximations in equations (25) and (26) are made considering that both I_1 and I_2 are small as a consequence of the assumptions made in Section 5. The main contribution to C_{F_i} is produced by I_2.

7 Example

In trying to check the approximate linearized method presented here, lets consider the problem of a straight inlet with a ramp of constant slope tan ϕ placed between points E and F.

The Schwarz-Christoffel mapping which transforms this inlet in a half plane τ' (similar to τ plane) is given by

$$\frac{dz}{d\tau'}=\frac{\tau'-1}{\tau'}\left(\frac{\tau'-\xi_F'}{\tau'-\xi_E'}\right)^{\phi/\pi}. \tag{27}$$

As in the previous section, a sink of strength $2\pi\beta$ should exits in the origin K' of τ' plane, where $\pi\beta$ is the flow crossing the inlet duct (line K^-K^+). Equation (27) defines a normalized transformation since at the infinity ($\tau'\rightarrow\infty$) $dz/d\tau'=1$. In the τ' plane the velocity is generated by the free stream and the sink, so that

$$W'(\tau')=1-\beta/\tau'.$$

Dividing by equation (27) we obtain the complex velocity in the z plane

$$W(z)=\frac{\tau'-\beta}{\tau'-1}\left(\frac{\tau'-\xi_E'}{\tau'-\xi_F'}\right)^{\phi/\pi}. \tag{28}$$

In the section K^-K^+ ($\tau'\rightarrow 0$) the velocity should be α, thus from equation (28) in this limit

$$\alpha=\beta\left(\frac{\xi_E'}{\xi_F'}\right)^{\phi/\pi}. \tag{29}$$

By substituting β from equation (29) into equation (28) the complex velocity is fully determined. The suction force is proportional to the coefficient of the sharp lip singularity in A ($\tau'\rightarrow 1$) which, with the notation introduced in Section 6, is

$$B=\lim_{\tau'\rightarrow 1}(\tau'-1)W(\tau')=\left[1-\alpha\left(\frac{\xi_F'}{\xi_E'}\right)^{\phi/\pi}\right]\left[\frac{1-\xi_E'}{1-\xi_F'}\right]^{\phi/\pi}. \tag{30}$$

As ϕ is small the angle can be substituted by the tangent so that ϕ has either meaning. Furthermore, the ϕ/π powered terms can be expanded to obtain

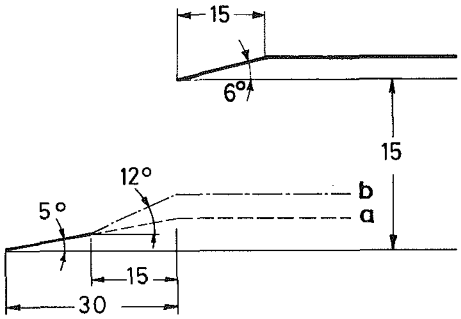

Fig. 4 Examples of inlets studied in Huang (1982): (a) ramp surface of slope 5 deg; (b) ramps surface divided in two parts with slope 5 and 12 deg, respectively.

$$B\simeq\left\{1-\alpha\left[1+\frac{\phi}{\pi}\,ln\,\frac{\xi_F'}{\xi_E'}\right]\right\}\left\{1+\frac{\phi}{\pi}\,ln\,\frac{1-\xi_E'}{1-\xi_F'}\right\}=1+I_1$$

$$-\alpha(1+I_1-I_2)+0\left[\left(\frac{\phi}{\pi}\right)^2\right], \tag{31}$$

which clearly match with the value given in equation (20) after calculation of I_1 and I_2 in equation (21) for $f(\xi)\equiv\phi$. A point should be made concerning ξ_E' and ξ_F'. They are not the same as those obtained from transformation (3). However, for small ϕ the difference between them should be $0(\phi/\pi)$ and the contribution of these corrections to equation (31) should be $0[(\phi/\pi)^2]$.

8 Discussion and Conclusions

For $\alpha=1$, which is the common range of validity, equation (20) gives $W'(1)=I_2$, which expressed as in equation (24) coincides with the result of Huang. It can be shown that by performing a similar approximation process like that explained in Sections 4 and 5, using the complex velocity conservation method, the same solution as in equation (20) would be obtained.

In what follows we consider the examples studied by Huang (1982) and sketched in Fig. 4. The ramp surfaces of the inlet has constant slope, simplifying the integrations in equation (21). However, it raises a problem because $f(\xi)$ is not a C^o function. It experiences jumps at the ramp ends that generate singularities at F and B of the type appearing in equation (28). Nevertheless, following the approach explained in Section 5 these singularities would be neglected in deriving equation (17) as long as ξ is far enough from the singularities (in this case, $\xi=1$). Anyway, the effect of each jump is retained, and it appears in the form of a logarithmic singularity when performing integration of I_1 and I_2. For the suction in the cases explained in Fig. 4 we obtain the following results:

$$C_{sa}=1.08(0.99-1.11\alpha)^2, \quad C_{sb}=1.23(1.01-1.07\alpha)^2,$$

which compared with those obtained by Huang (1982)

$$C_{sa}=1.08(0.83-0.93\alpha)^2, \quad C_{sb}=1.23(0.74-0.81\alpha)^2,$$

indicate that there exists differences in coefficients of some 20 percent although the values coincide for $\alpha=0(1)$, as mentioned above.

We should remark that in the formulation in Section 4, the only simplification is the transference of boundary conditions, which only implies proximity of the inlet surfaces to the skeleton, although $f(\xi)$ is allowed to be discontinuous except at point A in which it should be continuous. Otherwise the suction force calculation method should change because the sharp lip singularity changes. Obviously, to solve the non-simplified problem, even without singularities, is far more complicated and requires additional effort.

Concerning the comments of Huang on the small influence of the inside wall of the inlet, it is true as far as the second term of I_2 is concerned but it is not for the first term, which represents the asymptotic width of the ramp. Additionally, it could be shown that, if $\alpha \neq 1$, I_1 has a significant influence, and therefore the effect of both the external and internal surfaces are of the same order. As Fig. 3 shows, this occurs because the inside upper wall of the inlet maps close to the lip A', thus appreciably contributing to the velocity at this point.

In Huang's example $I_1 \sim (1/3)I_2$ over the cowl and $I_1 \sim (1/2)I_2$ over the ramp.

Acknowledgments

The author would like to thank Professor I. Da Riva for fruitful discussions of the work.

References

Ashley, H., and Landahl, M., 1965, "Aerodynamics of Wings and Bodies," Dover Publications, New York, pp. 90.

Donovan, A. F., and Lawrence, H. R., 1957, "Aerodynamic Components of Aircraft at High Speeds," *High Speed Aerodynamics and Jet Propulsion*, Princeton University Press, Princeton, N.J. Vol. VII, Section E.

Huang, M. K., 1982, "Two-Dimensional Theory of Incompressible Flow over Inlets," ASME JOURNAL OF APPLIED MECHANICS, Vol. 49, pp. 444-446.

Küchemann, D., and Weber, J., 1953, *Aerodynamics of Propulsion*, McGraw-Hill, New York, pp. 61-63.

Lissaman, P. B. S., 1968, "A Linear Theory for the Jet Flap in Ground Effect," *AIAA Journal*, Vol. 6, No. 7, pp. 1356-1362.

Milne-Thompson, L. M., 1952, *Theoretical Aerodynamics*, McMillan and Co., London, pp. 123-124.

Ruden, P., 1950, "Two-Dimensional Symmetrical Inlets with External Compression," NACA TM 1279.

Journal of Applied Mechanics

Brief Notes

A Brief Note is a short paper that presents a specific solution of technical interest in mechanics but which does not necessarily contain new general methods or results. A Brief Note should not exceed 1500 words *or equivalent* (a typical one-column figure or table is equivalent to 250 words; a one line equation to 30 words). Brief Notes will be subject to the usual review procedures prior to publication. After approval such Notes will be published as soon as possible. The Notes should be submitted to the Technical Editor of the JOURNAL OF APPLIED MECHANICS. Discussions on the Brief Notes should be addressed to the Editorial Department, ASME, United Engineering Center, 345 East 47th Street, New York, N. Y. 10017, or to the Technical Editor of the JOURNAL OF APPLIED MECHANICS. Discussions on Brief Notes appearing in this issue will be accepted until two months after publication. Readers who need more time to prepare a Discussion should request an extension of the deadline from the Editorial Department.

Dynamic Plastic Response of Circular Plates With Transverse Shear

A. Kumar[1] **and V. V. Krishna Reddy**[2]

Introduction

In this brief note, the motion of a simply supported circular plate, made of rigid-plastic material, is studied. The plate material is assumed to obey the Tresca yield criterion which retains the transverse shear force; the resulting yield criterion is of the form proposed by Sawczuk and Duszek (1963) and adopted, for example, by Jones and Gomes de Oliveira (1980). The plate is subjected to a uniformly distributed load which is applied suddenly at time $t=0$, kept constant at an intensity p during $0 \le t \le \tau$ and suddenly removed at $t=\tau$.

In a similar study undertaken by Jones and Gomes de Oliveira (1980) for circular plates subjectd to blast loading idealized by an instantaneous uniform velocity, it was concluded that the pattern of velocity profile depends on a dimensionless parameter $\nu = RQ_0/2M_0$ (i.e., the relative importance of the product of the radius of the plate and the shear capacity per unit length over the moment capacity per unit length). Accordingly, the plates have been classified into three categories, Class I being in the range $0 \le \nu \le 1.5$, Class II in the range $1.5 \le \varphi \le 2$, and Class III in the range $\nu \ge 2$. It is found that the shear sliding at the supports is possible only when

$$\frac{p}{p_o} > 2(\nu - 1)\ , \ p_o = \frac{6M_o}{R^2} \tag{1}$$

for Class II plates, and

$$\frac{p}{p_o} > \frac{2\nu}{(1-\rho_o/R)(2+\rho_o/R)}\ , \ \frac{\rho_o}{R} = [(4\nu^2 - 8\nu + 1)^{1/2} - 1]/2\nu \tag{2}$$

for Class III plates. If these conditions are not satisfied, the problem has the bending solution only which is similar to the one presented by Hopkins and Prager (1954), and, also, by Kumar and Hegde (1982).

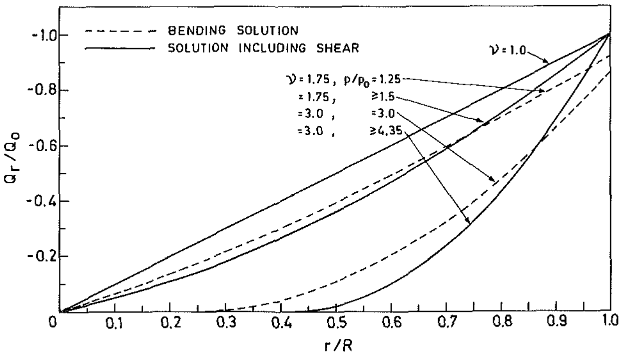

Fig. 1 *Variation of dimensionless shear forces (Q_r/Q_o) with dimensionless radius (r/R) for different values of ν and pressure intensity ratio (p/p_o)*

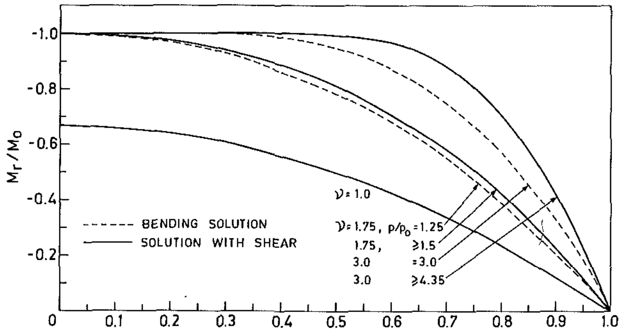

Fig. 2 Variation of dimensionless radial moment (M_r/M_o) with dimensionless radius (r/R) for different values of ν and pressure intensity ratio (p/p_o)

Results

Following a procedure similar to the one adopted by Jones and Gomes de Oliveira (1980), the expressions for shear force, bending moment, and the plate deflection are obtained analytically and, wherever necessary, numerically. Relations between the radius of the plate and the shear force as well as between the radius and the radial bending moment (all in nondimensional forms) are plotted in Figs. 1 and 2, respectively. The solution of the problem including shear in the yield criterion shows smaller shear forces in the inner regions of the plate and larger in outer regions and the radial moments are greater throughout the plate, when compared with the bending solution. In Fig. 3, for a given ratio of p/p_o, the variation of dimensionless deflections (with respect to a standard deflection of $10\, p_o \tau^2/\mu$) with radius is plotted. It can be observed

---

[1] Professor, Civil Engineering Department, Indian Institute of Technology Kanpur, Kanpur, India 208 016.

[2] Former Research Student, Civil Engineering Department, Indian Institute of Technology Kanpur, Kanpur, India 208 016.

Manuscript received by ASME Applied Mechanics Division, March 3, 1986; final revision May 21, 1986.

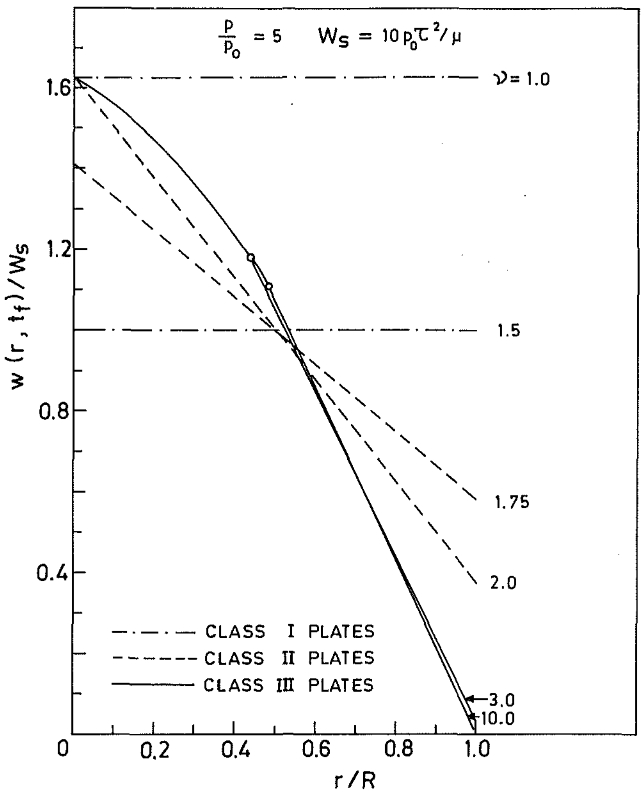

Fig. 3 Variation of dimensionless transverse deflection across plate, with ν, for constant pressure intensity (the circles indicate the positions of the stationary hinge circles)

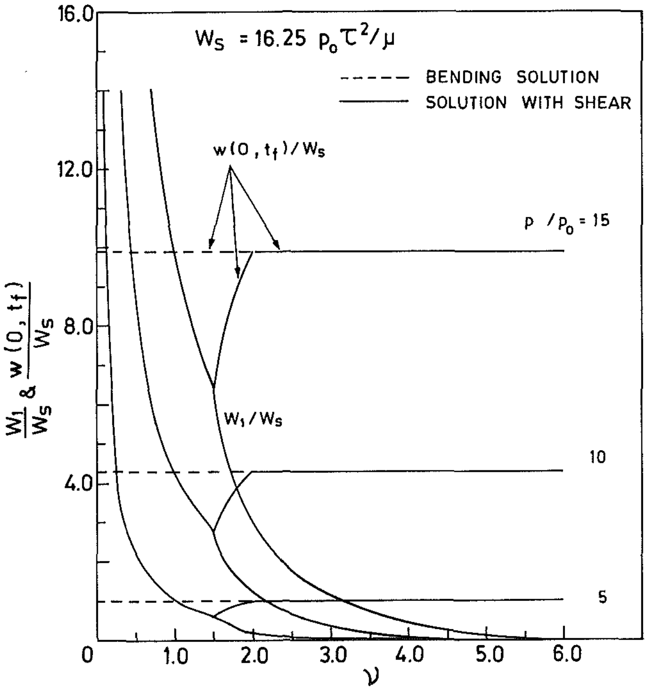

Fig. 4 Variation of dimensionless central, edge deflections of plate with ν, for different load intensities

that as the value of ν increases the shear deformations are less. It is interesting to note that, for a given p/p_o ratio, there exists a value of the dimensionless radius at which the deflections are more or less the same, irrespective of the value of ν, for Class III plates. Figure 4 shows the variation in the dimensionless central $\bar{w}(0,t_f)$ and edge $(\bar{W}_1)$ deflections (with respect to a standard deflection of $16.25\, p_o\tau^2/\mu$) with ν. It is observed that if ν is decreased from 1.5 to some lower values, the plate will yield at the support indefinitely. This figure also represents the variation in deflection with the ratio p/p_o.

References

Hopkins, H. G., and Prager, W., 1954, "On the Dynamics of Plastic Circular Plates," *J. App. Math. Phys.* (ZAMP), Vol. 5, pp. 317-330.

Jones, N., and Gomes de Oliveira, J., 1980, "Dynamic Plastic Response of Circular Plates with Transverse Shear and Rotary Inertia," ASME JOURNAL OF APPLIED MECHANICS, Vol. 47, pp. 27-34.

Kumar, A., and Hegde, M., 1982, "Dynamic Response of Rigid Plastic Circular Plates in a Damping Medium," ASME JOURNAL OF APPLIED MECHANICS, Vol. 49, pp. 240-241.

Sawczuk, A., and Duszek, M., 1963, "A Note on the Interaction of Shear and Bending in Plastic Plates," *Arch. Mech. Stosow.*, Vol. 15, pp. 411-426.

Note on Southwell's Method for Buckling Tests of Struts

W.-T. Tsai[3]

Introduction

Southwell (1931) devised a method by which linear elastic test data from a strut with initial curvature could be analyzed to determine the buckling capacity which the strut would have if it were perfectly straight. The capacity is estimated from the measured lateral deflection and the applied axial force. The method proved to be very practical and efficient in most applications (Donnell, 1938; Horton, et al., 1971). It is especially useful in nondestructive testing to demonstrate strength and stiffness properties of an actual structural component since the strut would be required to be loaded within the elastic limit. However, the accuracy of the predicted buckling capacity and the associated stiffness properties become poor if the initial curvature is small. The reason, among others, is that the actual deflection dwells within the deviation range of the employed gauges. Errors introduced by the uncertainties in gauge measurements become the dominating factor of the measurements taken during the test. This should not be surprising since the method is not applicable to a perfectly straight strut. The difficulty in obtaining an accurate result for a strut of small initial bow was also recognized by Donnell (1938).

Due to improvements in manufacturing control nowadays, a strut can be made with very little initial imperfection. The buckling capacity of such a strut becomes hard to estimate without loaded into yield range. In order to obtain an accurate buckling capacity for the strut to remain within the elastic limit at low axial force, an alternate method of testing is proposed. This method introduces an eccentricity at both ends of the strut (Fig. 1). Such eccentricity, together with any existing initial bow, produces a moment which in turn induces a lateral deflection in the strut. The magnitude of the lateral deflection is directly influenced by the magnitude of introduced eccentricity. It can be made large enough to overcome the difficulty of measurement error. Although the same idea was briefly discussed by Donnell (1938), he did not pursue it further since he anticipated difficulties in using harmonic series to treat the eccentricity. In this note, a closed-form solution is obtained to relate the introduced eccentricity to the lateral deflection of a strut.

Governing Differential Equation and the Solution

Accounting for the effect of an initial bow and an eccentricity, the governing differential equation of a strut is

$$EI(y'' - y_o'') + P(y + e) = 0 \tag{1}$$

---

[3] President, Tsais & Associates, South Pasadena, Calif. 91030.

Manuscript received by ASME Applied Mechanics Division, March 18, 1986; final revision June 6, 1986.

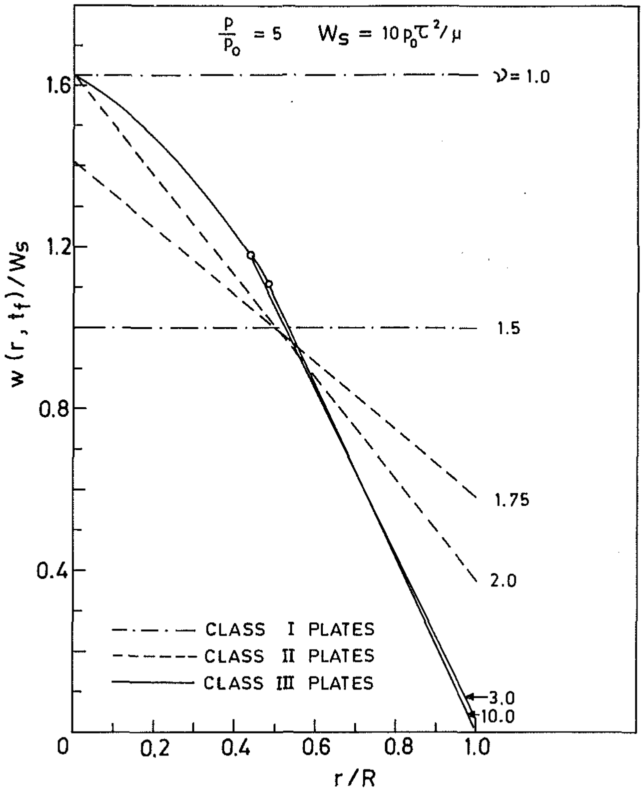

Fig. 3 Variation of dimensionless transverse deflection across plate, with ν, for constant pressure intensity (the circles indicate the positions of the stationary hinge circles)

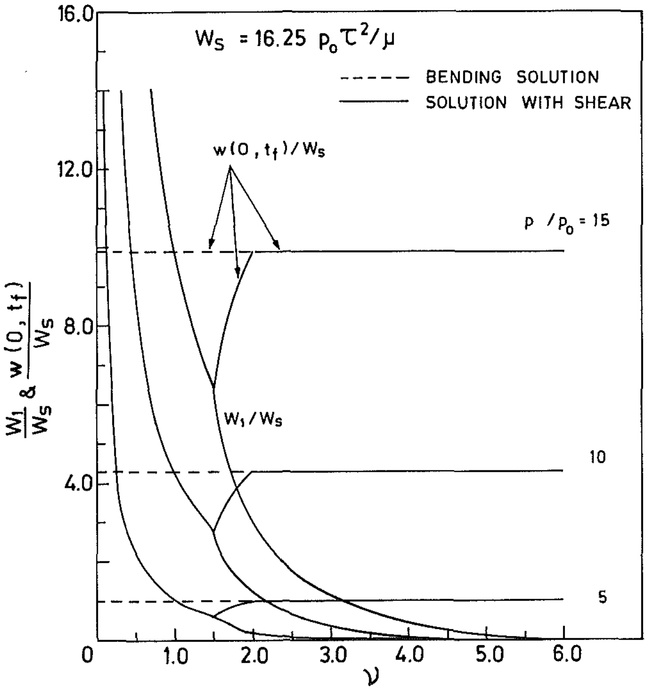

Fig. 4 Variation of dimensionless central, edge deflections of plate with ν, for different load intensities

that as the value of ν increases the shear deformations are less. It is interesting to note that, for a given p/p_o ratio, there exists a value of the dimensionless radius at which the deflections are more or less the same, irrespective of the value of ν, for Class III plates. Figure 4 shows the variation in the dimensionless central $\bar{w}(0,t_f)$ and edge ($\bar{W}_1$) deflections (with respect to a standard deflection of $16.25\, p_o\tau^2/\mu$) with ν. It is observed that if ν is decreased from 1.5 to some lower values, the plate will yield at the support indefinitely. This figure also represents the variation in deflection with the ratio p/p_o.

References

Hopkins, H. G., and Prager, W., 1954, "On the Dynamics of Plastic Circular Plates," *J. App. Math. Phys.* (ZAMP), Vol. 5, pp. 317-330.

Jones, N., and Gomes de Oliveira, J., 1980, "Dynamic Plastic Response of Circular Plates with Transverse Shear and Rotary Inertia," ASME Journal of Applied Mechanics, Vol. 47, pp. 27-34.

Kumar, A., and Hegde, M., 1982, "Dynamic Response of Rigid Plastic Circular Plates in a Damping Medium," ASME Journal of Applied Mechanics, Vol. 49, pp. 240-241.

Sawczuk, A., and Duszek, M., 1963, "A Note on the Interaction of Shear and Bending in Plastic Plates," *Arch. Mech. Stosow.*, Vol. 15, pp. 411-426.

Note on Southwell's Method for Buckling Tests of Struts

W.-T. Tsai[3]

Introduction

Southwell (1931) devised a method by which linear elastic test data from a strut with initial curvature could be analyzed to determine the buckling capacity which the strut would have if it were perfectly straight. The capacity is estimated from the measured lateral deflection and the applied axial force. The method proved to be very practical and efficient in most applications (Donnell, 1938; Horton, et al., 1971). It is especially useful in nondestructive testing to demonstrate strength and stiffness properties of an actual structural component since the strut would be required to be loaded within the elastic limit. However, the accuracy of the predicted buckling capacity and the associated stiffness properties become poor if the initial curvature is small. The reason, among others, is that the actual deflection dwells within the deviation range of the employed gauges. Errors introduced by the uncertainties in gauge measurements become the dominating factor of the measurements taken during the test. This should not be surprising since the method is not applicable to a perfectly straight strut. The difficulty in obtaining an accurate result for a strut of small initial bow was also recognized by Donnell (1938).

Due to improvements in manufacturing control nowadays, a strut can be made with very little initial imperfection. The buckling capacity of such a strut becomes hard to estimate without loaded into yield range. In order to obtain an accurate buckling capacity for the strut to remain within the elastic limit at low axial force, an alternate method of testing is proposed. This method introduces an eccentricity at both ends of the strut (Fig. 1). Such eccentricity, together with any existing initial bow, produces a moment which in turn induces a lateral deflection in the strut. The magnitude of the lateral deflection is directly influenced by the magnitude of introduced eccentricity. It can be made large enough to overcome the difficulty of measurement error. Although the same idea was briefly discussed by Donnell (1938), he did not pursue it further since he anticipated difficulties in using harmonic series to treat the eccentricity. In this note, a closed-form solution is obtained to relate the introduced eccentricity to the lateral deflection of a strut.

Governing Differential Equation and the Solution

Accounting for the effect of an initial bow and an eccentricity, the governing differential equation of a strut is

$$EI(y'' - y_o'') + P(y+e) = 0 \tag{1}$$

---

[3] President, Tsais & Associates, South Pasadena, Calif. 91030.

Manuscript received by ASME Applied Mechanics Division, March 18, 1986; final revision June 6, 1986.

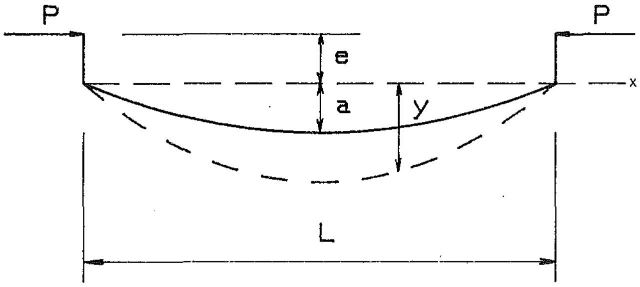

Fig. 1 Geometry of a strut

where EI is the bending rigidity of the strut, e the eccentricity, P the axial force, y the total deflection, and y_o the initial bow. In order to simplify the analysis, the initial bow is assumed to be a simple sine function

$$y_o = a \sin \frac{\pi x}{L} \tag{2}$$

This was shown by Southwell to be a good approximation for determination of the lateral deflection. Upon introduction of equation (2) and the boundary conditions, $y = 0$ at $x = 0$ and $x = L$, into equation (1), the total deflection is given by Tsai (1977)

$$y = \frac{a}{1 - P/P_{cr}} \sin \frac{\pi x}{L} + e\left[\frac{\cos \lambda \ (L/2 - x)}{\cos \ (\lambda L/2)} - 1\right] \tag{3}$$

where $P_{cr} = \pi^2 EI/L^2$ is the buckling capacity of the strut if it were perfectly straight, and $\lambda = \sqrt{P/EI} = \sqrt{P/P_{cr}}\pi/L$.

Application of Southwell's Method

To apply equation (3) to Southwell's test, the net deflection at the middle point is to be measured. By introducing $x = L/2$ into equation (3), the net deflection, $d = y - y_o$, is given by

$$d = \frac{a}{P_{cr}/P - 1} + e\left[\frac{1}{\cos(\lambda L/2)} - 1\right] \tag{4}$$

This expression may be rewritten into an alternate form upon multiplying equation (4) by a factor, $P_{cr}/P - 1$, and defining $v = d/P$, the result reads

$$P_{cr}v - d = a + e\left[\frac{1}{\cos(\lambda L/2)} - 1\right]\left(\frac{P_{cr}}{P} - 1\right) \tag{4'}$$

The left-hand side together with the first term of the right-hand side of equation (4′) is the typical form of Southwell's approach. By plotting v as the abscissa and d as the ordinate, a straight line is obtained. The slope of this straight line is the buckling capacity and the negative intercept of the d axis is the initial bow at the mid-span. It can be seen from this relation that the buckling capacity cannot be obtained at a testing load level below P_{cr} if there is no initial bow since a perfectly straight strut would not show any lateral deflection until the strut collapses at $P = P_{cr}$.

With an eccentricity added to the possible initial bow, the entire right-hand side of equation (4′) would be applied. The effect of eccentricity appears to be coupled with λL and P/P_{cr} in a form much more complicated than that of an initial bow alone. Actually, a simplified approximation as elegant as that of an initial bow can be obtained. The simplification starts with a series expansion of the cosine function. It is then followed by a series inversion and a multiplication. The final results of equation (4′), with the help of $\lambda L = \pi\sqrt{P/P_{cr}}$, becomes

$$P_{cr}v - d = a + \frac{\pi^2}{8} e\left[1 + \left(\frac{5\pi^2}{48} - 1\right)\frac{P}{P_{cr}} + \frac{5\pi^2}{48}\left(\frac{61\pi^2}{600} - 1\right)\left(\frac{P}{P_{cr}}\right)^2 + \ldots\right]$$

$$= a + 1.234e\left[1 + 0.028\left(\frac{P}{P_{cr}}\right) + 0.004\left(\frac{P}{P_{cr}}\right)^2 + \ldots\right] \tag{5}$$

An examination of the coefficients indicates that the maximum contribution of the P/P_{cr} term is less than three percent of P/P_{cr}. By neglecting the effect of P/P_{cr} in the right-hand side of equation (5), one obtains a form of first order approximation

$$P_{cr}v - d = a + 1.234e \tag{6}$$

Therefore, the effect of load eccentricity correlates to the critical buckling load in the same fashion as of the initial bow except that the negative intercept is now the sum of the initial bow and 1.234 times of the eccentricity. Explicitly, with a larger eccentricity, the buckling capacity can be estimated at a larger lateral deflection for the same axial force. In other words, it can be estimated at the same deflection with a smaller axial force. Effectively, the result would have less error introduced by measuring gauges for a larger eccentricity. The initial bow would be the negative intercept of the d axis subtracted by $1.234e$.

Conclusion

The buckling capacity and the associated stiffness properties of a strut can be accurately estimated at tests of low axial forces if the strut is loaded with an eccentricity. The initial bow is obtained by subtracting a factor of the eccentricity from the negative intercept of d axis.

Acknowledgment

The author is grateful to Pin-Fun Tsai for her beneficial suggestions and discussions.

References

Donnell, L. H., 1938, "On the Application of Southwell's Method for the Analysis of Buckling Tests," *S. Timoshenko 60th Anniversary Volume*, McGraw-Hill, New York, pp. 27–38.

Horton, W. H., Cundari, F. L., and Johnson, R. W., 1971, "Applicability of the Southwell Plot to the Interpretation of Test Data Obtained from Stability Studies of Elastic Column and Plate Structures," U.S. Army Air Mobility Research and Development Laboratory, Fort Eustis, VA, Contract DA 44-177-AMC-258(T).

Southwell, R. V., 1969, *An Introduction to the Theory of Elasticity*, Dover Publications Inc., New York, pp. 424–429.

Tsai, W. T., 1977, "Nonlinear Behavior of Compression Members," ASCE Structural Div., pp. 1484–1489.

Mode II Loading of a Cracked Strip

D. M. Parks[4]

Energy methods have been widely used in the analysis of fracture mechanics problems, making use of the equivalence of compliance (stiffness) changes with respect to crack length and the energy release rate, J (Rice, 1968). One approach to the analysis of certain configurations, such as the double cantilever beam, has been to idealize the total compliance of the body using, e.g., assumptions of beam theory in relatively compliant portions of the body and of rigid bodies in relatively stiffer regions. Most analyses of this sort have been applied to Mode I problems. The purpose of this note is to present an elementary energy analysis of a Mode II problem which seems

---

[4] Department of Mechanical Engineering, Massachusetts Institute of Technology, Cambridge, Mass. 02139.

Manuscript received by ASME Applied Mechanics Division, May 19, 1986.

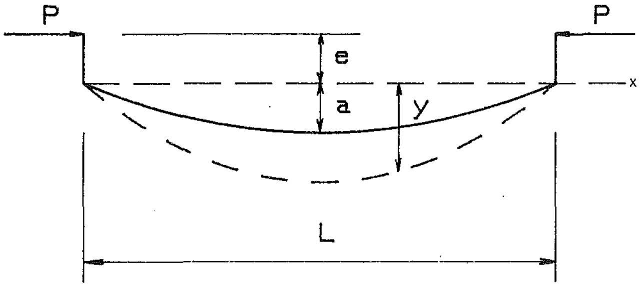

Fig. 1 Geometry of a strut

where EI is the bending rigidity of the strut, e the eccentricity, P the axial force, y the total deflection, and y_o the initial bow. In order to simplify the analysis, the initial bow is assumed to be a simple sine function

$$y_o = a \sin \frac{\pi x}{L} \tag{2}$$

This was shown by Southwell to be a good approximation for determination of the lateral deflection. Upon introduction of equation (2) and the boundary conditions, $y = 0$ at $x = 0$ and $x = L$, into equation (1), the total deflection is given by Tsai (1977)

$$y = \frac{a}{1 - P/P_{cr}} \sin \frac{\pi x}{L} + e\left[\frac{\cos \lambda\ (L/2 - x)}{\cos\ (\lambda L/2)} - 1\right] \tag{3}$$

where $P_{cr} = \pi^2 EI/L^2$ is the buckling capacity of the strut if it were perfectly straight, and $\lambda = \sqrt{P/EI} = \sqrt{P/P_{cr}}\pi/L$.

Application of Southwell's Method

To apply equation (3) to Southwell's test, the net deflection at the middle point is to be measured. By introducing $x = L/2$ into equation (3), the net deflection, $d = y - y_o$, is given by

$$d = \frac{a}{P_{cr}/P - 1} + e\left[\frac{1}{\cos(\lambda L/2)} - 1\right] \tag{4}$$

This expression may be rewritten into an alternate form upon multiplying equation (4) by a factor, $P_{cr}/P - 1$, and defining $v = d/P$, the result reads

$$P_{cr}v - d = a + e\left[\frac{1}{\cos(\lambda L/2)} - 1\right]\left(\frac{P_{cr}}{P} - 1\right) \tag{4'}$$

The left-hand side together with the first term of the right-hand side of equation (4′) is the typical form of Southwell's approach. By plotting v as the abscissa and d as the ordinate, a straight line is obtained. The slope of this straight line is the buckling capacity and the negative intercept of the d axis is the initial bow at the mid-span. It can be seen from this relation that the buckling capacity cannot be obtained at a testing load level below P_{cr} if there is no initial bow since a perfectly straight strut would not show any lateral deflection until the strut collapses at $P = P_{cr}$.

With an eccentricity added to the possible initial bow, the entire right-hand side of equation (4′) would be applied. The effect of eccentricity appears to be coupled with λL and P/P_{cr} in a form much more complicated than that of an initial bow alone. Actually, a simplified approximation as elegant as that of an initial bow can be obtained. The simplification starts with a series expansion of the cosine function. It is then followed by a series inversion and a multiplication. The final results of equation (4′), with the help of $\lambda L = \pi\sqrt{P/P_{cr}}$, becomes

$$\begin{aligned} P_{cr}v - d &= a + \frac{\pi^2}{8} e\left[1 + \left(\frac{5\pi^2}{48} - 1\right)\frac{P}{P_{cr}} + \frac{5\pi^2}{48}\left(\frac{61\pi^2}{600} - 1\right)\left(\frac{P}{P_{cr}}\right)^2 + \ldots\right] \\ &= a + 1.234e\left[1 + 0.028\left(\frac{P}{P_{cr}}\right) + 0.004\left(\frac{P}{P_{cr}}\right)^2 + \ldots\right] \end{aligned} \tag{5}$$

An examination of the coefficients indicates that the maximum contribution of the P/P_{cr} term is less than three percent of P/P_{cr}. By neglecting the effect of P/P_{cr} in the right-hand side of equation (5), one obtains a form of first order approximation

$$P_{cr}v - d = a + 1.234e \tag{6}$$

Therefore, the effect of load eccentricity correlates to the critical buckling load in the same fashion as of the initial bow except that the negative intercept is now the sum of the initial bow and 1.234 times of the eccentricity. Explicitly, with a larger eccentricity, the buckling capacity can be estimated at a larger lateral deflection for the same axial force. In other words, it can be estimated at the same deflection with a smaller axial force. Effectively, the result would have less error introduced by measuring gauges for a larger eccentricity. The initial bow would be the negative intercept of the d axis subtracted by $1.234e$.

Conclusion

The buckling capacity and the associated stiffness properties of a strut can be accurately estimated at tests of low axial forces if the strut is loaded with an eccentricity. The initial bow is obtained by subtracting a factor of the eccentricity from the negative intercept of d axis.

Acknowledgment

The author is grateful to Pin-Fun Tsai for her beneficial suggestions and discussions.

References

Donnell, L. H., 1938, "On the Application of Southwell's Method for the Analysis of Buckling Tests," *S. Timoshenko 60th Anniversary Volume*, McGraw-Hill, New York, pp. 27–38.

Horton, W. H., Cundari, F. L., and Johnson, R. W., 1971, "Applicability of the Southwell Plot to the Interpretation of Test Data Obtained from Stability Studies of Elastic Column and Plate Structures," U.S. Army Air Mobility Research and Development Laboratory, Fort Eustis, VA, Contract DA 44-177-AMC-258(T).

Southwell, R. V., 1969, *An Introduction to the Theory of Elasticity*, Dover Publications Inc., New York, pp. 424–429.

Tsai, W. T., 1977, "Nonlinear Behavior of Compression Members," ASCE Structural Div., pp. 1484–1489.

Mode II Loading of a Cracked Strip

D. M. Parks[4]

Energy methods have been widely used in the analysis of fracture mechanics problems, making use of the equivalence of compliance (stiffness) changes with respect to crack length and the energy release rate, J (Rice, 1968). One approach to the analysis of certain configurations, such as the double cantilever beam, has been to idealize the total compliance of the body using, e.g., assumptions of beam theory in relatively compliant portions of the body and of rigid bodies in relatively stiffer regions. Most analyses of this sort have been applied to Mode I problems. The purpose of this note is to present an elementary energy analysis of a Mode II problem which seems

---

[4] Department of Mechanical Engineering, Massachusetts Institute of Technology, Cambridge, Mass. 02139.

Manuscript received by ASME Applied Mechanics Division, May 19, 1986.

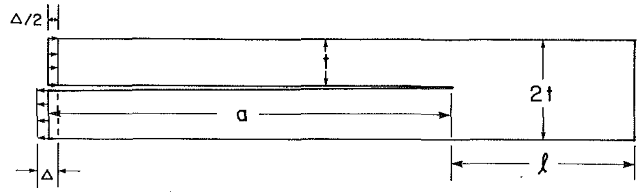

Fig. 1 A long symmetrically cracked strip subject to a uniform relative end displacement of magnitude Δ

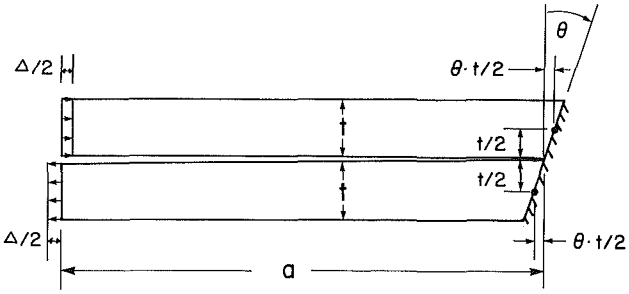

Fig. 2 Idealized model consisting of beam/column kinematics

to have been inappropriately analyzed in a well-known compendium of stress intensity factors (Tada et al., 1985).

Consider in Fig. 1 the long strip of unit thickness and height $2t$ containing a crack of length $a >> t$ which divides a portion of the body into two strips, each of height t. Ahead of the crack tip is an uncracked ligament of length ℓ, which is also much greater than t. Loading is imposed at the end of the body by uniform displacements parallel to the crack. On the upper strip, the displacement is positive, of magnitude $\Delta/2$, while on the lower strip, a displacement of equal magnitude, but opposite sign, is imposed. The relative offset of the ends of the two strips is Δ. Such loading nominally places the upper strip in compression and the lower strip in tension. A closer examination, however, reveals additional complexity. For example, if the resultant forces in the two strips are $\mp P$, we note that since they are offset by a distance t, bending moments must also be sustained in each strip.

Figure 2 presents an idealized kinematical model of the deformation in the two strips which allows for an effective rigid body rotation of angle θ in the ligament material far ahead of the tip. In the general case of unequal strips, the "base" at the crack tip should also be permitted a free displacement δ in the crack direction, but in the present case, symmetry considerations show that $\delta = 0$.

We see from Fig. 2 that each strip is in combined bending and tension (bottom) or compression (top). The mid-section strain, ϵ, in the bottom strip is:

$$\epsilon = (\Delta/2 - \theta \cdot t/2)/a \tag{1}$$

while the curvature is:

$$\kappa = \theta/a. \tag{2}$$

The top strip has the same curvature and midsection strain equal to $-\epsilon$.

In this displacement-loaded problem, the potential energy, π, per unit thickness is the strain energy, W. For isotropic elastic response, the total strain energy in the two strips is

$$\begin{aligned} W &= 2 \cdot [1/2E' \cdot ta \cdot \epsilon^2 + 1/2E'I \cdot \kappa^2 \cdot a] \\ &= E't/4a \cdot [(t\theta - \Delta)^2 + \theta^2/3]. \end{aligned} \tag{3}$$

In equation (3), $I = t^3/12$ is the strip section moment of inertia per unit thickness, E' is the Young's modulus, E, for generalized plane stress, and $E/(1-\nu^2)$, where ν is Poisson's ratio, for plane strain. Evidently, W depends on the kinematical parameters Δ and θ. Since no external moment is applied to the ligament region, Castigliano's theorem requires $\partial W/\partial\theta = 0$, furnishing

$$\theta = 3\Delta/4t. \tag{4}$$

When equation (4) is substituted into equation (5), the strain energy becomes

$$\pi = W = E' \cdot t \cdot \Delta^2/16a \tag{5}$$

and the energy release rate is

$$J = -\partial\pi/\partial a = E' \cdot t \cdot \Delta^2/16a^2. \tag{6}$$

From the symmetry of the problem, only Mode II is present so $J = K_{\mathrm{II}}^2/E'$ and thus

$$K_{\mathrm{II}} = \Delta/4a \cdot E'\sqrt{t}. \tag{7}$$

Tada's result can be obtained by setting $\theta = 0$, with resulting W and J values four times that of equations (5), (6) and thus K_{II} values twice that of equation (7).

By permitting the additional kinematic freedom corresponding to nonzero θ, a decidedly lower strain energy is obtained, so presumably equations (6) and (7) are more correct. This has been verified numerically by Sharples (1985), who analyzed this problem in a strip with $a/t = 36.5$ and $\ell/t = 3.5$ using the virtual crack extension (VCE) capabilities of the ABAQUS finite element program (Hibbitt, et al., 1982). His numerical results for J on each of several VCE contours were in excellent agreement with equation (6).

The methodology of beam/columns applied in this example could be straightforwardly generalized to include strips of unequal section area and moment of inertia. In addition, analysis for nonlinear material response could be accommodated by using standard nonlinear models of cylinders under combined bending and axial load.

Acknowledgment

This problem was brought to my attention by David Hibbitt. I am grateful to John Sharples of UKAEA for performing corroboratory finite element analysis.

References

Hibbitt, H. D., Karlsson, B. I., and Sorensen, E. P., 1982, ABAQUS User's Manual, Theory Manual, HKS Inc., Providence, R.I.

Rice, J. R., 1968, "Mathematical Analysis in the Mechanics of Fracture," in *Fracture, Vol. II*, Leibowitz, H., ed., Academic Press, N.Y., pp. 191–311.

Sharples, J. K., 1985, Private communication to H. D. Hibbitt.

Tada, H., Paris, P. C., and Irwin, G. R., 1985, *The Stress Analysis of Cracks Handbook*, Paris Productions Inc., St. Louis, MO, p. 8–29.

Proof of a Conjecture in Elastic Membrane Theory

D. J. Steigmann[5]

Analyses of problems in elastic membrane theory usually employ the ad hoc assumption that an equilibrium configuration cannot be stable or neutrally stable unless the principal stresses are everywhere nonnegative (e.g., Kydoniefs and Spencer, 1969). We show that this result follows directly from the principle of minimum potential energy, where the potential energy $E[\mathbf{x}]$ is given by

$$E[\mathbf{x}] = \int_{\Omega} \phi(\mathbf{x},\mathbf{a}_\alpha)\sqrt{A}\,d\theta^1 d\theta^2 - \int_{\partial\Omega_t} \zeta(\mathbf{x})ds. \tag{1}$$

---

[5] Division of Engineering, Brown University, Providence, R.I. 02912.

Manuscript received by ASME Applied Mechanics Division, February 28, 1986; final revision June 23, 1986.

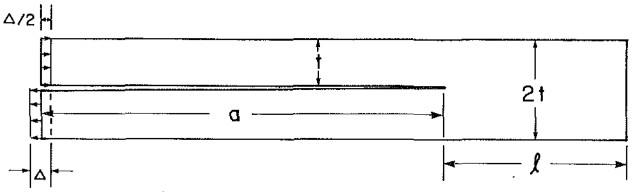

Fig. 1 A long symmetrically cracked strip subject to a uniform relative end displacement of magnitude Δ

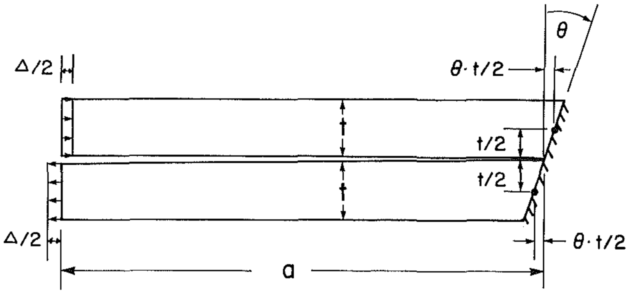

Fig. 2 Idealized model consisting of beam/column kinematics

to have been inappropriately analyzed in a well-known compendium of stress intensity factors (Tada et al., 1985).

Consider in Fig. 1 the long strip of unit thickness and height $2t$ containing a crack of length $a >> t$ which divides a portion of the body into two strips, each of height t. Ahead of the crack tip is an uncracked ligament of length ℓ, which is also much greater than t. Loading is imposed at the end of the body by uniform displacements parallel to the crack. On the upper strip, the displacement is positive, of magnitude $\Delta/2$, while on the lower strip, a displacement of equal magnitude, but opposite sign, is imposed. The relative offset of the ends of the two strips is Δ. Such loading nominally places the upper strip in compression and the lower strip in tension. A closer examination, however, reveals additional complexity. For example, if the resultant forces in the two strips are $\mp P$, we note that since they are offset by a distance t, bending moments must also be sustained in each strip.

Figure 2 presents an idealized kinematical model of the deformation in the two strips which allows for an effective rigid body rotation of angle θ in the ligament material far ahead of the tip. In the general case of unequal strips, the "base" at the crack tip should also be permitted a free displacement δ in the crack direction, but in the present case, symmetry considerations show that $\delta = 0$.

We see from Fig. 2 that each strip is in combined bending and tension (bottom) or compression (top). The mid-section strain, ϵ, in the bottom strip is:

$$\epsilon = (\Delta/2 - \theta \cdot t/2)/a \tag{1}$$

while the curvature is:

$$\kappa = \theta/a. \tag{2}$$

The top strip has the same curvature and midsection strain equal to $-\epsilon$.

In this displacement-loaded problem, the potential energy, π, per unit thickness is the strain energy, W. For isotropic elastic response, the total strain energy in the two strips is

$$\begin{aligned} W &= 2\cdot[1/2E' \cdot ta \cdot \epsilon^2 + 1/2E'I \cdot \kappa^2 \cdot a] \\ &= E't/4a \cdot [(t\theta - \Delta)^2 + \theta^2/3]. \end{aligned} \tag{3}$$

In equation (3), $I = t^3/12$ is the strip section moment of inertia per unit thickness, E' is the Young's modulus, E, for generalized plane stress, and $E/(1-\nu^2)$, where ν is Poisson's ratio, for plane strain. Evidently, W depends on the kinematical parameters Δ and θ. Since no external moment is applied to the ligament region, Castigliano's theorem requires $\partial W/\partial\theta = 0$, furnishing

$$\theta = 3\Delta/4t. \tag{4}$$

When equation (4) is substituted into equation (5), the strain energy becomes

$$\pi = W = E' \cdot t \cdot \Delta^2/16a \tag{5}$$

and the energy release rate is

$$J = -\partial\pi/\partial a = E' \cdot t \cdot \Delta^2/16a^2. \tag{6}$$

From the symmetry of the problem, only Mode II is present so $J = K_{\rm II}{}^2/E'$ and thus

$$K_{\rm II} = \Delta/4a \cdot E'\sqrt{t}. \tag{7}$$

Tada's result can be obtained by setting $\theta = 0$, with resulting W and J values four times that of equations (5), (6) and thus $K_{\rm II}$ values twice that of equation (7).

By permitting the additional kinematic freedom corresponding to nonzero θ, a decidedly lower strain energy is obtained, so presumably equations (6) and (7) are more correct. This has been verified numerically by Sharples (1985), who analyzed this problem in a strip with $a/t = 36.5$ and $\ell/t = 3.5$ using the virtual crack extension (VCE) capabilities of the ABAQUS finite element program (Hibbitt, et al., 1982). His numerical results for J on each of several VCE contours were in excellent agreement with equation (6).

The methodology of beam/columns applied in this example could be straightforwardly generalized to include strips of unequal section area and moment of inertia. In addition, analysis for nonlinear material response could be accommodated by using standard nonlinear models of cylinders under combined bending and axial load.

Acknowledgment

This problem was brought to my attention by David Hibbitt. I am grateful to John Sharples of UKAEA for performing corroboratory finite element analysis.

References

Hibbitt, H. D., Karlsson, B. I., and Sorensen, E. P., 1982, ABAQUS User's Manual, Theory Manual, HKS Inc., Providence, R.I.

Rice, J. R., 1968, "Mathematical Analysis in the Mechanics of Fracture," in *Fracture, Vol. II*, Leibowitz, H., ed., Academic Press, N.Y., pp. 191-311.

Sharples, J. K., 1985, Private communication to H. D. Hibbitt.

Tada, H., Paris, P. C., and Irwin, G. R., 1985, *The Stress Analysis of Cracks Handbook*, Paris Productions Inc., St. Louis, MO, p. 8-29.

Proof of a Conjecture in Elastic Membrane Theory

D. J. Steigmann[5]

Analyses of problems in elastic membrane theory usually employ the ad hoc assumption that an equilibrium configuration cannot be stable or neutrally stable unless the principal stresses are everywhere nonnegative (e.g., Kydoniefs and Spencer, 1969). We show that this result follows directly from the principle of minimum potential energy, where the potential energy $E[\mathbf{x}]$ is given by

$$E[\mathbf{x}] = \int_\Omega \phi(\mathbf{x}, \mathbf{a}_\alpha)\sqrt{A}\,d\theta^1 d\theta^2 - \int_{\partial\Omega_t} \zeta(\mathbf{x})\,ds. \tag{1}$$

---

[5] Division of Engineering, Brown University, Providence, R.I. 02912.

Manuscript received by ASME Applied Mechanics Division, February 28, 1986; final revision June 23, 1986.

Here $\theta^\alpha\,(\alpha=1,2)$ are embedded coordinates of a material point on the membrane surface, $\mathbf{x}(\theta^1,\theta^2)$ is the position, $\mathbf{a}_\alpha \equiv \partial\mathbf{x}/\partial\theta^\alpha$ span the tangent plane at $\mathbf{x}$, $A \equiv \det(A_{\alpha\beta})$, $A_{\alpha\beta} \equiv \mathbf{A}_\alpha \cdot \mathbf{A}_\beta$, $\mathbf{A}_\alpha \equiv \partial\mathbf{X}/\partial\theta^\alpha$, $\mathbf{X}(\theta^1,\theta^2)$ is the position on the reference surface, $\zeta(\mathbf{x})$ is a potential for the force $\mathbf{t}(=\zeta_{\mathbf{x}})$ per unit reference arc length s applied to the edge $\partial\Omega_t$ of the reference surface Ω, and

$$\phi(\mathbf{x},\mathbf{a}_\alpha) = w(\mathbf{a}_\alpha) - \psi(\mathbf{x},\mathbf{a}_\alpha), \tag{2}$$[2]

where w is the strain energy and ψ is a load potential.

We adopt the energy criterion of elastic stability, according to which a stable or neutrally stable configuration $\mathbf{x}$ is a strong relative minimizer of $E[\mathbf{x}]$. Following Graves (1939), we conclude that $\phi(\mathbf{x},\mathbf{a}_\alpha)$ must be rank-one convex in $\mathbf{a}_\alpha$:

$$\phi(\mathbf{x},\mathbf{a}_\beta+\mathbf{f}n_\beta) - \phi(\mathbf{x},\mathbf{a}_\beta) - n_\alpha\mathbf{f}\cdot\phi_{\mathbf{a}_\alpha}(\mathbf{x},\mathbf{a}_\beta) \geq 0 \tag{3}$$[3]

for all vectors $\mathbf{f} = f^\alpha\mathbf{a}_\alpha + f\mathbf{a}_3$ and $\mathbf{n} = n_\alpha\mathbf{A}^\alpha$, where $\mathbf{A}^\alpha$ is the dual basis on the reference surface: $\mathbf{A}^\alpha \cdot \mathbf{A}_\beta = \delta^\alpha_\beta$. We consider load potentials ψ which are rank-one affine in $\mathbf{a}_\alpha$:

$$\psi(\mathbf{x},\mathbf{a}_\beta+\mathbf{f}n_\beta) - \psi(\mathbf{x},\mathbf{a}_\beta) - n_\alpha\mathbf{f}\cdot\psi_{\mathbf{a}_\alpha}(\mathbf{x},\mathbf{a}_\beta) \equiv 0. \tag{4}$$

An important example is uniform lateral pressure loading of constant intensity p. For a closed membrane we have $\int\psi\sqrt{A}d\theta^1 d\theta^2 = pV$, where the enclosed volume is $V = (1/3)\int\mathbf{x} \cdot \mathbf{a}_3\sqrt{a}d\theta^1 d\theta^2$; $a \equiv \det(a_{\alpha\beta})$, $a_{\alpha\beta} \equiv \mathbf{a}_\alpha \cdot \mathbf{a}_\beta$, and $\mathbf{a}_3 = e^{\alpha\beta}\mathbf{a}_\alpha \times \mathbf{a}_\beta/2\sqrt{a}$ is the unit normal to the deformed surface. $e^{\alpha\beta}$ is the two-dimensional alternator taking values 1, -1 according as $(\alpha,\beta) = (1,2), (2,1)$, respectively, and zero otherwise. The load potential is

$$\psi(\mathbf{x},\mathbf{a}_\alpha) = (p/6)\mu^{\alpha\beta}\mathbf{x}\cdot\mathbf{a}_\alpha \times \mathbf{a}_\beta;\ \mu^{\alpha\beta} \equiv e^{\alpha\beta}/\sqrt{A}. \tag{5}$$

Then $\psi_{\mathbf{a}_\alpha} = (p/3)\mu^{\alpha\beta}\,\mathbf{a}_\beta \times \mathbf{x}$, and after some calculation we find

$$n_\alpha\mathbf{f}\cdot\psi_{\mathbf{a}_\alpha} = (p/3)\mu^{\alpha\beta}\,n_\beta\,\mathbf{x}\cdot\mathbf{a}_\alpha \times \mathbf{f} \text{ and } \psi(\mathbf{x},\mathbf{a}_\gamma+\mathbf{f}n_\gamma)$$
$$= \psi(\mathbf{x},\mathbf{a}_\gamma) + (p/3)\mu^{\alpha\beta}n_\beta\mathbf{x}\cdot\mathbf{a}_\alpha \times \mathbf{f},$$

so that (4) is identically satisfied. Then (2) and (4) require that w be rank-one convex:

$$w(\mathbf{a}_\beta+\mathbf{f}n_\beta) - w(\mathbf{a}_\beta) - n_\alpha\mathbf{f}\cdot w_{\mathbf{a}_\alpha}(\mathbf{a}_\beta) \geq 0,\ \forall\mathbf{f}n_\alpha. \tag{6}$$

According to the principle of material frame indifference, the strain energy must be insensitive to transformations $\mathbf{a}_\alpha \rightarrow \mathbf{Q}\mathbf{a}_\alpha$ for all proper orthogonal $\mathbf{Q}$. Then Cauchy's theorem on isotropic functions (Truesdell and Noll, 1965) requires that w be a function of the metric components $a_{\alpha\beta}$, so that

$$w_{\mathbf{a}_\alpha} = 2(\partial w/\partial a_{\alpha\beta})\mathbf{a}_\beta. \tag{7}$$

From (6), (7) and the mean value theorem, we derive the Legendre-Hadamard condition:

$$\mathbf{f}\cdot\mathbf{E}^{\alpha\beta}(\hat{\mathbf{a}}_\gamma)n_\alpha n_\beta\cdot\mathbf{f} \geq 0;\ \hat{\mathbf{a}}_\gamma \equiv \mathbf{a}_\gamma + t\mathbf{f}n_\gamma,\ t\epsilon(0,1), \tag{8}$$

where

$$\mathbf{E}^{\alpha\beta}(\mathbf{a}_\gamma) \equiv 4(\partial^2 w/\partial a_{\alpha\gamma}\partial a_{\beta\epsilon})\mathbf{a}_\gamma \otimes \mathbf{a}_\epsilon + 2(\partial w/\partial a_{\alpha\beta})\mathbf{1} \tag{9}$$

and $\mathbf{1} = \mathbf{a}_\alpha \otimes \mathbf{a}^\alpha + \mathbf{a}_3 \otimes \mathbf{a}_3$ is the unit tensor. The choice $f^\alpha = 0$ in (8) gives

$$n_\alpha n_\beta \partial w/\partial a_{\alpha\beta} \geq 0. \tag{10}$$

Let n_α be the unit normal to a curve in the reference surface. The unit normal $\boldsymbol{\nu} = \nu_\alpha\mathbf{a}^\alpha$ to the image of the curve in the deformed surface is given by $\nu_\alpha = \sqrt{(a/A)}n_\alpha/\lambda$, where λ is the stretch of the curve (Naghdi, 1972). Then (10) is equivalent to

$$N^{\alpha\beta}\nu_\alpha\nu_\beta \geq 0, \tag{11}$$

where $N^{\alpha\beta} = 2\sqrt{(A/a)}\,\partial w/\partial a_{\alpha\beta}$ are the Cauchy stresses. Thus an equilibrium configuration of a membrane subjected to conservative loading is stable or neutrally stable only if the principal Cauchy tensions are pointwise nonnegative. The choice $f \equiv \mathbf{f}\cdot\mathbf{a}_3 = 0$ in (8) gives the two-dimensional analogue of the classical Legendre-Hadamard condition:

$$4n_\alpha n_\beta f_\gamma f_\epsilon(\partial^2 w/\partial a_{\alpha\gamma}\partial a_{\beta\epsilon}) + \sqrt{(a/A)}N^{\alpha\beta}n_\alpha n_\beta f^\gamma f_\gamma \geq 0,\ \forall f^\alpha n_\beta. \tag{12}$$

Pipkin (1985) has derived conditions equivalent to (11) and (12) for the special case of an initially plane isotropic membrane with fixed edges and $\psi = 0$, and has shown that the classical Baker-Ericksen inequality (Baker and Ericksen, 1954) is implied by (12).

Acknowledgment

The support of the Materials Research Lab in the Division of Engineering at Brown University is gratefully acknowledged.

References

Baker, M., and Ericksen, J. L., 1954, "Inequalities Restricting the Form of the Stress-Deformation Relations for Isotropic Solids and Reiner-Rivlin Fluids," *Journal of the Washington Academy of Sciences*, Vol. 44, pp. 33–35.

Graves, L. M., 1939, "The Weierstrass Condition for Multiple Integral Variation Problems," *Duke Mathematical Journal*, Vol. 5, p. 656.

Kydoniefs, A. D., and Spencer, A. J. M., 1969, "Finite Axisymmetric Deformations of an Initially Cylindrical Elastic Membrane," *Quarterly Journal of Mechanics and Applied Mathematics*, Vol. 22, pp. 87–95.

Naghdi, P. M., 1972, "The Theory of Plates and Shells," *Handbuch der Physik*, Vol. VIa/2, Flügge, S., ed., Springer-Verlag.

Pipkin, A. C., 1985, "The Relaxed Energy Density for Isotropic Elastic Membranes," Division of Appl. Math., Brown University.

Truesdell, C., and Noll, W., 1965, "The Nonlinear Field Theories of Mechanics," *Handbuch der Physik*, Vol. III/3, Flügge, S., ed., Springer-Verlag.

Pneumatic Chamber Nonlinearities

Ying-Tsai Wang[6,8] and Rajendra Singh[7,8]

1 Introduction

This note examines the nature of nonlinearities associated with a closed pneumatic chamber coupled to a linear mechanical system as shown in Fig. 1. This simple model could represent several practical applications dealing with passive vibration isolators, shock absorbers, and cushioning type actuators. The feasibility of finding an approximate analytical solution for such systems using perturbation techniques has not been investigated, with the exception of a paper by Chen (1977), who analyzed a symmetric, double-sided closed pneumatic chamber system coupled to a cam-actuated mechanism. His study considered only the nonlinearity induced by the gas compressibility; the dynmic response was obtained by the Krylov-Bogoliubov method of slowly varying parameters. Even though no numerical or experimental validation was given, his analysis found that the resonant peak shifted toward a lower frequency as the excitation amplitude was increased. However, he did not examine some of the critical issues dealing with singularities, mean value shifting,

---

[2] ϕ may depend on θ^α explicitly, as in the case of nonhomogeneous material, for example.

[3] Graves considered functionals of the form (1) without the boundary integral. In arriving at (3), he employed variations in $\mathbf{x}$ which vanish on the boundary, so the result is unaffected by the presence of the extra term.

[6] Currently with the National Taiwan Institute of Technology, Republic of China.

[7] Associate Professor, Mem. ASME.

[8] Fluid Power Laboratory, Department of Mechanical Engineering, The Ohio State University, Columbus, Ohio 43210.

Manuscript received by the ASME Applied Mechanics Division June 25, 1985; final revision March 4, 1986.

Here $\theta^\alpha (\alpha=1,2)$ are embedded coordinates of a material point on the membrane surface, $\mathbf{x}(\theta^1,\theta^2)$ is the position, $\mathbf{a}_\alpha \equiv \partial\mathbf{x}/\partial\theta^\alpha$ span the tangent plane at $\mathbf{x}$, $A \equiv \det(A_{\alpha\beta})$, $A_{\alpha\beta} \equiv \mathbf{A}_\alpha \cdot \mathbf{A}_\beta$, $\mathbf{A}_\alpha \equiv \partial\mathbf{X}/\partial\theta^\alpha$, $\mathbf{X}(\theta^1,\theta^2)$ is the position on the reference surface, $\zeta(\mathbf{x})$ is a potential for the force $\mathbf{t}(=\zeta_{\mathbf{x}})$ per unit reference arc length s applied to the edge $\partial\Omega_t$ of the reference surface Ω, and

$$\phi(\mathbf{x},\mathbf{a}_\alpha)=w(\mathbf{a}_\alpha)-\psi(\mathbf{x},\mathbf{a}_\alpha), \qquad (2)$$[2]

where w is the strain energy and ψ is a load potential.

We adopt the energy criterion of elastic stability, according to which a stable or neutrally stable configuration $\mathbf{x}$ is a strong relative minimizer of $E[\mathbf{x}]$. Following Graves (1939), we conclude that $\phi(\mathbf{x},\mathbf{a}_\alpha)$ must be rank-one convex in $\mathbf{a}_\alpha$:

$$\phi(\mathbf{x},\mathbf{a}_\beta+\mathbf{f}n_\beta)-\phi(\mathbf{x},\mathbf{a}_\beta)-n_\alpha\mathbf{f}\cdot\phi_{\mathbf{a}_\alpha}(\mathbf{x},\mathbf{a}_\beta)\geq 0 \qquad (3)$$[3]

for all vectors $\mathbf{f} = f^\alpha\mathbf{a}_\alpha + f\mathbf{a}_3$ and $\mathbf{n} = n_\alpha\mathbf{A}^\alpha$, where $\mathbf{A}^\alpha$ is the dual basis on the reference surface: $\mathbf{A}^\alpha \cdot \mathbf{A}_\beta = \delta^\alpha_\beta$. We consider load potentials ψ which are rank-one affine in $\mathbf{a}_\alpha$:

$$\psi(\mathbf{x},\mathbf{a}_\beta+\mathbf{f}n_\beta)-\psi(\mathbf{x},\mathbf{a}_\beta)-n_\alpha\mathbf{f}\cdot\psi_{\mathbf{a}_\alpha}(\mathbf{x},\mathbf{a}_\beta)\equiv 0. \tag{4}$$

An important example is uniform lateral pressure loading of constant intensity p. For a closed membrane we have $\int\psi\sqrt{A}d\theta^1 d\theta^2 = pV$, where the enclosed volume is $V = (1/3)\int\mathbf{x} \cdot \mathbf{a}_3\sqrt{a}d\theta^1 d\theta^2$; $a \equiv \det(a_{\alpha\beta})$, $a_{\alpha\beta} \equiv \mathbf{a}_\alpha \cdot \mathbf{a}_\beta$, and $\mathbf{a}_3 = e^{\alpha\beta}\mathbf{a}_\alpha \times \mathbf{a}_\beta/2\sqrt{a}$ is the unit normal to the deformed surface. $e^{\alpha\beta}$ is the two-dimensional alternator taking values 1, -1 according as $(\alpha,\beta) = (1,2), (2,1)$, respectively, and zero otherwise. The load potential is

$$\psi(\mathbf{x},\mathbf{a}_\alpha)=(p/6)\mu^{\alpha\beta}\mathbf{x}\cdot\mathbf{a}_\alpha\times\mathbf{a}_\beta;\ \mu^{\alpha\beta}\equiv e^{\alpha\beta}/\sqrt{A}. \tag{5}$$

Then $\psi_{\mathbf{a}_\alpha} = (p/3)\mu^{\alpha\beta}\,\mathbf{a}_\beta \times \mathbf{x}$, and after some calculation we find

$$n_\alpha\mathbf{f}\cdot\psi_{\mathbf{a}_\alpha}=(p/3)\mu^{\alpha\beta}\,n_\beta\,\mathbf{x}\cdot\mathbf{a}_\alpha\times\mathbf{f} \text{ and } \psi(\mathbf{x},\mathbf{a}_\gamma+\mathbf{f}n_\gamma)$$
$$=\psi(\mathbf{x},\mathbf{a}_\gamma)+(p/3)\mu^{\alpha\beta}n_\beta\mathbf{x}\cdot\mathbf{a}_\alpha\times\mathbf{f},$$

so that (4) is identically satisfied. Then (2) and (4) require that w be rank-one convex:

$$w(\mathbf{a}_\beta+\mathbf{f}n_\beta)-w(\mathbf{a}_\beta)-n_\alpha\mathbf{f}\cdot w_{\mathbf{a}_\alpha}(\mathbf{a}_\beta)\geq 0,\ \forall\mathbf{f}n_\alpha. \tag{6}$$

According to the principle of material frame indifference, the strain energy must be insensitive to transformations $\mathbf{a}_\alpha\rightarrow\mathbf{Q}\mathbf{a}_\alpha$ for all proper orthogonal $\mathbf{Q}$. Then Cauchy's theorem on isotropic functions (Truesdell and Noll, 1965) requires that w be a function of the metric components $a_{\alpha\beta}$, so that

$$w_{\mathbf{a}_\alpha}=2(\partial w/\partial a_{\alpha\beta})\mathbf{a}_\beta. \tag{7}$$

From (6), (7) and the mean value theorem, we derive the Legendre-Hadamard condition:

$$\mathbf{f}\cdot\mathbf{E}^{\alpha\beta}(\hat{\mathbf{a}}_\gamma)n_\alpha n_\beta\cdot\mathbf{f}\geq 0;\ \hat{\mathbf{a}}_\gamma\equiv\mathbf{a}_\gamma+t\mathbf{f}n_\gamma,\ t\in(0,1), \tag{8}$$

where

$$\mathbf{E}^{\alpha\beta}(\mathbf{a}_\gamma)\equiv 4(\partial^2 w/\partial a_{\alpha\gamma}\partial a_{\beta\epsilon})\mathbf{a}_\gamma\otimes\mathbf{a}_\epsilon+2(\partial w/\partial a_{\alpha\beta})\mathbf{1} \tag{9}$$

and $\mathbf{1} = \mathbf{a}_\alpha \otimes \mathbf{a}^\alpha + \mathbf{a}_3 \otimes \mathbf{a}_3$ is the unit tensor. The choice $f^\alpha = 0$ in (8) gives

$$n_\alpha n_\beta\partial w/\partial a_{\alpha\beta}\geq 0. \tag{10}$$

Let n_α be the unit normal to a curve in the reference surface. The unit normal $\boldsymbol{\nu} = \nu_\alpha\mathbf{a}^\alpha$ to the image of the curve in the deformed surface is given by $\nu_\alpha = \sqrt{(a/A)}n_\alpha/\lambda$, where λ is the stretch of the curve (Naghdi, 1972). Then (10) is equivalent to

$$N^{\alpha\beta}\nu_\alpha\nu_\beta\geq 0, \tag{11}$$

where $N^{\alpha\beta} = 2\sqrt{(A/a)}\ \partial w/\partial a_{\alpha\beta}$ are the Cauchy stresses. Thus an equilibrium configuration of a membrane subjected to conservative loading is stable or neutrally stable only if the principal Cauchy tensions are pointwise nonnegative. The choice $f \equiv \mathbf{f}\cdot\mathbf{a}_3 = 0$ in (8) gives the two-dimensional analogue of the classical Legendre-Hadamard condition:

$$4n_\alpha n_\beta f_\gamma f_\epsilon(\partial^2 w/\partial a_{\alpha\gamma}\partial a_{\beta\epsilon})+\sqrt{(a/A)}N^{\alpha\beta}n_\alpha n_\beta f^\gamma f_\gamma\geq 0,\ \forall f^\alpha n_\beta. \tag{12}$$

Pipkin (1985) has derived conditions equivalent to (11) and (12) for the special case of an initially plane isotropic membrane with fixed edges and $\psi = 0$, and has shown that the classical Baker-Ericksen inequality (Baker and Ericksen, 1954) is implied by (12).

Acknowledgment

The support of the Materials Research Lab in the Division of Engineering at Brown University is gratefully acknowledged.

References

Baker, M., and Ericksen, J. L., 1954, "Inequalities Restricting the Form of the Stress-Deformation Relations for Isotropic Solids and Reiner-Rivlin Fluids," *Journal of the Washington Academy of Sciences*, Vol. 44, pp. 33–35.

Graves, L. M., 1939, "The Weierstrass Condition for Multiple Integral Variation Problems," *Duke Mathematical Journal*, Vol. 5, p. 656.

Kydoniefs, A. D., and Spencer, A. J. M., 1969, "Finite Axisymmetric Deformations of an Initially Cylindrical Elastic Membrane," *Quarterly Journal of Mechanics and Applied Mathematics*, Vol. 22, pp. 87–95.

Naghdi, P. M., 1972, "The Theory of Plates and Shells," *Handbuch der Physik*, Vol. VIa/2, Flügge, S., ed., Springer-Verlag.

Pipkin, A. C., 1985, "The Relaxed Energy Density for Isotropic Elastic Membranes," Division of Appl. Math., Brown University.

Truesdell, C., and Noll, W., 1965, "The Nonlinear Field Theories of Mechanics," *Handbuch der Physik*, Vol. III/3, Flügge, S., ed., Springer-Verlag.

Pneumatic Chamber Nonlinearities

Ying-Tsai Wang[6,8] **and Rajendra Singh**[7,8]

1 Introduction

This note examines the nature of nonlinearities associated with a closed pneumatic chamber coupled to a linear mechanical system as shown in Fig. 1. This simple model could represent several practical applications dealing with passive vibration isolators, shock absorbers, and cushioning type actuators. The feasibility of finding an approximate analytical solution for such systems using perturbation techniques has not been investigated, with the exception of a paper by Chen (1977), who analyzed a symmetric, double-sided closed pneumatic chamber system coupled to a cam-actuated mechanism. His study considered only the nonlinearity induced by the gas compressibility; the dynmic response was obtained by the Krylov-Bogoliubov method of slowly varying parameters. Even though no numerical or experimental validation was given, his analysis found that the resonant peak shifted toward a lower frequency as the excitation amplitude was increased. However, he did not examine some of the critical issues dealing with singularities, mean value shifting,

---

[2] ϕ may depend on θ^α explicitly, as in the case of nonhomogeneous material, for example.

[3] Graves considered functionals of the form (1) without the boundary integral. In arriving at (3), he employed variations in $\mathbf{x}$ which vanish on the boundary, so the result is unaffected by the presence of the extra term.

[6] Currently with the National Taiwan Institute of Technology, Republic of China.

[7] Associate Professor, Mem. ASME.

[8] Fluid Power Laboratory, Department of Mechanical Engineering, The Ohio State University, Columbus, Ohio 43210.

Manuscript received by the ASME Applied Mechanics Division June 25, 1985; final revision March 4, 1986.

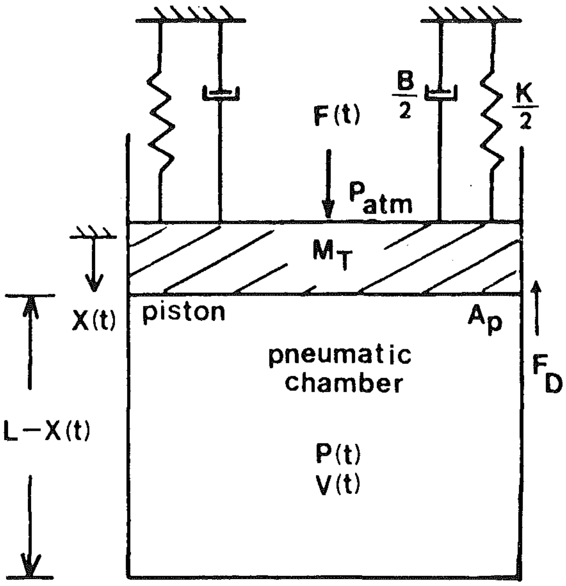

Fig. 1 Schematic of an example case: closed pneumatic chamber

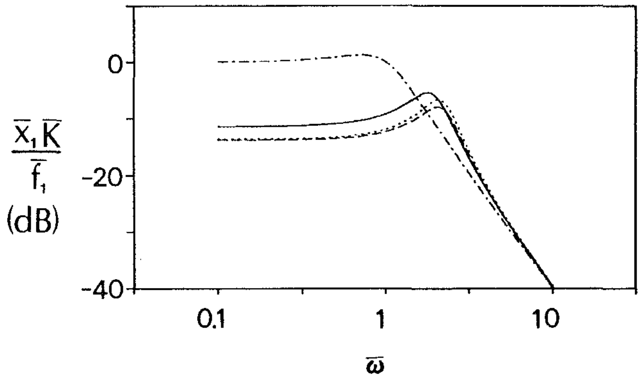

Fig. 2 Magnitude frequency response for various nonlinearities at $\bar{f}_1 = 0.6$: -·-· pure mechanical system ($H = 0$); ——— compressibility; · · · · compressibility and sliding friction effects; ---- all nonlinearities included

role of nonlinear damping (only the viscous damping was considered), and the justification of the selection of his perturbation method. Some of these issues will be discussed here.

2 Mathematical Formulation

For the thermodynamic compression process, we assume a polytropic model

$$P(t)[V(t)]^n = P(0)[V(0)]^n;\ V(0) = A_pL \text{ and } V(t) = A_p(L - X(t)) \qquad (1)$$

where n denotes the polytropic constant, P is the absolute pressure, V is the gas volume, A_p is the chamber or piston area, L is the initial height of the chamber, and X indicates the piston displacement from the initial point. The equation of motion is given as

$$M_T\ddot{X}(t) + B\dot{X}(t) + KX(t) = F(t) + M_Tg + (P_{atm} - P(t))A_p - F_D(t) \qquad (2)$$

where M_T is the total mass, B is the linear mechanical damping coefficient, K is the linear mechanical spring stiffness, $F(t)$ is the external force, P_{atm} is the atmosphere pressure, and $F_D(t)$ is the total damping force which is assumed to be of the following form: $F_D = \mu_{\dot{x}}\dot{X} + \mu_p P^q + \mu_g[\text{sign}(\dot{X})]$, where sign$(\dot{X}) = 1$ for $\dot{X} > 0$, sign$(\dot{X}) = 0$ for $\dot{X} = 0$ and sign$(\dot{X}) = -1$ for $\dot{X} < 0$, and $\mu_{\dot{x}}$ is the viscous friction coefficient (in force/velocity unit), μ_p is the scaled sliding friction coefficient (in force/pressure unit) to account for P_{atm}, q is the friction exponent, and μ_g is the dry (Coulomb) friction coefficient (in force unit). Note that $\mu_{\dot{x}}$, μ_p, q, and μ_g are unique to the physical system chosen.

Table 1 Comparison of results at $\bar{f}_1 = 0.6$ and $\bar{\omega} = 2.09$

Harmonic coefficient	Numerical integration		The method of harmonic balance	
	$\bar{x}_m/\bar{x}_1$	$\bar{p}_k/\bar{p}_1$	$\bar{x}_m/\bar{x}_1$	$\bar{p}_k/\bar{p}_1$
os	−0.261	0.019	−2.60	0.021
1	1	1	1	1
2	0.088	0.356	0.094	0.371
3	0.019	0.135	0	0
4	0.005	0.052	0	0
5	0.002	0.019	0	0
Reference values	$\bar{x}_1 = 0.464$	$\bar{p}_1 = 0.637$	$\bar{x}_1 = 0.468$	$\bar{p}_1 = 0.656$

From the initial point ($t = 0$), we define the excitation $F(t)$ and responses $X(t)$ and $P(t)$ as $F(t) = f_o + f(t)$, $X(t) = x_o + x(t)$, and $P(t) = p_o + p(t)$, where f_o is the time-averaged value of $F(t)$. Now, define response operating points x_o and p_o corresponding to f_o. Using equations (1) and (2), we get

$$K(L - x_o)^{nq+1} + (f_o + P_{atm}A_p + M_Tg - KL)(L - x_o)^{nq} - P(0)A_pL^n(L - x_o)^{nq-n} - \mu_pP(0)^qL^{nq} = 0 \qquad (3)$$

We find that equation (3) has unique solution at any f_o, i.e., $x_o \equiv x_o(f_o)$ and $p_o \equiv p_o(f_o)$, provided $x_o < L$. Note that $L = x_o$ indicates that the piston will compress the gas down to zero volume—an impossible condition to achieve. However, x_o could approach L which is somewhat realistic for the cushioning type actuation and isolation cases.

3 Nature of Nonlinearity

First, define dimensionless parameters and variables as follows.

$$\bar{f} = f/[p_oA_p],\ \bar{p} = p/p_o,\ \bar{x} = x/[L - x_o],\ \bar{\mu}_p = \mu_p p_o{}^q/[p_oA_p],$$
$$\bar{\mu}_g = \mu_g/[p_oA_p],\ \bar{K} = K(L - x_o)/[p_oA_p],$$
$$\omega_n = \sqrt{K/M_T},\ \bar{\omega} = \omega/\omega_n,\ \xi = [B + \mu_{\dot{x}}]/[2\sqrt{KM_T}]$$

where ω is the excitation frequency and ω_n is the undamped natural frequency of the mechanical system. The governing equations, equations (1) and (2), are reduced to the following dimensionless form:

$$\bar{p}(t) = (1 - \bar{x}(t))^{-n} - 1 \qquad (4)$$

$$\ddot{\bar{x}}(t) + 2\xi\omega_n\dot{\bar{x}}(t) + \omega_n^2\bar{x}(t) = \frac{\omega_n^2}{\bar{K}}\bar{f}(t) - H(\bar{x}(t), \dot{\bar{x}}(t)), \qquad (5)$$

where $H(\bar{x},\dot{\bar{x}}) = \dfrac{\omega_n^2}{\bar{K}}\{\bar{p} + \bar{\mu}_p[(1 + \bar{p})^q - 1] + \bar{\mu}_g[\text{sign}(\dot{\bar{x}})]\}$

$$= \frac{\omega_n^2}{\bar{K}}\{[(1 - \bar{x})^{-n} - 1] + \bar{\mu}_p[(1 - \bar{x})^{-nq} - 1] + \bar{\mu}_g[\text{sign}(\dot{\bar{x}})]\}$$

Note that the system is completely described by equation (5) in terms of $\bar{x}$ which is related to $\bar{p}$ through equation (4). The nonlinear function $H(\bar{x},\dot{\bar{x}})$ consists of the following terms: (*i*) nonlinearity induced by the gas compressibility; (*ii*) nonlinearity induced by the sliding friction model; and (*iii*) nonlinearity induced by the dry (Coulomb) friction. For both compressibility and sliding friction effects, we note that $H \to \infty$ as $\bar{x} \to 1.0$, $H = 0$ at $\bar{x} = 0$ and H is unsymmetrical about $\bar{x} = 0$. The unbounded behavior of H close to $\bar{x} \to 1.0$ indicates that the nonlinearities are very large. The nature of such a singularity can be termed as "hard"—as defined by Bota and Mickens (1984). The unsymmetrical behavior about $\bar{x}=0$ is somewhat similar to Mahaffey's problem (1976) on plasma oscillations—he called such oscillations "anharmonic".

For weakly nonlinear systems, many perturbation methods (Mickens, 1981; Nayfeh and Mook, 1979; and Siljak, 1969) may work. But for those cases where nonlinear effects are large, it is not clear which method will work. However, Mickens (1984) claims that the method of harmonic balance can be applied to such problems. Also, Bota and Mickens (1984) claim that only the method of harmonic balance will work for "hard" singularity type, one-dimensional oscillatory problems. Since our example case fits into such a description, the method of harmonic balance seems to be the most logical technique that can be applied.

4 Results

Now, we apply the method of harmonic balance to evaluate the frequency response. Since the nonlinear function H is not symmetric about $\bar{x}=0$, the mean value shift must be considered even though the excitation $\bar{f}(t)$ may have a zero mean value. The excitation $\bar{f}(t)$ and responses $\bar{x}(t)$ and $\bar{p}(t)$ are assumed to be given as follows:

$$\bar{f}(t)=\bar{f}_1\cos(\omega t),$$

$$\bar{x}(t)\simeq\bar{x}_{os}+\bar{x}_1\cos(\omega t+\theta_{x1})+\bar{x}_2\cos(2\omega t+\theta_{x2}) \text{ and}$$

$$\bar{p}(t)\simeq\bar{p}_{os}+\bar{p}_1\cos(\omega t+\theta_{p1})+\bar{p}_2\cos(2\omega t+\theta_{p2})$$

where $\bar{x}_{os}/\bar{x}_1=\bar{x}_2/\bar{x}_1=\bar{x}_1=0(\epsilon)$, $\bar{p}_{os}/\bar{p}_1=\bar{p}_2/\bar{p}_1=\bar{p}_1=0(\epsilon)$ and the subscript *os* denotes the mean value shift or zeroth harmonic. Since lower frequencies are of interest in practical pneumatic systems, the series solution is limited here up to the second harmonic. Numerical parameters used to illustrate this example case are: $\bar{K}=0.511$, $\bar{\mu}_p=0.2$, $q=2$, $\xi=0.5$, $\bar{\mu}_g=0.07$, and $\omega_n=0.5$ (see Wang, 1986, for more details).

Figure 2 shows frequency response curves, the magnitude of the first harmonic versus the dimensionless frequency $\bar{\omega}=\omega/\omega_n$, for various values of $H(\bar{x},\dot{\bar{x}})$. Note that the overall system with all nonlinearities included is still a second order system, but the resonant frequency is shifted to $\bar{\omega}=2.09$ as shown in Fig. 2. It is apparent that the compressibility term is the most dominant, followed by the sliding friction term which is also related to the pressure (per our assumption). Both of these nonlinear effects increase stiffness as well as damping. Conversely, the dry friction is influential only at the resonance, thereby adding only to the damping, as one would expect. We must caution that in a practical system the real damping mechanism could dictate the response.

In order to validate the results obtained by the method of harmonic balance, we compare these with the results yielded by the numerical integration of equations (4) and (5). In Table 1, the zeroth and first five harmonics are examined for both $\bar{x}$ and $\bar{p}$ at the resonant frequency ($\bar{\omega}=2.09$); an order analysis has been performed using the first harmonic results as reference values. We find that some of the harmonic coefficients as predicted by the numerical integration are higher than those assumed for the method of harmonic balance. Hence, there is some ambiguity regarding our order approximation! Nonetheless, we still obtain very accurate results with considerably less computer time.

Acknowledgment

We gratefully acknowledge the support of OSU Fluid Power Laboratory Industrial Consortium.

References

Bota, K. B., and Mickens, R. E., 1984, "Approximate Analytic Solutions for Singular Nonlinear Oscillators," *Journal of Sound and Vibration*, Vol. 96, No. 2, pp. 277-279.

Chen, F. Y., 1977, "Dynamic Response of a Cam-Actuated Mechanism with Pneumatic Coupling," *ASME Journal of Engineering for Industry*, Vol. 99, No. 3, pp. 598-603.

Mahaffey, R. A., 1976, "Anharmonic Oscillator Description of Plasma Oscillations," *Physics of Fluids*, Vol. 19, No. 9, pp. 1387-1391.

Mickens, R. E., 1981, *Nonlinear Oscillations*, Cambridge Press, Cambridge.

Mickens, R. E., 1984, "Comments on the Method of Harmonic Balance," *Journal of Sound and Vibration*, Vol. 94, No. 3, pp. 456-460.

Nayfeh, A. H., and Mook, D. T., 1979, *Nonlinear Oscillations*, Wiley, New York.

Siljak, D. D., 1969, *Nonlinear Systems, The Parameter Analysis and Design*, Wiley, New York.

Wang, Y. T., 1986, "Frequency Response of Nonlinear Pneumatic Systems," Ph.D. Dissertation, The Ohio State University, Columbus, Ohio.

Journal of Applied Mechanics
Discussion

Stability of a Clamped-Free Rotor Partially Filled With Liquid[1]

F. G. Kollmann.[2] A problem very similar to that treated in this paper has been solved by the discusser's former assistant G. Lichtenberg [1]. The author states that the inviscid analysis presented in the main body of his paper is unable to predict the stability of the rotating system since the rotor is unstable at any speed. Clearly this instability is due to the external damper. However, external damping seems to be a secondary effect in this analysis which deals mainly with the three-dimensional motion of the trapped fluid.

Lichtenberg analyzed the motion of an overhung rotor partially filled with an inviscid fluid. External damping of this rotor was not considered. He derived analytical expressions for the characteristic equation of the rotor motion. For the three-dimensional motion of the trapped fluid this solution contains Bessel functions of the first and second kind. The Bessel functions lead to dense sequences of singularities in a certain region of the $\Omega - \tau -$plane (Ω = nondimensional angular speed, τ = eigenvalue). Therefore, it would be interesting if the author could comment in some more detail on his remark, that "the common Bessel functions are not numerically independent in the range of interest."

Due to the mathematical difficulties mentioned, Lichtenberg confined his numerical analysis to the planar motion of the enclosed fluid. His computed stability diagram for one rotor showed very good correspondence with experimental results. For the rotor investigated by Lichtenberg, the "planar" theory predicts all measured effects with sufficient accuracy. For completeness it is mentioned that the discusser's former assistant R. Wohlbrück [2] solved a more general problem. He considered again an overhung rotor. However, the cavity of this rotor was not formed by a cylinder—as in Lichtenberg's analysis—but by an arbitrary surface of revolution. Again external rotor damping was not included and the fluid was considered as inviscid. Due to the more complex shape of the interior surface of the rotor, no analytical solution could be derived. Therefore, Wohlbrück used the Finite Element Method. His numerically computed stability diagrams for two different rotors (ellipsoidal and doubly conical interior surface) again showed very good correspondence with experimental results.

References

[1] Lichtenberg, G., 1982, "Vibrations of an Ellastically Mounted Spinning Rotor Partially Filled With Liquid," *ASME Journ. Mech. Des.*, Vol. 104, No. 2, pp. 345–355.

[2] Wohlbrück, R., 1985, "Stabilty of a Rotor Whose Cavity has an Arbitrary Meridian and is Partially Filled With Fluid," *ASME Journ. of Vibration, Acoustics, Stress, and Reliability in Design*, Vol. 107, pp. 440–445.

Author's Closure

The author appreciates Professor Kollman's interest in the paper and the additional references. The paper by Lichtenberg should have been included in the references. The fact that it was not cited is an oversight for which I apologize. The paper by Wohlbruck appeared after the present paper was submitted for publication.

While damping was not highlighted in this paper, the calculations did include the effect of the external damper. The damping made it necessary to use Bessel Functions with complex argument. In order to solve the equations numerically it was necessary to use Hankel functions (which are simply linear combinations of the Bessel Functions J_n and Y_n). This was necessary because the more common Bessel Functions were not numerically independent in the range of interest. This is analogous to the situation which occurs in the solution of $\ddot{x} - x = 0$. The solution may be written in terms of $\cosh(x)$ and $\sinh(x)$, however these are not numerically different for large values of x. This lack of independence of the fundamental solutions leads to numerical singularities in the solution process. For large x it is necessary to write the solution in terms of e^x and e^{-x} (which are just linear combinations of $\cosh(x)$ and $\sinh(x)$) in order to have two independent fundamental solutions to the differential equation.

Hydrodynamic Lubrication in Hemispherical Punch Stretch Forming[3]

W. R. D. Wilson[4] **and L. Hector**[5]**.** The authors are to be congratulated for an interesting paper which couples, for the first time, a sophisticated finite-element plasticity model with a hydrodynamic lubrication model. This approach will eventually provide computer models of forming processes which will accurately reflect the complex interactions between metal deformation, lubrication and friction.

However, we believe that there is a serious flaw in the

---

[1] By S. L. Hendricks and published in the March 1986 issue of the ASME Journal of Applied Mechanics, Vol. 53, pp. 166–172.

[2] Professor, Technische Hochschule Darmstadt, Fachgebiet Maschinenelemente und Getriebe, Magdalenenstr. 8-10, Germany.

[3] By Kuo-Kuang Chen and D. C. Sun, and published in the June 1986 issue of the ASME Journal of Applied Mechanics, Vol. 53, pp. 440–449.

[4] Professor and Director of the Center for Manufacturing Engineering, Northwestern University, Evanston, IL 60201.

[5] Graduate Research Student, Northwestern University, Evanston, IL 60201.

Journal of Applied Mechanics

Book Reviews

Finite Element Methods in Structural Mechanics, by C. T. F. Ross. Ellis Horwood Limited, West Sussex, England, 1985. 319 pages. Price: $33.95/paperback; $61.95/hardcover.

REVIEWED BY W. K. LIU[1]

This book is indeed an introductory text for undergraduate students and practicing engineers. The emphasis is on the simplicity of procedures, and mathematical details are kept to the minimum. Several examples are worked out and the adequacy of current micro-computers for most applications is emphasized. Static analysis and vibrations are the two main topics covered. Matrix displacement methods and the energy methods are used to derive the element stiffness and mass matrices. Vibration analysis is performed by modal analysis techniques (nothing is mentioned on direct time integration). Structural elements such as bars, torque bars, beams, frames, grillages, plates and quadrilateral continuum elements are described. The book concludes with a brief chapter on nonlinear structural mechanics.

A separate chapter is devoted to grillages, which seems quite unnecessary as a grillage is merely a combination of a beam and a torque bar. The reviewer feels that this material can be distributed in Chapters 4 and 7.

The sections on plate/shell finite elements are out of date. In present day finite element plate/shell analysis, C^0 elements are rapidly supplanting C^1 elements because of their superior performance and versatility.

A few words of caution should be included regarding the limitations of some finite elements; for example, locking phenomena in an incompressible continuum, shear and membrane locking in plate/shell elements, and numerical instability arising from spurious modes. More up-to-date references should also be included.

The author defines material nonlinearity, in Chapter 9, as "the material undergoing plastic deformation." Certainly, this is just an example of material nonlinearities and there are other nonlinearities such as the more elementary nonlinear elasticity.

The author mentions in the preface that "the book would fill the gap between the numerous texts on traditional Strength of Material and the postgraduate books that have been recently written on Finite Element Methods." This is a questionable statement as there are numerous introductory texts such as "Introduction to Matrix Structural Analysis," by H. C. Martin, "Theory of Matrix Structural Analysis," by J. S. Przemieniecki, "Applied Finite Element Analysis," by L. J. Segerlind, "Finite Element Methods for Engineers," by R. T. Fenner and "Concepts and Applications of Finite Element Analysis," by R. D. Cook, to name a few. In total, this book is suitable as a matrix approach to finite element primer.

Computerized Buckling Analysis of Shells, by D. Bushnell. Martinus Nijhoff Publishers, The Netherlands, 1985. 423 pages. Price: $85.

REVIEWED BY J. ARBOCZ[2]

The publication of Dave Bushnell's book could not have happened at a better moment. It is the reviewers opinion that with the large scale introduction of computerized structural analysis in the practice and lately also at many technical schools, the teaching of and the approach to solving technical problems has been shifting in the wrong direction.

Twenty-five years ago it was so, that numerical results were looked upon with a certain amount of distrust and they were only accepted if supported by experimental results or some other facts. Today, as the older generation of engineers (the ones who obtained their degrees before the advent of computers) retire and the younger ones with extensive training in the ever-so-popular finite element technique take over, one begins to encounter in technical discussions a new mentality; the insight of how structures behave under loading of the older generation is being replaced more and more by the nearly religious faith of the younger ones in the predictions of their favorite computer codes. This is especially true when making buckling predictions for complex structures.

Bushnell's book represents a very important contribution to the discussion of how one should introduce computers when one is teaching or performing structural analysis of buckling sensitive thin-walled shells. On hand from many practical examples Bushnell shows that a shell design specialist, who is aware of the latest theoretical developments and who is familiar with the theories upon which the nonlinear structural analysis codes he uses are based, can achieve very accurate modeling of the collapse behavior of complex structures. On the other hand, he also demonstrates the danger that can arise by the use of sophisticated computational tools by persons of inadequate theoretical background. It is to be hoped that the failures because of unexpected buckling of the large, expensive shell structures described in the text will convince all people that contrary to the beliefs of some, computer codes are no replacements for engineering know-how and engineering expertise.

---

[1] Associate Professor, Department of Mechanical and Nuclear Engineering, Northwestern University, Evanston, Ill. 60201. Mem. ASME.

[2] Professor of Aircraft Structures, Delft University of Technology, Department of Aerospace Engineering, The Netherlands.

The book is divided into nine chapters. In Chapter One the author initially presents examples of catastrophic failure of several large, expensive structures followed by a discussion of what is buckling. The difference between the various types of bifurcation buckling and nonlinear collapse is particularly well documented. The chapter concludes with a richly illustrated discussion of "classical" buckling of cylindrical and spherical shells, whereby experimental results are used for comparison with theoretical predictions.

Chapter Two deals with nonlinear collapse and its relationship to bifurcation buckling models. The following examples are treated: the elastic-plastic axisymmetric creep collapse of axially compressed monocoque cylinders and the creep collapse of ring-stiffened cylinders under external hydrostatic pressure; the general collapse of curved and straight pipes under uniform bending and external pressure; the collapse of cylindrical panels and shells with concentrated loads and cutouts and the collapse of axially compressed noncircular cylinders. The chapter closes with the axisymmetric collapse of a complex rocket interstage, where the local load-path eccentricity of the axial compression gives rise to concentrated bending and local plastic flow.

In Chapter Three the author discusses bifurcation buckling cases where nonuniformity or nonlinearity of the prebuckling state is important. Initially nonsymmetric bifurcation buckling in the neighborhood of an edge is illustrated on a cylindrical shell under axial compression and on externally pressurized spherical caps with end rings. Next buckling due to localized hoop compression caused by prebuckling shape changes is discussed. Three examples are treated: an "infinite" cylinder heated uniformly over half its length, a clamped cylinder with an axial thermal gradient near the edge and the buckling of an internally pressurized rocket fuel tank. In the following examples of nonsymmetric bifurcation buckling of shells of revolution in which meridional tension is combined with circumferential compression are presented. Besides the buckling of complete spheres and of truncated spherical shell segments subjected to axial tension, particular emphasis is given to the elastic-plastic bifurcation buckling of internally pressurized torispherical shells. The chapter closes with the presentation of a detailed simulation study of the failure of a large steel water tower, whereby a complex elastic-plastic model is used which includes the effects of certain fabrication processes such as cold bending and welding.

Chapter Four deals with the effect of boundary conditions and eccentric loading and is devoted mostly to cylindrical shells. Inextensional buckling results are presented for an axially compressed 5 deg cone and for a spherical shell under external pressure both supported at the edges by rings of square cross section. The simulation of local plastic flow by appropriate constraint condition is illustrated for a cone-cylinder specimen under external pressure.

Chapter Five describes the buckling of shells of revolution subjected to combined uniform loadings and to nonsymmetric loads. Interaction curves are presented for isotropic and for anisotropic shells under combined axial compression and internal or external pressure and under combined torsion and external pressure. Modeling consideration for shells of revolution under nonsymmetric static or dynamic loading are discussed. Especially interesting are the examples in which buckling under nonsymmetric loading is estimated by a one-dimensional numerical analysis. Also included are thermal buckling problems of nonsymmetrically heated shells. The chapter closes with buckling estimates for a nuclear containment vessel due to ground motion during an earthquake.

Chapter Six deals with the buckling of ring-stiffened shells. Initially the effect of boundary conditions on the elastic buckling of ring-stiffened cylinders under external hydrostatic pressure is treated. This is followed by elastic-plastic buckling results. Comparisons between theory and tests are included. Next the effects of residual stresses and deformations on plastic buckling of ring-stiffened shells of revolution are discussed. Modeling tips for using BOSOR 5 to calculate the buckling loads including residual effects due to cold bending and welding are presented. The chapter closes with a section dealing with the effect on buckling of deformations of the ring cross sections. General and local instability and modal interaction are discussed and comparisons with tests in which local ring deformations are important are presented.

In Chapter Seven Dave Bushnell presents a method to use a computer code for shells of revolution to predict buckling loads of prismatic shells and panels. The author has pioneered this method and demonstrates its validity by analyzing a circular cylinder under external pressure as a portion of a torus. Next the method is applied to obtain predictions of bifurcation buckling loads of noncircular cylindrical shells under axial compression or external pressure and failure loads of corrugated and beaded panels under axial compression. The chapter closes with a long section on the modal interaction and imperfection sensitivity of axially compressed prismatic structures.

Chapter Eight contains a very concise and readable presentation of the imperfection sensitivity theory by Koiter and the Harvard school under Budiansky and Hutchinson. The author presents the most important results of twenty-five years of intensive research by many investigators in a single chapter that excels in clarity and readability.

In Chapter Nine the buckling of hybrid bodies of revolution is discussed, that is of shells that contain combinations of one and two-dimensionally discretized domains, another method where the author has made pioneering contributions. The following examples are treated: buckling of ring-stiffened cylindrical shells under uniform hydrostatic pressure in which each ring and small regions on either side are modeled with 8-mode quadrilaterals of revolution, spherical shells embedded in structural foam and the elastic-plastic instability of an axially compressed shell of revolution with axisymmetric frangible joints.

Most of the numerical results in this excellent book have been obtained with one of the well known computer codes of the BOSOR or STAGS family. What makes this book unique is that the author has succeeded in providing a "feel" for shell buckling based on a careful mixture of theoretical, analytical, and numerical procedures. Many of the richly illustrated examples are written in a tutorial form, a guide-by-example for the modeling and solving of complex nonlinear problems. It shows convincingly that the modern structural engineer must have a very thorough understanding of how structures behave if he is to use the advanced computational tools successfully. This book is a must for all those who work in the field of shell stability.

Linear Variations, by P. C. Müller and W. O. Schiehlen. Martinus Nijhoff Publishers, The Netherlands, 1985. 327 pages. Price: $65.50.

REVIEWED BY R. ABEYARATNE[3]

This book is concerned with the vibrations of discrete, linearized systems with many degrees of freedom. The primary aim of the authors in writing this book was to present the sub-

---

[3] Associate Professor, Department of Mechanical Engineering, Massachusetts Institute of Technology, Cambridge, Mass. 02139. Assoc. Mem. ASME.

ject in a form "allowing the use of computers for finding solutions." The book consists of four parts: Mathematical Description of Vibrating Systems (56 pages), Time-Invariant Vibrating Systems (200 pages), Time-Variant Vibrating Systems (33 pages), and Mathematical Background (30 pages).

Part I begins with an introductory discussion of the various classifications of vibrations. This is followed by a very brief review of kinematics, Lagrange's equations, and the momentum principles. The section closes with a chapter on the linearization of the equations of motion and their state-space representation.

Part II is devoted to the study of autonomous systems. It begins with a chapter on the fundamental matrix of the system and its use in generating the general solution of the equations of motion. A chapter on stability and boundedness follows. Here, stability criteria based on the characteristic equation as well as on Liapunov's matrix equation are discussed. This is followed by chapters on free vibrations, forced vibrations, and resonance. Mode shapes, lightly damped systems, periodic excitation, vibration absorption, and parameter identification are some of the topics explored. The final chapter of this section is devoted to random vibrations.

Part III consists of two chapters: the first is concerned with the solution of the (nonautonomous) equations of motion and its stability, while the second addresses parametrically excited and forced vibrations. The final part of the book presents background material on matrix algebra – one chapter on its analytical aspects and a second on its numerical aspects. It also has a brief chapter on controllability and observability.

I beleive the authors do achieve their aim of presenting the results in a form convenient for computer implementation. The results are presented in such a way that when analyzing a given system, one merely needs to select a set of generalized coordinates and write down the position vectors of the various particles in terms of these coordinates. It is then a matter of "substituting into a sequence of appropriate formulas". In fact, even the simplest of examples (e.g., the double pendulum) is worked out in the book in this mechanistic manner.

This book is concerned with the mathematical results associated with various aspects of linear vibration theory. The physics of the subject is underplayed. My primary criticism of the book is that I found it to be extremely concise; often, the authors simply state results (both elementary and advanced) without explanation, e.g., the section on Floquet Theory in Chapter 10.

On the positive side, this book is a comprehensive source for mathematical results in linear vibration theory of discrete systems. It discusses the subject through both a state-space formulation as well as directly through the equations of motion. This is a useful feature, since it helps link the traditional mechanical engineering approach to vibrations with the more modern literature. A second attractive feature is that in order to illustrate the theory, the authors repeatedly use the same four mechanical systems throughout the text, thereby giving the book additional coherence.

Parametric Random Vibration, by R. A. Ibrahim, Wiley, New York, 1985. 342 pages. Price: $59.95.

REVIEWED BY T. FANG[4] AND E. H. DOWELL[5]

This is the first book devoted to parametric random vibrations. It systematically presents the methods and recent results on the subject. The book is really a summary of the state-of-the-art culled from hundreds of published papers and technical reports. It consists of nine chapters, dealing with the mathematical basis, analytical techniques, and theoretical and experimental results for the behavior of random parametric systems.

The first chapter is an introduction, in which different kinds of motions, i.e., chaotic responses, random responses due to pseudo-random excitations or random initial conditions, and parametric random vibrations, are briefly reviewed.

The next four chapters introduce the related mathematics of stochastic analysis. Fundamental concepts of random processes and elements of stochastic calculus are outlined in Chapters 2 and 3, respectively. Chapters 4 and 5 contain the essential tools for modeling and analyzing random parametric systems, i.e., the Itô and Stratonovich stochastic calculus, the Wong-Zakai and Khas'miniskii Limit theorems, the Fokker-Planck-Kolmogorov equation and its applications, and the moment equation method. The latter two chapters are particularly well written with an emphasis on clarifying the controversies and disputes which occurred in the 1960's.

The last four chapters discuss parametric random vibrations per se. Chapter 6 describes various stochastic averaging methods, together with their applications to the study of stochastic behavior of linear or nonlinear systems. The recently developed method of stochastic averaging of the energy envelope appears to be very useful for "quasi-conservative" nonlinear systems. Chapter 7 is devoted to parametric stochastic stability. Various types of stochastic stability are summarized. Two of them, i.e., the stability of moments and almost sure stability, are discussed in some detail. Stability boundaries obtained by different theorems for typical problems are compared. Parametric random responses are considered in Chapter 8. A number of techniques are presented here to determine the random responses of linear and nonlinear dynamic systems, including helicopter rotor blades in atmospheric turbulent flow, liquid sloshing under parametric random excitations, and coupled beams with autoparametric resonance. Special attention is given to the moment equation method. Both Gaussian and non-Gaussian closure techniques are used and the corresponding results are compared with each other and also compared with those obtained by stochastic averaging methods. It appears that non-Gaussian closure schemes are more reasonable for nonlinear systems. The last chapter compiles the experimental results reported in the literature.

Historical reviews of the techniques, theories, and their applications are distributed in related chapters. An extensive list of references is appended. Among the total of 545 references, 408 of them are cited explicitly.

The book is of a graduate level, well written, and useful to engineering researchers and scientists working in those fields involving parametric random vibrations.

Numerical Simulation of Fluid Flow and Heat/Mass Transfer Processes (Lecture Notes in Engineering), edited by N. C. Markatos, D. G. Tatchell, M. Cross, and N. Rhodes. Springer-Verlag, New York, 1986. 482 pages. Price: $36.00.

REVIEWED BY P. D. RICHARDSON[6]

The first decision one faces in implementing numerical studies in applied mechanics is whether to generate one's own

---

[4] Visiting Professor on leave from Northwestern Polytechnical University, Xian, China.

[5] J. A. Jones Professor, Dean, School of Engineering, Duke University, Durham, North Carolina 27706.

[6] Professor of Engineering and Physiology, Brown University, Providence, RI 02912. Fellow ASME.

ject in a form "allowing the use of computers for finding solutions." The book consists of four parts: Mathematical Description of Vibrating Systems (56 pages), Time-Invariant Vibrating Systems (200 pages), Time-Variant Vibrating Systems (33 pages), and Mathematical Background (30 pages).

Part I begins with an introductory discussion of the various classifications of vibrations. This is followed by a very brief review of kinematics, Lagrange's equations, and the momentum principles. The section closes with a chapter on the linearization of the equations of motion and their state-space representation.

Part II is devoted to the study of autonomous systems. It begins with a chapter on the fundamental matrix of the system and its use in generating the general solution of the equations of motion. A chapter on stability and boundedness follows. Here, stability criteria based on the characteristic equation as well as on Liapunov's matrix equation are discussed. This is followed by chapters on free vibrations, forced vibrations, and resonance. Mode shapes, lightly damped systems, periodic excitation, vibration absorption, and parameter identification are some of the topics explored. The final chapter of this section is devoted to random vibrations.

Part III consists of two chapters: the first is concerned with the solution of the (nonautonomous) equations of motion and its stability, while the second addresses parametrically excited and forced vibrations. The final part of the book presents background material on matrix algebra – one chapter on its analytical aspects and a second on its numerical aspects. It also has a brief chapter on controllability and observability.

I beleive the authors do achieve their aim of presenting the results in a form convenient for computer implementation. The results are presented in such a way that when analyzing a given system, one merely needs to select a set of generalized coordinates and write down the position vectors of the various particles in terms of these coordinates. It is then a matter of "substituting into a sequence of appropriate formulas". In fact, even the simplest of examples (e.g., the double pendulum) is worked out in the book in this mechanistic manner.

This book is concerned with the mathematical results associated with various aspects of linear vibration theory. The physics of the subject is underplayed. My primary criticism of the book is that I found it to be extremely concise; often, the authors simply state results (both elementary and advanced) without explanation, e.g., the section on Floquet Theory in Chapter 10.

On the positive side, this book is a comprehensive source for mathematical results in linear vibration theory of discrete systems. It discusses the subject through both a state-space formulation as well as directly through the equations of motion. This is a useful feature, since it helps link the traditional mechanical engineering approach to vibrations with the more modern literature. A second attractive feature is that in order to illustrate the theory, the authors repeatedly use the same four mechanical systems throughout the text, thereby giving the book additional coherence.

Parametric Random Vibration, by R. A. Ibrahim, Wiley, New York, 1985. 342 pages. Price: $59.95.

REVIEWED BY T. FANG[4] AND E. H. DOWELL[5]

This is the first book devoted to parametric random vibrations. It systematically presents the methods and recent results on the subject. The book is really a summary of the state-of-the-art culled from hundreds of published papers and technical reports. It consists of nine chapters, dealing with the mathematical basis, analytical techniques, and theoretical and experimental results for the behavior of random parametric systems.

The first chapter is an introduction, in which different kinds of motions, i.e., chaotic responses, random responses due to pseudo-random excitations or random initial conditions, and parametric random vibrations, are briefly reviewed.

The next four chapters introduce the related mathematics of stochastic analysis. Fundamental concepts of random processes and elements of stochastic calculus are outlined in Chapters 2 and 3, respectively. Chapters 4 and 5 contain the essential tools for modeling and analyzing random parametric systems, i.e., the Itô and Stratonovich stochastic calculus, the Wong-Zakai and Khas'miniskii Limit theorems, the Fokker-Planck-Kolmogorov equation and its applications, and the moment equation method. The latter two chapters are particularly well written with an emphasis on clarifying the controversies and disputes which occurred in the 1960's.

The last four chapters discuss parametric random vibrations per se. Chapter 6 describes various stochastic averaging methods, together with their applications to the study of stochastic behavior of linear or nonlinear systems. The recently developed method of stochastic averaging of the energy envelope appears to be very useful for "quasi-conservative" nonlinear systems. Chapter 7 is devoted to parametric stochastic stability. Various types of stochastic stability are summarized. Two of them, i.e., the stability of moments and almost sure stability, are discussed in some detail. Stability boundaries obtained by different theorems for typical problems are compared. Parametric random responses are considered in Chapter 8. A number of techniques are presented here to determine the random responses of linear and nonlinear dynamic systems, including helicopter rotor blades in atmospheric turbulent flow, liquid sloshing under parametric random excitations, and coupled beams with autoparametric resonance. Special attention is given to the moment equation method. Both Gaussian and non-Gaussian closure techniques are used and the corresponding results are compared with each other and also compared with those obtained by stochastic averaging methods. It appears that non-Gaussian closure schemes are more reasonable for nonlinear systems. The last chapter compiles the experimental results reported in the literature.

Historical reviews of the techniques, theories, and their applications are distributed in related chapters. An extensive list of references is appended. Among the total of 545 references, 408 of them are cited explicitly.

The book is of a graduate level, well written, and useful to engineering researchers and scientists working in those fields involving parametric random vibrations.

Numerical Simulation of Fluid Flow and Heat/Mass Transfer Processes (Lecture Notes in Engineering), edited by N. C. Markatos, D. G. Tatchell, M. Cross, and N. Rhodes. Springer-Verlag, New York, 1986. 482 pages. Price: $36.00.

REVIEWED BY P. D. RICHARDSON[6]

The first decision one faces in implementing numerical studies in applied mechanics is whether to generate one's own

---

[4] Visiting Professor on leave from Northwestern Polytechnical University, Xian, China.

[5] J. A. Jones Professor, Dean, School of Engineering, Duke University, Durham, North Carolina 27706.

[6] Professor of Engineering and Physiology, Brown University, Providence, RI 02912. Fellow ASME.